



BİNGÖL  
ÜNİVERSİTESİ

e-ISSN 2149-6366

Cilt 13, Sayı 3, Eylül 2024

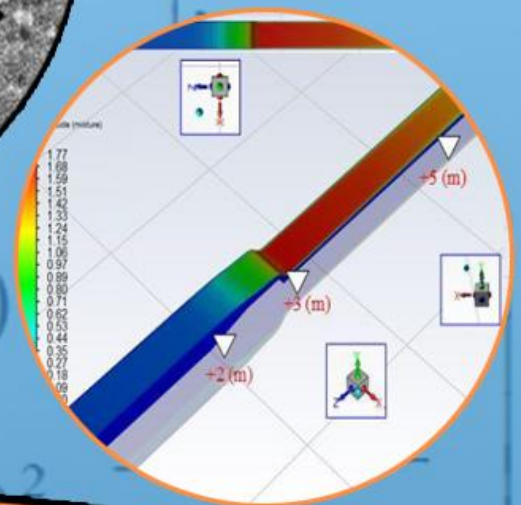
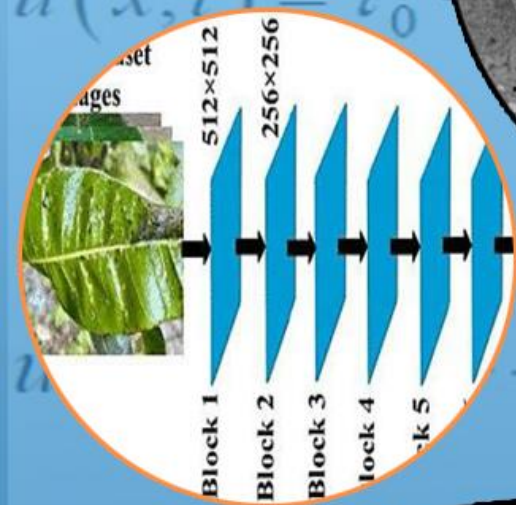
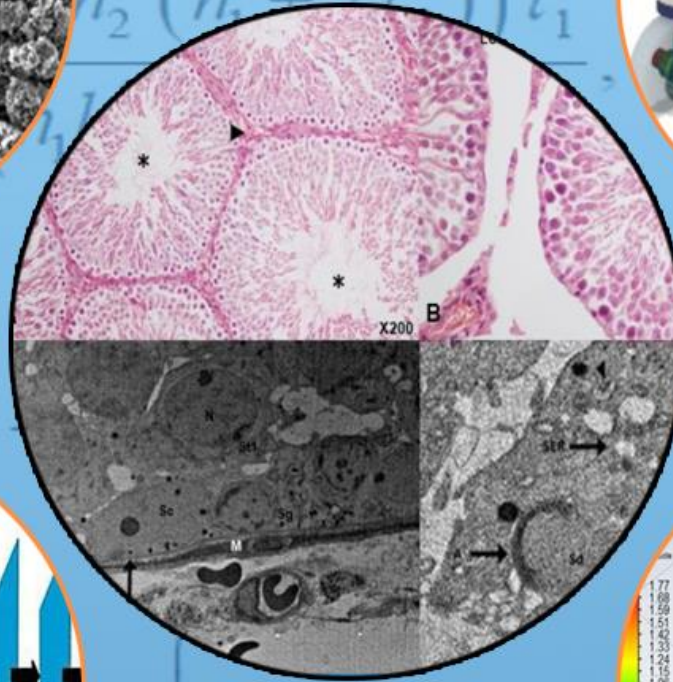
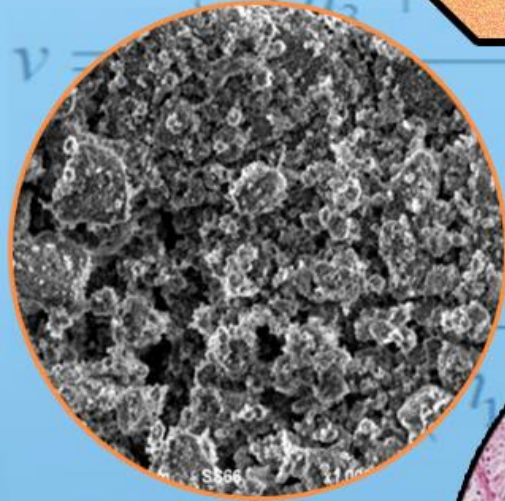
Volume 13, Issue 3, September 2024

**TDFD**

**TÜRK DOĞA ve FEN DERGİSİ**

TURKISH JOURNAL OF NATURE AND SCIENCE

**TJNS**



[www.dergipark.gov.tr/tdfd](http://www.dergipark.gov.tr/tdfd)

Bingöl Üniversitesi Fen Bilimleri Enstitüsü tarafından  
yayımlanmaktadır.

Published by Bingöl University Institute of Science

ULAKBİM

**TRDİZİN**

# TÜRK DOĞA VE FEN DERGİSİ

## Amaç

Türk Doğa ve Fen Dergisi, Dergipark tarafından yayınlanan Bingöl Üniversitesi Fen Bilimleri Enstitüsüne ait ulusal ve hakemli bir dergidir. Türk Doğa ve Fen Dergisi, Türkiye ve dünyanın her yerinden gelen doğa ve fen bilimlerinin her alanında özgün, yayımlanmamış, yayımlanmak üzere başka yere gönderilmemiş makale, derleme ve sempozyum değerlendirmesi gibi çalışmaların bilim alemine sunulması amacıyla kurulmuştur.

## Kapsam

Türk Doğa ve Fen Dergisinde Mühendislik, Ziraat, Veterinerlik, Fen ve Doğa Bilimleri alanlarından olmak üzere Türkçe ve İngilizce hazırlanmış orijinal makale, derleme ve sempozyum değerlendirmesi gibi çalışmalar yayımlanır. Türk Doğa ve Fen Dergisi sadece online sistemde yayımlanmakta olup ayrıca kağıt baskısı bulunmamaktadır.

## Merhaba...

Türk Doğa ve Fen Dergisi, Dergipark tarafından yayımlanmakta olup Bingöl Üniversitesi Fen Bilimleri Enstitüsüne aittir. Bahar ve güz dönemi olmak üzere yılda iki defa çıkarılan ulusal hakemli bir dergi olarak ilk sayısını 2012 bahar döneminde yayımlamıştır. Türk Doğa ve Fen Dergisi, Türkiye ve dünyanın her yerinden gelen doğa ve fen bilimlerinin her alanında özgün, yayımlanmamış, yayımlanmak üzere başka yere gönderilmemiş makale, derleme ve sempozyum değerlendirmesi gibi çalışmaların bilim alemine sunulması amacıyla kurulmuştur. İlk sayısından bugüne kesintisiz olarak faaliyetlerini sürdürmektedir.

Türk Doğa ve Fen Dergisi sadece online sistemde yayımlanmakta olup ayrıca kağıt baskısı bulunmamaktadır. Dergimize gelen her çalışma öncelikle Turnitin intihal programında taranmaktadır. Dergimizde editörlerin, hakemlerin ve yazarların, uluslararası yayım etik kurallarına uyması ve makalelerin yazım kurallarına uyumlu olması zorunluluğu vardır.

Yazarlar yayımlanmak üzere dergimize gönderdikleri çalışmalarını ile ilgili telif haklarını zorunlu olarak Bingöl Üniversitesi Türk Doğa ve Fen Dergisi'ne devretmiş sayılırlar. Yazarlardan herhangi bir ücret talep edilmemektedir. Yazarların değerlendirmeleri, dergimizin resmi görüşü olarak kabul edilemez. Çalışmaların her türlü sorumluluğu yazarlarına aittir. Araştırma ürünleri için etik kurul raporu gerekli ise, çalışma üzerinde bu raporun alınmış olduğu belirtilmeli ve kurul raporu sisteme kaydedilmelidir. Araştırma ile ilgili intihal, atıf manipülasyonu, sahte veri uydurma vb. suistimallerin tespit edilmesi halinde yayım ve etik ilkelerine göre davranılır. Bu durumda çalışmanın yayımlanmasını önlemek, yayımdan kaldırmak ya da başka işlemler yapmak için gerekli işlemler takip edilmektedir.

Dergimizde, kaynak gösteriminde uluslararası Vancouver sistemine geçilmiştir. Ayrıca dergimiz, Creative Commons ile lisanslanmak suretiyle dergimizde yayımlanan makalelerin paylaşımı, kaynak gösterimi ve yayımlanmasında dergi ve yazar haklarını korumaya almıştır. 2018 yılı güz döneminden itibaren makaleler, uluslararası yazar kimlik numarası ORCID No'su ile yayımlanmaktadır.

Dergi ekibi, dergimizin ulusal ve uluslararası indekslerce taranan bir dergi olması yönünde çalışmalarını titizlikle sürdürmektedir. Dergimize gösterilen ilgi bu yönde bizleri teşvik etmeye devam edecektir.

Bingöl Üniversitesi Fen Bilimleri Enstitüsü tarafından yayımlanmaktadır

## EDİTÖRLER (YAYIN) KURULU

### BAŞEDİTÖR

**Dr. Öğr. Üyesi Mücahit ÇALIŞAN**

Bingöl Üniversitesi, Mühendislik-Mimarlık Fakültesi, Bilgisayar Mühendisliği

E-Mail: [mcalisan@bingol.edu.tr](mailto:mcalisan@bingol.edu.tr)

### EDİTÖR YARDIMCILARI

**Doç. Dr. Ekrem DARENDELİOĞLU**

Bingöl Üniversitesi, Fen-Edebiyat Fakültesi, Moleküler Biyoloji ve Genetik  
Bölümü

E-Mail: [edarendelioglu@bingol.edu.tr](mailto:edarendelioglu@bingol.edu.tr)

**Doç. Dr. Adnan AYNA**

Bingöl Üniversitesi, Fen-Edebiyat Fakültesi, Kimya Bölümü

E-Mail: [aayna@bingol.edu.tr](mailto:aayna@bingol.edu.tr)

### EDİTÖRLER

#### Fen ve Doğa Bilimleri

**Doç. Dr. İkram ORAK**

Bingöl Üniversitesi, Sağlık Hizmetleri Meslek Yüksekokulu, Tıbbi Hizmetler ve  
Teknikler

E-Mail: [iorak@bingol.edu.tr](mailto:iorak@bingol.edu.tr)

**Prof. Dr. Selami SELVİ**

Balıkesir Üniversitesi, Altınoluk Meslek Yüksekokulu, Bitkisel ve Hayvansal  
Üretim Bölümü

E-Mail: [sselvi2000@yahoo.com](mailto:sselvi2000@yahoo.com)

**Prof. Dr. Refik KESKİN**

Sakarya Üniversitesi, Fen-Edebiyat Fakültesi, Matematik Bölümü

E-Mail: [rkeskin@sakarya.edu.tr](mailto:rkeskin@sakarya.edu.tr)

**Prof. Dr. Halim ÖZDEMİR**

Sakarya Üniversitesi, Fen-Edebiyat Fakültesi, Matematik Bölümü

E-Mail: [hozdemir@sakarya.edu.tr](mailto:hozdemir@sakarya.edu.tr)

**Prof. Dr. Zafer ŞİAR**

Bingöl Üniversitesi, Fen-Edebiyat Fakültesi, Matematik Bölümü  
E-Mail: [zsiar@bingol.edu.tr](mailto:zsiar@bingol.edu.tr)

**Prof. Dr. Uğur ÇAKILCIOĞLU**

Munzur Üniversitesi, Pertek Sakine Genç Meslek Yüksekokulu, Bitki Morfolojisi  
ve Anatomisi Bölümü  
E-Mail: [ucakilcioglu@yahoo.com](mailto:ucakilcioglu@yahoo.com)

**Doç. Dr. Kamuran DİLSİZ**

Bingöl Üniversitesi, Fen-Edebiyat Fakültesi, Fizik Bölümü  
E-Mail: [kdilsiz@bingol.edu.tr](mailto:kdilsiz@bingol.edu.tr)

**Doç. Dr. Şükran KONCA**

Bakırçay Üniversitesi, Mühendislik ve Mimarlık Fakültesi, Temel Bilimler,  
Matematik Bölümü  
E-Mail: [sukran.konca@bakircay.edu.tr](mailto:sukran.konca@bakircay.edu.tr)

**Doç. Dr. İdris YAZGAN**

Kastamonu Üniversitesi, Fen Edebiyat Fakültesi, Biyoloji  
E-Mail: [idrisyazgan@gmail.com](mailto:idrisyazgan@gmail.com)

**Doç. Dr. Abdulcabbar YAVUZ**

Gaziantep Üniversitesi, Mühendislik Fakültesi, Metalurji ve Malzeme Mühendisliği  
E-Mail: [ayavuz@gantep.edu.tr](mailto:ayavuz@gantep.edu.tr)

**Doç. Dr. Bünyamin ALIM**

Bayburt Üniversitesi, Teknik Bilimler Meslek Yüksekokulu, Elektrik ve Enerji  
Bölümü  
E-Mail: [balim@bayburt.edu.tr](mailto:balim@bayburt.edu.tr)

**Dr. Öğr. Üyesi Mustafa Şükrü KURT**

Erzurum Teknik Üniversitesi, Fen Fakültesi, Temel Bilimler  
E-Mail: [mustafa.kurt@erzurum.edu.tr](mailto:mustafa.kurt@erzurum.edu.tr)

**Dr. Öğr. Üyesi Sinan SAĞIR**

Karamanoğlu Mehmetbey Üniversitesi, Fizik  
E-Mail: [sinansagir@kmu.edu.tr](mailto:sinansagir@kmu.edu.tr) / [sinan.sagir@cern.ch](mailto:sinan.sagir@cern.ch)

**Doç. Dr. Murat AYDEMİR**

Erzurum Teknik Üniversitesi, Fen Fakültesi, Temel Bilimler

E-Mail: [murat.aydemir@erzurum.edu.tr](mailto:murat.aydemir@erzurum.edu.tr)

**Mühendislik Bilimleri**

**Prof. Dr. Figen KOREL**

İzmir Yüksek Teknoloji Enstitüsü, Gıda Mühendisliği Bölümü

E-Mail: [figenkorel@iyte.edu.tr](mailto:figenkorel@iyte.edu.tr)

**Prof. Dr. Kubilay ASLANTAŞ**

Afyon Kocatepe Üniversitesi, Teknoloji Fakültesi, Makine Mühendisliği Bölümü

E-Mail: [aslantas@aku.edu.tr](mailto:aslantas@aku.edu.tr)

**Prof. Dr. Hamit Özkan GÜLSOY**

Marmara Üniversitesi, Teknoloji Fakültesi, Metalurji ve Malzeme Mühendisliği  
Bölümü

E-Mail: [ogulsoy@marmara.edu.tr](mailto:ogulsoy@marmara.edu.tr)

**Prof. Dr. Ali Adnan HAYALOĞLU**

İnönü Üniversitesi, Mühendislik Fakültesi, Gıda Mühendisliği Bölümü

E-Mail: [adnan.hayaloglu@inonu.edu.tr](mailto:adnan.hayaloglu@inonu.edu.tr)

**Prof. Dr. Barbara SAWICKA**

University of Life Sciences in Lublin, Department of Plant Production Technology  
and Commodities Sciences

E-Mail: [barbara.sawicka@gmail.com](mailto:barbara.sawicka@gmail.com)

**Prof. Dr. İbrahim GÜNEŞ**

Giresun Üniversitesi, Mühendislik Fakültesi, İnşaat Mühendisliği Bölümü

E-Mail: [ibrahim.gunes@giresun.edu.tr](mailto:ibrahim.gunes@giresun.edu.tr)

**Doç. Dr. Serhat ŞAP**

Bingöl Üniversitesi, Teknik Bilimler Meslek Yüksekokulu, Elektrik ve Enerji  
Bölümü

E-Mail: [ssap@bingol.edu.tr](mailto:ssap@bingol.edu.tr)

**Doç. Dr. Sırma YEĞİN**

Ege Üniversitesi, Mühendislik Fakültesi, Gıda Mühendisliği Bölümü  
E-Mail: [sirma.yegin@ege.edu.tr](mailto:sirma.yegin@ege.edu.tr)

**Doç. Dr. Hasan OĞUL**

Sinop Üniversitesi, Mimarlık ve Mühendislik Fakültesi, Nükleer Enerji  
Mühendisliği  
E-Mail: [hogul@sinop.edu.tr](mailto:hogul@sinop.edu.tr)

**Doç. Dr. Murat YILMAZTEKİN**

İnönü Üniversitesi, Mühendislik Fakültesi, Gıda Mühendisliği Bölümü  
E-Mail: [murat.yilmaztekin@inonu.edu.tr](mailto:murat.yilmaztekin@inonu.edu.tr)

**Doç. Dr. Ferhat AYDIN**

Sakarya Uygulamalı Bilimler Üniversitesi, Teknoloji Fakültesi, İnşaat  
Mühendisliği Bölümü  
E-Mail: [ferhata@subu.edu.tr](mailto:ferhata@subu.edu.tr)

**Dr. Öğr. Üyesi Nurullah DEMİR**

Bingöl Üniversitesi, Mühendislik ve Mimarlık Fakültesi, Gıda Mühendisliği  
Bölümü  
E-Mail: [ndemir@bingol.edu.tr](mailto:ndemir@bingol.edu.tr)

**Doç. Dr. Ahmet GÜNER**

Bingöl Üniversitesi, Mühendislik ve Mimarlık Fakültesi, Elektrik ve Elektronik  
Mühendisliği Bölümü  
E-Mail: [aguner@bingol.edu.tr](mailto:aguner@bingol.edu.tr)

**Dr. Öğr. Üyesi Tahir AKGÜL**

Sakarya Uygulamalı Bilimler Üniversitesi, Teknoloji Fakültesi, İnşaat  
Mühendisliği Bölümü  
E-Mail: [tahirakgul@subu.edu.tr](mailto:tahirakgul@subu.edu.tr)

**Dr. Erhan Sulejmani**

University of Tetova, Faculty of Food Technology and Nutrition  
E-Mail: [erhan.sulejmani@unite.edu.mk](mailto:erhan.sulejmani@unite.edu.mk)

**Dr. Hacène Medjoudj**

Larbi Ben M'Hidi University of Oum El Bouaghi, Food Science Department  
E-Mail: [medjoudjh@yahoo.com](mailto:medjoudjh@yahoo.com)

**Dr. Avinash Lakshmikanthan**

Nitte Meenakshi Institute of Technology, Department of Mechanical Engineering,  
Karnataka, India  
E-Mail: [avinash.laks01@gmail.com](mailto:avinash.laks01@gmail.com)

**Dr. Manjunath Patel GC**

PES Institute of Technology and Management, Department of Mechanical  
Engineering, Karnataka, India  
E-Mail: [manju09mpm05@gmail.com](mailto:manju09mpm05@gmail.com)

**Sağlık Bilimleri**

**Doç. Dr. Aydın Şükrü BENGÜ**

Bingöl Üniversitesi, Sağlık Hizmetleri Meslek Yüksekokulu, Tıbbi Hizmetler ve  
Teknikler  
E-Mail: [abengu@bingol.edu.tr](mailto:abengu@bingol.edu.tr)

**Dr. Öğr. Üyesi Dilhun Keriman ARSERİM UÇAR**

Bingöl Üniversitesi, Sağlık Bilimleri Fakültesi, Beslenme ve Diyetetik Bölümü  
E-Mail: [dkucar@bingol.edu.tr](mailto:dkucar@bingol.edu.tr)

**Dr. Öğr. Üyesi Abdullah TUNÇ**

Bingöl Üniversitesi, Sağlık Bilimleri Fakültesi, İş Sağlığı ve Güvenliği Bölümü  
E-Mail: [atunc@bingol.edu.tr](mailto:atunc@bingol.edu.tr)

**Dr. Öğr. Üyesi Ramazan GÜNDOĞDU**

Bingöl Üniversitesi, Sağlık Hizmetleri Meslek Yüksekokulu, Eczane Hizmetleri  
E-Mail: [rgundogdu@bingol.edu.tr](mailto:rgundogdu@bingol.edu.tr)

**Dr. Alexander HERGOVICH**

UCL Cancer Institute, Faculty of Medical Sciences, Department of Cancer Biology,  
UCL, London, UK  
E-Mail: [a.hergovich@uc.ac.uk](mailto:a.hergovich@uc.ac.uk)

**Dr. Valenti GOMEZ**

UCL Cancer Institute, Faculty of Medical Sciences, Department of Oncology,  
UCL, London, UK

E-Mail: [valentin.gomez@ucl.ac.uk](mailto:valentin.gomez@ucl.ac.uk)

**Veterinerlik Bilimleri**

**Prof. Dr. Fatih Mehmet KANDEMİR**

Atatürk Üniversitesi, Veteriner Fakültesi, Veteriner Hekimliği Temel Bilimler

E-Mail: [fmehmet.kandemir@atauni.edu.tr](mailto:fmehmet.kandemir@atauni.edu.tr)

**Doç. Dr. Akın KIRBAŞ**

Bozok Üniversitesi, Veteriner Fakültesi, Klinik Bilimler Bölümü

E-Mail: [akindahiliye55@yahoo.com](mailto:akindahiliye55@yahoo.com)

**Doç. Dr. Emrah Hicazi AKSU**

Atatürk Üniversitesi, Veteriner Fakültesi, Klinik Bilimler Bölümü

E-Mail: [emrahaksu@atauni.edu.tr](mailto:emrahaksu@atauni.edu.tr)

**Ziraat Bilimleri**

**Doç. Dr. Zeynep DUMANOĞLU**

Bingöl Üniversitesi, Ziraat Fakültesi, Biyosistem Mühendisliği Bölümü

E-Mail: [zdumanoglu@bingol.edu.tr](mailto:zdumanoglu@bingol.edu.tr)

**Prof. Dr. Kağan KÖKTEN**

Bingöl Üniversitesi, Ziraat Fakültesi, Tarla Bitkileri Bölümü

E-Mail: [kahafe1974@yahoo.com](mailto:kahafe1974@yahoo.com)

**Prof. Dr. Mustafa SÜRME**

Adnan Menderes Üniversitesi, Ziraat Fakültesi, Tarla Bitkileri Bölümü

E-Mail: [mustafa.surmen@adu.edu.tr](mailto:mustafa.surmen@adu.edu.tr)

**Prof. Dr. Banu YÜCEL**

Ege Üniversitesi, Ziraat Fakültesi, Hayvan Yetiştirme Anabilim Dalı, Zootekni  
Bölümü

E-Mail: [banu.yucel@ege.edu.tr](mailto:banu.yucel@ege.edu.tr)



**Doç. Dr. Hakan İNCİ**

Bingöl Üniversitesi, Ziraat Fakültesi, Zootekni Bölümü  
E-Mail: [hinci@bingol.edu.tr](mailto:hinci@bingol.edu.tr)

## TEKNİK EDİTÖRLER

**Dr. Nimetullah KORKUT**







Bingöl Üniversitesi, BİNUZEM, Bilgisayar Teknolojileri  
E-Mail: [nkorkut@bingol.edu.tr](mailto:nkorkut@bingol.edu.tr)









## DİL EDİTÖRÜ

**Öğr. Gör. Dr. Ahmet KESMEZ**






Bingöl Üniversitesi, Yabancı Diller Yüksekokulu, İngilizce Bölümü  
E-Mail: [akesmez@bingol.edu.tr](mailto:akesmez@bingol.edu.tr)

İÇİNDEKİLER/CONTENTS

<p><b>Deep Learning Approaches and Motor Current Signature Analysis in Detection of Broken Rotor Bar Faults</b></p> <p><b>Özgür AYDIN<sup>1*</sup> , Erhan AKIN<sup>2</sup> </b></p> <p><sup>1</sup> Bingöl University, Informatics Department, Bingöl, Türkiye <sup>2</sup> Fırat University, Engineering Faculty, Elazığ, Türkiye Özgür AYDIN ORCID No: 0000-0001-8130-277X Erhan AKIN ORCID No: 0000-0001-6476-9255</p> <p><i>*Corresponding author: iamozguraydin@gmail.com</i></p> <p>(Received: 21.05.2024, Accepted: 23.06.2024, Online Publication: 26.09.2024)</p>	<p><b>1</b></p>
<p><b>Detection of Bean Rust (<i>Uromyces appendiculatus</i>) Disease Under Field Conditions Using Thermal Imaging</b></p> <p><b>Hilal ERDOĞAN<sup>1*</sup> </b></p> <p><sup>1</sup> Bursa Uludağ University, Agricultural Faculty, Department of Biosystems, Bursa, Türkiye Hilal ERDOĞAN ORCID No: 0000-0002-0387-2600</p> <p><i>*Corresponding author: hilalerdogan@uludag.edu.tr</i></p> <p>(Received: 05.01.2024, Accepted: 08.07.2024, Online Publication: 26.09.2024)</p>	<p><b>8</b></p>
<p><b>MPROVIOT - Multi-Purpose IoT Rover Robot</b></p> <p><b>Ahmet BAĞBARS<sup>1*</sup> , Muhammed Fatih TALU<sup>2</sup> , Nuh ALPASLAN<sup>3</sup> </b></p> <p><sup>1</sup> İnönü University, Faculty of Engineering, Computer Engineering Department, Malatya, Türkiye <sup>2</sup> İnönü University, Faculty of Engineering, Computer Engineering Department, Malatya, Türkiye <sup>3</sup> Bingöl University, Faculty of Engineering, Computer Engineering Department, Bingöl, Türkiye Ahmet BAĞBARS ORCID No: 0009-0000-2074-5462 Muhammed Fatih TALU ORCID No: 0000-0003-1166-8404 Nuh ALPASLAN ORCID No: 0000-0002-6828-755X</p> <p><i>*Corresponding author: a_bagbars@hotmail.com</i></p> <p>(Received: 19.05.2024, Accepted: 15.07.2024, Online Publication: 26.09.2024)</p>	<p><b>14</b></p>

<p><b>Typing of <i>Mannheimia haemolytica</i> Isolated From Respiratory Tract and Investigation of Virulence Genes</b></p> <p><b>Cihat ÖZTÜRK<sup>1*</sup>  , İsmail Hakkı EKİN<sup>2</sup> </b></p> <p><sup>1</sup> Kırşehir Ahi Evran University, Faculty of Medicine, Department of Medical Microbiology, Kırşehir, Türkiye</p> <p><sup>2</sup> Van Yüzüncü Yıl University, Faculty of Veterinary Medicine, Department of Microbiology, Van, Türkiye</p> <p>Cihat ÖZTÜRK ORCID No: 0000-0003-2868-2317 İsmail Hakkı EKİN ORCID No: 0000-0001-5029-8130</p> <p><i>*Corresponding author: cihat.ozturk@ahievran.edu.tr</i></p> <p>(Received: 15.01.2024, Accepted: 19.07.2024, Online Publication: 26.09.2024)</p>	<p><b>21</b></p>
<p><b>Economic Analysis of Automatic Meter Reading on Web Based in Türkiye Using Nginx Load Balancer Technology</b></p> <p><b>Şükrü KARAASLAN<sup>1*</sup>  , Mazhar KAYAOĞLU<sup>2</sup>  , Mehmet GEDİKPİNAR<sup>3</sup>  , Abdulkadir ŞENGÜR<sup>4</sup> </b></p> <p><sup>1</sup> Fırat University, Organized Industrial Zone Vocational School, Department of Electricity and Energy, Elazığ, Türkiye</p> <p><sup>2</sup> Bingöl University, Department of Informatics, Bingöl, Türkiye</p> <p><sup>3</sup> Fırat University, Faculty of Technology, Department of Electricity and Electronics, Elazığ, Türkiye</p> <p><sup>4</sup> Fırat University, Faculty of Technology, Department of Electricity and Electronics, Elazığ, Türkiye</p> <p>Şükrü KARAASLAN ORCID No: 0000-0001-8511-0388 Mazhar KAYAOĞLU ORCID No: 0000-0002-5807-9781 Mehmet GEDİKPİNAR ORCID No: 0000-0002-1045-7384 Abdulkadir ŞENGÜR ORCID No: 0000-0003-1614-2639</p> <p><i>*Corresponding author: s.karaaslan@firat.edu.tr</i></p> <p>(Received: 29.12.2023, Accepted: 20.07.2024, Online Publication: 26.09.2024)</p>	<p><b>31</b></p>
<p><b>Comparative Investigation of Deep Convolutional Networks in Detection of Plant Diseases</b></p> <p><b>Fikriye ATAMAN<sup>1*</sup>  , Halil EROĞLU<sup>2</sup> </b></p> <p><sup>1</sup> Van Yüzüncü Yıl University, Engineering Faculty, Computer Engineering Department, Van, Türkiye</p> <p><sup>2</sup> Van Yüzüncü Yıl University, Institute of Natural and Applied Sciences, Artificial Intelligence and Robotics Department, Van, Türkiye</p> <p>Fikriye ATAMAN ORCID No: 0000-0002-0257-7730 Halil EROĞLU ORCID No: 0009-0008-8576-2771</p> <p><i>*Corresponding author: fataman@yyu.edu.tr</i></p> <p>(Received: 02.05.2024, Accepted: 20.07.2024, Online Publication: 26.09.2024)</p>	<p><b>37</b></p>

<p><b>Effect Of Tool Tilt Angle On The Mechanical Properties Of Friction Stir Lap Welds Of AZ31B Magnesium Alloy Sheets</b></p> <p><b>Ömer EKİNCİ<sup>1</sup>  , Anıl İMAK<sup>2*</sup> </b></p> <p><sup>1</sup> Sivas University of Science and Technology, Faculty of Aviation and Space Sciences, Astronautical Engineering, Sivas, Türkiye</p> <p><sup>2</sup> Bingöl University, Faculty of Engineering and Architecture, Mechanical Engineering, Bingöl, Türkiye</p> <p>Ömer Ekinci ORCID No: 0000-0002-0179-6456 Anıl İMAK ORCID No: 0000-0001-6091-1584</p> <p><i>*Corresponding author: aimak@bingol.edu.tr</i></p> <p>(Received: 09.05.2024, Accepted: 26.07.2024, Online Publication: 26.09.2024)</p>	50
<p><b>Evaluation of Sun Protection Factor of Northern Iraqi Propolis</b></p> <p><b>Adnan AYNA<sup>1*</sup>  , Farhan NERWAY<sup>2</sup> </b></p> <p><sup>1</sup>Department of Chemistry, Faculty of Arts and Sciences, Bingöl University, Bingöl, Türkiye</p> <p><sup>2</sup>Department of Bee and Bee Products, Bingöl University, Bingöl, Türkiye</p> <p>Adnan AYNA ORCID No: 0000-0001-6801-6242 Farhan NERWAY ORCID No: 0009-0006-9324-5526</p> <p><i>*Corresponding author: aayna@Bingöl.edu.tr</i></p> <p>(Received: 09.05.2024, Accepted: 29.07.2024, Online Publication: 26.09.2024)</p>	57
<p><b>Partial Purification and Biochemical Characterization of Cellulase from <i>Bacillus pumilus</i> ND8 Isolated from Garden Waste</b></p> <p><b>Neslihan DİKBAŞ<sup>1*</sup>  , Waleed SALİH SALMAN AL DAHLUZ<sup>1</sup>  , Şeyma ALİM<sup>1</sup>  , Sevda UÇAR<sup>2</sup> </b></p> <p><sup>1</sup> Ataturk University, Agricultural Faculty, Department of Agricultural Biotechnology, Erzurum, Türkiye</p> <p><sup>2</sup> Sivas Science and Technology University, Faculty of Agricultural Sciences and Technology, Department of Herbal Production and Technologies, Sivas, Türkiye</p> <p>Neslihan DİKBAŞ ORCID No: 0000-0001-9096-2761 Waleed Salih Salman Al Dahluz ORCID No: 0009-0002-9275-7328 Şeyma ALİM ORCID No: 0000-0001-6684-7974 Sevda UÇAR ORCID No: 0000-0002-3612-457X</p> <p><i>*Corresponding author: neslidikbas@atauni.edu.tr</i></p> <p>(Received: 01.07.2024, Accepted: 29.07.2024, Online Publication: 26.09.2024)</p>	62

<p><b>Modeling of the Linear Equations of Langmuir Isotherm in the Adsorption of Cd (II) Ion with Siirt Kurtalan Koçpınar Clay</b></p> <p><b>Mehmet Can DAL<sup>1*</sup></b> </p> <p><sup>1</sup>Dicle University, Institute of Natural and Applied Science, Chemistry Department, Diyarbakır, Türkiye Mehmet Can DAL ORCID No: 0000-0001-6474-6053</p> <p><i>*Corresponding author: mcandal123@dicle.edu.tr</i></p> <p>(Received: 17.08.2024, Accepted: 02.08.2024, Online Publication: 26.09.2024)</p>	<p><b>67</b></p>
<p><b>Testing the Reliability of Numerical Model Studies for a Broad-Crested Weir</b></p> <p><b>Mahmut AYDOĞDU<sup>1*</sup></b> </p> <p><sup>1</sup> Malatya Turgut Özal University, Engineering and Natural Sciences Faculty, Civil Engineering Department, Malatya, Türkiye Mahmut AYDOĞDU ORCID No: 0000-0002-7339-2442</p> <p><i>*Corresponding author: mahmut.aydogdu@ozal.edu.tr</i></p> <p>(Received: 21.05.2024, Accepted: 19.08.2024, Online Publication: 26.09.2024)</p>	<p><b>73</b></p>
<p><b>Role of KU70, SIRT1, and SIRT6 Proteins in Diabetic Rat Testis Tissue</b></p> <p><b>Selim DEMİRTAŞ<sup>1*</sup></b> , <b>Onur ERSOY<sup>2</sup></b> , <b>Gülnur KIZILAY<sup>3</sup></b> </p> <p><sup>1</sup> Mardin Artuklu University, Medicine Faculty, Histology and Embriology Department, Mardin, Türkiye <sup>2</sup> Trakya University, Vocational School of Health Services, Pathology Laboratory Techniques Program, Edirne, Türkiye <sup>3</sup> Trakya University, Medicine Faculty, Histology and Embriology Department, Edirne, Türkiye</p> <p>Selim DEMİRTAŞ ORCID No: 0000-0001-7249-3092 Onur ERSOY ORCID No: 0000-0001-9829-7903 Gülnur KIZILAY ORCID No: 0000-0003-1793-7003</p> <p><i>*Corresponding author: selindemirtas@artuklu.edu.tr</i></p> <p>(Received: 14.05.2024, Accepted: 19.08.2024, Online Publication: 26.09.2024)</p>	<p><b>82</b></p>

## Green Synthesis of Apricot Kernel Silver Nanoparticles and Their Biological Activity

İbrahim BAYAV<sup>1\*</sup>, Adnan AYNA<sup>2</sup>, Sevda SAĞ<sup>1</sup>, Muhammet Veysel NAZLI<sup>3</sup>, Faruk ALTINBAŞAK<sup>4</sup>, İlay BOZ<sup>5</sup>, Ekrem DARENDELİOĞLU<sup>3</sup>

<sup>1</sup> Pamukkale University, Faculty of Medicine, Department of Medical Biology, Denizli, Türkiye

<sup>2</sup> Bingöl University, Faculty of Arts and Sciences, Department of Chemistry, Bingöl, Türkiye

<sup>3</sup> Bingöl University, Faculty of Arts and Sciences, Department of Molecular Biology and Genetics, Bingöl, Türkiye

<sup>4</sup> Hitit University, Faculty of Medicine, Department of Histology and Embryology, Çorum, Türkiye

<sup>5</sup> Pamukkale University, Faculty of Medicine, Department of Histology and Embryology, Denizli, Türkiye

İbrahim BAYAV ORCID No: 0000-0002-3533-3935

Adnan AYNA ORCID No: 0000-0001-6801-6242

Sevda SAĞ ORCID No: 0000-0001-8258-7324

Muhammet Veysel NAZLI ORCID No: 0000-0002-8847-4694

Faruk ALTINBAŞAK ORCID No: 0000-0002-6816-1367

İlay BOZ ORCID No: 0009-0003-8856-1602

Ekrem DARENDELİOĞLU ORCID No: 0000-0002-0630-4086

\*Corresponding author: [ibayav22@posta.pau.edu.tr](mailto:ibayav22@posta.pau.edu.tr)

(Received: 09.07.2024, Accepted: 21.08.2024, Online Publication: 26.09.2024)

92

## Investigation Antioxidant, Antimicrobial and *In Vitro* Cytotoxic Effects on PC-3 Cancer Lines of *Alchemilla holotricha* Juz. in Different Polarities Extracts

Bülent KAYA<sup>1\*</sup>, Yekta ARTUVAN<sup>2</sup>, Fatma CAF<sup>3</sup>, Yusuf MENEMEN<sup>4</sup>

<sup>1\*</sup> Bülent Kaya, Faculty of Sciences and Arts, Molecular Biology and Genetics Department, University of Bingöl, 12000 Bingöl, Türkiye

<sup>2</sup> Yekta Artuvan, Faculty of Sciences and Arts, Biology Department, University of Bingöl, 12000 Bingöl, Türkiye

<sup>3</sup> Fatma Caf, Vocational School of Food, Agriculture, and Livestock, University of Bingöl, 12000 Bingöl, Türkiye

<sup>4</sup> Yusuf Menemen, Faculty of Sciences and Arts, Biology Department, University of Kırıkkale, 71450, Kırıkkale, Türkiye

Bülent KAYA ORCID No: 0000-0002-1216-6441

Yekta ARTUVAN ORCID No: 0000-0002-6321-7181

Fatma CAF ORCID No: 0000-0002-0363-4848

Yusuf MENEMEN ORCID No: 0000-0002-9546-7986

\*Corresponding author: [b\\_kaya\\_tr@yahoo.com](mailto:b_kaya_tr@yahoo.com),

(Received: 18.04.2024, Accepted: 22.08.2024, Online Publication: 26.09.2024)





99

<p align="center"><b>Evaluation of Missing Data Imputation Methods and PCA Techniques for Machine Learning Models in Breast Cancer Diagnosis Using WBCD</b></p> <p align="center"><b>Yavuz Bahadır KOCA<sup>1*</sup> , Elif AKTEPE<sup>2</sup> </b></p> <p><sup>1</sup> Afyon Kocatepe University, Engineering Faculty, Electrical Engineering Department, Afyonkarahisar, Türkiye</p> <p><sup>2</sup> Afyon Kocatepe University, Afyon Vocational School, Electronics and Automation Department, Afyonkarahisar, Türkiye</p> <p align="center">Yavuz Bahadır KOCA ORCID No: 0000-0002-0317-1417 Elif AKTEPE ORCID No: 0000-0002-2375-2040</p> <p align="center"><i>*Corresponding author: ybkoca@aku.edu.tr</i></p> <p align="center">(Received: 28.03.2024, Accepted: 25.08.2024, Online Publication: 26.09.2024)</p>	<b>109</b>
<p align="center"><b>Classification of Skin Diseases with Different Deep Learning Models and Comparison of the Performances of the Models</b></p> <p align="center"><b>Ferdi DOĞAN<sup>1*</sup> , Mikat AKTAŞ<sup>2</sup> , Mehmet İsmail GÜRSOY<sup>3</sup> </b></p> <p><sup>1</sup> Adıyaman University, Faculty of Engineering, Computer Engineering, Adıyaman, Türkiye</p> <p><sup>2</sup> Fırat University, Faculty of Technology, Software Engineering, Elazığ, Türkiye</p> <p><sup>3</sup> Adıyaman University, Technical Sciences Vocational School, Electrical Department, Adıyaman, Türkiye</p> <p align="center">Ferdi DOĞAN ORCID No: 0000-0002-9203-697X Mikat AKTAŞ ORCID No: 0000-0002-0731-5668 Mehmet İsmail GÜRSOY SOYAD ORCID No: 0000-0002-2285-5160</p> <p align="center"><i>*Corresponding author: fdogan@adiyaman.edu.tr</i></p> <p align="center">(Received: 18.06.2024, Accepted: 25.08.2024, Online Publication: 26.09.2024)</p>	<b>117</b>
<p align="center"><b>Some Identities Concerning Generalized Fibonacci and Lucas Numbers by Matrix Methods</b></p> <p align="center"><b>Gülsüm LİMAN<sup>1*</sup> , Refik KESKİN<sup>2</sup> </b></p> <p><sup>1</sup> Kağıthane Profilo Vocational and Technical Anatolian High School, İstanbul, Türkiye</p> <p><sup>2</sup> Department of Mathematics, Sakarya University, Sakarya, Türkiye</p> <p align="center">Gülsüm LİMAN ORCID No: 0000-0003-0214-6102 Refik KESKİN ORCID No: 0000-0003-2547-2082</p> <p align="center"><i>*Corresponding author: rkeskin@sakarya.edu.tr</i></p> <p align="center">(Received: 15.12.2023, Accepted: 26.08.2024, Online Publication: 26.09.2024)</p>	<b>124</b>

<p align="center"><b>Evaluation of the Efficacy of Propolis Extracts Based on Different Solvents Against Some Plant Pathogenic Fungi</b></p> <p align="center"><b>Abdullah GÜLLER<sup>1*</sup>  , Işıl SARAÇ SİVRİKAYA<sup>2</sup>  , Ersin KARAKAYA<sup>3</sup>  , Gözdenur ÇAKAR KILIÇ<sup>4</sup> </b></p> <p><sup>1,2</sup> Bingöl University, Agriculture Faculty, Plant Protection Department, Bingöl, Türkiye</p> <p><sup>3</sup> Bingöl University, Agriculture Faculty, Biosystems Engineering Department, Bingöl, Türkiye</p> <p><sup>4</sup> Ankara University, Agriculture Faculty, Plant Protection Department, Ankara, Türkiye</p> <p>Abdullah GÜLLER ORCID No: 0000-0003-3887-4208  Işıl SARAÇ SİVRİKAYA ORCID No: 0000-0002-5991-2173  Ersin KARAKAYA ORCID No: 0000-0002-6734-4962  Gözdenur ÇAKAR KILIÇ ORCID No: 0000-0002-2359-1312</p> <p align="center"><i>*Corresponding author: aguller@bingol.edu.tr</i></p> <p align="center">(Received: 31.05.2024, Accepted: 27.08.2024, Online Publication: 26.09.2024)</p>	127
<p align="center"><b>Investigation of Effects of Apilarnil and Imatinib Use on Liver and Kidney Tissues in Rats via PI3K/AKT/mTOR and JAK2/STAT3 Signaling Pathways</b></p> <p align="center"><b>Cüneyt ÇAĞLAYAN<sup>1*</sup>  , Aydın GENÇ<sup>2</sup>  , Sefa KÜÇÜKLER<sup>3</sup>  , Hakan İNCİ<sup>4</sup> </b></p> <p><sup>1</sup> Bilecik Şeyh Edebali University, Medicine Faculty, Medical Biochemistry Department, Bilecik, Türkiye</p> <p><sup>2</sup> Bingöl University, Veterinary Faculty, Biochemistry Department, Bingöl, Türkiye</p> <p><sup>3</sup> Atatürk University, Veterinary Faculty, Biochemistry Department, Erzurum, Türkiye</p> <p><sup>4</sup> Bingöl University, Agriculture Faculty, Animal Science Department, Bingöl, Türkiye</p> <p>Cüneyt ÇAĞLAYAN ORCID No: 0000-0001-5608-554X  Aydın GENÇ ORCID No: 0000-0001-5367-0743  Sefa KÜÇÜKLER ORCID No: 0000-0002-8222-5515  Hakan İNCİ ORCID No: 0000-0002-9791-0435</p> <p align="center"><i>*Corresponding author: cuneyt.caglayan@bilecik.edu.tr</i></p> <p align="center">(Received: 02.08.2024, Accepted: 06.09.2024, Online Publication: 26.09.2024)</p>	134
<p align="center"><b>Investigation of the Effects of Rutin in Sprague Dawley Rats with Biochemical Parameters in Colistin-Induced Lung Injury</b></p> <p align="center"><b>Özge KANDEMİR<sup>1*</sup>  , Sefa KÜÇÜKLER<sup>2</sup> </b></p> <p><sup>1</sup> Aksaray University, Aksaray Vocational School of Technical Sciences, Food processing Department, Aksaray, Türkiye</p> <p><sup>2</sup> Atatürk University, Veterinary Faculty, Veterinary Biochemistry Department, Erzurum, Türkiye</p> <p>Özge KANDEMİR ORCID No: 0000-0001-8884-4168  Sefa KÜÇÜKLER ORCID No: 0000-0002-8222-5515</p> <p align="center"><i>*Corresponding author: ozgekandemir@aksaray.edu.tr</i></p> <p align="center">(Received: 07.07.2024, Accepted: 06.09.2024, Online Publication: 26.09.2024)</p>	140



<p><b>Investigation of the Effects of Maleic Acid and Vanillic Acid on Copper Toxicity in the <i>Drosophila melanogaster</i> Model</b></p> <p><b>Emine TORAMAN<sup>1*</sup>  , Melike KARAMAN<sup>1</sup> </b></p> <p><sup>1</sup> Atatürk University, Science Faculty, Molecular Biology and Genetics Department, Erzurum, Türkiye Emine TORAMAN ORCID No: 0000-0001-7732-6189 Melike KARAMAN ORCID No: 0000-0002-0973-2561</p> <p><i>*Corresponding author: emine.toraman@atauni.edu.tr</i></p> <p>(Received: 16.03.2024, Accepted: 06.09.2024, Online Publication: 26.09.2024)</p>	<p>148</p>
<p><b>Investigation of Friction Welding Dissimilar AISI 304 And AISI 1040 Steels</b></p> <p><b>Zülküf BALALAN<sup>1*</sup>  , Mehmet YAZ<sup>2</sup>  , Sedat BULDAĞ<sup>3</sup> </b></p> <p><sup>1</sup> Bingöl University, Faculty of Engineering and Architecture, Mechanical Engineering, Bingöl, Türkiye <sup>2</sup> Fırat University, Vocational School Of Technical Sciences/Department Of Machinery And Metal Technologies/Machinery, Elazığ, Türkiye <sup>3</sup> Bingöl University, Faculty of Engineering and Architecture, Mechanical Engineering, Bingöl, Türkiye</p> <p>Zülküf BALALAN ORCID No: 0000-0001-5808-6263 Mehmet YAZ ORCID No: 0000-0002-5422-7433 Sedat BULDAĞ ORCID No: 0009-0000-3877-6320</p> <p><i>*Corresponding author: zbalalan@bingol.edu.tr</i></p> <p>(Received: 28.05.2024, Accepted: 09.09.2024, Online Publication: 26.09.2024)</p>	<p>154</p>
<p><b>Anticholinergic Evaluation, Antioxidant Effects, and DNA Protection Potential of <i>Chenopodium spp</i> Depending on Its Phenolic Content</b></p> <p><b>Enver Fehim KOÇPINAR<sup>1*</sup> </b></p> <p><sup>1</sup> Muş Alparslan University, Vocational School of Health Services, Department of Medical Laboratory Techniques, Mus, Türkiye Enver Fehim KOÇPINAR ORCID No: 0000-0002-6031-4664</p> <p><i>*Corresponding author: ef.kocpinar@alparslan.edu.tr</i></p> <p>(Received: 07.05.2024, Accepted: 10.09.2024, Online Publication: 26.09.2024)</p>	<p>161</p>
<p><b>SAR Ship Detection Using Image Histograms and Machine Learning Approach</b></p> <p><b>Kazım HANBAY<sup>1*</sup>  , Mücahit ÇALIŞAN<sup>2</sup>  , Taha Burak ÖZDEMİR<sup>3</sup> </b></p> <p><sup>1</sup> İnönü University, Engineering Faculty, Software Engineering Department, Malatya, Türkiye <sup>2</sup> Bingöl University, Engineering-Architecture Faculty, Computer Engineering Department, Bingöl, Türkiye <sup>3</sup> İnönü University, Engineering Faculty, Computer Engineering Department, Malatya, Türkiye</p> <p>Kazım HANBAY ORCID No: 0000-0003-1374-1417 Mücahit ÇALIŞAN ORCID No: 0000-0003-2651-5937 Taha Burak ÖZDEMİR ORCID No: 0000-0002-8546-9662</p> <p><i>*Corresponding author: kazimhanbay@gmail.com</i></p> <p>(Received: 05.08.2024, Accepted: 12.09.2024, Online Publication: 26.09.2024)</p>	<p>171</p>

<p><b>Classification of Temporary and Real E-mail Addresses with Machine Learning Techniques</b></p> <p><b>Caner BALIM<sup>1*</sup> , Nevzat OLGUN<sup>2</sup> </b></p> <p><sup>1</sup> Afyon Kocatepe University, Engineering Faculty, Software Engineering Department, Afyonkarahisar, Türkiye</p> <p><sup>2</sup> Afyon Kocatepe University, Engineering Faculty, Software Engineering Department, Afyonkarahisar, Türkiye</p> <p>Caner BALIM ORCID No: 0000-0002-1010-129X Nevzat OLGUN ORCID No: 0000-0003-2461-4923</p> <p><i>*Corresponding author: cbalim@aku.edu.tr</i></p> <p>(Received: 20.07.2024, Accepted: 12.09.2024, Online Publication: 26.09.2024)</p>	<p><b>176</b></p>
<p><b>Microbial Quality of Drinking and Utility Water in Tourism Facilities in Antalya</b></p> <p><b>Riřan Elif NURAL<sup>1</sup> , Nadide SEYHUN<sup>1*</sup> </b></p> <p><sup>1</sup> Bursa Technical University, Faculty of Engineering and Natural Sciences, Department of Food Engineering, Bursa, Türkiye</p> <p>Riřan Elif NURAL ORCID No: 0000-0002-6073-890X Nadide SEYHUN ORCID No: 0000-0002-0086-8374</p> <p><i>*Corresponding author: nadide.seyhun@btu.edu.tr</i></p> <p>(Received: 26.08.2024, Accepted: 12.09.2024, Online Publication: 26.09.2024)</p>	<p><b>184</b></p>

## Deep Learning Approaches and Motor Current Signature Analysis in Detection of Broken Rotor Bar Faults

Özgür AYDIN<sup>1</sup> , Erhan AKIN<sup>2</sup> 

<sup>1</sup> Bingöl University, Informatics Department, Bingöl, Türkiye

<sup>2</sup> Fırat University, Engineering Faculty, Elazığ, Türkiye

Özgür AYDIN ORCID No: 0000-0001-8130-277X

Erhan AKIN ORCID No: 0000-0001-6476-9255

\*Corresponding author: iamozguraydin@gmail.com

(Received: 21.05.2024, Accepted: 23.06.2024, Online Publication: 26.09.2024)

### Keywords

Induction Motor,  
Fault Diagnosis,  
Broken Rotor  
Bar,  
Vision Transformer  
Model,  
Image Processing

**Abstract:** Induction motors are preferred in industrial applications due to their simple and robust structure, cost-effectiveness, self-starting capability, high efficiency, and reliability. However, faults like broken rotor bars occasionally encountered in these motors can lead to reduced performance and increased operating costs. Deep learning models are increasingly being used for the early detection of such faults. These models can recognize complex patterns in motor data to identify potential faults in advance, allowing for timely intervention, extending motor life, and ensuring production continuity. In this study, the diagnosis of broken rotor bars in induction motors was performed using four different deep learning models. Binary classification was conducted based on images obtained from current signals using a pre-existing dataset. The study achieved over 90% accuracy, thereby proving the effectiveness of deep learning models on induction motors.

1

## Kırık Rotor Çubuğu Arızalarının Belirlenmesinde Derin Öğrenme Yaklaşımları ve Motor Akım İmza Analizi

### Anahtar Kelimeler

Asenkron Motor,  
Arıza Teşhisi,  
Kırık Rotor  
Çubuğu,  
Vision Transformer  
Model,  
Görüntü İşleme

**Öz:** Asenkron motorlar, endüstriyel uygulamalarda sağladıkları basit ve sağlam yapı, maliyet etkinliği, kendiliğinden başlama kabiliyeti, yüksek verimlilik ve güvenilirlik gibi avantajlarla tercih edilir. Ancak, bu motorlarda zaman zaman karşılaşılan kırık rotor çubuğu gibi arızalar, performans düşüklüğüne ve işletme maliyetlerinin artmasına neden olabilir. Bu tür arızaların erken teşhisi için derin öğrenme modelleri giderek daha fazla kullanılmaktadır. Bu modeller, motor verilerinden karmaşık desenleri tanıyarak potansiyel arızaları önceden belirleyebilir, böylece zamanında müdahale ile motor ömrü uzatılabilir ve üretim sürekliliği sağlanabilir. Bu çalışma dört farklı derin öğrenme modeli kullanılarak asenkron motorlardaki kırık rotor çubuğu teşhisi gerçekleştirilmiştir. Hazır veri seti kullanılan çalışmada akım sinyalleri ile elde edilen görüntüler üzerinden ikili sınıflandırma yapılmıştır. Yapılan çalışma sonucunda %90 üzerinde başarımla sonuçlandırılmıştır. Böylece derin öğrenme modellerinin asenkron motorlar üzerinde etkinliği kanıtlanmıştır.

### 1. INTRODUCTION

Induction motors are efficient and economical devices that are particularly preferred in industrial applications among electric motors. These motors primarily consist of two main components: the stator and the rotor. The stator, located on the outer part of the motor, comprises windings powered by alternating current (AC). When AC is applied, the stator generates a variable magnetic field. This magnetic field induces electric currents in the

inner component known as the rotor, and these currents produce the torque that causes the rotor to start rotating. However, the rotor cannot fully synchronize with the speed of the stator's magnetic field, a phenomenon known as "slip." This characteristic of the motor gives it the name "asynchronous."

The simple structure, low cost, and minimal maintenance requirements of induction motors make them ideal for a wide range of applications. They are particularly widely

used in equipment such as pumps, fans, air compressors, and conveyor belts, where high reliability and resistance to overload conditions are required. These motors are indispensable elements of industrial automation systems and reduce operational costs by providing energy efficiency [1-4].

Fault types encountered in induction motors generally develop due to mechanical, electrical, or environmental factors. Mechanical issues include bearing damage, shaft bending, and coupling faults; these damages typically result from insufficient lubrication, incorrect installation, or overloading. Electrical faults directly affect the motor's performance due to problems in the electrical supply, such as phase imbalances, voltage drops, and high harmonic content. Moreover, situations like short circuits in the stator windings and overheating caused by environmental factors can also shorten the motor's lifespan and lead to insulation degradation. Broken rotor bars, in particular, are one of the most severe mechanical faults in induction motors. The breaking of rotor bars causes the motor to vibrate abnormally, overheat, and reduce energy efficiency. This type of damage usually results from overloading, material fatigue, or installation errors and can lead to significant performance reductions in the motor. Preventing these issues through regular maintenance and proper usage ensures that the motor operates efficiently and has a long service life [4-6]. To detect and classify the faults described, studies have been conducted using vibration signals [7-20], current signals [21-24], and frequency-based analyses [25].

The early detection of faults in induction motors is vital for improving the motor's reliability and operational efficiency. Various methods used for this purpose help identify any potential issues by monitoring the motor's condition. Vibration analysis reveals mechanical problems by measuring the motor's abnormal vibrations, while the thermography method detects overheating and insulation problems by analyzing the temperature distribution on the motor surface. Ultrasonic inspection identifies cracks or structural degradation inside the motor using ultrasonic waves, and oil analysis shows the motor's internal wear condition by examining the metal particles and chemical components in the motor oil. Motor Current Signature Analysis (MCSA), in particular, stands out in detecting electrical faults. By evaluating abnormalities in the motor current, it identifies critical issues such as stator winding damage and broken rotor bars. The use of MCSA provides a deeper analysis of electrical problems, offering more detailed information compared to other methods and playing a central role in motor maintenance strategies. The effective use of these techniques not only reduces repair and maintenance costs by identifying motor faults at an early stage but also extends the motor's lifespan and improves the overall system performance [26-27].

The use of MCSA method for fault diagnosis in induction motors is quite common. For instance, Akkurt and Arabacı (2019) utilized current signal analysis and artificial neural networks to detect bearing faults in induction motors. In their experiments, current signals

obtained from artificially damaged bearings were examined and compared with signals from healthy bearings. Statistical and spectral features were determined, and the artificial neural network was trained, enabling the classification of bearing faults with an accuracy of 95.3% [28]. In their study, Kaya and Ünsal (2022) used artificial neural network models to detect and classify various faults in a 3 kW wound-rotor induction motor. The motor was tested with different fault combinations and operated under full load. As a result of the tests, the detection and classification of multiple faults were achieved with an 87% success rate. These results demonstrate that the proposed method can be applied effectively [29]. These studies have shown that MCSA is an effective tool for fault detection in induction motors. Additionally, by combining it with advanced techniques such as machine and deep learning, the efficiency of this method can be further enhanced.

In this study, it has been shown that different deep learning methods (Vision Transformer, gMLP, MLP Mixer, FNet) can be successfully applied to current signals for fault diagnosis in induction motors. Among the methods used, the highest accuracy rate achieved was between 100%.

## 2. METHODOLOGY

### 2.1. Data Collection

Our study was conducted using the publicly available broken rotor bar dataset. This dataset contains electrical and mechanical signals collected from three-phase induction motors. The data was obtained through tests conducted with varying degrees of broken bar faults in the motor's rotor under different mechanical loads; the dataset also includes data from a faultless rotor. The induction motor used operates at 3-phase, 1 horsepower (hp), 220/380V voltage, 4 poles, and a nominal speed of 1785 rpm. The experimental dataset contains four different fault classes and one healthy condition class. The data is organized according to load conditions at torque values ranging from 0.5 to 4.0 Nm. A total of ten experiments were conducted to create each data group. In this paper, the phase current signal ( $I_a$ ) was used for analysis. The sampling frequency of the electrical signals was set at 50 kHz, and that of the mechanical vibration signals at 7600 Hz [30].

### 2.2. Classification Algorithms (Deep Learning Models)

#### 2.2.1. Vision Transformer

Vision Transformer (ViT) is a deep learning model that effectively works in visual tasks by dividing images into fixed-size patches and processing these patches through the attention mechanism of the Transformer. ViT, an adaptation of the Transformer model originally developed for natural language processing, performs at a level comparable to the best available CNN models, especially when trained on large-scale datasets. The model creates visual representations by considering the

global context, providing comprehensive learning processes [31-32].

### 2.2.2. gMLP

gMLP (Gated Multi-Layer Perceptron) is an artificial neural network structure developed as an alternative to Transformer models, incorporating gated units and not relying on attention mechanisms. This model aims to effectively capture interactions between data points by adding gates that control information flow between traditional multilayer perceptrons. gMLP is particularly notable because it is more computationally efficient and requires fewer parameters [33-34].

### 2.2.3. MLP-Mixer

MLP-Mixer is an innovative deep learning architecture introduced by Google Brain that learns visual representations solely using multilayer perceptrons (MLPs) without resorting to attention mechanisms or convolutional layers. The model first divides the image into patches and then processes these patches using two types of MLPs: one designed to capture interactions across patches (along channels) and another within patches (across patches). This approach allows the MLP-Mixer to handle spatial and feature-based information separately, and it can achieve high performance when trained on large datasets [35-37].

### 2.2.4. F-Net

F-Net is a deep learning model that does not use an attention mechanism but instead relies on Fourier transformations. It replaces the computationally expensive self-attention layers of the original Transformer model with simple Fourier transformation operations, performing frequency analysis on the data. This allows F-Net to offer a more computationally efficient alternative for natural language processing and other sequential modeling tasks. F-Net's performance can approach that of models trained using attention mechanisms in some tasks while operating much faster and using fewer resources. The model's benefit is particularly notable in large datasets and situations requiring the processing of long sequences [38].

## 2.3. Performance Metrics

Deep learning performance metrics are used to determine how models perform in classification or regression tasks. Among these metrics: Accuracy shows the percentage of correct predictions among all predictions. Precision indicates how much of a predicted class actually belongs to that class. Recall shows the proportion of actual positives that were correctly predicted. F1 Score is calculated as the harmonic mean of precision and recall and represents the balanced performance of the model. ROC Curve and AUC Value evaluate a classifier's performance from a broader perspective. In this study, metrics such as accuracy, precision, recall, F1 score, and ROC AUC value were used to measure the classification capabilities of deep

learning models. These metrics reveal the model's overall accuracy, reliability, and efficiency in detail. Accuracy, precision, recall formulas are given in equations 1-3.

$$Accuracy = \frac{TP + TN}{TP + TN + FP + FN} \quad (1)$$

$$Precision = \frac{TP}{TP + FP} \quad (2)$$

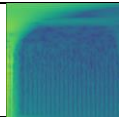
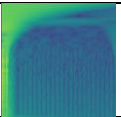
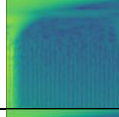
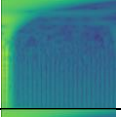
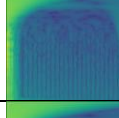
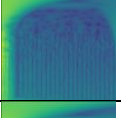
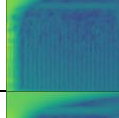
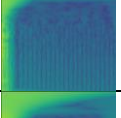
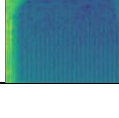
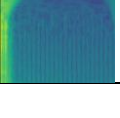
$$Recall = \frac{TP}{TP + FN} \quad (3)$$

## 3. EXPERIMENTAL STUDIES

During the studies, powerful hardware resources were used for data processing and model training. Specifically, a computer with an Intel Xeon E5-2630 v3 processor and 64 GB RAM was chosen. For running deep learning algorithms, the NVIDIA RTX A5000 GPU with 45 GB RAM was utilized. The stages of reading data from the dataset and processing images were carried out using MATLAB, while the deep learning models were implemented through the Python programming language and its specialized libraries. This hardware and software infrastructure ensured that the study was conducted efficiently and effectively.

In this study, images were generated from the Ia current signals in the dataset. The duration of each signal was set to 18 seconds, and analysis was conducted using non-overlapping windows of 1 second each, between 11 and 15 seconds. With this method, 400 time-frequency representations were obtained for each class of Ia signals under a 0.5 Nm load, resulting in a total of 2000 representations. These representations are presented in Table 1 under five different groups. The image creation process followed the procedural steps taken from the experimental studies conducted by Dişli and colleagues in 2023 [39]. This method provided a detailed framework for signal analysis and interpretation, forming the basis of experimental studies.

**Table 1.** Time-Frequency Representations Obtained from Ia Data

	400 Sample			
Healthy		...		
Broken Bar 1		...		
Broken Bar 2		...		
Broken Bar 3		...		
Broken Bar 4		...		

In the following sections of our study, we will evaluate the performance of different deep learning models. In this process, binary classification analysis was performed using four different deep learning models. Our dataset consists of images of healthy and unhealthy rotor currents. In total, there are 400 healthy images versus 1600 unhealthy images. This significant imbalance could potentially lead to problems during model training. To address this imbalance, the dataset was restructured. First, 400 images of healthy rotor currents were selected directly. From the unhealthy group, 100 images were randomly selected from each of the four different subgroups, all containing broken rotor bars. With this selection, each unhealthy subgroup was equally represented, resulting in a total of 400 unhealthy images. Consequently, for binary classification analysis, a balanced dataset containing an equal number of images (400 each) from both healthy and unhealthy groups was created. This approach allows the model to generalize training data better and minimize biases that could arise from imbalanced data distribution.

In our study, the deep learning models gMLP, MLP Mixer, and FNet were used alongside ViT. Figure 2 shows the architecture of the ViT deep learning model. In this model, images of 224x224 pixels are divided into patches of 32x32 pixels. Each image contains a total of 49 patches, meaning that patches are repeated seven times along each dimension of the image. Each patch contains a total of 3,072 data points, indicating that each pixel has three color channels, and thus each patch contains  $32 \times 32 \times 3 = 3,072$  elements. These structural details provide a fundamental framework for understanding how the model processes images.

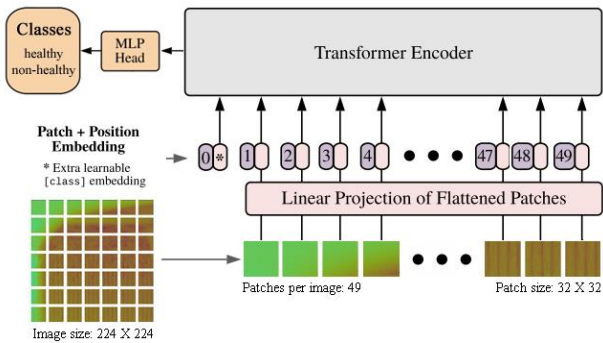


Figure 1. Fault Detection Using the ViT Model

The other deep learning models we used in our study are structurally similar deep learning models. Therefore, the gMLP deep learning model, which achieved the highest performance in our study, is shown in Figure 3. This deep learning model resizes the input images to 512x512 pixels. The model extracts patches from these images with a size of 32x32 pixels and works on each patch. This patch size allows the image to be divided into smaller, manageable parts, enabling the model to learn more detailed and local features on these patches. In total,  $(512 / 32)^2$ , which is 256 patches are obtained from each image, allowing the model to process a wider image in more detail. Each patch is then transformed into a 256-dimensional embedding vector.

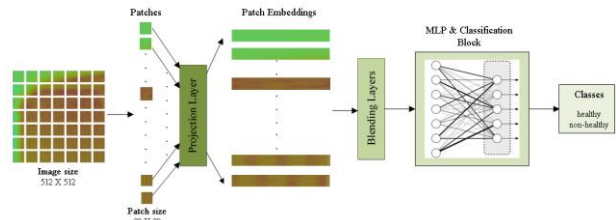
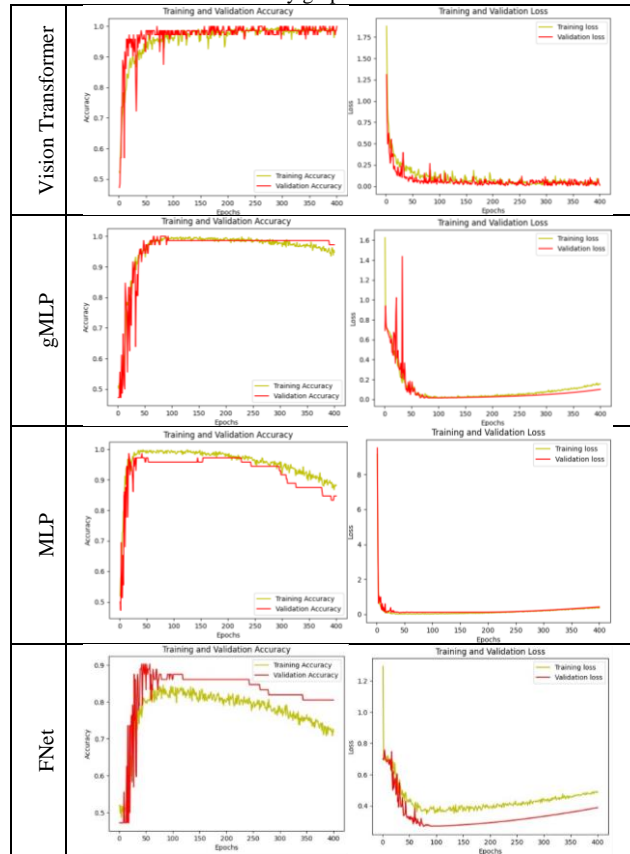


Figure 2. Representation of the gMLP model for fault diagnosis

The training process for all models lasted a total of 400 epochs. Additionally, a dropout rate of 20% was applied to prevent overfitting of the model. These parameters play a significant role in both the configuration and training process of the model.

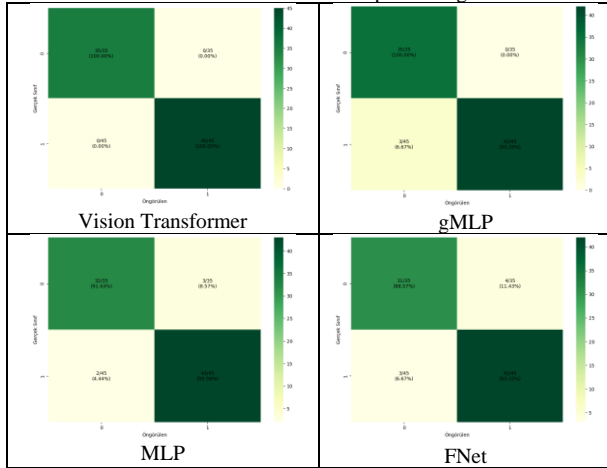
Table 2. The Loss and Accuracy graphs



The Loss and Accuracy graphs of the models examined are presented in Table 2. The Vision Transformer (ViT) model accurately performed all classifications, as documented by the Confusion Matrix. Additionally, this model began to exhibit stable performance after approximately the 100th epoch. When examining the gMLP model, three healthy samples were mistakenly classified as unhealthy. This model began to make stable predictions from the 100th epoch but experienced performance declines after the 250th epoch. The MLP model, on the other hand, generally showed successful performance, making accurate predictions after the 50th epoch, but inconsistencies and performance declines occurred after the 150th epoch. This situation was confirmed by the Confusion Matrix, where four unhealthy samples were classified as healthy, and three healthy samples were classified as unhealthy. The FNet model stands out as the only model that did not show

stable performance throughout the study. Due to the fluctuations in both the accuracy and loss graphs of this model, it was concluded that it did not demonstrate sufficient performance in this study.

**Table 3.** Confusion Matrix Results of Deep Learning Models



The confusion matrix results of the study are presented in Table 3. In Table 4, the performance metrics for each model have been calculated and interpreted according to the following formulas. **The Vision Transformer** has demonstrated excellent performance with 100% accuracy, precision and recall.

$$\text{Accuracy} : \frac{TP+TN}{TP+TN+FP+FN} = \frac{35+45}{35+45+0+0} = 1.00 \text{ (%100\%)}$$

$$\text{Precision} : \frac{TP}{TP+FP} = \frac{35}{35+0} = 1.00 \text{ (%100\%)}$$

$$\text{Recall} : \frac{TP}{TP+FN} = \frac{35}{35+0} = 1.00 \text{ (%100\%)}$$

**gMLP** has demonstrated quite good performance with an accuracy rate of 96.25%. The precision value is 92.1% and the recall value is 100%.

$$\text{Accuracy} : \frac{TP+TN}{TP+TN+FP+FN} = \frac{35+42}{35+42+3+0} = \frac{77}{80} = 0.9625$$

$$\text{Precision} : \frac{TP}{TP+FP} = \frac{35}{35+3} = \frac{35}{38} = 0.921$$

$$\text{Recall} : \frac{TP}{TP+FN} = \frac{35}{35+0} = 1.00 \text{ (%100\%)}$$

**MLP** is performing with an accuracy rate of 93.75%. The precision value is 94.1% and the recall value is 91.4%.

$$\text{Accuracy} : \frac{TP+TN}{TP+TN+FP+FN} = \frac{32+43}{32+43+2+3} = \frac{75}{80} = 0.9375$$

$$\text{Precision} : \frac{TP}{TP+FP} = \frac{32}{32+2} = \frac{32}{34} = 0.941$$

$$\text{Recall} : \frac{TP}{TP+FN} = \frac{32}{32+3} = \frac{32}{35} = 0.914$$

**FNet** is performing with an accuracy rate of 91.25%. The precision value is 91.2% and the recall value is 88.6%.

$$\text{Accuracy} : \frac{TP+TN}{TP+TN+FP+FN} = \frac{31+42}{31+42+3+4} = \frac{77}{80} = 0.9125$$

$$\text{Precision} : \frac{TP}{TP+FP} = \frac{31}{31+3} = \frac{31}{34} = 0.912$$

$$\text{Recall} : \frac{TP}{TP+FN} = \frac{31}{31+4} = \frac{31}{35} = 0.886$$

Other metrics and all results are provided in Table 4.

**Table 4.** Performance Metrics of Deep Learning Models

Model	Accuracy	precision	recall	F1 score	Cohens Kappa	ROC AUC
Vision Transformer	%100	1.00	1.00	1.00	1.00	1.00
gMLP	%96,25	0.921	1.00	0.959	0.925	0.967
MLP mixer	%93,75	0.941	0.914	0.927	0.875	0.933
FNet	%91,25	0.912	0.886	0.899	0.825	0.909

In Table 4, the performance metrics of four different deep learning models—Vision Transformer, gMLP, MLP and FNet are examined comparatively. The Vision Transformer model achieved perfect values (1.00) in accuracy, precision, and recall, with an accuracy rate of 100%. This indicates that the model classified all examples in the test set flawlessly. The gMLP model demonstrated very high performance with an accuracy rate of 96.25%, achieving precision and recall values of 0.921 and 1.00, respectively. Additionally, it has a high F1 score of 0.959 and a ROC AUC value of 0.967, indicating the model's balance in classification and overall success as a classifier. The MLP model, with an accuracy of 93.75%, precision of 0.941, and recall of 0.914, showed slightly lower performance compared to the gMLP model. Nevertheless, the F1 score of 0.927 and the ROC AUC value of 0.933 indicate that the model is still a strong classifier. The FNet model, which performed lower than the other three models, has an accuracy rate of 91.25%. However, its precision value of 0.912 shows a high level of correct positive predictions. The recall value of 0.886 indicates a weakness in detecting positive class examples, while the F1 score of 0.899 and the ROC AUC value of 0.909 demonstrate that the model can still deliver acceptable performance under limited conditions.

#### 4. RESULTS

Bu In this study, deep learning models that have recently gained prominence such as ViT, gMLP, MLP Mixer, and FNet were used to perform fault diagnosis on a preprocessed dataset based on current information from electrical motors. These data were analyzed to classify motor conditions as "healthy" and "unhealthy". Experimental results indicated that the Vision Transformer model outperformed the other models; this observation is supported by the stability of the model and its remarkable accuracy rate of 100%. These findings suggest that Vision Transformer is a promising candidate for real-time fault diagnosis applications in electric motors. Particularly, the role this technology could play in the development of real-time fault detection and preventive maintenance strategies could enhance efficiency in industrial processes, thus reducing operational costs. Further studies aim to explore in more detail how effective this model can be under real-world conditions using current and vibration data obtained from asynchronous motors. This could provide valuable insights not only for fault diagnosis but also for process optimization and resource management.

## REFERENCES

- [1] Pelly, Brian R. "Thyristor phase-controlled converters and cycloconverters: operation, control, and performance." (No Title) (1971).
- [2] Hughes, Austin, and Bill Drury. *Electric motors and drives: fundamentals, types and applications*. Newnes, 2019.
- [3] Nasar, Syed A., and Ion Boldea. "The induction machine handbook." *Electric Power Engineering Series*, Boca raton, Florida, USA: CRC Press LLC (2002).
- [4] Sen, Paresh Chandra. *Principles of Electric Machines and Power Electronics*, International Adaptation. John Wiley & Sons, 2021.
- [5] Pillay, Pragasen, and Ramu Krishnan. "Modeling, simulation, and analysis of permanent-magnet motor drives. I. The permanent-magnet synchronous motor drive." *IEEE Transactions on industry applications* 25.2 (1989): 265-273.
- [6] Singh, Arvind, et al. "A review of induction motor fault modeling." *Electric Power Systems Research* 133 (2016): 191-197.
- [7] Jing, Luyang, et al. "A convolutional neural network based feature learning and fault diagnosis method for the condition monitoring of gearbox." *Measurement* 111 (2017): 1-10.
- [8] Lou, Xinsheng, and Kenneth A. Loparo. "Bearing fault diagnosis based on wavelet transform and fuzzy inference." *Mechanical systems and signal processing* 18.5 (2004): 1077-1095.
- [9] Zhu, Huibin, et al. "Bearing fault feature extraction and fault diagnosis method based on feature fusion." *Sensors* 21.7 (2021): 2524.
- [10] Banerjee, Tribeni Prasad, and Swagatam Das. "Multi-sensor data fusion using support vector machine for motor fault detection." *Information Sciences* 217 (2012): 96-107.
- [11] Bera, Arka, Arindam Dutta, and Ashis K. Dhara. "Deep learning based fault classification algorithm for roller bearings using time-frequency localized features." *2021 International Conference on Computing, Communication, and Intelligent Systems (ICCCIS)*. IEEE, 2021.
- [12] Lu, Chen, Zhenya Wang, and Bo Zhou. "Intelligent fault diagnosis of rolling bearing using hierarchical convolutional network based health state classification." *Advanced Engineering Informatics* 32 (2017): 139-151.
- [13] Janssens, Olivier, et al. "Convolutional neural network based fault detection for rotating machinery." *Journal of Sound and Vibration* 377 (2016): 331-345.
- [14] Shen, Sheng, et al. "A physics-informed deep learning approach for bearing fault detection." *Engineering Applications of Artificial Intelligence* 103 (2021): 104295.
- [15] Hu, Jie, and Sier Deng. "Rolling bearing fault diagnosis based on wireless sensor network data fusion." *Computer communications* 181 (2022): 404-411.
- [16] Oh, Jin Woo, and Jongpil Jeong. "Data augmentation for bearing fault detection with a light weight CNN." *Procedia Computer Science* 175 (2020): 72-79.
- [17] Chen, ZhiQiang, Chuan Li, and René-Vinicio Sanchez. "Gearbox fault identification and classification with convolutional neural networks." *Shock and Vibration* 2015 (2015).
- [18] Liu, Shuangjie, et al. "Bearing fault diagnosis based on improved convolutional deep belief network." *Applied Sciences* 10.18 (2020): 6359.
- [19] Sun, Wenjun, et al. "A sparse auto-encoder-based deep neural network approach for induction motor faults classification." *Measurement* 89 (2016): 171-178.
- [20] Kumar, Dileep, et al. "Towards soft real-time fault diagnosis for edge devices in industrial IoT using deep domain adaptation training strategy." *Journal of Parallel and Distributed Computing* 160 (2022): 90-99.
- [21] Kao, I-Hsi, et al. "Analysis of permanent magnet synchronous motor fault diagnosis based on learning." *IEEE Transactions on Instrumentation and Measurement* 68.2 (2018): 310-324.
- [22] Hoang, Duy Tang, and Hee Jun Kang. "A motor current signal-based bearing fault diagnosis using deep learning and information fusion." *IEEE Transactions on Instrumentation and Measurement* 69.6 (2019): 3325-3333.
- [23] Aydin, İlhan, Mehmet Karakose, and Erhan Akin. "An approach for automated fault diagnosis based on a fuzzy decision tree and boundary analysis of a reconstructed phase space." *ISA transactions* 53.2 (2014): 220-229.
- [24] Ince, Turker, et al. "Real-time motor fault detection by 1-D convolutional neural networks." *IEEE Transactions on Industrial Electronics* 63.11 (2016): 7067-7075.
- [25] Jia, Feng, et al. "Deep neural networks: A promising tool for fault characteristic mining and intelligent diagnosis of rotating machinery with massive data." *Mechanical systems and signal processing* 72 (2016): 303-315.
- [26] Bonnett, Austin H. "Root cause AC motor failure analysis with a focus on shaft failures." *IEEE transactions on industry applications* 36.5 (2000): 1435-1448.
- [27] Thomson, William T., and Ronald J. Gilmore. "Motor Current Signature Analysis To Detect Faults In Induction Motor Drives-Fundamentals, Data Interpretation, And Industrial Case Histories." *Proceedings of the 32nd turbomachinery Symposium*. Texas A&M University. Turbomachinery Laboratories, 2003.
- [28] Akkurt, İbrahim, and Hayri Arabacı. "Sürücüden Beslenen Asenkron Motorlarda Rulman Arızalarının Stator Akımı Kullanarak Tespiti." *Uluslararası Doğu Anadolu Fen Mühendislik ve Tasarım Dergisi* 1.2 (2019): 122-134.
- [29] Kaya, Kadir, and Abdurrahman Ünsal. "Yapay sinir ağlarıyla asenkron motor çoklu arızalarının tespiti ve sınıflandırılması." *Politeknik Dergisi* 25.4 (2022): 1687-1699.
- [30] Treml, Aline Elly, et al. "Experimental database for detecting and diagnosing rotor broken bar in a



- three-phase induction motor." IEEE DataPort (2020).
- [31] Dosovitskiy, Alexey, et al. "An image is worth 16x16 words: Transformers for image recognition at scale." arXiv preprint arXiv:2010.11929 (2020).
- [32] Khan, Salman, et al. "Transformers in vision: A survey." ACM computing surveys (CSUR) 54.10s (2022): 1-41.
- [33] Liu, Hanxiao, et al. "Pay attention to mlps." Advances in neural information processing systems 34 (2021): 9204-9215.
- [34] Gorishniy, Yury, et al. "Revisiting deep learning models for tabular data." Advances in Neural Information Processing Systems 34 (2021): 18932-18943.
- [35] Tolstikhin, Ilya O., et al. "Mlp-mixer: An all-mlp architecture for vision." Advances in neural information processing systems 34 (2021): 24261-24272.
- [36] Melas-Kyriazi, Luke. "Do you even need attention? a stack of feed-forward layers does surprisingly well on imagenet." arXiv preprint arXiv:2105.02723 (2021).
- [37] Hou, Qibin, et al. "Vision permutator: A permutable mlp-like architecture for visual recognition." IEEE transactions on pattern analysis and machine intelligence 45.1 (2022): 1328-1334.
- [38] Lee-Thorp, James, et al. "Fnet: Mixing tokens with fourier transforms." arXiv preprint arXiv:2105.03824 (2021).
- [39] Dişli, Fırat, Mehmet Gedikpınar, and Abdulkadir Sengur. "Deep transfer learning-based broken rotor fault diagnosis for Induction Motors." Turkish Journal of Science and Technology 18.1 (2023): 275-290.

## Detection of Bean Rust (*Uromyces appendiculatus*) Disease Under Field Conditions Using Thermal Imaging

Hilal ERDOĞAN<sup>1\*</sup> 

<sup>1</sup> Bursa Uludağ University, Agricultural Faculty, Department of Biosystems, Bursa, Türkiye  
Hilal ERDOĞAN ORCID No: 0000-0002-0387-2600

\*Corresponding author: [hilalerdogan@uludag.edu.tr](mailto:hilalerdogan@uludag.edu.tr)

(Received: 05.01.2024, Accepted: 08.07.2024, Online Publication: 26.09.2024)

### Keywords

Bean,  
Thermal imaging,  
*Uromyces  
appendiculatus*

**Abstract:** Among the factors causing yield losses in agricultural fields, plant diseases are known to be one of the most significant. For many years, pesticides have been used to control these diseases. However, due to the unintended toxic effects of pesticides on non-target organisms in recent years, there have been restrictions on their usage. At this point, early warning systems aiming to reduce the use of pesticides have come to the forefront. This study aims to detect bean rust disease (*Uromyces appendiculatus*) at an early stage using thermal imaging methods. Surface temperatures of healthy and infected leaves were measured at 60-minute intervals over a three-week period. Throughout this period, it was observed that the average daily temperatures of both infected and healthy leaves were below ambient temperatures. According to the obtained results, it was determined that leaves infected with the pathogen exhibited temperatures approximately 2°C lower than those of healthy leaves. Consequently, thermal imaging is considered to play a crucial role in the potential early detection of bean rust disease.

8

## Termal Görüntüleme ile Fasulye Pası (*Uromyces appendiculatus*) Hastalığının Arazi Koşullarında Tespiti

### Anahtar Kelimeler

Fasulye,  
Termal  
görüntüleme,  
*Uromyces  
appendiculatus*

**Öz:** Tarım alanlarında verim kayıplarına neden olan faktörler arasında bitki hastalıklarının en önemlilerinden biri olduğu bilinmektedir. Yıllardır, bu hastalıkları kontrol etmek için pestisitler kullanılmaktadır. Ancak, son yıllarda pestisitlerin istenmeyen toksik etkileri nedeniyle, bunların kullanımına yönelik kısıtlamalar getirilmiştir. Bu noktada, pestisit kullanımını azaltmayı amaçlayan erken uyarı sistemleri ön plana çıkmıştır. Bu çalışma, termal görüntüleme yöntemlerini kullanarak fasulye pas hastalığını (Etmen: *Uromyces appendiculatus*) erken bir aşamada tespit etmeyi amaçlamaktadır. Sağlıklı ve enfekte yaprakların yüzey sıcaklıkları üç haftalık bir süre boyunca 60 dakikalık aralıklarla ölçülmüştür. Bu süre boyunca hem enfekte hem de sağlıklı yaprakların ortalama günlük sıcaklıklarının çevre sıcaklıklarının altında olduğu gözlemlenmiştir. Elde edilen sonuçlara göre, patojenle enfekte yaprakların, sağlıklı yaprakların sıcaklıklarından yaklaşık olarak 2°C daha düşük olduğu belirlenmiştir. Sonuç olarak, termal görüntülemenin fasulye pasının potansiyel erken tespitinde kritik bir rol oynadığı düşünülmektedir.

### 1. INTRODUCTION

The increase in the world's population has led to an escalation in food demand over the years [1, 2]. This situation highlights the increasing significance of agricultural production and emphasizes measures to reduce crop losses in agricultural production. Among the most critical factors leading to product losses in agricultural production are plant diseases and pests [3-5].

Pesticides have been used for many years in the fight against plant diseases and pests. However, due to the emergence of unwanted side effects of pesticides, there have been restrictions on their usage [6, 7].

Restrictions on pesticide use have brought other alternative methods to the forefront. One of the most significant among these is precision agriculture methods. Precision agriculture aims for the right input, in the right

amount, at the right place, at the right time [8, 9]. The use of precision agriculture methods is crucial in detecting diseases, especially at an early stage, before spreading throughout the entire area [10-12]. Early-stage detection without spreading throughout the entire area enables less chemical usage. In recent years, thermal imaging methods, potentially used for early disease detection, have gained prominence in this regard [13, 14].

Infrared rays are part of the electromagnetic spectrum and are emitted depending on the temperature of objects. Each object in nature has its own heat energy, invisible to the human eye, emitted into the environment. In thermal imaging systems, this heat energy is captured and, based on the degree of heat, a picture is obtained by colorizing it. It is challenging to perceive an object that has the same color as the background for RGB cameras, as they require light and color. Near Infrared (NIR), Mid-Wave Infrared (MWIR), and Long-Wave Infrared (LWIR) are distinct divisions of the infrared spectrum, which is a subset of the electromagnetic spectrum, categorized based on their applications. However, for thermal cameras, the situation is very different. Even if both objects have the same color, the difference in heat enables the object's appearance to be easily captured as an image [15]. Thermal cameras can detect infrared energy from various distances based on the sizes of their lenses without physically touching the object. Thermal cameras detect the infrared energy emitted by the object in the environment through the camera's lens and send this information to the infrared detector inside the camera for image processing [16]. As a result of these processes, the information is converted into an image that we can see. This process is called thermography, converting infrared rays into a visible image. This technique is used in many fields, especially in evaluating seedling vitality [17-19], predicting soil moisture status, estimating plant water stress, planning irrigation, identifying plants affected by diseases and pathogens [20-24], and assessing the ripeness of fruits and vegetables in agricultural activities and the food industry. Thermal imaging advantages include non-contact, rapid results, and high sensitivity [25]. Additionally, modern thermal cameras can operate at room temperature, making their usage widespread. The intensity of radiation emitted by an object is a function dependent on the surface temperature; the higher the temperature of an object, the greater the intensity of the infrared radiation emitted by the object [26]. Thermal imaging is a technique that converts the radiation emitted by an object into temperature data without physical contact. Thermal imaging methods are based on detecting the localized temperature increase or decrease resulting from the stress a plant develops in response to the infection of diseases in the area where the infection occurs. Studies have shown that it is possible to detect many diseases based on temperature differences at an early stage [24, 27-29].

Bean rust disease (*Uromyces appendiculatus* Pers. C.K.) (Pucciniales: Pucciniaceae) is a fungal disease-causing varying level of intensity, density, and yield and quality

losses depending on the severity of the disease and the host reaction. This disease causes spots on the leaves, stems, and even fruits of plants [30-32]. Bean rust disease is characterized by yellow, orange, or brown spots on the upper surface of the leaves. This pathogen, which has no alternate hosts, spends all its stages on the same plant. During winter, it appears on leaves as teliospores, mostly in dark brown, and during summer, it appears as uredospores, which are red in color, seen on the leaves [33-36]. Bean rust disease spreads through spores, which can be transmitted from one plant to another through wind or irrigation. Additionally, not removing infected plant residues from the field facilitates the spread of the disease [34, 37]. This disease agent, causing yield losses in beans consumed as food worldwide, holds economic importance.

The purpose of this study is to determine the potential use of thermal imaging methods for the early diagnosis of bean rust disease in bean plants. Early diagnosis of infection will enable the control of the disease agent before spreading to all healthy plants, allowing for the application of appropriate control methods. Thus, the early detection of the disease through thermal imaging can identify the economic damage threshold at the right time and prevent excessive pesticide usage. Moreover, with thermal cameras integrated into robotic systems in subsequent studies, the density of the disease can be detected in areas where infection has started but is not visible to the naked eye, allowing for proper spraying in the right place and amount.

## 2. MATERIAL AND METHOD

This study was carried out in the plant production areas where bean cultivation belongs to Bursa Uludağ University TUAM Farm Directorate. The potential detection of bean rust disease on bean plants (May Magnum®) due to the stress caused by the temperature change on the plant was investigated using thermal imaging methods.

### 2.1. Temperature Data and Disease Diagnosis

In this study, LWIR cameras have been acknowledged as more suitable for the accurate detection of plant diseases due to their capability of determining only the temperatures emitted by the target object without being influenced by many other factors during measurement [24, 38]. Within the LWIR range (8-14  $\mu\text{m}$ ), most objects, including plants, exhibit high emissivity, meaning they efficiently emit infrared radiation. This high emissivity leads to more precise temperature measurements and improved thermal imaging. The study employed a portable LWIR camera with a resolution of 464 x 348 pixels and a thermal sensitivity of less than 40 millikelvin (mK) [39]. To achieve more accurate results, the emissivity was set to approximately 1, and a lens with a resolution of 0.90 m/rad pixel was utilized [24].

Measurements were conducted using a thermal camera on the leaves of both diseased and healthy plants present in an area of 250 m<sup>2</sup>. Additionally, ambient temperatures

were determined using a portable thermometer. Throughout the study, all thermal measurements were manually taken using a portable thermal camera (FLIR T530® Teledyne FLIR LLC, U.S.) from randomly selected diseased and healthy leaves of individual plants. The average temperatures of leaves infected by *U. appendiculatus* were monitored and recorded simultaneously with the temperatures of healthy leaf surfaces, along with the average environmental temperature. Teledyne FLIR Thermal Studio® software was employed to compute the average temperatures of leaf surfaces from thermal images. Healthy leaves were used as controls. This study was conducted during the flowering stage of bean plants.

Samples obtained from the field were processed to prepare *U. appendiculatus* disease specimens and were identified under a microscope [40-42]. A diagnostic method similar to the one used by Shaik and Steadman (1989) was employed.

## 2.2. Measurement Time and Distance

In the area where the study took place, thermal measurements were conducted on the leaves of both diseased and healthy plants using a thermal camera. During the temperature measurements on the leaves, environmental factors such as the intensity of sunlight can affect leaf temperatures [24, 43]. Therefore, thermal images of all labeled leaves were obtained every 60 minutes from 06:00 to 17:00 for a duration of 3 weeks (21 days). Temperature measurements were taken from 7 different points (replicates) for each hourly measurement. After 21 days, the thermal imaging process was concluded due to the healthy plants becoming infected. Additionally, a handheld thermometer was used to record ambient temperatures. The thermal imaging process was conducted manually. High-resolution (pixel) cameras and close-range shots reduce the margin of error in temperature measurements [24]. In this research, measurements were taken from a distance of 0.3 meters from the leaf surface using a thermal camera to enhance the precision of temperature measurements. All temperature measurements on the leaves were conducted at approximately the same angle (90°) and distance (0.3 m) [24, 43, 44]. The 'FLIR Thermal Studio' tool was utilized to calculate the average temperatures of infected and healthy leaf surfaces.

## 2.3. Statistical Analysis

The statistical analysis was conducted using data involving the daily average surface temperatures of leaves infected by *U. appendiculatus*, leaves with no infection, and concurrently measured ambient temperatures. Significant differences between temperature values were determined using variance analysis (ANOVA) employing the JMP 16.0® algorithm. Student's t-test was performed to examine average differences (at 0.05 significance level).

## 3. RESULTS

According to the obtained results, a decrease in temperature was observed in bean plant leaves infected with *U. appendiculatus*. Firstly, temperature values obtained from plant leaves between 06:00 and 17:00 were examined. The statistical analysis was performed by determining the average temperature values for 1, 2, and 3 weeks of ambient temperature, non-infected plant leaf temperature, and infected plant leaf temperature.

In Figure 1, although not easily noticeable to the naked eye, the area where the disease has spread is clearly depicted due to the temperature difference captured by the thermal camera. The leaf showing early-stage infection (B) was determined to have a temperature value of 9.7 °C. This value was found to be 7.3 °C for the infected leaf (A).



**Figure 1.** Temperature differences obtained using thermal imaging methods between a leaf where the infection has spread and a leaf where the infection has just started in an infected plant.

Upon examining Figure 2, a homogeneous color distribution is observed on the surface of a healthy leaf. When compared with Figure 1, both appear healthy in RGB imaging, yet in reality, Figure 1 indicates the onset and spread of the disease in those leaves.

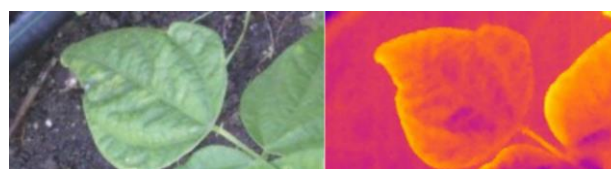


**Figure 2.** Thermal image obtained from the surface of a healthy leaf.

Figure 3 displays advanced stage rust disease in the thermal and RGB images. Upon examining the results, it was observed that the obtained thermal images showed higher temperature values compared to healthy leaves (Figure 3) and leaves where the infection had just begun (Figure 1).



**Figure 3.** Thermal image of a leaf surface severely affected by infection.

According to the obtained results, at the end of the 1<sup>st</sup>, 2<sup>nd</sup>, and 3<sup>rd</sup> weeks, ambient temperature values were determined as 20.5, 21.1, and 21.3 °C, respectively. Examining the temperature values obtained from non-infected bean leaves revealed readings of 13.42, 13.81,

and 13.96 °C, respectively. Lastly, for bean plant leaves infected with *U. appendiculatus*, lower values were recorded as 11.95, 12.38, and 12.61 °C compared to the other obtained temperatures. On average, a temperature difference of 2 °C was identified between infected and non-infected bean leaves. In some plant leaves, this temperature difference reached approximately 3 °C (Figure 1). Upon considering all these values, statistically significant differences among the averages were obtained (Figure 4).

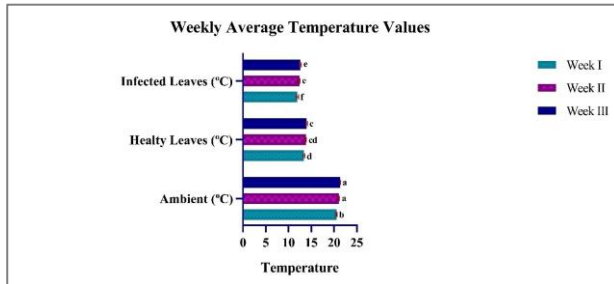


**Figure 4.** Average temperature values of ambient, infected, and non-infected leaves. Columns with the same letters represent no significant difference.

Throughout the three-week period, the daily average surface temperatures of infected and healthy leaves, along with the daily average ambient temperature, were statistically evaluated. The letters on top of the bars in Figure 4 indicate significant differences between the measurements ( $F: 806.13$ ,  $df: 8;54$ ,  $p < 0.0001$ ).

#### 4. DISCUSSION AND CONCLUSION

Fungal diseases cause stress or dead in plants. This stress can affect various physiological processes in plants such as photosynthesis, respiration, and transpiration. These factors can lead to temperature changes, particularly in plant parts, especially in leaves [45-48]. Recent studies employing thermal imaging techniques have facilitated the early detection of plant diseases without spreading across the entire field [24, 49, 50]. The use of thermal imaging techniques for the detection of plant diseases, especially those not showing any symptoms in plant parts at an early stage, is becoming increasingly prevalent [38, 51]. Therefore, the aim of this study was to potentially detect bean rust using thermal imaging techniques and to determine the temperature differences caused by stress. The study revealed that bean leaves infected with *U. appendiculatus* were cooler compared to the leaves unaffected by *U. appendiculatus* infection.

Previous studies have demonstrated the effective detection of virus and fungal infections through thermal imaging. For instance, Pineda et al. [50] observed the accumulation of local salicylic acid (SA) and consequent temperature increase in plant areas exhibiting hypersensitive response (HR) to Tobacco Mosaic Virus (TMV) infection. Conversely, in the conducted study, a decrease in temperature was observed in bean leaves infected with *U. appendiculatus*. This is believed to be due to the spores formed on bean leaves, which could hinder photosynthesis. Hellebrand et al. [52] investigated the response of powdery mildew disease (*Blumeria* [syn.

*Erysiphe] graminis* DC. f. sp. *tritici*) in wheat plants using thermal imaging. According to their findings, they determined an average temperature of 20.1 °C in infected plants and 21.0 °C in healthy, non-infected plants.

In the study conducted by Erdoğan et al. [24], the potential detection of powdery mildew (*Sphaerotheca fuliginea* Schlech. Polacci) in zucchini plants using thermal imaging methods was evaluated. Examination of the temperature values in zucchini leaves infected with *S. fuliginea* revealed an average temperature of 8.2 °C, whereas in non-infected leaves, this value was observed to be around 10.2 °C. The results obtained from this study align with the findings of the current research. Oerke et al. [53] investigated the potential of thermal imaging methods in detecting *Pseudoperonospora cubensis* Berk. and Curt., which causes mildew in cucumbers. Their results indicated that infected plant tissues had lower temperatures compared to non-infected plant tissues. Therefore, these findings corroborate with the results obtained from the present study.

In the study conducted by Zhu et al. [49], the temperature variations induced by stress caused by mosaic virus in tomatoes and rust diseases in wheat plants were examined. The results indicated that the mosaic virus in tomatoes led to a temperature difference ranging from 0.2°C to 1.7°C, while the rust in wheat caused a temperature variance of 0.4°C to 2°C. It was observed that with the increasing spread of the disease within the plant, there was a decrease in the temperature observed in the plants. These findings align with the outcomes of the current research. Bhakta et al. [48] integrated thermal imaging methods with Decision Trees (DTs) models, enabling the early detection of bacterial leaf blight in rice based on temperature changes in the plant. Similarly, Singh et al. [29] utilized DTs models to identify the onset of wheat yellow rust disease by detecting temperature variations in the plants at the early stages of symptoms.

Disease-causing agents, environmental conditions, time, or plant-related factors can lead to an increase or decrease in leaf surface temperature. It has been observed that these temperature changes, although not visually discernible, can be detected using thermal imaging methods. This suggests a significant potential for early disease detection. The ability to control diseases at an early stage could contribute to preventing diseases before spreading throughout the entire field, thereby reducing yield losses and benefiting the agricultural sector. Additionally, this approach may enhance environmental sustainability by reducing the use of environmentally harmful chemicals. Finally, the integration of thermal imaging methods with models such as Convolutional Neural Networks (CNN) and YOLO holds great promise for agricultural mechanization.

#### Acknowledgement

I thank Yavuz Selim Şahin for diagnosing the disease and getting images. Also, I extend my gratitude to

Alperen Kaan Bütüner and Teledyne FLIR Türkiye for their technical support during the thermal imaging phase.

## REFERENCES

- [1] Gundersen C, Ziliak JP. Food insecurity and health outcomes. *Health affairs*. 2015; 34(11): 1830-1839.
- [2] Zurek M, Hebinck A, Selomane O. Climate change and the urgency to transform food systems. *Science* 2022; 376(6600): 1416-1421.
- [3] Meier MS, Stoessel F, Jungbluth N, Juraske R, Schader C, Stolze M. Environmental impacts of organic and conventional agricultural products—Are the differences captured by life cycle assessment?. *Journal of Environmental Management*. 2015; 149: 193-208.
- [4] Clark M, Tilman D. Comparative analysis of environmental impacts of agricultural production systems, agricultural input efficiency, and food choice. *Environmental Research Letters*. 2017; 12(6): 064016.
- [5] Arora NK. Impact of climate change on agriculture production and its sustainable solutions. *Environmental Sustainability*. 2019; 2(2): 95-96.
- [6] Alengebawy A, Abdelkhalek ST, Qureshi SR, Wang MQ. Heavy metals and pesticides toxicity in agricultural soil and plants: Ecological risks and human health implications. *Toxics*. 2021; 9(3): 42.
- [7] Şahin YS, Erdiñç A, Bütüner AK, Erdođan H. Detection of *Tuta absoluta* larvae and their damages in tomatoes with deep learning-based algorithm. *International Journal of Next-Generation Computing*. 2023a.; 14(3): 555-565
- [8] Kurtulmuş F, Sefil K, Kargacı K, Arslan S. Bilgisayarlı görme esaslı deđişken oranlı bir alev makinası için görüntü alma sisteminin optimizasyonu. *Bursa Uludađ Üniversitesi Ziraat Fakültesi Dergisi*. 2020; 34(1): 135-147.
- [9] Erdođan H, Ünal H, Susurluk İA, Lewis EE. Precision application of the entomopathogenic nematode *Heterorhabditis bacteriophora* as a biological control agent through the Nemabot. *Crop Protection*. 2023a.; 106429.
- [10] Nawaz M, Mabubu JI, Hua H. Current status and advancement of biopesticides: microbial and botanical pesticides. *Journal of Entomology and Zoology Studies*. 2016; 4(2): 241-246.
- [11] Duhan JS, Kumar R, Kumar N, Kaur P, Nehra K, Duhan S. Nanotechnology: The new perspective in precision agriculture. *Biotechnology Reports*. 2017; 15: 11-23.
- [12] Samada LH, Tambunan USF. Biopesticides as promising alternatives to chemical pesticides: A review of their current and future status. *Online Journal of Biological Sciences*. 2020; 20(2): 66-76.
- [13] Puri V, Nayyar A, Raja L. Agriculture drones: A modern breakthrough in precision agriculture. *Journal of Statistics and Management Systems*. 2017; 20(4): 507-518.
- [14] Sishodia RP, Ray RL, Singh SK. Applications of remote sensing in precision agriculture: A review. *Remote Sensing*. 2020; 12(19): 3136.
- [15] Ballester C, Jiménez-Bello MA, Castel JR, Intrigliolo DS. Usefulness of thermography for plant water stress detection in citrus and persimmon trees. *Agricultural and forest Meteorology*. 2013; 168, 120-129.
- [16] Khanal S, Fulton J, Shearer S. An overview of current and potential applications of thermal remote sensing in precision agriculture. *Computers and Electronics in Agriculture*. 2017; 139, 22-32.
- [17] Kranner I, Kastberger G, Hartbauer M, Pritchard HW. Noninvasive diagnosis of seed viability using infrared thermography. *Proceedings of the National Academy of Sciences*. 2010; 107(8), 3912-3917.
- [18] Men S, Yan L, Liu J, Qian H, Luo Q. A classification method for seed viability assessment with infrared thermography. *Sensors*. 2017; 17(4), 845.
- [19] ElMasry G, ElGamal R, Mandour N, Gou P, Al-Rejaie S, Belin E, Rousseau D. Emerging thermal imaging techniques for seed quality evaluation: Principles and applications. *Food Research International*. 2020; 131, 109025.
- [20] Grant OM, Chaves MM, Jones HG. Optimizing thermal imaging as a technique for detecting stomatal closure induced by drought stress under greenhouse conditions. *Physiologia Plantarum*. 2006; 127(3), 507-518.
- [21] Wiriya-Alongkorn W, Spreer W, Ongprasert S, Spohrer K, Pankasemsuk T, Mueller J. Detecting drought stress in longan tree using thermal imaging. *Maejo International Journal of Science and Technology*. 2013; 7(1), 166.
- [22] Hong M, Bremer DJ, van der Merwe D. Thermal imaging detects early drought stress in turfgrass utilizing small unmanned aircraft systems. *Agrosystems, Geosciences & Environment*. 2019; 2(1), 1-9.
- [23] Bilgili A. Thermal Image Processing for Automatic Detection of Fusarium Root and Crown Rot Disease In Tomato Plants. *Dicle Üniversitesi Mühendislik Fakültesi Mühendislik Dergisi*. 2023; 14(4), 611-619.
- [24] Erdođan H, Bütüner AK, Şahin YS. Detection of Cucurbit Powdery Mildew, *Sphaerotheca fuliginea* (Schlech.) Polacci by Thermal Imaging in Field Conditions. *Scientific Papers Series Management, Economic Engineering in Agriculture and Rural Development*. 2023b; 23(1): 189-192.
- [25] Vadivambal R, ve Jayas DS. Applications of thermal imaging in agriculture and food industry—a review. *Food and Bioprocess Technology*. 2011; 4: 186-199.
- [26] Meola C, Carlomagno GM. Recent advances in the use of infrared thermography. *Measurement Science and Technology*. 2004; 15(9): R27.
- [27] Mutka AM, Bart RS. Image-based phenotyping of plant disease symptoms. *Frontiers in plant science*. 2015; 5: 734.
- [28] Kim J, Kweon SG, Park J, Lee H, Kim KW. Digital infrared thermal imaging of crape myrtle leaves infested with sooty mold. *The Plant Pathology Journal*. 2016; 32(6): 563.
- [29] Singh RN, Krishnan P, Singh VK, Das B. Estimation of yellow rust severity in wheat using visible and thermal imaging coupled with machine

- learning models. Geocarto International. 2023; 38(1): 2160831.
- [30] Sandlin CM, Steadman JR, Araya CM, Coyne DP. Isolates of *Uromyces appendiculatus* with specific virulence to landraces of *Phaseolus vulgaris* of Andean origin. Plant disease. 1999; 83(2): 108-113.
- [31] Araya CM, Alleyne AT, Steadman JR, Eskridge KM, Coyne DP. Phenotypic and genotypic characterization of *Uromyces appendiculatus* from *Phaseolus vulgaris* in the Americas. Plant Disease. 2004; 88(8): 830-836.
- [32] Acevedo M, Steadman JR, Rosas JC. *Uromyces appendiculatus* in Honduras: pathogen diversity and host resistance screening. Plant disease. 2013; 97(5): 652-661.
- [33] Bhairi SM, Staples RC, Freve P, Voder OC. Characterization of an infection structure-specific gene from the rust fungus *Uromyces appendiculatus*. Gene. 1989; 81(2): 237-243.
- [34] Mersha Z, Hau B. Effects of bean rust (*Uromyces appendiculatus*) epidemics on host dynamics of common bean (*Phaseolus vulgaris*). Plant pathology. 2008; 57(4): 674-686.
- [35] Abo-Elyousr KA, Abdel-Rahim IR, Almasoudi NM, Alghamdi SA. Native endophytic *Pseudomonas putida* as a biocontrol agent against common bean rust caused by *Uromyces appendiculatus*. Journal of Fungi. 2021; 7(9): 745.
- [36] Makhumbila P, Rauwane ME, Muedi HH, Madala NE, Figlan S. Metabolome profile variations in common bean (*Phaseolus vulgaris* L.) resistant and susceptible genotypes incited by rust (*Uromyces appendiculatus*). Frontiers in Genetics. 2023; 14: 1141201.
- [37] Sharma N, Sharma S, Gupta SK, Sharma M. Evaluation of fungicides against bean rust (*Uromyces appendiculatus*). Plant Disease Research. 2018; 33(2): 174-179.
- [38] Ishimwe R, Abutaleb K, Ahmed F. Applications of thermal imaging in agriculture—A review. Advances in Remote Sensing. 2014; 3(03): 128.
- [39] Şahin YS, Bütüner AK, Erdoğan H. Potential For Early Detection Of Powdery Mildew In Okra Under Field Conditions Using Thermal Imaging. Scientific Papers Series Management, Economic Engineering in Agriculture & Rural Development. 2023b; 23(3), 863-870.
- [40] Shaik M, Steadman JR. The effect of leaf developmental stage on the variation of resistant and susceptible reactions of *Phaseolus vulgaris* to *Uromyces appendiculatus*. Phytopathology. 1989; 79(10), 1028-1035.
- [41] Miller SA, Beed FD, Harmon CL. Plant disease diagnostic capabilities and networks. Annual review of phytopathology. 2009; 47, 15-38.
- [42] Kumari HMPS, Pastor Corrales MA, Rajapaksha RGAS, Bandaranayake PCG, Weebadde C. Characterization of *Uromyces appendiculatus* First Races in Sri Lanka and Identification of Genes for the Development of Rust-Resistant Snap Beans. Plant Disease. 2023; 107(8), 2431-2439.
- [43] Faye E, Dangles O, Pincebourde S. Distance makes the difference in thermography for ecological studies. Journal of Thermal Biology. 2016; 56: 1-9.
- [44] Liyo S, Bianchi E, Biglia A, Bessone M, Laurino D, Porporato M. Viability of thermal imaging in detecting nests of the invasive hornet *Vespa velutina*. Insect Science. 2021; 28: 271-277.
- [45] Chelle M. Phylloclimate or the climate perceived by individual plant organs: what is it? How to model it? What for?. New Phytologist. 2005; 166(3):781-90.
- [46] Chaerle L, Leinonen I, Jones HG, Van Der Straeten, D. Monitoring and screening plant populations with combined thermal and chlorophyll fluorescence imaging. Journal of experimental botany. 2007; 58(4): 773-784.
- [47] Murchie EH, Lawson T. Chlorophyll fluorescence analysis: a guide to good practice and understanding some new applications. Journal of Experimental Botany. 2013; 64(13): 3983-3998.
- [48] Bhakta I, Phadikar S, Majumder K, Mukherjee H, Sau A. A novel plant disease prediction model based on thermal images using modified deep convolutional neural network. Precision Agriculture. 2023; 24(1), 23-39.
- [49] Zhu W, Chen H, Ciechanowska I, Spaner D. Application of infrared thermal imaging for the rapid diagnosis of crop disease. IFAC-PapersOnLine. 2018; 51(17): 424-430.
- [50] Pineda M, Barón M, Pérez-Bueno ML. Thermal imaging for plant stress detection and phenotyping. Remote Sensing. 2020; 13(1): 68-88.
- [51] Farber C, Mahnke M, Sanchez L, Kurouski D. Advanced spectroscopic techniques for plant disease diagnostics. A review. TrAC Trends in Analytical Chemistry. 2019; 118: 43-49.
- [52] Hellebrand HJ, Herppich WB, Beuche H, Dammer KH, Linke M, Flath K. Investigations of plant infections by thermal vision and NIR imaging. International Agrophysics. 2006; 20: 1-10.
- [53] Oerke EC, Steiner U, Dehne HW, Lindenthal M. Thermal imaging of cucumber leaves affected by downy mildew and environmental conditions. Journal of Experimental Botany. 2006; 57(9): 2121-2132.

## MPROVIOT - Multi-Purpose IoT Rover Robot

Ahmet BAĞBARS<sup>1\*</sup>, Muhammed Fatih TALU<sup>2</sup>, Nuh ALPASLAN<sup>3</sup>

<sup>1</sup> İnönü University, Faculty of Engineering, Computer Engineering Department, Malatya, Türkiye

<sup>2</sup> İnönü University, Faculty of Engineering, Computer Engineering Department, Malatya, Türkiye

<sup>3</sup> Bingöl University, Faculty of Engineering, Computer Engineering Department, Bingöl, Türkiye

Ahmet BAĞBARS ORCID No: 0009-0000-2074-5462

Muhammed Fatih TALU ORCID No: 0000-0003-1166-8404

Nuh ALPASLAN ORCID No: 0000-0002-6828-755X

\*Corresponding author: a\_bagbars@hotmail.com

(Received: 19.05.2024, Accepted: 15.07.2024, Online Publication: 26.09.2024)

### Keywords

Arduino,  
Rover robot,  
Object detection,  
Sensor,  
IoT

**Abstract:** Robots can be used in various fields due to their flexibility and diversity. This research focuses on designing and developing a multifunctional rover robot for research, exploration, and educational purposes. The main objective of the research is to design a Rover robot platform with remote control, IoT technology. Various scenarios have been created to test the robot's different capabilities, and its performance has been observed. The collected data have been analyzed using both qualitative and quantitative methods. The developed rover robot can be successfully controlled both through RC and IoT controls. Moreover, a web server has been developed for the IoT aspect of the robot, and both arm and head camera images of the robot are transmitted as IoT. The robot's modular design ensures suitability for various tasks and makes it suitable for educational purposes. The results of this study indicate the potential of multifunctional rover robots for various applications and their effectiveness as educational tools.

## MPROVIOT – Çok Amaçlı IoT Rover Robot

### Anahtar

### Kelimeler

Arduino,  
Rover robot,  
Nesne tespiti,  
Sensör,  
IoT

**Öz:** Robotlar esneklik ve çeşitlilikleriyle farklı alanlarda kullanılmaktadır. Bu çalışma, araştırma, keşif ve eğitim amaçları için çok amaçlı bir robot tasarlama ve geliştirme üzerine odaklanmaktadır. Araştırmanın ana amacı, uzaktan kumandalı ve IoT teknolojisine sahip bir Rover robot platformu tasarlamaktır. Robotun farklı yeteneklerini test etmek için çeşitli senaryolar oluşturulmuş ve robotun performansı gözlemlenmiştir. Elde edilen veriler hem nitel hem de nicel yöntemlerle analiz edilmiştir. Geliştirilen Rover robotu hem RC hem de IoT kontrolleriyle başarıyla yönetilebilmektedir. Ayrıca, robotun IoT yönü için bir web sunucusu geliştirilmiştir ve robotun hem kol hem de kafa kamerası görüntüleri IoT olarak iletilmektedir. Robotun modüler tasarımı, farklı görevler için uygun olmasını sağlamakta ve eğitim amaçlı kullanıma uygun hale getirmektedir. Bu araştırmanın sonuçları, çok amaçlı rover robotlarının farklı alanlarda kullanım potansiyeline sahip olduğunu ve eğitimde de etkili bir araç olabileceğini göstermektedir.

## 1. INTRODUCTION

In the robotics industry, multi-purpose designs are preferred over single-purpose robots for specific emergency tasks to achieve higher efficiency/cost ratios in future robots. A robot must be multifunctional to address today's challenges, to be cost-effective, and to increase an organization's productivity [1]. Many traditional robots are designed for a specific purpose or usage area. Two different types of robots may be required for two different types of tasks [2]. This entails

complexity in coordinating different robots for different tasks, as well as cost. Therefore, designing a multi-purpose robot that can perform multiple tasks on a single platform would be more cost-effective [3, 4]. Multi-purpose robots can perform multiple tasks simultaneously, thus saving both cost and time. Our research indicates that emergency robots are frequently encountered in the Robotics Industry, but upon detailed examination, most of them are specifically designed for a particular purpose, and due to the challenges in their usage, they are often deployed too late in emergency



situations [5]. A point emphasized in speeches at the United Nations Conference is that robotic technology will play a critical role in emergency response, rescue, and emergency preparedness in the future [6].

Multi-purpose IoT rover robots have garnered significant attention in recent research. These robots are designed for various applications such as exploration, environmental monitoring, and educational purposes. The integration of IoT technology allows these rovers to collect and transmit data efficiently, enhancing their capabilities. In the realm of planetary exploration, researchers have focused on improving vision systems for planetary rovers to enhance their exploration capabilities [7]. Some studies focus on intelligent physical robots in healthcare. While the primary focus is on healthcare applications, the systematic literature review conducted in this research offers valuable insights into the broader use of robots, including multi-purpose IoT rover robots [8]. Additionally, the development of autonomous navigation systems using advanced algorithms has enabled rovers to navigate challenging terrains effectively [9]. Similarly, introduced a new potential field method for rough terrain path planning using genetic algorithms for a 6-wheel rover, demonstrating advancements in motion planning for wheeled mobile robots [10]. Moreover, the utilization of IoT technology has led to the creation of low-cost environmental monitoring mini rovers equipped with sensors for data collection and surveillance in confined spaces [11]. These compact rovers offer a cost-effective solution for monitoring various environments. In the context of multi-robot systems, the deployment of multiple robots operating as a team has shown significant benefits over single large rovers, including increased fault tolerance and parallel exploration capabilities [12]. This approach enhances the overall efficiency and robustness of exploration missions.

Educational robotics has emerged as a promising field with the potential to enhance teaching and learning processes. Research has shown that robots can improve engagement and elicit novel social behaviors, particularly in individuals with autism [13]. The development of open-source educational robots like the Mona robot has provided affordable platforms for teaching and research [14]. These robots offer opportunities to design pedagogically sound curricula and adequately train teachers to effectively incorporate educational robotics in K-12 settings [15]. Furthermore, the use of social robots as educational tools shows promise in supporting second language learning through interaction and repeated practice. Studies emphasize the importance of integrating educational robotics into teacher education to enhance pedagogical methods and improve learning outcomes [16]. Additionally, the design of educational robotics kits, such as those simulating sustainable cities, demonstrates the potential for hands-on, experiential learning in primary education [17]. Chronis & Varlamis, presented an open source and open design robot that can be used for educational purposes at all levels of the educational system, supporting many different activities and teaching

scenarios [18]. Darmawansah et al. focused on trends and research foci of robotics-based STEM education, shedding light on the evolving role of robotics in educational settings [19]. Yu & Wang, 2022 provided a review of dexterous manipulation techniques for multi-fingered robotic hands, emphasizing advancements in reinforcement learning methodologies for robotic manipulation tasks [20]. Lastly, Wang et al. discussed distributed reinforcement learning for robot teams, highlighting the potential applications of multi-robot systems in various fields such as automated manufacturing and disaster relief [21]. Overall, the literature review highlights the diverse applications and technological advancements in multi-purpose IoT rover robots, showcasing their potential in various fields ranging from planetary exploration to environmental monitoring and educational initiatives.

The main objective of the study is to design a highly useful robot that can be used in many emergency situations. The developed robot has its web interface-based control, the platform also incorporates a radio control (RC) functionality. It has mobility capabilities in challenging terrain conditions and is equipped with IoT features, sensors, and cameras. The camera and sensor data are transmitted via IOT. It is partially autonomous and can be directed to a desired location remotely using GPS navigation. It can easily grasp and carry objects thanks to its arm. It can determine the distance of objects using the angle between two cameras and it can detect depth with an ultrasonic sensor. Besides, it can observe the surroundings by extending its arm into places that the robot cannot enter with the camera on the arm.

The developed robot offers a cost-effective solution while performing safe destruction tasks with explosion risk. The robot's arm is used to carry suspicious objects and remove danger from the environment. It can autonomously extinguish fires with its liquid tank and pump in partial fire-fighting tasks. It can be used in tasks such as detecting gas leaks or toxic chemicals in hazardous areas where humans are present. Moreover, it has the capability to spray disinfectant in scenarios with infection risks such as COVID-19. Its ability to be used in challenging terrain conditions provides a significant advantage in disaster areas for rescue operations.

## 2. MATERIAL AND METHOD

In this paper, a Rover robot platform has been designed with remote control, IoT technology. This section will discuss the methods used in the development stage. The development phase of the robot is analyzed in two parts: hardware and software. The hardware was further divided into mechanical and electronic design. In the mechanical design phase, we based our initial model on NASA's Perseverance Rover Robot, incorporating Ackermann steering and rocker-bogie suspension systems. We then customized and evolved this design to better suit our specific requirements. The mechanical design involves creating the robot's structural body and ensuring its mobility. Key mechanical components include the main carrier body made from 20x20 mm T-

slot aluminum profiles and the suspension system made from 20 mm aluminum pipes. The electronic design integrates various components to achieve the desired functionality. We used a Raspberry Pi-4 as the central processing unit and an Arduino Mega control card to manage sensor data and motor controls. Sensors such as the HC-SR04 ultrasonic distance sensor, DHT21 temperature and humidity sensor, MQ-135 air quality sensor, and Ublox GY-GPSV1 NEO-8M GPS module are included for environmental monitoring and navigation. The robot's movement and interactions are powered by servo motors. The software phase focuses on developing the control system for the robot, which is managed via a web interface. The control system is responsible for processing data from the sensors, sending commands to the actuators, and ensuring the robot's operations are performed as intended. The web interface allows users to remotely control the robot, monitor sensor data in real-time, and program the robot for various tasks. Our robot aims to minimize human risk in emergency situations, particularly in search and rescue operations where accessibility is a significant challenge. By combining programmable and radio-controlled features, the robot can be rapidly deployed and operated in disaster scenarios, providing critical assistance and improving the efficiency of rescue efforts.

## 2.1. General Design of Robot

The development process of our robot began with the completion of the mechanical components. This involved constructing the main body and implementing the mobility systems. Once the mechanical assembly was finished, microcontrollers and sensors were integrated onto the structure. The final stage involved programming the robot and conducting tests to ensure it performed the intended functions effectively. The general diagram of the robot is depicted in Fig. 1, illustrating the arrangement and connections of the electronic components used.

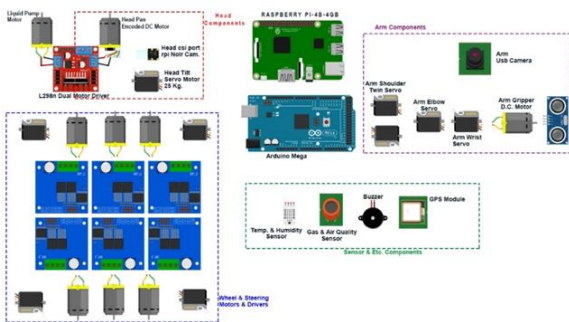


Figure 1. Diagram of the general electronic components of the robot.

Our robot utilizes both Ackermann steering and rocker-bogie suspension systems. The initial tests revealed that our suspension system was inadequate for off-road conditions. To address this, we redesigned the suspension using articulated axles, resulting in a two-axis suspension system. This improvement enhanced the robot's ability to navigate rough terrains. Additionally, the robot's body and wheel dimensions were enlarged, and we equipped it with more powerful motors.

Specifically, we used 18-kilo torque motors with 110 RPM to boost its performance. The robot's control system allows for remote operation via the Flask Web interface, providing users with a user-friendly platform to manage and control the robot's movements and functions.

## 2.2. Body and Mechanical Design

The initial step in our study involved selecting components that are both cost-effective and high-performance. The main carrier body of the robot is constructed from 20x20 mm T-slot 6-channel aluminum sigma profile, providing a robust and flexible framework as shown in Fig. 4. The bogie suspension and articulated axle system, crucial for the robot's mobility, are made from 20mm aluminum pipe, as depicted in Fig. 3. To ensure precision and reliability, the connection and engine assembly parts of the robot were designed and manufactured using a 3D printer with Autodesk Fusion 360 software. This process is illustrated in Fig. 2, where the prepared parts are shown being printed and successfully tested.

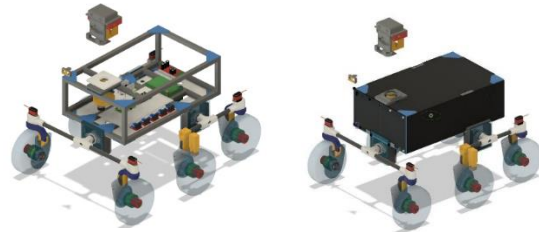


Figure 2. The Design of the Robot's Body Frame is shown in these images taken from the Fusion 360 Engineering Design Application.

Rocker-Bogie Suspension has been chosen for the robot. The Bogie system was used on NASA's Mars rover Sojourner and has been the preferred suspension system ever since. This system has been used on several missions, including the 2003 Mars Exploration Rovers Spirit and Opportunity, the 2012 Mars Science Laboratory (MSL) rover Curiosity, and the Mars 2020 rover Perseverance.

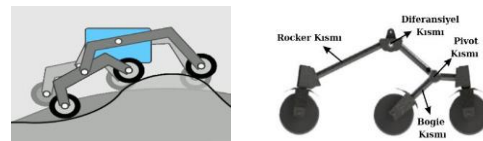


Figure 3. Rocker-Bogie suspension system



Figure 4. The body frame of the robot

Our robot's arm design features five movable joints across three axes, optimized for interaction with the

environment. The visuals of the Robot Arm are shown in Fig. 5. The horizontal deviation axis is powered by a DC motor with an encoder, providing 360-degree rotation capacity. We used dual 25 kg-cm servo motors in the shoulder joint to meet the high torque requirements. The main structural element for the arm is a 20mm sigma profile. Cameras placed on the head and arm facilitate depth perception for object interaction.



**Figure 5.** Images of the Designed Robot Arm. These images show the D.O.F. structure of the robot arm, the way it grips objects, the design structure of the arm, motors, camera and distance sensor.

### 2.2.1. Motion motors, ackermann steering geometry and wheel motors

The robot utilizes Ackermann Steering Geometry as its steering algorithm, enabling the calculation of the turning radius based on the geometry of the steering mechanism. This system is implemented through a function that calculates the angles of the steering servos and the speeds of the wheel motors simultaneously, executed on the Arduino Mega microcontroller.

In our design, we opted to increase the driving speed using 110 RPM glass lifting motors paired with larger wheels. The choice of glass lifting motors is driven by their cost-effectiveness and their ability to deliver adequate power in terms of both torque and rotation speed. For more demanding tasks, we selected high-torque glass lifting motors with worm gear reducers. These motors provide a rotational speed of 110 RPM and a torque of 18 kg.cm (1.7658 N.m), offering a balance of speed and power suitable for a variety of terrains.

The wheels, which are 25.4 cm (10 inches) in diameter, enhance the robot's ability to traverse different surfaces. Using the provided Eq. (1), the force exerted per wheel is calculated to be 27.76 N.

$$F_{onewheel} = \frac{Torque}{R_{wheel}} = \frac{36kg.cm}{12.7cm} = 2.83kgf \quad (1)$$

### 2.3. Electronic Design, Microcontroller and Sensor Components

IoT (Internet of Things) refers to the ability of everyday objects to communicate and exchange data with each

other via the internet. This technology enables various smart devices (e.g., thermostats, lights, cameras) to connect to the internet, share data, and be controlled over a network [22]. MQTT (Message Queuing Telemetry Transport) is a lightweight and low-resource-consuming message-based protocol used for machine-to-machine communication. It is especially preferred in the IoT ecosystem. Almost all IoT cloud platforms support the MQTT protocol due to its practical use and resource friendliness [23]. The reason for using IoT in our study is to obtain sensor data for detecting the robot's surroundings and to facilitate the transmission of user-designed program codes for remote control, along with manual control commands. Additionally, IoT is utilized for transmitting images captured by the robot's two cameras.

This section describes the electronic modules used in the robot, their features, and the tasks that these modules undertake in the robot. Raspberry Pi 4 and Arduino Mega 2560 were utilized in the study. Raspberry Pi is a single-board computer that includes basic components of a computer such as processor, RAM memory, input/output units, all on a single card. These computers can be used as desktop computers in robotic projects, smart home systems, embedded systems due to its compact design. The Arduino Mega 2560 was used for tasks such as the operation of sensors and motors and the transmission of data received from the controller to the Raspberry Pi. Moreover, the HC-SR04 ultrasonic sensor was used for the robot to avoid obstacles. The Ublox GYGPSV1 NEO-8M GPS module is used to determine the robot's position in the terrain and also to enable autonomous progress between locations. This module can communicate with both GPS and GNSS satellites and has a location accuracy of 2-2.5 meters. It also supports 72-channel satellite communication. The DHT21 digital temperature and humidity sensor was used to measure the temperature and humidity of the physical environment. The MQ-135 air quality sensor is used to detect gases such as NH<sub>3</sub>, NO<sub>x</sub>, alcohol, benzene, smoke, and CO<sub>2</sub> in the environment. The measurement accuracy can be adjusted with a potentiometer.

### 2.4. Software Components for Robot

#### 2.4.1. Software to send sensor data with wifi module

The software running on Raspberry Pi is developed in Python. This software creates scripts from the movement and arm position commands coming from the remote control computer via MQTT messages using the Paho-MQTT library. These created scripts are transmitted to Arduino Mega in JSON format via the I2C protocol and the robot's movements are controlled in a coordinated and precise manner. In addition, data from sensors and cameras are transferred to the control computer via the MQTT protocol. This configuration allows Raspberry Pi to transmit sensor and image data to the control computer in real time.

The software on Arduino Mega performs basic microcontroller functions and reads data from sensors via serial, analog and digital ports, transmits and receives data from Raspberry Pi via I2C in JSON format, controls the motors and in addition, since our robot can also be controlled with RC, it manages the robot's movements and modes according to the RC-Control signals coming via sBUS with the RC receiver. In addition, the Ackermann Steering Geometry Algorithm is used for the Steering system and the data is converted in the range of 0-180 degrees according to the angle of the joystick.

#### 2.4.2. Control computer flash web server software

A Python Flask Web Server based software has been developed for control. Separate web pages are designed for sensor data collection, control, monitoring, and programming functions in this platform. The home page lists the block coding instruction sets previously saved in the SQLite3 database and these instructions can be selected and loaded into the robot. The selected instruction sets are transferred to the Arduino Mega via Raspberry Pi and executed.

### 3. RESULTS

Our robot is controlled in two different ways considering various usage scenarios. These are Radio Controlled (RC) programmable with Python Flask Web server with IoT method.

In this study, RC control method is chosen in real-time image acquisition scenarios that require rapid response. Control is provided at a range of approximately 1 km using a RadioLink AT 10 remote control and a 2.4 GHz RadioLink R12DS receiver. The signals from the controller are monitored by sending an interrupt request to the Arduino Mega microcontroller. The Raspberry Pi processes the images with the Python OpenCV library and transmits them via a 5.8 GHz FPV transmitter. This ensures effective image communication.

IoT and MQTT are used for the robot to perform autonomous or manual tasks remotely. Special pages are designed for control and monitoring on Flask Web Server. Data communication is performed using the Python Flask web server and the Paho-MQTT library. Schematic representation of IoT control using Wi-Fi Signals is shown in Fig. 6.

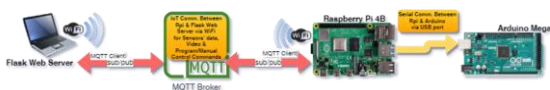


**Figure 6.** Schematic representation of IoT control using Wi-Fi Signals.

The communication method between the Python Flask Web Server on the Control Computer and the RPi and Arduino Mega on the robot is shown. Thanks to the suspension system of our robot, its mobility skills in off-road conditions have reached the desired level. The robot can be controlled manually in real time and with RC controller. Communication range is at the intended level. It is seen that the robot gave the desired results in IoT

control tests from the website. It is also observed that the MQTT communication protocol works efficiently in terms of stability and speed. The robot can be effectively utilized in various scenarios. AI models in our robot will be of great benefit in emergency operations as they can be used for different purposes in many different tasks.

The robot arm can lift objects weighing approximately 1 kg as a result of calculating joint angles with a moment-reducing algorithm. With the special 3D joint apparatus designed, double servo motors were added to the joints to increase the force. Moreover, it can perform functions such as agricultural irrigation, autonomous spraying, and disinfectant spraying with a multi-purpose liquid tank pump.

The developed robot is compared with FOSSBot [18] in terms of mobility, sensor capacity, processing power, and manipulation capabilities as shown in Table 1. Our robot features Ackermann steering geometry and a rocker-bogie suspension system, providing high mobility and stability in challenging terrain conditions. The five-jointed robotic arm, with a 360-degree rotating axis and high-torque servo motors, allows significant interaction with the environment. Additionally, it is equipped with various environmental sensors and a dual-camera system. With Raspberry Pi 4 and Arduino Mega 2560 processors, the robot has high processing power and can be remotely controlled using Python and MQTT protocols. The robot also includes artificial intelligence and object detection capabilities, making it suitable for complex and challenging tasks such as search and rescue, environmental monitoring, and exploration. In contrast, FOSSBot [18] is a simpler platform designed for movement on flat surfaces, lacking a suspension system and robotic arm. It uses basic sensors and does not have a dual-camera system. FOSSBot is primarily intended for educational and research purposes, suitable for simple projects and basic robotic applications but limited in performance for complex and challenging tasks.

**Table1.** Developed Robot and FOSSBot Comparison Table

Criteria	Developed Robot	FOSSBot [18]
Mobility and Suspension	Ackermann steering geometry and rocker-bogie suspension system	Four-wheeled simple mobile platform, no suspension
Robotic Arm and Manipulation	Five-jointed robotic arm, 360-degree rotating axis	No robotic arm
Sensors and Sensing	HC-SR04 ultrasonic sensor, DHT21 temperature and humidity sensor, MQ-135 air quality sensor, Ublox GYGPSV1 NEO-8M GPS module, dual cameras	Basic sensors (ultrasonic or IR sensors), no dual cameras
Processing Power and Control Systems	Raspberry Pi 4, Arduino Mega 2560, and MQTT	Raspberry Pi or similar single-board computer
Task and Application Areas	Search and rescue, environmental monitoring, exploration, remote control	Educational and research purposes, simple projects

#### 4. DISCUSSION AND CONCLUSION

In this study, an emergency response robot has been developed that allows people to assess the area, make detections, and perform the necessary interventions before entering dangerous environments. The developed rover robot can be successfully controlled both through RC and IoT controls. Furthermore, an IoT-focused web server has been established to cater to the IoT functionalities of the robot, facilitating the transmission of both arm and head camera imagery via both IoT and FPV channels. The robot's modular design ensures suitability for various tasks and makes it suitable also for educational purposes. The robot exhibits the potential for international utilization across diverse tasks, facilitated by its open software architecture for further development and the ability to integrate additional models onto the Raspberry Pi platform. The developed robot can be used in a variety of industrial applications like hazardous material handling and inspection. The robot can be used to safely assess and interact with dangerous environments, reducing human risk. Furthermore, the robot's ability to navigate rough terrains and obstacles makes it ideal for search and rescue operations. The developed robot can also be used as an excellent teaching tool for various STEM (Science, Technology, Engineering, and Mathematics) disciplines. Its open software architecture allows students and educators to experiment with programming, sensor integration, and robotics principles. By working with a real-world application, students gain hands-on experience in developing and controlling robotic systems, enhancing their understanding of both hardware and software components. Additionally, the robot's modularity allows for the inclusion of various educational modules, such as AI, computer vision, and IoT, offering a comprehensive learning platform that evolves with the curriculum. In future work, we are planning to expand the AI capabilities of the robot by using NVIDIA Jetson instead of Raspberry Pi. In this way, computer vision tasks will be carried out faster. In addition, we are planning to use a stereo robot camera for depth perception and an advanced LIDAR sensor for three-dimensional mapping of the environment. This expansion will not only enhance the robot's performance in terms of speed and accuracy but also open up new avenues for its application in more complex industrial tasks and advanced educational projects. The integration of more sophisticated AI and sensory systems will further solidify the robot's role as a versatile and practical tool in both industry and education.

#### Acknowledgement

We would like to thank Bingöl STEM and Science Center for providing us with equipment and workshop support in this study.

#### REFERENCES

- [1] Johnson J. Children, robotics, and education. *Artificial Life and Robotics* 2003; 7: 16–21.
- [2] Tadeusz M, Janusz M, Lukasz R, et al. Multipurpose Mobile Robot. *Applied Mechanics and Materials* 2013; 282: 152–157.
- [3] Zaman MTU, Ahmed MS, Sabbir H, et al. Design and Construction of a Multipurpose Robot. *International Journal of Automation, Control and Intelligent Systems*; 1, [https://www.researchgate.net/publication/279965085\\_Design\\_and\\_Construction\\_of\\_a\\_Multipurpose\\_Robot](https://www.researchgate.net/publication/279965085_Design_and_Construction_of_a_Multipurpose_Robot) (2015, accessed 17 May 2024).
- [4] Evripidou S, Georgiou K, Doitsidis L, et al. Educational Robotics: Platforms, Competitions and Expected Learning Outcomes. *IEEE Access* 2020; 8: 219534–219562.
- [5] Qin H, Shao S, Wang T, et al. Review of Autonomous Path Planning Algorithms for Mobile Robots. *Drones* 2023, Vol 7, Page 211 2023; 7: 211.
- [6] Tadokoro S. UN World Conference on Disaster Risk Reduction [Society News]. *IEEE Robot Autom Mag* 2015; 22: 176–177.
- [7] Matthies L, Maimone M, Johnson A, et al. Computer vision on Mars. *Int J Comput Vis* 2007; 75: 67–92.
- [8] Huang R, Li H, Suomi R, et al. Intelligent Physical Robots in Health Care: Systematic Literature Review. *J Med Internet Res* 2023;25:e39786 <https://www.jmir.org/2023/1/e39786> 2023; 25: e39786.
- [9] Fue K, Porter W, Barnes E, et al. Autonomous Navigation of a Center-Articulated and Hydrostatic Transmission Rover using a Modified Pure Pursuit Algorithm in a Cotton Field. *Sensors* 2020, Vol 20, Page 4412 2020; 20: 4412.
- [10] Raja R, Dutta A, Venkatesh KS. New potential field method for rough terrain path planning using genetic algorithm for a 6-wheel rover. *Rob Auton Syst* 2015; 72: 295–306.
- [11] Pauzi NAM, Mustaza SM, Yahya I. Low-cost environmental monitoring mini rover based on IoT technology. *International Journal of Advanced Technology and Engineering Exploration* 2021; 8: 64–72.
- [12] Kalita H, Gholap AS, Thangavelautham J. Dynamics and Control of a Hopping Robot for Extreme Environment Exploration on the Moon and Mars. *IEEE Aerospace Conference Proceedings*. Epub ahead of print 1 March 2020. DOI: 10.1109/AERO47225.2020.9172617.
- [13] Scassellati B, Henny Admoni, Matorić M. Robots for use in autism research. *Annu Rev Biomed Eng* 2012; 14: 275–294.
- [14] Arvin F, Espinosa J, Bird B, et al. Mona: an Affordable Open-Source Mobile Robot for Education and Research. *Journal of Intelligent and Robotic Systems: Theory and Applications* 2019; 94: 761–775.
- [15] An H, Sung W, Yoon SY. Implementation of learning by design in a synchronized online

- environment to teach educational robotics to inservice teachers. *Educational Technology Research and Development* 2022; 70: 1473–1496.
- [16] Boyarinov DA, Samarina AE. The Potential of Educational Robotics in Teacher Education. *ARPHA Proceedings* 3: 259-276 2020; 3: 259–276.
- [17] Vicente FR, Zapatera Llinares A, Montes Sánchez N. Curriculum analysis and design, implementation, and validation of a STEAM project through educational robotics in primary education. *Computer Applications in Engineering Education* 2021; 29: 160–174.
- [18] Chronis C, Varlamis I. FOSSBot: An Open Source and Open Design Educational Robot. *Electronics* 2022, Vol 11, Page 2606 2022; 11: 2606.
- [19] Darmawansah D, Hwang GJ, Chen MRA, et al. Trends and research foci of robotics-based STEM education: a systematic review from diverse angles based on the technology-based learning model. *Int J STEM Educ* 2023; 10: 1–24.
- [20] Yu C, Wang P. Dexterous Manipulation for Multi-Fingered Robotic Hands With Reinforcement Learning: A Review. *Front Neurorobot* 2022; 16: 861825.
- [21] Wang Y, Damani M, Wang P, et al. Distributed Reinforcement Learning for Robot Teams: a Review. *Current Robotics Reports* 2022; 3: 239–257.
- [22] Çiğdem Ş, Meidute-Kavaliauskiene I, Yıldız B. Industry 4.0 and Industrial Robots: A Study from the Perspective of Manufacturing Company Employees. *Logistics* 2023, Vol 7, Page 17 2023; 7: 17.
- [23] Garcia CA, Montalvo-Lopez W, Garcia M V. Human-Robot Collaboration Based on Cyber-Physical Production System and MQTT. *Procedia Manuf* 2020; 42: 315–321.

## Typing of *Mannheimia haemolytica* Isolated From Respiratory Tract and Investigation of Virulence Genes

Cihat ÖZTÜRK<sup>1\*</sup>, İsmail Hakkı EKİN<sup>2</sup>

<sup>1</sup> Kırşehir Ahi Evran University, Faculty of Medicine, Department of Medical Microbiology, Kırşehir, Türkiye

<sup>2</sup> Van Yüzüncü Yıl University, Faculty of Veterinary Medicine, Department of Microbiology, Van, Türkiye

Cihat ÖZTÜRK ORCID No: 0000-0003-2868-2317

İsmail Hakkı EKİN ORCID No: 0000-0001-5029-8130

\*Corresponding author: [cihat.ozturk@ahievran.edu.tr](mailto:cihat.ozturk@ahievran.edu.tr)

(Received: 15.01.2024, Accepted: 19.07.2024, Online Publication: 26.09.2024)

### Keywords

*Mannheimia*  
*haemolytica*,  
Typing,  
Virulence genes

**Abstract:** This study aimed to determine the biochemical properties and distribution of important virulence genes of *Mannheimia haemolytica* isolates from the respiratory tracts of diseased and healthy cattles and sheeps. Forty-eight *Mannheimia haemolytica* isolates from naso-pharyngeal and trachea-bronchial swabs were identified by Real Time-PCR. According to the differences in arginine and sorbitol tests, four different biochemical profiles were determined in the isolates examined. Three virulence gene profiles were detected in the isolates examined by Real-Time PCR. 37.5%, 33.3%, and 12.5% of the isolates examined were identified as profiles I, III and II, respectively. At the same time, it was determined that biochemical profile II was associated with disease cases and this was related to arginine negativity. In addition, it was determined that isolates with virulence gene profile I were associated only with the biochemical profile I and that this was due to arginine negativity. In contrast, the relationship between arginine-positive isolates and virulence gene profile III was found to be significant. As a result; arginine negativity and *gcp*, *gs60*, *tbpB*, *lktC*, *adh* positive, *nmaA* negative isolates may be the epidemiological criteria that can be used to differentiate commensal and pathogen *Mannheimia haemolytica* isolates and new studies on the subject should be done.

21

## Solunum Yollarından İzole Edilen *Mannheimia haemolytica* İzolatlarının Tiplendirilmesi ve Virülens Genlerinin Araştırılması

### Anahtar Kelimeler

*Mannheimia*  
*haemolytica*,  
Tiplendirme,  
Virülens genler

**Öz:** Bu çalışmada, hasta/sağlıklı sığır ve koyunların solunum yollarından izole edilen *Mannheimia haemolytica* izolatlarının biyokimyasal özellikleri, önemli virülens genlerinin dağılımı tespit edilmesi amaçlandı. Nazo-farengiyal ve trake-bronşiyal svap örneklerinden izole edilen ve Real-Time PCR ile tanımlanan 48 (%87.3) adet *Mannheimia haemolytica* izolatu kullanıldı. İncelenen izolatlarda, hastalık ve virülens genleri ile ilişkili biyokimyasal özelliklerin arginin ve sorbitol testlerindeki farklılıklara göre 4 farklı biyokimyasal profil belirlendi. Real Time-PCR yöntemiyle virülens genleri incelenen izolatlarda, %37.5'i profil I, %33.3'ü profil III ve %12.5'i profil II olmak üzere 3 farklı virülens gen profili tespit edildi. Bununla birlikte biyokimyasal profil II'nin hastalık olguları ile ilişkili ve bunun arginin negatiflik ile ilişkili olduğu belirlendi. Ayrıca virülens gen profil I özelliğine sahip izolatların sadece biyokimyasal profil I ile ilişkili olduğu ve bunun arginin negatiflikten kaynaklandığı belirlenirken, arginin pozitif izolatlar ile virülens gen profil III arasındaki ilişkinin önemli olduğu gözlemlendi. Sonuç olarak; arginin negatiflik ile *gcp*, *gs60*, *tbpB*, *lktC*, *adh* pozitif, *nmaA* negatif izolatların kommensal ve patojen *Mannheimia haemolytica* izolatlarının ayırımında kullanılabilecek epidemiyolojik kriter olabileceği ve konu ile ilgili yeni çalışmaların yapılması gerektiği düşünülmektedir.

## 1. INTRODUCTION

The importance of animal husbandry in terms of both economy and health has brought animal health to the

agenda [1, 2]. According to the Global Animal Medicine Association [3], one out of every five farm animals dies around the world every year due to completely preventable diseases and approximately 20 billion

dollars are lost [4, 5, 6]. Researchers have reported that pneumonic pasteurellosis is responsible for 50% of small ruminant deaths and 30% of cattle deaths [7, 8]. The effect of the disease on the global economy has been recognized all over the world, and it has been reported that it causes an annual economic loss of approximately 1 billion dollars in some countries [9, 6]. In bacterial investigations performed in pneumonia cases in cattle and sheep, *Mannheimia haemolytica* (*M. haemolytica*), *Pasteurella multocida* (*P. multocida*), *Mycoplasma* spp., *Histophilus somni*, *Trueperella pyogenes*, *Streptococcus* spp. and *Staphylococcus* spp. are the primary and secondary factors in the formation of the disease. In addition, viruses and parasites are other infectious agents that cause pneumonia [10, 11, 12, 13, 14]. Pneumonia caused by *M. haemolytica* is characterized by acute cranio-ventral fibrinous pneumonia and fibrinopurulent pleura pneumonia [15]. Although *M. haemolytica* is found as a primary and secondary bacterial agent in respiratory tract infections due to its commensal presence in the respiratory tract flora of various animal species, there are not enough epidemiological studies especially in Turkey. Whether there is a difference between commensal and pathogenic *M. haemolytica* and the mechanism by which the strains in the flora become pathogenic in disease cases are still the subjects of interest to researchers. [16, 17, 18]. *M. haemolytica* is included in Pasteurellaceae family, *Mannheimia* genus [19, 20, 21, 22, 23, 24]. Twelve different serotypes were detected in the serotyping performed according to the capsular surface antigens of the agent [25, 26]. *M. haemolytica* is a Gram-negative, non-motile, bipolar stainable, coccobacilli-shaped encapsulated bacterium [24, 27]. It has many virulence factors that allow *M. haemolytica* to evade host defense and colonize and play an important role in the pathogenesis of the disease. Adhesins, capsular polysaccharide, outer membrane proteins, lipopolysaccharide, neurominidase, leukotoxin, lipoprotein, sialoglycoprotease, serotype-specific protein and transferrin binding proteins detected in studies among these factors have been reported by many researchers [28, 29, 30, 31, 32, 33, 34, 35, 36, 37, 38, 39]. Outside of conventional bacteriological methods for the identification of *M. haemolytica* isolates, PCR methods using 12S rRNA and 16S rRNA gene regions and specific primers for different genes related to the virulence of the agent have also been frequently used [39, 40, 41, 42, 43, 44, 45, 46, 47].

This study investigated the biochemical properties and virulence-related genes of *M. haemolytica* isolates obtained from the respiratory tract of healthy and diseased cattle and sheep. It also evaluated possible relationships between the isolates' phenotypic and genotypic characteristics and the animals' disease status.

## 2. MATERIAL AND METHOD

In this study, 650 swab samples taken from the nasopharyngeal (NF) and tracheobronchial (TB) regions of 157 (157 NF and 138 TB) cattle and 182 sheep (186 NF and 173 TB) slaughtered, and diagnosed with

pneumonia in veterinary clinics in Van province between 2018-2019 were examined (Table 3).

Forty-eight *M. haemolytica* strains examined in the study were isolated and identified from the swab samples. *M. haemolytica* reference strain were supplied by Prof. Dr. Arzu Findık from Ondokuz Mayıs University Faculty of Veterinary Medicine Department of Microbiology.

In the study, swab samples were placed in Stuart transport medium and delivered to the laboratory of the Microbiology Department of the Faculty of Veterinary Medicine of Van Yüzüncü Yıl University in a short time [48].

The study was approved by the Animal Ethics Committee of Van Yuzuncu Yil University (approval date and no: 06/03/2018, YUHADYEK-17310).

### 2.1. Isolation and Identification of *M. haemolytica* Isolates

Swab samples taken from cattle and sheep were cultured on 7% blood agar for bacteriological culture and incubated at 37°C for 24-72 hours under aerobic conditions. Mucoid and haemolytic, 1-2 mm in diameter, greyish, transparent, smooth, round bacterial colonies were selected and stored at -20°C until identification [23, 49, 50]

In the preliminary identification of the isolates examined, Gram-negative small bacilli, oxidase and catalase positive bacterial isolates that formed acid (yellow colour) at the bottom of TSI agar, could and/or could not grow on MacConkey agar and were immobile on SIM medium were accepted as suspected *M. haemolytica* in preliminary identification [51]. BD™ Pheonix automated bacterial identification system (Becton Dickinson, USA) was used for identification and biochemical characteristics of suspected isolates, BD Pheonix identification panel (BD Pheonix™ NMIC-308, USA) containing 45 different biochemical tests was used [52].

### 2.2. Identification by Real Time-PCR

**DNA isolation:** According to the recommended protocol, the genomic DNA of suspected *M. haemolytica* isolates was obtained using a commercial bacterial DNA isolation kit (Cat# GF-BA-100, Vivantis, Malaysia).

**Real Time-PCR:** Identification of *M. haemolytica* at species level was performed according to the optimised protocol of Hawari et al. [53] with minor modifications. In Real Time-PCR, commercial SYBR Green qPCR Master Mix (Amplicon (2X), 5000830, Denmark) was used according to the recommended protocol. To prepare the PCR mixture, 12 µl of Master Mix, 2 µl of genomic DNA and 1 µl of each primer (10 mM) (Table 1) were added and the mixture was completed to 25 µl with PCR grade water. The PCR mixture was pre-denatured in a thermal cycler (Qiagen, Corbet Rotor Gene, 6000, USA) at 94°C for 5 minutes. Then, in the amplification process



including 35 cycles; denaturation at 94°C for 1 min; annealing at 56°C for 45 s; elongation at 72°C for 1 min and final elongation at 72°C for 5 min protocol was applied and the dynamic sigmoidal curves obtained in the software of the Real Time-PCR device were evaluated. For the confirmation of PCR products obtained at the amplification stage, electrophoresis (Owl Easycast, B1-BP, USA) was performed in 1% agarose gel (1xTAE solution) for one hour and then visualised in the imaging system (ImageSCI, GL 5000, USA). The detected amplicons were compared with a 100 bp DNA ladder (VC 100 bp plus, Vivantis, Malaysia) and samples with a 325 bp band were considered positive for *M. haemolytica*. Reference *M. haemolytica* strain was used as positive control, and DNA/RNA free PCR grade water was used as negative control.

**Table 1.** *M. haemolytica* specific oligonucleotide sequence [53].

Gene	Primer Sequence (5'-3')	Amplicon (bp)
PHSSA	F TTCACATCTTCATCCTC	325
	R TTTTCATCCTCTTCGTC	

## 2. Detection of Virulence Related Genes of *M. haemolytica*

In the study, O-sialoglycoprotease (*gcp*), outer membrane lipoprotein (*gs60*), transferrin binding protein (*tbpB*), leukotoxin (*lktC*), UDP-N-acetyl-D-glucosamine-2-epimerase (which is associated with virulence in *M. haemolytica* isolates) (*nmaA*) and adhesion (*adh*) genes were investigated by Real Time-PCR. The oligonucleotide sequences and binding temperatures used for each virulence-related gene are given in Table 2 [54].

**Table 2.** Oligonucleotide sequences and binding temperatures of virulence related genes [54].

Gen	Primer Sequence (5'-3')	Annealing (°C)/Cycles
<i>gcp</i>	F CGCCCTTTTGGTTTTCTAA	54/35
	R GTAAATGCCCTTCATATGG	
<i>gs60</i>	F GCACATTATATTCTATTGAG	50/40
	R AGGCATACTCTAACTTTTGC	
<i>tbpB</i>	F CTACTTGCTGCTTGTTCCTC	56/35
	R AGAACCCTTACTGTACGTC	
<i>lktC</i>	F GGAAACATTACTTGGCTATGG	54/40
	R TGTGCCAGCTCTTCTTGATA	
<i>nmaA</i>	F CTGTAGAAGCCGGAACAGTA	56/35
	R CATCGCCATAAGGGTTGTGA	
<i>adh</i>	F CTGCAAGTAAGCAACATTG	54/35
	R GAATCCGCACCAATAGCAAT	

Commercial SYBR Green qPCR Master Mix (Ampliqon, 5000830, Denmark) was used for Real Time

PCR for Real-Time PCR for virulence-related genes. After optimization of the PCR mix, 2 µl of genomic DNA and 1 µl of each primer (10 mM) (Table 2) were added into 10 µl of Master Mix, and the mixture was completed to 20 µl with PCR grade water. The mixture was incubated for 5 min at 95 °C for preliminary denaturation in a Thermal cycler (Qiagen, Corbet Rotor Gene, 6000, USA). Denaturation at 94°C for 30 s, binding for 60 s at the temperatures specified for each gene in Table 2, elongation at 72°C for 60 s, and finally final elongation at 72°C for 8 min were applied. The protocol was applied as 35 amplification cycles for *adh*, *gcp*, *nmaA* and *tbpB* genes and 40 cycles for *gs60* and *lktC* genes. Sigmoidal curves obtained dynamically in the software of the Real Time-PCR device were evaluated as positive.

## 2.3. Statistical Analysis

The SPSS (2013) package program was used to determine the degree of affinity of *M. haemolytica* isolates according to their biochemical properties by dendrogram analysis. The Z ratio test (Two-Sample proportion test) and Chi-square test methods were used by using the Minitab (Demo version 15-Access 15.11.2019) statistical program to determine the correlation between the biochemical properties of isolates and genes related to disease and virulence [55].

## 3. RESULTS

### 3.1. Identification with Real-Time PCR

After preliminary identification for 650 swabs samples, 48 isolates were identified as *M. haemolytica* by Real Time-PCR using primers specific to the *M. haemolytica* gene (Figure 1, Figure 2).

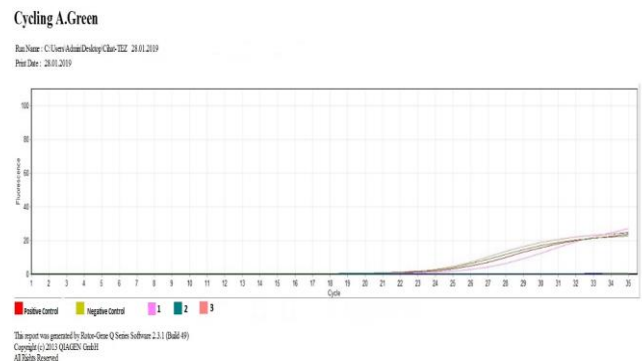


**Figure 1.** Positive amplification results from *M. haemolytica* isolates analyzed by Real Time-PCR.

Of the 48 isolates identified as *M. haemolytica* in the study, 44 (91.6%) were obtained from sheep and 4 (8.4%) from cattle (Table 3).

**Table 3.** Distribution of *M. haemolytica* isolates according to animal species and health/disease conditions.

Animal Species	Material Source	Number of Animals	Number of Isolates		Total Number of Isolates	Isolation Rate (%)
			NF	TB		
Cattle	Slaughterhouse/Healthy	133	–	–		
Cattle	Slaughterhouse/Diseased	5	–	1	4	2.54
Cattle	Field/Diseased	19	3	–		
Sheep	Slaughterhouse/ Healthy	133	19	–		
Sheep	Slaughterhouse/Diseased	40*	11	10	44	24.17
Sheep	Field/Diseased	9	4	–		
<b>Total</b>		<b>339</b>	<b>37</b>	<b>11</b>	<b>48</b>	<b>26.71</b>

\*: Six different *M. haemolytica* were isolated from the NF (Naso-Pharyngeal) and TB (Trache-Bronchial) regions of three patient sheep.

–: *M. haemolytica* was not isolated.

**3.2. Distribution of Biochemical Properties**

Biochemical characteristics of 48 isolates identified as *M. haemolytica* by Real Time-PCR were determined by the BD Phoenix™ automated bacterial identification system using a test panel containing 45 biochemical tests. According to the differences in arginine and sorbitol tests, four different biochemical profiles were determined in the isolates examined (Table 4).

**3.3. Identifying virulence associated genes**

Of the isolates analysed by Real Time-PCR, 95.8% were positive for *gcp*, 87.5% for *gs60*, 58.3% for *tbpB*, 93.8% for *IktC*, 16.7% for *nmaA* and 91.7% for *adh* genes (Table 4).

**3.4. Determining Gene Profiles Associated with Virulence**

It was determined that different gene profiles were found according to the distribution of virulence-related genes in the isolates. Isolates with three or more virulence-associated genes were considered as a separate profile, while isolates with less than three virulence-associated genes were not considered as virulence gene profiles. Accordingly, three different gene profiles were detected in the isolates (Table 4).

**3.5. Distribution of Virulence-Related Gene Profiles in the Main Biochemical Profiles Determined in *M. haemolytica* Isolates**

Biochemical profile I, which was determined in 17 (42.5%) of the *M. haemolytica* isolates, was determined in 12 (66.66%), 4 (66.66%) and 1 (6.25%) of virulence-related gene profiles I, II, and III respectively. Biochemical profile II, which was determined in 6 (15%) of the isolates, was detected in 2 (11.11%) of 18 virulence gene profile I and 4 (25%) of 16 virulence gene profile II. Biochemical profile III, which was determined in 8 (20%) of the *M. haemolytica* isolates, was determined in 1 (5.55%), 1 (16.66%) and 6 (37.5%) of virulence-related gene profiles I, II, and III respectively. Biochemical profile IV, which was determined in 9 (22.5%) of the isolates, was detected in 3 (16.66%) of 18 virulence gene profile I, 1 (16.66%) of 6 virulence gene profile II and 5 (31.25%) of 16 virulence gene profile III (Table 4). Isolates belonging to profiles IV, V, VI, VII, VIII and IX are presented in Table 4, but they were not evaluated because of their poor correlation with biochemical profiles.

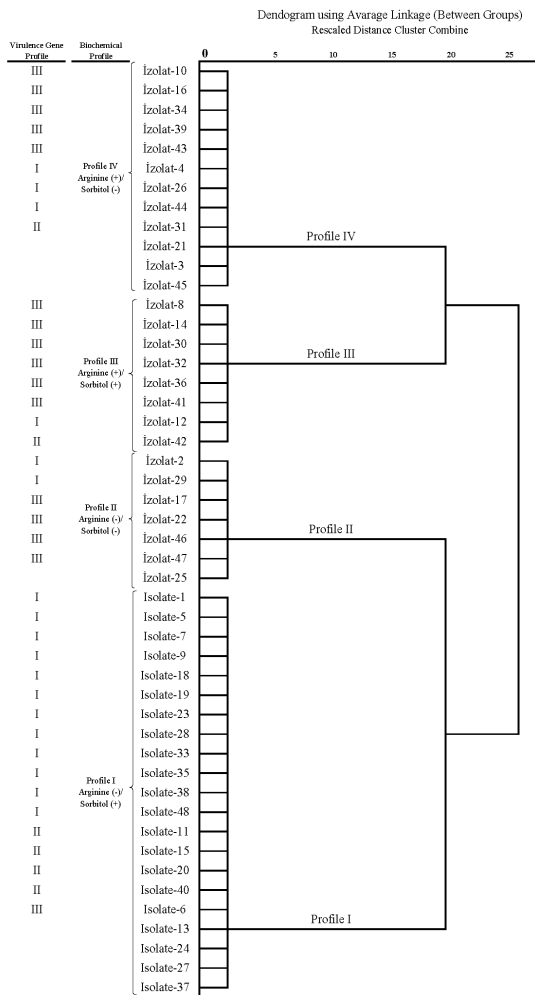


**Figure 2.** Dendrogram analysis of biochemical profiles determined according to arginine and sorbitol test results and virulence-related gene profiles, and the distribution of antimicrobial resistance genes in *M. haemolytica* isolates.

**Table 4.** Distribution of virulence-related gene profiles detected in *M. haemolytica* isolates in major biochemical profiles.

Virulence-Related Gene Profile							n	Biochemical Profile (%)			
Profile	<i>gcp</i>	<i>gs60</i>	<i>tbpB</i>	<i>lktC</i>	<i>nmaA</i>	<i>adh</i>		I	II	III	IV
								Arg – Sor +	Arg – Sor –	Arg+ Sor+	Arg+ Sor –
I	+	+	+	+	-	+	18	12 (66.66)	2 (11.11)	1 (5.55)	3 (16.66)
II	+	+	+	+	+	+	6	4 (66.66)	-	1 (16.66)	1 (16.66)
III	+	+	-	+	-	+	16	1 (6.25)	4 (25)	6 (37.5)	5 (31.25)
IV	+	-	+	+	-	+	2	1	1	-	-
V	+	-	-	-	+	-	1	-	-	-	1
VI	+	-	-	-	-	-	1	-	-	-	1
VII	-	-	-	-	-	-	1	1	-	-	-
VIII	-	+	-	+	-	+	2	1	-	-	-
IX	+	+	+	+	-	-	1	1	-	-	1
<b>Total</b>							<b>48</b>	<b>21</b>	<b>7</b>	<b>8</b>	<b>12</b>

Arg: Arginine, Sor: Sorbitol, Profiles IV, V, VI, VII, VIII, IX: Isolates that were not evaluated as virulence gene profile.

### 3.6. Relation of biochemical profiles to virulence-related gene profile and animal health status

In the evaluation made according to the statistical analysis of the obtained data; the isolates with biochemical profile I were associated only with virulence gene profile I ( $p < 0.01$ ), while biochemical profile II was associated with isolates obtained from disease cases ( $p < 0.01$ ) (Table 5), and this was determined that it was caused by only arginine negativity ( $p < 0.05$ ) (Table 5).

On the other hand, it was determined that isolates with virulence gene III profile were not associated with biochemical profile I ( $p > 0.05$ ), but the relationship between arginine positive isolates and virulence gene profile III was found as significant ( $p < 0.01$ ) (Table 5).

Also, it was determined that sorbitol positive or negative isolates were not associated with disease cases ( $p > 0.05$ ). In addition, no correlation was found between sorbitol positive or negative isolates and virulence gene profiles (Table 5). In contrast virulence gene profile II was not associated with biochemical profiles and disease cases ( $p > 0.05$ ).

**Table 5.** The relationship of arginine positive/negative *M. haemolytica* isolates with health situations and virulence factors.

	Arginine(+) n=20	Arginine (-) n=28	Sorbitol (+) n=29	Sorbitol (-) n=19
<b>Health situation</b>				
Diseased (%)	9 (45)	20 (71) <sup>a</sup>	17 (59)	12 (63)
Healthy (%)	11(55)	8 (29)	12 (41)	7 (37)
<b>Virulence gene profile II</b>				
Positive (%)	4 (25)	14 (50) <sup>b</sup>	13 (45)	5 (26)
Negative (%)	16 (75)	14 (50)	16 (55)	14 (74)
<b>Virulence gene profile V</b>				
Positive (%)	11 (55) <sup>c</sup>	5 (18)	7 (24)	9 (47)
Negative (%)	9 (45)	23 (82)	22 (76)	10 (53)

**a;** The relationship between arginine negative isolates and disease cases ( $p < 0.05$ ), **b;** The relationship between arginine negative isolates and virulence gene profile I ( $p < 0.05$ ), **c;** The relationship between arginine positive isolates and virulence gene profile III ( $p < 0.01$ ).

## 4. DISCUSSION AND CONCLUSION

This study investigated the biochemical properties and virulence-related genes of *M. haemolytica* isolates obtained from the respiratory tract of healthy/diseased cattle and sheep. In addition, possible relationships between the isolates' phenotypic and genotypic characteristics and the animals' disease status were evaluated.

A study conducted in Antakya reported that *M. haemolytica* was not isolated from 122 bovine lung samples [56]. In a similar study conducted in Kars and its surroundings, it was reported that *M. haemolytica* was isolated from 61 (26.4%) of the lung samples taken from a total of 231 cattle and sheep examined [57]. Önat et al. [50] reported that *M. haemolytica* was isolated from 5 (10.6%) of bilateral nasal swab samples taken from 47 cattle. Noyes et al. (58) *M. haemolytica* was isolated from 1596 (29%) of the naso-pharyngeal swab samples taken from 5498 cattle with respiratory tract infection symptoms. Castillo et al. [59] reported that they isolated *M. haemolytica* from 70 (79.5%) of the nasal swab samples taken from 88 cattle with respiratory tract infection. Demissie et al. [60] reported that *M. haemolytica* was isolated from 57 (34.1%) of 167 sheep lung samples with macroscopic pneumonia lesions. In studies conducted in some other regions (Aydın and Urfa) [61, 62], Kırkan et al. (61) reported that they isolated *M. haemolytica* from 22 (11%) of 200 sheep lung samples with pneumonia lesions, and Tel and Keskin [62] reported that they isolated *M. haemolytica* from 30 (12.5%) of 240 sheep lung samples.

In this study, four (2.54%) of the *M. haemolytica* isolates were obtained from cattle, while four were isolated from diseased and healthy sheep (Table 3). While the *M. haemolytica* isolation rate obtained from cattle was determined to be higher than the rates reported by Ülker et al. [56], it was higher than the isolation rates reported by Gürbüz [57], Önat et al. [50], Noyes et al. [58] and Castillo et al. [59]. was found to be low. However, the isolation rate obtained from sheep was found to be higher than the isolation rates reported by

Gürbüz [57] and Demissie et al. (2014) and Kırkan and Kaya [61], Tel and Keskin [62]. It was thought that the differences observed in the studies were due to the differences in cultivation methods, climate and barn conditions from region to region.

Biochemical properties of *M. haemolytica* isolates show great variability. Bisgaard [63] reported that indole, MR, VP, arabinose, and esculin test results were negative in *M. haemolytica* strains isolated from the tracheal cavity of cattle, while lactose fermentation showed variability. Daphal et al. [64] also reported that indole, MR-VP and citrate test results of 7 *M. haemolytica* isolates obtained from small ruminants were negative. Angen et al. [65] reported that indole, sorbitol and MacConkey agar growth test results of 246 trehalose negative *M. haemolytica* isolates isolated from cattle and sheep showed variability. In the study in which ten different biogroups were determined among the isolates, it was reported that growth on MacConkey agar was variable in 5 biogroups and isolates in the other five biogroups did not grow on MacConkey agar. In a study conducted in Baghdad [45], it was reported that all 5 *M. haemolytica* isolates, 3 of which were identified from lung tissue and 2 of which were identified from the nasal cavity, were positive for rhamnose, indole, nitrate and negative for gelatinase, urea, inositol, xylose, mannitol, arabinose, maltose with commercial identification kit. Taunde et al. [66] found that 16 (15%) of 40 *M. haemolytica* isolates obtained from goats with severe respiratory infection symptoms were  $\beta$ -haemolytic, 34 (85%) of them were non-haemolytic, all of the isolates were esculin positive, ONPG negative and did not grow on MacConkey agar (atypical strain). The researchers reported that *M. haemolytica* case isolates may have atypical characteristics under unfavourable environmental conditions. Gürbüz [57] reported that all *M. haemolytica* isolates (61 isolates) obtained from cattle and sheep were indole negative, and reactions to arabinose, xylose, salicin, and trehalose were variable. In a study conducted by İlhan and Keleş [67] in Van region, it was reported that 57 (86.3%) of 66 (11.3%) *M. haemolytica* isolates isolated from lung samples of sheep slaughtered in slaughterhouse were identified as biotype A and 9 (13.6%) as biotype T according to arabinose, xylose and trehalose fermentation test results. Another study [68] determined that all 16 *M. haemolytica* isolates obtained from sheep were trehalose negative, arabinose and xylose positive, and 13 (81.3%) were lactose positive. According to the results obtained, the researchers reported that all of the isolates were defined as biotype A (xylose and arabinose positive). The present study determined that all 48 *M. haemolytica* isolates were  $\beta$  haemolytic on blood agar but did not grow on MacConkey agar and were indole negative. However, among the biochemical tests in the commercial kits used to identify the isolates, it was determined that the isolates had four different biochemical profiles according to arginine-arginine and sorbitol fermentation properties. It was observed that biochemical profile II was associated with the isolates obtained from disease cases and this relationship was observed only in arginine negative isolates. It is thought that biochemical characteristics

may differ among *M. haemolytica* case isolates and this may be caused by unfavourable environmental conditions, host differences and genetic transmission among Gram negative bacteria.

In a study on the detection of the leukotoxin (*lktA*) gene in 248 *M. haemolytica* and *Biberstenia trehalosi* isolates obtained from different animal groups [69], the leukotoxin gene was detected in 108 of the isolates. The study, it was reported that leukotoxin was the major virulence factor in the formation of pneumonic pasteurellosis, and other virulence factors played a role in inducing factors in the colonization of the agent and disease formation. In a similar study conducted in our country [70], the *lktA* gene was detected in all 22 *M. haemolytica* and 2 *Biberstenia trehalosi* isolates isolated from sheep with pneumonic lesions in their lungs, and it was reported that the leukotoxin gene is the most important virulence factor in cases of pneumonic pasteurellosis. On the other hand, it was reported that 7 (13%) of 54 *M. haemolytica* isolates obtained from lung samples taken from calves with respiratory tract infection in Siberia and Kazakhstan did not contain the leukotoxin gene [27]. In an experimental study conducted on *M. haemolytica* isolates obtained from 29 calves infected with *M. haemolytica* [32], it was reported that *lkt*, *gs60*, *adh* and *gcp* genes were expressed in the lung tissue in all isolates. In contrast, *tbp* and *nma* genes were not detected. The study reported that the most important virulence factor in *M. haemolytica* isolates was leukotoxin, and the failure to detect *nma* and *tbp* genes may be related to the infection stage of the disease. El Dokmak et al. [71] conducted another study on the virulence-related genes of 7 *M. haemolytica* isolates isolated from cattle and sheep, it was reported that *gcp* and *gs60* genes were detected in all of the isolates. In another study in which 16 genes related to virulence were examined in 121 *M. haemolytica* isolates obtained from sheep [72], *lktA*, *tbpA*, *tbpB* and *tonB* genes were detected in all isolates, while *adh* (97.5%), *fhaC* (94.2%), *gcp* (79.3%), *hf* (79%), *irp* (59.5%), *lpsA* (65%), *nanH* (99.2%), *pilA* (95.8%), *plpD* (95.8%), *pomA* (97.6%), *sodA* (91.7%) and *sodC* (19%) genes have been reported to be present in different proportions. In the study, it was reported that only the *irp* gene was found to be associated with the disease in isolates obtained from sheep with pneumonia, and it was concluded that the distribution of virulence-related genes was homogeneous between *M. haemolytica* isolates isolated from diseased and healthy animals.

In this study, *gcp* genes were detected in 46 (95.8%), *gs60* in 42 (87.5%), *tbpB* in 28 (58.3%), *lktC* in 45 (93.8%), *nmaA* in 8 (16.7%) and *adh* in 44 (91.7%) of 48 *M. haemolytica* isolates obtained from the respiratory tract of cattle and sheep. The number of leukotoxin gene positive isolates detected in the study was higher than reported by Fisher et al. [69] and Nefedchenko et al. [27] and lower than reported by Kırkan [70], Lo et al. [32] and Garcia-Alvarez et al. [72]. It was concluded that the detection of leukotoxin genes at different rates may be due to the presence of more than one gene region encoding leukotoxin, and the presence of genes may also

vary according to regional conditions and animal species. The number of positive isolates in the direction of *nma*, iron binding protein *tbp*, *adh* gene was higher than reported by Lo et al. [32] and Garcia-Alvarez et al. [72]. The number of *gcp* and *gs60* gene positive isolates was lower than that found by Lo et al. [32] and higher than that found by El Dokmak et al. [71]. In the present study, it was thought that the high rate (95.8% and 87.5%) of *gcp* and *gs60* genes in the field isolates of *M. haemolytica* may differ from strain to strain in terms of the need for synthesis against immune response in adverse environmental conditions and in vivo environments.

In this study, it was concluded that the heterogeneity in *tbpB* genes was high in *M. haemolytica* isolates and since it could be detected in isolates obtained from disease cases, it was thought that it could be a criterion that could be used to distinguish between pathogenic and commensal *M. haemolytica* isolates. *nmaA* gene was not detected in the majority of isolates (91.7%), and it is thought that there may be other gene regions encoding the capsule gene. However, different gene profiles were determined according to the distribution of virulence-related genes in the isolates. While all virulence-related genes were found in all isolates with profile II, *nmaA* was not detected in isolates with profile I, and *nmaA* and *tbpB* genes were not detected in isolates with profile III. Virulence gene profile I (37.5%), III (33.3%) and II (12.5%) were detected in 83.3% of the isolates. Isolates with virulence gene profile I were associated with arginine-arginine negative isolates, and isolates with virulence gene profile III were associated with arginine-arginine positive isolates. In general, virulence genes in *M. haemolytica* isolates have heterogeneity and one of the most important reasons for this is that the agent causes mixed infection with different bacterial species. Therefore, it was concluded that new genes encoding some virulence factors may be transferred via extrachromosomal genetic materials such as plasmids and transposons, and the other reason may be due to the control of virulence factors by more than one gene.

It was concluded that arginine negativity and virulence gene I profile (*gcp*, *gs60*, *tbpB*, *lktC* and *adh* positive; *nmaA* negative) may be epidemiological criteria that can be used to distinguish between commensal and pathogenic *M. haemolytica* isolates and further studies should be conducted on the subject.

### Acknowledgement

This research was supported by Van Yüzüncü Yıl University Scientific Research Projects Coordination Unit with the project number TDK-2018-7156.

This study is summarised from a part of the first author's PhD thesis.

### REFERENCES

- [1] Et ve Süt Kurumu. Et ve Süt Kurumu sektör değerlendirme raporu. Ankara. 2016.
- [2] TÜİK Hayvancılık İstatistikleri (İnternet). 2019. [Erişim tarihi: 29.03.2020]. Erişim adresi: <https://biruni.tuik.gov.tr/medas/?kn=101&locale=tr>.
- [3] Global Animal Health Association, Animal breeding [İnternet]. 2019, [Erişim tarihi 17 Mayıs 2019]. Erişim adresi: <https://healthforanimals.org/zoonoses.html>.
- [4] Bell S. Respiratory disease in sheep: 2. Treatment and control. In Practice. 2008; 30: 278-283.
- [5] Ermilio EM, Smith MC. Treatment of emergency conditions in sheep and goats. Vet Clin Food Anim. 2011; 27: 33-45.
- [6] Statham J. Respiratory disease in cattle a practical approach. Livestock. 2018; 23 (5): 206-13.
- [7] Kumar A, Tikoo SK, Malik P, Kumar AT. Respiratory diseases of small ruminants. Hindawi Publishing Corporation Veterinary Medicine International. 2014; 373642: 2.
- [8] Şentürk B. Türkiye’de salgın hayvan hastalık sorunu ve yeni model önerileri. Harran Üniv Vet Fak Derg. 2015; 4 (1), 27-9.
- [9] Rahal A, Ahmad AH, Prakash A, Mandil R, Kumar RT. Environmental attributes to respiratory diseases of small ruminants. Vet Med INT. 2014; 853627: 10.
- [10] Öztürk D, Çorlu M. Pnömonili Koyun akciğerlerinden izole edilen bakteriler ve antibiyotik duyarlılıkları. Vet. Bil. Derg. 2006; 22 (1-2): 59-63
- [11] Yüzbaşıgil AF (2010). Kuzu pnömonilerinde patolojik ve bakteriyolojik incelemeler ile *Parainfluenza 3* (PI 3) virüsünün etiyolojideki rolü. Selçuk Üniversitesi Sağlık Bilimleri Enstitüsü, Doktora Tezi.
- [12] Rosadio R, Cirilo E, Manchego A, Rivera H. *Respiratory syncytial* and *parainfluenza type 3* viruses coexisting with *Pasteurella multocida* and *Mannheimia hemolytica* in acute pneumonias of neonatal alpacas. Small Ruminant Res. 2011; 97: 110–6.
- [13] Arslan HH, Özcan U. Current approach to bovine respiratory disease. Dairy and Vet Sci J. 2018; 5 (2): 1-3
- [14] Jesse FFA, Mubin HNA, Hambali IU, Lila MAM, Chung ELT, Abba Y, et al. Review on clinical management involving respiratory diseases in ruminants. Adv Anim. Vet. Sci. 2019; 7(4): 321-5.
- [15] Confer AW. Update on bacterial pathogenesis in BRD. Anim Health Res Rev. 2009 Dec;10(2):145-8. doi: 10.1017/S1466252309990193. PMID: 20003651.
- [16] Tomassini L, Gonzales B, Weiser GC, Sischo W. An ecologic study comparing distribution of *Pasteurella trehalosi* and *Mannheimia haemolytica* between Sierra Nevada bighorn sheep, White Mountain Bighorn Sheep, and Domestic sheep. J Wildl Dis. 2009; 45 (4): 930-40.
- [17] Hossain MM, Islam MS, Kamal AHM, Rahman AKMA, Cho HS. Dairy cattle mortality in an

- organized herd in Bangladesh. *VeterinaryWorld*. 2014; 7 (5): 331-6.
- [18] Caswell JL, Williams KJ. Respiratory system. Maxie M.G. (Ed.) Jubb, Kennedy and Palmer's Pathology of Domestic. 5. baskı. Edinburgh: Elsevier; 2016.
- [19] Angen O, Ahrens P, Kuhnert P, Christensen H, Mutters R. Proposal of *Histophilus somni* gen. nov., sp. nov. for the three species *incertae sedis* *Haemophilus somnus*, *Haemophilus agni* and *Histophilus ovis*. *Int J Syst Evol Microbiol*. 2003; 53: 1449-56.
- [20] Christensen H, Bisgaard M. Revised definition of *Actinobacillus* sensu stricto isolated from animals. A review with special emphasis on diagnosis. *Vet. Microbiol*. 2004; 99: 13-30.
- [21] Blackall PJ, Bojesen AM, Christensen H, Bisgaard M. Reclassification of *Pasteurella trehalosi* as *Bibersteinia trehalosi* gen. nov., comb. nov. *Int J Syst Evol Microbiol*. 2007; 57: 666-74.
- [22] Yavrucu E. *Mannheimia haemolytica*'nın sığır epitel hücreleri üzerindeki apoptotik etkisi [Yüksek Lisans tezi]. Ankara: Ankara Üniversitesi; 2008.
- [23] Quinn PJ (Editor), Markey BK, Leonard FC, Fitzpatrick ES, Fanning S, Hartigan PJ. *Veterinary Microbiology and Microbial Disease*, UK: John Wiley and Sons Ltd; 27: 300-308. 2011.
- [24] Mutters R, Angen Q, Bisgaard M. *Bergey's manual of systematics of archaea and bacteria*, Online *Bergey's Manual Trust*. (e-book). Published by John Wiley and Sons. in association with *Bergey's Manual Trust*. 2015. Doi: [10.1002/9781118960608.gbm01200](https://doi.org/10.1002/9781118960608.gbm01200).
- [26] Angen Ø, Mutters R, Caugant DA, Olsen JE, Bisgaard M. Taxonomic relationships of the [*Pasteurella*] *haemolytica* complex as evaluated by DNA-DNA hybridizations and 16S rRNA sequencing with proposal of *Mannheimia haemolytica* gen. nov., comb. nov., *Mannheimia granulomatis* comb. nov., *Mannheimia glucosida* sp. nov., *Mannheimia ruminalis* sp. nov. and *Mannheimia varigena* sp. nov. *Int J Syst Evol Microbiol* 1999; 49: 67-86.
- [27] Omaleki L, Browning FG, Allen JL, Barber SR. Molecular epidemiology of *Mannheimia haemolytica* and *Mannheimia glucosida* associated with ovine mastitis. *JVDI*. 2012; 24(4): 730-4.
- [28] Nefedchenko AV, Glotova TI, Glotov AG. Isolation and antimicrobial resistance of *Mannheimia haemolytica* on dairy farms in Siberia. *Bulg J Vet Med*. 2019; 22 (4): 428-38.
- [29] Highlander SK. Molecular genetic analysis of virulence in *Mannheimia* (*Pasteurella*) *haemolytica*, *Frontiers in Bioscience*. 2001; 6: 1128-50.
- [30] Lee RWH, Pool AN, Ziauddin A, Lo RYC, Shewen PE, Strommer JN. Edible vaccine development: stability of *Mannheimia haemolytica* A1 leukotoxin 50 during post-harvest processing and storage of field-grown transgenic white clover. *Kluwer Academic Publishers Molecular Breeding*. 2003; 11: 259-66.
- [31] Zecchinon L, Fett T, Desmecht D. How *Mannheimia haemolytica* defeats host defence through a kiss of death mechanism. *Vet Res*. 2005; 36: 133-56.
- [32] De la Mora A, Trigo F, Jaramillo L, Garfies Y, Solórzano C, Agundis C et al. The N-acetyl-D-glucosamine specific adhesin from *Mannheimia haemolytica* activates bovine neutrophils oxidative burst. *Vet Immunol Immunopathol*. 2006; 113 (1-2): 148-56.
- [33] Lo RYC, Sathiamoorthy S, Shewen PE. Analysis of *in vivo* expressed genes in *Mannheimia haemolytica* A1. *FEMS Microbiol Lett*. 2006; 265: 18-25.
- [34] Lee RWH, Cornelisse M, Ziauddin A, Slack PJ, Hodgins DC, Strommer JN, et al. Expression of a modified *Mannheimia haemolytica* *gs60* outer membrane lipoprotein in transgenic alfalfa for the development of an edible vaccine against Bovine Pneumonic Pasteurellosis. *J Biotechnol*. 2008; 135: 224-31.
- [35] Mohamed RA, Abdelsalam EB. A review on Pneumonic Pasteurellosis (Respiratory Mannheimiosis) with emphasis on pathogenesis, virulence mechanisms and predisposing factors. *Bulg J Vet Med*. 2008; 11 (3): 139-60.
- [36] Rice JA, Carrasco-Medina L, Hodgins DC, Shewen PE. *Mannheimia haemolytica* and bovine respiratory disease. *Anim Health Res Rev*. 2008; 8 (2): 117-28.
- [37] Hounscome JDA. Comparative outer membrane proteomic analyses of bovine and ovine isolates of *Mannheimia haemolytica* and *Mannheimia glucosida* [PhD thesis]. UK; University of Glasgow. 2012.
- [38] Puchalski A, Chmiel RU, Dec M, Wernicki A. An electrophoretic characterization of iron-transporting proteins in *Mannheimia haemolytica* A1. *Pol J Vet*. 2013; 3: 527-32.
- [39] Legesse A, Abayneh T, Mamo G, Gelaye E, Tesfaw L, Yami M, et al. Molecular characterization of *Mannheimia haemolytica* Isolates associated with Pneumonic cases of sheep in selected Areas of Central Ethiopia. *BMC Microbiol*. 2018; 18: 205.
- [40] Singh F, Sonawane GG, Meena RK. Molecular detection of virulent *Mannheimia haemolytica* and *Pasteurella multocida* in lung tissues of pneumonic sheep from semiarid tropics, Rajasthan, India. *Turk J Vet Anim Sci*. 2018; 42: 556-1.
- [41] Özbey G, Muz A. Pnömonili Koyun ve Keçilerin Akciğerlerinden Aerobik Bakteri izolasyonları ve İzole *Pasteurella multocida* ve *Mannheimia haemolytica*'nın Polimeraz Zincir Reaksiyonu ile Saptanması. *Turk J Vet Anim Sci*. 2004; 28: 209-16.
- [42] Gioia J, Qin X, Jiang H, Clinkenbeard K, L0 R, Liu Y, et al. The genome sequence of *Mannheimia haemolytica* A1: Insights into virulence, natural competence, and *Pasteurellaceae* phylogeny. *J. Bacteriol*. 2006; 7257-66.
- [43] Alexander TW, Cook SR, Yanke LJ, Booker CW, Morley PS, Read RR, et al. A multiplex polymerase

- chain reaction assay for the identification of *Mannheimia haemolytica*, *Mannheimia glucosida* and *Mannheimia ruminalis*. Vet Microbiol. 2008; 130 (1-2): 166-75.
- [44] Kumar J, Shivendra D, Kumar R. Rapid detection of *Mannheimia haemolytica* in lung tissues of sheep and from bacterial culture. Veterinary World. 2015; 8 (9): 1073-7.
- [45] Shanthalingam S, Goldy A, Bavananthasivam J, Subramaniam R, Batra SA, Kugadas A, et al. PCR assay detects *Mannheimia haemolytica* in culture negative pneumonic lung tissues of Bighorn Sheep (*Ovis Canadensis*) from outbreaks in the Western Usa, 2009–2010. J Wildl Dis. 2014; 50 (1): 1-10.
- [46] Ahmed WA, Mohammed RJ, Khalaf IA. Molecular and phenotypical characterization of *Mannheimia haemolytica* isolated from goats in Baghdad Province. AIM. 2017; 7: 304-14.
- [47] Dağ S, Gürbüz A, Özen H, Büyük F, Çelebi Ö, Karaman M, et al. Immunohistochemical and molecular detection of *Mannheimia* spp. and *Pasteurella* spp. in sheep with pneumonia in Kars Province – Turkey. Kafkas Univ Vet Fak Derg. 2018; 24 (2): 281-8.
- [48] Rawat N, Gilhare VR, Kushwaha KK, Hattimare DD, Khan FF, Shende RK et al. Isolation and molecular characterization of *Mannheimia haemolytica* and *Pasteurella multocida* associated with pneumonia of goats in Chhattisgarh. Vet World. 2019; 12 (2): 331-6.
- [49] Koneman EW (Editor), Allen SD, Dowell VR, Janda WM, Sommers HM, Winn WC. Color Atlas and Text Book of Diagnostic Microbiology. Third Edition. Lippincott Comp., Philadelphia, USA. 1988.
- [50] Carter GR (1984). *Pasteurella*, *Yersinia* and *Francisella*, chapter 11, in “Diagnostic Procedures in Veterinary Bacteriology and Mycology” Fourth Edition, 111-121, Charles C Thomas, U.S.A.
- [51] Önat K, Kahya S, Çarlı T. Frequency and antibiotic susceptibility of *Pasteurella multocida* and *Mannheimia haemolytica* isolates from nasal cavities of Cattle. Turk J Vet Anim Sci. 2010; 34 (1): 91-4.
- [52] Angen Ø, Ahrens P, Bisgaard M. Phenotypic and genotypic characterization of *Mannheimia* (*Pasteurella*) *haemolytica*-like strains isolated from diseased animals in Denmark. Vet Mic. 2002; 84: 103-14.
- [53] Laishevtcev AI, ОСОБЕННОСТИ БИОХИМИЧЕСКОЙ ИДЕНТИФИКАЦИИ И ДИФФЕРЕНЦИАЦИИ БАКТЕРИЙ ВИДА *Mannheimia haemolytica* (Features of biochemical identification and differentiation of *Mannheimia haemolytica*). RJOAS. 2016; 6 (54): 70-7.
- [54] Hawari AD, Hassawi DS, Sweiss M. Isolation and identification of *Mannheimia haemolytica* and *Pasteurella multocida* in sheep and goats using biochemical tests and Random Amplified Polymorphic DNA (RAPD) Analysis. J Biol Sci. 2008; 8(7): 1251-4.
- [55] Klima CL, Alexander TW, Hendrick S, McAllister AT. Characterization of *Mannheimia haemolytica* isolated from feedlot cattle that were healthy or treated for bovine respiratory disease. Can J Vet Res. 2014; 78 (1): 38-45.
- [56] Gülaydın Ö, Gürtürk K. Identification of *Pasteurella multocida* strains isolated from respiratory tract of healthy and diseased cattle and determination of capsular types by PCR in Van Region. Van Vet J. 2018; 29 (3): 143-6.
- [57] Ülker H, Kucuk D, Cantekin Z, Solmaz H (2012). Hatay yöresinde kesimhanede kesilen sığır akciğerlerinden *Pasteurella multocida* ve *Mannheimia haemolytica* izolasyonu ve antibiyotiklere duyarlılığı. AVKAE Derg, 2, 2, 10-14.
- [58] Gürbüz A. Sığır ve koyunlara ait pnömonili akciğerlerden *Pasteurella haemolytica*'nın izolasyonu, identifikasyonu, biyotiplendirilmesi ve antibiyotiklere olan duyarlılıklarının belirlenmesi. [Doktora Tezi]. Kars: Kafkas Üniversitesi. 2003.
- [59] Noyes NR, Benedict KM, Gow SP, Booker CW, Hannon SJ, McAllister TA, Morley PS (2015). *Mannheimia haemolytica* in feedlot cattle: prevalence of recovery and associations with antimicrobial use, resistance, and health outcomes. Journal of Veterinary Internal Medicine 29, 705–713.
- [60] Castillo JLR, Valencia GL, Monge-Navara FJ, Medina-Basulto GE, Hori-Oshima S, Cueto-Gonzalez SA, ve ark. Detection and economic impact related to bovine respiratory disease, shrink, and traveling distance in feedlot cattle in Northwest Mexico. Turk J Vet Anim Sci. 2017; 41: 294-301.
- [61] Demissie T, Dawo F, Sisay T. Biochemical and antigenic characterization of *Mannheimia*, *pasteurella* and *Mycoplasma* species from naturally infected pneumonic sheep and goats, Bishoftu, Ethiopia. AJBAS. 2014; 6 (6): 198-204.
- [62] Kırkan Ş, Kaya O. Serotyping of *Mannheimia haemolytica* Strains Isolated from Pneumonic Lungs of Sheep in the Aydın Region of Turkey. Turk J Vet Anim Sci. 2005; 29: 491-4.
- [63] Tel OY, Keskin O. Koyun akciğerlerinden *Pasteurella multocida* ve *Mannheimia haemolytica* izolasyonu ve antibiyotiklere duyarlılığı. YYÜ Vet Fak Derg. 2010; 21 (1): 31.
- [64] Bisgaard M. Incidence of *Pasteurella haemolytica* in the respiratory tract of Apparently healthy chickens and chickens with infectious bronchitis. Characterisation of 213 Strains. Avian Pathology. 1977; 6: 285-292.
- [65] Daphal SH, Mhasa PP, Pawade MM, Shelke PP, Sangle JD, Kolhe RP. Emergence of virulent *Pasteurella multocida* and *Mannheimia hemolytica* in sheep and goats of Western Maharashtra, India. Int J Curr Microbiol App Sci. 2018; 7 (9): 1990-1998.
- [66] Angen Q, Aalbjek B, Falsen E, Olsen JE, Bisgaard M. Relationships among strains classified with the ruminant *Pasteurella haemolytica*-complex using quantitative evaluation of phenotypic Data. Zbl. Bakt. 1997; 285: 459-79.
- [67] Taunde PA, Argenta FF, Bianchi RM, De Cecco BS, Vielmo A, Lopes BC, et al. *Mannheimia*

- haemolytica* pleuropneumonia in goats associated with shipping stress. *Ciencia Rural*. 2019; 49(1): 1-6.
- [68] İlhan Z, Keleş İ. Biotyping and serotyping of *Mannheimia (Pasteurella) haemolytica* isolated from lung samples of slaughtered sheep in the Van Region. *Turk J Vet Anim Sci*. 2007; 31 (2): 137-41
- [69] Şahin İ. Samsun ili ve çevresinde koyun pnömonilerinden izole edilen *Mannheimia haemolytica* türlerinin fenotipik karakterizasyonu ve antibiyotik duyarlılıklarının belirlenmesi. Samsun, Ondokuz Mayıs Üniversitesi. 2017.
- [70] Fisher MA, Weiser GC, Hunter DL, Ward ACS. Use of a Polymerase Chain Reaction method to detect the leucotoxine gene *lktA* in biogrup and biovariant isolates of *Pasteurella haemolytica* and *Pasteurella trehalosi*. *Am. J. Vet. Res.* 1999; 11: 1402-6.
- [71] Kırkan Ş. Aydın yöresinde koyunların solunum sisteminde infeksiyon nedeni *Mannheimia (Pasteurella) haemolytica*'nın biyotip ve Serotip tayini, elektroforez ve PCR ile tanısı. [Doktora Tezi]. Aydın: Adnan Menderes Üniversitesi. 2003.
- [72] El Dokmak MM, Khalil SA, Ebied SKHM. Genetic diversity of *Mannheimia haemolytica* strains. *AJVS*. 2015; 47: 166-74.
- [73] Garcia-Alvarez A, Garayzabal JF, Chaves F, Pinto C, Cid D. Ovine *Mannheimia haemolytica* Isolates from Lungs with and without Pneumonic Lesions Belong to Similar Genotypes. *Vet Microbiol*. 2018; 219: 80-6.



## Economic Analysis of Automatic Meter Reading on Web Based in Türkiye Using Nginx Load Balancer Technology

Şükrü KARAASLAN<sup>1\*</sup>, Mazhar KAYAOĞLU<sup>2</sup>, Mehmet GEDİKPİNAR<sup>3</sup>, Abdulkadir ŞENGÜR<sup>4</sup>

<sup>1</sup> Fırat University, Organized Industrial Zone Vocational School, Department of Electricity and Energy, Elazığ, Türkiye

<sup>2</sup> Bingöl University, Department of Informatics, Bingöl, Türkiye

<sup>3</sup> Fırat University, Faculty of Technology, Department of Electricity and Electronics, Elazığ, Türkiye

<sup>4</sup> Fırat University, Faculty of Technology, Department of Electricity and Electronics, Elazığ, Türkiye

Şükrü KARAASLAN ORCID No: 0000-0001-8511-0388

Mazhar KAYAOĞLU ORCID No: 0000-0002-5807-9781

Mehmet GEDİKPİNAR ORCID No: 0000-0002-1045-7384

Abdulkadir ŞENGÜR ORCID No: 0000-0003-1614-2639

\*Corresponding author: [s.karaaslan@firat.edu.tr](mailto:s.karaaslan@firat.edu.tr)

(Received: 29.12.2023, Accepted: 20.07.2024, Online Publication: 26.09.2024)

### Keywords

Automatic meter reading, Techno economic analysis, Load balancer

**Abstract:** Electricity meters, which are read manually, bring a great financial burden to companies in terms of workload, time and economy. In this study, examined the reading of electric meters automatically process, Türkiye focused on cost-benefit analysis performed. With the ever-increasing electricity consumption, the number of electricity expenses and accordingly the number of subscribers increases. Along with the increasing number of electricity consumers, the number of subscribers and consequently electricity consumption increases. Automatic Meter Reading Systems is one of the recommended solution packages for Energy Management Systems. It is for python programming language and its frameworks as software infrastructure. Nginx is used as a web server, and Web Server Gateway Interface and Gunicorn frameworks are used for the connection between the application and the web server. Thanks to automatic meter reading system, which has an extremely fast reading structure, it is predicted that tens of thousands of electricity meters can be read over the internet in seconds. Nginx Load Balancer software technology is capable of transferring tens of thousands of indexes to the database at once. This technology is able to distribute data load and respond to data traffic. In addition, the effect of reading cost on Energy Management Systems is analyzed in meters that are read manually. Türkiye's Elazığ province, economic research analysis was conducted on a total of 334 thousand electricity subscribers. According to survey data, 47 million has electricity subscribers in Türkiye. In addition, cost-benefit analysis of the meters that are foreseen to be read in Nginx load balancer software technology is performed.

## Nginx Yük Dengeleyicisi Kullanılarak Web Tabanlı Otomatik Sayaç Okumanın Türkiye'deki Ekonomik Analizi

### Anahtar

### Kelimeler

Otomatik sayaç okuma, Tekno ekonomik analiz, Yük dengeleyici

**Öz:** Manuel olarak okunan elektrik sayaçları iş yükü, zaman ve ekonomik açıdan şirketlere büyük bir mali yük getirmektedir. Bu çalışmada elektrik sayaçlarının otomatik olarak okunması işlemi incelenerek Türkiye odaklı maliyet-fayda analizi yapılmaktadır. Sürekli olarak artan elektrik tüketimi ile birlikte elektrik tüketici sayısı ve buna bağlı olarak da abone sayısı artmaktadır. Otomatik Sayaç Okuma Sistemleri, Enerji Yönetim Sistemleri çözüm paketlerinden bir tanesidir. Yazılım alt yapısı olarak python programlama dili ve onun frameworkleri kullanılmaktadır. Web sunucusu olarak Nginx, uygulaması ile web sunucusu arasındaki bağlantı için de Web Server Gateway Interface ve Gunicorn framework yapıları kullanılmaktadır. Uygulama Flask framework yapısı üzerine kurulu olup veritabanı olarak gelişmiş bir yapıya sahip olan PostgreSQL framework'ü kullanılmaktadır. Son derece hızlı bir okuma yapısına sahip olan otomatik sayaç okuma sistemi sayesinde on binlerce elektrik sayacının internet ağı üzerinden saniyeler içerisinde okunabilmesi öngörülmektedir. Nginx Load Balancer yazılım teknolojisi, on binlerce sayaç

endeksini tek seferde veritabanına aktarabilme özelliğindedir. Bu teknoloji veri yük dağılımını yapabilmekte ve veri trafiğine cevap verebilmektedir. Ayrıca manuel olarak okunan sayaçlarda okuma maliyetinin, enerji yönetim sistemleri üzerindeki etkisi incelenmektedir. Araştırmanın ekonomik analizi ise Türkiye'nin Elazığ ilinde bulunan toplam 334 bin elektrik abonesi üzerinde yapılmıştır. Araştırma verilerinden yola çıkarak Türkiye'de bulunan 47 milyon elektrik abonesi bulunmaktadır. Nginx yük dengeleyici yazılım teknolojisiyle okunması öngörülen sayaçların maliyet-fayda analizi yapılmaktadır.

## 1. INTRODUCTION

Intelligent measurement technology in electricity distribution has made it necessary to meet the increasing data from demand of electricity consumers and to obtain healthy electricity networks. Therefore, web-based reading of the electricity meter in residential, commercial and industrial areas and the use of related applications are increasing [1]. In terms of energy efficiency and Energy Management Systems (EMS), it is very important for electrical measuring devices to interact with each other over the Internet without the need for people.

These systems combined under the umbrella of Automatic Meter Reading (AMR) Systems are important applications for the automation of electrical network measurement processes [2]. Existing electricity meter reading procedures used in Türkiye is done largely manually. However, automatic reading is made in narrow areas and pilot study areas. Automatic readings are also extremely inefficient and contain a limited number of electricity meters. Using existing automatic readings can cause some other communication problems, especially the internet connection problem. With Nginx Load Balancer (NLB) software technology, web-based electricity meters can read many electricity meters instantly, and thanks to the developed smart software, they can perform operations such as billing, leakage electricity detection, on-off very quickly [3]. In Figure 1, the operation of the automatic meter reading system is schematized.

In order to meet the rapidly increasing demands for power, power systems are undergoing a transition from analogue to digital control and communication systems. While this modernisation brings numerous benefits, the introduction of new hardware and software in power systems also introduces vulnerabilities. These vulnerabilities can be exploited to alter electricity meter readings, potentially leading to significant financial losses. In order to prevent such attacks on electricity meter readings, it is necessary to develop software models for automatic reading methods [8,9]. As numerous studies have demonstrated, the implementation of smart meters around the globe is encountering a multitude of challenges [10,11]. Consequently, the slow pace of progress and mounting concerns have prompted the necessity for the development of novel applications of smart meters in domains such as the protection and monitoring of the evolving distribution system [12,13]. Additionally, the smart meter can be employed to monitor the power

consumption of individual devices, thereby offering insights into customers' power usage patterns [14].

This paper proposes a software model for efficient reading of a large number of electricity meters. This software model is envisaged to perform tasks such as reading electricity meters, billing and reducing electricity leakage. In addition, in this study, the electrical data in an electricity meter is read automatically by means of the developed software. The economic analysis of the automatic meter reading system to the energy management system is also carried out in the paper. For this purpose, Elazığ province of Türkiye is taken as the research region and the necessary technical and economic analyses are carried out comparatively.

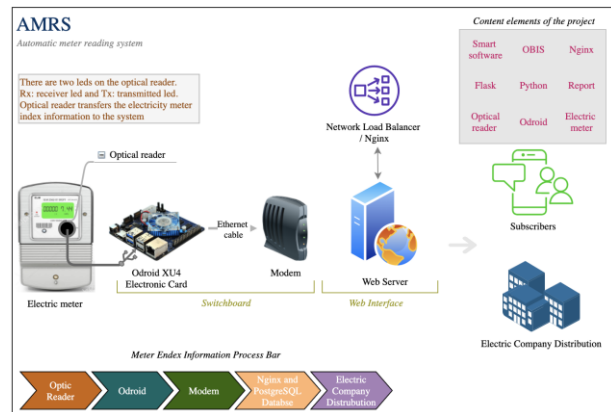


**Figure 1.** The path of the meter index data between the hardware units (The data is taken from the meter and reaches the electricity distribution company or the subscriber)

## 2. NLB TECHNOLOGY AND SMART SOFTWARE

NLB performs the task of balancing thousands of meters of index information with Load Balancer and distributing it to web servers. In this way, electricity consumption can be monitored instantly.

### 2.1. Material and Method NLB and Python Frameworks Configurations

NLB is a load balancing job. It is also a technology of sharing a data collection between computers, processors, web servers and their framework structures. For automatic meter reading, NLB can be defined as software technology that shares requests from users and transmits index information from the meters to the user quickly by reducing response time [3]. In the software scheme shown in Figure 2, when the meter readers or end consumers at the electricity distribution company make a request, the request data is balanced in the Nginx Load Balancer structure and sent to the Gunicorn frame

structure. It is the gateway to the Web Server Gateway Interface (WSGI).

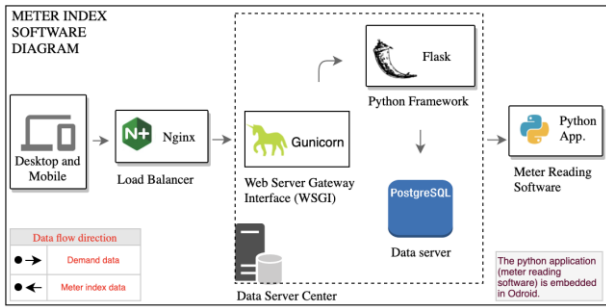


**Figure 2.** Load distribution of the counter index on web servers and its frameworks (Requests from computer and mobile application are balanced with the help of load balancer and transferred to the relevant framework structures. Index information from the meter is followed by the user by following the same path)

The request data is then transferred to the Flask frame server, a framework of meter reading software. Finally, a python application with meter reading software alerts the relevant counters based on this meter data and, after performing an authentication, collects the index information on the meters and saves them in the buffer section. The next process is the display of meter data in the meter reading software. Index information can be viewed by users by following the path of Flask, Gunicorn, Nginx Load Balancer.

## 2.2. Smart Software

After the meter index information is shown to the electricity distribution company representative and the end user, this data billed by a smart software. With this software, which can map the electricity consumption instantly, it is thought that it will provide an important feedback contribution in the future of electrical energy investments.

## 3. RESEARCH METHODS AND SYSTEM DEFINITION

### 3.1. Research Methods

The number of electricity customers in the electricity distribution companies in Türkiye in 2020 and 2021 are shown in Table 1. [4]. The financial analysis of meter reading manually within one year is examined in this section. Türkiye's Elazig province made research on electricity meters and 334 thousand subscribers is projected to reach some conclusions. The distribution of financial expenses of companies that read meters in Türkiye is shown in Table 3 as a percentage. In Table 2 based on the results of the research indicated in Türkiye's Elazig province electricity meters are read within 30 days.

**Table 1.** Number of subscribers in electricity distribution regions

Region	2020	2021	Change %
Boğaziçi	5.206.237	5.309.628	1.99
Başkent	4.364.492	4.450.587	1.97
Toroslar	4.095.347	4.199.880	2.55
Gdz	3.524.199	3.642.279	3.35
Uludağ	3.380.111	3.461.642	2.41
İ. Anadolu	2.986.337	3.036.679	1.69
Akdeniz	2.261.116	2.317.587	2.5
Yeşilirmak	2.206.997	2.278.063	3.22
Adm	2.021.409	2.127.291	5.24
Dicle	1.993.050	2.055.864	3.15
Sakarya	1.963.823	2.022.256	2.98
Osmanğazi	1.888.406	1.932.244	2.32
Çoruh	1.431.106	1.468.083	2.58
Trakya	1.168.941	1.207.476	3.3
Aras	1.059.704	1.095.423	3.37
Firat	1.012.087	1.059.759	4.71
Çamlıbel	1.017.033	1.037.517	2.01
Kayseri	770.120	788.102	2.33
Vangölu	745.985	775.669	3.98
Akedaş	758.175	764.761	0.87
<b>Total</b>	<b>46.081.856</b>	<b>47.311.976</b>	<b>2.67</b>

**Table 2.** Research data of meters in Elazığ province

Expenses monthly	Unit	Price
Workplace rent	USD	300
Number of staff	Unit	51
Salaries of staff	USD	60000
Number of vehicles	Unit	12
Vehicle expense	USD	18000
Number of subscribers	Unit	334000
Profit share	USD	19575 %25
Meter readers/ Fixture	USD/Unit	135000 - 45
Other	USD	450

**Table 3.** Share of some economic factors in the cost of manuel meter reading in Türkiye

Description	Percentile
Staff expenses	59.3%
Transportation expenses	17.7%
Company profit share	19.3%
<b>Total</b>	<b>100%</b>

### 3.2. Time Loss Calculation

Manual meter reading has an economical cost and causes a decrease in work efficiency in terms of labor and time loss. 8935 personnel in Türkiye are constantly read the meter. As it is known that the number of electricity subscriber increases day by day, the time lost is constantly increasing. These decreases work efficiency by increasing the human-based workforce. We can symbolize the number of meters that a staff read in a day (8 hours) with RCD (Number of reading counters in a day). The related expression is shown in Equation 1 and Equation 2.

$$RCD = \frac{\text{Number of subscriber}}{\text{Number of personel}} \quad (1)$$

$$RCD = \frac{334.000 SN}{45 PN} \times \frac{1}{30 \text{ day}} = 247.4 SN / (PN \cdot \text{day}) \quad (2)$$

At the same time, we can call the waste of time reading a meter, WOT (Waste of time). Number of subscriber (SN) is shown as number of staff (PN). The related expression is shown in Equation 3 and Equation 4. The graph of the total time loss by years depending on the number of subscribers is shown in Figure 3.

$$WOT = \frac{\text{Working time}}{RCD} \quad (3)$$

$$WOT = \frac{\frac{8 \text{ hours}}{\text{day}} \times \frac{60 \text{ min}}{\text{hours}} \times \frac{1}{PN}}{247.4 \frac{SN}{PN \cdot \text{day}}} = 1.92 \text{ min}/SN \quad (4)$$

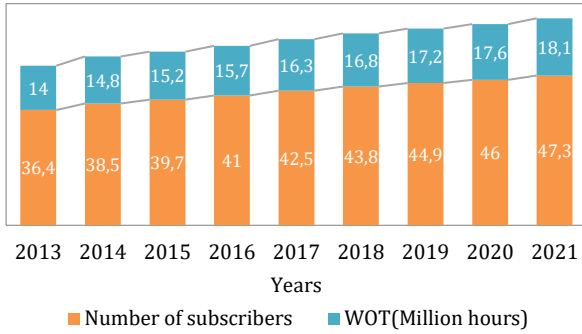


Figure 3. Total time loss graph depending on the number of subscribers (from 2013 to 2021)

### 3.3. Real State of the System

The real state of the system includes a digital electricity meter, optical port reader with USB output and single board computer components produced according to TSE (Turkish Standards Institute) standards. In the designed experimental setup, a 105 W incandescent bulb is connected to the meter output and it is aimed to monitor the consumption data of the measuring device instantly. An optical port reader is attached to the relevant part to enable communication with the measuring device. The data in the measuring device is read and saved in the temporary memory of the single board computer running the Linux operating system and then transferred to the web servers. The compatibility between the software blocks is very important for the data rate to be high and for the system to respond to heavy data traffic. In this study, a harmony between the software blocks has been achieved in order to reduce the data rate and to read a large number of meters at once. Especially Linux operating system and other framework structures are preferred because it is python based. Because the meter reading software created is based on python. The meter reading software is embedded locally in the single board computer shown in Figure 4. The system can work with wired internet network or it can work with wireless internet network after the SIM card module is integrated into the system. This study, which realizes the remote-control event, also resolves the subscriber's electrical energy on-off event to a large extent.

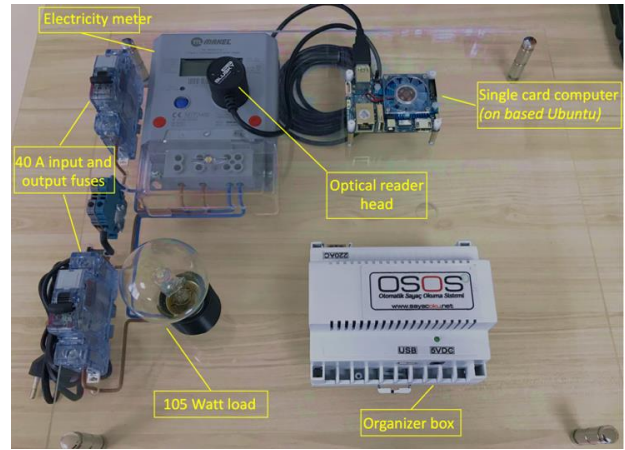


Figure 4. Prototype of automatic meter reading system

The electrical parameters inside the meter have a memory. In other words, each address belongs to an electrical data. These addresses are called Object Identification System (OBIS). Intelligent software improves its operations according to OBIS codes and generates the necessary reports. In this case, the smallest information packet is in the state of electricity stored in OBIS. Some important ones of OBIS code definitions are given in Table 4 and the necessary usage is explained [5].

Table 4. Counter object identification system (OBIS) codes

OBIS Codes	Codes Definition	Unit	Format
0.9.2	Date	-	yyyy-mm-dd
0.9.1	Time	-	hh:mm:ss
1.8.0	T Total active energy	kWh	1234.567
5.8.0	Ri, Inductive reactive energy	kVArh	1234.567
6.8.0	Rc, Capacitive reactive energy	kVArh	1234.567
1.6.0	Maximum active power demand	kW	1234.567

### 3.4. Run of Meter Reading Software

Meter reading codes on a single board computer are run by PyCharm, a python compiler, and the results are observed [6,7]. After reading the meter reading codes, the index data from the meter is shown in Figure 5 and Figure 6. The connection between the meter and python application is provided in accordance with the IEC 62056-21 protocol. In order to get data from the meter, an authentication process must be made between the meter and the python application. In Figure 5, the python application sends an identification query code to the measuring device.

```

serialport = "/dev/ttyUSB0"
init_seq = bytes('?!\\r\\n', 'ascii')
request = bytearray('\\x06000r\\n', 'ascii')

serial = serial.Serial(serialport, 300, bytesize=serial.SEVENBITS,
                       parity=serial.PARITY_EVEN, timeout=5, interCharTimeout=2)

serial.flushInput()
serial.write(init_seq)
print("send init:\n> {}".format((init_seq.decode('iso-8859-9'))[:-2]))
response = bytes()
newlines = 0
try:
    while newlines < 1:
        response += serial.read()
        length = len(response)
        # count newlines
        if (0x0a or 0x0d) in response:
            newlines += 1
            ehz_id = response
            print("got id:\n< {}".format((ehz_id.decode('iso-8859-9'))[:-2]))
except Exception as e:
    print("No ID")

***THIS PART OF THE CODE IS RESERVED***

try:
    wait = 1.0
    time.sleep(wait)
    print("send ACK:\n> {}".format((request.decode('iso-8859-9'))[:-2]))
    new = 'false'
    while new == 'false':
        response2 = bytes()
        time.sleep(0.5)
        serial.baudrate = 300
        print("switch to 300 baud")
        serial.write(request)
        time.sleep(0.5)
        print("send hex: {}".format(request))
        # print (os.popen('stty -F /dev/ehz-hz').read())
        serial.baudrate = new_ascii_baudrate
        serial.timeout = 1
        print("switch to {} baud".format(new_ascii_baudrate))
        # print (os.popen('stty -F /dev/ehz-hz').read())
        response2 += serial.read()
        # print (response2.decode('iso-8859-9'))
        if len(response2) > 0:
            if 0x02 in response2:
                print("got STX")
                end = 'false'
            while end == 'false':
                response2 += serial.read()
                # print ("RESPONSE:{}".format(response2.decode('iso-8859-9')))
                if (0x03 in response2) and (0x21 in response2):
                    print("got ETX")
                    end = 'true'
                print("FINISH:\n{}".format(response2.decode('iso-8859-9')))
                new = 'true'
except Exception as e:
    print("ERROR: {}".format(e))

```

Figure 5. Embedded system python code written to communicate with the electricity meter and read the data in it.

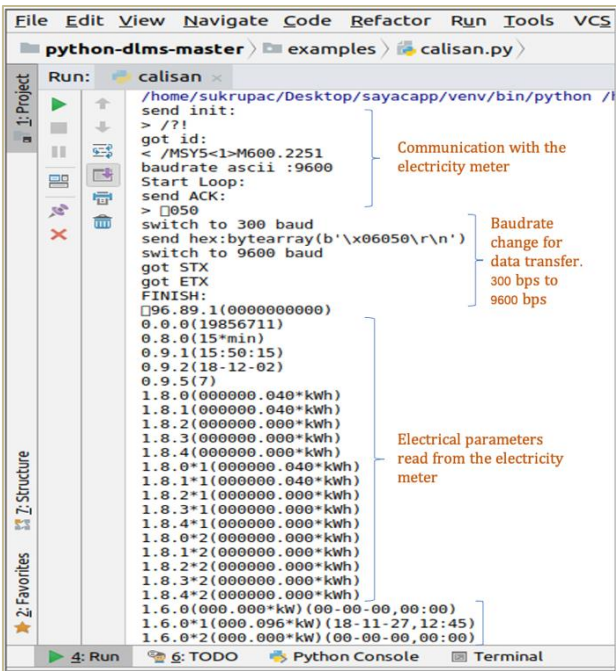


Figure 6. Monitoring the data received from the electricity meter on the PyCharm interface

The counter wakes up with this code and sends "counter identification information" to the python application, such as brand, model and year of manufacture in the memory of the meter. If the counter shows credentials, it means that it accepts communication. This initial communication with the meter takes place at 300 bps. When the index information of the meter is read, it is the second part of the communication. The second communication with the meter takes place at 9600 bps. Communication between the meter and the python

application ends automatically after it is received from the meter. In addition, in Figure 6, the meter data has been successfully obtained with the OBIS codes representing the electrical index data. A python-based meter reading software has been developed that can communicate with the optical communication part of the meter. This developed software has been tested on various brands and models of electricity meters. Success rate has been achieved with high accuracy.

#### 4. DISCUSSION AND CONCLUSIONS

Manual reading / control of electricity meters brings a huge workload and financial burden to companies. In this study, it is aimed to reduce the loss of labor and save time by reading the electricity meters automatically. Overall, the study focuses on local Elazig province in the Türkiye. In this context, the necessity of working with cost-benefit analysis was examined. With the increasing electricity consumption, the number of electricity consumers and subscribers increases accordingly. Thus, some studies have been made and many solutions have been proposed to use the energy produced efficiently. One of the important solutions proposed by Energy Management Systems (EMS) for the solution of existing problems is the addition of Automatic Meter Reading Systems (AMRS). In the study, Python programming language and frameworks are used as software infrastructure. Nginx web server and Web Server Gateway Interface (WSGI) and Gunicorn frameworks are used for connection. The application is based on the Flask framework structure and PostgreSQL framework, which has an advanced structure as a database, has been tried. Based on the data obtained from the studies, it is thought that many (tens of thousands) of electricity meters can be read over the Internet network in a short time (seconds). In addition, Nginx Load Balancer (NLB) software technology has the ability to transfer many electricity meters indexes to the database at once. This technology can make data-load distribution and respond to two-way intensive data traffic. An important dimension of the study is in the context of researching and examining the effect of reading cost on energy management systems in meters that are read manually. The economic analysis of the research was carried out on 334 thousand electricity subscribers in Elazig province. Based on the survey data towards Elazig, 47 million in Türkiye of electricity subscribers through this methodology, the impact could be detailed techno-economic efficiency.

#### REFERENCES

- [1] Amer W, Attique Y, Ghafoor A. "Comprehensive e-Monitoring, e-Management and e-Billing (eM2B) system with Zoom\_in and Zoom-Out capabilities to reduce electricity distribution loses for developing countries". *IEEE 2010 International Systems Conference*, San Diego, USA, 05-08 April 2010.
- [2] Wibisino G, Saktiaji GP, Ibrahim I. "Techno economiz analysis of smart meter reading implementation in PLN Bali using LoRa technology". *2017 International Conference on*

*Broadband Communication, Wireless Sensors and Powering (BCWSP)*, Jakarta, Indonesia, 21-23 November 2017.

- [3] Chi X, Liu B, Niu Q, Wu Q. “Web Load Balance and Cache Optimization Design Based Nginx under High-Concurrency Environment”. *2012 Third International Conference on Digital Manufacturing & Automation*, Guilin, China, 31 July – 02 August 2012.
- [4] Republic of Türkiye, Energy Market Regulatory Authority. “Electricity Market Sector Report 2013-2021”. Republic of Türkiye, Energy Market Regulatory Authority, Ankara, Türkiye, 2021.
- [5] International Standard, IEC 62056-21. “Electricity metering, data exchange from meter reading, tariff and load control”. International standard 2018.
- [6] Fernandes SL, Bala GJ. “Odroid XU4 based implementation of decision level fusion approach for matching computer generated sketches”, *2016 Journal of Computational Science*, Tamil Nadu, India, September 2016.
- [7] Qusay IS, Szatmari A, Toth R, Beszedes A. “CharmFL: A Fault Localization Tool for Python”. *2021 IEEE 12th International Working Conference on Source Code Analysis and Manipulation (SCAM)*, Luxembourg, 27-28 September 2021.
- [8] Xia, X., Xiao, Y., Liang, W., & Cui, J. (2022). Detection methods in smart meters for electricity thefts: A survey. *Proceedings of the IEEE*, *110*(2), 273-319.
- [9] Chakraborty, S., Das, S., Sidhu, T., & Siva, A. K. (2021). Smart meters for enhancing protection and monitoring functions in emerging distribution systems. *International Journal of Electrical Power & Energy Systems*, *127*, 106626.
- [10] Gaggero, G. B., Marchese, M., Moheddine, A., & Patrone, F. (2021). A possible smart metering system evolution for rural and remote areas employing unmanned aerial vehicles and internet of things in smart grids. *Sensors*, *21*(5), 1627.
- [11] Sharma, R., Gandhi, R., Sungheetha, A., Chinnaiyan, R., & Deepaletchumi, N. (2024, February). Smart Measuring Device for Power with Digital Debiting System Using Mobile Application Tool. In *2024 4th International Conference on Innovative Practices in Technology and Management (ICIPTM)* (pp. 1-6). IEEE.
- [12] Vlasa, I., Gligor, A., Dumitru, C. D., & Iantovics, L. B. (2020). Smart metering systems optimization for non-technical losses reduction and consumption recording operation improvement in electricity sector. *Sensors*, *20*(10), 2947.
- [13] Dimkpa, V. C., Agba, J. C., & Ogu, V. U. Design and Construction of a GSM Based Energy Meter Reader and Load Control System.
- [14] Shunmugalatha, A., Balamurugan, K., Aravind, D. S., & ShanmugaSundarapandi, B. (2023, August). Design and Development of Autonomous Smart Energy Meter with Remote Management Control. In *2023 Second International Conference on Augmented Intelligence and Sustainable Systems (ICAISS)*(pp. 1782-1785). IEEE.

## Comparative Investigation of Deep Convolutional Networks in Detection of Plant Diseases

Fikriye ATAMAN<sup>1\*</sup>, Halil EROĞLU<sup>2</sup>

<sup>1</sup> Van Yüzüncü Yıl University, Engineering Faculty, Computer Engineering Department, Van, Türkiye

<sup>2</sup> Van Yüzüncü Yıl University, Institute of Natural and Applied Sciences, Artificial Intelligence and Robotics Department, Van, Türkiye

Fikriye ATAMAN ORCID No: 0000-0002-0257-7730

Halil EROĞLU ORCID No: 0009-0008-8576-2771

\*Corresponding author: fataman@yyu.edu.tr

(Received: 02.05.2024, Accepted: 20.07.2024, Online Publication: 26.09.2024)

### Keywords

Deep learning,  
Image processing,  
Convolutional  
neural networks,  
Plant disease  
detection

**Abstract:** Preserving plant health and early detection of diseases are crucial in modern agriculture. Artificial intelligence techniques, particularly deep learning networks, are employed for this purpose. In this study, disease recognition was conducted using leaf images from various plant species. The study encompassed important agricultural products such as apples, strawberries, grapes, corn, peppers, and potatoes among the plant species considered. Among the deep learning networks, popular architectures like AlexNet, Vgg16, MobileNetV2, and Inception were compared. The Inception V3 model achieved the highest success rate of 92%, followed by the AlexNet architecture with a success rate of 91%. Among these networks, the InceptionV3 model yielded the best results. The InceptionV3 model effectively learned from plant leaf images and accurately distinguished between diseased and healthy leaves. These findings demonstrate that AI-based systems can be efficiently utilized for disease recognition and prevention in the agriculture sector. In this study, the performance of the InceptionV3 model in disease recognition on plant leaves was analyzed in detail, emphasizing the role of deep learning networks in agricultural applications.

## Bitki Hastalıklarının Tespitinde Derin Evrişimli Ağların Karşılaştırmalı İncelenmesi

### Anahtar Kelimeler

Derin öğrenme,  
Görüntü işleme,  
Evrişimli sinir  
ağları,  
Bitki hastalıkları  
tespiti

**Öz:** Modern tarımda bitki sağlığını korumak ve hastalıkları erken teşhis etmek çok önemlidir. Bu amaçla yapay zekâ tekniklerinden, özellikle de derin öğrenme ağlarından yararlanılmaktadır. Bu çalışmada, çeşitli bitki türlerine ait yaprak görüntülerini kullanarak hastalık tanıma işlemi gerçekleştirilmiştir. Çalışmada ele alınan bitki türleri arasında elma, çilek, üzüm, mısır, biber, patates gibi önemli tarım ürünleri bulunmaktadır. Derin öğrenme ağları arasında ise AlexNet, Vgg16, MobileNetV2 ve Inception gibi yaygın mimariler karşılaştırılmıştır. %92 ile en yüksek başarı oranı Inception V3 modeline aittir. Inception V3 modelini ise %91 başarı oranı ile AlexNet mimarisi takip etmektedir. Bu ağlar arasında en iyi sonucu, InceptionV3 modeli vermiştir. InceptionV3 modeli, bitki yapraklarının görüntülerini etkili bir şekilde öğrenerek hastalıklı ve sağlıklı yaprakları doğru bir şekilde ayırt edebilmiştir. Bu sonuçlar, yapay zekâ tabanlı sistemlerin tarım sektöründe hastalık tanıma ve önleme konusunda etkin bir şekilde kullanılabileceğini göstermektedir. Bu çalışmada, InceptionV3 modelinin bitki yaprakları üzerinde hastalık tanıma konusundaki performansı ayrıntılı bir şekilde analiz edilmiş, derin öğrenme ağlarının tarımsal uygulamalardaki rolü vurgulanmıştır.

### 1. INTRODUCTION

Agriculture has vital importance for humanity's nutrition. Therefore, it is required to use the sources efficiently and effectively. One of the key factors to achieve increasing sustainable efficiency is having healthy agricultural products and early diagnoses of diseases. The health of

plants generally depends on the conditions of the plant's leaves, and the analysis of those leaves is essential for early diagnosis of any diseases.

The diagnosis and monitoring of plant diseases are generally done by hand in traditional ways by experts. However, these traditional ways are disadvantageous in

terms of both time and cost. Therefore, artificial intelligence techniques, particularly deep learning networks, provide an alternative and efficient fast, and accurate solution to diagnose plant diseases. Deep learning networks are able to define complicated patterns through large quantities of data[1] and this provides a great advantage for diagnosing plant diseases.

Four different convolutional deep neural network models were used in this study to define the best model for diagnosing plant diseases. An open data set which includes images of different plants is used in this analysis. A detailed explanation of the dataset is given in the following section entitled "Materials". The comparison between four different models described and analyzed in this study will contribute to the studies on diagnosing plant diseases.

There is much research on defining plant diseases through deep learning networks in the literature. The literature shows that previous research has mostly tested different modeling with data from one or a few different plants. A wider dataset which includes data from 38 different categories and deep network models which has not been used previously for plant diseases are used in this study.

The most recent studies on defining plant diseases in the literature are listed below:

Benfenati et al. [2] has developed two different deep learning approaches to automatically define the powdery mildew disease on cucumber leaves. They concentrated on investigating the use of unsupervised techniques which were used to eliminate the need for images that were mostly tagged by hand. For this purpose, autoencoder networks were applied using the following methods for unsupervised detection of disease symptoms[2].

Ahmed et al. [3] used the "Plant Village" data set, which includes 17 basic diseases. These diseases include 4 bacterial diseases, 2 virus-related diseases, 2 fungal diseases, and 1 mite-related disease. Additionally, the dataset covers a total of 12 different plant species with images of healthy leaves. Support vector machines, gray-level co-occurrence matrices, and convolutional neural networks have been used as machine-learning approaches to develop predictive models[3].

Shovon et al. [4] have proposed a new and powerful deep learning group model, named PlantDet, based on InceptionResNetV2, EfficientNetV2L, and Xception models. PlantDet can solve poor data compliance problems and provide powerful performance for a limited dataset that includes limited background images at the same time. PlantDet consists of efficient data boost, preprocessing, average pooling layering worldwide, L2 regulators, PreLU activation functions, batch normalization layers, and many more layers. As a result, in comparison to all other models, it provides a more durable model to sustain high performance when

working on poor data compliance and high data compliance problems [4].

Bouguettaya et al. [5] have analyzed the most recent developments in diagnosing plant diseases and their treatment by using deep learning algorithms and computer aid visualization techniques based on IHA technology[5].

Ahmad et al. [6] has evaluated the possibility of generalizing using DL models for the prediction of corn diseases with different datasets and environmental conditions. They used five different datasets which include images of leaf diseases in corn plants. Multiple DL-based image classification models were trained and evaluated with different datasets. Five different pre-trained deep learning neural network architectures (InceptionV3, ResNet50, VGG16, DenseNet169, and Xception) were used with the transfer learning method. After the models were trained, the ability of DL models to generalize was evaluated by using the images of corn diseases from different datasets as testing data. It was observed that DenseNet169 modeling indicated the best performance. DenseNet169 model indicated the highest generalization accuracy of 81.60% when it was trained by using red, green, blue, and alpha (RGBA) images from CD&S corn disease datasets with removed backgrounds. An accuracy of 77.50% to 80.33% was observed when the PlantVillage dataset was used with images from the field and with PlantDoc or CD&S datasets[6].

Moupojou et al. [7] have suggested the FieldPlant dataset which contains 5.170 images of plant diseases directly from the field. Each leaf in the images was tagged individually by hand under the supervision of plant pathologists to ensure the quality of the process. Therefore, through 27 disease classification, 8.629 individual leaves were tagged. Lately, comparison tests were carried out on this dataset to evaluate classification and object detection models, and it was found that classification tasks were more successful through FieldPlant compared to PlantDoc[7].

In the study by Guan E. [8], the model trained using the dynamic learning rate reduction strategy achieved 99.80% accuracy on the Plant Village plant disease and pest dataset. Moreover, through transfer learning on the IP102 dataset, which represents real-world environmental conditions, the Dise-Efficient model achieves 64.40% accuracy in plant disease and pest identification. In light of these results, the proposed Dise-Efficient model has a high potential to become a valuable reference for the future deployment of automatic plant disease and pest detection applications on mobile and embedded devices[8].

In the study conducted by Shoaib E. [9], the latest developments in the use of machine learning (ML) and deep learning (DL) techniques for the identification of plant diseases are investigated. The research focuses on studies published between 2015 and 2022, and the experiments



discussed in this study demonstrate the effectiveness of using these techniques in improving the accuracy and efficiency of plant disease detection. The study also addresses the challenges and limitations associated with plant disease detection using ML and DL. These challenges and limitations include data availability, image quality, and distinguishing between healthy and diseased plants. The research provides valuable information for plant disease detection researchers, practitioners, and industry professionals by providing solutions to these challenges and limitations, comprehensively understanding the current state of research in this field, highlighting the benefits and limitations of these methods, and proposing potential solutions to overcome implementation issues[9].

Pandian et al. [10], a new 14-layer deep convolutional neural network (14-DCNN) is proposed to detect plant leaf diseases using leaf images. A new data set was created using various data sets from open sources. Data augmentation techniques were used to eliminate the sampling imbalance of classes in the data set. Three different image augmentation techniques were used; basic image processing, deep convolutional generator-discriminator networks (DCGAN), and neural style transfer. The created dataset consists of 147,500 images, including 58 unique healthy and diseased plant leaf classes and a non-leaf class. The proposed DCNN model was trained for 1000 epochs in a multi-graphics processing unit environment. To select the most appropriate hyperparameter values to improve training performance, a random search method based on a fine-grained search technique from a coarse-grained search was used. On 8850 images in the test set, the proposed DCNN model achieved 99.9655% overall classification accuracy, 99.7999% weighted average precision, 99.7966% weighted average recall, and 99.7968% weighted average F1 score. In addition, the overall performance of the proposed DCNN model yielded better results than existing transfer learning approaches [10].

Alzahrani et al. [11] compared the performances of three different deep learning models: DenseNet169, ResNet50V2, and the ViT model, which is an image transformer model. The comparison was carried out on the diagnosis of diseases affecting tomato plants. An image dataset consisting of diseased and healthy tomato leaves was used to train and test the models. The DenseNet169 model achieved the best results, reaching the highest overall accuracy rate with 99.88% training accuracy and 99.00% testing accuracy. ResNet50V2 and ViT models also achieved high accuracy, with test accuracy rates of 95.60% and 98.00%, respectively. The findings demonstrate the potential of deep learning in detecting tomato diseases accurately and efficiently. This can improve crop yield and quality by aiding early disease management. Experimental findings show that the proposed ensemble models stand out due to their short training and testing times and superior classification performance. Thanks to this study, experts will be able to make early diagnoses of tomato plant

diseases easily and quickly, thus preventing the emergence of new infections[11].

Khalid et al. [12] included Explainable Artificial Intelligence methods using the Grad-CAM method. This method provides a visual interpretation of disease symptoms in plant images by explaining the decision-making process of the models. After extensive testing, the CNN model achieves 89% accuracy, 96% precision and recall, and 96% F1 score. Although the MobilNet architecture achieved 96% accuracy, it recorded slightly lower values such as 90% precision, 89% recall, and 89% F1-score[12].

Bouacida et al. [13] propose a new deep learning-based system that gives the system the ability to recognize diseased and healthy leaves of different plants for which it has not been trained. The basic idea is to focus on recognizing small diseased leaf areas and determining the prevalence rate of the disease over the entire leaf, rather than the entire appearance of the diseased leaf. For efficient classification and to leverage the excellence of the Inception model in disease recognition, a small Inception model architecture that can handle small regions without sacrificing performance has been used. To verify the method's effectiveness, training and testing were carried out using the PlantVillage dataset, which is known as the most used dataset due to its comprehensive and diverse coverage. The method reaches an accuracy rate of 94.04%. Additionally, when tested on new data sets, an accuracy rate of 97.13% is achieved. This innovative approach not only improves the accuracy of plant disease detection but also addresses the critical issue of generalizing the model to different crops and diseases. It also outperforms existing methods with its ability to identify any disease in any plant species, suggesting broad applicability and potential contribution to global food security initiatives [13].

Yang et al. [14] focus on the inability of traditional convolutional neural networks to effectively recognize similar plant leaf diseases. To overcome this problem and more accurately detect diseases on plant leaves, an effective plant disease image recognition method called aECA-ResNet34 is proposed in this study. This method is based on the ResNet34 model, and the improved aECANet, which has a symmetric structure, is added to the first and last layers of this network, respectively. The aECA-ResNet34 model was compared with different plant disease classification models on the pistachio seed dataset created in this study and the open-source PlantVillage dataset. Experimental results show that the aECA-ResNet34 model proposed in this study offers higher accuracy, better performance, and greater robustness. As a result, it appears that the proposed aECA-ResNet34 model can recognize multiple plant leaf diseases with high accuracy[14].

Joseph et al. [15] developed data sets that were applied to eight fine-tuned deep-learning models with the same training hyperparameters. Experimental results based on eight fine-tuned deep learning models reveal that Xception and MobileNet models perform best in

recognizing maize leaf diseases, with testing accuracy of 0.9580 and 0.9464, respectively. Similarly, in recognizing wheat leaf diseases, MobileNetV2 and MobileNet models showed the best performance with a test accuracy of 0.9632 and 0.9628, respectively. In recognizing rice leaf diseases, Xception and Inception V3 models showed the best performance with a test accuracy of 0.9728 and 0.9620, respectively. The research also proposes a new convolutional neural network model to be trained from scratch on all three developed cereal plant datasets. The proposed model performs well on corn, rice, and wheat datasets with a test accuracy of 0.9704, 0.9706, and 0.9808, respectively [15].

The main purpose of the study conducted by Saraswat et al [16] is to provide advanced detection of fungal and bacterial diseases in plants by using artificial intelligence techniques. The proposed approach is to identify and classify plant diseases using neural networks and the dynamic SURF (DSURF) method. The DSURF method supports dynamic feature extraction and classifier combinations to create image clustering. The deep learning model is used to train and test the classifier. The researchers claim that they achieved a high overall accuracy of 99.5% with the proposed DNNM and DSURF method, and the result is much better than other methods previously proposed in this field. This study aims to find best practices for detecting bacterial and fungal infections in plants to provide access to healthy food necessary for human health[16].

Kumar et al. [17] suggest using computer vision technology along with fuzzy logic to identify the disease and discover the condition. GLCM is used to extract features from the tissue and fuzzy logic is applied to determine the disease degree. K-means clustering is used to identify defective areas. GLCM is used to detect defective areas and fuzzy logic is used to diagnose the disease. The model provides approximately 70% classification accuracy[17].

Chin et al. [18] aim to observe the performance of the YOLOv8 model, which performs better than previous models, on a small-scale plant disease dataset. It also proposes to improve the accuracy and efficiency of plant disease detection and classification methods by optimizing the YOLOv8 algorithm by integrating the GhostNet module into the backbone to reduce the number of parameters for a faster calculation algorithm. Additionally, the architecture includes the Coordinate Attention (CA) mechanism module, which further improves the accuracy of the proposed algorithm. Our results show that the combination of YOLOv8s with the CA mechanism and transfer learning achieves the best result, achieving a score of 72.2%, exceeding studies using the same dataset. Without transfer learning, its best result is shown by its score of 69.3% achieved by YOLOv8s with GhostNet and CA mechanism [18].

Kolluri et al. [19] created a deep convolutional neural network for this purpose, using a dataset consisting of images of more than 54,000 controlled patients and

healthy plant leaves to identify 14 plants and 26 associated diseases. The model delivers a successful result with a test set endurance training accuracy rate of 99.06%. In general, device-assisted plant disease diagnosis is achieved with the ability to train deep-learning models using large and ever-expanding public image datasets[19].

Korra et al. [20] propose a new deep learning framework that utilizes pre-trained deep learning models along with transfer learning to achieve faster convergence and higher accuracy. Moreover, the proposed model is enhanced by region of interest calculation to improve detection accuracy and reduce computational complexity. An algorithm known as LbPDD-GBROIC (Learning-Based Plant Disease Detection with Region of Interest Computation Using Directed Backpropagation) is proposed. The proposed algorithm uses pre-trained deep models such as AlexNet, DenseNet169, Inception V3, ResNet50, Squeezenet v1, and VGG19 along with transfer learning and ROI calculation. The empirical study using the PlantVillage dataset reveals that ROI calculation has a significant impact on all models. The Inception V3 model outperformed other models with 99.76% accuracy[20].

Bhagat et al. [21] pass state-of-the-art networks such as InceptionV3, VGG16, ResNet50, DenseNet, MobileNet, MobileNetV3, NASNet, and EfficientNetB0 with 94.14% accuracy on the proposed chickpea dataset. Importantly, the method delivers results at 34 frames per second (FPS) on an NVIDIA P100 GPU. Moreover, its performance has been validated on publicly available datasets, including the plant village dataset, cassava, and apple leaf datasets, achieving an accuracy of 99.78%, 86.4%, and 97.2%, respectively[21].

Aliff et al. [22] propose a system that enables the automatic detection and classification of banana diseases by applying deep learning-based Convolutional Neural Networks using MATLAB together with the DJI drone. Thanks to this technology, the system can automatically detect and classify the main diseases seen in banana plants. In the study, various hyperparameters were carefully fine-tuned to achieve impressive training and testing accuracy levels. The results revealed that the model achieved the highest training accuracy of 81.27% in the 8th epoch and the lowest accuracy of 78.40% in the 4th epoch. This success demonstrates its potential to aid early disease detection and classification in banana plants[22].

In the study conducted by Sofuoglu and Birant [23], a new deep-learning model that accurately classifies plant leaf diseases for the agriculture and food sectors is proposed. The study focuses on disease detection in potato leaves by designing a new CNN architecture. By applying filters to the input images, CNN methodology extracts key features, reduces dimensions while preserving important features, and finally performs classification. Experimental results conducted on a real-world dataset have shown that the proposed model (98.28%) provides a significant accuracy increase (8.6%)

on average compared to state-of-the-art models in the literature (89.67%). The weighted averages of recall, precision, and F1-score metrics were obtained around 0.978, which means that the method is quite successful in diagnosing the disease[23].

Najim et al. [24] mentioned that tomato leaf diseases are a big problem for producers and the difficult of finding a single method to combat these diseases. Deep learning techniques, especially CNNs, are promising in recognizing early signs of diseases and could help manufacturers avoid costly problems in the future. This study presents a CNN-based model for early diagnosis of tomato leaf diseases to protect yield and increase yield. A dataset from the plantvillage database containing 11,000 photos from 10 different disease categories was used to train the model. While our CNN is trained on this dataset, the proposed model achieves a surprising 96% accuracy. This suggests that our method is potentially effective in detecting tomato leaf diseases at an early stage and can therefore assist producers in managing and reducing disease outbreaks, ultimately resulting in higher crop yields[24].

Too E et al. [25] focused on fine-tuning and evaluating pioneering deep convolutional neural networks for image-based plant disease classification. An empirical comparison of deep learning architectures has been made. Architectures evaluated include VGG 16, Inception V4, ResNet with 50, 101, and 152 layers, and DenseNets with 121 layers. The dataset used for the experiment contains 38 different classes, which are the sum of diseased and healthy leaves of 14 plants from plantVillage. DenseNets tends to consistently improve in accuracy with an increasing number of epochs and has shown no signs of overfitting and performance degradation. Additionally, it has been stated that DenseNets requires very few parameters and a reasonable computation time to achieve pioneering performances in the field[25].

In the study conducted by Forentinos K [26], convolutional neural network models were developed to detect and diagnose plant diseases using simple leaf images of healthy and diseased plants. Training of these models was carried out through deep learning methodologies. An open database containing 58 different combinations of 25 different plant species and a total of 87,848 images, including healthy plants, was used to train the models. Various model architectures have been trained and the best-performing model is capable of recognition with a success rate of 99.53%[26].

Chohan M et al. [27] propose a deep learning-based model called plant disease detector. The model can detect various diseases using photographs of plants' leaves. The plant disease detection model was developed using a neural network. First, the number of samples was increased by applying augmentation to the dataset. Then, a Convolutional Neural Network (ESA) was used with multiple convolution and pooling layers. The plantVillage dataset was used to train the model. Once the model is trained, the model is appropriately tested to

verify the results. Different experiments have been carried out using this model. 15% of PlantVillage data was used for testing purposes, including images of healthy and diseased plants. The proposed model achieved 98.3% testing accuracy[27].

It is conducted by Liu J and Wang X [28], a definition of the plant diseases and pests detection problem was presented and compared with traditional plant diseases and pests detection methods. According to the difference in network structure, this study summarizes the research on deep learning-based plant diseases and pest detection in recent years on three bases: classification network, detection network, and segmentation network, and the advantages and disadvantages of each method are summarized. Common datasets are introduced and the performance of existing studies is compared. On this basis, the study discusses possible challenges in practical applications of deep learning-based plant disease and pest detection. Additionally, possible solutions and research ideas for these challenges are suggested and some recommendations are offered. Finally, this study analyzes and evaluates the future trends of deep learning-based plant diseases and pest detection[28].

Jakjoud F. et al. [29] a Convolutional Neural Network (ESA) model based on the VGGnet16 architecture was presented for the recognition of diseased and healthy leaves. Various optimizers have been tested and the best results were obtained with Adadelta and SGD optimizer to study accuracy and model stability. These models were tested on a computer and Raspberry Pi Model B[29].

Wan H. et al. [30] proposed a suitable and accurate method for agricultural disease detection. Finally, approximately 87% accuracy was achieved on a relatively large dataset[30].

The study by Barbedo J. [31] is based on an image database containing 12 plant species, each with very different characteristics in terms of the number of samples, number of diseases, and variety of conditions. Experimental results show that while technical limitations associated with automatic plant disease classification have been largely overcome, the use of limited image datasets for training still leads to many unintended consequences that hinder the effective deployment of such technologies[31].

In the study by Akshai K. and Anitha J. [32], a deep learning model was trained to classify different plant diseases. The convolutional Neural Network (ESA) model has been used as it has achieved great success in image-based classification. The deep learning model provides faster and more accurate predictions than manual observation of the plant leaf. In this study, the CNN model and pre-trained models such as VGG, ResNet, and DenseNet were trained using the dataset. Among these models, the DenseNet model achieved the highest accuracy[32].

This study highlights the importance of using deep learning techniques for early detection and prevention of plant diseases in modern agriculture. The study demonstrates the potential of artificial intelligence in the agricultural sector by showing that the InceptionV3 model outperforms other models with a 92% accuracy rate on a large dataset.

**2. MATERIAL AND METHOD**

This section describes the methods and data set used in the study. The data set used in this study is studied with four different deep convolutional learning models. Selected models are AlexNet, VGG16, MobileNetV2, and InceptionV3. These models are proven to be successful and state-of-the-art models. Therefore, no time was wasted for hyperparameter optimization. Using deep learning models for detecting plant disease constitutes the basic methodology of this study. This section gives a detailed explanation of these four different deep learning models and how these models are trained.

**2.1. Dataset**

In this section, the data set used in the study is explained. The data set is the New Plant Diseases Dataset, which consists of healthy and diseased crop leaves divided into 38 different classes [33]. The process of developing a deep learning model for plant disease detection is a challenging task. Because a large amount of training data needs to be collected. Data augmentation methods are used on the New Plant Diseases Dataset used in the study, to overcome this problem. Data augmentation increases the diversity of training data for machine learning algorithms without collecting new data. In this study, the data set was enriched by using basic image manipulation such as image rotation, cropping, rotation, color transformation, color enhancement, and deep learning-based image augmentation techniques. A total of 100,000 images were obtained. 70,000 images are allocated as training data, 15,000 as validation data, and 15,000 as test data. Images are in color. The entire

dataset was divided into training, validation, and testing datasets in a 70/30 ratio, preserving the index structure. The classes of plants in the dataset are as follows: Apple, Blueberry, Cherry, Corn, Grape, Orange, Peach, Pepper, Tomato, Raspberry, Bean, Pumpkin, and Strawberry [33]. The data set used in the study consists of JPG images. Figure 1 shows some examples of classes.

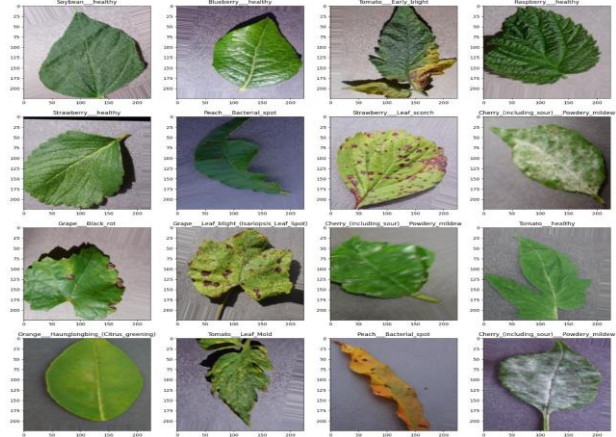


**Figure 1.** Example images of plant classes in the dataset.

When Figure 1 is examined, it is possible to see some diseased plant leaves in the data set. In addition, the volume of training data was increased by applying data augmentation methods to this data set. In this way, it is aimed that deep learning models to recognize different features.

Table 1 shows the names and numbers of the classes in the training and validation data set used in the models in table format. In addition, the images used in training are subjected to data enrichment steps such as data enlargement and rotation, thus increasing the number of training data and aiming to increase the generalization accuracy of the models. In this way, it is aimed to improve the training success of the models and to provide some benefit to the problems of overlearning and overfitting.

**Table 1.** Details of Dataset

No	Dataset Classes	Train Data Records	Test Data Records
1	Apple__Apple_scab	2 016	504
2	Apple__Black_rot	1 987	497
3	Apple__Cedar_apple_rust	1 760	440
4	Apple__healthy	2 008	502
5	Blueberry__healthy	1 816	454
6	Cherry_(including_sour)__Powdery_mildew	1 683	421
7	Cherry_(including_sour)__healthy	1 826	456
8	Corn_(maize)__Cercospora_leaf_spot Gray_leaf_spot	1 642	410
9	Corn_(maize)__Common_rust_	1 907	477
10	Corn_(maize)__Northern_Leaf_Blight	1 908	477
11	Corn_(maize)__healthy	1 859	465
12	Grape__Black_rot	1 888	472
13	Grape__Esca_(Black_Measles)	1 920	480
14	Grape__Leaf_blight_(Isariopsis_Leaf_Spot)	1 722	430
15	Grape__healthy	1 692	423
16	Orange__Huanglongbing_(Citrus_greening)	2 010	503
17	Peach__Bacterial_spot	1 838	459
18	Peach__healthy	1 728	432
19	Pepper_bell__Bacterial_spot	1 913	478
20	Pepper_bell__healthy	1 988	497
21	Potato__Early_blight	1 939	485

No	Dataset Classes	Train Data Records	Test Data Records
22	Potato___Late_blight	1 939	485
23	Potato___healthy	1 824	456
24	Raspberry___healthy	1 781	445
25	Soybean___healthy	2 022	505
26	Squash___Powdery_mildew	1 736	434
27	Strawberry___Leaf_scorch	1 774	444
28	Strawberry___healthy	1 824	456
29	Tomato___Bacterial_spot	1 702	425
30	Tomato___Early_blight	1 920	480
31	Tomato___Late_blight	1 851	463
32	Tomato___Leaf_Mold	1 882	470
33	Tomato___Septoria_leaf_spot	1 745	436
34	Tomato___Spider_mites Two-spotted_spider_mite	1 741	435
35	Tomato___Target_Spot	1 827	457
36	Tomato___Tomato_Yellow_Leaf_Curl_Virus	1 961	490
37	Tomato___Tomato_mosaic_virus	1 790	448
38	Tomato___healthy	1 926	481

## 2.2. AlexNet

AlexNet is a deep convolutional neural network, a milestone in the history of deep learning. AlexNet is a revolutionary model in deep learning, recognized by winning the ImageNet Large Scale Visual Recognition Challenge (ILSVRC) competition in 2012. AlexNet announced it in 2012 in a paper titled “ImageNet Classification with Deep Convolutional Neural Networks” [34]. In this article, the AlexNet model and its successes in the ImageNet competition are described in detail[34].

AlexNet is a deep learning model that was announced during the ImageNet ILSVR competition held in 2012 and won this competition. This competition was organized to evaluate visual recognition performance on a huge dataset containing 1.2 million training data and 1000 different classes. AlexNet achieved revolutionary success in deep learning at that time and inspired subsequent studies. AlexNet has the following key features:

**Architecture:** AlexNet consists of eight layers. It consists of five convolutional layers and three fully connected layers[34].

**Convolutional layers:** Convolutional layers are used to extract different features of input images. In AlexNet, these layers scan the image with various filters and create feature maps. At the same time, convolutional layers highlight local connections, which helps the model generalize better [34].

**Fully connected layers:** Fully connected layers are used for flattening feature maps and classification. The AlexNet is capable of recognizing 1000 different classes by using these layers[34].

**Activation Functions:** ReLU (Rectified Linear Activation) activation function is used in AlexNet[34]. Activation functions help to model to train faster and achieve better results.

**Regularization:** Techniques, such as dropout and data augmentation are used to reduce overlearning in AlexNet[34].

**Training data:** AlexNet is trained on a large training dataset. This increased the generalization ability of the model[34].

AlexNet was a turning point that increased the popularity of the deep learning field and laid the foundation for later deep learning models.

This model is considered an important starting point in the field of visual recognition and classification and has contributed greatly to advances in the field of deep learning. Figure 2 shows the architecture of AlexNet.

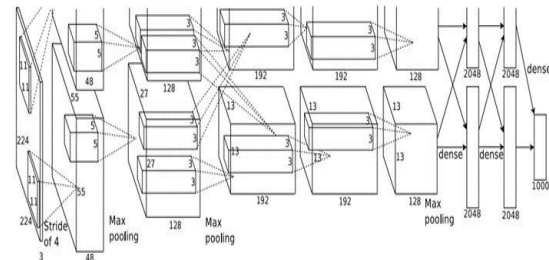


**Figure 2.** Architecture of the Alexnet[34]

As shown in Figure 2, the network contains eight weighted layers. The first five are convolutional layers and the remaining three are fully connected layers. The output of the last fully connected layer is passed to a softmax function that produces a probability distribution over 1000 class labels. The kernels of the second, fourth, and fifth convolutional layers are linked to the kernel maps of the previous layer only with those located on the same GPU. The kernels of the third convolutional layer are connected to all kernel maps in the second layer. Neurons in fully connected layers are connected to all neurons in the previous layer. After the first and second convolutional layers come the response normalization layers. After the third and fifth convolutional layers, the maximum pooling layers come. ReLU is applied to the output of each convolutional and fully connected layer[34]. The first convolutional layer processes the input image of size 224x224x3 with 96 cores of size 11x11x3. It is processed with 4 pixels which is the distance between the receptive field centers of two

kernel maps. The second convolutional layer takes the output of the first convolutional layer (response normalized and pooled) and processes it with 256 cores of size 5x5x48. The third, fourth, and fifth convolutional layers are interconnected with no intervening pooling or normalization layer. The third convolutional layer depends on the outputs of the second convolutional layer (normalized and pooled) with 384 cores of size 3x3x256. The fourth convolutional layer contains 384 cores of size 3x3x192, and the fifth convolutional layer is processed with 256 cores of size 3x3x192. Each fully connected layer consists of 4096 neurons [34].

### 2.3. VGG16

VGG16 was announced in a paper titled "Very Deep Convolutional Networks for Large-Scale Image Recognition." This article was published by Karen Simonyan and Andrew Zisserman in 2014 [35]. It introduces several deep learning models as part of the VGG (Visual Geometry Group) family developed by researchers from the University of Oxford. The VGG16 is the largest and most complex model, in this family [35]. It has achieved great success in the ImageNet Large Scale Visual Recognition Challenge competition.

**Architecture:** VGG16 is a CNN model with 16 layers [35]. The majority of layers consist of convolutional layers [35]. The model consists of 13 convolutional layers, two consecutive fully connected layers, and three fully connected classification layers [35].

**Convolutional layers:** VGG16's convolutional layers have 3x3 frame filters [35]. In each layer, 64, 128, 256, 512 and 512 feature collections are produced [35]. After successive layers of evolution, each one concludes with a pooling layer [35].

**Fully connected layers:** VGG16 ends with two fully connected layers with 4096 contents [35]. These layers are used to assign feature classes [35].  
**Classification layers:** The top three fully connected layers are used for their distribution [35]. The first two distributions have 4096 distributions, and the last one can be adapted according to the ranges in the class of the given task [35].  
**Learning:** VGG16 provides very successful results for training on large amounts of data [35]. The training process generally includes common deep-learning techniques such as backpropagation and stochastic gradient descent [35].

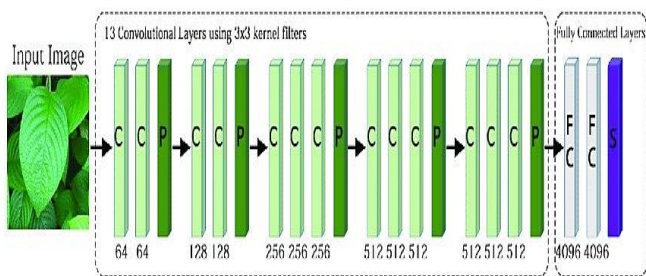


**Figure 3.** Architecture of the VGG-16 [35].

The VGG-16 architecture is shown in Figure 3. As can be seen, it is connected to the softmax layer with 2 fully connected layers of 4096.

### 2.4. MobileNetV2

MobileNetV2 is a deep learning model introduced by Google in 2018 in an article titled "Inverted Residuals and Linear Bottlenecks" [36]. This model is designed for fast and effective object recognition and classification, especially on resource-limited platforms such as portable devices [36].

Important features of MobileNetV2 are:

**Architecture:** MobileNetV2 includes two basic structures called "Inverted Residuals" and "Linear Bottlenecks". These structures are designed to offer a lighter and more effective architecture [36]. Inverted Residuals differ from traditional CNN architectures and reduce the computational intensity of the model while creating deeper [36]. MobileNetV2's architecture has a lighter and more efficient structure compared to CNN.

**Inverted residuals:** This is one of the most important features of MobileNetV2. Inverse layers work like a traditional CNN layer but are used to increase the depth of the network. These layers operate oppositely to traditional Convolutional Layers. First, they make the model deeper by adding one step at a time to a low-dimensional layer. This helps share more parameters and keep the model lightweight [36].

**Linear bottlenecks:** This is another feature designed to make the network more efficient. Linear bottlenecks are used at every layer of the network. It is used to size incoming feature maps. This reduces the computational intensity of the network while minimizing information loss [36].

**Depthwise separable convolution:** A special type of convolution called "depth decomposition convolution" is used in each layer [36]. This type of convolution requires fewer calculations than traditional convolutions and is used with fewer parameters. This lightens the network [36].

**Global average pooling:** At the end of the network, the global average pooling layer is used. This smooths the results by averaging each feature map and is used for classification [36].

**Output layers:** MobileNetV2's output layers are used to perform result classification [36]. These layers determine which class the model will classify a given image [36]. Figure 4 shows the general architecture of MobileNet V2.

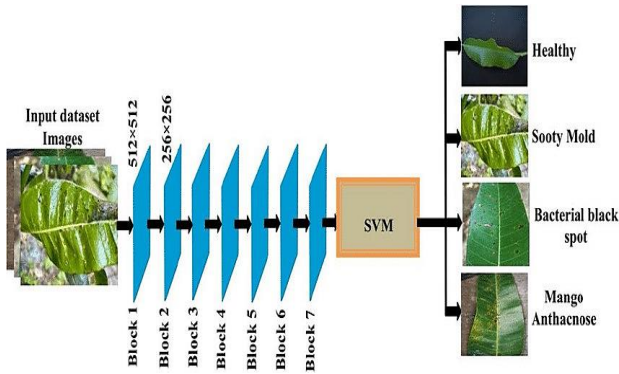


**Figure 4.** Architecture of the MobileNetV2 [36].

**Lightweight:** MobileNetV2 is specifically optimized for resource-limited devices. The model can run fast on mobile devices because it has lower memory and computational requirements[36].

**Generalization ability:** Although it's generally used in object recognition tasks, this model gives successful results in transfer learning applications[36]. The pre-trained MobileNetV2 network can be used for different tasks, that allow you to get good results in new tasks with less data[36].

**Various applications:** It is successfully used in many tasks such as image classification, object detection, and face recognition. Additionally, it is an ideal option for real-time applications and embedded systems.

### 3. RESULTS

This section includes the findings obtained from the tests performed on the models explained in detail in the methods section. For each model, the values given in Table 3 are applied and the results are examined.

**Table 3.** Applied parameters on models

Parameters	Models			
	AlexNet	Vgg16	MobileNetV2	InceptionV3
Optimizer	Adam	Adam	Adam	Adam
Activation	Relu	Relu	Relu	Relu
Loss	Categorical	Categorical	Categorical	Categorical
Epoch	100	100	100	100
Metrics	Accuracy	Accuracy	Accuracy	Accuracy

When Table 3 is examined, it is seen that the same metrics are applied to each model. These values are important to make an accurate comparison. Models were trained on Google Colab using GPU. Data enrichment and early-stopping methods were used to prevent overlearning.

**Table 4.** Precision, recall, and f1-score values of the Inception V3 model.

Metrics	Precision	Recall	F1-Score
Inception V3	0.93	0.91	0.92
AlexNet	0.93	0.89	0.91
MobileNetV2	0.91	0.90	0.90
VGG16	0.90	0.88	0.89

Table 4 shows the precision, sensitivity, and f1-score values of the Inception model. When these values are checked, it can be seen that the model performs well.

Figure 6 shows the loss and accuracy graphs of the 4 models. It was concluded that the model that gave the highest accuracy value and performed best among the models trained with the parameters in Table 2 was the inceptionv3 model.

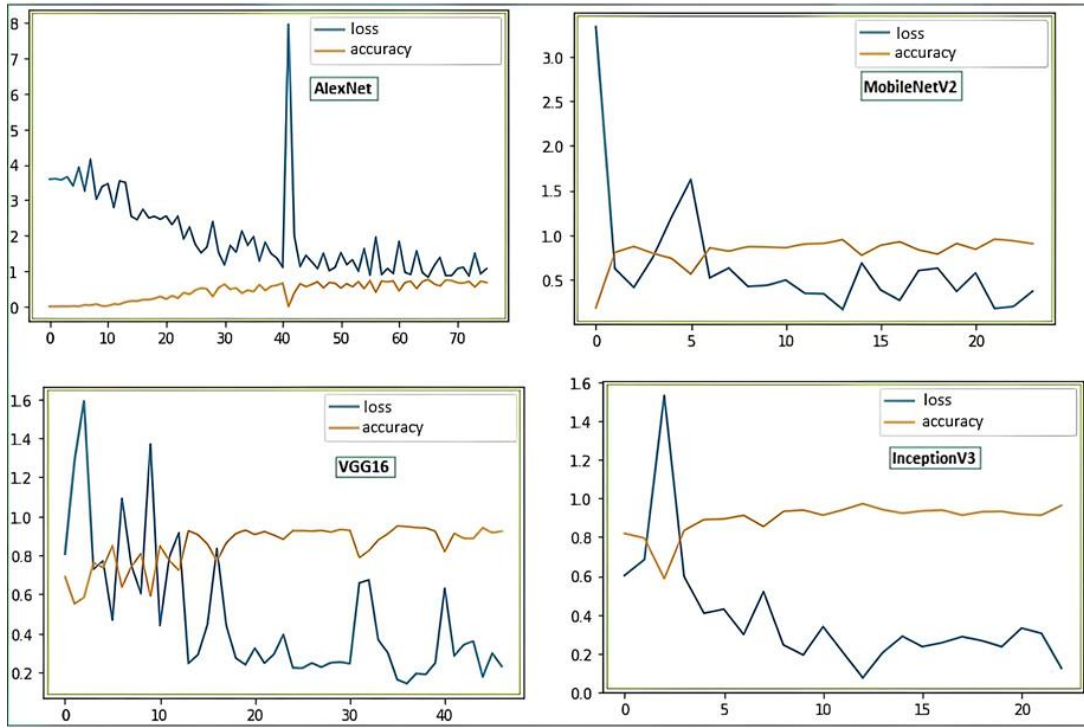


Figure 6. Performance graph of models as a result of training

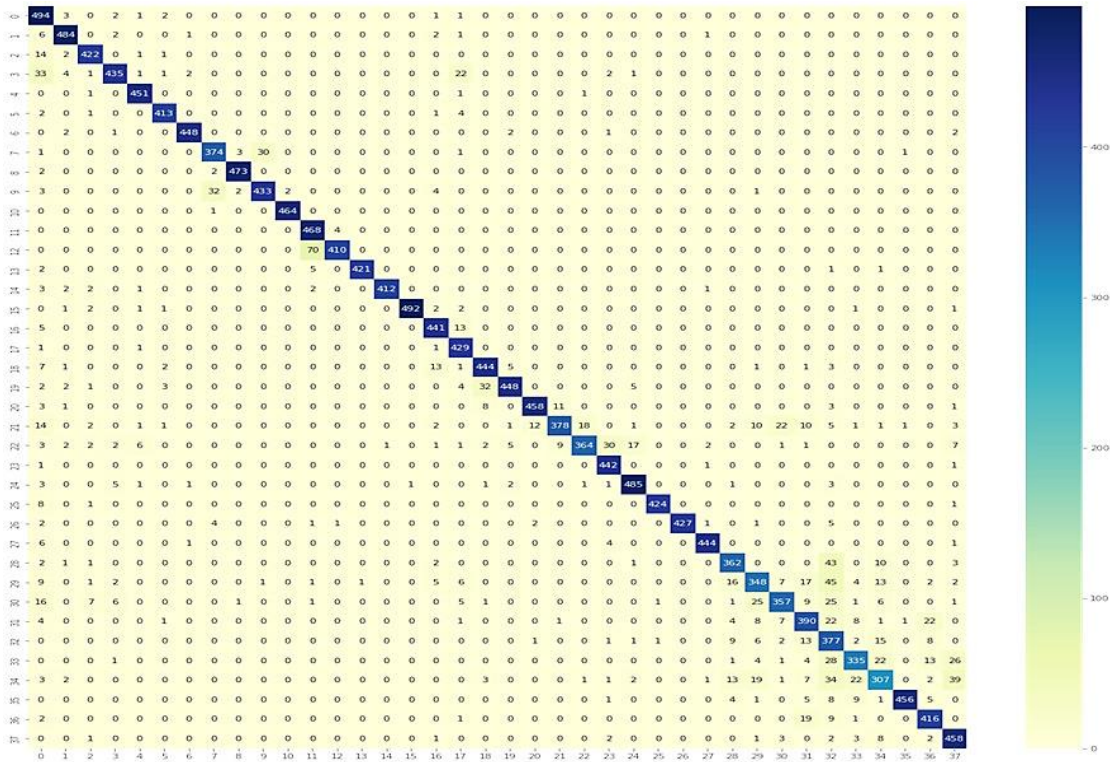


Figure 7. Error Matrix for the InceptionV3 Model

Figure 7 shows the error matrix of the Inception V3 model, which is the most successful model according to the data in Table 3. It is seen that the InceptionV3 model can successfully detect and classify diseases on the validation data set containing 38 different plant disease types on which the model was trained.

#### 4. DISCUSSION AND CONCLUSION

This study researched the performance of deep learning networks in recognizing diseases on plant leaves. A dataset containing leaf images of various plant species was used in the study. Four deep-learning models AlexNet, Vgg16, MobileNetV2, and InceptionV3 are trained and tested on this dataset. According to the results obtained, the InceptionV3 model had a higher accuracy rate than other models with an accuracy rate of



92%. This study showed that the InceptionV3 model can accurately distinguish diseased and healthy leaves by effectively learning images of plant leaves. Thus, it turned out that the Inception V3 model is more effective than other used deep-learning models in plant disease diagnosis. The study shows that deep learning networks can be an effective tool for disease prevention and control in the agricultural sector. In this way, efficiency and quality in agriculture production can be increased.

Deep learning models have been trained with only one or a few different plant species in the literature. This study also reveals its novelty and originality by using 38 different classes of plants. However, the study also has some limitations. For example, its performance can be tested by training the model on more plant species and diseases. Additionally, more research is needed on how the model will yield real-life results. To address this gap, future studies aim to increase the performance of deep learning models by using a larger and more diverse dataset.

Additionally, it is planned to develop the model as a mobile application that can take images of plant leaves in real time and diagnose diseases. When the studies were examined, it was seen that there is no mobile application that detects artificial intelligence-based plant diseases in the IOS or Android markets. In the study planned for the mobile application, the InceptionV3 model, which was trained within the scope of this study and provides the best performance, will be used. The model trained in this study and its weights recorded will be transformed using Tensorflow Lite. Techniques such as quantization and model optimization offered by TensorFlow Lite will also be added to overcome problems such as memory and processing power limitations on mobile devices. Afterward, it is planned to use federated learning techniques to solve the problem of big data and different plant species. Because training models used for plant disease diagnosis usually require large amounts of data. This data may contain sensitive information about farmers' fields or crops.

The planned federated learning model can be set up like this: It collects images of plant leaves from farmers' devices. The data is stored on the device. The InceptionV3 model is trained locally on each device. For this training, model updates are performed with the data on the device, using the time when the device is most inactive. Updates to local models are sent to a central server. Model weights of the data are shared. Thus, information security and responsible artificial intelligence ethics are protected. Then, the central server combines the updates from different devices and creates a general model. In this way, the best model is obtained. Combined model updates are returned to the devices and training continues locally with these models. This cycle is repeated regularly to update and improve the model constantly.

In this scenario, of course, some difficulties will be encountered. It can be difficult to update data on different devices simultaneously and regularly. Poor or

intermittent internet connection can make it difficult to deliver timely updates. Additional measures may be required to protect the security and confidentiality of data on devices. The limited processing power and memory of mobile devices can slow down the process of training and updating the model. Effectively combining model updates from different devices can be technically complex.

However, there are precautions that can be taken against these difficulties. By performing model updates asynchronously, the need for constant connection of devices can be reduced. Additionally, updates will be stored locally and pushed to the server at the appropriate time. A mechanism is created that temporarily stores updates when the connection is lost and sends them to the server when the connection is restored. Data transfer is minimized by using compression and optimization techniques. Strong encryption methods are used in data transfer between devices. Additionally, user data is protected with data anonymization techniques. Models are optimized with TensorFlow Lite and quantization techniques. By combining model updates from different devices with a weighted average, the performance of the overall model is improved. Additionally, the defragmentation process is optimized by adapting updates according to device performance and data quality.

Federated learning can increase privacy and data security by ensuring that this data remains on the device and that only updates necessary to improve the model are sent to the cloud. Or it could allow models to be trained on the device without needing to be trained in the cloud. This may enable faster and more accurate detection of plant diseases. It also allows the model to be customized to the types of diseases in a particular region or farm. This may make diagnoses more accurate. A technology similar to this is the specialized message completion technology anticipated in virtual keyboards used on phones. In this way, more field studies and test problems will be solved to evaluate real-world applicability. As a result of this study, deep learning-based systems will be disseminated in the agricultural sector.

This study showed that the InceptionV3 model can accurately detect diseases on plant leaves and increase productivity in the agricultural sector. Suggestions for future research include the use of larger and more diverse datasets and the application of federated learning techniques, which can improve the performance of the model and provide security.

**Dataset Access:** The dataset used in this study is open and can be accessed from the relevant source link. Access: <https://www.kaggle.com/datasets/vipoooool/new-plant-diseases-dataset>.

## REFERENCES

- [1] Hinton G, LeCun Y, Bengio Y. Deep learning. *Nature*. 2015;521(7553):436–44.
- [2] Benfenati A, Causin P, Oberti R, Stefanello G. Unsupervised deep learning techniques for automatic detection of plant diseases: reducing the need of manual labelling of plant images. *Journal of Mathematics in Industry*. 2023 Dec 1;13(1).
- [3] Ahmed I, Yadav PK. A systematic analysis of machine learning and deep learning based approaches for identifying and diagnosing plant diseases. *Sustainable Operations and Computers*. 2023 Jan 1;4:96–104.
- [4] Shovon MSH, Mozumder SJ, Pal OK, Mridha MF, Asai N, Shin J. PlantDet: A Robust Multi-Model Ensemble Method Based on Deep Learning For Plant Disease Detection. *IEEE Access*. 2023;11:34846–59.
- [5] Bouguettaya A, Zarzour H, Kechida A, Taberkit AM. A survey on deep learning-based identification of plant and crop diseases from UAV-based aerial images. *Cluster Computing*. 2023 Apr 1;26(2):1297–317.
- [6] Ahmad A, Gamal A El, Saraswat D. Toward Generalization of Deep Learning-Based Plant Disease Identification Under Controlled and Field Conditions. *IEEE Access*. 2023;11:9042–57.
- [7] Moupojou E, Tagne A, Retraint F, Tadonkemwa A, Wilfried D, Tapamo H, et al. FieldPlant: A Dataset of Field Plant Images for Plant Disease Detection and Classification With Deep Learning. *IEEE Access*. 2023;11:35398–410.
- [8] Guan H, Fu C, Zhang G, Li K, Wang P, Zhu Z. A lightweight model for efficient identification of plant diseases and pests based on deep learning. *Frontiers in Plant Science*. 2023;14.
- [9] Shoaib M, Shah B, EI-Sappagh S, Ali A, Ullah A, Alenezi F, et al. An advanced deep learning models-based plant disease detection: A review of recent research. Vol. 14, *Frontiers in Plant Science*. Frontiers Media SA; 2023.
- [10] Pandian JA, Kumar VD, Geman O, Hnatiuc M, Arif M, Kanchanadevi K. Plant Disease Detection Using Deep Convolutional Neural Network. *Applied Sciences (Switzerland)*. 2022 Jul 1;12(14).
- [11] Alzahrani MS, Alsaade FW. Transform and Deep Learning Algorithms for the Early Detection and Recognition of Tomato Leaf Disease. *Agronomy*. 2023 May 1;13(5).
- [12] Khalid MM, Karan O. Deep Learning for Plant Disease Detection. *International Journal of Mathematics, Statistics, and Computer Science*. 2023 Nov 18;2:75–84.
- [13] Bouacida I, Farou B, Djakhdjakha L, Seridi H, Kurulay M. Innovative deep learning approach for cross-crop plant disease detection: A generalized method for identifying unhealthy leaves. *Information Processing in Agriculture*. 2024;
- [14] Yang W, Yuan Y, Zhang D, Zheng L, Nie F. An Effective Image Classification Method for Plant Diseases with Improved Channel Attention Mechanism aECANet Based on Deep Learning. *Symmetry [Internet]*. 2024 Apr 8;16(4):451. Available from: <https://www.mdpi.com/2073-8994/16/4/451>
- [15] Joseph DS, Pawar PM, Chakradeo K. Real-Time Plant Disease Dataset Development and Detection of Plant Disease Using Deep Learning. *IEEE Access*. 2024;12:16310–33.
- [16] Saraswat S, Singh P, Kumar M, Agarwal J. Advanced detection of fungi-bacterial diseases in plants using modified deep neural network and DSURF. *Multimedia Tools and Applications*. 2024 Feb 1;83(6):16711–33.
- [17] Kumar A, Kumar P, Suman K. Deep Learning for Automated Diagnosis of Plant Diseases: A Technological Approach. Vol. 20, *J. Electrical Systems*. 2024.
- [18] Chin PW, Ng KW, Palanichamy N. Plant Disease Detection and Classification Using Deep Learning Methods: A Comparison Study. *Journal of Informatics and Web Engineering*. 2024 Feb 14;3(1):155–68.
- [19] Kolluri J, Dash SK, Das R. International Journal of Intelligent Systems and Applications In Engineering Plant Disease Identification Based on Multimodal Learning [Internet]. Vol. 2024, Original Research Paper International Journal of Intelligent Systems and Applications in Engineering IJISAE. 2024. Available from: [www.ijisae.org](http://www.ijisae.org)
- [20] Korra S, Bhaskar T, Ramana N, Bhukya S, Rajender N. International Journal of Intelligent Systems And Applications In Engineering An Efficient Guided Backpropagation Approach for Detection of Plant Diseases Using Deep Learning Models [Internet]. Vol. 2024, Original Research Paper International Journal of Intelligent Systems and Applications in Engineering IJISAE. 2024. Available from: [www.ijisae.org](http://www.ijisae.org)
- [21] Bhagat S, Kokare M, Haswani V, Hambarde P, Taori T, Ghante PH, et al. Advancing real-time plant disease detection: A lightweight deep learning approach and novel dataset for pigeon pea crop. *Smart Agricultural Technology*. 2024 Mar 1;7.
- [22] Aliff M, Luqman M, Yusof MI, Sani NS, Syafiq MU, Sadikan SFN, et al. Utilizing Aerial Imagery and Deep Learning Techniques for Identifying Banana Plants Diseases. *ITM Web of Conferences*. 2024;60:00013.
- [23] Sofuoglu CI, Birant D. Potato Plant Leaf Disease Detection Using Deep Learning Method. *Tarim Bilimleri Dergisi*. 2024 Sep 1;30(1):153–65.
- [24] Najim MH, Abdulateef SK, Alasadi AH. Early detection of tomato leaf diseases based on deep learning techniques. *IAES International Journal of Artificial Intelligence*. 2024 Mar 1;13(1):509–15.
- [25] Too EC, Yujian L, Njuki S, Yingchun L. A comparative study of fine-tuning deep learning models for plant disease identification. *Computers and Electronics in Agriculture*. 2019 Jun 1;161:272–9.
- [26] Ferentinos KP. Deep learning models for plant disease detection and diagnosis. *Computers and Electronics in Agriculture*. 2018 Feb 1;145:311–8.

- [27] Chohan\* M, Khan A, Chohan R, Katpar SH, Mahar MS. Plant Disease Detection using Deep Learning. *International Journal of Recent Technology and Engineering (IJRTE)* [Internet]. 2020 May 30;9(1):909–14. Available from: <https://www.ijrte.org/portfolio-item/A2139059120/>
- [28] Liu J, Wang X. Plant diseases and pests detection based on deep learning: a review. Vol. 17, *Plant Methods*. BioMed Central Ltd; 2021.
- [29] Jakjoud F, Hatim A, Bouaaddi A. Deep learning application for plant diseases detection. In: *ACM International Conference Proceeding Series*. Association for Computing Machinery; 2019.
- [30] Wan H, Lu Z, Qi W, Chen Y. Plant disease classification using deep learning methods. In: *ACM International Conference Proceeding Series*. Association for Computing Machinery; 2020. p. 5–9.
- [31] Barbedo JGA. Factors influencing the use of deep learning for plant disease recognition. *Biosystems Engineering*. 2018 Aug 1;172:84–91.
- [32] Akshai KP, Anitha J. Plant disease classification using deep learning. In: *2021 3rd International Conference on Signal Processing and Communication, ICPSC 2021*. Institute of Electrical and Electronics Engineers Inc.; 2021. p. 407–11.
- [33] Bhattarai S. New plant diseases dataset. 2024.
- [34] Krizhevsky A, Sutskever I, Hinton GE. ImageNet Classification with Deep Convolutional Neural Networks [Internet]. 2012 [cited 2023 Oct 22]. Available from: [https://papers.nips.cc/paper\\_files/paper/2012/file/c399862d3b9d6b76c8436e924a68c45b-Paper.pdf](https://papers.nips.cc/paper_files/paper/2012/file/c399862d3b9d6b76c8436e924a68c45b-Paper.pdf)
- [35] Simonyan K, Zisserman A. Very Deep Convolutional Networks for Large-Scale Image Recognition. 2014 Sep 4; Available from: <http://arxiv.org/abs/1409.1556>
- [36] Sandler M, Howard A, Zhu M, Zhmoginov A, Chen LC. MobileNetV2: Inverted Residuals and Linear Bottlenecks. 2018 Jan 12; Available from: <http://arxiv.org/abs/1801.04381>
- [37] Szegedy C, Vanhoucke V, Ioffe S, Shlens J. Rethinking the Inception Architecture for Computer Vision [Internet]. 2015 [cited 2023 Oct 28]. Available from: <https://arxiv.org/pdf/1512.00567.pdf>

## Effect Of Tool Tilt Angle On The Mechanical Properties Of Friction Stir Lap Welds Of AZ31B Magnesium Alloy Sheets

Ömer EKİNCİ<sup>1</sup> , Anıl İMAK<sup>2\*</sup> 

<sup>1</sup> Sivas University of Science and Technology, Faculty of Aviation and Space Sciences, Astronautical Engineering, Sivas, Türkiye

<sup>2</sup> Bingöl University, Faculty of Engineering and Architecture, Mechanical Engineering, Bingöl, Türkiye  
Ömer Ekinci ORCID No: 0000-0002-0179-6456  
Anıl İMAK ORCID No: 0000-0001-6091-1584

\*Corresponding author: [aimak@bingol.edu.tr](mailto:aimak@bingol.edu.tr)

(Received: 09.05.2024, Accepted: 26.07.2024, Online Publication: 26.09.2024)

### Keywords

Friction stir lap welding, AZ31B magnesium alloy, Tool tilt angle, Microhardness, Tensile shear load

**Abstract:** Friction stir lap welding of AZ31B magnesium alloy sheet pairs was conducted under various welding tool tilt angles (0°, 1°, 2°, 3° and 4°) while keeping other variables constant. Tensile shear load capacity and microhardness of the welds were obtained. Furthermore, the fracture mechanism of the weld was examined. The tilt angle significantly affected the weld cross-sectional area structure and tensile load capacity of the weld. A tunnel defect formed at the tilt angle of 0°. It was determined that the strongest weld with a 5083 N tensile load made at the 1° tilt angle is slightly more than three times as strong as the weakest one with a 1584 N made at 4°. The weld strength considerably decreased with increasing the tilt angle after 1° because the effective top sheet thickness on the advancing side was highly reduced because of more tool shoulder penetration. Hardness in the heat-affected and weld zones of the weld decreased when the tilt angle was improved due to the more heat input. The average hardness in the heat-affected and the weld zones of the welds made at 0° and 4° inclination angles are (62 and 61 HV) and (56.7 and 50.7 HV), respectively. The fact that no breakage occurred from the weld areas during the tensile test is proof of strong joining.

## Takım Eğim Açısının AZ31B Magnezyum Alaşımli Levhaların Sürtünme Karıştırma Bindirme Kaynaklarının Mekanik Özelliklerine Etkisi

### Anahtar Kelimeler

Sürtünme karıştırma bindirme kaynağı, AZ31B magnezyum alaşımı, Takım eğim açısı, Mikrosertlik, Çekme kesme mukavemeti

**Öz:** AZ31B magnezyum alaşımli levha çiftlerinin sürtünme karıştırma bindirme kaynağı, diğer değişkenler sabit tutularak çeşitli kaynak takımı eğim açıları (0°, 1°, 2°, 3° ve 4°) altında gerçekleştirildi. Kaynakların çekme kesme yükü taşıma kapasitesi ve mikrosertliği elde edildi. Ayrıca kaynağın kırılma mekanizması da incelenmiştir. Eğim açısı, kaynak kesit alanı yapısını ve kaynağın çekme yükü kapasitesini önemli ölçüde etkilemiştir. 0° eğim açısında tünel kusuru oluştu. 1° eğim açısında üretilen 5083 N çekme yüküne sahip en güçlü kaynağın, 4° eğim açısında üretilen 1584 N çekme yüküne sahip en zayıf kaynaktan üç kattan biraz daha fazla mukavemete sahip olduğu tespit edildi. Kaynak mukavemeti, 1°den sonra eğim açısının artmasıyla önemli ölçüde azaldı çünkü ilerleyen taraftaki etkin üst plaka kalınlığı, daha fazla takım omuzu nüfuzu nedeniyle oldukça azaldı. Eğim açısı artırıldığında, daha fazla ısı girdisi nedeniyle ısıdan etkilenen ve kaynak bölgelerindeki sertlik azalmıştır. 0° ve 4° eğim açılarında yapılan kaynakların ısıdan etkilenen ve kaynak bölgelerindeki ortalama sertlikleri sırasıyla (62 ve 61 HV) ve (56,7 ve 50,7 HV)'dir. Çekme testi sırasında kaynak bölgelerinden herhangi bir kırılmanın meydana gelmemesi birleştirmenin sağlam olduğunun kanıtıdır.

### 1. INTRODUCTION

Reducing the weight of ground and air vehicles effectively improves fuel efficiency and mitigates

environmental pollutants. Magnesium (Mg) alloys are the lightest and almost most excellent weight-reducing structural metals. Furthermore, they can replace steel and aluminum in many structural applications as they have

low density, high specific strength, good sound-damping capacity, castability, machinability, electromagnetic interference shielding capacity, recyclability, and plentiful [1]. For this reason, they are utilized in sectors like automotive, aviation, and transportation [2-4]. According to several reports, Mg alloys are vital for future developments in the automotive and aerospace industries [5-7]. Joining technology plays a critical role in increasing the applications of Mg alloys. Nevertheless, since they have low melting points, low boiling points, high thermal conductivity, and active chemical properties, it is difficult to weld them. For example, imperfections (cracks, pores, and oxide inclusions) that are detrimental to the joint mechanical properties take place in the joint when joined by general fusion welding techniques [8-11]. Friction stir welding (FSW), the solid-state joining method created by TWI, is thought excellent for welding light metals [12]. FSW has demonstrated to offer a number of advantages over traditional arc welding techniques involving a notable decrease in distortion and elimination of solidification cracking [13-15]. Since melting of the materials does not occur in the FSW process, there are no flaws associated with the fusion welding, and thus high-strength joints can be produced. Researchers have shown that this welding technology is successful in combining light metallic materials like Mg alloys, Al alloys and Ti alloys [16-19]. Lap joints are frequently seen in the production of components and structures. For instance, the majority of sheet metal structures used in aerospace and aircraft include lap joints [20, 21]. Therefore, the lap joint appears to be quite important in the assembly of bodies in industries. Normally, rivets have been dominant for lap joining aerospace and aircraft structures at the beginning, however, since rivet holes likely lead to the formation and propagation of cracks and corrosion, and FSW can generate stronger joints and also provides significant weight and cost reductions, FSW has replaced most rivets [22]. FSW has been used mostly for butt joining of especially aluminum alloys, but there are also studies made on lap joining materials by FSW. Based on my research, there are fewer investigations into the lap joining Mg alloys via FSW. FSW process parameters determining the weld quality in terms of microstructure and mechanical properties are the welding tool geometry, tilt angle, plunge depth, rotation and travel speeds [23-25]. Cao and Jahazi [26] investigated the influence of tool rotation rate (500, 750, 1000, 1500 and 2000 rpm) and probe length (2, 2.25, 2.75 and 3.5 mm) on the microstructure, defects, hardness and tensile shear strength of the lap welds of 2 mm thick AZ31B-H24 Mg sheets made at 20 mm/s constant welding speed and 0.5° tool tilt angle by FSW. They found that weld tensile shear load increased when tool rotation speed increased up to 1000 rpm, but then decreased with further increase in tool rotation speed. On the other hand, weld load carrying capacity increased with increasing tool probe length and penetration depth into the lower sheet. Cao and Jahazi [27] researched influence of welding speed (5, 10, 15, 20, 25 and 30 mm/s) on the lap joint tensile shear load of 2 mm AZ31B-H24 Mg alloy sheets produced at constant 2000 rpm tool rotation speed clockwise and 0.5° tool tilt angle through FSW. High

quality of lap joints was successfully fabricated. It was found that tensile shear load of lap joint enhanced when welding speed increased up to 15 mm/s and then remained stable with further increase. Yang et al. [28] studied the effect of tool pin geometry on the lap weld load carrying capacity of 2 mm thick AZ31-H24 Mg alloy sheets with FSW. They determined that welds produced by tool with triangular pin had much higher strength compared to the tool having cylindrical threaded pin. Because, triangular pin reduced the hook height growth as a result of providing more material to flow sideways.

Most of the friction stir lap welding investigations were carried out on the influence of welding parameters such as tool geometry, rotation speed, plunge depth, and travel speed on the microstructural and mechanical characteristics of the weld. It is also worth investigating the effect of tool tilt angle parameter on weld properties. Furthermore, No study has been found in the literature on the role of tool inclination angle on the mechanical and microstructural properties of friction stir lap welding (FSLW) of magnesium alloys. Hence, this study focused on tool tilt angle on mechanical properties of the (FSLW) of AZ31B magnesium alloy sheets.

## 2. MATERIAL AND METHOD

AZ31B magnesium alloy sheets with a 2 mm thickness, 100 mm length, and 100 mm width were purchased. Chemical and mechanical characteristics of the AZ31B alloy are presented in Tables 1 and 2. AZ31B sheet pairs were lap-welded for various welding tool inclination angles clockwise (0°, 1°, 2°, 3° and 4°) by the friction stir welding technique. Welding operations were carried out on a Falco FMH-4 model universal milling machine as shown in Figure 1. The welding tool was produced from H13 steel and its profile is shown in Figure 1. The tool has a conical-shaped pin without thread. Tool rotation speed of 1325 rpm, plunge depth of 3.7 mm, and feed rate of 37 mm.min<sup>-1</sup> were kept constant. Welding parameters are also given in Table 3. Welding configuration is given in Figure 2. The photo of the sheets joined at different tool tilt angles is provided in Figure 3. The tensile shear test specimens with 25 mm width were obtained as in Figure 4, cutting the joined sheets with a bandsaw. The tensile shear specimens were tested on an Instron 2736-004 machine using 1 mm.min<sup>-1</sup> constant tensile speed at room temperature as in Figure 5. To examine the cross-sectional areas of the welds, cross-sectional area samples were attained by cutting the joined sheets, and then they were sanded and polished with sandpaper up to 1500 grit. Microhardness of the welds was measured from cross-sections of the welds along the line just above the interface of the sheets from the base metal to the weld center via an AOB THV-1D Vickers tester using a 0.3 kg load and 11 seconds dwell time.

**Table 1.** Chemical composition

Material	Element (wt.%)								
	Fe	Ni	Cu	Si	Mn	Zn	Al	Ca	Mg
AZ31B Mg alloy	0.005	0.005	0.05	0.1	0.2-1	0.6-1.4	2.3-3.5	0.04	Rest

**Table 2.** Mechanical properties

Material	Yield strength	Tensile strength	Elongation	Vickers hardness
AZ31B Mg alloy	185 N.mm <sup>-2</sup>	270 N.mm <sup>-2</sup>	% 12	68.5 HV

**Table 3.** Welding parameters

Tool profile	Tool inclination angle	Tool rotation	Tool plunge	Tool feed rate
With conical pin and 8° concave shoulder	0° 1° 2° 3° 4°	1325 rpm	3.7 mm	37 mm.min <sup>-1</sup>

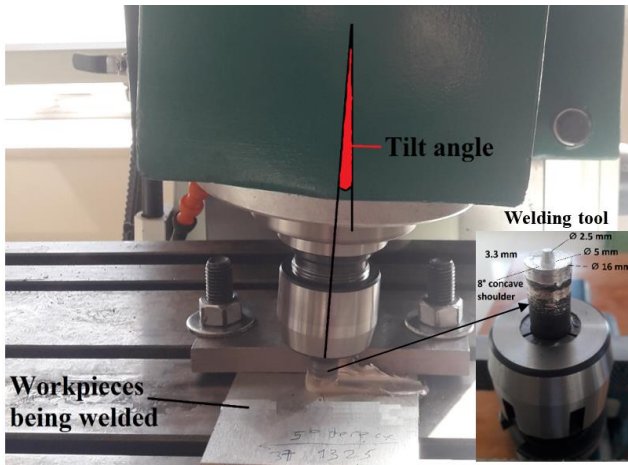


**Figure 1.** Friction stir lap welding operation and the welding tool

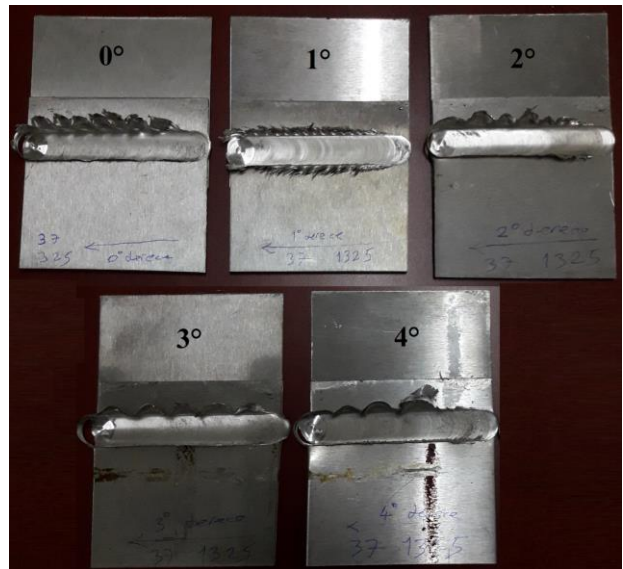


**Figure 3.** The joined sheets

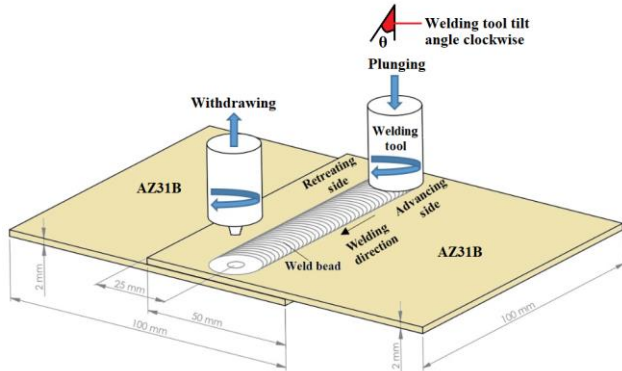


**Figure 2.** Friction stir lap welding configuration

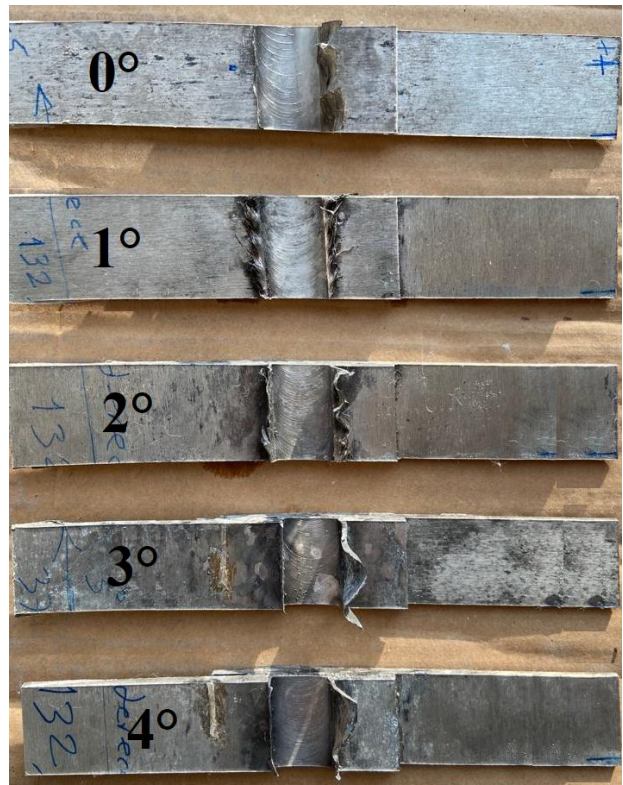


**Figure 4.** The weld specimens for the tensile shear test



Figure 5. The tensile shear test of the weld specimens

### 3. RESULTS AND DISCUSSION

Macro cross-sectional areas of the produced welds are shown in Figure 6. It can be seen that a tunnel defect formed in the weld created with the  $0^\circ$  tool inclination angle. This tunnel most likely occurred due to insufficient tool shoulder pressing pressure on the upper sheet because there is no tool tilt and thus insufficient compression of the sheets at the interface. The effective upper sheet thicknesses exposed to tensile force (the lowest distance between the interface of the sheets and the top of the upper sheet) on the advancing sides of the welds were measured. The effective thicknesses on the advancing sides of welds made at  $0^\circ$  and  $1^\circ$  are very close and nearly equal. However, it significantly decreased with an increase in the tilt angle above  $1^\circ$ , reaching the lowest value of 0.45 mm at  $4^\circ$ . Additionally, as the tool inclination angle increases, it is seen that more material is headed upwards from the top part of the upper sheet by flowing. This is because the back side of the tool shoulder immersed more into the top sheet. Moreover, the lowest upper sheet thicknesses on the retreating sides of the welds were obtained. Accordingly, the weld created at  $0^\circ$  tilt angle had the smallest value while the weld created at  $1^\circ$  had the biggest. Furthermore, it became thinner with increasing tilt angle from  $1^\circ$  to  $4^\circ$ . Vickers microhardness values of the welds obtained along the red line just above the interfaces of the sheets on their cross-sections are given in Figure 7. The hardness of the AZ31B base metal (BM) was found to be around 68.5 HV. In general, hardness gradually decreased from base metal (BM) to heat-affected zone (HAZ) and then weld zone (WZ). The average hardness in the HAZs of the welds made at  $0^\circ$ ,  $1^\circ$ ,  $2^\circ$  and  $4^\circ$  tilt angles is 62, 59.5, 57.7 and 56.7 HV, respectively while it is 61, 55.5, 52.9 and 50.7 HV in their WZ. The smallest hardness values were found in the WZs of the welds. In addition, the hardness of HAZ and WZ of the weld declined when the tool tilt angle was enhanced, therefore it became maximum at the smallest tilt angle of  $0^\circ$  and minimum at the highest tilt angle of  $4^\circ$ . This is due to the greater immersion of the tool shoulder into the upper sheet with a higher inclination angle, resulting in more heat input at the interface of the sheets. Cao and Jahazi [26] also found that the lowest hardness values are in the weld zone in the FSLW of AZ31B-H24 Mg alloy sheets, and higher tool rotation

speed led to lower hardness because of higher heat input resulted in larger grains in the weld zone.

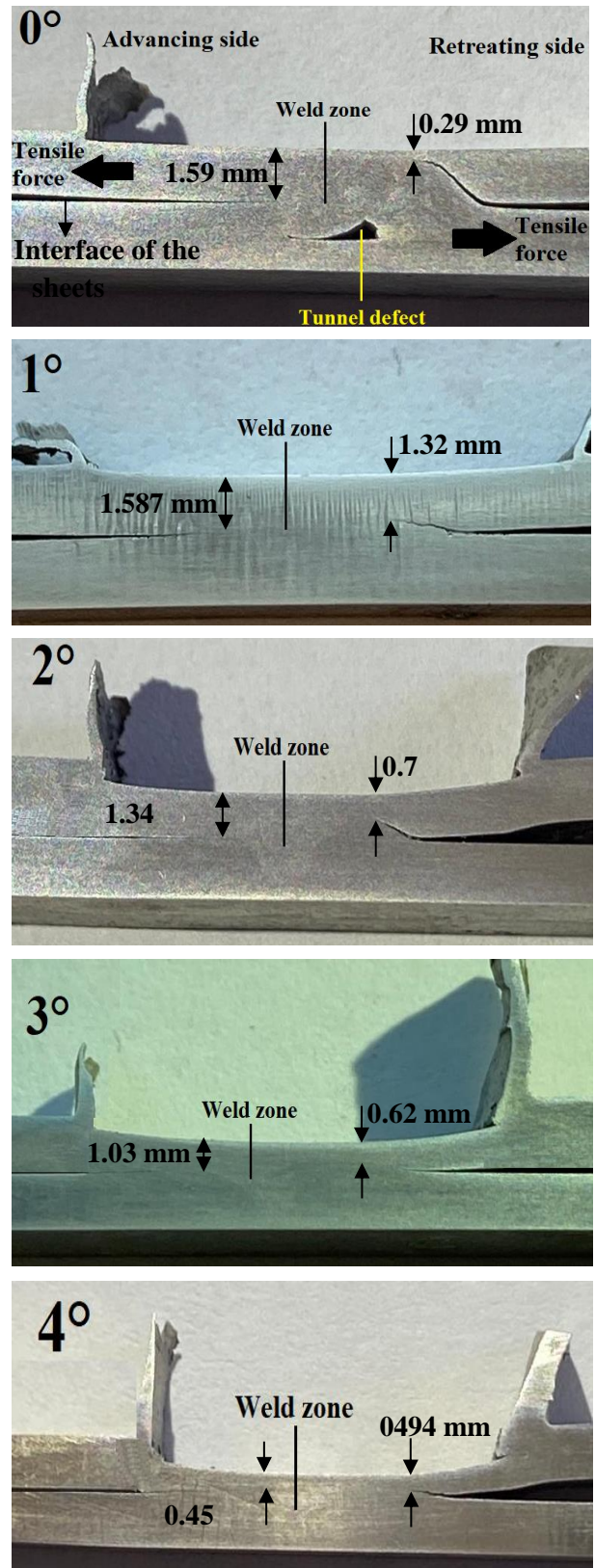


Figure 6. Cross-sections of the welds

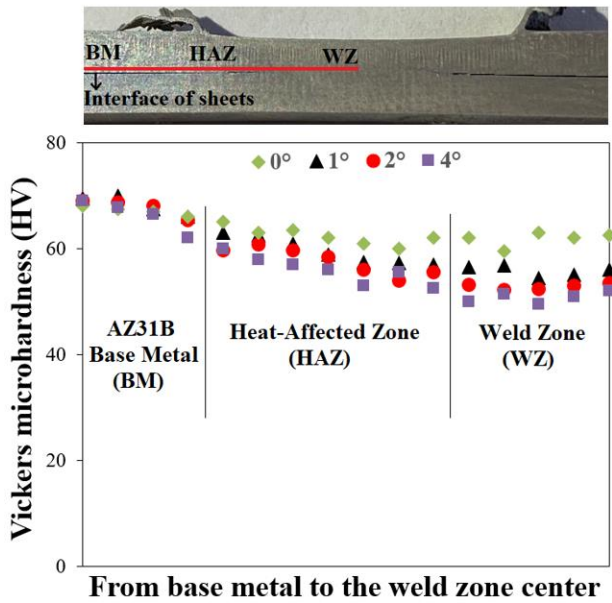


Figure 7. Microhardness of the welds created at various tool tilt angles

The tensile shear load properties of the welds are shown in Figure 8. It is obvious that the tool tilt angle has a significant effect on the tensile shear load of the weld. The tensile shear load increased to the maximum value of 5083 N with an increase in tilt angle from 0° to 1°. However, increasing the inclination angle up to 4° caused a dramatic decrease in the load value. This is because the tool shoulder plunged into the top of the upper sheet more with a higher tilt angle, and resulted in an important reduction in the effective upper sheet load-bearing thickness on the advancing side of the weld as seen in Figure 6. In other words, the effective upper sheet load-bearing thickness considerably got thinner owing to more tool shoulder plunging with increasing tilt angle. The weld formed with the 4° tilt angle has had the lowest tensile shear load of 1584 N. Also, the welds produced at high tilt angles (2°, 3° and 4°) had lower tensile elongation. Rajendran et al. [29] investigated the effect of tool tilt angle (0°-4°) on tensile shear load of the weld for FSSW of 2014-T6 aluminum alloy. They claimed that the weld made at 1° was defect-free, but the strongest one made at 2°, and the weld made at 3° had a low tensile load capacity because of unbalanced material flow.

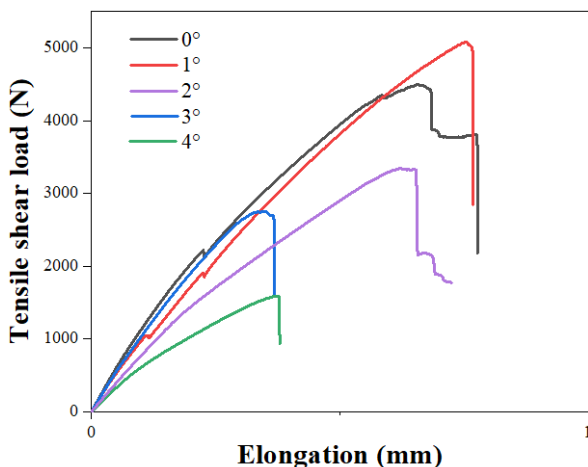


Figure 8. Tensile shear loads of the welds

Photos of the failure of welds during the tensile shear test are shown in Figure 9. It can be seen that all the welds failed away from the weld zones. Since there are no any failures from the weld zones, it can be said that weld zones are stronger than the acquired results. All the welds indicated a tensile mode fracture from the upper sheet material on the advancing side. The welds produced at 0°, 1° and 2° fractured from their upper sheet HAZs, their advancing sides, and almost vertically to the tensile force direction. But, the weld made at 1° broke slightly more away from the weld zone. The welds made with 3° and 4° failed from the top sheets just outside the plunging place of the tool shoulder due to excessive penetration of the tool shoulder into the top side of the upper sheet and the upper sheet becoming very thin.

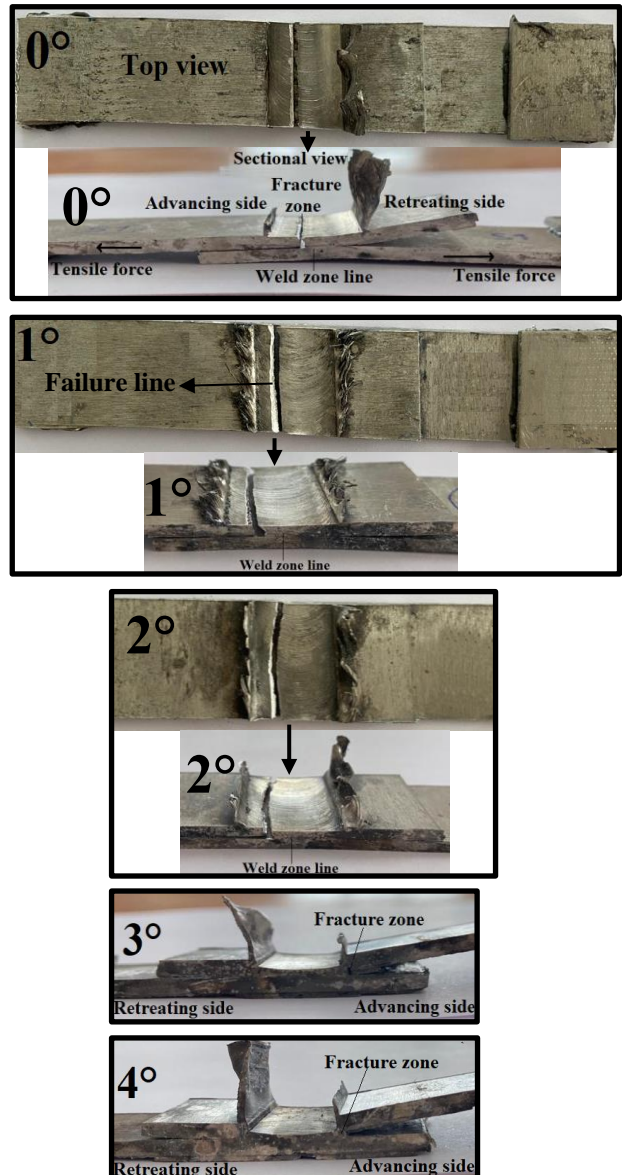


Figure 9. Fracture views of the welds after tensile test operation

#### 4. CONCLUSIONS

Friction stir lap welding of AZ31B magnesium alloy sheets was successfully carried out. Outcomes from evaluating cross-sections and mechanical tests of the welds are as below.



Increasing the tool tilt angle led to the thinning of the upper sheet as the tool shoulder penetrated more. The weld produced at 1° appeared to be the strongest with a tensile shear load of 5083 N because it had no visible defects and an effective high upper sheet load-bearing thickness on the advancing side. The weakest weld with a tensile shear load of 1584 N was made at 4° because, at this angle, the load carrier thickness of the upper sheet became extremely thin. On the other hand, the welds made at 0°, 2° and 3° inclination angles had a tensile shear load of 4497, 3342 and 2751 N, respectively. Weld tensile shear load increased with rising inclination angle from 0° to 1°. However, a further increase in the inclination angle resulted in a significant decrease in weld tensile shear load. The hardness of AZ31B alloy was determined to be around 68.5 HV. As the inclination angle was increased, the hardness in the heat-affected and weld zones of the weld decreased slightly and the lowest hardness values measured in the weld zones. The reason for this is probably more tool shoulder penetration into the upper sheet and generating more friction heat input. The average hardness in HAZ and the WZ is 62 and 61 HV, and 56.7 and 50.7 HV for the welds obtained at 0° and 4° inclination angles, respectively. All the welds failed from the top sheet on the advancing side and in tensile mode during the tensile test. Since no welds failed from their weld areas, we can say that the load carrying capacity of the weld areas is greater than the tensile loads obtained. Mg alloys, which are very difficult to weld with fusion welding, can be welded by friction stir welding method for use in applications such as aerospace and automotive, on condition that appropriate welding parameters are selected, for example, by choosing the tool inclination angle of 1 degree or slightly larger like between 1 and 2 degrees.

## REFERENCES

- [1] Cao X, Jahazi M, Immarigeon JP, Wallace W. A review of laser welding techniques for magnesium alloys. *J Mater Process. Technol.* 2006;171:188-204.
- [2] Liu FJ, Li YP, Sun ZY, Ji Y. Corrosion resistance and tribological behavior of particles reinforced AZ31 magnesium matrix composites developed by friction stir processing. *J Mater Res Technol.* 2021;11:1019-30.
- [3] Eivani AR, Mehdizade M, Chabok S, Zhou J. Applying multipass friction stir processing to refine the microstructure and enhance the strength, ductility and corrosion resistance of WE43 magnesium alloy. *J Mater Res Technol.* 2021;12:1946-57.
- [4] Wang W, Han P, Peng P, Guo H, Huang L, Qiao K, et al. Superplastic deformation behavior of fine-grained AZ80 magnesium alloy prepared by friction stir processing. *J Mater Res Technol.* 2020;9(3):5252-63.
- [5] Zhang X, Chen Y, Hu J. Recent advances in the development of aerospace materials. *Pro Aerosp Sci.* 2018;97:22-34.
- [6] Vedernikov A, Safonov A, Tucci F, Carlone P, Akhatov I. Pultruded materials and structures: a review. *J Compos Mater.* 2020;54:4081-4117.
- [7] Imran M, Khan R.A. Characterization of Al-7075 metal matrix composites: a review. *J Mater Res. Technol.* 2019;8:3347-3356.
- [8] Qin B, Yin F-c, Zeng C-z, Xie J-c, Shen J. Microstructure and mechanical properties of TIG/A-TIG welded AZ61/ZK60 magnesium alloy joints. *Trans Nonferrous Met Soc. China.* 2019;29(9):1864-1872.
- [9] Gao M, Wang H, Hao K, Mu H, Zeng X. Evolutions in microstructure and mechanical properties of laser lap welded AZ31 magnesium alloy via beam oscillation. *J Manuf Process.* 2019;45:92-99.
- [10] Hao K, Wang H, Gao M, Wu R, Zeng X. Laser welding of AZ31B magnesium alloy with beam oscillation. *J Mater Res Technol.* 2019;8(3):3044-3053.
- [11] Song G, Diao Z, Lv X, Liu L. TIG and laser-TIG hybrid filler wire welding of casting and wrought dissimilar magnesium alloy. *J Manuf Process.* 2018;34:204-214.
- [12] Thomas WM, Nicholas ED, Needham JC, Murch MG, Templesmith P, Dawes CJ. Friction Stir Welding. In *Pat. App.* 1991;8 PCT/GB92102203 and Great Britain patent application no. 9125978.
- [13] Golbabaei P, Besharati Givi MK, Molaiekiya. Investigating effects of process parameters on microstructural and mechanical properties of Al5052/SiC metal matrix composite fabricated via friction stir processing. *Mater Des.* 2012;37:458-464.
- [14] Barmouz M, Givi MK. Fabrication of in situ Cu/SiC composites using multi-pass friction stir processing: Evaluation of microstructural, porosity, mechanical and electrical behavior. *Comp Part A: App Sci Manuf.* 2011;50(10):1445-1453.
- [15] Zohoor M, Besharati Givi MK, Salami P. Effect of processing parameters on fabrication of Al-Mg/Cu composites via friction stir processing. *Mater Des.* 2012;39:5004-5014.
- [16] Liu HJ, Fujii H, Maeda M, Nogi K. Tensile properties and fracture locations of friction-stir-welded joints of 2017-T351 aluminum alloy. *J Mater Process Technol.* 2003;142(3):692-696.
- [17] Zhou M, Morisada Y, Fujii H, Ishikawa T. Mechanical properties optimization of AZX612-Mg alloy joint by double-sided friction stir welding. *J Mater Process Technol.* 2018;254:91-99.
- [18] Fujii H, Sun Y, Kato H, Nakata K. Investigation of welding parameter dependent microstructure and mechanical properties in friction stir welded pure Ti joints. *Mater Sci Eng A.* 2010;527(15):3386-3391.
- [19] Tsujikawa M, Abe Y, C. SW, Oki S, Higashi K, Hiraki I, M. Kamita. Cold-rolled Mg-14 mass% Li-1 mass% Al alloy and its friction stir welding. *Mater Trans.* 2006;47(4):1077-1081.
- [20] Salari E, Jahazi M, Khodabandeh A, Ghasemi-Nanesa H. Influence of tool geometry and rotational speed on mechanical properties and

- defect formation in friction stir lap welded 5456 aluminum alloy sheets. *Mater Des.* 2014;58:381-389.
- [21] Galvão I, Verdera D, Gesto D, Loureiro A, Rodrigues DM. Influence of aluminium alloy type on dissimilar friction stir lap welding of aluminium to copper. *J Mater Process Technol.* 2013;213(11):1920-1928.
- [22] Thornton PH, Krause AR, Davies RG. Aluminum Spot Weld. *Weld J.* 1996;75:101.
- [23] Mishra RS, M ZY. Friction stir welding and processing. *Mater Sci Eng R.* 2005;50:1-78.
- [24] Cam G, Mistikoglu S. Recent developments in friction stir welding of Al-alloys. *J Mater Eng Perform.* 2014;23:1936-53.
- [25] Singh K, Singh G, Singh H. Review on friction stir welding of magnesium alloys. *J Magnes All.* 2018;6:399-416.
- [26] Cao X, Jahazi M. Effect of tool rotational speed and probe length on lap joint quality of a frictionstir welded magnesium alloy. *Mater Des.* 2011;32(1):1-11.
- [27] Cao X, Jahazi M. Effect of welding speed on lap joint quality of friction stir welded AZ31 magnesium alloy. *Trends in Welding Research, Proceedings of the 8th International Conference,* 2008;72-80.
- [28] Yang Q, Li X, Chen1 K, Shi YJ. Effect of tool geometry and process condition on static strength of a magnesium friction stir lap linear weld. *Mater Sci Eng A.* 2011;528:2463-2478.
- [29] Rajendran C, Srinivasan K, Balasubramanian V, Balaji H, Selvaraj P. Effect of tool tilt angle on strength and microstructural characteristics of friction stir welded lap joints of AA2014-T6 aluminum alloy. *Tran Nonferrous Met. Soc China.* 2019;29:1824-1835.

## Evaluation of Sun Protection Factor of Northern Iraqi Propolis

Adnan AYNA<sup>1\*</sup>, Farhan NERWAY<sup>2</sup>

<sup>1</sup>Department of Chemistry, Faculty of Arts and Sciences, Bingöl University, Bingöl, Türkiye

<sup>2</sup>Department of Bee and Bee Products, Bingöl University, Bingöl, Türkiye

Adnan AYNA ORCID No: 0000-0001-6801-6242

Farhan NERWAY ORCID No: 0009-0006-9324-5526

\*Corresponding author: aayna@bingol.edu.tr

(Received: 09.05.2024, Accepted: 29.07.2024, Online Publication: 26.09.2024)

### Keywords

Propolis,  
Sun protection  
factor,  
Ethanol extract,  
Photoaging,  
Antioxidant

**Abstract:** One of the main risk factors for skin cancer and photoaging is excessive sun exposure combined with the lack of sun protection. Incorporating natural antioxidant and anti-inflammatory agents into sunscreens and taking natural antioxidant extracts orally are two recent photoprotection approaches. Propolis and its plant precursors have the potential to be used as active components in pharmaceutical and skin care products that mitigate the effects of ultraviolet radiation from the sun. To date, no research has been carried out on the photoprotective effects of Northern Iraqi propolis. Ethanol and water extracts of propolis were used in the current research due to its potential sun protection factor. This investigation aimed to assess the sun protection factor (SPF) of Northern Iraqi propolis collected from Erbil, Mosul and Sulaymaniyah regions. The SPF of propolis extracts were assessed using the methods of Mansur. According to the findings, the extracts' SPF varied from 5.1 to 17.9. The Musol propolis ethanol extract had the greatest SPF at a concentration of 20 ppm (17.9). At 0.5 ppm (5.1), the Erbil water extract had the lowest SPF. Overall, it was noticed that the SPF value of the propolis ethanolic extract was higher than the water extract for each concentration studied.

## Kuzey Irak Propolisinin Güneş Koruma Faktörünün Değerlendirilmesi

### Anahtar Kelimeler

Propolis,  
Güneş koruma  
faktörü,  
Etanol ekstraktı,  
Fotoyaşlanma,  
Antioksidan

**Öz:** Cilt kanseri ve fotoyaşlanma için ana risk faktörlerinden biri güneşe aşırı maruz kalma ve güneşten korunma eksikliğidir. Güneş kremlerine doğal antioksidan ve antiinflamatuvar ajanların dahil edilmesi ve doğal antioksidan ekstraktlarının ağızdan alınması fotokorunmaya yönelik yeni ilki yaklaşımdır. Propolis güneşten gelen ultraviyole radyasyonun etkilerini azaltan farmasötik ve cilt bakım ürünlerinde aktif bileşenler olarak kullanılmaya potansiyeline sahiptir. Şu ana kadar Kuzey Irak propolisinin fotokoruyucu etkileri üzerine herhangi bir araştırma yapılmamıştır. Potansiyel güneş koruma faktörü nedeniyle bu çalışmada propolisin etanol ve su ekstraktları kullanılmıştır. Bu araştırma, Erbil, Musul ve Süleymaniye'den toplanan Kuzey Irak propolisinin güneş koruma faktörünü değerlendirmeyi amaçlamıştır. Propolis ekstraktlarının güneş koruma faktörü Mansur'un geliştirmiş olduğu yöntem kullanılarak hesaplanmıştır. Bulgulara göre ekstraktların güneş koruma faktörü 5,1 ile 17,9 arasında değişmektedir. Musol propolis etanol ekstraktının 20 ppm (17,9) konsantrasyonda en yüksek güneş koruma faktörüne sahip olduğu gözlemlenmiştir. 0,5 ppm (5,1) ile Erbil propolisinin su ekstraktının en düşük güneş koruma faktörüne sahip olduğu sonuçlardan anlaşılmaktadır. Genel olarak, incelenen her konsantrasyon için propolis etanolik ekstraktının güneş koruma faktörü değerinin su ekstraktından daha yüksek olduğu sonucuna varılmıştır.

## 1. INTRODUCTION

Over the years, propolis has acquired reputation all over the world as a unique naturally derived resinous medicine with a wide range of medical applications. Significant clinical trials are underway to highlight the

therapeutic value of propolis and advance its use in the nutraceutical and pharmaceutical industries. In addition to providing beeswax, propolis, royal jelly, venom and apitherapy as dietary and therapeutic resources for human health, honey bees also serve as pollinators in natural environments [1-5]. Propolis has a wide range of

components and these components change according to the type of honeybee species, the plant that bees use to produce propolis, the environment and the time of year when it is harvested [6-8].

Propolis's bioactive profile is correlated with habitats, particularly with regard to the wide range of floral resources that are essential to bee survival and biodiversity [9]. Propolis contains more than 300 chemical components that have biological activities, such as chalcones, phenolic acids, benzofuranes, benzopyranes and flavonoids [10]. Numerous large-scale experimental studies have documented the biomedical benefits of propolis, particularly that sourced from Brazil, China, Taiwan, and Iran, as well as its constituents' anti-inflammatory, antioxidant, anticancer, immunomodulatory, antibacterial, antiviral, antifungal and antidiabetic properties [11].

Numerous studies have demonstrated the protective effects of polyphenols against UV radiation exposure. Overexposure to UV light can harm a cell's DNA and result in negative reactions [12]. Natural polyphenols are often UV-absorbing pigments that are yellow, red, or purple in color. Several *in vitro* and clinical investigations have demonstrated that skin disorders, melanoma, dry skin, ageing skin, vasodilation and skin cancers may all be directly caused by exposure to UV radiation [13]. Phenolic chemicals are distinguished by their absorption spectrum, which filters out UV radiation to lessen oxidative stress, DNA damage and the penetration of harmful UV rays into the skin [14]. Using natural polyphenol compounds, which have photoprotective as well as antioxidant and anti-inflammatory qualities, can help to protect against the harmful effects of UV radiation from the sun [14].

Natural polyphenol compounds, which possess both antioxidant and anti-inflammatory qualities in addition to photoprotective effects, can be used to protect against the harmful effects of UV radiation from the sun [15]. As an active component in skin care products and pharmaceutical formulations for the prevention of sun UV radiation, propolis and its botanical antecedents are promising options [16]. There hasn't been any research done on the photoprotective qualities of Northern Iraqi propolis or its plant precursors. The aim of this study was to evaluate the possible photoprotective effects of Northern Iraqi propolis collected from Erbil, Musol and Sulaymaniyah.

## 2. MATERIAL AND METHOD

### 2.1. Chemicals Used and Material Collection

All chemicals were provided by Sigma Chemical Co. (USA) and were of the reagent grade. Deionized water that has been purified with the Milli-Q® water purification system (Millipore, Burlington, MA, USA). Spectrophotometric measurements were taken by using a Shimadzu UV-1800 double-beam UV-Vis instrument. Samples of propolis were gathered from several areas in the northern Iraqi regions of Erbil, Musol and

Sulaymaniyah. The propolis samples were obtained directly from beekeepers and were not purchased from marketplaces. Table 1 displays the geographical locations of the samples. The samples were collected on July, 2021.

**Table 1.** Coordinates of the locations of the propolis samples

Locations	Coordinate	Altitude
1 Erbil	N 36°23'18.6792" E 44°12'07.6356"	1063.0m
2 Musol	N 36°48'53.6796" E 42°17'07.6956"	406.0m
3 Sulaymaniyah	N 35°43'12.3888" E 45°34'12.5724"	1170.0m

### 2.2. Hexane Extraction

Using a grinding tool, the raw propolis was crushed and ground into a fine grain in order to maximize the amount of surface area that could be extracted using hexane solution. Subsequently, 10 g of propolis were weighed, put into appropriate containers, and put in a vacuum machine to reduce the possibility of poisoning. 100 ml of hexane was then added, and the propolis was tightly sealed with aluminum paper and paraffin. After that, the containers were maintained at 40°C and 150 rpm for a whole day in an orbital shaker. The solutions were vacuum-filtered the next day using paper filters, and the resulting mixtures were then put in an oven set at 37°C to evaporate the leftover hexane together with the ingredients.

### 2.3. Ethanol Extraction

The propolis sample was kept at room temperature while it was extracted using ethanol by shaking and extraction. Following that, Whatman No. 1 filter paper was used to filter the propolis extracts. After the filtrates were evaporated using a vacuum incubator, the produced propolis was kept dry for storage.

### 2.4. Water Extraction

The remaining propolis from the ethanol extraction were collected and 100 ml of distilled water was then added. Afterwards, the propolis were put in an orbital shaker system at 150 rpm for 24 hours at 37°C. The following day, the extracts were filtered via Whatman 1 paper filters, and heated at 37°C to evaporate any remaining water.

### 2.5. Photoprotective Effects of Propolis

The sun protection factor (SPF) of water and ethanol extracts of Northern Iraqi propolis (Erbil, Musol and Sulaymaniyah) was assessed according to Mansur et al. with minor modifications [17]. Through the investigation, each extract was diluted with 96% ethanol (v/v) to a concentration of 0.5, 1, 5, 10 and 20 ppm (µg/mL). The absorption spectrum of the test samples was obtained in the range of 290–320 nm. A 1 cm quartz element was used for the study. Absorbance data were obtained from 290 to 320 nm in 5 nm increments. 96% ethanol (v/v) was used as a blank.

SPF values were calculated according to Mansur et al. equation [17]:

$$CF \times \sum EE(\lambda) \times I(\lambda) \times Abs(\lambda)$$

EE ( $\lambda$ )—erythral effect spectrum; I ( $\lambda$ )—solar intensity spectrum; Abs ( $\lambda$ )—absorbance of extract; CF—correction factor (= 10).

## 2.6. Statistical Analysis

Results were expressed standard deviation of three measurements. These data were calculated using Microsoft Excel software.

## 3. RESULTS

The SPF of the ethanolic and water extracts of Erbil, Musol and Sulaymaniyah propolis were assessed spectrophotometrically (Table 2-4). The results showed that the SPF of extracts ranged from 5.1 to 17.9. The highest SPF was found in the ethanol extract of Musol propolis at 20 ppm concentration (17.9). The lowest SPF was found in the water extract of Erbil at 0.5 ppm (5.1). In general, it could be observed that the SPF value of the ethanolic extract of propolis for each concentration is greater than that of water extract.

The SPF analysis of ethanolic and water extracts of Erbil propolis demonstrated that greatest SPF value was obtained at 20 ppm ethanol extract (9.9) while this value was 35% lesser (6.7) for the same concentration of water extract. On the other hand, the lowest SPF was obtained at 0.5 ppm concentration of water extract (5.1).

**Table 2.** The SPF analysis of ethanolic and water extracts of Erbil propolis. E denoted ethanol extract, W denotes water extract

Concentration (ppm)	SPF (E, Erbil)	SPF (W, Erbil)
20	9.9±0.2	6.7±0.16
10	6.6±0.12	6±0.14
5	5.9±0.14	5.7±0.14
1	5.5±0.12	5.6±0.1
0.5	5.4±0.1	5.1±0.12

The SPF analysis of ethanolic and water extracts of Musol propolis demonstrated that greatest SPF value was obtained at 20 ppm ethanol extract (17.9) while this value was almost 3 fold lesser (6.6) for the same concentration of water extract. On the other hand, the lowest SPF was obtained at 0.5 ppm concentration of water extract (5.4). The analysis also revealed that SPF of ethanolic extract of Musol propolis was twofold greater than that of Erbil propolis.

**Table 3.** The SPF analysis of ethanolic and water extracts of Musol propolis. E denoted ethanol extract, W denotes water extract

Concentration (ppm)	SPF (E, Musol)	SPF (W, Musol)
20	17.9±0.45	6.6±0.16
10	10±0.24	5.9±0.1
5	7.5±0.22	5.7±0.15
1	5.7±0.12	5.4±0.12
0.5	5.5±0.15	5.4±0.1

The results of the SPF study of the ethanolic and water extracts of Sulaymaniyah propolis showed that the

highest SPF value was achieved at 20 ppm ethanol extract (11.9), whereas the value for the same concentration of water extract was nearly 2 fold lesser (6.5). Conversely, the water extract concentration of 0.5 ppm produced the lowest SPF (5.5).

**Table 4.** The SPF analysis of ethanolic and water extracts of Sulaymaniyah propolis. E denoted ethanol extract, W denotes water extract

Concentration (ppm)	SPF (E, Sulaymaniyah)	SPF (W, Sulaymaniyah)
20	11.9±0.32	6.5±0.21
10	8.7±0.23	5.9±0.22
5	6.9±0.20	5.7±0.14
1	5.9±0.14	5.5±0.16
0.5	5.5±0.11	5.5±0.11

## 4. DISCUSSION AND CONCLUSION

The ultraviolet (UV) radiation emitted by the sun are classified into three groups based on their wavelengths: UVA (320–400 nm), UVB (290–320 nm) and UVC (100–280 nm) [18]. Since UVA and UVB may reach the earth's surface, unlike UVC, which is absorbed by the atmosphere's ozone layer, they have the potential to cause a wide range of skin conditions, from moderate sunburns and minor skin inflammations to serious cancers [19,20]. UVB rays can reach a depth of 160–180  $\mu$ m in the skin, which increases the risk of melanoma and skin cancer as well as causing wrinkles, scaling, dryness and blood vessel dilatation. UVA rays can cause reactive oxygen species, which can harm proteins, lipids, and DNA structures by penetrating deeper into the epidermis and dermis [21]. As a result, efforts to produce a sun protection formulation have accelerated in recent decades. The sun protection benefits of sunscreens are attributed to either of two processes: chemical (i.e., radiation absorption) or physical (i.e., radiation blocking) [22]. SPF unit explains how well they protect the skin [23]. This phrase describes the level of skin protection against the sun's piercing rays. Common synthetic sunscreen ingredients like oxybenzone, avobenzene, ecamsule and octocrylene, however, can penetrate the skin and cause major adverse effects, such as allergic reactions, DNA damage, antiandrogenic effects, the development of cancer and other health problems [24]. Consequently, a lot of research is being done to create a natural sunscreen that should have less adverse consequences.

Attributable to the protective effects of propolis on the skin, it has been deliberated as a decent candidate for integration in skin-care cosmeceuticals such as sunscreens [25]. Propolis also has strong anti-inflammatory properties, making it a good treatment for sunburns and other skin conditions that are influenced by radiation [26]. Concurrently, preserving the collagen contents of the skin, it can act as an anti-aging product [27]. Furthermore, since propolis contains various flavonoids and antioxidants, it can protect the skin from UV rays.

Spectrophotometric analysis of SPF of Lithuanian propolis revealed that SPF of the ethanolic extracts 10  $\mu$ g/mL had SPFs ranging from 2.010 to 4.851. The

propolis extract has the highest SPF of 4.851. The pine buds extract had the lowest SPF [28], all which are lower than Northern Iraqi propolis. Using topical formulations based on a Brazilian red propolis hydroalcoholic extract was shown to provide photoprotective effects in a mouse model [29]. Furthermore, these findings imply that the biological impact may have something to do with anti-inflammatory and antioxidant processes. These results suggest that the Hydroalcoholic Extract of Red Propolis is a natural substance with promise for photoprotection applications in cosmetic formulations. The study showed how crucial it is to incorporate green propolis extracts into Gel Permolen TR-1 sunscreen preparations since significant antioxidant and SPF activity was noted, which may enhance the phytopharmaceutical product's ability to protect skin. The HET-CAM test indicated that the formulation made with Gel Permolen TR-1 and enhanced with EEP was safe to apply directly to the skin. In their study, all EEPs of 70% and 75% (at room temperature and high temperature) increased sun protection at the tested concentrations in the experimental settings of this investigation. This composition can therefore be applied to photoprotective materials [29].

As seen in the experiments deposited in the literature, when the extract was added to the Polawax cream sunscreen, the outcomes show that the ethanolic red propolis extracts had photoprotective qualities [30]. This study was reported as the first investigation into the photoprotective properties of red propolis ethanolic extracts added to a cream sunscreen formulation like Polawax. Their research comes to a different conclusion, despite the fact that many writers demonstrate a correlation between antioxidant activity, flavonoid concentration, and phenol content in the importance of UV protection. The antioxidant activity was strong, however the extraction procedure was insufficient to remove numerous phenols and flavonoids. As a result, they linked antioxidant activity to the high benefit of sun protection that was only discovered. Furthermore, the findings demonstrated that the addition of propolis ethanol extract to photoprotective formulations not only enhanced the sun protection values but also guaranteed the preservation of propolis's other qualities, including antimicrobial, anti-inflammatory, antioxidant and healing. As a result, their study indicates that it is a potential source of natural chemicals for the creation of novel formulations that offer photoprotection [31].

The purpose of this study was to evaluate the level of sun protection provided by Northern Iraqi propolis that was gathered in Sulaymaniyah, Mosul and Erbil. Mansur's method was used to evaluate the propolis extracts' sun protection factor. The results showed that the SPF of the extracts ranged from 5.1 to 17.9. At a dosage of 20 ppm, the Musol propolis ethanol extract exhibited the highest level of sun protection (17.9). The Erbil water extract had the lowest SPF at 0.5 ppm (5.1). Overall, it was shown that at every concentration under investigation, the propolis ethanolic extract's SPF value was higher than the water extract's. Conducting in vivo experiments to evaluate the effectiveness of propolis or

investigating other extraction techniques, would offer a good guide for future investigations.

### Acknowledgement

The Bingöl University Independent Research Projects Office (BÜBAP), in Turkey, provided funding for this project. (Grant Number: BAP-FBE.2022.002).

### REFERENCES

- [1] Belmehtdi, O., El Menyiy, N., Bouyahya, A., El Baaboua, A., El Omari, N., Gallo, M., ... & Abrini, J. (2023). Recent advances in the chemical composition and biological activities of propolis. *Food Reviews International*, 39(9), 6078-6128.
- [2] Ayna, A., Tunc, A., Özbolat, S. N., Bengü, A. Ş., Aykutoğlu, G., Canli, D., ... & Darendelioğlu, E. (2021). Anticancer, and antioxidant activities of royal jelly on HT-29 colon cancer cells and melissopalynological analysis. *Turkish Journal of Botany*, 45(8), 809-819.
- [3] Bengü, A. Ş., Ayna, A., Özbolat, S., Tunç, A., Aykutoğlu, G., Çiftci, M., & Darendelioğlu, E. (2020). Content and antimicrobial activities of Bingöl royal jelly. *Türk Tarım ve Doğa Bilimleri Dergisi*, 7(2), 480-486.
- [4] Bava, R., Castagna, F., Musella, V., Lupia, C., Palma, E., & Britti, D. (2023). Therapeutic Use of Bee venom and potential applications in veterinary medicine. *Veterinary Sciences*, 10(2), 119.
- [5] Page, M. L., & Williams, N. M. (2023). Honey bee introductions displace native bees and decrease pollination of a native wildflower. *Ecology*, 104(2), e3939.
- [6] Shehata, M. G., Ahmad, F. T., Badr, A. N., Masry, S. H., & El-Sohaimy, S. A. (2020). Chemical analysis, antioxidant, cytotoxic and antimicrobial properties of propolis from different geographic regions. *Annals of Agricultural Sciences*, 65(2), 209-217.
- [7] Stojanović, S. T., Najman, S. J., Popov, B. B., & Najman, S. S. (2020). Propolis: chemical composition, biological and pharmacological activity—a review. *Acta Medica Medianae*, 59(2).
- [8] Dezmirean, D. S., Paşca, C., Moise, A. R., & Bobiş, O. (2020). Plant sources responsible for the chemical composition and main bioactive properties of poplar-type propolis. *Plants*, 10(1), 22.
- [9] Durazzo, A., Lucarini, M., Plutino, M., Lucini, L., Aromolo, R., Martinelli, E., ... & Pignatti, G. (2021). Bee products: A representation of biodiversity, sustainability, and health. *Life*, 11(9), 970.
- [10] Chavda, V. P., Chaudhari, A. Z., Teli, D., Balar, P., & Vora, L. (2023). Propolis and their active constituents for chronic diseases. *Biomedicines*, 11(2), 259.
- [11] Popova, M., Trusheva, B., & Bankova, V. (2021). Chemistry and Applications of Propolis. In *Gums, Resins and Latexes of Plant Origin: Chemistry, Biological Activities and Uses* (pp. 1-33). Cham: Springer International Publishing.

- [12] Vechtomova, Y. L., Telegina, T. A., Buglak, A. A., & Kritsky, M. S. (2021). UV radiation in DNA damage and repair involving DNA-photolyases and cryptochromes. *Biomedicines*, 9(11), 1564.
- [13] Farris, P. K., & Valacchi, G. (2022). Ultraviolet light protection: is it really enough?. *Antioxidants*, 11(8), 1484.
- [14] Boo, Y. C. (2020). Emerging strategies to protect the skin from ultraviolet rays using plant-derived materials. *Antioxidants*, 9(7), 637.
- [15] Salian, A., Dutta, S., & Mandal, S. (2021). A roadmap to UV-protective natural resources: Classification, characteristics, and applications. *Materials Chemistry Frontiers*, 5(21), 7696-7723.
- [16] Karapetsas, A., Voulgaridou, G. P., Konialis, M., Tsochantaridis, I., Kynigopoulos, S., Lambropoulou, M., ... & Pappa, A. (2019). Propolis extracts inhibit UV-induced photodamage in human experimental in vitro skin models. *Antioxidants*, 8(5), 125.
- [17] Mansur, J. D. S., Breder, M. N., Mansur, M. C., & Azulay, R. D. (1986). Determination of sun protection factor by spectrophotometry. *An Bras Dermatol*, 61(3), 121-124.
- [18] Dwivedi, A., Tripathi, A. K., Singh, J., & Pal, M. K. (2018). Ultraviolet radiation (UVR): An introduction. *Photocarcinogenesis & Photoprotection*, 1-8.
- [19] Hoisington, R. D., Whiteside, M., & Herndon, J. M. (2023). Unequivocal detection of solar ultraviolet radiation 250-300 nm (UV-C) at Earth's surface. *European Journal of Applied Sciences-Vol*, 11(2).
- [20] Sumali, S. M. (2023). A comparative study of UVA and UVB radiation: Mechanisms of DNA damage and repair. *Indonesia Journal of Biomedical Science*, 17(2), 239-243.
- [21] Robinson, J., Begum, R., & Maqbool, M. (2023). Ultraviolet Radiation: Benefits, Harms, Protection. *An Introduction to Non-Ionizing Radiation*, 2, 62.
- [22] Serpone, N. (2021). Sunscreens and their usefulness: have we made any progress in the last two decades?. *Photochemical & Photobiological Sciences*, 20, 189-244.
- [23] Schalka, S., & Reis, V. M. S. D. (2011). Sun protection factor: meaning and controversies. *Anais brasileiros de dermatologia*, 86, 507-515.
- [24] Benson, H. A. (2007). Sunscreens: efficacy, skin penetration, and toxicological aspects. In *Dermatologic, Cosmeceutic, and Cosmetic Development* (pp. 433-450). CRC Press.
- [25] Fu, Y., Wan, R., Yang, L., Xiong, L., Hu, J., Tang, J., ... & Li, Y. (2022). Propolis inspired sunscreens for efficient UV-protection and skin barrier maintenance. *Nano Research*, 15(9), 8237-8246.
- [26] Batista, C. M., Alves, A. V. F., Queiroz, L. A., Lima, B. S., Araújo, A. A. S., de Albuquerque Júnior, R. L. C., & Cardoso, J. C. (2018). The photoprotective and anti-inflammatory activity of red propolis extract in rats. *Journal of Photochemistry and Photobiology B: Biology*, 180, 198-207.
- [27] Kim, D. H., Auh, J. H., Oh, J., Hong, S., Choi, S., Shin, E. J., ... & Byun, S. (2020). Propolis suppresses UV-induced photoaging in human skin through directly targeting phosphoinositide 3-kinase. *Nutrients*, 12(12), 3790.
- [28] Stanciauskaite, M., Marksa, M., Rimkiene, L., & Ramanauskiene, K. (2022). Evaluation of Chemical Composition, Sun Protection Factor and Antioxidant Activity of Lithuanian Propolis and Its Plant Precursors. *Plants*, 11(24), 3558.
- [29] Batista, C. M., Alves, A. V. F., Queiroz, L. A., Lima, B. S., Araújo, A. A. S., de Albuquerque Júnior, R. L. C., & Cardoso, J. C. (2018). The photoprotective and anti-inflammatory activity of red propolis extract in rats. *Journal of Photochemistry and Photobiology B: Biology*, 180, 198-207.
- [30] Almeida, W. A. D. S., Sousa, L. R. D., dos Santos Antunes, A., de Azevedo, A. S., do Nascimento, A. M., Amparo, T. R., ... & dos Santos, V. M. R. (2020). Green propolis: In vitro photoprotective and photostability studies of single and incorporated extracts in a sunscreen formulation. *Revista Brasileira de Farmacognosia*, 30(3), 436-443.
- [31] Valverde, T. M., Soares, B. N. G. D. S., Nascimento, A. M. D., Andrade, Â. L., Sousa, L. R. D., Vieira, P. M. D. A., ... & Santos, V. M. R. D. (2023). Anti-Inflammatory, antimicrobial, antioxidant and photoprotective investigation of red propolis extract as sunscreen formulation in polawax cream. *International Journal of Molecular Sciences*, 24(6), 5112.

## Partial Purification and Biochemical Characterization of Cellulase from *Bacillus pumilus* ND8 Isolated from Garden Waste

Neslihan DİKBAŞ<sup>1\*</sup>, Waleed SALİH SALMAN AL DAHLUZ<sup>1</sup>, Şeyma ALİM<sup>1</sup>, Sevda UÇAR<sup>2</sup>

<sup>1</sup> Ataturk University, Agricultural Faculty, Department of Agricultural Biotechnology, Erzurum, Türkiye

<sup>2</sup> Sivas Science and Technology University, Faculty of Agricultural Sciences and Technology, Department of Herbal Production and Technologies, Sivas, Türkiye

Neslihan DİKBAŞ ORCID No: 0000-0001-9096-2761

Waleed Salih Salman Al Dahluz ORCID No: 0009-0002-9275-7328

Şeyma ALİM ORCID No: 0000-0001-6684-7974

Sevda UÇAR ORCID No: 0000-0002-3612-457X

\*Corresponding author: neslidikbas@atauni.edu.tr

(Received: 01.07.2024, Accepted: 29.07.2024, Online Publication: 26.09.2024)

### Keywords

*Bacillus pumilus*,  
Cellulase,  
Partial  
purification

**Abstract:** Cellulose, one of the most abundant carbohydrates on Earth, is a promising candidate for the production of second-generation biofuels such as ethanol and various everyday products. This polysaccharide is degraded by the enzyme cellulase, which is usually produced by microorganisms. Microbial cellulases are widely used in various industries (such as textiles, detergents, pharmaceuticals, food and paper).

In the present study, cellulase enzyme was partially purified from *Bacillus pumilus* ND8 strain isolated from garden waste and the pH and temperature values at which the enzyme showed optimum activity were determined. *B. pumilus* ND8 strain exhibited a cellulase activity of 8.6 U/mL as a result of partial purification and the protein concentration of the enzyme was measured as 6.72 mg/mL. The pH and temperature values at which the partially purified cellulase showed optimum activity were pH 5.5 and 60 °C, respectively.  $K_m$  and  $V_{max}$  values of the enzyme were determined as 0.81 mM and 14.2 µmol/min, respectively. In conclusion, cellulase purified from *B. pumilus* ND8 strain was found to possess unique properties that make it suitable for industrial applications.

## Bahçe Atıklarından İzole Edilen *Bacillus pumilus* ND8'den Selülazın Kısmi Saflaştırılması ve Biyokimyasal Karakterizasyonu

### Anahtar Kelimeler

*Bacillus pumilus*,  
Selülaz,  
Kısmi  
saflaştırma

**Öz:** Dünyada bol miktarda bulunan karbonhidratlardan biri olan selüloz, etanol gibi ikinci nesil biyoyakıtların ve çeşitli günlük ürünlerin üretimi için umut verici bir adaydır. Bu polisakkarit, genellikle mikroorganizmalar tarafından üretilen selülaz enzimi tarafından parçalanır. Mikrobiyal selülazlar çeşitli endüstrilerde (tekstil, deterjan, ilaç, gıda ve kağıt gibi) yaygın olarak kullanılmaktadır.

Mevcut çalışmada, bahçe atıklarından izole edilen *Bacillus pumilus* ND8 suşundan selülaz enzimi kısmi olarak saflaştırıldı ve enzimin optimum aktivite gösterdiği pH ve sıcaklık değerleri belirlendi. *B. pumilus* ND8 suşu kısmi saflaştırma sonucunda 8.6 U/mL'lik bir selülaz aktivitesi sergiledi ve enzimin protein konsantrasyonu 6.72 mg/mL olarak ölçüldü. Kısmi olarak saflaştırılan selülazın optimum aktivite gösterdiği pH ve sıcaklık değerleri sırasıyla pH 5.5 ve 60 °C olarak bulundu. Enzimin  $K_m$  ve  $V_{max}$  değerleri ise sırasıyla 0.81 mM ve 14.2 µmol/min olarak belirlendi. Sonuç olarak, *B. pumilus* ND8 suşundan saflaştırılan selülazın endüstriyel uygulamalarda kullanılmasını uygun kılan kendine özgü niteliklere sahip olduğu tespit edilmiştir.



## 1. INTRODUCTION

The continued increase in global industrialization has led researchers in various industrial fields (textiles, animal feed, paper, detergents, food, etc.) to search for solutions that are economically viable and do not cause environmental damage [1]. Cellulose is the most abundant renewable energy source in the world, easily and cheaply available for the production of different biotechnologically important products [2].

Cellulose is the main component of the plant cell wall and is a polysaccharide formed by D-glucose units linked by  $\beta$ -1,4 bonds [1,3,4]. Cellulose is mainly broken down by the enzyme cellulase, which is widely produced by microorganisms [1,5]. Cellulases efficiently hydrolyze cellulose into glucose units through the synergistic effects of endo- $\beta$ -1,4-glucanase,  $\beta$ -D-glucosidase and cellobiohydrolase enzymes [4,6,7]. Known for their fast growth rates compared to fungi, bacteria have become a preferred choice for industrial enzyme production due to their ability to produce high purity cellulase under a variety of growth media [8,9].

Cellulases are of great interest due to their wide-ranging applications in various industries (detergent, food, textile, paper, feed, leather industry, etc.) [6,10,11,12]. They also play important roles in fiber modification, biomass fermentation and pharmaceutical development [6,13,14]. The widespread use of these enzymes in various industries requires the discovery of robust enzymes that can operate efficiently at high temperature and pH levels [6,11].

In this study, which was designed to add a new cellulase enzyme to the cellulase enzymes used industrially in various fields, isolation and identification of cellulotic bacteria from garden wastes and partial purification and characterization of cellulase enzyme from *B. pumilus* showing the highest activity were carried out.

## 2. MATERIAL AND METHOD

### 2.1. Bacterial Strains

The garden waste used in the study was collected from Atatürk University campus. Samples were collected with a sterile spatula and collected in a sterile ziplock bag. 0.1 g samples were suspended in physiological saline (9 mL) by vortexing for 2 min. A 10x dilution series was made and 1 mL of each dilution was transferred to Nutrient Agar (NA). Petri dishes were incubated at 28 °C for 72 hours. According to their morphological characteristics (shape, size and color), 60 bacterial colonies were selected and inoculated into NA by drawing method. After incubation at 28 °C for 2 days, they were stored at -80 °C in 50% glycerol stocks.

### 2.2. Molecular Identification by 16S rRNA Gene Sequencing

EurX GeneMATRIX Bacterial & Yeast DNA isolation kit (Poland) was used for DNA isolation of the strains. The 16S rRNA gene was amplified from the genomic DNA of

the strain by polymerase chain reaction (PCR) using universal primers (27F 5' AGAGTTTGATCMTGGCTCAG 3' and 1492R 5' TACGGYTACCTTTGTTACGACTT 3'). Sequence analysis of the strains was outsourced to BM Lab and the strains were identified by comparing the sequence results in the NCBI database.

### 2.3. Assay of Cellulase Activity

Dinitrosalicylic acid (DNS) method was used to determine the cellulase activity of bacterial strains. 0.5 mL of enzyme solution and 0.5 mL of substrate were incubated at 37 °C for 30 minutes. Then 1 mL of DNS solution was added. The experiments were carried out in 3 repetitions and the results are given as the average of the three repetitions. The mixture was boiled for 5 min and after cooling, enzyme activity was determined by measuring at OD540 nm [15].

### 2.4. Purification of Cellulase

Partial purification of cellulase enzyme was carried out according to Dikbaş et al. [16] with minor modifications. *B. pumilus* ND8 strain grown in CMC broth at 35 °C for 2 days was centrifuged (8000 rpm at 4°C for 10 min). Cellulase was partially purified in the range of 0-80% ammonium sulfate. The partially purified enzyme was dissolved in 0.1 M sodium acetate buffer with pH 5.5 and stored at +4 °C.

### 2.5. Protein Determination

Protein concentration was determined using bovine serum albumin as a standard according to Bradford [17] and color change was measured spectrophotometrically at 595 nm.

### 2.6. Effect of pH on The Activity of Purified Cellulase

Substrate solutions were prepared using sodium acetate (pH 2.0-3.0), sodium citrate (pH 4.0-5.0-6.0), Tris-HCl (pH 7.0-8.0-9.0) and sodium carbonate (pH 10.0-11.0) buffers to determine the pH at which cellulase showed optimum activity. The experiments were carried out in 3 repetitions and the results are given as the average of the three repetitions. The pH at which the cellulase enzyme showed the highest activity was determined spectrophotometrically at 540 nm [16].

### 2.7. Effect of Temperature on The Activity of Purified Cellulase

To determine the optimum temperature at which cellulase showed the highest activity, reactions were carried out in the range of 10-90 °C with temperature increments of 10 °C. The experiments were carried out in 3 repetitions and the results are given as the average of the three repetitions. The optimum temperature of the enzyme was determined by measuring activity in a spectrophotometer (540 nm) at each temperature range [16].

## 2.8. Determination of $K_m$ and $V_{max}$ Values

Cellulase activity was measured at different substrate concentrations under optimum conditions and  $K_m$  and  $V_{max}$  values were determined by drawing Lineweaver-Burk graph [18].

## 3. RESULTS

### 3.1. Determination of cellulase activity of strains

Seven strains isolated from garden waste were tested for cellulase activity and strain ND8 showed the highest cellulase activity with a value of 43 U/mL (Figure 1). This strain was identified as *B. pumilus* in NCBI (Accession number: PP940105).

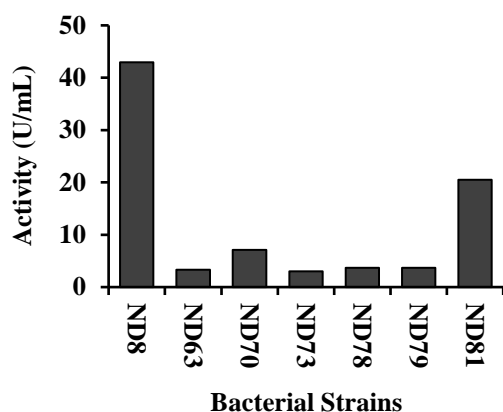


Figure 1. Cellulase activity results of seven different strains

### 3.2. Partial Purification Results of Cellulase

The cellulase enzyme partially purified by ammonium sulfate precipitation from the isolated and identified *B. pumilus* ND8 strain showed the best activity in the purification range 0-20% with an activity of 8.6 U/mL (Figure 2). The protein concentration in the range 0-20% was measured as 6.72 mg/mL.

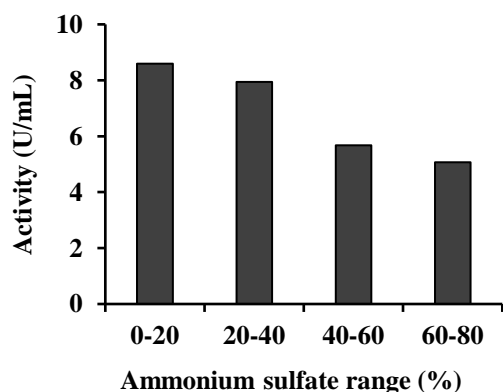


Figure 2. Cellulase activity of ammonium sulfate precipitation intervals

### 3.3. Optimum pH Results of Cellulase Enzyme

The pH value at which the cellulase enzyme partially purified from *B. pumilus* ND8 strain showed optimum

activity was determined as pH 5.5. Cellulase showed an activity of 10.1 U/mL at pH 5.5 (Figure 3).

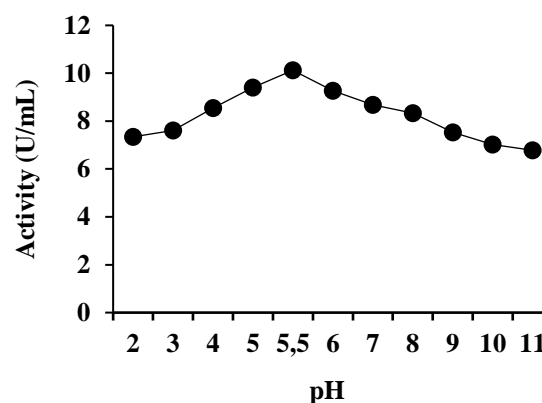


Figure 3. Effect of pH on activity of cellulase enzyme

### 3.4. Optimum Temperature Results of Cellulase Enzyme

The optimum temperature at which the cellulase enzyme partially purified from *B. pumilus* ND8 showed optimum activity was determined to be 60 °C and it showed 14.1 U/mL activity at this temperature (Figure 4).

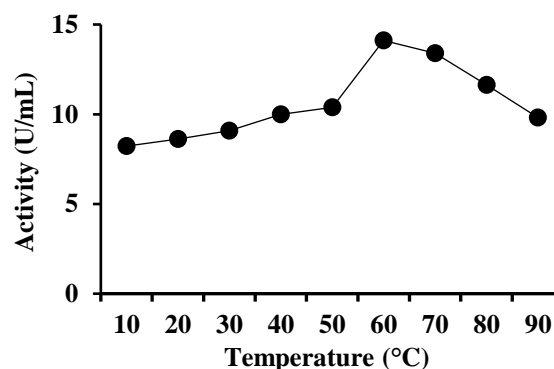


Figure 4. Effect of temperature on activity of cellulase enzyme

### 3.5. $K_m$ and $V_{max}$ Values

When the partially purified cellulase from *B. pumilus* ND8 was tested against carboxymethyl cellulose, the enzyme exhibited a  $K_m$  value of 0.81 mM and a  $V_{max}$  value of 14.2  $\mu\text{mol}/\text{min}$  (Figure 5).

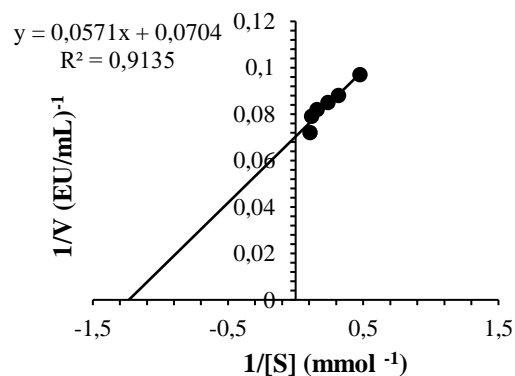


Figure 5. Graph for determining  $K_m$  and  $V_{max}$  values of cellulase enzyme for carboxymethyl cellulose

#### 4. DISCUSSION AND CONCLUSION

Cellulases are evaluated as potential biocatalysts by various industries worldwide due to their capacity to hydrolyze cellulose [19]. Due to their industrial importance, interest in the isolation of new bacterial strains that have higher catalytic activity, produce stable cellulase under variable conditions, and are easy to modify and optimize is increasing day by day [20]. Numerous studies have documented the discovery of bacterial cellulases from different environments (soil, water, etc.) and highlighted their potential for industrial use [21,22,23,24,25]. In this study, 7 bacteria isolated from garden waste were tested for cellulase production, and the strain showing the highest activity was identified as *B. pumilus* ND8. The cellulase enzyme from this strain was partially purified and some of its biochemical properties were determined.

The ammonium sulfate precipitation range in which *B. pumilus* ND8 strain showed the highest cellulase activity was determined as 0-20 and cellulase was purified in this range. The activity of the purified enzyme was determined as 8.6 U/mL. It was observed that *B. pumilus* ND8 strain had a better cellulase activity than other cellulase producing bacteria in the literature (*Aneurinibacillus aneurinilyticus* BKT-9 [21], *Pseudomonas* sp. D1-PT [26], *Bacillus* sp. T2-D2 [26], *Arthrobacter woluwensis* TDS9 [23]).

A wide pH range is required for enzymes to be used in different application areas [27]. In the study, the pH value at which cellulase showed optimum activity was determined as 5.5 and it was observed that it did not completely lose its activity in the pH 2-11 range. These results are in agreement with *B. subtilis* CD001 (pH 5.0), *B. subtilis* subsp. *subtilis* JJBS300 (pH 5.0) and *B. licheniformis* PANG L (pH 5.0) cellulase, which show optimum activity under acidic conditions [28,29,30]. However, there are reports in the literature on the production of alkaline and neutral cellulases by *Bacillus* species [27,31,32,33]. As a result, the optimum pH for cellulase activity is enzyme specific and may vary depending on the type and source of cellulase.

It was determined that partially purified cellulase was thermostable and showed its optimum activity at 60 °C. Results are consistent with *B. subtilis* BC1 (60 °C) and *B. pumilus* EWBCM1 (50 °C) isolated from the gut of *Zeuzera pyrina* and *Eudrilus eugeniae* [31,32]. In addition, *B. subtilis* CD001 isolated from cow manure and *B. subtilis* F3 strain isolated from hot spring water showed optimum cellulase activity at 60 °C and 50 °C, respectively. [29,33]. The thermostability of purified cellulase will give it advantages such as high desirability in various industries, competitiveness, longer enzyme lifetime and versatility in applications.

The kinetic parameters of the purified enzyme were determined as  $K_m$  (0.81 mM) and  $V_{max}$  (14.2  $\mu\text{mol}/\text{min}$ ), respectively. Considering the results, *B. pumilus* ND8 cellulase has a high affinity for its substrate. This suggests that it may be more effective in the hydrolysis of cellulase [9].

In conclusion, *B. pumilus* ND8 isolated from garden waste was able to produce a cellulase with thermostable and acidic properties. Further studies are needed to better characterize the usefulness of this bacterium, which has an important industrial role, and the secondary metabolites it produces in different fields (food, feed, textile, soil improvement, etc.).

#### REFERENCES

- [1] Bhardwaj N, Kumar B, Agrawal K, Verma, P. Current perspective on production and applications of microbial cellulases: a review. *Bioresour Bioprocess.* 2021; 8:1-34.
- [2] Ilić N, Milić M, Beluhan S, Dimitrijević-Branković S. Cellulases: from lignocellulosic biomass to improved production. *Energies.* 2023;16(8):3598.
- [3] Ikegami W, Kamitakahara H, Teramoto Y, Takano T. Synthesis of optically inactive cellulose via cationic ring-opening polymerization. *Cellulose.* 2021;28(10):6125-6132.
- [4] Niranjana K, Ranganathan K, Yapa N. Isolation, characterization and identification of cellulase (Endo- $\beta$ -1, 4-glucanase) producing bacteria from diverse locations. *Vidyodaya Journal of Science.* 2023; 26(01).
- [5] Liu L, Huang WC, Liu Y, Li M. Diversity of cellulolytic microorganisms and microbial cellulases. *Int Biodeterior Biodegrad.* 2021;163:105277.
- [6] Islam F, Roy, N. Screening, purification and characterization of cellulase from cellulase producing bacteria in molasses. *BMC Res Notes.* 2018;11:1-6.
- [7] Kaur P, Taggar MS, Kaur J. Cellulolytic microorganisms: diversity and role in conversion of rice straw to bioethanol. *Cell Chem Technol.* 2020;54:613-34.
- [8] Bhagat SA, Kokitkar SS. Isolation and identification of bacteria with cellulose-degrading potential from soil and optimization of cellulase production. *J App Biol Biotech.* 2021;9(6):154-161.
- [9] Malik WA, Javed S. Enhancement of cellulase production by cellulolytic bacteria SB125 in submerged fermentation medium and biochemical characterization of the enzyme. *Int J Biol Macromol.* 2024;130415.
- [10] Hamdan NT, Jasim HM. Purification and characterization of cellulase enzyme from *Trichoderma longibrachiatum* isolated in Iraqi soil. *IOSR J Biotechnol Biochem (IOSR-JBB).* 2018;4:32-41.
- [11] Megha SV, Maragathavalli S, Brindha S, Karthikeyan V, Annadurai B, Gangwar SK. Isolation and purification of cellulase. *Int J Sci. Nat.* 2019;6(3):474-479.
- [12] Vara S, Karnena MK. Fungal enzymatic degradation of industrial effluents—A review. *Curr Res Environ Appl Mycol.* 2020;10(1):417-442.
- [13] Verma N, Kumar V, Bansal MC. Valorization of waste biomass in fermentative production of cellulases: a review. *Waste Biomass Valor.* 2021;12:613-640.

- [14] Ejaz U, Sohail M, Ghanemi A. Cellulases: from bioactivity to a variety of industrial applications. *Biomimetics*. 2021;6(3):44.
- [15] Biçen HEI. Biochemical characterization of cellulase enzyme by *Bacillus cereus* isolated from cellulotic waste [dissertation]. Turkey: University of Düzce; 2022.
- [16] Dikbaş N, Uçar S, Alım Ş. Purification of phytase enzyme from *Lactobacillus brevis* and biochemical properties. *Biologia*. 2023;78(9):2583-2591.
- [17] Bradford MM. A rapid and sensitive method for the quantitation of microgram quantities of protein utilizing the principle of protein-dye binding. *Anal Biochem*. 1976;72(1-2):248-254.
- [18] Demir Y, Dikbaş N, Beydemir Ş. Purification and biochemical characterization of phytase enzyme from *Lactobacillus coryniformis* (MH121153). *Mol Biotechnol*. 2018; 60:783-790.
- [19] Balla A, Silini A, Cherif-Silini H, Bouket AC, Boudechicha A, Luptakova L, et al. Screening of cellulolytic bacteria from various ecosystems and their cellulases production under multi-stress conditions. *Catalysts*. 2020;12(7):769.
- [20] Inan Bektas K, Nalcaoğlu A, Ceylan E, Colak DN, Caglar P, Agirman S, et al. Isolation and characterization of detergent-compatible amylase-, protease-, lipase-, and cellulase-producing bacteria. *Braz J Microbiol*. 2023;54(2):725-737.
- [21] Ahmad T, Sharma A, Gupta G, Mansoor S, Jan S, Kaur B, et al. Response surface optimization of cellulase production from *Aneurinibacillus aneurinilyticus* BKT-9: An isolate of urban Himalayan freshwater. *Saudi J Biol Sci*. 2020;27(9):2333-2343.
- [22] An X, Zong Z, Zhang Q, Li Z, Zhong M, Long H, et al. Novel thermo-alkali-stable cellulase-producing *Serratia* sp. AXJ-M cooperates with *Arthrobacter* sp. AXJ-M1 to improve degradation of cellulose in papermaking black liquor. *J Hazard Mater*. 2022;421:126811.
- [23] Das T, Ali F, Rahman MS. Cellulase activity of a novel bacterial strain *Arthrobacter woluwensis* TDS9: Its application on bioconversion of paper mill sludge. *J Genet Eng Biotechnol*. 2022;20(1):87.
- [24] Krishnaswamy VG, Sridharan R, Kumar PS, Fathima MJ. Cellulase enzyme catalyst producing bacterial strains from vermicompost and its application in low-density polyethylene degradation. *Chemosphere*. 2022;288:132552.
- [25] Roy D, Gunri SK, Pal KK. Isolation, screening and characterization of efficient cellulose-degrading fungal and bacterial strains and preparation of their consortium under in vitro studies. *3 Biotech*. 2024;14(5):1-15.
- [26] Biswas S, Saber MA, Tripty IA, Karim MA, Islam MA, Hasan MS, et al. Molecular characterization of cellulolytic (endo-and exoglucanase) bacteria from the largest mangrove forest (Sundarbans), Bangladesh. *Ann Microbiol*. 2020;70:1-11.
- [27] Elsabayt ZE, Abdel-Aziz SH, Ibrahim AM, Guirgis AA, Dawwam GE. Purification, biochemical characterization, and molecular cloning of cellulase from *Bacillus licheniformis* strain Z9 isolated from soil. *J Genet Eng Biotechnol*. 2022;20(1):34.
- [28] Anu Kumar S, Kumar A, Kumar V, Singh B. Optimization of cellulase production by *Bacillus subtilis* subsp. *subtilis* JJBS300 and biocatalytic potential in saccharification of alkaline-pretreated rice straw. *Prep Biochem Biotechnol*. 2021;51(7):697-704.
- [29] Malik WA, Javed S. Biochemical characterization of cellulase from *Bacillus subtilis* strain and its effect on digestibility and structural modifications of lignocellulose rich biomass. *Front Bioeng Biotechnol*. 2021;9:800265.
- [30] Shyaula M, Regmi S, Khadka D, Poudel RC, Dhakal A, Koirala D, et al. Characterization of thermostable cellulase from *Bacillus licheniformis* PANG L Isolated from the Himalayan Soil. *Int J Microbiol*. 2023;(1):3615757.
- [31] Dehghanikhah F, Shakarami J, Asoodeh A. Purification and biochemical characterization of alkalophilic cellulase from the symbiotic *Bacillus subtilis* BC1 of the leopard moth, *Zeuzera pyrina* (L.)(Lepidoptera: Cossidae). *Curr Microbiol*. 2020;77:1254-1261.
- [32] Shankar T, Sankaralingam S, Balachandran C, Chinnathambi A, Nasif O, Alharbi SA, et al. Purification and characterization of carboxymethylcellulase from *Bacillus pumilus* EWBCM1 isolated from earthworm gut (*Eudrilus eugeniae*). *J King Saud Univ Sci*. 2021;33(1):101261.
- [33] Fouda A, Alshallash KS, Atta HM, El Gamal MS, Bakry MM, Alawam AS, et al. Synthesis, optimization, and characterization of cellulase enzyme obtained from thermotolerant *Bacillus subtilis* F3: an insight into cotton fabric polishing activity. *J Microbiol Biotechnol*. 2024;34(1):207.

## Modeling of the Linear Equations of Langmuir Isotherm in the Adsorption of Cd (II) Ion with Siirt Kurtalan Koçpınar Clay

Mehmet Can DAL<sup>1\*</sup> 

<sup>1</sup>Dicle University, Institute of Natural and Applied Science, Chemistry Department, Diyarbakır, Türkiye  
Mehmet Can DAL ORCID No: 0000-0001-6474-6053

\*Corresponding author: [mcandal123@dicle.edu.tr](mailto:mcandal123@dicle.edu.tr)

(Received: 17.08.2024, Accepted: 02.08.2024, Online Publication: 26.09.2024)

### Keywords

Cadmium,  
Langmuir,  
Linear  
regression,  
Adsorption  
constants,  
Isotherm,  
Clay

**Abstract:** Langmuir isotherm model has been widely used by researchers in adsorption isotherm studies for more than a century. During the process, 6 linear equations have been derived from the Langmuir model, which is a non-linear model. However, the degree of compatibility of these mathematically derived linear equations with experimental data is different. In addition, the constants obtained from the equations are also different. This study focuses on these 6 equations which are rarely given together. Thus, it was possible to compare the degree of fit of the equations with experimental data.

In this study, the performance of clay mineral in the removal of a heavy metal known for its harmful effect, such as cadmium, from solution was measured. The data obtained as a result of adsorption of cadmium (II) ion with clay from Siirt Koçpınar region at a temperature of 298 K were applied to 6 linear equations derived from Langmuir isotherm model. As a result, it was determined that the degree of suitability of the models for adsorption was type 3 = type 6 < type 1 = type 4 < type 2 = type 5 and the most suitable R<sup>2</sup> values belonged to type 2 and type 5 with values of 0.992. The largest q<sub>m</sub> value was found to belong to type 4 with a value of 86.608 mg g<sup>-1</sup>.

67

## Cd (II) İyonunun Siirt Kurtalan Koçpınar Kili ile Adsorpsiyonunda Langmuir İzotermine Ait Doğrusal Denklemlerinin Modellenmesi

### Anahtar Kelimeler

Kadmiyum,  
Langmuir,  
Doğrusal  
regresyon,  
Adsorpsiyon  
sabitleleri,  
İzoterm,  
Kil

**Öz:** Langmuir izoterm modeli yüzyılı aşkın bir süredir adsorpsiyon izoterm çalışmalarında araştırmacılar tarafından yaygın olarak kullanılmaktadır. Non-lineer bir model olan Langmuir modelinden süreç içerisinde 6 doğrusal denklem türetilmiştir. Ancak matematiksel olarak türetilen bu doğrusal denklemlerin deneysel veriler ile uyum derecesi farklıdır. Ayrıca denklemlerden elde edilen sabitler de farklı olmaktadır. Bu çalışma çok ender olarak beraber verilen bu 6 denkleme odaklanmıştır. Böylelikle denklemlerin deneysel verilerle uyum derecelerinin karşılaştırılması mümkün olmuştur.

Bu çalışmada, ucuz ve etkin oluşu nedeniyle kil mineralinin kadmiyum gibi zararlı etkisi ile bilinen bir ağır metalin çözümlenmiş haliyle giderimindeki performansı ölçülmüştür. Kadmiyum (II) iyonunun Siirt Koçpınar bölgesinden alınmış kil ile 298 K sıcaklığında adsorpsiyonu sonucunda elde edilen veriler, Langmuir izoterm modelinden türetilmiş 6 doğrusal denkleme uygulanmıştır. Regresyon modeli olarak en küçük kareler yöntemi kullanılarak denklemler karşılaştırılmıştır. Sonuç olarak; modellerin adsorpsiyona uygunluk derecelerinin; tip 3 = tip 6 < tip 1 = tip 4 < tip 2 = tip 5 olduğu ve en uygun R<sup>2</sup> değerleri 0,992 değerleri ile tip 2 ve tip 5'e ait olduğu görülmüştür. En büyük q<sub>m</sub> değerinin 86,608 mg g<sup>-1</sup> değeri ile tip 4'e ait olduğu tespit edilmiştir.

## 1. INTRODUCTION

Today, environmental pollution has reached a point that threatens the future of the world. Industrial residues play a major role in this. Heavy metals pollute water and land and cause health problems that may even result in death for living things, especially humans.

Cadmium, one of the most toxic elements, has the symbol Cd, atomic mass of 112.411 and atomic number 48 [1]. It is a non-abundant metallic element. Cadmium is often associated with minerals such as ZnS and other zinc ores. One mineral form, greenockite (CdS), is important, but the usual source of Cd is the oxide in industrial slag associated with the refining of Zn or Pb [2].

Cadmium is mainly used in battery production [3-5], alloys [6-8], solar cells [9-10], as a plastic stabilizer [11-12] and pigment [13-15] in the industry and its wastes pose pollution and risk for the environment [16-18]. Various studies have been done on the removal of cadmium from solutions. The primary ones of these studies are coagulation method [19], ion exchange method [20], lime softening method [21], reverse osmosis method [22]. However, those conducted by adsorption method [23-25] attract the most attention.

Adsorption can be defined as the accumulation of a substance from a liquid or gas on a solid. If adsorption is in equilibrium at constant temperature, there is adsorption isotherm, if not, it can be mentioned as adsorption kinetics. There are many studies [26-48] on adsorption isotherm, adsorption kinetics and thermodynamics of it. Studying the adsorption isotherm gives insight into the nature of adsorption. A typical isotherm is a curve.

Among adsorption isotherms, Langmuir and Freundlich isotherms are prominent. While Freundlich isotherm model is considered suitable for heterogenous surfaces models [49], the Langmuir is associated with homogeneous surfaces [50], and monolayer adsorption [51]. This is largely due to the fact that Freundlich model anticipates multilayer adsorption while Langmuir isotherm anticipates monolayer adsorption.

### 1.1. Langmuir Isotherm Model

Irving Langmuir published a paper in 1916 [52] that laid the foundation for the model that bears his name. Langmuir isotherm model anticipates a monolayer adsorption. Therefore, it is based on a limited adsorption. In chemical adsorption, multilayer adsorption does not occur because the atoms or molecules specifically bind one-to-one with the adsorbent. The Langmuir isotherm equation is essentially a non-linear equation. The equation is expressed as follows:

$$q_e = q_m \frac{K_L C_e}{1 + K_L C_e} \quad (1)$$

Where;

$q_e$ ; Amount adsorbed at equilibrium per gram of adsorbent ( $\text{mgg}^{-1}$ )

$q_m$ ; Maximum amount adsorbed at equilibrium per gram of adsorbent ( $\text{mgg}^{-1}$ )

$C_e$ ; Equilibrium concentration ( $\text{mgL}^{-1}$ )

$K_L$ ; Langmuir constant ( $\text{mgL}^{-1}$ )

Despite the fact that the Langmuir isotherm equation is nonlinear, six linearized equations derived from eq. 1 have gradually replaced it in the literature. However, 6 equations can hardly be found in the same study. But the sequence number of the equations is given randomly in the literature. These equations can be expressed as follows:

$$\text{Type 1} \quad \frac{1}{q_e} = \frac{1}{K_L q_m} \frac{1}{C_e} + \frac{1}{q_m} \quad (2)$$

$$\text{Type 2} \quad \frac{C_e}{q_e} = \frac{1}{q_m} C_e + \frac{1}{K_L q_m} \quad (3)$$

$$\text{Type 3} \quad q_e = -\frac{1}{K_L} \frac{q_e}{C_e} + q_m \quad (4)$$

$$\text{Type 4} \quad \frac{1}{C_e} = K_L q_m \frac{1}{q_e} - K_L \quad (5)$$

$$\text{Type 5} \quad C_e = q_m \frac{C_e}{q_e} - \frac{1}{K_L} \quad (6)$$

$$\text{Type 6} \quad \frac{q_e}{C_e} = -K_L q_e + K_L q_m \quad (7)$$

## 2. MATERIAL AND METHOD

In this study, mixed type clay from Siirt Koçpınar village was used as adsorbent. As adsorbate Sigma-Aldrich brand  $\text{Cd}(\text{NO}_3)_2 \cdot 4\text{H}_2\text{O}$  was used. Adsorption experiment was carried out with Memmert brand WNB 14 model heated shaking water bath at 298 K temperature. Equilibrium concentrations ( $C_e$ ) were determined by Agilent 400 model atomic absorption spectrophotometer (AAS) Calculations were made as follows:

$$q_e = \frac{(C_i - C_e)V}{m1000} \quad (8)$$

Here;

$q_e$ : The amount of substance adsorbed per gram by the adsorbent at equilibrium ( $\text{mgg}^{-1}$ ),

$C_i$ : Initial concentration ( $\text{mgL}^{-1}$ ),

$C_e$ : Concentration at equilibrium ( $\text{mgL}^{-1}$ ),

$V$ : Solution volume (mL) and

$m$ : Mass of adsorbent (g).

The data were applied to the linearized 6 types of Langmuir isotherm model. Plot of type 1 was obtained by plotting  $1/q_e$  versus  $1/C_e$ , plot of type 2 by plotting  $C_e/q_e$  versus  $C_e$ , plot of type 3 by plotting  $q_e$  versus  $q_e/C_e$ , plot of type 4 by plot plotting  $1/C_e$  versus  $1/q_e$ , plot of type 5 by plotting  $C_e$  versus  $C_e/q_e$ , and the plot of type 6 by plotting  $q_e/C_e$  versus  $q_e$ . For each type of plot equations,  $K_L$ ,  $q_m$  ve  $R^2$  constants were obtained, and these plots were comparized and tabulated. Microsoft Excel 2010 program was used for the operations and the

least squares method was adopted for regression analysis.

### 3. RESULTS

The isotherm plot giving the relationship between the independent variable  $C_e$  and the dependent variable  $q_e$  obtained as a result of the experiment and the calculations made afterwards is given in Figure 1:

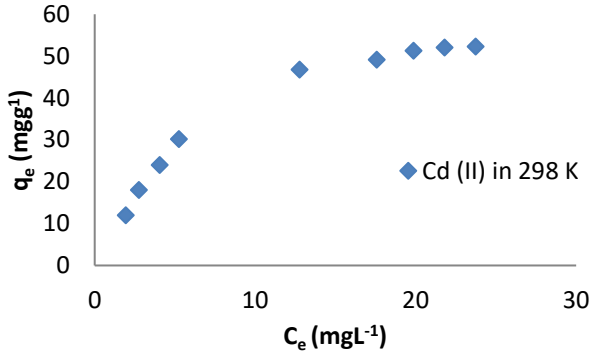


**Figure.1.** Isotherm curve of Cd (II) ion adsorption with Siirt Koçpınar clay at 298 K temperature

The plots generated by fitting the experimental data to the linear equations of the Langmuir model are given in Figures 2-7:

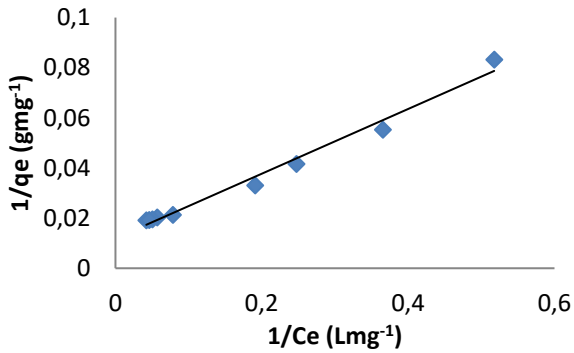


**Figure.2.** Linear plot of Langmuir type 1 linear equation for the adsorption of Cd (II) ion with Siirt Koçpınar clay at 298 K

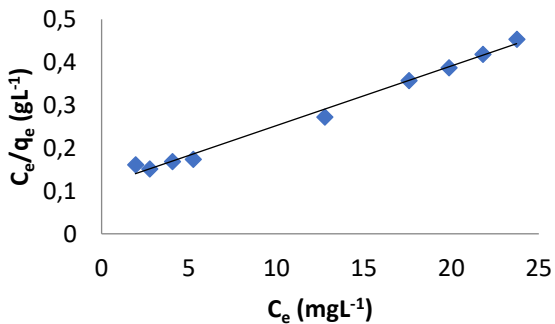


**Figure.3.** Linear plot of Langmuir type 2 linear equation for the adsorption of Cd (II) ion with Siirt Koçpınar clay at 298 K temperature

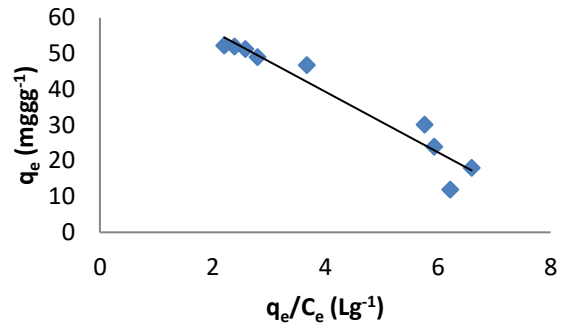


**Figure.4.** Linear plot of Langmuir type 3 linear equation for the adsorption of Cd (II) ion with Siirt Koçpınar clay at 298 K temperature

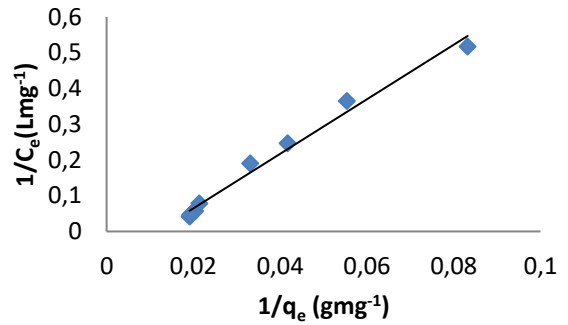


**Figure.5.** Linear plot of Langmuir type 4 linear equation for the adsorption of Cd (II) ion with Siirt Koçpınar clay at 298 K temperature

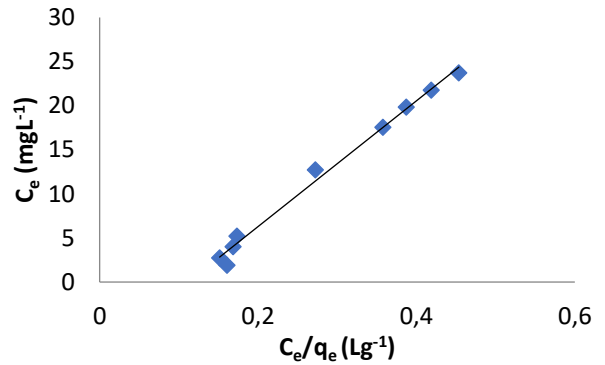


**Figure.6.** Linear plot of Langmuir type 5 linear equation for the adsorption of Cd (II) ion with Siirt Koçpınar clay at 298 K temperature

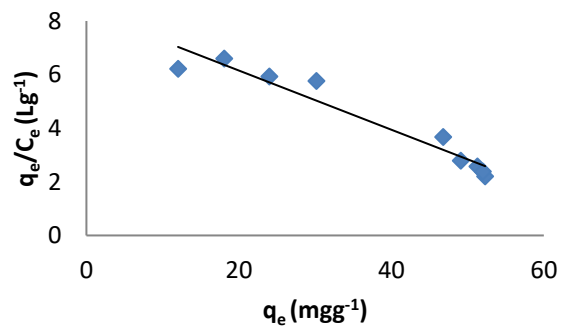


**Figure.7.** Linear plot of Langmuir type 6 linear equation for the adsorption of Cd (II) ion with Siirt Koçpınar clay at 298 K temperature

The constants obtained from the above 6 plots are given in table 1:

**Table.1.** Constants of the linear type equations of the Langmuir isotherm model

Linear Types	$K_L$ (Lmg <sup>-1</sup> )	$q_m$ (mgg <sup>-1</sup> )	$R^2$
Type 1	0.092	84.034	0.985
Type 2	0.123	71.942	0.992
Type 3	0.118	73.246	0.936
Type 4	0.088	86.608	0.985
Type 5	0.125	71.303	0.992
Type 6	0.110	75.715	0.936

Results that given table. 1 were showed that the degree of suitability of the models for adsorption; type 3 = type 6 < type 1 = type 4 < type 2 = type 5. The most suitable  $R^2$  values belong to type 2 and type 5 with values of 0.992.  $q_m$  values; type 5 < type 2 < type 3 < type 6 < type 1 < type 4 and  $K_L$  values were found to be type 4 < type 1 < type 6 < type 3 < type 2 < type 5. It was determined that the largest  $q_m$  value was belong to type 4 with a value of 86.608 mgg<sup>-1</sup>. It is no coincidence that the smallest  $K_L$  value which is 0.088 Lmg<sup>-1</sup> belongs to the same linear type. Low  $K_L$  values indicate high affinity, high  $q_m$  values indicate high adsorption capacity in accordance with affinity, and high  $R^2$  values indicate a measure of the fit of the experimental data to the linear equation. As a result, the experimental data were found to be in high agreement with the theory.

#### 4. DISCUSSION AND CONCLUSION

Recently, environmental pollution has become a global issue and has received much attention. One of the main causes of environmental pollution is heavy metal pollution. Due to the harm and widespread use of cadmium, a separate parenthesis can be opened here.

In this adsorption study carried out to remove cadmium pollution, 6 linearized equations of the Langmuir isotherm equation, which are rarely given together in the literature, constituted the main core of the study. Each of these 6 equations, which are almost never encountered in thesis studies and scientific articles in our country, means a new possibility for the Langmuir model. Because each equation will give different  $K_L$  and  $q_m$  values. Also, the degree of linearity of each equation will be different. As the adsorbent, adsorbed and other conditions affecting adsorption vary, the degree and sequence of concordance of each equation with the experimental data changes.

In this study, mixed type clay taken from Koçpınar region of Siirt Kurtalan district was used as adsorbent. As for adsorbed material, Cd (II) ion was used. The raw data obtained in the experiment carried out in a water bath with shaker at 298 K temperature were processed and applied to 6 linear equations of the Langmuir isotherm model. Least squares method was used as regression model for the comparison of the equations. As a result of the regression analysis, it was determined that the degree of suitability of the models for adsorption; type 3 = type 6 < type 1 = type 4 < type 2 = type 5. The most suitable  $R^2$  values belong to type 2 and type 5 with

values of 0.992.  $K_L$  values, a measure of affinity, were found to be type 4 < type 1 < type 6 < type 3 < type 2 < type 5 and  $q_m$  values were found to be type 5 < type 2 < type 3 < type 6 < type 1 < type 4. It was determined that the largest  $q_m$  value was belong to type 4 with a value of 86.608. It is no coincidence that the smallest  $K_L$  value which is 0.088 belongs to the same linear type. Because low  $K_L$  value indicates high affinity, in this context, maximum adsorption is inevitable. The same is true for the vice versa. Namely,  $K_L$  value of type 5 was found to be the highest and  $q_m$  value was found to be the lowest. As a result, the experimental data were found to be in high agreement with the theory.

#### REFERENCES

- [1] Smith, K.S. (1998). Cadmium. In: Geochemistry. Encyclopedia of Earth Science. Springer, Dordrecht, 50-51. [https://doi.org/10.1007/1-4020-4496-8\\_37](https://doi.org/10.1007/1-4020-4496-8_37)
- [2] Van Horn JD. Cadmium, Physical and Chemical Properties. In: Kretsinger, R.H., Uversky, V.N., Permyakov, E.A. (eds) Encyclopedia of Metalloproteins. Springer, New York, NY. 2013. p 383–384. [https://doi.org/10.1007/978-1-4614-1533-6\\_32](https://doi.org/10.1007/978-1-4614-1533-6_32)
- [3] Blumbergs E, Serga V, Platacis E, Maiorov M, Shishkin A. Cadmium Recovery from Spent Ni-Cd Batteries: A Brief Review. Metals 2021;11(11):1714. <https://doi.org/10.3390/met11111714>.
- [4] Assefi M, Maroufi S, Yamauchi Y, Sahajwalla V. Pyrometallurgical recycling of Li-ion, Ni–Cd and Ni–MH batteries: A minireview. Curr. Opin. Green Sustain. Chem. 2020;24:26–31.
- [5] Fernandes A, Afonso, JC, Bourdot D, Junqueira A. Hydrometallurgical route to recover nickel, cobalt and cadmium from spent Ni–Cd batteries. J. Power Sources. 2012;220:286–291.
- [6] Sarholt L, Jensen ASB, Touboltsev VS, Johansen A, Johnson E. Nanoscale Lead-Cadmium Alloy Inclusions in Silicon. In Journal of Metastable and Nanocrystalline Materials.2001;10:283-288. <https://doi.org/10.4028/www.scientific.net/jmmm.10.283>
- [7] Mason HJ, Davison AG, Wright AL, Guthrie CJ, Fayers PM, Venables KM, et al. Relations between liver cadmium, cumulative exposure, and renal function in cadmium alloy workers. Br. J. Ind. Med. 1988;45:793–802.
- [8] Lombaert N, Gilles M, Verougstraete V. Cadmium Monitoring at the Workplace: Effectiveness of a Combination of Air and Biomonitoring. Toxics. 2023;11:354. <https://doi.org/10.3390/toxics11040354>.
- [9] Kartopu G, Oklobia O, Turkay D, Diercks DR, Gorman BP, Barrioz V, et al. Study of thin film poly-crystalline CdTe solar cells presenting high acceptor concentrations achieved by in-situ arsenic doping. Sol. Energy Mater. Sol. Cells. 2019;194:259–267.
- [10] Oklobia O, Kartopu G, JC Irvine S. Properties of Arsenic-Doped ZnTe Thin Films as a Back Contact for CdTe Solar Cells. Materials.2019;12:3706. <https://doi.org/10.3390/ma12223706>.
- [11] Frye AH, Horst RW. The mechanism of poly(vinyl chloride) stabilization by barium, cadmium, and zinc carboxylates . I. Infrared Studies, J. Polym. Sci. 1959;40:419–431 .
- [12] Batzer H.(1983). Use and possibilities for substitution of cadmium stabilizers. Ecotoxicology and Environmental Safety. 1983;7(1):117-121.



- [13] Pisu FA, Ricci PC, Porcu S, Carbonaro CM, Chiriu D. Degradation of CdS Yellow and Orange Pigments: A Preventive Characterization of the Process through Pump-Probe, Reflectance, X-ray Diffraction, and Raman Spectroscopy. *Materials*. 2022;15:5533. <https://doi.org/10.3390/ma15165533>.
- [14] Rosi F, Grazia C, Gabrieli F, Romani A, Paolantoni M, Vivani R. UV-Vis-NIR and micro Raman spectroscopies for the non destructive identification of Cd<sub>1-x</sub>Zn<sub>x</sub>S solid solutions in cadmium yellow pigments. *Microchem. J*. 2016;124:856–867.
- [15] Traill RJ, Boyle RW. Hawelite, Isometric Cadmium Sulphide, A New Mineral. *Am. Mineral. J. Earth Planet. Mater.* 1955;40:555–559.
- [16] Genchi G, Sinicropi MS, Lauria G, Carocci A, Catalano A. The Effects of Cadmium Toxicity. *Int J Environ Res Public Health*. 2020;17(11):3782. doi: 10.3390/ijerph17113782.
- [17] Hogervost J, Plusquin M, Vangronsveld J, Nawrot T, Cuypers A, Van Hecke E, et al. House dust as possible route of environmental exposure to cadmium and lead in the adult general population. *Environ. Res.* 2007;103:30–37. doi:10.1016/j.envres.2006.05.009.
- [18] Satarug S, Vesey DA, Gobe GC. Mitigation of Cadmium Toxicity through Modulation of the Frontline Cellular Stress Response. *Stresses*. 2022;2(3):355-372. <https://doi.org/10.3390/stresses2030025>.
- [19] Zhou J, Liu Y, Li B, Huashou Li, Guikui C, Rongliang Q. Coagulation of trace arsenic and cadmium from drinking water using titanium potassium oxalate. *npj CleanWater*.2023;6(9). <https://doi.org/10.1038/s41545-023-00227-z>.
- [20] Bai Y, Bartkiewicz B. Removal of cadmium from wastewater using ion exchange resin Amberjet 1200H columns. *Pol J Environ Studies*. 2009;18(6):1191–1195.
- [21] Holmes RR., Hart ML, Kevern JT. Reuse of Drinking Water Treatment Waste for Remediation of Heavy Metal Contaminated Groundwater. *Groundw. Monit. Remediat*. 2019; 39:69–79.
- [22] Kheriji J, Tabassi D, Hamrouni B. Removal of Cd(II) ions from aqueous solution and industrial effluent using reverse osmosis and nanofiltration membranes. *Water Sci Technol*. 2015;72(7):1206-16. doi: 10.2166/wst.2015.326.
- [23] Liu W, Zhao C, Wang S, Niu L, Wang L, Liang S, et al. (2018). Adsorption of cadmium ions from aqueous solutions using nano-montmorillonite: kinetics, isotherm and mechanism evaluations. *Res Chem Intermed*. 2018;44:1441–1458. <https://doi.org/10.1007/s11164-017-3178-y>.
- [24] Montazer-Rahmati MM, Rabbani P, Abdolali A, Keshtkar AR. Kinetics and equilibrium studies on biosorption of cadmium, lead, and nickel ions from aqueous solutions by intact and chemically modified brown algae. *J Hazard Mater*. 2011;185(1):401-7. doi:10.1016/j.jhazmat.2010.09.047.
- [25] Pawar RR, Lalmhunsiam, Munui K, Jae-Gyu K, Hong SM, Sawant SY. Efficient removal of hazardous lead, cadmium, and arsenic from aqueous environment by iron oxide modified clay-activated carbon composite beads. *Applied Clay Science*. 2018;162:339-350.
- [26] Onursal N. Adsorpsiyon Kinetiğine Ve Modellerine Genel Bir Bakış. *Fen Bilimleri ve Matematik Alanında Yeni Trendler*. Platanus yayınları. 2022; p. 255-272.
- [27] Onursal N. Adsorpsiyon izotermi ve termodinamiğinin deneysel verilere dayanarak incelenmesi. *Serüven yayınları. Fen bilimleri ve matematikte uluslararası araştırmalar*. 2022; p. 145-158.
- [28] Onursal N. Malahit yeşilinin sulu çözeltilerden karışık tip kil ile sulu çözeltilerden uzaklaştırılması. 3. Anadolu Uluslararası Uygulamalı Bilimler Kongresi. Diyarbakır: UBAK Yayınları; 2019. s. 644-657.
- [29] Onursal N, Kul A, Baran M. Cu (II) iyonlarının aktive edilmiş karışık tipteki kil ile sudan uzaklaştırılması, izoterm, kinetik ve termodinamik parametrelerin incelenmesi, *Eurasia Journal Of Mathematics, Engineering, Natural & Medical Sciences*. 2019;7:63-85.
- [30] Onursal, N, Kul, R, Yavuz, Ö. Pb (II) İyonlarının Aktive Edilmiş Karışık Tipteki Kil İle Sudan Uzaklaştırılması İzoterm Kinetik ve Termodinamik Parametrelerin İncelenmesi. *Euroasia of Mathematics Engineering Natural & Medical Sciences*. . 2019; 6 (7); s. 9-22.
- [31] Onursal N, Dal MC. Altı Tip Yalancı-İkinci Dereceli Kinetik Denkleminin Malahit Yeşilinin Siirt Kili ile Adsorpsiyonunda Karşılaştırmalı Doğrusal Yöntemler. *International Siirt Scientific Research Congress*. Siirt: 2001. p. 399-409.
- [32] Onursal N. Removal of Ni(II) Ions from aqueous solutions with Siirt Koçpınar mixed type clay investigation of isotherm, thermodynamic and kinetic parameters. *Desalination and Water Treatment*. 2022;276:150-159.
- [33] Dal MC, Onursal N, Arıca E, Yavuz Ö. Diyarbakır Karacadağ Kırmızı Tepe skoryası ile Cu (II) adsorpsiyon kinetiğinin incelenmesi. *Dicle Üniversitesi Mühendislik Fakültesi Mühendislik Dergisi*. 2021;12(2):337-346. doi:10.24012/dumf.881650.
- [34] Onursal N, Dal MC. Altı tip yalancı- ikinci dereceli kinetik denkleminin malahit yeşilinin Siirt kili ile adsorpsiyonunda karşılaştırılmalı doğrusal yöntemler. *International Siirt Conference on Scientific Research Conference Proceedings Book*. Siirt. 2021. p. 398-409.
- [35] Kul A R , Benek V, Selçuk A, Onursal N. Using Natural Stone Pumice in Van Region on Adsorption of Some Textile Dyes. *Journal of the Turkish Chemical Society Section A: Chemistry*. 2017;4(2):525-536.
- [36] Kul AR, Benek V, Alacabey İ, Onursal N. Kinetics Studies of Zinc Adsorption on Van Pumice. *International Congress of Healty and Environment*. Adana:2017. p.406.
- [37] Onursal N, Altunkaynak Y, Baran A, Dal MC. Adsorption of nickel(II) ions from aqueous solutions using Malatya clay: Equilibrium, kinetic, and thermodynamic studies. *Environ Prog Sustainable Energy*. 2023;e14150. doi:10.1002/ep.1415.
- [38] Altunkaynak, Yalçın. "Using Chemically Unprocessed Orange Peel to Effectively Remove Hg(II) Ions From Aqueous Solutions: Equivalent, Thermodynamic, And Kinetic Investigations". *Sakarya University Journal of Science* 27/1 (Şubat 2023), 189-203. <https://doi.org/10.16984/saufenbilder.1081514>.
- [39] Canpolat, M., Altunkaynak, Y., & Yavuz, Ö. (2022). Kimyasal olarak işlenmemiş Midyat taşı kullanılarak sulu çözeltilerden Pb(II) iyonlarının etkin bir şekilde uzaklaştırılması: İzoterm, kinetik ve termodinamik çalışmalar. *Niğde Ömer Halisdemir Üniversitesi Mühendislik Bilimleri Dergisi*, 11(4), 1085-1096. <https://doi.org/10.28948/ngumuh.1089310>.
- [40] Canpolat, M., Altunkaynak, Y., & Yavuz, Ö. (2022). Bakır(II) İyonlarının Sulu Çözeltilerden Atık Portakal Kabuğu İle Uzaklaştırılması: Denge, Kinetik Ve Termodinamik Çalışmalar. *Afyon Kocatepe Üniversitesi Fen Ve Mühendislik Bilimleri Dergisi*, 22(3), 498-507. <https://doi.org/10.35414/akufemubid.1101318>.
- [41] Onursal, N., Dal, M.C. (2024). Investigation of isotherm and thermodynamic parameters of adsorption of copper (II) ions in aqueous solution with natural mixed type Siirt clay (NMTSC-2) and new (second) linear equation

- derived from Harkins–Jura isotherm. Chem. Pap. 78, 749–760. <https://doi.org/10.1007/s11696-023-03116-4>.
- [42] Altunkaynak, Y., Canpolat, M., & Yavuz, Ö. (2023). Sulu Çözeltilerden Pb<sup>2+</sup> İyonlarının Uzaklaştırılmasında Atık Portakal Kabuklarının Kullanılması: Kinetik ve Termodinamik Çalışmalar. Düzce Üniversitesi Bilim Ve Teknoloji Dergisi, 11(2), 1105-1120. <https://doi.org/10.29130/dubited.1089013>.
- [43] Canpolat, M., Altunkaynak, Y., & Yavuz, Ö. (2022). Bakır(II) İyonlarının Sulu Çözeltilerden Atık Portakal Kabuğu İle Uzaklaştırılması: Denge, Kinetik Ve Termodinamik Çalışmalar. Afyon Kocatepe Üniversitesi Fen Ve Mühendislik Bilimleri Dergisi, 22(3), 498-507. <https://doi.org/10.35414/akufemubid.1101318>.
- [44] Uçar, S., Evcin, A., Uçar, M., Alibeyli, R., et al. (2015). Removal of Phenol and Chlorophenols from Aquatic System Using Activated Clinoptilolite. Hacettepe Journal of Biology and Chemistry, 43(3), 235-249.
- [45] Altunkaynak, Y., Canpolat, M., & Yavuz, Ö. (2023). Sulu Çözeltilerden Pb<sup>2+</sup> İyonlarının Uzaklaştırılmasında Atık Portakal Kabuklarının Kullanılması: Kinetik ve Termodinamik Çalışmalar. Düzce Üniversitesi Bilim Ve Teknoloji Dergisi, 11(2), 1105-1120. <https://doi.org/10.29130/dubited.1089013>.
- [46] Altunkaynak, Y., & Canpolat, M. (2022). Sulu Çözeltilerden Nikel(II) İyonlarının Uzaklaştırılmasında Portakal Kabuğu Atığının Kullanılması: Denge, Kinetik Ve Termodinamik Çalışmalar. Journal of Advanced Research in Natural and Applied Sciences, 8(2), 322-339. <https://doi.org/10.28979/jarnas.1000133>.
- [47] Uçar, M. (2019). Adsorption of chlorophenolic compounds on activated clinoptilolite. Adsorption Science & Technology. 37(7–8) 664–679.
- [48] Altunkaynak, Y., & Canpolat, M., Yavuz, O. (2024). Adsorption of mercury (II) ions on kaolinite from aqueous solutions: Isothermal, kinetic, and thermodynamic studies. Environmental Progress & Sustainable Energy, 43(2), e14295, <https://doi.org/10.1002/ep.14295>.
- [49] Ayawei N, Ebelegi AN, Wankasi D. Modelling and Interpretation of adsorption isotherms. Hindawi Journal of Chemistry. 2017; 11 pages. <https://doi.org/10.1155/2017/3039817>.
- [50] Khayyun TS, Mseer AH. Comparison of the experimental results with the Langmuir and Freundlich models for copper removal on limestone adsorbent. Applied Water Science. 2019;9:170. <https://doi.org/10.1007/s13201-019-1061-2>.
- [51] Alnaief M, Sandouqa A, Altarawneh I, Al-Shannag M, Alkasrawi M, Al-hamamre Z. Adsorption Characteristics and Potential of Olive Cake Alkali Residues for Biodiesel Purification. Energies. 2021;14(1):16. <https://doi.org/10.3390/en14010016>.
- [52] Langmuir I. The constitution and fundamental properties of solids and liquids. Journal of the American Chemical Society. 1916;38 (11):2221-2295.

## Testing the Reliability of Numerical Model Studies for a Broad-Crested Weir

Mahmut AYDOĞDU<sup>1\*</sup> 

<sup>1</sup> Malatya Turgut Özal University, Engineering and Natural Sciences Faculty, Civil Engineering Department, Malatya, Türkiye

Mahmut AYDOĞDU ORCID No: 0000-0002-7339-2442

\*Corresponding author: mahmut.aydogdu@ozal.edu.tr

(Received: 21.05.2024, Accepted: 19.08.2024, Online Publication: 26.09.2024)

### Keywords

Weir,  
Flow rate,  
Broad-crested  
weir,  
Ansys-fluent,  
Free water  
surface profile

**Abstract:** The increase in population causes the need for water to increase day by day. The fact that water resources are limited further emphasizes the effective use of water. For this purpose, level-flow control of water transmitted through open channels is very important. Broad-crested weir types are widely used in these controls carried out through weirs. This study used a newly designed broad-crested weir type that had not been used before. The model created in the laboratory environment was tested for  $Q=7.84$  l/s and  $Q=14.86$  l/s flow rates. The experiments measured water surface profile, flow depths, and velocity values. The same model was tested in the numerical environment under similar flow conditions. For this purpose, three-dimensional solutions were performed with Ansys-Fluent software. The Realizable k- $\epsilon$  turbulence model, which has been tested for reliability in previous studies and is suitable for this type of broad-crested weir flows, was preferred. In the numerical solution, the VOF method was used for the water-air interface. Thus, the data belonging to the numerical model was verified using experimental data. In general, it was observed that there was an agreement between the experimental and numerical data in terms of water surface profile, flow depths and velocities. As a result of this study, it can be said that it allows different broad-crested weir designs to be tested with less cost before moving on to field applications.

## Geniş Başlıklı Bir Savak İçin Sayısal Model Çalışmaların Güvenilirliğinin Test Edilmesi

### Anahtar Kelimeler

Savak,  
Debi,  
Geniş-başlıklı  
savak,  
Ansys-fluent,  
Serbest su  
yüzü profili

**Öz:** Nüfusun artması suya olan ihtiyacın da her geçen gün artmasına neden olmaktadır. Su kaynaklarının kısıtlı olması ise, suyun etkin kullanımını daha da ön plana çıkarmaktadır. Bu amaçla açık kanallar vasıtasıyla iletilen suların seviye-debi kontrolü çok önemlidir. Savaklar aracılığıyla yapılan bu kontrollerde geniş başlıklı savak tipleri yaygın olarak kullanılmaktadır. Bu çalışma kapsamında daha önce kullanılmamış yeni tasarlanmış geniş başlıklı bir savak tipi kullanılmıştır. Laboratuvar ortamında oluşturulan model,  $Q=7.84$  l/s ve  $Q=14.86$  l/s debi değerleri için test edildi. Yapılan deneylerde su yüzü profili, akım derinlikleri ve hız değerleri ölçüldü. Aynı model benzer akım koşullarında sayısal ortamda da teste tabi tutuldu. Bu amaçla Ansys-Fluent yazılımı ile üç boyutlu çözümler gerçekleştirildi. Daha önce yapılmış çalışmalarda güvenilirliği test edilmiş ve bu tip geniş başlıklı savak akımlarına uygun olan Realizable k- $\epsilon$  türbülans modeli tercih edilmiştir. Sayısal çözümde su-hava arakesiti için VOF metodu kullanılmıştır. Böylece sayısal modele ait veriler, deneysel veriler kullanılarak doğrulandı. Genel olarak deneysel ve sayısal veriler arasında; su yüzü profili, akım derinlikleri ve hızları bakımından uyum olduğu görülmüştür. Bu çalışma neticesinde saha uygulamalarına geçmeden önce, yapılacak farklı geniş başlıklı savak tasarımlarının daha az maliyetle test edilmesine imkân sağladığı söylenebilir.

### 1. INTRODUCTION

For the effective and sustainable use of limited water resources, it is necessary to determine the distribution of

water over time and space in terms of properties and volume. In Türkiye, water consumption is mostly used for agricultural purposes and is transmitted through open channels. In this type of transmission, the amount of

water in the channel must be measured regularly and reliable records must be kept. Because this is essential to protect existing water and increase usage efficiency. In general, flow measurements are made with a method that is costly and requires intense effort, such as velocity-area measurements [1]. However, low-cost, reliable, and practical methods are needed for flow measurement in open-channel flows. One of these methods is measurement weirs. Weirs are widely used in irrigation channels and environmental projects. Built-in streams and open channels increase the irrigation capacity by raising the water level upstream, storing water, or directing the flow by weirs [2]. Weirs are constructed in various geometric types (labyrinth, ogee, broad-crested, and sharp-edged) depending on the need. The broad-crested weir type is widely used in field practices [3]. Compared to other types, broad-crested weirs have many advantages, such as structural stability, low cost, and extremely low sensitivity to tailwater submergence [4]. In literature, the hydraulic properties of broad-crested weirs with different geometries and designs were examined and many experiments were conducted for this purpose [4]–[7]. These studies focused on determining the flow coefficient and revealing the effect of geometries on the flow pattern.

Many studies have been carried out previously on the broad-crested weir structure. Clemmens et al. [8] examined the flow change and energy loss in upstream and downstream conditions using a rectangular broad-crested weir. They reported that upstream face slopes of 3:1 and 2:1 were acceptable to accurately predict flow. They stated that the water surface profile decreased continuously from the front face slope to the end of the narrowing part of the weir, and did not affect the flow estimation of the downstream water level. Flow over a trapezoidal broad-crested weir at different upstream and downstream slopes was investigated by Sargison, J. E., & Percy, A. [9]. In general, pressure and water surface profiles were similar for all test cases. Vertically increasing the upstream slope reduced the height of the water surface profile and the static pressure affected the weir. They also stated that it also reduced the flow coefficient. Azimi et al. [10] examined the flows passing over the broad-crested weir sloped upstream and downstream directions. They also collected experimental results available in the literature and suggested useful correlations for the flow coefficient. Madadi et al. [11] investigated the effect of the upstream front slope of rectangular broad-crested weirs on wavy weir flow. The results obtained showed that when the weir upstream slope decreased from the standard angle, that was, from 90° to 40°, the relative wave height decreased by up to 78% and the relative wavelength increased by up to 55%.

However, in some cases, experimental studies cause an economic burden and serious time loss. The solution is to use today's technology effectively and efficiently. Nowadays, physical modeling can be done quickly and practically in a digital environment with advanced computer and software technologies. In particular, computational fluid dynamics (CFD) simulations are

advantageous over physical modeling by easily solving many different parameters and flow situations [12]. In addition, numerical model results are verified with physical models, providing the opportunity to analyze different flow environments and water structures. There are recent studies in the literature for this purpose. Sarker and Rhodes [13] investigated the open channel flow over a rectangular broad-crested weir experimentally and theoretically. The basic equations governing the flow were solved numerically using the CFD-based Fluent program. The findings obtained from the studies were compared and found to be consistent with each other. Bal [14] measured the velocity field of the flow passing over a broad-crested weir under two different flow conditions using one-dimensional Laser Doppler Anemometer. He used the Ansys-Fluent package program based on the finite volume method for numerical solutions. As a result of the comparison of numerical and experimental data, it was stated that the RNG  $k-\epsilon$  turbulence model gave more successful results. Felder et al. [15] carried out an experimental study to determine the water surface profile, velocity, and pressure distributions on a broad-crested weir flow. They analyzed the flow characteristics on the crest by considering non-uniform velocity distributions and non-hydrostatic pressure distributions. They stated that the data differed from the smooth turbulent boundary layer theory but were consistent with previous studies on this subject. Soydan et al. [16] tested and compared the trapezoidal cross-section broad-crested weir structure with experimental data with the help of an Ansys-Fluent numerical solver. In the numerical solution, Standard  $k-\epsilon$ , Renormalization group  $k-\epsilon$ , and Realizable  $k-\epsilon$  turbulence models were used. Water surface profiles were determined with VOF. The flow profiles were compared with numerical and experimental data and it was stated that the turbulence models used were quite successful in predicting the flow profiles.

İlkentapar & Öner [17] examined the water surface profiles and velocity distributions upstream and downstream of the rectangular broad-crested weir by using three different flow rate values. Again, they created numerical models under the same flow conditions as the experiments and realized solutions with the FLOW-3D package program. Using different mesh structures and Standard  $k-\epsilon$  turbulence models, water surface profiles were determined by the volume of fluid method. The water surface profiles and velocity distributions obtained from the solution were compared with experimental data. Yıldız & Yazar [18] experimentally examined the effects of broad-crested weir models with different slope angles on the flow. 41 different flow rates were tested for three different broad-crested weir models. They also performed numerical solutions under the same flow conditions with Ansys-Fluent, a CFD software. It has been concluded that the experimental and numerical model results are compatible.

This study used a newly designed broad-crested weir type that had not been used before. Such a design aims with different surface slopes weir, to experimentally

measure the water flow movement in the channel and investigate its numerical reliability. For this purpose, the upstream surface of the broad-crested weir was designed as trapezoidal and the downstream surface as circular in the model created in the laboratory environment. The experiments were carried out for  $Q=7.84$  l/s and  $Q=14.86$  l/s flow rates. In the experiments, the water surface profile, flow depths, and velocity values were measured. Then, the same model was tested in the numerical environment under similar flow conditions. In the numerical study, three-dimensional numerical simulations were carried out with the Ansys-Fluent software, which provides solutions with the finite volume method. The reliability of the previous studies was tested and the Realizable  $k-\epsilon$  turbulence model, which is suitable for this type of broad-crested weir flows, was preferred. The water surface profile was calculated with the Volume Of Fluid (VOF) method and the solutions were carried out in three dimensions. The water surface profiles, flow depth, and velocity values of the numerical solution were compared with the experimental measurement results.

**2. MATERIAL AND METHOD**

The flow over a broad-crested weir under commonly used free-flow conditions is shown in Figure 1 below [19].

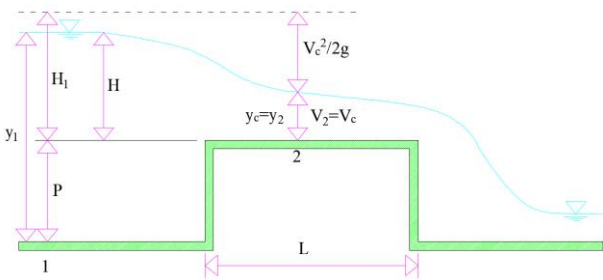


**Figure 1.** Flow conditions over a broad-crested weir

In Figure 1,  $H$  is the water height above the weir surface at the upstream,  $H_1$  is the total energy height at the upstream,  $y_1$  is the water depth at the upstream,  $y_c$  is the critical depth,  $V_c$  is the critical velocity and  $P$  is the weir height. The total energy height  $H_1$  at the upstream is calculated as in Equation 1.

$$H_1 = y_c + \frac{V_c^2}{2g} = \left(\frac{3}{2}\right) y_c \tag{1}$$

The critical velocity is calculated as in Equation 2.

$$V_c = \sqrt{gy_c} \tag{2}$$

In literature, broad-crested weirs are classified according to  $H/L$  value. Accordingly, if  $0.1 \leq H/L \leq 0.35$ , the critical flow control is upstream of the weir, and the flow coefficient changes slowly in this range and is called a broad-crested weir [19].

In this study, experimental measurements were carried out by taking two different flow rates into account to

determine the flow velocity and water surface profiles passing over the broad-crested weir with different upstream and downstream surfaces. The experiments were carried out with the help of a rectangular cross-section open channel model in the Civil Engineering Hydraulics Laboratory of İnönü University (Figure 2).



**Figure 2.** Open channel model used in the experimental

The bearing elements of the experimental setup were made of steel. The channel side walls were made of transparent plexiglass material for easy observation of the flow. There are two reservoirs at the beginning and end of the channel, which circulated the water in the channel. This open channel model had a length of 12.8 m, a width of 0.40 m, and a height of 0.5 m. A digital limnimeter with a sensitivity of 0.1 mm in the depth of the flow was used, and a pump with a capacity of 0-360  $m^3$ /hour with an inlet and outlet diameter of 8 inches was used to circulate the water in the channel arrangement. To measure the flow rate, a TMF2011-C model electromagnetic flowmeter with  $\pm 0.5\%$  accuracy was used between the pump and the inlet valve. In addition, the flow control was monitored precisely and instantly using the Programmable Logic Controller (PLC) control method, which works with a remote sensing system. PLC software can be controlled via smartphone and second-by-second flow rate readings can be easily viewed. Figure 3 showed the PLC control system working mechanism.

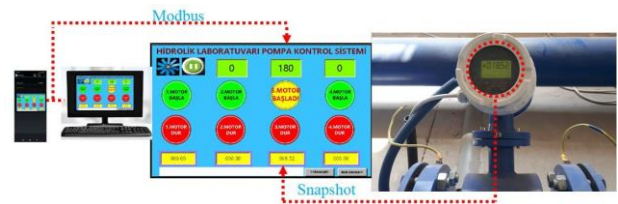


**Figure 3.** PLC control system working mechanism

The broad-crested weir was placed 6.5 m downstream from the point where the water inlet the channel. Since this 6.5 m point was the starting point of the weir, it was taken into account as the 0 (zero) point in the measurements. The total weir length was 1 m, and flow depth measurements were taken at 0.1 m intervals towards the downstream way, starting from the zero point upstream at -0.6 m. Flow depths over the weir were measured at 0.05 m intervals. Schiltknecht MiniAir20 model velocity meter with  $\pm 0.5\%$  accuracy was used to measure the flow velocity. It can detect velocity values up to a maximum of 5 m/s with a measurement velocity of 2 measurements/second. The average button for all velocity values was activated and at least 240 seconds were waited for each measurement. The velocity meter was placed on a scale with a wheeled mechanism that

can move forward-backward and left-right on the flow channel. To minimize experimental setup errors, the devices and equipment used in experiments were provided by İnönü University administration at regular intervals (once every 6 months). However, in model studies, some inevitable errors caused by scale effects are also known to affect the results. On the other hand, the fact that the equations that manage the movement of the water contain viscosity and turbulence expressions makes it difficult to solve such problems. Nowadays, the widespread use of CFD methods for solutions of water structures-flow interaction problems has enabled significant developments in calculations and economic, fast, and easy solutions in the analysis of open-channel flows.

## 2.1. Numerical Model Setup and Basic Equations

Within this study, the physical model, whose experiments were carried out in a laboratory environment, was also created in a numerical environment through Ansys-Fluent software. For this purpose, free surface flow over a broad-crested weir was examined. To examine the mean flow characteristics of broad-crested flows, the Navier-Stokes equations were used. The main equations used in the numerical model and defining the flow are presented below [20]:

$$\frac{\partial \rho}{\partial t} + \nabla \cdot (\rho \mathbf{U}) = 0 \quad (3)$$

$$\frac{\partial (\rho \mathbf{U})}{\partial t} + \nabla \cdot (\rho \mathbf{U} \otimes \mathbf{U}) = -\nabla p + \nabla \cdot \boldsymbol{\tau} + S_M \quad (4)$$

$$\boldsymbol{\tau} = \mu \left( \nabla \mathbf{U} + (\nabla \mathbf{U})^T - \frac{2}{3} \boldsymbol{\delta} (\nabla \cdot \mathbf{U}) \right) \quad (5)$$

Here,  $\rho$  is defined as density,  $\nabla$  as gradient operator,  $\mathbf{U}$  as velocity vector,  $t$  as time,  $\boldsymbol{\tau}$  as stress tensor,  $S_M$  as source term,  $\mu$  as viscosity,  $\boldsymbol{\delta}$  as identity matrix. Equation 3 refers to the continuity equation, and Equation 4 refers to the conservation of momentum [21].

In this study, the two-equation Realizable k- $\varepsilon$  model was preferred. Two-equation turbulence models allow the determination of a turbulent length and time scale by solving two separate convection equations. The Realizable k- $\varepsilon$  model is a model based on model transport equations for turbulent kinetic energy ( $k$ ) and its dissipation rate ( $\varepsilon$ ). The Realizable k- $\varepsilon$  model differs from the Standard k- $\varepsilon$  model with two important features. The Realizable k- $\varepsilon$  model includes an alternative turbulent viscosity formula. A modified convection equation for the dissipation ratio  $\varepsilon$  is derived from an exact equation for the transport of mean-square vorticity fluctuation. In the Realizable k- $\varepsilon$  model, the transport equations for  $k$  and  $\varepsilon$  values are as follows.

$$\frac{\partial}{\partial t} (\rho k) + \frac{\partial}{\partial x_j} (\rho k u_j) = \frac{\partial}{\partial x_j} \left[ \left( \mu + \frac{\mu_t}{\sigma_k} \right) \frac{\partial k}{\partial x_j} \right] + G_k + G_b - \rho \varepsilon - Y_M + S_k \quad (6)$$

$$\frac{\partial}{\partial t} (\rho \varepsilon) + \frac{\partial}{\partial x_j} (\rho \varepsilon u_j) = \frac{\partial}{\partial x_j} \left[ \left( \mu + \frac{\mu_t}{\sigma_\varepsilon} \right) \frac{\partial \varepsilon}{\partial x_j} \right] + \rho C_1 S_\varepsilon - \rho C_2 \frac{\varepsilon^2}{k + \sqrt{v \varepsilon}} + C_{1\varepsilon} \frac{\varepsilon}{k} C_{3\varepsilon} G_b + S_\varepsilon \quad (7)$$

Here;  $G_k$  denotes the formation of turbulent kinetic energy depending on the gradient of the average velocity,  $G_b$  denotes the formation of turbulent kinetic energy due to buoyancy,  $Y_M$  denotes the contribution of undulating expansion in compressible turbulence to the total dissipation rate.  $C_2$  and  $C_{1\varepsilon}$  are constants.  $\sigma_k$  and  $\sigma_\varepsilon$  are the turbulent Prandtl numbers for  $k$  and  $\varepsilon$  respectively, and  $S_k$  and  $S_\varepsilon$  are user-defined source terms. Except for the constants in the model, the  $k$  equation here is the same as the k- $\varepsilon$  model and the RNG k- $\varepsilon$  model. However, the  $\varepsilon$  equation is quite different from standard and RNG-based equations. The validity of this model has been widely recognized for a wide variety of flows, including rotating homogeneous shear flows, free flows containing jets and mixing layers, and channel and boundary layer flows. Compared to the Standard k- $\varepsilon$  model, the Realizable k- $\varepsilon$  model yields better predictions for certain flows. One example is the round jet, for which the Standard k- $\varepsilon$  model overestimates the spreading rate. Generally, since the realizability conditions are approached asymptotically, the turbulence characteristics are more consistent than for the Standard k- $\varepsilon$  model. The Realizable k- $\varepsilon$  model uses wall functions and has the same default initial conditions and scalings as the Standard k- $\varepsilon$  model [21].

## 2.2. Solution Region Boundary Conditions with Volume of Fluid Method

In open channel flows, the interface between two-phase immiscible fluids (such as water and air) can be examined using the volume of fluid method, which can be applied to a constant Eulerian relation [22]. This method determines the parts of the solution region that are filled with water and air. The working principle of the numerical modeling system is defined by the fluid volume, which indicates the volumetric occupancy rate in the created solution region. The method called VOF is used as a powerful and successful technique in determining the free surface shape in open channel flows. This method is based on a process that determines the filling rates of the element volumes of the fluid entering a given numerical calculation network at certain time intervals and accordingly calculates the free surface profile in the flow at selected time intervals. The VOF method tracks the moving front by adopting an implicit formulation using the volume fraction of one phase in each cell of a discretized domain. This method has the advantage of conserving the total volume by construction. However, its main disadvantage is that it increases the model complexity and should be preferred only when there are multiphase problems. If the element in the calculation network within the solution region is fully filled, it takes the value  $F=1$ , and when it is empty, that is, filled with air, it takes the value  $F=0$ . For  $0 < F < 1$ , the network element is partially filled. VOF was also preferred for this study examining the broad-crested weir structure.

In this study, the model geometry was created with Solidworks software and transferred to Ansys-Fluent software with (.step) extension. Since channel length and mesh number directly affect the solution time, especially in numerical solutions, the channel geometry was kept a little shorter so as not to change the flow conditions. For the numerical solution; flow rate values, flow velocities, and weir size values were taken as the same as the experimental values at the channel inlet. Here,  $y_1$  is the water depth upstream, and  $V_1$  is the inlet velocity water in the channel,  $Y$  is channel height,  $b$  is channel wide, and  $Z$  total channel length. The  $Y$  value was taken as 0.3 m for the numerical solution, while the experimental model channel size was 0.5 m. The  $Z$  value in the experimental model was 12.8 m, it was taken as 7 m in the numerical model. For the numerical solution, the weir was placed 2 m from the upstream. Table 1 includes experimental and numerical data.

**Table 1.** Summary of experimental and numerical data

Q (l/s)	$y_1$ (m)	$V_1$ (m/s)	Numerical Channel Dimensions (b*Y*Z) (m)	Experimental Channel Dimensions (b*Y*Z) (m)
7.84	0.1775	0.11	0.4*0.3*7	0.4*0.5*12.8
14.86	0.2064	0.18	0.4*0.3*7	0.4*0.5*12.8

Also, the dimensions of the broad-crested weir used in the numerical solution were given schematically in Figure 4. FD represents the direction of the flow.

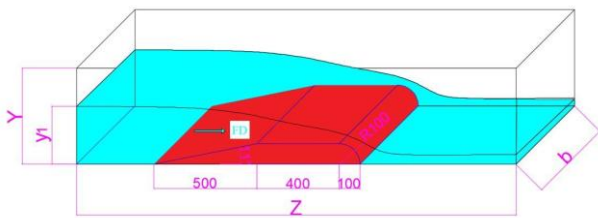


**Figure 4.** Schematic drawing of the broad-crested weir (Figure numerical dimensions are in mm)

The mesh designate was first made appropriate with the numerical solution's channel structure. Linear mesh structure was preferred because the channel geometry and weir structure did not have too many curvilinear and variable surfaces. The optimum number of meshes was achieved by running the model several times with different numbers of meshes and convergence of the solution network. In this study, instead of considering the effect of different mesh types on modeling, linear mesh structure was preferred. Because the model geometry was not too complex and there were not very small areas on the weir. For solution sensitivity, Orthogonal Quality and Skewness values were taken into account and solutions were performed for Coarse, Medium, and Fine mesh structures. As a result, the Fine mesh structure, which obtained the closest result to the experimental data, was considered. As a result of the solutions, the Average Orthogonal Quality value was obtained as 0.99863 and 0.99864. Again, the Average Skewness value was obtained as 0.00948 and 0.0092. These values indicate that the mesh quality was within the accepted limits [21]. Figure 5 shows an image where

the mesh structure and boundary conditions were defined. In Figure 5, B inlet was defined to the system as "velocity inlet" and the experimentally measured flow velocity value was taken into account. F channel outlet is defined as "pressure outlet". In addition, the part of the D channel outside the flow area is defined as a "pressure outlet" since it is a surface opening to the atmosphere. A and E represent the right and left side surfaces of the channel, respectively, and are defined as "wall". C is the bottom of the channel and is defined in the system as a "wall".

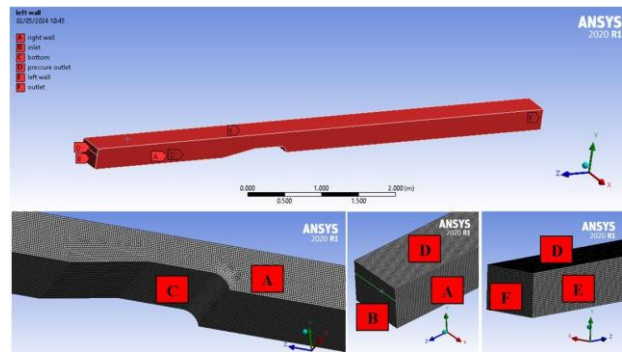


**Figure 5.** Boundary conditions defined for the numerical model

After data entry was provided at all these stages with Ansys-Fluent software, the analysis was started by taking  $\Delta t = 0.02$  seconds and Number of time steps = 3500. The iteration convergence value for all solutions was taken into account as 0.000001 ( $1 \times 10^{-6}$ ) in all equation values to stay on the safe side. As a result of the analysis, water surface profiles, flow depths, and velocity values were obtained numerically, taking into account the experimental measurement points in the channel. Thus, the reliability of the study was tested by comparing the experimental and numerical solution results.

### 3. RESULTS AND DISCUSSION

This study measured the velocities of the flow passing over the broad-crested weir, whose upstream surface was trapezoidal and its downstream surface was circular, and the depths at certain points over the weir and along the experimental set were measured. Thus, water surface profiles were obtained. Solutions were taken for two different flow rates in experimental and numerical measurements, considering the same flow conditions. Numerical simulations were carried out with Ansys-Fluent software, which works with the finite volume method. Using the Realizable  $k-\epsilon$  turbulence model, the water surface profile was calculated with the VOF method, and the solutions were obtained in three dimensions. Then, the water surface profiles of the numerical solution were compared with the experimental measurement results. Figure 6 shows the water surface profiles obtained experimentally and numerically along the (z) channel direction for  $Q=7.84$  l/s and  $Q=14.86$  l/s. The values were measured at 10 cm intervals, starting 60 cm before the weir in the upstream direction, in both the experimental and numerical models. The part where the weir begins was accepted as the zero (0) starting point, and flow depths were measured at 5 cm intervals on the

weir. After the weir, flow depths were again measured at 10 cm intervals, and at the points where the depth change decreased, measurements continued at 20 cm intervals until the end of the channel. The flow depths measured ( $h$ ) in the figure were made dimensionless by dividing by the maximum flow depth ( $h_{max}$ ), and a water surface profile was created along the direction ( $z$ ) in the channel. It had been observed that the flow depths were generally compatible with two flow rates each other. It was seen that more sensitive results were obtained in numerical solutions, especially in the circular surface transition from upstream to downstream. In this section, separations in the streamlines can be seen due to the increase in flow velocity. It can also be said that experimentally and numerically closer flow depths were obtained towards the downstream of the channel. When we compare the flow depths for  $Q=7.84$  l/s and  $Q=14.86$  l/s flow rates, a slight difference was revealed. For  $Q=7.84$  l/s flow rate, the experimentally measured flow depths after the broad-crested weir were higher than the numerical study, while for  $Q=14.86$  l/s flow rate, the numerical results were lower. This situation showed that the numerical studies achieve more sensitive results with the appropriate mesh structure. In addition, since the external human intervention of the flow field was less and the roughness conditions of the weir and inside the channel were clearer, such a difference was acceptable. Once more, the differences between the numerical and experimental solutions may be affected by the mesh structure of the flow in the channel, the mesh type, the selected solution model, the vortex, and turbulence movements of the flow in the channel due to the weir structure. Therefore, the values may change in cases where the flow accelerates or passes downstream from the weir surface. As can be seen from the flow topology, for flow rates  $Q=7.84$  l/s and  $Q=14.86$  l/s, there was no separation of boundary layers upstream and at the top of the broad-crested weir. This reflects the difference between our designed weir and one of the other broad-crested weirs with different cross sections [14].

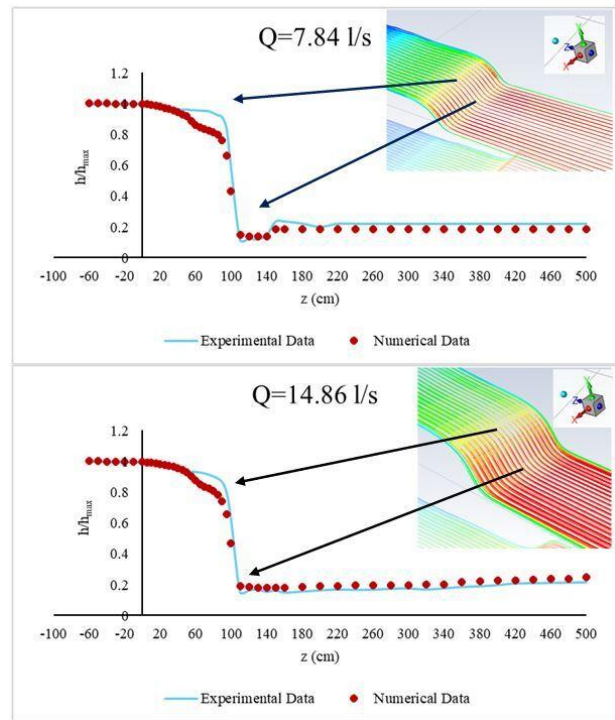


**Figure 6.** Experimental and numerical water surface profile for  $Q=7.84$  l/s and  $Q=14.86$  l/s

Figure 7 showed that the static pressure values affected over the channel bottom. In general, a high-pressure value that would cause deformation at the channel bottom was not observed. Maximum static pressure values were observed on the upstream aspect for  $Q=7.84$  l/s and  $Q=14.86$  l/s. When the two flow rates were compared, higher static pressure values were obtained for the flow rate  $Q=14.86$  l/s. Both of two flow rates it was observed that the pressure decreased to negative values only at the weir exit, on the curved surface where the flow started to accelerate. For the broad-crested weir surface, only the curved surface can be coated with a more durable coating material against the risk of cavitation. Thus, possible damage to the weir surface was prevented.



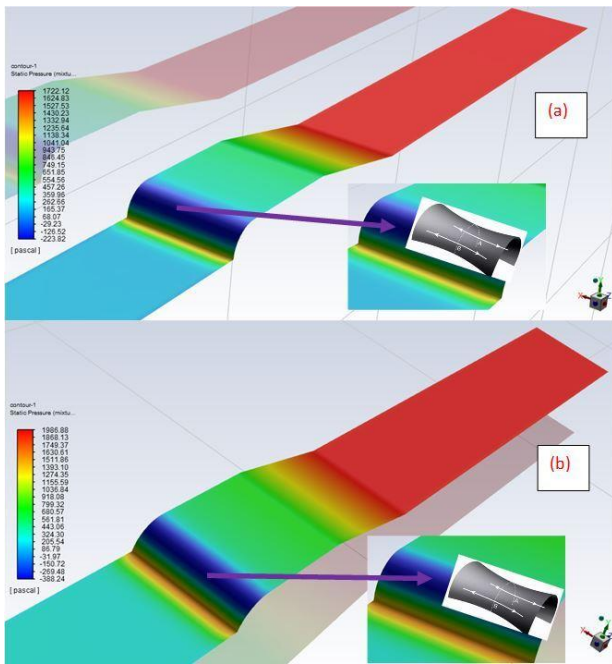


**Figure 7.** Static pressure values for (a)  $Q=7.84$  l/s, (b)  $Q=14.86$  l/s, and material example for the surface to be coated

Again, the velocity values obtained for  $Q=7.84$  l/s and  $Q=14.86$  l/s flow rates were given in Figure 8. The measured velocity values were the average velocity values taken at  $x=0.2$  m for the central axis of the channel. In the numerical solution, the channel length was taken as 7 m to shorten the number of meshes and solution time. The zero (0) point in Figure 8 was the starting point of the 2 m section before the broad-crested weir upstream. In other words, the 2 m point represents where the weir begins, the beginning of the trapezoidal surface. These levels were also indicated on the velocity magnitude contours. The velocimeter average button for all experimental velocity values was activated and at least 240 seconds were waited for each measurement. Flow velocities, for  $Q=7.84$  l/s and  $Q=14.86$  l/s flow rates were found to be compatible numerically and experimentally. Both flow rates in upstream, flow velocity remained at very low values. Hereby, the experimental and numerically measured values were very close.

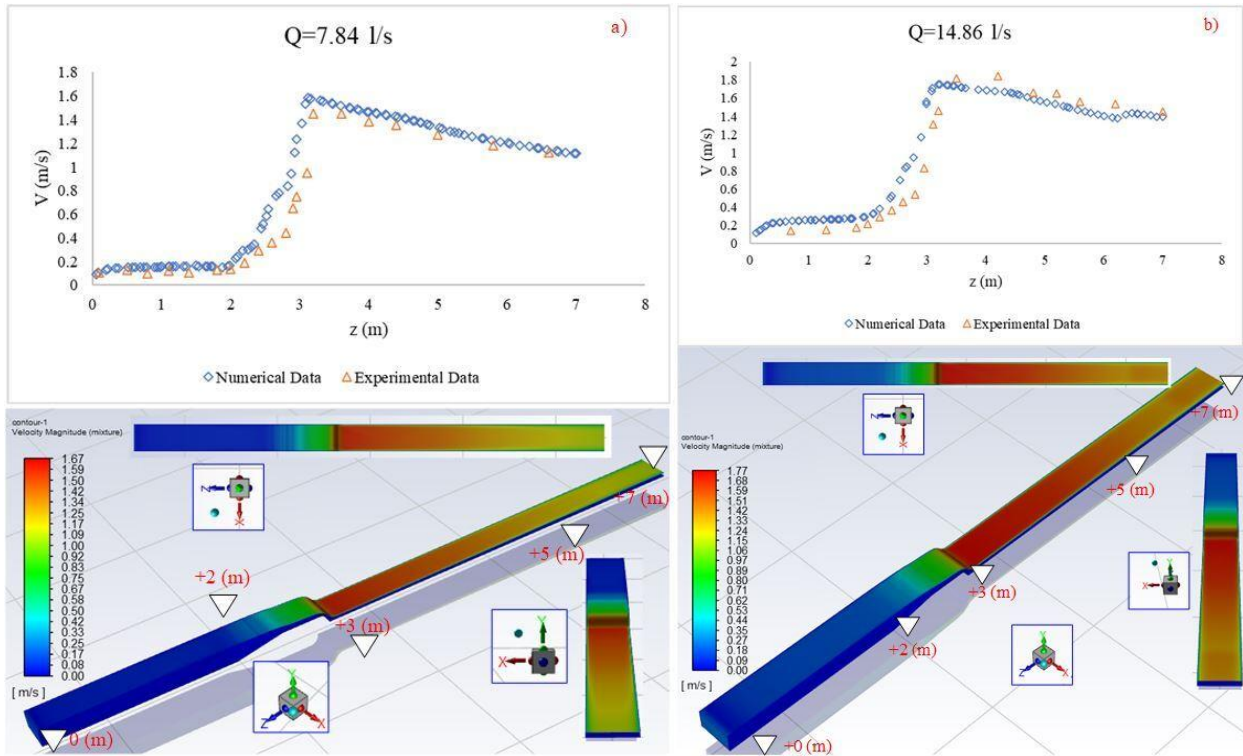


**Figure 8.** a) For  $Q=7.84$  l/s experimental and numerical velocity values and velocity magnitude contours, b) For  $Q=14.86$  l/s experimental and numerical velocity values and velocity magnitude contours

Velocity values began to increase on the weir surface and towards the points where the critical flow depth began to form, and the difference between the values obtained in the numerical and experimental solutions partially increased. When both flow rate values were compared  $Q=14.86$  l/s flow rate value, it can be said that the experimental velocity measurements in the section after the weir are slightly higher than the numerical solution. It can be said that more precise values are obtained in the numerical solution depending on the sensitivity of the measuring device, the mesh structure of the model, and the increase in flow velocity.

#### 4. CONCLUSION

In the context of this study, a broad-crested weir model which owns a trapezoidal upstream surface and a circular downstream surface, inhearse the channel in a laboratory environment was used. Passing over the weir flow rates, depth, and velocity, were measured. Experiments were carried out for two different flows. Then, numerical simulations were carried out to determine the flow velocity and depth over the broad-crested weir, considering the same flow conditions. Ansys-Fluent package program, which provides solutions using the

finite volume method, was used. Realizable  $k-\varepsilon$  turbulence model was used. The water-air surface interface was calculated by the VOF method. As a result of numerical solutions, three-dimensional velocity, static pressure contours, and water surface profiles were obtained.

- The water surface profiles of the numerical solution were compared with the experimental measurement results. In general, the water surface profiles were quite compatible with the experimental data. This further increased the reliability of numerical solutions in flow estimation.

- In addition, it had been observed that the flow velocities measured at certain points along the channel axis have values close to the experimental data. Separations in the streamlines were also observed in the numerical solution at the point where the flow started to accelerate after reaching the critical depth.

- When the static pressure values affecting the channel bottom were examined, maximum values were obtained on the upstream aspect for both flow rates. In addition, negative pressure values were obtained in the region where the flow reached the critical depth and left the weir. This causes the risk of cavitation. For this reason, it may be recommended to cover the part where the negative pressure zone occurs with a more durable material.

In addition to all these, numerical solutions provide more precise solutions with new software developed every day. Its importance is gradually increasing. Different turbulence models, using this new design model, more sensitive results can be achieved. For this purpose, the effects of this type of broad-crested weir structure on the flow behavior can be seen in the numerical environment before being used in area applications. Especially durable materials can be preferred against the risk of wear on the weir surface. Appropriate design changes and measures can be taken accordingly. This broad-crested weir design can enable more efficient flow utilization in irrigation channels and environmental projects.

### Acknowledgement

The author would like to thank the Inonu University Department of Civil Engineering for providing the use of the laboratory for the experiments and Dr. Fatih Kantarcı for helping.

### REFERENCES

- [1] Soydan Oksal NG, Aköz MS, Simsek O. Numerical modelling of trapezoidal weir flow with RANS, LES and DES models. *Sādhanā*. 2020;45(1):91.
- [2] Felder S, Islam N. Hydraulic performance of an embankment weir with rough crest. *J Hydraul Eng*. 2017;143(3):4016086.
- [3] Özlük A. Trapez Geniş Başlıklı Savaklara Ait Debi Katsayısının Yapay Zeka Yöntemleri İle Belirlenmesi. 2022.
- [4] Hager WH, Schwalt M. Broad-crested weir. *J Irrig Drain Eng*. 1994;120(1):13–26.
- [5] Tracy HJ. Discharge characteristics of broad-crested weirs. Vol. 397. US Department of the Interior, Geological Survey; 1957.
- [6] Isaacs LT. Effects of laminar boundary layer on a model broad-crested weir. 1981;
- [7] Faltas MS, Hanna SN, Abd-el-Malek MB. Linearised solution of a free-surface flow over a trapezoidal obstacle. *Acta Mech*. 1989;78:219–33.
- [8] Clemmens AJ, Replogle JA, Reinink Y. Field predictability of flume and weir operating conditions. *J Hydraul Eng*. 1990;116(1):102–18.
- [9] Sargison JE, Percy A. Hydraulics of broad-crested weirs with varying side slopes. *J Irrig Drain Eng*. 2009;135(1):115–8.
- [10] Azimi AH, Rajaratnam N, Zhu DZ. Discharge characteristics of weirs of finite crest length with upstream and downstream ramps. *J Irrig Drain Eng*. 2013;139(1):75–83.
- [11] Madadi MR, Dalir AH, Farsadizadeh D. Control of undular weir flow by changing of weir geometry. *Flow Meas Instrum*. 2013;34:160–7.
- [12] Şimşek O, İşlek H, Aköz MS. Ağ Elemanı Özelliklerinin Sayısal Model Sonuçları Üzerine Etkisinin Belirlenmesi. *Çukurova Üniversitesi Mühendislik-Mimarlık Fakültesi Derg*. 2020;35(1):195–210.
- [13] Sarker MA, Rhodes DG. Calculation of free-surface profile over a rectangular broad-crested weir. *Flow Meas Instrum*. 2004;15(4):215–9.
- [14] Bal H. Geniş başlıklı savak içeren açık kanal akımının sayısal modellenmesi. *Çukurova Üniversitesi, Adana, Türkiye*. 2011;
- [15] Felder S, Chanson H. Free-surface profiles, velocity and pressure distributions on a broad-crested weir: A physical study. *J Irrig Drain Eng*. 2012;138(12):1068–74.
- [16] Soydan NG, Aköz MS, Şimşek O, Gümüş V. Trapez Kesitli Geniş Başlıklı Savak Akımının ke Tabanlı Türbülans Modelleri ile Sayısal Modellenmesi. *Çukurova Üniversitesi Mühendislik-Mimarlık Fakültesi Derg*. 2012;27(2):47–58.
- [17] İlkentapar M, Öner AA. Geniş Başlıklı Savak Etrafındaki Akımın İncelenmesi. *Niğde Ömer Halisdemir Üniversitesi Mühendislik Bilim Derg*. 2017;6(2):615–26.
- [18] YILDIZ MC, Yarar A. Geniş Başlıklı Savaklardaki Savak Yüklerinin Deneysel Ve Sayısal Olarak Modellenmesi. *Konya J Eng Sci*. 2020;8(1):164–74.

- [19] Subramanya K. Flow in open channels. Tata McGraw-Hill; 2009.
- [20] Raupach MR, Shaw RH. Averaging procedures for flow within vegetation canopies. *Boundary-layer Meteorol.* 1982;22(1):79–90.
- [21] Guide AFT. ANSYS FLUENT Theory Guide. Release 18.2, 15317 (November). 2013;
- [22] Hirt CW, Nichols BD. Volume of fluid (VOF) method for the dynamics of free boundaries. *J Comput Phys.* 1981;39(1):201–25.

## Role of KU70, SIRT1, and SIRT6 Proteins in Diabetic Rat Testis Tissue

Selim DEMİRTAŞ<sup>1\*</sup>, Onur ERSOY<sup>2</sup>, Gülnur KIZILAY<sup>3</sup>

<sup>1</sup> Mardin Artuklu University, Medicine Faculty, Histology and Embriology Department, Mardin, Türkiye

<sup>2</sup> Trakya University, Vocational School of Health Services, Pathology Laboratory Techniques Program, Edirne, Türkiye

<sup>3</sup> Trakya University, Medicine Faculty, Histology and Embriology Department, Edirne, Türkiye

Selim DEMİRTAŞ ORCID No: 0000-0001-7249-3092

Onur ERSOY ORCID No: 0000-0001-9829-7903

Gülnur KIZILAY ORCID No: 0000-0003-1793-7003

\*Corresponding author: [selimdemirtas@artuklu.edu.tr](mailto:selimdemirtas@artuklu.edu.tr)

(Received: 14.05.2024, Accepted: 19.08.2024, Online Publication: 26.09.2024)

### Keywords

Bax/Bcl2-  
ratio,  
TUNEL assay,  
Rat,  
Apoptosis,  
Histology

**Abstract:** Diabetic male infertility/subfertility is an important complication of diabetes. The molecular mechanisms responsible for this complication have not been thoroughly investigated. We aimed to elucidate the role of KU70, SIRT1, and SIRT6 proteins in diabetic testis. Sprague–Dawley male rats were maintained under stable laboratory conditions. The rats were divided into a control group (n=8) and a diabetes group (n=8 treated with a single dose of 50 mg/kg streptozotocin). At the end of the 1-month experimental period, animals were sacrificed under anesthesia. Both testicles were removed, processed lightly, and studied through electron transmission microscopy and western blotting. Blood samples were collected for biochemical analysis. Histopathological analysis revealed that, in the diabetes group, the diaphragmatic tubule diameters and serum testosterone levels were decreased. KU70 immunoreactivity was statistically significantly increased, whereas SIRT1 and SIRT6 expression was significantly decreased compared with that observed in the control group. This is the first study to examine the expression of KU70, SIRT1, and SIRT6 in diabetic testicular tissue for the first time. According to the results, KU70, SIRT1, and SIRT6 may play an important role in cell apoptosis in diabetic testicular tissue. Importance of these proteins should be investigated further in additional quantitative studies.

## Diyabetik Rat Testis Dokusunda KU70, SIRT1 ve SIRT6 Proteinlerinin Rolü

### Anahtar Kelimeler

Bax/Bcl2-  
oranı,  
TUNEL metodu,  
Rat,  
Apoptoz,  
Histoloji

**Öz:** Diyabetik erkek infertilite/subfertilitesi, günümüzde diyabetin önemli komplikasyonları arasında yerini almıştır. Diyabetik erkek infertilitesinin altında yatan moleküler mekanizmalar henüz tam olarak aydınlatılamamıştır. Çalışmamızda; KU70, SIRT1 ve SIRT6 proteinlerinin bu mekanizmalar içerisindeki rolünün aydınlatılmasına katkı sağlanması amaçlanmıştır. Stabil laboratuvar koşulları altında tuttuğumuz Sprague Dawley erkek sıçanlardan, kontrol grubu (n=8) ve tek doz 50 mg/kg streptozotosin uygulanan diyabet grubu (n=8) olmak üzere iki grup oluşturulmuştur. Diyabet grubunda; ışık ve elektron mikroskopik incelemelerimizde diyabetik testis dokusunda şimdiye kadar literatürde yer alan tüm histopatolojik bulgular gözlenmiş, morfometrik olarak da seminifer tübül çaplarının azaldığı tespit edilmiştir. Çalışmamızda, KU70, SIRT1 ve SIRT6 ifadeleri incelendiğinde KU70 diyabet grubunda istatistiksel anlamlılıkla artarken, SIRT1 ve SIRT6 ifadelerinin diyabetik grupta, kontrol grubuna göre anlamlı şekilde düştüğü belirlenmiştir. Sonuç olarak, diyabetik erkek hastalarda karşılaşılan subfertilite/infertilite olgularında, KU70, SIRT1 ve SIRT6 proteinlerinin önemli bir rolü olabileceği ve bu proteinlerin, kantitatif başka çalışmalarla da desteklenerek öneminin vurgulanması gerektiği kanısındayız.

## 1. INTRODUCTION

Diabetes mellitus (DM) is a chronic metabolic disease that occurs due to defects in insulin secretion [1]. Neuropathy, retinopathy, nephropathy, and microvascular and macrovascular pathologies are the

main complications associated with diabetes [2, 3]. In addition, abnormal sperm production and sexual dysfunctions in men with diabetes are considered among the long-term complications of diabetes. Studies on diabetic rats revealed a decrease in testicular weight, testosterone levels, and sperm count and motility, along

with an increase in abnormal spermatogenesis [4-7]. The molecular mechanisms underlying testicular dysfunction in individuals with diabetes have not been fully elucidated. However, numerous proteins involved in apoptotic pathways are thought to play a role in this process.

Non-homologous end joining (NHEJ) is one of the two main mechanisms involved in the repair of DNA double-strand breaks. KU70 is a protein involved in this process, and it has been shown that double-strand breaks ends are stabilized by KU70 and KU80 [8]. KU70 and KU80 form the KU heterodimer and, together with the DNA-related protein kinase catalytic subunit, they play a role in the repair mechanism. Apart from DNA repair, KU proteins are involved in cell signal, proliferation, replication, transcription activation, and apoptosis. KU70 is involved in the regulation of apoptosis by suppressing Bax activity. It is localized both in the cytoplasm and nucleus [9].

Sirtuins (SIRT) constitute a family of nicotinamide adenine dinucleotide (NAD<sup>+</sup>)-dependent, class III deacetylase enzymes. There are seven sirtuins found in mammals (SIRT1–SIRT7). SIRT1 plays an important role in apoptosis by targeting proteins, such as p53, p73, E2 factor-1 (E2F1), and KU70. Studies have shown that it also affects insulin metabolism and, when overexpressed in pancreatic beta ( $\beta$ ) cells, it increases insulin secretion and adenosine 3'-triphosphate (ATP) production. KU70 deacetylation by SIRT1 in NHEJ, suppresses Bax and participates in DNA repair. Moreover, KU70 deacetylation by SIRT1 in the cytoplasm leads to KU70/Bax binding and inhibits apoptosis [10-12].

SIRT6 is involved in the repair mechanism of DNA single-strand breaks and base excision repair (BER) pathway. It also plays a role in repairing double-strand breaks by stabilizing the DNA-related protein kinase in NHEJ. Studies investigating the effects of SIRT6 gene suppression demonstrated that this gene plays a role in the DNA repair mechanism in various diseases, such as spinal curvature, metabolic disorders, and aging before maturation [13-15]. SIRT6 is involved in KU70 deacetylation and KU70/Bax binding and suppresses apoptosis [16].

In this study, we investigated the possible roles of KU70, SIRT1, and SIRT6 proteins in diabetic testicular tissues, aiming to contribute to the development of new treatment protocols.

## 2. MATERIAL AND METHOD

### 2.1. Experimental Procedure

The present study was approved by the Trakya University Animal Experiments Local Ethics Committee (TUHADYEK-2017/17). Sixteen Sprague–Dawley male rats (age: 3 months; weight: 250–320 g) were obtained from Istanbul University, Institute of Experimental Medicine Research. The rats were maintained under

stable laboratory conditions ( $22 \pm 1.0^\circ\text{C}$ , 12 h light/dark cycle) with ad libitum access to water and feed pellets containing crude 21% protein (Purina, Istanbul, Turkey).

The rats were divided into two groups: control and diabetes ( $n=8$ , respectively). We intraperitoneally injected 50 mg/kg body weight streptozotocin (STZ) (Sigma–Aldrich, Taufkirchen, Germany) dissolved in 0.1 M citrate buffer, pH 4.2, into rats of the latter group to induce diabetes. Blood glucose levels were measured using a glucometer (IME-DC, Hof, Germany) in blood samples obtained from the tail vein of the rats prior to initiating the experiment, 48 h after STZ administration, and once weekly for 1 month. Following STZ administration, the rat with blood glucose levels  $>250$  mg/dl were considered “diabetic” [17]. At the end of the experimental period, all animals were sacrificed under anesthesia; both testes were removed, processed for light microscopy and transmission electron microscopy and western blotting. Blood samples were collected for biochemical analysis.

### 2.2. Enzyme-linked Immunosorbent Assay (ELISA)

Testosterone levels were measured in supernatants obtained from cardiac blood samples collected prior to sacrifice. The rat testosterone ELISA kit (Bioassay Technology Laboratory, Shanghai, China) was used in accordance with the instructions provided by the manufacturer.

### 2.3. Histopathological Evaluations

Light microscopic routine staining and immunohistochemical examinations were conducted. After fixing the testis tissues with Bouin’s fixative, they were washed, dehydrated, and embedded in paraffin. Tissue sections (thickness: 5  $\mu\text{m}$ ) were stained with hematoxylin-eosin (H+E) (Sigma-Aldrich, Missouri, USA) and subjected to histological and morphometric analyses to reveal the structural features of the testes. After sealing with Entellan™ (Merck Millipore, Darmstadt, Germany), the slides were examined under an Olympus BX-51 (Olympus Corporation, Tokyo, Japan) microscope and photographed at different magnifications. Spermatogenesis was evaluated using the Johnsen scoring system for five areas/sections for each animal in 10 different fields/seminiferous tubules which were randomly selected. The evaluation was performed using an Olympus BX51 microscope (magnification:  $\times 400$ ) [6].

### 2.4. Transmission Electron Microscopy

Testicular tissues were pre-fixed for 1.5 h with 2.5% glutaraldehyde and post-fixed for 1 h with 1% osmium tetroxide (OsO<sub>4</sub>). Subsequently, the tissues were passed through a graded alcohol series and propylene oxide, and blocked using araldite. Semi-thin sections taken by an ultramicrotome (RMC-MTX, Tucson, USA) were stained with toluidine blue to determine the cutting regions of the blocks. Thin sections were obtained from the determined regions and stained with uranyl acetate

and Reynold's lead citrate. Subsequently, the sections were examined using a Jeol 1010 (Jeol Ltd., Tokyo, Japan) transmission electron microscope.

## 2.5. Terminal Deoxynucleotidyl Transferase UTP Nick End Labeling (TUNEL) Assay

The TUNEL assay was used to determine the apoptosis in testicular tissue sections. Tissue sections (thickness: 5  $\mu$ m) were incubated overnight at 37°C. The sections were passed through toluene and a graded alcohols series, washed with phosphate-buffered saline (pH 7.4; Invitrogen, Carlsbad, CA, USA), and treated with proteinase K subsequently, they were examined using the ApopTaq Plus Peroxidase In Situ Apoptosis Detection Kit (Merck Millipore, Darmstadt, Germany) according to the instructions provided by the manufacturer. Finally, the sections were passed through an ascending alcohol series and toluene, and mounted with Entellan™.

## 2.6. Immunohistochemistry and Western Blotting

Bax, Bcl-2, and Caspase-3 (CASP3) were evaluated immunohistochemically. KU70, SIRT1, and SIRT6 were evaluated through both immunohistochemistry and western blotting. Five  $\mu$ m sections from paraffin blocks were deparaffinized, rehydrated, exposed to antigen retrieval through boiling in citrate buffer (pH: 6.0), and H<sub>2</sub>O<sub>2</sub> for inhibition of endogenous peroxidase activity. Samples were incubated with blocking solution to prevent non-specific binding at ambient temperature then antibodies of Bax (1/100 dilution; Abcam, Cambridge, MA, USA), Bcl-2 (1/200 dilution; LifeSpan BioSciences, Seattle, WA, USA), CASP3 (1/500 dilution; Abcam, Cambridge, MA, USA), KU70 (1/100 dilution; FnTest, Hubei, China), SIRT1 (1/500 dilution; Novus Biologicals, Centennial, CO, USA), SIRT6 (1/1,000 dilution; Novus Biologicals, Briarwood Avenue, CO, USA) at 4°C for overnight. The following steps were performed with a ready to use detection kit and DAB chromogen (Invitrogen, Thermo Fisher Scientific, Waltham, MA, USA) according to manufacturer's instructions. The samples counterstained with hematoxylin, mounted with entellan and examined under a light microscope.

The frozen tissue samples were homogenized in RIPA buffer with protease and phosphatase inhibitors. The prepared lysates were centrifuged at 10,000 rpm at 4°C for 10 min and supernatants were used for Western blotting. Total protein concentration was measured with Nanodrop device (Optizen NanoQ; Mecasy, Daejeon, South Korea). Equal volume of proteins was loaded and run on Nupage Novex 4–12% Bis-tris (Invitrogen, Thermo Fisher Scientific, Waltham, MA, USA) precast gels. The separated proteins were transferred on nitrocellulose membranes and the membranes were incubated with antibodies of KU70 (LS-C358891), SIRT1 (LS-B1564), SIRT6 (NB100-2522), and  $\beta$ -Actin (NB600-503) as internal control. The chemiluminescence developed bands were examined

under Chemidoc™ MP Imaging System Biorad (Model No: Universal Hood 3; Biorad, California, USA) and captured images were analyzed with Image J 1.48v software (Wayne Rasband; National Institutes of Health, Bethesda, MD, USA).

## 2.7. Quantitative and Statistical Analysis

Measurement of seminiferous tubule diameters (MSTD) in H+E stained slides was carried out using an ocular micrometer at  $\times 200$  magnification. Round or nearly round tubules were randomly selected and assessed non-blinded and blinded investigators by selecting the cross section of 10 seminiferous tubules in each slide [18, 19]. In the evaluation of TUNEL slides, the 'apoptotic tubule index' was calculated by counting the seminiferous tubules that contained at least three apoptotic cells in an average of 100 seminiferous tubules. The 'apoptotic cell index' was evaluated by counting apoptotic cells in an average of 1,000 cells in the seminiferous tubules in  $\times 200$  magnification [20].

The immunoreactivity of Bax, Bcl-2, KU70, SIRT1, and SIRT6 was evaluated semiquantitatively using histological scoring methods. Changes between the groups were determined by calculating the Bax/Bcl-2-ratio. Immunoreactivity was assessed in five areas which were randomly selected in the tissue section for each animal through  $\times 200$  magnification. Immunoreactivities were scored as the number of immunopositive cells using H-score. [19, 21, 22]. In the evaluation of CASP3 slides, assessed non-blinded and blinded investigators, scoring was performed through  $\times 200$  magnification, according to the number of immunopositive cells in 1,000 cells in each slide [20].

Statistical analysis was conducted using the SPSS 20.0 software (IBM, New York, USA) Values are presented as the mean  $\pm$  standard deviation. P-values  $< 0.05$  denoted statistically significant differences. Student's t-test was used to analyze glucose levels in blood. MSTD, Johnsen scoring, apoptotic tubule and apoptotic cell indices, and biochemical and immunohistochemical data were evaluated by applying the Mann–Whitney U test.

## 3. RESULTS

### 3.1. Blood Glucose and Testosterone Results

There was no difference in the blood glucose levels measured prior to the experiment between the control and diabetes groups ( $P=0.584$ ). At the end of the experiment, the levels of the diabetes and control groups remained stable ( $P<0.001$ ) (Table 1).

The ELISA method was used to measure the levels of testosterone in blood samples obtained by cardiac puncture following the experiment. Testosterone levels in the diabetes group were significantly decreased compared with measured for the control group ( $P<0.001$ ) (Table 1).

**Table 1.** Blood glucose, testosterone, MSTD, and Johnsen scoring.

	Initial blood glucose levels (mg dl <sup>1</sup> )	End of experiment blood glucose levels (mg dl <sup>1</sup> )	Testosterone (mIU dl <sup>1</sup> )	MSTD (μm)	Johnsen scoring
Control group	102.25 ± 5.17 P=0.584	106.50 ± 7.19	16.25 ± 1.67	345.63 ± 14.77	9.12 ± 0.83
Diabetes group	110.13 ± 4.64	463.75 ± 118.91 P<0.001*	7.73 ± 1.14 P<0.001*	275.38 ± 1.14 P<0.001*	7.37 ± 0.51 P<0.001*

Note: Results are shown as the means ± standard deviation.

\*Statistically significant compared with the control group.

MSTD, measurement of seminiferous tubule diameters.

### 3.2. Morphometry

Comparison of the MSTD measurements between the two groups showed that the values of the diabetes group were significantly decreased compared with those of the control group ( $P<0.001$ ). In addition, Johnsen's score was significantly decreased in the diabetes group versus the control group ( $P=0.002$ ) (Table 1).

### 3.3. Histopathology

#### 3.3.1. Light and electron microscopy

The control group exhibited a normal seminiferous tubule epithelium structure. In seminiferous tubules, spermatogenic serial cells from the basement membrane to the lumen, and respectively as spermatogonium, spermatocyte-I, spermatocyte-II, early and late spermatid. Sperms are in the lumen, while Sertoli cells are located in the basement membrane (Figures 1A, 1B, 1E, 1F). Spermatids were observed close to the lumen with their darkly stained nuclei, and the sperms were located in the lumen with their long, spindle-shaped nuclei (Figures 1A, 1B, 1E, 1F). Leydig cells, which exhibit a polygonal-shaped structure in interstitial connective tissue, demonstrated oval-shaped nuclei and

eosinophilic-stained cytoplasm (Figure 1B). In addition to the seminiferous tubules formed by Sertoli cells and few spermatogenic serial cells in the diabetes group, tubules containing spermatogonia, spermatocytes-I, spermatids, and sperms were also observed (Figure 1C). Due to the degeneration of Sertoli and spermatogenic cells, large vacuoles appeared in the germinal epithelium in various locations (Figures 1C, 1D, 1G, 1H). The accumulation of electron-dense bodies in the cytoplasm of spermatogenic cells was remarkable. Particularly with spermatids located close to the lumen and containing residual bodies, there was electron-dense body accumulation and large vacuoles observed in the sperm (Figures 1G, 1H). Irregular nuclei, extensive vacuole formation, loss of crystals in mitochondria, and reduction in smooth endoplasmic reticulum (SER) were detected in Sertoli cells (Figures 1G, 1H). Vacuole formation, thickening of the outer membrane in mitochondria, SER reduction, and changes in the appearance of chromatin in the nuclei were observed in the cytoplasm of some spermatogonia and spermatids (Figures 1G, 1H). It is suggested that the corrugations observed in the seminiferous tubule basement membranes also occurred due to the degenerations noted in the tubular epithelial cells (Figures 1C, 1D, 1G).

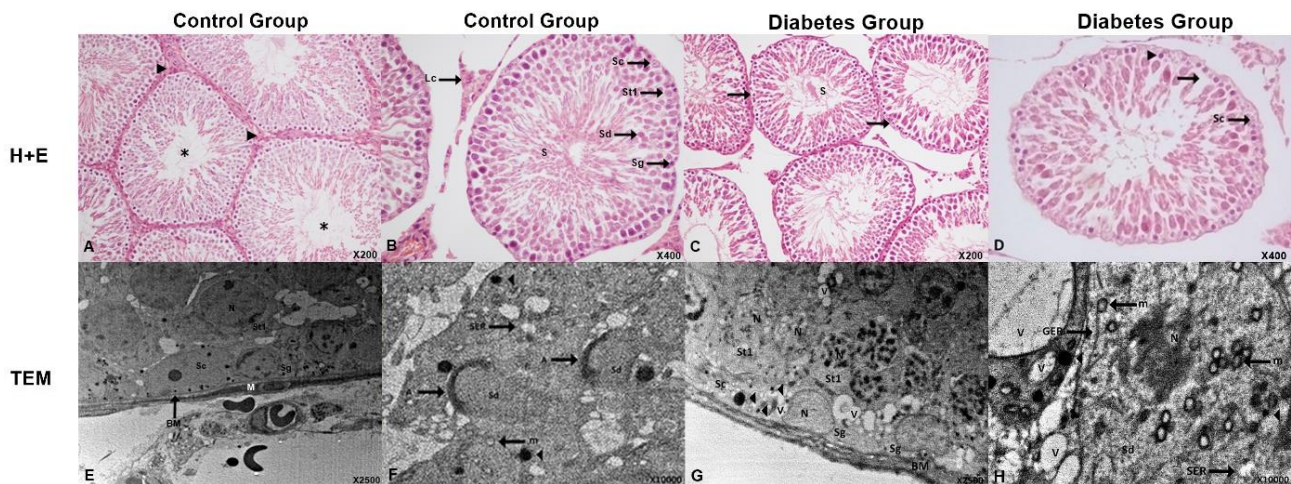


**Figure 1.** Sections with H+E stains (A–D), TEM micrographs (E–H). A. Interstitial connective tissue (▶), seminiferous tubules (\*). B. Spermatogonia (Sg), spermatocytes-I (St1), spermatids (Sd), sperms (S), Sertoli cells (Sc), and Leydig cells (Lc). C. Sperms (S), seminiferous tubules (→). D. Disorganization in cells (→) and picnotic cell nuclei (▶). E. Basal membrane (BM), peritubular myoid cell (M), Sertoli cell (Sc), spermatogonium (Sg), spermatocyte-I (St1), and nucleus (N). F. Spermatids (Sd), acrosom (A), mitochondria (m), smooth endoplasmic reticulum (SER), and electron-dense bodies (▶). G. Sertoli cell (Sc), spermatogonium (Sg), vacuole (V), spermatocyte-I (St1), and electron-dense bodies (▶) with irregular basement membrane (BM). H. The cytoplasm contains degenerated nucleus (N), multiple vacuoles (V), mitochondria (m), granular endoplasmic reticulum (GER), smooth endoplasmic reticulum (SER), and spermatids (Sd) containing electron-dense bodies (▶). Magnifications: x200 (A&C), x400 (B&D), x2500 (E&G), x10000 (F&H). Abbreviations: TEM, transmission electron microscopy.

### 3.3.2. TUNEL assay

In the tissue sections of the control group, TUNEL-positive cells were observed in a small number of cells in seminiferous tubules, especially in spermatogonia (Figure 2A). However, in the seminiferous tubules of the tissue sections of the diabetes group, a large number of TUNEL reactions was observed in other cells (besides spermatogonia) belonging to the spermatogenic series (Figure 2B). The apoptotic cell index in the diabetes group ( $34.75 \pm 3.37$ ) was significantly increased compared with that recorded in the control group ( $2.75 \pm 1.48$ ) ( $P < 0.001$ ) (Figure 2C). In addition, the apoptotic tubule index in the diabetes group ( $14.13 \pm 2.32$ ) was significantly increased compared with that noted in the control group ( $3.25 \pm 1.83$ ) ( $P < 0.001$ ) (Figure 2D).

### 3.3.3. Immunohistochemistry and western blotting

The examination of CASP3 immunoreactivity showed that the cellular localization was nuclear and cytoplasmic in both groups. In the control group, a small number of cells were stained, and mild staining was observed in spermatogenic serial cells and Sertoli cells (Figure 2E). However, in the diabetes group, a large number of immunopositive cells were detected in the seminiferous tubules (Figure 2F). CASP3 immunoreactivity was generally observed only in spermatogonia and Sertoli cells in both groups. CASP3 immunoreactivity in the diabetes group ( $16.75 \pm 1.9$ ) was significantly higher than that recorded in the control group ( $7.5 \pm 1.3$ ) ( $P < 0.001$ ) (Figure 2E).

Bax immunoreactivity was cytoplasmic for both groups. In the control group, weak staining was observed in the spermatogenic cell lines in seminiferous tubules. Of

note, staining was not observed in Sertoli cells, while spermatogonia and other spermatogenic serial cells exhibited weak and moderate staining, respectively (Figure 2H). In the diabetes group, Sertoli cells were not stained, spermatogonia were weakly stained, and spermatocytes-I and other spermatogenic serial cells were moderately stained (Figure 2I). Bax immunoreactivity was significantly higher in the diabetes group ( $234.38 \pm 18.48$ ) versus the control group ( $121.13 \pm 7.18$ ) ( $P < 0.001$ ) (Figure 2J).

Considering that staining showed cytoplasmic Bcl-2 immunoreactivity in cells in seminiferous tubules, moderate and strong cytoplasmic staining was observed in testicular tissue sections of the control group.

Spermatogonia showed weak and spermatocyte-I cells moderate cytoplasmic immunoreactivity, while there was no staining observed in Sertoli cells (Figure 2K). In the diabetes group, there was no staining observed in spermatogonia and Sertoli cells, whereas other serial cells showed weak staining (Figure 2L). Bcl-2 immunoreactivity in the diabetes group ( $113.13 \pm 5.93$ ) was significantly decreased compared with that noted in the control group ( $204.38 \pm 4.95$ ) ( $P < 0.001$ ) (Figure 2M). The Bax/Bcl-2-ratio is a frequently used method to determine whether cells in tissues will undergo apoptosis. An increase in Bax and Bcl-2 expression indicates cell apoptosis and survival, respectively. In this study, the Bax/Bcl-2-ratio was significantly higher in the diabetes group ( $2.07 \pm 0.204$ ) versus the control group ( $0.59 \pm 0.38$ ) ( $P < 0.001$ ) (Figure 2N). This finding indicates that the number of cells which are prone to apoptosis were significantly increased in the diabetes group.

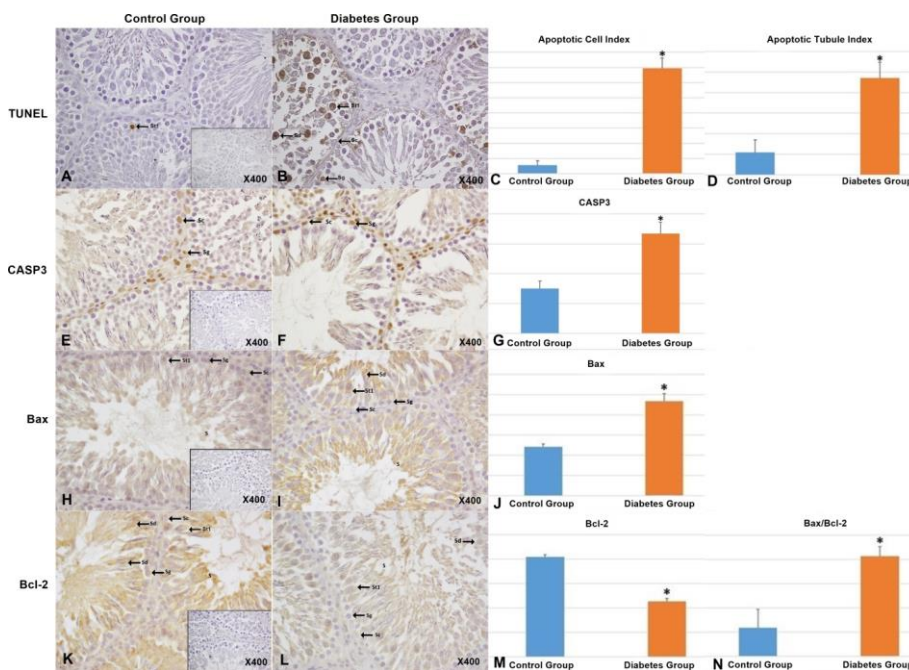


**Figure 2.** TUNEL sections (A, B), apoptotic cell and apoptotic tubule index (C, D). Immune-positive cells of all groups are monitored (→). Caspase 3 (CASP3) sections (E, F), CASP3 immunoreactivity values in G. Bax sections (H, I), Bax immunoreactivity values in J. Bcl-2 sections (K, L). Bcl-2 immunoreactivity values in (M) and Bax/Bcl-2-ratio in (N). Inner shape; negative control. \* $P < 0.05$  denotes statistically significant difference compared with the control group.

Abbreviations: S, sperms; Sc, Sertoli cells; Sd, spermatids; Sg, spermatogonium; St1, spermatocytes-I; TUNEL, terminal deoxynucleotidyl transferase UTP nick end labeling.



Of note, the cellular localization of KU70 in the sections was both nuclear and cytoplasmic. KU70 immunoreactivity examination revealed that, in the control group, spermatogonia and Sertoli cells showed very limited staining. Spermatocytes-I and other spermatogenic serial cells exhibited weak and moderate staining (Figure 3A). In the diabetes group, cells in the seminiferous tubules generally demonstrated moderate and strong staining. Notably, Sertoli cells showed weak staining, whereas spermatogonia, spermatocytes-I and other spermatogenic serial cells exhibited moderate and strong staining (Figure 3B). KU70 immunoreactivity was significantly higher in the diabetes group ( $248.75 \pm 5.82$ ) versus the control group ( $106.88 \pm 5.30$ ) ( $P < 0.001$ ). Western blotting analysis determined that KU70 protein expression was significantly higher in the diabetes group ( $1.17 \pm 0.16$ ) versus the control group ( $0.64 \pm 0.17$ ) ( $P = 0.004$ ) (Figures 3C, 3D). The results of the present immunohistochemistry and western blotting analyses were consistent, clearly demonstrating that the expression of KU70 increases in diabetic testicular tissues.

The immunoreactivity examination revealed that the cellular localization of SIRT1 in tissue sections was both nuclear and cytoplasmic. In the control group, immunoreactivity was exhibited by a large number of cells. There was no staining observed in Sertoli cells, while spermatogonia, spermatocytes-I, and other spermatogenic serial cells demonstrated moderate and strong staining (Figure 3E). In the diabetes group, weakly immunoreactivity was observed in the seminiferous tubules. Staining was not detected in

Sertoli cells, while spermatogonia were weakly stained, (Figure 3F). SIRT1 immunoreactivity in the diabetes group ( $98.75 \pm 7.44$ ) were found to be significantly lower than that in the control group ( $193.13 \pm 4.58$ ) ( $P < 0.001$ ). Moreover, western blotting analysis revealed that the expression of SIRT1 was significantly lower in the diabetes group ( $0.68 \pm 0.19$ ) versus the control group ( $1.33 \pm 0.48$ ) ( $P = 0.004$ ) (Figures 3G, 3H). The results of the immunohistochemistry and western blotting analyses were consistent, demonstrating that SIRT1 expression was significantly lower in diabetic testicular tissues versus control tissues.

The cellular localization of SIRT6 in the tissue sections was both nuclear and cytoplasmic. In the control group, there were numerous SIRT6-immunopositive cells observed. Sertoli cells exhibited weak and moderate staining, while spermatogonia, spermatocytes-I, and other spermatogenic cells showed moderate and strong staining (Figure 3I). In the diabetes group, the staining intensity was weak. Spermatogonia and Sertoli cells showed weak immunoreactivity, while other serial cells exhibited weak and moderate staining (Figure 3J). SIRT6 immunoreactivity was significantly lower in the diabetes group ( $64.63 \pm 7.44$ ) versus the control group ( $145.88 \pm 8.56$ ) ( $P < 0.001$ ). Western blotting analysis revealed that the expression of SIRT6 protein was significantly lower in the diabetes group ( $0.70 \pm 0.22$ ) versus the control group ( $1.88 \pm 0.40$ ) ( $P < 0.001$ ) (Figures 3K, 3L). The results of both immunohistochemistry and western blotting analyses demonstrated that SIRT6 expression was significantly lower in diabetic testicular tissues versus control tissues.

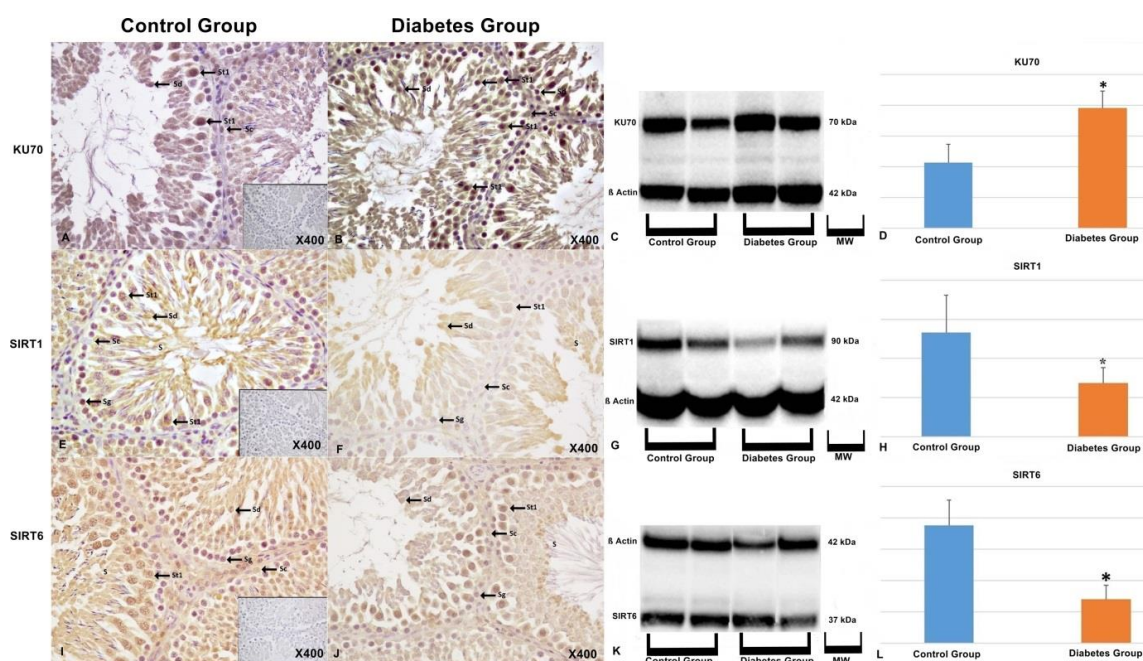


**Figure 3.** KU70 sections, western blotting bands, and graph of analysis (A–D). SIRT1 sections, western blotting bands, and graph of analysis (E–H). SIRT6 sections, western blotting bands, and graph of analysis (I–L). Inner shape; negative control. \* $P < 0.05$  denotes statistically significant difference compared with the control group.

Abbreviations: MW, molecular weight; S, sperms; Sc, Sertoli cells; Sd, spermatids; SIRT1, sirtuin 1; Sg, spermatogonium; S1, spermatocytes-I.

#### 4. DISCUSSION AND CONCLUSION

Studies have shown that diabetes affects the hypothalamus-pituitary-testicular axis and decreases

testosterone synthesis and secretion. In addition, conditions such as increased prostate glandular volume, decreased spermatogenesis and sperm quality, erectile dysfunction, retrograde ejaculation, and decreased libido

have also been reported in diabetes studies of diabetes [5, 7, 23]. Numerous studies have also recorded serious changes in the diameters of diaphragmatic tubules as a result of the decreased number of spermatogenic cells in the seminiferous tubules and their degeneration, accompanied by a decrease in the serum testosterone levels of diabetic rats [4, 24]. Cameron et al. [25] showed that tubule alimentation is impaired by thickening of capillary and seminiferous tubule basement membranes due to diabetes. Öztürk et al. [26] argued that diabetes led to Leydig cell dysfunction and a consequent decrease in testosterone. Owing to the thickening of the tubule basement membranes, the difficulty of diffusion of testosterone into the tubule may prevent the continuity of spermatogenesis.

Through electron microscopic studies, Trindade et al. [7] reported an irregular basement membrane structure, disruption of the seminiferous tubules, disruption of the structure of Sertoli cells and spermatogonia, and vacuole formation in the cytoplasm of Sertoli cells. In addition to degeneration of spermatogenic cells, Koroglu et al. [27] observed deformation of the acrosomal structures and tails of sperms. Other studies showed thickening and irregularity in seminiferous tubular basement membranes, vacuolization in Sertoli cells, and disruption of the structure of the SER [28-32]. In the nuclei of spermatogenic serial cells, condensation, and disruptions of mitochondria and the SER were also noted. Along with a decrease in the number of mitochondria, changes in the shape of the organelle and irregularities in the cristae were observed [28-32]. Trindade et al. [7] and Kianifard et al. [28] suggested that vacuolization and reduction in SER negatively affect the function and spermatogenesis process in Sertoli cells. Mitochondria degeneration and decrease in number due to diabetes has been shown. It has been stated that inadequate ATP production and increased reactive oxygen species production in spermatogenic cells may cause infertility [7, 28]. When the underlying causes of infertility were examined, it was observed that degeneration in mitochondria plays an important role [7]. Owing to mitochondria degeneration, the accumulation of electron-dense bodies and lipofuscin in the cytoplasm of spermatogenic serial cells leads to an increase in reactive oxygen species, thereby causing a degenerative effect and lipid peroxidation in cells [7, 28, 29].

In this study, the findings of apoptotic cell and apoptotic tubule indices were consistent with those of previous studies [33, 34]. Ghosh et al. [24] and Ding et al. [30] reported that the expression of Bax was significantly increased in diabetic testicular tissues, and Bax played a role in the apoptotic process. Liu et al. [35] suggested that the expression of Bax was increased in diabetic testicular tissues, and that this change was important in the damage mechanism involved in diabetic testicles. Other studies confirmed that Bax expression in diabetic testicular tissues was significantly increased and played a role in the apoptotic pathway [3, 36, 37]. Collectively, these studies showed that Bax protein plays an important role in the apoptotic process, especially in diabetes. A previous study revealed a significant increase and

decrease in the expression of the Bax and Bcl-2 genes, respectively, in testicular tissues of diabetic rats [19]. It was also shown that the Bax/Bcl-2-ratio was significantly increased [19]. Another study reported that Bcl-2 expression was significantly decreased in diabetic testicular tissues versus control tissues [38]. In a study investigating the expression of proteins belonging to the Bcl-2 family (Bcl-2, Bcl-XL, Bax, and Bad) in testicular tissues of diabetic rats was, the expression of anti-apoptotic proteins was decreased in the diabetes group [37]. Khamis et al. [39] showed that CASP3 mRNA expression was significantly increased in diabetic testicular tissue. In another study investigator showed that CASP3 expression was significantly increased in the diabetic testicular tissues; increased CASP3 expression induced caspase-activated DNase activation, leading to DNA fragmentation [36].

This was the first study to investigate the expression of KU70 in diabetic testicular tissues through immunohistochemistry and western blotting. Ahmed et al. [40] showed that expression and localization of KU70 in the nucleus of Sertoli cells, type A spermatogonia, late spermatocytes I, secondary spermatocytes and round spermatids as well as in the cytoplasm of metaphases I and II cells in mice testis by immunofluorescence, and this findings consistent with our study. They observed that KU70 impairment leads to reduced testis size, limited spermatogenesis and DNA repair, limited sperm production and increased metaphase I apoptosis. In a diabetic nephropathy study conducted by Tuncdemir et al. [41] the investigators stated that the expression of KU70 was significantly increased in the diabetes group versus the control group. In another study examining KU70, the anesthetic substance bupivacaine was administered to mouse dorsal root ganglion neurons cultured in a hyperglycemic environment. The results suggested that hyperglycemia leads to inactivation of the DNA-related protein kinase catalytic subunit and causes KU70 inhibition, thereby resulting in DNA damage and apoptosis [42]. Another study examined the expression of KU70 in cultured cardiomyocyte cells in a hyperglycemic environment. The results demonstrated that hyperglycemia increased KU70 acetylation and, accordingly, increased Bax activity. They found that KU70 acetylation was decreased, KU70/Bax binding was increased, and apoptosis was inhibited in the treated groups [43]. It is thought that KU70, which shows increased expression in diabetes, may play an important role in the apoptotic pathway. Other studies reported that KU70 binds to Bax in the cytoplasm, thereby isolating Bax from mitochondria, preventing the formation of pore, and blocking apoptosis [44, 45].

A mouse study showed that spermatocytes expressed high levels of SIRT1 during the spermatogenesis process. Interestingly, sperm anomalies and infertility were observed after silencing the SIRT1 gene [46]. It has been stated that SIRT1 is expressed in numerous tissues during embryonic development. In a study, SIRT1 expression was demonstrated during the fetal period in the neuroepithelium, dorsal root ganglion, trigeminal ganglion, eye, heart, kidney, testis, liver and lung tissues.

These findings suggested that SIRT1 expression is important in fetal development. Strong SIRT1 immunoreactivity has been demonstrated, especially in the testes, during embryonic development [47]. In a study investigating SIRT1 immunoreactivity in testicular tissues of rats with type 1 diabetes, SIRT1 expression was decreased in the diabetes group compared with the control group. SIRT1 increases insulin sensitivity and decreases glucotoxicity in testicles. Poly (ADP-ribose) polymerase-1 (PARP)/SIRT1 interaction is thought to be involved in the testicular apoptotic pathway [48, 49]. Several studies have shown that SIRT1 activation is reduced in diabetic testes, similar to our findings [50-52]. Wang et al. [53] has reported that, in Type 2 diabetes rats testes, SIRT1 expression decreased compared to control groups and SIRT1 expression increased in melatonin treated groups. In a recent study, researchers were fed mice with high fat diet and showed that, long-term calorie restriction increase obese male fertility, likely by relieves oxidative stress via activation of SIRT1 signaling [54]. Consistent with our findings, another two studies revealed that SIRT1 expression was decreased in diabetic testes. They have been suggested that, in diabetic testes, miR-34a expression increases, whereas SIRT1 expression decreases; therefore miR-34a may suppress SIRT1 and induce apoptosis [55, 56]. Zhao et al. [57] examined the effects of zinc deficiency on testes and measured SIRT1 protein expression in mouse testicular tissues with type 1 diabetes. The results indicated that SIRT1 expression was significantly decreased in the diabetes groups. The investigators suggested that zinc regulates SIRT1 activity in diabetic testicular tissues.

Currently, there is a limited number of research studies examining the expression of SIRT6. SIRT6 and SIRT1 are involved in the maturation processes of spermatids [58]. A study of mouse testicles showed that SIRT6 was expressed in both the nuclei and cytoplasm of spermatogonia, spermatocytes, and early spermatids [59]. An obesity study based on a high-fat diet did not find a significant difference in SIRT6 expression between the control and diet groups, showing nuclear immunoreactivity in early and late spermatids. A significant decrease in SIRT6 expression led to a decrease in sperm protamination. Of note, in testicular germ cells, a decrease in SIRT6 expression was associated with an increase in H3K9 acetylation and DNA damage [60]. Fan et al. [61] stated that, in diabetic nephropathy, apoptosis increases due to a decrease in SIRT6 expression in podocytes; particularly in adenosine 5' monophosphate-activated protein kinase (AMPK) dephosphorylation and mitochondrial dysfunction. Liu et al. [62] suggested that SIRT6 is the regulator of the Wnt signal and exerts anti-inflammatory and antiapoptotic effects by inhibiting H3K9 deacetylation and Notch1/Notch4 transcription factors. However, Tao et al. [16] revealed for the first time that SIRT6, similarly to SIRT1, deacetylated KU70 and inhibited KU70/Bax-related apoptosis in a hepatocellular carcinoma cell culture model. Zhang et al. [63] examined the expression of SIRT6 and KU70 in human dental pulp cells undergoing apoptosis induced by bacterial

lipopolysaccharides. They reported that SIRT6 increased KU70/Bax binding and inhibited apoptosis by deacetylation of KU70. A recent study has reported that SIRT6 expression on mice testes. It has shown that SIRT6 expression may be associated with fertility [64].

In conclusion, the results of the present study may contribute to the knowledge regarding the possible roles of KU70, SIRT1, and SIRT6 proteins in diabetic testicular tissues, apoptosis, and infertility, as well as provide directions for the development of new treatment protocols.

### Acknowledgement

This study was supported by a grant from the Trakya University Scientific Research Committee, Edirne, Turkey (Project number: 2017/184).

The authors also thank Istanbul Bilgi University for contributing to the proofreading service.

### REFERENCES

- [1] Gökdemir GŞ, Baylan M. The effect of gliclazide use on BDNF and NGF levels in rats with diabetes mellitus. *South Clin Ist Euras*. 2023;34(4):306-311.
- [2] Raffaele M, Li Volti G, Barbagallo IA, Vanella L. Therapeutic efficacy of stem cells transplantation in diabetes: role of heme oxygenase. *Front Cell Dev Biol*. 2016;4:80.
- [3] Zha W, Bai Y, Xu L, et al. Curcumin attenuates testicular injury in rats with streptozotocin-induced diabetes. *BioMed Res Int*. 2018;2018:7468019.
- [4] Alves MG, Martins AD, Rato L, Moreira PI, Socorro S, Oliveira PF. Molecular mechanisms beyond glucose transport in diabetes-related male infertility. *Biochim Biophys Acta*. 2013;1832(5):626-635.
- [5] Amaral S, Oliveira PJ, Ramalho-Santos J. Diabetes and the impairment of reproductive function: possible role of mitochondria and reactive oxygen species. *Curr Diabetes Rev*. 2008;4(1):46-54.
- [6] Ersoy O, Kizilay G. Effects of fucoidan on diabetic rat testicular tissue. *Biotech Histochem*. 2018;93(4):277-285.
- [7] Trindade AA, Simoes AC, Silva RJ, Macedo CS, Spadella CT. Long term evaluation of morphometric and ultrastructural changes of testes of alloxan-induced diabetic rats. *Acta Cir Bras*. 2013;28(4):256-265.
- [8] Fell, VL, Schild-Poulter C. The Ku heterodimer: function in DNA repair and beyond. *Mutat Res Rev Mutat Res*. 2015;763:15-29.
- [9] Hada M, Kwok RP. Regulation of Ku70-Bax complex in cells. *J Cell Death*. 2014;7:11-13.
- [10] Bayram A, İğci M. Sirtuin genes and functions. *Fırat Med J*. 2013;18(3):136-140.
- [11] Chalkiadaki A, Guarente L. The multifaceted functions of sirtuins in cancer. *Nat Rev Cancer*. 2015;15(10):608-624.
- [12] Gomez JA, Gama V, Yoshida T, Sun W, Hayes P, Leskov K, et al. Bax-inhibiting peptides derived

- from Ku70 and cell-penetrating pentapeptides. *Biochem Soc Trans.* 2007;35(Pt 4):797-801.
- [13] Michan S, Sinclair D. Sirtuins in mammals: insights into their biological function. *Biochem J.* 2007;404(1):1-13.
- [14] Sharma A, Diecke S, Zhang WY, Lan F, He C, Mordwinkin NM, et al. The role of SIRT6 protein in aging and reprogramming of human induced pluripotent stem cells. *J Biol Chem.* 2013;288(25):18439-18447.
- [15] Wang W, Sun W, Cheng Y, Xu Z, Cai L. Role of sirtuin-1 in diabetic nephropathy. *J Mol Med (Berl).* 2019;97(3):291-309.
- [16] Tao NN, Ren JH, Tang H, Ran LK, Zhou HZ, Liu B, et al. Deacetylation of Ku70 by SIRT6 attenuates Bax-mediated apoptosis in hepatocellular carcinoma. *Biochem Biophys Res Commun.* 2017;485(4):713-719.
- [17] Nasirian F, Sarir H, Moradi-kor N. Antihyperglycemic and antihyperlipidemic activities of *Nannochloropsis oculata* microalgae in streptozotocin-induced diabetic rats. *Biomol Concepts.* 2019;10(1):37-43.
- [18] Franca L, Suescun M, Miranda J, Giovambatista A, Perello M, Spinedi E, et al. Testis structure and function in a nongenetic hyperadipose rat model at prepubertal and adult ages. *Endocrinology.* 2006;147(3):1556-1563.
- [19] Sadik NA, El-Seweidy MM, Shaker OG. The antiapoptotic effects of sulphurous mineral water and sodium hydrosulphide on diabetic rat testes. *Cell Physiol Biochem.* 2011;28(5):887-898.
- [20] Bayram S, Kizilay G, Topcu-Tarlacalisir Y. Evaluation of the Fas/FasL signaling pathway in diabetic rat testis. *Biotech Histochem.* 2016;91(3):204-211.
- [21] Li C, Wang L, Zheng L, et al. SIRT1 expression is associated with poor prognosis of lung adenocarcinoma. *OncoTargets Ther.* 2015;8:977.
- [22] Choi EK, Lee YH, Choi YS, Kwon HM, Choi MS, Ro JY, et al. Heterogeneous expression of Ku70 in human tissues is associated with morphological and functional alterations of the nucleus. *J Pathol.* 2002;198(1):121-130.
- [23] Jangir RN, Jain GC. Diabetes mellitus induced impairment of male reproductive functions: a review. *Curr Diabetes Rev.* 2014;10(3):147-157.
- [24] Ghosh S, Chowdhury S, Das AK, Sil PC. Taurine ameliorates oxidative stress induced inflammation and ER stress mediated testicular damage in stz-induced diabetic Wistar rats. *Food Chem Toxicol.* 2019;124:64-80.
- [25] Cameron DF, Murray FT, Drylie DD. Interstitial compartment pathology and spermatogenic disruption in testes from impotent diabetic men. *Anat Rec.* 1985;213(1):53-62.
- [26] Öztürk F, Gül M, Ağkadir M, Yağmurca M. Histological alterations of rat testes in experimental diabetes. *Turkiye Klinikleri J Med Sci.* 2002;22(2):173-178.
- [27] Koroglu P, Senturk GE, Yucel D, Ozakpinar OB, Uras F, Arbak S. The effect of exogenous oxytocin on streptozotocin (STZ)-induced diabetic adult rat testes. *Peptides.* 2015;63:47-54.
- [28] Kianifard D, Sadrkhanlou RA, Hasanzadeh S. The ultrastructural changes of the Sertoli and leydig cells following streptozotocin induced diabetes. *Iran J Basic Med Sci.* 2012;15(1):623-635.
- [29] Cambay Z, Baydas G, Tuzcu M, Bal R. Pomegranate (*Punica granatum L.*) flower improves learning and memory performances impaired by diabetes mellitus in rats. *Acta Physiol Hung.* 2011;98(4):409-420.
- [30] Ding C, Wang Q, Hao Y, Ma X, Wu L, du M, et al. Vitamin D supplement improved testicular function in diabetic rats. *Biochem Biophys Res Commun.* 2016;473(1):161-167.
- [31] Öztaş E, Yılmaz TE, Güzel E, Sezer Z, Okyar A, Özhan G. Gliclazide alone or in combination with atorvastatin ameliorated reproductive damage in streptozotocin-induced type 2 diabetic male rats. *Saudi Pharm J.* 2019;27(3):422-431.
- [32] Wankeu-Nya M, Florea A, Bâlici S, Watcho P, Matei H, Kamanyi A. *Dracaena arborea* alleviates ultra-structural spermatogenic alterations in streptozotocin-induced diabetic rats. *BMC Compl Alternative Med.* 2013;13(1):71.
- [33] Yin Y, DeWolf WC, Morgentaler A. Experimental cryptorchidism induces testicular germ cell apoptosis by p53-dependent and-independent pathways in mice. *Biol Reprod.* 1998;58(2):492-496.
- [34] Li Y-J, Song T-B, Cai Y-Y, et al. Bisphenol A exposure induces apoptosis and upregulation of Fas/FasL and caspase-3 expression in the testes of mice. *Toxicol Sci.* 2009;108(2):427-436.
- [35] Liu Y, Yang Z, Kong D, Zhang Y, Yu W, Zha W. Metformin ameliorates testicular damage in male mice with streptozotocin-induced type 1 diabetes through the PK2/PKR pathway. *Oxid Med Cell Longev.* 2019;2019:5681701.
- [36] Koh PO. Streptozotocin-induced diabetes increases apoptosis through JNK phosphorylation and Bax activation in rat testes. *J Vet Med Sci.* 2007;69(9):969-971.
- [37] Koh PO. Streptozotocin-induced diabetes increases the interaction of Bad/Bcl-XL and decreases the binding of pBad/14-3-3 in rat testis. *Life Sci.* 2007;81(13):1079-1084.
- [38] İrtegün S, Deveci E. Examining the expression level of VEGF and Bcl-2 by immunohistochemistry and western blot in testis tissue of diabetic rats. *Dicle Med J.* 2016;43(4):527-533.
- [39] Khamis T, Abdelalim AF, Abdallah SH, Saeed AA, Edress NM, Arisha AH. Early intervention with breast milk mesenchymal stem cells attenuates the development of diabetic-induced testicular dysfunction via hypothalamic Kisspeptin/Kiss1r-GnRH/GnIH system in male rats. *Biochim Biophys Acta Mol Basis Dis.* 2020;1866(1):165577.
- [40] Ahmed EA, Sfeir, A, Takai H, Scherthan H. Ku70 and non-homologous end joining protect testicular cells from DNA damage. *J Cell Sci.* 2013;126(14):3095-104.

- [41] Tuncdemir M, Ozturk M. Regulation of the Ku70 and apoptosis-related proteins in experimental diabetic nephropathy. *Metabolism*. 2016;65(10):1466-1477.
- [42] Wang Y, Lai L, Guo W, Peng S, Liu R, Hong P, et al. Inhibition of Ku70 in a high-glucose environment aggravates bupivacaine-induced dorsal root ganglion neurotoxicity. *Toxicol Lett*. 2020;318:104-113.
- [43] Xu T, Liu Y, Li P, Xu X, Zeng J. Insulin in combination with selenium inhibits HG/Pal-induced cardiomyocyte apoptosis by Cbl-b regulating p38MAPK/CBP/Ku70 pathway. *Eur Rev Med Pharmacol Sci*. 2016;20(15):3297-3303.
- [44] Kerr E, Holohan C, McLaughlin KM, et al. Identification of an acetylation-dependant Ku70/FLIP complex that regulates FLIP expression and HDAC inhibitor-induced apoptosis. *Cell Death Differ*. 2012;19(8):1317-1327.
- [45] Matsuyama S, Palmer J, Bates A, Poventud-Fuentes I, Wong K, Ngo J, et al. Bax-induced apoptosis shortens the life span of DNA repair defect Ku70-knockout mice by inducing emphysema. *Exp Biol Med*. 2016;241(12):1265-1271.
- [46] McBurney MW, Yang X, Jardine K, Hixon M, Boekelheide K, Webb JR, et al. The mammalian SIR2 protein has a role in embryogenesis and gametogenesis. *Mol Cell Biol*. 2003;23(1):38-54.
- [47] Ogawa T, Wakai C, Saito T, et al. Distribution of the longevity gene product, SIRT1, in developing mouse organs. *Congenit Anom*. 2011;51(2):70-79.
- [48] Al-Bader M, Kilarkaje N. Effects of Trans-Resveratrol on hyperglycemia-induced abnormal spermatogenesis, DNA damage and alterations in poly (ADP-ribose) polymerase signaling in rat testis. *Toxicol Appl Pharmacol*. 2016;311:61-73.
- [49] Al-Bader M, Kilarkaje N. Dataset of Trans-Resveratrol on diabetes-induced abnormal spermatogenesis, poly (ADP-ribose) polymerase-1 (PARP1) expression in intra-testicular blood vessels, and stage-dependent expression of PARP1 and Sirtuin 1 in the rat testis. *Data Brief*. 2017;10:230-237.
- [50] He W, Liu H, Hu L, Wang Y, Huang L, Liang A, et al. Icaritin improves testicular dysfunction via enhancing proliferation and inhibiting mitochondria-dependent apoptosis pathway in high-fat diet and streptozotocin-induced diabetic rats. *Reprod Biol Endocrinol*. 2021;19(1):168.
- [51] Huang T, Zhou Y, Lu X, Tang C, Ren C, Bao X, et al. Cordycepin, a major bioactive component of *Cordyceps militaris*, ameliorates diabetes-induced testicular damage through the Sirt1/Foxo3a pathway. *Andrologia*. 2022;54(1):e14294.
- [52] Lei X, Huo P, Xie YJ, Wang Y, Liu G, Tu H, et al. *Dendrobium nobile* Lindl polysaccharides improve testicular spermatogenic function in streptozotocin-induced diabetic rats. *Mol Reprod Dev*. 2022;89(4):202-213.
- [53] Wang P, Zhang S, Lin S, Lv Z. Melatonin ameliorates diabetic hyperglycaemia-induced impairment of Leydig cell steroidogenic function through activation of SIRT1 pathway. *Reprod Biol Endocrinol*. 2022;20(1):117.
- [54] Zhang S, Zhang M, Sun S, Wei X, Chen Y, Zhou P, et al. Moderate calorie restriction ameliorates reproduction via attenuating oxidative stress-induced apoptosis through SIRT1 signaling in obese mice. *Ann Transl Med*. 2021;9(11):933.
- [55] Gaderpour S, Ghiasi R, Hamidian G, Heydari H, Keyhanmanesh R. Voluntary exercise improves spermatogenesis and testicular apoptosis in type 2 diabetic rats through alteration in oxidative stress and mir-34a/SIRT1/p53 pathway. *Iran J Basic Med Sci*. 2021;24(1):58-65.
- [56] Jiao D, Zhang H, Jiang Z, Huang W, Liu Z, Wang Z, et al. MicroRNA-34a targets sirtuin 1 and leads to diabetes-induced testicular apoptotic cell death. *J Mol Med*. 2018;96(9):939-949.
- [57] Zhao Y, Tan Y, Dai J, Wang B, Li B, Guo L, et al. Zinc deficiency exacerbates diabetic down-regulation of Akt expression and function in the testis: essential roles of PTEN, PTP1B and TRB3. *J Nutr Biochem*. 2012;23(8):1018-1026.
- [58] Tatone C, Di Emidio G, Barbonetti A, Carta G, Luciano AM, Falone S, et al. Sirtuins in gamete biology and reproductive physiology: emerging roles and therapeutic potential in female and male infertility. *Hum Reprod Update*. 2018;24(3):267-289.
- [59] Ki BS, Park M, Woo Y, Lee WS, Ko JJ, Choi Y. Expression of Sirt1, Sirt2, Sirt5, and Sirt6 in the mouse testis. *Reprod Dev Biol*. 2015;39(2):73-47.
- [60] Palmer NO, Fullston T, Mitchell M, Setchell BP, Lane M. SIRT6 in mouse spermatogenesis is modulated by diet-induced obesity. *Reprod Fertil Dev*. 2011;23(7):929-939.
- [61] Fan Y, Yang Q, Yang Y, Gao Z, Ma Y, Zhang L, et al. Sirt6 suppresses high glucose-induced mitochondrial dysfunction and apoptosis in podocytes through AMPK activation. *Int J Biol Sci*. 2019;15(3):701-713.
- [62] Liu M, Liang K, Zhen J, Zhou M, Wang X, Wang Z, et al. Sirt6 deficiency exacerbates podocyte injury and proteinuria through targeting Notch signaling. *Nat Commun*. 2017;8(1):1-15.
- [63] Zhang L, Bai L, Ren Q, Sun G, Si Y. Protective effects of SIRT6 against lipopolysaccharide (LPS) are mediated by deacetylation of Ku70. *Mol Immunol*. 2018;101:312-318.
- [64] Li L, Chen B, An T, Zhang H, Xia B, Li R, et al. BaZiBuShen alleviates altered testicular morphology and spermatogenesis and modulates Sirt6/P53 and Sirt6/NF-κB pathways in aging mice induced by D-galactose and NaNO<sub>2</sub>. *J Ethnopharmacol*. 2021;10;271:113810.

## Green Synthesis of Apricot Kernel Silver Nanoparticles and Their Biological Activity

İbrahim BAYAV<sup>1\*</sup>, Adnan AYNA<sup>2</sup>, Sevda SAĞ<sup>1</sup>, Muhammet Veysel NAZLI<sup>3</sup>, Faruk ALTINBAŞAK<sup>4</sup>, İlay BOZ<sup>5</sup>, Ekrem DARENDELİOĞLU<sup>3</sup>

<sup>1</sup> Pamukkale University, Faculty of Medicine, Department of Medical Biology, Denizli, Türkiye

<sup>2</sup> Bingöl University, Faculty of Arts and Sciences, Department of Chemistry, Bingöl, Türkiye

<sup>3</sup> Bingöl University, Faculty of Arts and Sciences, Department of Molecular Biology and Genetics, Bingöl, Türkiye

<sup>4</sup> Hitit University, Faculty of Medicine, Department of Histology and Embryology, Çorum, Türkiye

<sup>5</sup> Pamukkale University, Faculty of Medicine, Department of Histology and Embryology, Denizli, Türkiye

İbrahim BAYAV ORCID No: 0000-0002-3533-3935

Adnan AYNA ORCID No: 0000-0001-6801-6242

Sevda SAĞ ORCID No: 0000-0001-8258-7324

Muhammet Veysel NAZLI ORCID No: 0000-0002-8847-4694

Faruk ALTINBAŞAK ORCID No: 0000-0002-6816-1367

İlay BOZ ORCID No: 0009-0003-8856-1602

Ekrem DARENDELİOĞLU ORCID No: 0000-0002-0630-4086

\*Corresponding author: [ibayav22@posta.pau.edu.tr](mailto:ibayav22@posta.pau.edu.tr)

(Received: 09.07.2024, Accepted: 21.08.2024, Online Publication: 26.09.2024)

### Keywords

Apricot kernel,  
Silver nanoparticles,  
Cytotoxicity,  
Cancer,  
Antimicrobial

**Abstract:** Silver nanoparticles (AgNPs) exhibit cytotoxicity in various cancer cells, as well as high conductivity, chemical stability, catalytic, and antibacterial activity. A range of biological sources, including plants, fungi, and bacteria, are utilized for the synthesis of silver, gold, and other nanoparticles. The aim of this study is to synthesize environmentally friendly and cost-effective AgNPs from apricot kernel methanol extract and to investigate their antimicrobial and cytotoxic activities. The synthesized AgNPs were characterized using UV-vis spectroscopy, X-ray diffraction (XRD), scanning electron microscopy (SEM), and Fourier-transform infrared spectroscopy (FTIR). The UV-vis spectra revealed a surface plasmon resonance peak at 420 nm, confirming the formation of apricot kernel silver nanoparticles. Additionally, FTIR spectra indicated the involvement of biological compounds in the synthesis of AgNPs. The synthesized AgNPs inhibited the growth of both Gram-negative and Gram-positive bacteria, including *E. aerogenes* CCM 2531, *B. subtilis* IM 622, *S. aureus* 6538 P, *S. aureus* ATCC 29213, and *L. monocytogenes* NCTL 53448. Furthermore, AgNPs reduced the viability of SH-SY5Y neuroblastoma cells. Based on these findings, it can be suggested that the environmentally friendly synthesized AgNPs exhibit multifunctional properties with potential applications against infectious bacterial strains and cancer.

## Kayısı Çekirdeği Gümüş Nanopartiküllerinin Yeşil Sentezi ve Biyolojik Aktiviteleri

**Anahtar Kelimeler**  
Kayısı çekirdeği,  
Gümüş nanopartikül,  
Sitotoksosite,  
Kanser,  
Antimikrobiyal

**Öz:** Gümüş nanopartiküllerin (AgNP'ler), çeşitli kanser hücrelerinde sitotoksositeye, yüksek iletkenliğe, kimyasal stabiliteye, katalitik ve antibakteriyel aktiviteye sahiptir. Gümüş, altın ve diğer nanoparçacıkların sentezi için bitkiler, mantarlar ve bakteriler dahil olmak üzere birçok biyolojik kaynak kullanılmaktadır. Bu çalışmanın amacı, çevre dostu ve uygun maliyetli AgNP'lerin kayısı çekirdeği metanol ekstraktından sentezlenmesi ile antimikrobiyal ve sitotoksik aktivitelerini araştırmaktır. Sentezlenen AgNP'ler UV-vis, X-ışını kırınımı (XRD), Taramalı Elektron Mikroskobu (SEM) ve Fourier dönüşümlü kızılötesi spektroskopisi (FTIR) ile karakterize edildi. UV-vis spektrumları, kayısı çekirdeği gümüş nanoparçacıklarının oluşumunu doğrulayan 420nm'de yüzey plazmon rezonans pikini ortaya çıkardı. FTIR spektrumları ayrıca biyolojik bileşiklerin AgNP'lerin sentezine katılımını göstermiştir. Sentezlenen AgNP'ler *E. aerogenes* ccm 2531, *B. subtilis* IM 622, *S. Aureus*

6538 p., *S. Aureus ATCC 29213* ve *L. monocytogenes NCTL 53448* olmak üzere gram negatif ve gram pozitif bakterilerin büyümesini engelledi. AgNP'ler ayrıca, SHSY5Y nöroblastom hücrelerinin canlılığını azalttı. Bu bulgulara dayanarak, çevre dostu sentezlenen AgNP'lerin çok işlevli özellikler gösterdiği, bulaşıcı bakteri türlerine ve kansere karşı kullanılabilme potansiyeli sahip olduğu söylenebilir.

## 1. INTRODUCTION

Neuroblastoma (NB) is a type of pediatric tumor that arises from neural tissues within the central nervous system (CNS) [1, 2]. It is one of the most common cancers found in infants and children, following leukemia and brain tumors. Additionally, NB serves as a model in neuroprotection research, aiding in the development of new therapeutic and preventive strategies for CNS-related disorders. Treatment approaches for NB are influenced by the severity of the disease, the patient's age, and underlying biological factors [3, 4]. Given these complexities, there is a pressing need for research focused on discovering novel biochemical compounds and innovative treatment strategies for NB.

For many years herbal medicines have been used as the primary source of medical treatment. The apricot has been used in folk medicine as a remedy for various diseases attributed to its rich antioxidant, antimicrobial and anticancer content [5,6]. The apricot fruit constitutes carbohydrates, vitamins, beta carotene and thiamine. Apricot kernels (Ak) contain a significant amount of protein, oil and fibre. Apricot kernels also contain the toxic cyanogenic glycoside amygdalin [5,7-9].

The eco-friendly synthesis of silver nanoparticles (AgNPs) by biological materials has considerable attention in view of therapeutic aspects. Environmentally friendly synthesis of nanoparticles by biological resources extract is currently under investigation. The AgNPs are reported to have numerous different biological applications. The study of antimicrobial and anticancer activity of these biosynthesized nanoparticles gives an idea of the activity and association of these nanoparticles with biomolecules of living systems [10-12].

Numerous research regarding the physico-chemical features of Ak are presented in the literature Gupta et al. [8], but not much knowledge is found regarding the in vitro antioxidant activities of the Ak. Likewise, the anticancer and antimicrobial activities of Ak have been less studied and the lack of research related to the antibacterial and anticancer activity of the kernels along with their nanoparticles have motivated the present study. In the present study, single step synthesis of the AgNPs by the reduction of silver nitrate (AgNO<sub>3</sub>) at room temperature by Ak methanol extracts are presented. The synthesis of NPs has been monitored by UV-Visible spectroscopy (UV-Vis), Scanning Electron Microscopy (SEM), X-Ray Diffraction (XRD) and Fourier Transform Infrared Spectroscopy (FTIR). The synthesised AgNPs were evaluated for their anticancer and antimicrobial activity.

## 2. MATERIAL AND METHOD

### 2.1. Preparation of Ak Extracts

The extract was prepared from 200 gr Ak by granulating in a mortar and was extracted with 1 liter methanol. The mixture was sealed with aluminium foil and stirred for 24 hours. Following that, the extract was filtered with Whatman No.1 filter paper and the pellet was discarded while supernatant was stored at 4 °C.

### 2.2. Synthesis of Ak AgNPs (AkAgNPs)

100 ml of methanol extract was mixed with 900 ml of 1 mM AgNO<sub>3</sub> under magnetic stirring at room temperature. The greyish colour of the extract-AgNO<sub>3</sub> mixture at 0 min of reaction time changed to a dark brown in about 10 minutes after justifying pH of the mixture to alkali with NaOH. After observing the colour change, the absorbance of the dark brown mixture was measured at 430 nm by UV-vis spectrophotometer to observe the formation of AkAgNPs. Following that the mixture was centrifuged at 15000 rpm for 15 min and subsequently washed in pure water for 5 times at 15000 rpm to discard waste biological material.

### 2.3. Characterization of AkAgNPs

Initial characterisation of AkAgNPs were carried out by UV-Vis (Shimadzu UV-3600 UV-VIS-NIR Spectrophotometer) to determine the absorption spectra of the AkAgNPs between 200–800 nm.

The FTIR spectra were measured by the dried pellet method at resolution of between 4,000 to 400 cm<sup>-1</sup> (Perkin Elmer Spectrum 100) for the Ak extract powders and AkAgNPs.

The nanoparticles were further characterized by XRD using a Rigaku Optima IV diffractometer with Cu K $\alpha$  radiation ( $\lambda = 0.1542$  nm).

The morphology of the AkAgNPs was characterised by SEM (JEOL). Samples were examined on a graphite-coated surface to obtain a uniform image by providing conductivity.

### 2.4. Anti-microbial Activity Test

The antimicrobial activity of synthesised AkAgNPs were investigated against *Enterobacter aerogenes ccm 2531*, *Bacillus subtilis IM 622*, *Staphylococcus aureus 6538 p.*, *Staphylococcus aureus ATCC 29213* and *Listeria monocytogenes NCTL 5348*. The antimicrobial activity was tested using the spread plate agar method, in which 6 mm discs placed on plates based. Distilled water was

used as negative control, penicillin and streptomycin mixture was used as positive control, Ak extract, AgNO<sub>3</sub> and different doses of AkAgNPs were absorbed into the disks. After incubating the plates at 37°C for 24 h, the diameter of the inhibition zone was measured with image J [13].

## 2.5. Cell Culture

Human NB cells (SH-SY5Y; American Type Culture Collection (ATCC, USA)) were cultured in Dulbecco's Modified Eagle Medium (DMEM) containing 10% FBS and 1% penicillin-streptomycin solution (Biological Industries, Israel). The cells were cultured as described in [14].

## 2.6. Cell Proliferation Assay

WST-1 cell proliferation assay kit (Clontech, USA) was used to analyse cell proliferation and viability. Briefly,  $15 \times 10^3$  NB cells/well in a 100- $\mu$ l medium were cultured in 96 well plates. 24 hour later, different concentrations of Ak extracts and AkAgNPs (8 mg/ml and 4 mg/ml) were added into the wells. The assay was performed according to the instructions supplied with kit.

## 2.7. Statistical Analyses

All experiments were repeated at least 3 times, and biostatistical analysis was carried out with GraphPad Prism 5.0. Data sets were compared and the analyses were performed with by one-way ANOVA Newman-Keuls Post-Hoc Test

## 3. RESULTS

### 3.1. Characterisation of Nanoparticles

Green synthesis AkAgNPs from 1 mM aqueous solution of AgNO<sub>3</sub> (pH 11,2) with Ak extract was initially confirmed by UV-Vis spectral analysis.

The initial greyish colour of the reaction mixture of the extract with AgNO<sub>3</sub> solution changed to dark brown colour as a result of excitation of surface plasmon resonance vibration of AkAgNPs. The surface plasmon of AkAgNPs occurred at about 420 nm for Ak extract reacted with AgNO<sub>3</sub> (Fig. 1). It is worth noting the reduction of Ag<sup>+</sup> ions by the extract was occurred in about 10 minutes at room temperature.

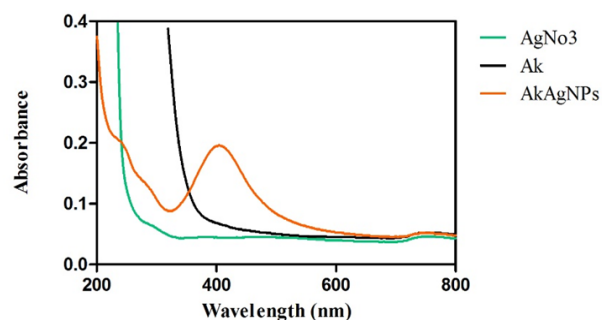


**Figure 1.** UV-Vis absorption spectra of AgNO<sub>3</sub>, Ak extract, AkAgNPs (AgNO<sub>3</sub>; silver nitrate, Ak Extract; apricot kernel extract; AkAgNPs; synthesized AgNPs with apricot kernel extract)

The FTIR measurements of biosynthesized AkAgNPs were performed to understand the interaction between biomolecules of the Ak extract and Ag<sup>+</sup> ions. FTIR spectra of AkAgNPs showed absorption peak situated at about 3336, 2925, 2853, 1742, 1638 and 1016 cm<sup>-1</sup>. The very intense broad band positioned at about 3336 cm<sup>-1</sup> position in the spectra of AkAgNPs could be attributed to O-H stretching. The peak placed at about 2925 and 2853 cm<sup>-1</sup> in the spectra could represent C-H stretching of alkyl group while stretching vibration at 2853 cm<sup>-1</sup> could be attributed to C-H stretching of aldehydes group. The absorption peaks located at 1,638 cm<sup>-1</sup> in both spectra represents N-H stretch of amines. The peak 1016 cm<sup>-1</sup> represents C-N stretching of aliphatic amines (Fig. 2).

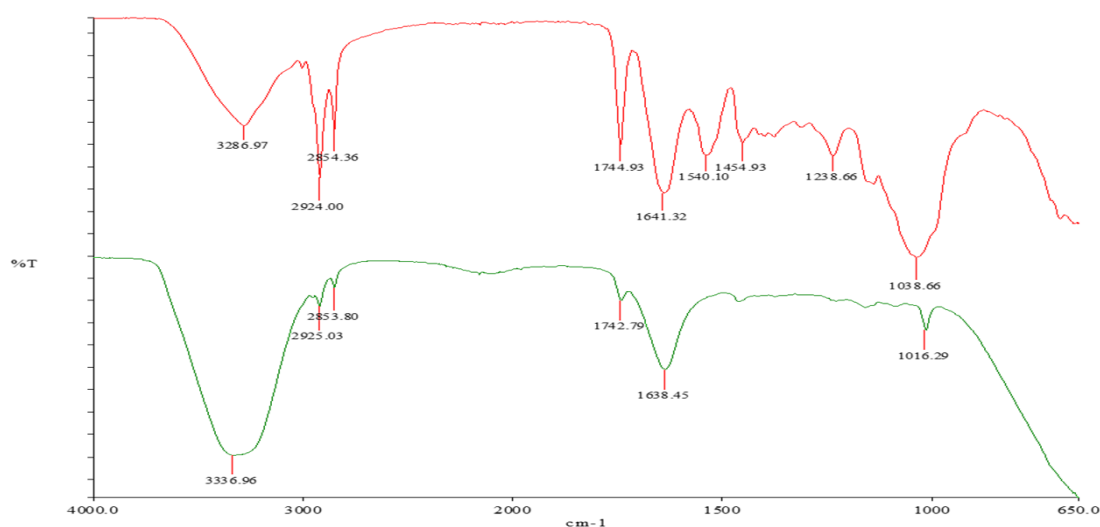


**Figure 2.** FTIR spectra of synthesized AkAgNPs (Green) and Ak Extract (Red)



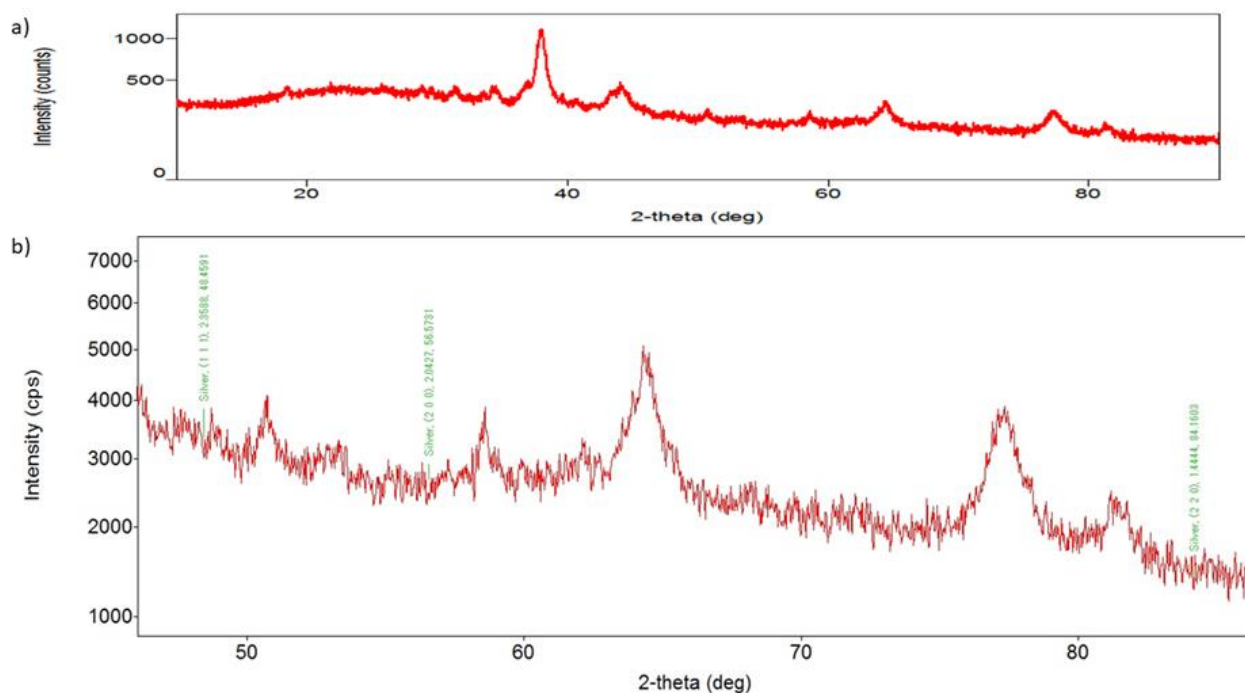


**Figure 3.** XRD spectrum of the nanoparticles. a) The nanoparticles revealed the presence of six distinct diffraction peaks at  $2\theta = 34.36^\circ, 37.885^\circ, 43.98^\circ, 64.42^\circ, 77.02^\circ, 81.65^\circ$ . b) The cubic silver indices of AkAgNPs crystals; 111, 200, 220, and 311

The presence of these vibrations at FTIR spectra suggests that some of the bio-organic molecules such as carbohydrates, proteins, oils, enzymes and amino acids are responsible for the reduction of  $\text{Ag}^+$  ions and hence nanoparticle formation.

The crystalline structure of the AkAgNPs were confirmed by XRD analyses. XRD spectrum of the nanoparticles revealed the presence of six distinct diffraction peaks at  $2\theta = 34.36^\circ, 37.885^\circ, 43.98^\circ, 64.42^\circ, 77.02^\circ, 81.65^\circ$  that can be indexed at 111, 200, 220, and 311 of the cubic silver suggesting that the AkAgNPs were crystalline (Fig. 3).

SEM micrographs of AkAgNPs at room temperature showed the presence of very well dispersed AkAgNPs. The analysis of particle size distribution revealed that the majority of the particles are between 0.4 to 0.9  $\mu\text{m}$  at 1000 magnification (Fig. 4).

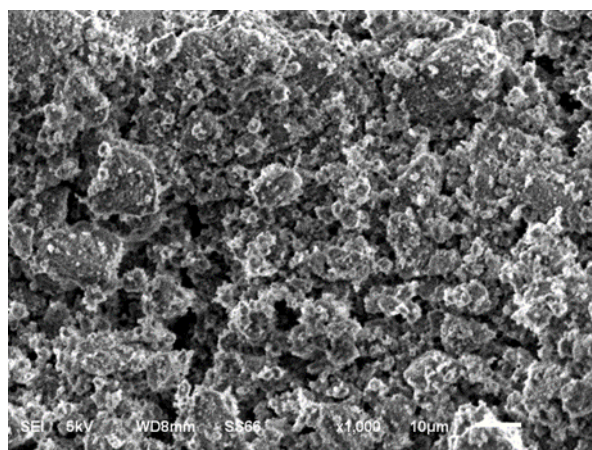


**Figure 4.** SEM micrograph of synthesised AkAgNPs

### 3.2. Antimicrobial Activity of AkAgNPs

The antimicrobial activity of AkAgNPs were tested against *E. aerogenes ccm 2531*, *B. subtilis IM 622*, *S. aureus 6538 p.*, *S. aureus ATCC 29213* and *L. monocytogenes NCTL 5348* using the disc diffusion method and the results were presented in table 1. The synthesised nanoparticles inhibited the growth of gram-negative bacterium *E. aerogenes ccm 2531* and gram positive bacteria such as *B. subtilis IM 622*, *S. aureus 6538 p.*, *S. aureus ATCC 29213* and *L. monocytogenes NCTL 5348* (2 and 4 mg/mL). 4 mg/ml  $\text{AgNO}_3$  and Ak extract did not inhibit the growth of the microorganisms.

**Table 1.** Antibacterial activity of AkAgNPs against gram negative and gram positive bacteria. The inhibition zones are given as cm.

Bacteria	AkAgNPs (4 mg/ml)	AkAgNPs (2 mg/ml)	Ak extract (4mg/ml)	Antibiotic	$\text{AgNO}_3$ (4mg/ml)	Water
<i>E. aerogenes ccm 2531</i> (Gr -)	0.840	0.775	0.696	1.940	0.631	0
<i>B. subtilis IM 622</i> (Gr +)	0.786	0.760	0.605	1.783	0.713	0
<i>S. aureus 6538 p.</i> (Gr +)	0.812	0.793	0.700	2.316	0.806	0
<i>S. aureus ATCC 29213</i> (Gr +)	0.660	0.700	0.512	2.037	0.643	0
<i>L. monocytogenes NCTL 5348</i> (Gr +)	0	0.89	0	2.260	0.655	0

### 3.3. Effects of AkAgNPs on SHSY5Y cell proliferation

The antiproliferative effect of the AkAgNPs and their extracts were assessed on NB cells. The cells were treated with different concentrations of AkAgNPs (4 and 8 mg/ml) over 24 hours, and the cell proliferations are given in Fig. 5. AkAgNPs significantly decreased cell viability at 4 and 8 mg/ml while the extract did not show anticancer activity on NB cells.

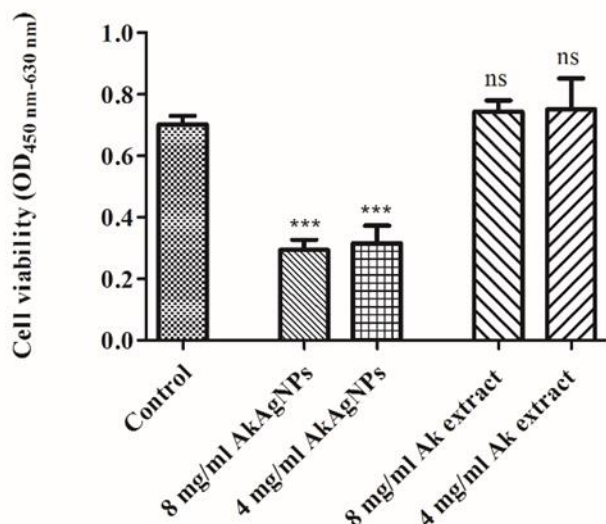


**Figure 5.** Anticancer activity of AkAgNPs in NB cell line. (\*\*\*) $p < 0.001$ ; Control vs other groups 8 mg/ml, 4 mg/ml; ns: not significant)

## 4. DISCUSSION AND CONCLUSION

Many studies regarding the physicochemical characteristics of Ak are reported in the literature Haciseferoğulları et al., Alpaslan et al. [15,16], but the in vitro anticancer and antimicrobial activities of Ak and their NPs have not been studied in detail and the lack of the research related to the antimicrobial and anticancer activity of the apricot seeds along with their nanoparticles have stimulated the present research. In the present study, single step synthesis of the AgNPs through the reduction of aqueous AgNO<sub>3</sub> at room temperature by Ak methanol extracts are presented.

Ak extracts contain high levels of amygdalin, protein, fat, and various antioxidant and anticancer molecules. However, these molecules are unable to cross lipid membranes, have large molecular sizes, are poorly absorbed, and are unstable, resulting in reduced bioavailability and efficacy. Therefore, using nanoparticles is essential to enhance their absorption and increase their stability by preventing oxidation. For this reason, AgNPs were synthesized from Ak extracts, and their biological activity was investigated. The different concentrations of Ak methanol extract (4 and 8 mg/mL) did not show an antiproliferative effect on NB cells, whereas AkAgNPs significantly decreased cell viability at both concentrations. Similarly, Grunathan et al. also demonstrated that AgNPs reduced cell viability in SH-SY5Y cells in a dose-dependent manner [17]. This

suggests that nanoparticle-based kernel extracts have the potential to increase the efficiency and safety of kernel biomolecules by enhancing their capacity, improving solubility, and controlling their release.

AgNPs are reported to show their antibacterial effect through interaction with the outer membranes of the bacteria thanks to their chemical stability and tiny size [18-21]. The silver ions leads toxicity by reacting thiol group of the enzymes located outer membranes of the microorganisms [22,23]. In addition to these antimicrobial activity of the NPs are reported to be arisen from ionic (electrostatic) interaction between negatively charged cell membrane and positively charged silver [24-26].

The antimicrobial activity of AkAgNPs was tested against *E. aerogenes ccm 2531*, *B. subtilis IM 622*, *S. aureus 6538 p.*, *S. aureus ATCC 29213* and *L. monocytogenes NCTL 5348*. Based on the results, it can be concluded that AkAgNPs inhibit the growth of both Gram-negative and Gram-positive bacteria. In recent years, some studies have suggested that Gram-positive bacteria may be resistant to the effects of nanoparticles due to differences in their cell wall structures [27-29]. Vadakkan et al. also reported that biogenic AgNPs exhibit strong antibacterial properties against a wide range of both Gram-positive and Gram-negative bacteria [30]. Additionally, Saied et al. demonstrated that Ak extract possesses antimicrobial properties [31]. The data obtained in this study are consistent with the literature, showing that AkAgNPs inhibit the growth of both Gram-negative and Gram-positive bacteria.

The anticancer and antimicrobial effects of AgNPs synthesized by reducing AgNO<sub>3</sub> with Ak methanol extracts at room temperature are presented. The environmentally friendly synthesized AkAgNPs demonstrated significant activity against both Gram-negative and Gram-positive bacteria. Additionally, their notable effectiveness against NB cancer cells suggests potential efficacy against other cancer types. In future studies, the effects of AkAgNPs on other cancer cell lines will be further explored.

### Acknowledgement

The authors wishes to thank Dr. Bülent Kaya and Dr. Fethi Ahmet Özdemir for their advices during experiments.

### REFERENCES

- [1] Maris J M. Recent advances in neuroblastoma. The New England journal of medicine. 2010;362 (23): 2202-2211.
- [2] Ricciardi V, Portaccio M, Piccolella S, Manti L, Pacifico S, Lepore M. Study of SH-SY5Y cancer cell response to treatment with polyphenol extracts using FT-IR spectroscopy. Biosensors. 2017;7(4): 57.
- [3] Kreissman S G, Villablanca J G, Diller L, London W B, Maris J M, Park J R. Response and toxicity to

- a dose-intensive multi-agent chemotherapy induction regimen for high risk neuroblastoma (HR-NB): a Children's Oncology Group (COG A3973) study. *J Clin Oncol Res.* 2007; 25(18): 9505-9505.
- [4] Jiang M, Stanke J, Lahti J M. The connections between neural crest development and neuroblastoma. In *Current topics in developmental biology.* Academic Press. 2011; 94: 77-127.
- [5] Fratianni F, Ombra M N, d'Acierno A, Cipriano L, and Nazzaro F. Apricots: biochemistry and functional properties. *Current Opinion in Food Science.* 2018; 19: 23-29.
- [6] Alexa E, Lalescu D, Berbecea A, Camen D, Poiana M A, Moigradean D, & Bala M. Chemical composition and antioxidant activity of some apricot varieties at different ripening stages. *Chilean journal of agricultural research.* 2018; 78(2): 266-275.
- [7] Naryal A, Bhardwaj P, Kant A, Chaurasia O P, Stobdan T. Altitude and seed phenotypic effect on amygdalin content in Apricot (*Prunus armeniaca* L.) kernel. *Pharmacognosy Journal.* 2019;11(2).
- [8] Gupta S, Chhajed M, Arora S, Thakur G, Gupta R. Medicinal value of Apricot: A Review. *Indian Journal of Pharmaceutical Sciences.* 2018;80(5): 790-794.
- [9] Dang T, Nguyen C, Tran P N. Physician beware: severe cyanide toxicity from amygdalin tablets ingestion. *Case Reports in Emergency Medicine.* 2017.
- [10] Chen B, Zhang Y, Yang Y, Chen S, Xu A, Wu L et al. Involvement of telomerase activity inhibition and telomere dysfunction in silver nanoparticles anticancer effects. *Nanomedicine.* 2018;13(16): 2067-2082.
- [11] Khatami M, Varma RS, Zafarnia N, Yaghoobi H, Sarani M, Kumar VG. Applications of green synthesized Ag, ZnO and Ag/ZnO nanoparticles for making clinical antimicrobial wound-healing bandages. *Sustainable Chemistry and Pharmacy,* 2018; 10:9-15.
- [12] Buttacavoli M, Albanese N N, Di Cara G, Alduina R, Faleri C, Gallo M et al. Anticancer activity of biogenerated silver nanoparticles: an integrated proteomic investigation. *Oncotarget.* 2018;9(11): 9685.
- [13] Abramoff M D, Magalhães P J, Ram S J. Image processing with ImageJ. *Biophotonics,* 2004;11(7): 36-42.
- [14] Waetzig V, Haeusgen W, Andres C, Frehse S, Reinecke K, Bruckmueller H et al. I. Retinoic acid-induced survival effects in SH-SY5Y neuroblastoma cells. *Journal of Cellular Biochemistry.* 2019;120(4): 5974-5986.
- [15] Haciseferoğullari H, Gezer I, Özcan M M, Murat Asma B. Post-harvest chemical and physical-mechanical properties of some apricot varieties cultivated in Turkey. *Journal of Food Engineering.* 2007;79(1): 364-373.
- [16] Alpaslan M, Hayta M. Apricot kernel: Physical and chemical properties. *Journal of The American Oil Chemists Society.* 2006;83(5): 469-471.
- [17] Gurunathan S, Jeyaraj M, Kang M H, & Kim J H. Mitochondrial peptide humanin protects silver nanoparticles-induced neurotoxicity in human neuroblastoma cancer cells (SH-SY5Y). *International journal of molecular sciences.* 2019; 20(18): 4439.
- [18] Sreekanth T V M, Nagajyothi P C, Supraja N, Prasad T N V K V. Evaluation of the antimicrobial activity and cytotoxicity of phyto-genic gold nanoparticles. *Applied Nanoscience.* 2015; 5(5): 595-602.
- [19] Grace A N, Pandian K. Antibacterial efficacy of aminoglycosidic antibiotics protected gold nanoparticles—A brief study. *Colloids and Surfaces A: Physicochemical and Engineering Aspects.* 2007;297(1-3): 63-70.
- [20] Tang S, Zheng J. Antibacterial activity of silver nanoparticles: structural effects. *Advanced healthcare materials.* 2018; 7(13): 1701503.
- [21] González-Fernández S, Lozano-Iturbe V, García B, Andrés LJ, Menéndez MF, Rodríguez, D, et al. Antibacterial effect of silver nanorings. *BMC microbiology.* 2020; 20:1-14.
- [22] Liu J, Sonshine D A, Shervani S, Hurt R H. Controlled release of biologically active silver from nanosilver surfaces. *American Chemical Society Applied Nano Materials.* 2010;4(11): 6903-6913.
- [23] Barros D, Pradhan A, Mendes VM, Manadas B, Santos PM, Pascoal C, Cássio F. Proteomics and antioxidant enzymes reveal different mechanisms of toxicity induced by ionic and nanoparticulate silver in bacteria. *Environmental Science. Nano.* 2019;6(4):1207-1218.
- [24] Bindhu M R, Umadevi M. Antibacterial activities of green synthesized gold nanoparticles. *American Chemical Society Materials Letters.* 2014;120: 122-125.
- [25] González-Fernández, S., Lozano-Iturbe, V., García, B., Andrés, L. J., Menéndez, M. F., Rodríguez, D., ... & Quirós, L. M. (2020). Antibacterial effect of silver nanorings. *BMC microbiology,* 20, 1-14.
- [26] Khina AG, Krutyakov YA. Similarities and differences in the mechanism of antibacterial action of silver ions and nanoparticles. *Applied Biochemistry and Microbiology.* 2021; 57:683-693.
- [27] Arasu M V, Arokiyaraj S, Viayaraghavan P, Kumar T S J, Duraipandiyan V, Al-Dhabi N A et al. One step green synthesis of larvicidal, and azo dye degrading antibacterial nanoparticles by response surface methodology. *Journal of Photochemistry and Photobiology B: Biology.* 2019;190: 154-162.
- [28] Silveira A P, Bonatto C C, Lopes C A P, Rivera L M R, Silva L P. Physicochemical characteristics and antibacterial effects of silver nanoparticles produced using the aqueous extract of *Ilex paraguariensis*. *Materials Chemistry and Physics.* 2018;216: 476-484.
- [29] Mukha I P, Eremenko A M, Smirnova N P, Mikhienkova A I, Korchak G I, Gorchev V F et al. Antimicrobial activity of stable silver nanoparticles of a certain size. *Applied*

Biochemistry and Microbiology. 2013;49(2): 199-206.

- [30] Vadakkan K, Rumjit N P, Ngangbam A K, Vijayanand S, Nedumpillil N K. Novel advancements in the sustainable green synthesis approach of silver nanoparticles (AgNPs) for antibacterial therapeutic applications. *Coordination Chemistry Reviews*, 2024; 499: 215528.
- [31] Saied M, Ward A, Hamieda S F. Effect of apricot kernel seed extract on biophysical properties of chitosan film for packaging applications. *Scientific Reports*. 2024; 14(1): 3430.

## Investigation Antioxidant, Antimicrobial and *In Vitro* Cytotoxic Effects on PC-3 Cancer Lines of *Alchemilla holotricha* Juz. in Different Polarities Extracts

Bülent KAYA<sup>1\*</sup>, Yekta ARTUVAN<sup>2</sup>, Fatma CAF<sup>3</sup>, Yusuf MENEMEN<sup>4</sup>

<sup>1\*</sup>Bülent Kaya, Faculty of Sciences and Arts, Molecular Biology and Genetics Department, University of Bingöl, 12000 Bingöl, Türkiye

<sup>2</sup>Yekta Artuvan, Faculty of Sciences and Arts, Biology Department, University of Bingöl, 12000 Bingöl, Türkiye

<sup>3</sup>Fatma Caf, Vocational School of Food, Agriculture, and Livestock, University of Bingöl, 12000 Bingöl, Türkiye

<sup>4</sup>Yusuf Menemen, Faculty of Sciences and Arts, Biology Department, University of Kırkkale, 71450, Kırkkale, Türkiye

Bülent KAYA ORCID No: 0000-0002-1216-6441

Yekta ARTUVAN ORCID No: 0000-0002-6321-7181

Fatma CAF ORCID No: 0000-0002-0363-4848

Yusuf MENEMEN ORCID No: 0000-0002-9546-7986

\*Corresponding author: [b\\_kaya\\_tr@yahoo.com](mailto:b_kaya_tr@yahoo.com),

(Received: 18.04.2024, Accepted: 22.08.2024, Online Publication: 26.09.2024)

### Keywords

*Alchemilla holotricha* Juz., Antimicrobial, Antioxidant, Anticytotoxic, Plant extracts

**Abstract:** The extracts of *Alchemilla holotricha* Juz. with different polarities were obtained using hexane, dichloromethane, ethyl acetate, methanol, and water. The samples were further analyzed for their overall antioxidant activity, ability to scavenge DPPH free radicals, capacity to chelate metals, total reducing power, ability to scavenging hydrogen peroxide, and hydroxy radical scavenging activity. The ethyl acetate extract exhibited the highest concentration of total phenols ( $67.63 \pm 0.88$  mg GAE/g extract), whereas both the ethyl acetate and dichloromethane extracts demonstrated the highest levels of total flavonoids ( $14.82 \pm 1.02$ - $14.82 \pm 0.03$  mg CE/g extract). On the other hand, the hexane extract displayed the highest content of phenolic acids ( $0.72 \pm 0.21$  mg SAE/g extract). The antimicrobial activity of each extract was assessed using the agar disk diffusion method. The *A. holotricha* strain's ethyl acetate fraction displayed the most potent antibacterial activity. The *Escherichia coli* exhibited the greatest antibacterial impact, measuring 17 mm, while the *Klebsiella pneumoniae* showed a somewhat lower effect of 15 mm. *Bacillus subtilis* had the highest level of resistance among the microorganisms tested, with a diameter of 8 mm. *A. holotricha* displayed the most potent antioxidant and antibacterial properties in the ethyl acetate extracts. The study showed that ethyl acetate, a solvent with moderate polarity, is more efficient at dissolving aromatic compounds in the above-ground portion of the plant compared to non-polar solvents like n-hexane and diethyl ether. Moreover, the water and methanol extracts exhibited cytotoxicity towards PC-3 cells at particular concentrations.

## *Alchemilla holotricha* Juz.'un Farklı Polaritelerdeki Ekstraktlarında Antioksidan, Antimikrobiyal ve PC-3 Kanser Hattı Üzerinde *In Vitro* Sitotoksik Etkilerinin Araştırılması

### Anahtar

### Kelimeler

*Alchemilla holotricha* Juz., Antimikrobiyal, Antioksidan, Antisitoksit, Bitki ekstraktları

*Alchemilla holotricha*'nın hekzan, diklorometan, etil asetat, metanol ve su ile farklı polariteli ekstraktları elde edildi. Daha sonra bu ekstraktların toplam antioksidan aktivite, DPPH serbest radikal uzaklaştırma aktivitesi, metal şelatlama kapasitesi, toplam indirgeme gücü, hidrojen peroksit uzaklaştırma, hidroksi radikal uzaklaştırma aktivitesi tespit edilmiştir. Toplam fenol içeriği  $67.63 \pm 0.88$  GAE/g ile en yüksek etil asetat, toplam flavonoid içeriği  $14.82 \pm 1.02$ - $14.82 \pm 0.03$  mg CE/g ile en yüksek etil asetat ve diklorometan, fenolik asit içeriği  $0.72 \pm 0.21$  mgSAE/g ile en yüksek hekzan özütünde elde edilmiştir. Antimikrobiyal aktivitenin belirlenmesinde agar disk difüzyon yöntemi kullanıldı. *Alchemilla holotricha*'nın etil asetat özütü en yüksek antibakteriyel aktiviteyi göstermiştir. En yüksek antibakteriyel etkiyi sırasıyla 17 mm çap ile *Escherichia coli*, ardından 15

mm ile *Klebsiella pneumoniae* göstermiştir. *Bacillus subtilis* 8 mm çap ile en dirençli mikroorganizma olarak tespit edilmiştir. *Alchemilla holotricha* hem antioksidan hem de antimikrobiyal etkinliğini en iyi etil asetat ekstraktında göstermiştir. Çalışmada kısmen polar bir çözücü olan etil asetatın bitkinin toprak üstü kısmındaki aromatik maddeleri n-hekzan ve dietil eter gibi polar olmayan çözücülere göre daha iyi çözdüğü görülmüştür. Ayrıca su ve metanol ekstireleri PC-3 hücreleri üzerinde belirli dozlarda toksik etki gösterdi.

## 1. INTRODUCTION

Current studies have revealed that; Plants have the ability to reduce and prevent many diseases, due to their high antioxidant activity and ability to eliminate free radicals. Free radicals, which are released as a result of some biochemical reactions in the body, cause damage to biopolymers such as lipids, proteins and DNA. Excessive production of these ROS (reactive oxygen species), RNS (reactive nitrogen species) and toxic agents, reactions such as DNA damage, carbonylation of cellular proteins or lipid peroxidation occur, resulting in many chronic and degenerative diseases, especially cancer. Antioxidants, which are molecules that reduce or slow down oxidation with their free radical scavenging effects, protect the body against diseases that can be caused by ROS (reactive oxygen species), RNS (reactive nitrogen species), and toxic agents. Exogenous antioxidant substances, especially the use of medicinal plants among the public, in which are a good source of antioxidants due to their secondary compound content such as phenolic and flavonoid, are used in many industrial areas [1]. In addition, the use of plant polyphenols, which are natural antioxidants, instead of carcinogenic synthetic antioxidants used in the food and pharmaceutical industry has increased [2]. For centuries, peoples have been using plants for the prevention and treatment of diseases and this is known as ethnobotany. In ethnobotany, *Alchemilla* L. is a plant believed to be healing. In Anatolia and the world geography, many species are mentioned in the category of medicinal plants in the ethnobotanical field [3]. In the ethnobotanical field, it is known that *Alchemilla* L. species improve wound healing by covering them on wounds. In many research articles, it has been shown that *Alchemilla* species have strong antibacterial effects and have antioxidant properties with high oxidant removal due to the presence of high phenolic and other bio compounds in their content. Anticancer properties have been demonstrated in the studies of this study group and in some other studies in recent years. Among the *Alchemilla* species, the antioxidant and antimicrobial properties of *A. alpina*, *A. cimilensis*, *A. mollis*, and *A. vulgaris* were studied [3-5]. In this study, the biological activities of different solvent extracts obtained from *Alchemilla holotricha* Juz, which have not been studied before, were evaluated. Our aim in this study was to determine the most effective of different extracts of *Alchemilla holotricha*. By identifying the most effective extract of this plant, we demonstrate its high biological activities are in the functional food concept that has developed in recent years and is expected to continue its development in the future. We think that adding plant-based compounds to foods instead of synthetic

preservatives will be effective in the short term and in the long term, because with the rise of industrial society, the daily diet of people and the consumption of ready-made and packaged foods from outside are increasing together. The increasing intake of these agents in the daily diet can lead to adverse health effects. Since the use of additives in foods is important not only for these properties but also for taste, smell and sensory properties, the use of added plant-based compounds will be effective in the long term approach.

## 2. MATERIAL AND METHODS

The plant samples used in this study were obtained from Trabzon-Gümüşhane Passage, Turkey. The taxonomic identification of this plant was confirmed by Y. Menemen. This plant was kept in the herbarium of Kırıkkale University (Yusuf 1504).

### 2.1. Extraction Procedure

The powdered plant samples were extracted from the nonpolar solvent to the polar solvent. Starting from the hexane fraction, extraction was performed in dichloromethane, ethyl acetate, methanol, and finally in distilled water in a shaking mixer at 150 rpm for 24 hours, respectively. The obtained filtrate was extracted by evaporating the solvent at low speed in a rota evaporator. The extract, which was transferred to a vacuum desiccator filled with CaCl<sub>2</sub>, was dried completely and protected from moisture. Extract in 5 different fractions was obtained to be used in the study [6].

### 2.2. Antioxidant Activity

The Folin Ciocalteu method was used to determine the total phenolic content. 0.5 mL of the plant extract was taken and 2.5 ml of Folin Ciocalteu reagent was added into it. Then, 7.5 mL of sodium carbonate solution was added into the test tube and kept at 25°C for 2 hours. The total amount of phenol was calculated in UV Spectrophotometer at 760 nm, as equivalent to gallic acid [7].

### 2.2.2. Determination of total flavonoid content

To calculate the total flavonoid content; we added 1.25 mL distilled water to 250  $\mu$ L plant extract. To this mixture 75  $\mu$ L of 5% NaNO<sub>2</sub> solution was added. 6 minutes later, 500  $\mu$ L NaOH was added, followed by 275  $\mu$ L distilled water and mixed gently. Total flavonoid content was calculated as mg/kg by reading at 415 nm according to the catechin standard calibration chart. [8].

### 2.2.3. Determination of total phenolic acid content

2 mL HCl (0.5 M) was added into 1 mL plant extract. 2 mL reagent prepared by dissolving 10 g NaNO<sub>2</sub> and 10 g Na<sub>2</sub>MoO<sub>4</sub> in 100 mL water. Then 2 mL NaOH (8.5%) was added into that mixture. Then 2 mL of NaOH (8.5%) was added. The final volume was made up to 10 mL. Total phenolic acid content was calculated as sinapic acid equivalent (mg/g) by reading at 505 nm [9].

### 2.2.4. Determination of total lycopene and B-carotene content

The method developed by Barros et al. was used to determine the total content of  $\beta$ -carotene and lycopene. For this, 100 mg of the plant extract was weighed and mixed with 10 mL of acetone-hexane (4:6). The mixture was filtered through filter paper. Beta-carotene and lycopene levels were calculated from absorbance values read at 453, 505 and 663 nm wavelengths. Use the formulas below to calculate beta-carotene and lycopene levels. [10].

$$\beta\text{-carotene (mg/100 ml)} = 0,216A_{663} - 0,304A_{505} + 0,452A_{453} \quad [1]$$

$$\text{Lycopene (mg/100 ml)} = -0,0458A_{663} + 0,372A_{505} - 0,0806A_{453} \quad [2]$$

### 2.2.5. Determination of DPPH radical scavenging

DPPH removal activity of the plant extracts was measured by the violet/purple decolorization abilities of the 2,2-diphenyl-1-picrylhydrazil radical. To determine the activity, 0.3 mL of plant extract was added to 2.7 mL of 0.1 mM DPPH. Afterwards, the solution was mixed and kept in the dark area for 1 hour. The DPPH radical scavenging effect of plant extracts was determined by measuring absorption at 517 nm. This radical scavenging activity was calculated using the following formula [11].

$$\% \text{ Inhibition} = (A_{\text{Control}} - A_{\text{Sample}} / A_{\text{Control}}) \times 100 \quad [3]$$

### 2.2.6. Assessment of the reductive force property

To determine the reducing power properties of plant extracts, 2.5 mL of sodium phosphate buffer and 2.5 mL of potassium ferrocyanide (1%) were added to 2.5 mL of plant samples. The resulting solution was incubated at 50°C for about 20 minutes. To this mixture was added 2.5 mL of 10% prepared trichloroacetic acid and centrifuged at 1000 rpm. The supernatant was taken and 5 mL of deionized water and 1 mL of ferric chloride (0.1%) were

added to it and read at 700 nm against BHA and  $\alpha$ -tocopherol standards. [12].

### 2.2.7. H<sub>2</sub>O<sub>2</sub> (Hydrogen Peroxide) removal activity

0.6 mL (40 mM) H<sub>2</sub>O<sub>2</sub> in phosphate buffer was added to 0.4 mL of plant extract solution at different concentrations prepared in water. The final mixture was quickly read at 230 nm against the blank. The removal activity of the plant extract was calculated using the following formula [12].

$$\text{H}_2\text{O}_2 \text{ Removal Activity} = (A_{\text{Control}} - A_{\text{Sample}} / A_{\text{Control}}) \times 100 \quad [4]$$

### 2.2.8. Assessment of the OH $\cdot$ removal activity

For hydroxyl radical scavenging activity, 60  $\mu$ L FeCl<sub>2</sub>, 90  $\mu$ L 1,10-phenanthroline, 2.4 mL phosphate buffer, 150  $\mu$ L H<sub>2</sub>O<sub>2</sub> were added to the plant extracts at different concentrations, respectively. Samples incubated at 25 °C for 5 minutes were read at 560 nm. The radical scavenging activity was carried out according to the following equation [13].

$$\text{Hydroxyl Radical Removal} = (A_1 - A_2 / A_0) \times 100 \quad [5]$$

Absorbance reading without plant extract was given as "A<sub>0</sub>", absorbance reading in the presence of plant extract was given as "A<sub>1</sub>" absorbance reading without 1,10-phenanthroline was given as "A<sub>2</sub>".

### 2.2.9. Iron chelating capacity

The plant extracts were tested for their ferrous metal chelating activity. For this, 0.5 mL samples were taken from different fractions of the plant extract and mixed with 1.6 mL distilled water and 0.05 mL FeCl<sub>2</sub> (2 mM). Then 0.1 mL of Ferrozine (5 mM) was added to the mixture. Measure the absorbance of the Fe-Ferrozine complex of the mixture at 562 nm. The iron chelate activity was calculated using the following equation [14].

$$\text{Iron chelating capacity} = (A_{\text{control}} - A_{\text{sample}} / A_{\text{control}}) \times 100 \quad [6]$$

### 2.2.10. Evaluation of the total antioxidant capacity

For the antioxidant activities of the samples, 0.4 mL of the sample dissolved in methanol was taken, mixed with 4 mL of 0.6 M sulfuric acid containing 4 mM ammonium molybdate and 28 mM sodium phosphate, and the final mixture was vortexed and kept at 95 °C for 90 minutes. The antioxidant activity was read at 695 nm [15]. ( $y = 0.001x + 0.062$ ,  $R^2 = 0.946$ ).

### 2.3. Determination of Antimicrobial Activity

For the measurement of antimicrobial activity of extracts, the plant extracts were prepared with dimethylsulfoxide at 0.1 g/mL. The resulting solution was filtered with 0.22  $\mu$ m Nylon membrane filters. 50  $\mu$ L of each extract was absorbed into the blank discs. 200  $\mu$ L of test organisms adjusted according to Mc Farland were taken and spread in a petri dish containing the medium. Then, these discs

were transferred to the petri dish under sterile conditions with the help of a forceps. Streptomycin was used as a reference antimicrobial agent and discs impregnated with dimethylsulfoxide were used as a negative control. Petri dishes were kept in the refrigerator at 4°C for 1 hour in order to spread the active ingredients in the extract absorbed into the discs to the medium and to keep the microorganism growth at the lowest level. At the end of the period, it was kept in an oven at 37°C for 24 hours in order to incubate for the development of microorganisms. For incubation, it was kept in an oven at 37°C for 24 hours. The antimicrobial activity of effective compounds in plant extracts was determined by measuring the zones formed around the discs. [16]. *Bacillus subtilis* (ATCC 6633), *Staphylococcus aureus* (ATCC 29213), *Escherichia coli* (ATCC 25922), *Klebsiella pneumoniae* (EMCS), *Candida albicans*, *Saccharomyces cerevisiae* obtained from Refik Saydam Hygiene Center were used for antimicrobial activity.

#### 2.4. Antiproliferative Potential of Methanolic and Aqueous Extracts

WST-1 cell viability test was performed using Human prostate cancer cells (PC-3) to determine the efficacy of plant extracts. Human prostate cancer cells (PC-3) incubated and grown in cell growth medium containing 10% FBS and 1% penicillin-streptomycin, and then seeded in 96-well cell plates. It is adjusted to have approximately  $5 \times 10^3$  cells in each well. The cells in the 96-well plates were incubated for 24 hours for penetration. Then, water and methanolic extracts of the plant extracts were added to the cells in the wells at different doses and left for incubation. After 24 hours, 5  $\mu$ L of 4-[3-(4-Iodophenyl)-2-(4-nitro-phenyl)-2H-5-tetrazolio]-1,3-benzene sulfonate (WST1) per well containing PC-3 added and incubated for 4 hours. The absorbance of each well at 450 nm was taken at the reference wavelength of 630 nm and read in ELISA.2.5. Statistical Analysis.

Student's t-test was used for analysis and measurements were made in three replicates.

### 3. RESULTS AND DISCUSSION

Since the antioxidant components in the content of plants remove the free radicals in the environment and thus prevent the oxidative stress that triggers many diseases, studies in this field are becoming more and more popular with each passing day. Numerous medicinal plants and their components, such as purified flavones, isoflavones, flavonoids, anthocyanin, coumarin lignans, catechins, and isocatechin, contain antioxidant compounds that show beneficial therapeutic potential [17]. Therefore, in this study, the antioxidant effect of the aerial parts of *Alchemilla holotricha* was determined. In the study, it was observed that ethyl acetate, which is a partially polar solvent, dissolves aromatic substances in the above-ground part of the plant better than nonpolar solvents such as n-hexane and diethyl ether [18].

### 3.1. Antioxidant Assay Results

#### 3.1.1. Total antioxidant capacity

The total antioxidant capacity results of the extracts are given in Table 1. The lowest antioxidant capacity was observed in the hexane fraction with 24.15 mg AAE/g plant, and the highest value was observed in the ethyl acetate fraction with 359.64 mg AAE/g. In a study conducted with *Alchemilla persica*, the total antioxidant capacity of ethyl acetate extract was found to be 292.18 mg AAE/g [3]. Extract yields of *Alchemilla holotricha* were also examined. The highest extract yield was obtained with 0.93% in ethyl acetate. In the study, the highest antioxidant activities were mostly obtained in this fraction.

#### 3.1.2. Total phenolic compounds

Total phenolic content was plotted using the Gallic acid calibration curve in the spectrophotometer at 760 nm. ( $y=0.002+0.052x$ ,  $R^2=0.920$ ). The ethyl acetate fraction has the highest total phenolic content as a solvent with relatively moderate polarity. Hexane, a nonpolar solvent, and its extract were observed to have the lowest phenolic content (Table 1). Similarly, in our study with *Alchemilla cimilensis*, the highest values of total phenolic content were obtained in the same solvent, namely ethyl acetate solvent [19].

#### 3.1.3. Total flavonoid content and Total Phenolic Acid content (TPA)

One of the basic compounds in plants that eliminate tissue damage caused by radicals and prevents cells from being damaged is active compounds such as phenolics [20]. Flavonoids are low molecular weight phenolic compounds responsible for the antioxidant potential of plants. The total flavonoid amounts of the plant extracts were read in the spectrophotometer at 415 nm, and calculations were made in milligrams according to the (+)-catechin standard calibration curve ( $y=0.163x-0.012$ ,  $R^2=0.977$ ). The total flavonoid content in the examined plant samples ranged from 9.85 to 14.82. As with the phenolic content, the flavonoid concentration was also high in the ethyl acetate fraction (Table 1). Sözmen U.E. et al. [21] evaluated the total phenol and flavonoid contents of the *Alchemilla mollis* plant and reported that the phenolic compounds of the water extract were higher than the alcohol (methanol) extracts. Total flavonoid substance amounts were higher in ethyl acetate and dichloromethane extract. It was observed that hexane and water extracts demonstrated the lowest total flavonoid content. The fact that *A. holotricha* plant exhibits high antioxidants in the ethyl acetate fraction can be interpreted as the high content of polyphenols and flavonoids in this fraction. The flavonoid profile revealed in the study makes the plant medicinally important. In another study examining the flavonoid content of dichloromethane, ethyl acetate, methanol, and water extracts of *A. cimilensis*, it was reported that the ethyl acetate solvent medium gave higher results [19].



The TPA (total phenolic acid) content of the plant extracts was determined at 505 nm according to the sinapic acid standard calibration curve. ( $y=6960x-501.2$ ,  $R^2=0.962$ ). The total amount of phenolic acid substance was the same in all studied fractions. While there are many studies on total phenolic acid content by chromatographic methods, studies with spectrometric measurement are limited. The TPA content was obtained in the hexane fraction in the spectrometric study with *A. persica* [3].

### 3.1.4. Evaluation of Total $\beta$ -Carotene and Lycopene Content

Carotenoids are secondary plant pigments and consist of an aliphatic chain with methyl groups attached and a conjugated double bond system that gives the carotenoids their color. Carotenoids show maximum absorbance at wavelengths of about 430-480 nm, and the color is the result of this conjugated double bond system. Since carotenoids are lipophilic compounds, they are more soluble in apolar organic solvents than alcohol [22]. In

this study, the best results were obtained in dichloromethane solvent for  $\beta$ -carotene and methanol for lycopene. Results were calculated in mg carotenoid and lycopene per g extract (Table 1). Total lycopene content in various solvent extracts for *A. holotricha* could be ordered as methanol > water = dichloromethane > hexane > ethyl acetate respectively. Total  $\beta$ -carotene content in various solvent extracts for *A. holotricha* could be ordered as extracts of dichloromethane > ethyl acetate > methanol > hexane > water respectively (Table 1). The biological importance of  $\beta$ -carotene is that it is a lipid antioxidant and neutralizes free radicals, especially singlet oxygen. Linoleic acid-free radical binds to highly unsaturated  $\beta$ -carotene models. In addition, the presence of carotenoids in the medium not only reduces the free radical concentration but also reduces  $Fe^{3+}$  to  $Fe^{2+}$  [23]. Lycopene has greater radical scavenging activity as an antioxidant in in-vitro systems than  $\beta$ -carotene [24]. Lycopene, one of the most powerful antioxidants, has a singlet oxygen holding capacity 2 times that of  $\beta$ -carotene and 10 times that of  $\alpha$ -tocopherol [25].

**Table 1.** Effect of solvent type on total antioxidant, total phenolic, total flavonoid, total phenolic acid, total  $\beta$ -carotene and total lycopene content of extracts from *A. holotricha*

Antioxidant Activity	H	D	E	M	W
Total antioxidant capacity (TAC), (mg $g^{-1}$ )	24.15	135.96	359.64	197.84	234.06
Total phenolic content (mg GAE $g^{-1}$ )	8.05	28.32	67.63	45.98	48.16
Total flavonoid content (mg CE $g^{-1}$ )	10.46	14.82	14.82	11.29	9.85
Total phenolic acid content (mg SAE $g^{-1}$ )	0.72	0.72	0.72	0.72	0.72
Total $\beta$ - carotene content (mg $g^{-1}$ )	1.04	1.68	1.62	1.47	0.92
Total lycopene content (mg $g^{-1}$ )	0.81	0.82	0.76	0.94	0.82

(H: hexane D: dichloromethane, E: ethyl acetate, M: methanol, W: distilled water)

### 3.1.5. DPPH Radical scavenging capacity (%)

The plant extracts showed close results with  $\alpha$ -tocopherol, BHT and BHA studied as standard in the medium of water, ethyl acetate, and methanol. DPPH results are given in Table 2 as a percentage. An increase in the percentage of DPPH radical removal was observed depending on the concentration increase of the plant extracts. In one study, it was found that the DPPH radical scavenging effect of *Alchemilla alpina* methanol extract increased in the range of 45.4% -94.4% depending on the increasing concentrations [26]. Percent inhibition of DPPH radical scavenging effect of *Alchemilla vulgaris* extract has been reported as  $71.8 \pm 4.1\%$  [27]. The DPPH radical scavenging effect of *Alchemilla ellenbergiana* Rothm, in which methanol and hexane extracts were used, was found to be  $243.1 \mu g mL^{-1}$  in the methanol extract. Low DPPH radical scavenging activity was also detected in hexane extract ( $7.1 \mu g mL^{-1}$ ) [28]. Similarly, in our study, the radical scavenging effect of methanol extract (87%) was significantly higher than hexane (47 %). In another study, it was observed that the radical scavenging efficiency of water and methanol extracts was low in the *Alchemilla mollis* species of this *Alchemilla* genus. This significant difference in the DPPH effectiveness of these two types in the same solvents may be attached to environmental impacts [21]. The variability of results depends on plant ecological conditions, harvest time, plant species, concentration studied and solvent used [5]. It is emphasized that there is a parallel relationship between phenolic content and antioxidant capacity,

especially with radical scavenging activities. In our study, this parallel relationship between phenolic content and DPPH was observed especially in the ethyl acetate extract [29]. Since the DPPH method is technically simple, it is a widely used method for measuring the antioxidant activity of plant extracts. However, DPPH does not react to all antioxidants at the same rate, and the reaction rate is very slow for some antioxidants. For this reason, it is not an adequate method for the determination of antioxidant activity, and it is recommended to be supported by other methods.

### 3.1.6. Reductive force property

The reducing force of *Alchemilla holotricha* and synthetic antioxidants (BHA, BHT and  $\alpha$ -tocopherol) are given in Table 2. As seen in Table 2, methanol, water and ethyl acetate showed a higher reduction than synthetic antioxidants. In the reducing power analysis, the presence of antioxidants in the plant extract reduces the  $Fe^{3+}$  / ferricyanide complex to the  $Fe^{2+}$  form.  $Fe^{3+}$  reduction is an indicator of electron-donating activity of phenolic antioxidants and is strongly associated with other antioxidant properties. In addition, it was observed that the reducing force activity increased in parallel with the increase in concentration at the studied concentrations. Therefore, the reductive force property of *Alchemilla holotricha* ethyl acetate extracts can generally be associated with phenolic hydroxyl groups. Because, in the same way, it was found in this solvent the most in phenolic groups. In a study, it was observed that the

reducing properties of *Alchemilla vulgaris* extracts, which were tested in ethanol, methanol, and ethyl acetate, were the most in ethyl acetate solvent [30].

### 3.1.7. Hydrogen peroxide removal activity assay

Percentage H<sub>2</sub>O<sub>2</sub> removal activity for each sample were calculated and displayed in Table 2.

In the study, there was a high removal of hydrogen peroxide in the hexane fraction at all concentrations studied. In other fractions of the studied plant, the scavenging effect increased from 0.1 mg. The hydrogen peroxide removal activity in the hexane fraction can be attributed to the saturation of the fatty acids in this fraction [3]. The highest removal was observed at the highest concentration of 0.2 mg/mL in all fractions studied. The hydrogen peroxide concentration in the environment is formed according to phenolic compounds and flavonoids. Since the phenolic compounds in the plant extract are good electron donors, they can accelerate the conversion of H<sub>2</sub>O<sub>2</sub> to H<sub>2</sub>O [31]. Being good electron donors also shows reduced power [32].

### 3.1.8. Hydroxyl radical removal property

The hydroxyl radical is a highly reactive compound that attacks most organic molecules, and they are highly oxidizing by nature. The OH radical scavenging activity of the studied plant extracts and standards (BHA, BHT,  $\alpha$ -tocopherol) is given in Table 2. The concentration ranges of the extracts prepared for the hydroxyl radical removal

method is 0.05-0.2 mg/mL. The highest % inhibition was observed in the fraction of dichloromethane (11%) and ethyl acetate (13 %) at 0.2 mg/mL. It was observed that the OH radical scavenging effect also increased depending on the concentration increase of the plant extracts. Kaya reported that the OH scavenging activity of *Alchemilla persica* was the best in dichloromethane, and this was due to the low polarity of dichloromethane, which resulted from functional groups binding free groups better [3].

### 3.1.9. Metal chelating activity

Metal chelating activity was evaluated according to the competition of plant extracts with ferrozine to bind Fe<sup>+2</sup> ions in solution. The metal chelation potential of the plant extracts used in the study is given in Table 2. Metal chelating activity of the hexane, dichloromethane and ethyl acetate extract were found to be high for *Alchemilla holotricha* solvent extracts, while methanol and water extracts showed very little activity. On the other hand, in the present study, *Alchemilla holotricha* solvent extracts showed stronger metal chelating activity than synthetic antioxidants. This proves that the plant extract is a peroxidation inhibitor. Boroja et al. [33] using ABTS<sup>•+</sup> and <sup>•</sup>OH assays showed that the methanol extract of *A. vulgaris* has a greater antioxidant potential than the synthetic antioxidant. However, they reported that the methanol extract of *Alchemilla vulgaris* L. did not have Fe<sup>2+</sup> reducing properties [33]. In our study where different solvent extracts were used, the lowest iron chelating activity was observed in methanol.

**Table 2.** Antioxidant activity of extracts from *Alchemilla holotricha* in different solvents

DPPH scavenging capacity (%)	0.05 mg mL <sup>-1</sup>	0.1 mg mL <sup>-1</sup>	0.15 mg mL <sup>-1</sup>	0.2 mg mL <sup>-1</sup>
Hexane	43.83±2.11	44.51±4.44	46.57±3.12	47.63±6.23
Dichlorometan	45.98±6.12	46.66±4.16	47.42±1.23	53.6±7.26
Ethyl acetate	85.50±3.21	86±6.21	86.57±3.12	88.14±4.12
Methanol	85.57±5.13	86.66±3.12	86.69±6.23	87.17±5.23
Water	86.93±0.23	87.27±3.31	87.48±3.21	87.62±8.21
$\alpha$ -tocopherol	83.19±1.26	85.44±3.23	85.52±4.03	85.72±6.36
BHA	83.81±3.32	85.18±5.36	85.33±5.06	85.66±4.44
BHT	75.91±6.19	79.42±6.12	82.22±3.96	83.58±4.00

Reducing power activity	0.05 mg mL <sup>-1</sup>	0.1 mg mL <sup>-1</sup>	0.15 mg mL <sup>-1</sup>	0.2 mg mL <sup>-1</sup>
Hexane	0.294±0.01	0.303±0.03	0.304±0.23	0.481±0.06
Dichlorometan	0.355±0.03	0.381±0.04	0.452±0.26	0.554±0.05
Ethyl acetate	2.194±0.23	2.891±0.32	3.158±0.12	3.333±0.24
Methanol	1.132±0.11	1.746±0.15	2.485±0.26	3.011±0.12
Water	1.439±0.12	2.340±0.42	2.758±0.46	2.775±0.23
$\alpha$ -tocopherol	0.375±0.05	0.622±0.46	0.944±0.05	0.994±0.11
BHA	0.788±0.07	1.433±0.59	2.068±1.12	2.441±0.28
BHT	0.247±0.12	0.265±0.71	0.355±0.08	0.385±0.02

%OH scavenging activity	0.05 mg mL <sup>-1</sup>	0.1 mg mL <sup>-1</sup>	0.15 mg mL <sup>-1</sup>	0.2 mg mL <sup>-1</sup>
Hexane	0.25±0.02	0.44±0.09	1.04±0.02	2.13±0.01
Dichloromethane	0.41±0.23	1.95±0.05	9.74±0.25	11.95±0.32
Ethyl acetate	2.96±0.36	3.34±0.02	12.48±0.51	13.29±0.12
Methanol	1.21±0.21	1.99±0.12	3.24±0.96	3.57±0.03
Water	1.36±0.06	1.81±0.08	2.38±0.74	2.62±0.12
$\alpha$ -tocopherol	0.86±0.05	1.32 ± 0.96	1.41 ± 0.58	2.50 ± 0.21
BHA	0.43±0.09	0.54 ± 1.16	0.65 ± 0.32	0.86 ± 0.45
BHT	0.15±0.11	0.16 ± 0.87	0.27 ± 0.74	0.33 ± 1.56

Metal chelating activity (%)	0.05 mg mL <sup>-1</sup>	0.1 mg mL <sup>-1</sup>	0.15 mg mL <sup>-1</sup>	0.2 mg mL <sup>-1</sup>
Hexane	60.62±2.02	64.54±0.21	69.28±0.32	73.15±0.21
Dichlorometane	57.88±2.14	66.87±0.12	71.47±0.12	96.46±1.23
Ethyl acetate	45.46±0.36	59.50±2.14	61.93±0.21	86.49±1.56
Methanol	44.43±0.13	44.94±1.15	45.43±0.15	45.78±3.25
Water	41.24±0.21	42.15±1.11	47.59±0.18	51.23±0.89
BHT	5.74± 2.03	13.17 ± 0.0	16.37 ± 1.4	36.57± 2.08
α-tocopherol	33.28±2.14	33.35 ± 0.0	34.56 ± 2.0	36.91± 1.78
BHA	33.58±0.21	34.32± 1.15	38.14± 1.61	43.67± 0.65
Trolox	3.84±0.52	34.95± 1.18	36.78± 0.74	36.94± 0.85

Hydrogen peroxide scavenging activity (%)	0.05 mg mL <sup>-1</sup>	0.1 mg mL <sup>-1</sup>	0.15 mg mL <sup>-1</sup>	0.2 mg mL <sup>-1</sup>
Hexane	52.24±0.12	54.76±1.23	58.44±0.89	59.92±1.25
Dichlorometane	46.40±0.56	47.67±0.13	47.69±4.25	53.12±4.12
Ethyl acetate	28.16±0.03	34.05±2.10	42.07±4.51	50.23±6.25
Methanol	41.03±0.13	42.61±1.36	52.37±3.23	53.21±4.65
Water	42.84±0.54	46.98±3.23	57.73±4.63	57.75±4.43

### 3.2. Antimicrobial Activity

Antimicrobial activity findings for *Alchemilla holotricha* strain are displayed in Table 3. The antibacterial activities of the extracts *A. holotricha* were tested against bacteria, and one yeast strain. As evident from Table 3, the hexane extracts from *A. holotricha* weak activity against bacteria. However, the ethyl acetate and methanol extract of *A. holotricha* was the most active showing a strong inhibitory effect against all tested Gram-positive bacteria, Gram-negative bacteria and yeast strain. On the other hand, the water and dichloromethane extracts showed low antimicrobial activity similar to that of *A. holotricha* extracts.

Studies on the antimicrobial activities of different strains of this *Alchemilla* are available in the literature, and different rates of antimicrobial activity were observed in

the same bacterial strains [26, 28, 34, 35, 36]. In the study with *Alchemilla ellenbergiana*, it showed an equal inhibition zone of 11 mm in ethanol and ethyl acetate extracts against *K. pneumoniae*, a gram-negative bacterium, while an 18 mm zone of inhibition against *C. albicans* in the ethanol extract, and *S. aureus* (MRSA) in ethyl acetate and methanol extracts of 13 mm and 12 mm, respectively. [28]. In another study, increasing concentrations of *Alchemilla glabra* Neygenf formed an inhibition zone of 12-22 mm in gram negative bacteria *E. coli*, 22-17 mm in *P. vulgaris*, and 13-15 mm in *K. pneumoniae*. It was determined that *S. aureus* showed antimicrobial activity at different rates with a 12-22 mm inhibition zone. In the same study, it formed a 14-16 mm inhibition zone against *C. albicans* at different concentrations [36-37].

**Table 3.** *In vitro* antimicrobial activities of *A. holotricha* different solvents

Microorganism	<i>Alchemilla holotricha</i> Extracts						
	H	D	E	M	W	S.	DMSO
	Inhibition zone (mm)						
<i>B. subtilis</i>	-	7±0,1	8±0,2	8±0,1	7±0,2	25±0,7	-
<i>S. aureus</i>	8±0,1	10±0,3	11±0,1	12±0,4	7±0,3	40±0,8	-
<i>E. coli</i>	7±0,1	12±0,4	17±0,3	10±0,4	8±0,5	40±1	-
<i>K. pneumoniae</i>	-	9±0,5	15±0,2	10±0,2	8±0,2	26±0,3	-
<i>C. albicans</i>	-	8±0,3	13±0,6	9±0,3	8±0,3	16±0,5	-
<i>S. cerevisiae</i>	-	-	8±0,1	11±0,2	7±0,2	23±0,4	-

\* Hexane (H), Dichloromethane (D), Ethyl acetate (E), Methanol (M), Water (W), Dimethylsulfoxide (DMSO), Streptomycin (S)

### 3.3. Antiproliferative Potential of Methanolic and Aqueous Extracts

PC-3 cell lines were used to evaluate the effect of the extracts on tumor cell growth. To determine the proliferation effects of methanol and water extracts of *Alchemilla holotricha* in the PC-3 cell line, applications at different concentrations between 125-1000 µg mL<sup>-1</sup> were performed. water and methanol extracts of *A. holotricha* decreased PC-3 cell proliferation significantly at concentrations from 125 to 1000 µg mL<sup>-1</sup> when compared to control cells (p <0.001). (Fig. 1a, b, c and d). All extracts showed cytotoxic effect on PC-3 cells. A study was conducted using L929 and MDA-MB 231 cells to determine the cytotoxic effects of extracts obtained from *A. mollis* roots. In this study, no toxic effects were

observed in the concentration range of 62.5 and 3.25 µg mL<sup>-1</sup> of different extracts, while it was reported that the ethyl acetate extract at a concentration of 250 µg mL<sup>-1</sup> had a higher toxic effect than the other extracts. [38-39]. In the study conducted to determine the cytotoxic effect of methanol and water extracts of *A. persica* on PC-3 cell line, methanol extract showed a higher antiproliferative effect when compared to the other two concentrations at 250 µg mL<sup>-1</sup> [3]. However, in this study, the cytotoxic activity of the methanol extract of *A. holotricha* on the cell PC-3 line was higher than the water.

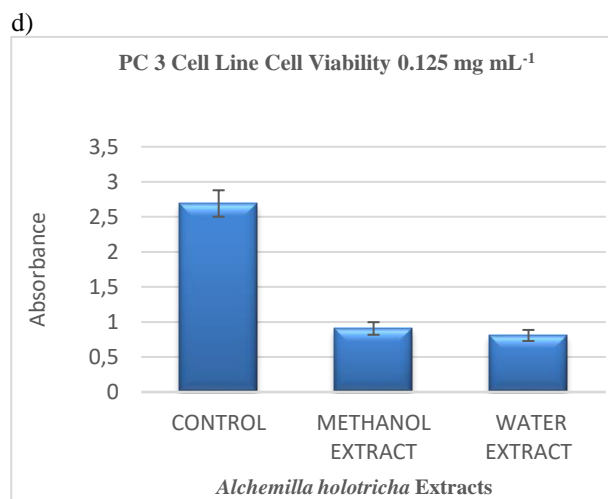
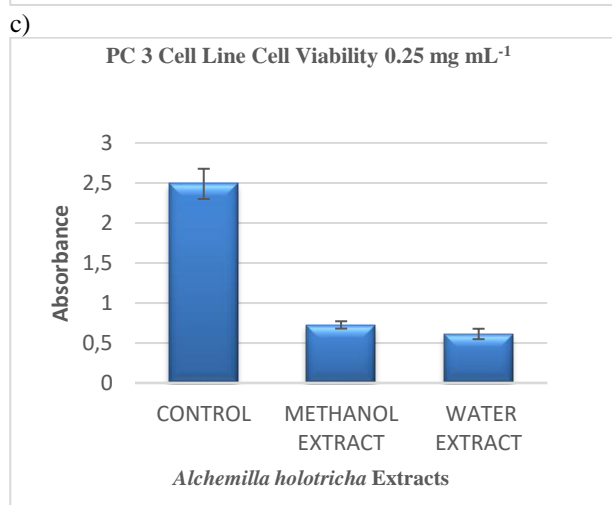
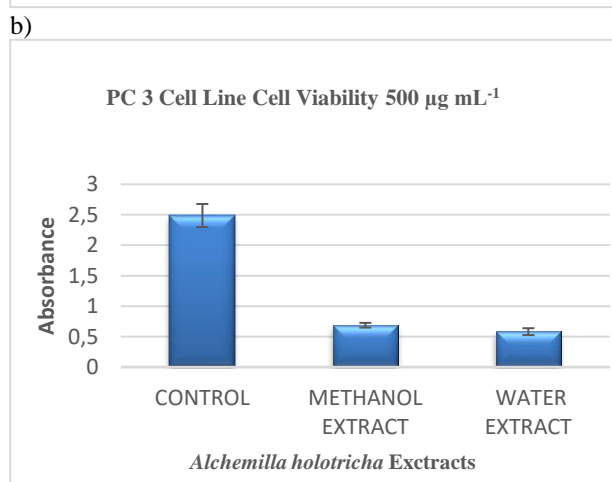
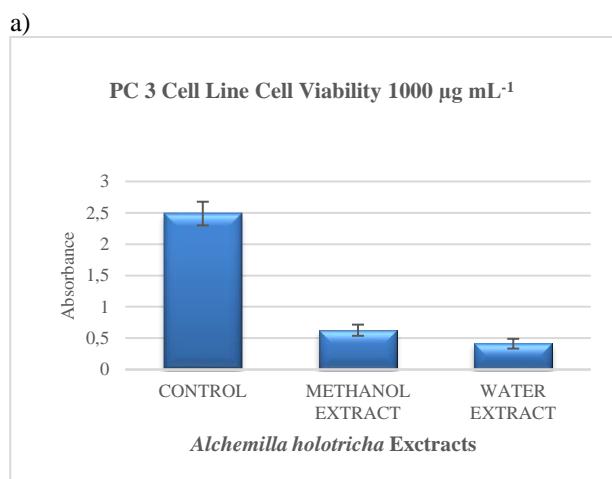


**Figure 1.** Antiproliferative potential of different concentrations of methanol and aqueous extracts of *A. holotricha*; a) 1000  $\mu\text{g mL}^{-1}$ , b) 500  $\mu\text{g mL}^{-1}$  c) 250  $\mu\text{g mL}^{-1}$  d) 125  $\mu\text{g mL}^{-1}$

#### 4. CONCLUSION

Natural antioxidants such as polyphenols, flavonoids, and phenolic compounds found in various parts of plants are responsible for preventing the harmful effects of stress by scavenging free radicals. As a result, due to its antioxidant content, *Alchemilla holotricha* is a natural source of antioxidants. The gram-negative bacteria were mainly affected by the ethyl acetate solvent. It also showed high antimicrobial activity in *C. albicans*, a pathogenic yeast. The water and methanol extract of *Alchemilla holotricha* showed significant cytotoxicity on the PC-3 cell line. In the light of the data obtained from this study, when antioxidant antimicrobial and anticancer were evaluated, it was determined that although the activities of the lion's claw (*Alchemilla holotricha*) plant in different solvents vary, the activity levels, in general, were high.

#### REFERENCES

- [1] Demiroz T, Nalbantsoy A, Kose FA, Baykan S. Phytochemical composition and antioxidant, cytotoxic and anti-inflammatory properties of *Psephellus goeksunensis* (Aytaç & H. Duman) Greuter & Raab-Straube. *S Afr J Bot.* 2020; 130: 1-7.
- [2] Jiangning G, Xinchu W, Hou W, Qinghua L, Kaishun B. Antioxidants from a Chinese medicinal herb – *Psoralea corylifolia* L. *Food Chem.* 2005; 91(2): 287-92.
- [3] Kaya, B. Determination of anticytotoxic, antioxidant and antimicrobial activities of *Alchemilla persica* extracts in different polarities. *TDFD.* 2020; 9(2): 157-169.
- [4] Yazıcı S.Ö. Optimization of the extraction conditions of phenolic compounds from *Alchemilla vulgaris* using response surface methodology. *Gıda.* 2021; 46(4): 1040-1052.
- [5] İnci Ş, Eren A, Kirbağ S. Determination of antimicrobial and antioxidant activity of *Alchemilla alpina* L. *TURJAF.* 2021; 9(12): 2260-2264.
- [6] Zhao M, Ito Y, Tu P. Isolation of a novel flavanone 6-glucoside from the flowers of *Carthamus*

- tinctorium* (Honghua) by high-speed counter-current chromatography. *J Chromatogr A*. 2005; 1090(1-2): 193-196.
- [7] Gamez-Meza N, Noriega-Rodriguez JA, Medina-Juarez LA, Ortega-Garcia J, Cazarez-Casanova R, Angulo-Guerrero O. Antioxidant activity in soybean oil of extracts from *Thompson grape* bagasse. *J Am Oil Chem Soc*. 1999; 76(12): 1445-1447.
- [8] Barros L, Calhella RC, Vaz JA, Ferreira ICFR, Baptista P, Estevinho LM. Antimicrobial activity and bioactive compounds of Portuguese wild edible mushrooms methanolic extracts. *Eur Food Res Technol*. 2007; 225(2): 151-156.
- [9] Koncic MZ, Kremer D, Gruz J, Strnad M, Bisevac G, Kosalec I, et al. Antioxidant and antimicrobial properties of *Moltkia petraea* (Tratt.) Griseb. flower, leaf and stem infusions. *Food Chem Toxicol*. 2010; 48(6): 1537-1542.
- [10] Barros L, Calhella RC, Vaz JA, Ferreira ICFR, Baptista P, Estevinho LM. Antimicrobial activity and bioactive compounds of Portuguese wild edible mushrooms. *Eur. Food Res Technol*. 2007; 225: 151-156.
- [11] Hatano T, Kagawa H, Yasuhara T, Okuda T. 2 new flavonoids and other constituents in Licorice Root - Their relative astringency and radical scavenging effects. *Chem Pharm Bull*. 1988; 36(6): 2090-2097.
- [12] Oyaizu M. Studies on product of browning reaction prepared from glucose amine. *Jpn J Nutri*. 1986; 44:307-315.
- [13] Ruch RJ, Cheng SJ, Klaunig JE. Prevention of cytotoxicity and inhibition of intercellular communication by antioxidant catechins isolated from Chinese green tea. *Carcinogenesis*. 1989; 10(6): 1003-1008.
- [14] Dinis TCP, Madeira VMC, Almeida LM. Action of phenolic derivatives (acetoaminophen, salicylate, and 5-aminosalicylate) as inhibitors of membrane lipid peroxidation and peroxy radicals scavengers. *Arch Biochem Biophys*. 1994; 315: 161-169.
- [15] Prieto P, Pineda M, Aguilar M. Spectrophotometric quantitation of antioxidant capacity through the formation of a phosphomolybdenum complex: Specific application to the determination of vitamin E. *Anal Biochem*. 1999; 269(2): 337-341.
- [16] Berghe VA. Screening methods for antibacterial and antiviral agents from higher plants. *Meth Plant Biochem*. 1991; 6: 47-68.
- [17] Aqil F, Ahmed I, Mehmood Z. Antioxidant and free radical scavenging properties of twelve traditionally used Indian medicinal plants. *Turk J Biol*. 2006; 30: 177-183.
- [18] Paixao, N., et al. (2007). "Relationship between antioxidant capacity and total phenolic content of red, ros?? and white wines." *Food Chemistry* 105: 204-214
- [19] Kaya B, Artuvan Y. Investigation of antioxidant and antimicrobial effect, phenolic compounds of *Alchemilla cimilensis* ECJSE. 2016; 3(1): 27-54.
- [20] Oreopoulou A, Tsimogiannis D, Oreopoulou V. Extraction of polyphenols from aromatic and medicinal plants: an overview of the methods and the effect of extraction parameters. In: *Polyphenols in plants*. Press Elsevier, Amsterdam, p. 243-259.
- [21] Sözmen EU, Eruygur N, Akpolat A, Çetin MD, Durukan H, Demirbaş A, et al. Sivas ili doğal florasından toplanan sarı kantaron (*Hypericum scabrum* L.) ve aslan pençesi (*Alchemilla mollis* (Buser) Rothm) bitkilerinin bazı kalite kriterlerinin belirlenmesi. *JIST*. 2020; 10(2): 1410-1418.
- [22] ByKirk L. Parkin, Owen R. Fennema. *Fennema's Food Chemistry*, 4th ed. Boca Raton. CRC Press; 2007.
- [23] Jayaprakasha GK, Singh RP, Sakariah KK. Antioxidant activity of grape seed (*Vitis vinifera*) extracts on peroxidation models in vitro. *Food Chem*. 2001; 73: 285-290.
- [24] Handelman GJ. The evolving role of carotenoids in human biochemistry. *Nutrition* 2001; 17(10): 818-22.
- [25] Mortensen A, Skibsted LH. Relative stability of carotenoid radical cations and homologue tocopheroxyl radicals. A real time kinetic study of antioxidant hierarchy. *FEBS Lett*. 1997; 417: 261-266.
- [26] Karatoprak GS, Ilgun S, Kosar M. Phenolic composition, anti-inflammatory, antioxidant, and antimicrobial activities of *Alchemilla mollis* (Buser) Rothm. *Chem. Biodivers*. 2017; 14: e1700150.
- [27] Oktyabrsky O, Vysochina G, Muzyka N, Samoilova Z, Kukushkina TG, Smirnova G. Assessment of antioxidant activity of plant extracts using microbial test systems. *J Appl Microbiol*. 2009; 106: 1175-1183.
- [28] Neuza Paixão, Rosa Perestrelo, José C. Marques, José S. Câmara, Relationship between antioxidant capacity and total phenolic content of red, rosé and white wines, *Food Chemistry*, Volume 105, Issue 1, 2007, Pages 204-214, ISSN 0308-8146, <https://doi.org/10.1016/j.foodchem.2007.04.017>.
- [29] Acet T, Kadriye Özcan K. Determination of antioxidant and antimicrobial properties of lady's mantle (*Alchemilla ellenbergiana*) extracts. *GUFBD*. 2018; 8 (1): 113-121.
- [30] Vlaisavljević S, Jelača S, Zengin G, Mimica-Dukić N, Berežni S, Miljić M, et al. *Alchemilla vulgaris* agg. (Lady's mantle) from central Balkan: antioxidant, anticancer and enzyme inhibition properties. *RSC Adv*. 2019; 9(64): 37474-37483.
- [31] Ruch RJ, Cheng SJ, Klaunig JE. Spin trapping of superoxide and hydroxyl radicals. *Methods Enzymol*. 1984; 105: 198-209.
- [32] Shon MY, Choi SD, Kahng GG, Nam SH, Sung NJ. Antimutagenic, antioxidant and free radical scavenging activity of ethyl acetate extracts from white, yellow and red onions. *FCT*. 2004; 42(4): 659-666.
- [33] Shafaghat A. Chemical constituents, antioxidant and antibacterial activities of the hexane extract of *Alchemilla sericata* Reichenb. *J Food Biochem*. 2019; 43: 9-14.
- [34] Boroja T, Mihailović V, Katanić J, Pan SP, Nikles S, Imbimbo P, et al. The biological activities of roots and aerial parts of *Alchemilla vulgaris* L. *S Afr J Bot*. 2018; 116: 175-184.

- [35] Kaya E, Şeker Karatoprak G, Koşar M, Özbilge H, Başer KHC. Antimicrobial Properties of *Alchemilla mollis*, Ankara, Türkiye, 23 June- 26 September 2009, 9th International Symposium on Pharmaceutical Sciences (ISOPS-9).
- [36] Denev P, Kratchanova M, Ciz M, Lojek A, Vasicek O, Blazheva D, Nedelcheva P, Vojtek L, Hyrsi P. Antioxidant, antimicrobial and neutrophil-modulating activities of herb extracts. Acta Biochim Plon. 2014; 61: 359–367.
- [37] Bengü, A. Ş., Adnan, A. Y. N. A., Özbolat, S., Abdullah, T. U. N. Ç., Aykutoğlu, G., Çiftci, M., & Darendelioğlu, E. (2020). Content and antimicrobial activities of bingol royal jelly. TTDB, 7(2), 480-486.
- [38] İlgün, S, Karatoprak GŞ. (*Alchemilla mollis* (Buser) Rothm bitkisi köklerinden elde edilen ekstirelerin antioksidan ve sitotoksik etkileri. MÜSBD. 2021; 14(2): 176-185.
- [39] Ayna, A., Tunc, A., Özbolat, S. N., Bengü, A. Ş., Aykutoğlu, G., Canli, D., & Darendelioğlu, E. (2021). Anticancer, and antioxidant activities of royal jelly on HT-29 colon cancer cells and melissopalynological analysis. Turk J Bot, 45(8), 809-819

## Evaluation of Missing Data Imputation Methods and PCA Techniques for Machine Learning Models in Breast Cancer Diagnosis Using WBCD

Yavuz Bahadır KOCA<sup>1\*</sup> , Elif AKTEPE<sup>2</sup> 

<sup>1</sup> Afyon Kocatepe University, Engineering Faculty, Electrical Engineering Department, Afyonkarahisar, Türkiye

<sup>2</sup> Afyon Kocatepe University, Afyon Vocational School, Electronics and Automation Department, Afyonkarahisar, Türkiye

Yavuz Bahadır KOCA ORCID No: 0000-0002-0317-1417

Elif AKTEPE ORCID No: 0000-0002-2375-2040

\*Corresponding author: ybkoca@aku.edu.tr

(Received: 28.03.2024, Accepted: 25.08.2024, Online Publication: 26.09.2024)

### Keywords

Breast cancer,  
Machine learning,  
Missing data  
management,  
PCA,  
Biomedical

**Abstract:** Cancer is one of the leading causes of human death, and breast cancer deaths are widespread among women. Early diagnosis of breast cancer is considered one of the main ways to reduce these deaths. Expert systems, artificial intelligence (AI), and machine learning (ML) techniques aim to assist doctors in the medical field in early disease detection. One of the main purposes of these technologies is to diagnose life-threatening diseases such as breast cancer earlier and accurately. This study analyses the Wisconsin Breast Cancer Dataset (WBCD) and evaluates the effects of different missing data imputation methods with Principal Component Analysis (PCA). PCA-based data reduction techniques are used in supervised ML methods. This study emphasizes combining ML approaches with missing data management strategies for breast cancer diagnosis. The study dataset consists of 699 data. 16 out of the data were identified as missing data. These missing data were processed using different data imputation methods. It was seen that the median filling technique provided the best performance. After filling the missing data with the median, PCA-based data reduction techniques were used on the dataset. The performances of Decision Trees (DT), Linear Regression (LR), Logistic Regression (LogR), k Nearest Neighbours (k-NN), Polynomial Regression (PR), Random Forest (RF) and Support Vector Machines (SVM) models were investigated for classifying tumours. The effects of these techniques were examined on ML algorithms with various PCA component numbers. The best performance was observed in SVM and k-NN algorithms. The success rates were 97.14% and 98.57%, respectively.

## WBCD Kullanılarak Meme Kanseri Tanısında Makine Öğrenme Modelleri İçin Eksik Veri Atama Yöntemlerinin ve PCA Tekniklerinin Değerlendirilmesi

### Anahtar

### Kelimeler

Meme kanseri,  
Makine  
öğrenmesi,  
Eksik veri  
yönetimi,  
PCA,  
Biyomedikal

**Öz:** Kanser, insan ölümlerinin önde gelen nedenlerinden biridir ve meme kanseri ölümleri kadınlar arasında yaygındır. Meme kanserinin erken teşhisi, bu ölümleri azaltmanın ana yollarından biri olarak kabul edilir. Uzman sistemler, yapay zekâ (AI) ve makine öğrenmesi (ML) teknikleri, tıp alanındaki doktorlara erken hastalık tespitinde yardımcı olmayı amaçlamaktadır. Bu teknolojilerin temel amaçlarından biri, meme kanseri gibi yaşamı tehdit eden hastalıkları daha erken ve doğru bir şekilde teşhis etmektir. Bu çalışmada, Wisconsin Meme Kanseri Veri Seti (WBCD) analiz edilmiş ve Temel Bileşen Analizi (PCA) ile farklı eksik veri atama yöntemlerinin etkileri değerlendirilmiştir. PCA tabanlı veri indirgeme teknikleri, denetimli ML yöntemlerinde kullanılmaktadır. Bu çalışmada, meme kanseri teşhisi için ML yaklaşımlarının eksik veri yönetimi stratejileriyle birleştirilmesi vurgulanmaktadır. Çalışmanın veri seti 699 veriden oluşmaktadır. Verilerden 16'sı eksik veri olarak tanımlanmıştır. Bu eksik veriler, farklı veri atama yöntemleri kullanılarak işlenmiştir. Medyan tekniğinin en iyi performansı sağladığı görülmüştür. Eksik veriler medyan değer ile doldurulduktan sonra, veri seti üzerinde PCA tabanlı veri indirgeme teknikleri kullanılmıştır. Tümörleri sınıflandırmak için Karar Ağaçları (DT), Doğrusal Regresyon (LR), Lojistik Regresyon (LogR), k En Yakın Komşular (k-NN), Polinom Regresyon (PR), Rastgele Orman (RF) ve Destek Vektör Makineleri (SVM) modellerinin performansları incelenmiştir. Bu tekniklerin etkileri çeşitli PCA bileşen sayılarına sahip ML algoritmaları üzerinde değerlendirilmiştir. En iyi performans SVM ve k-NN algoritmalarında gözlenmiştir. Başarı oranları sırasıyla %97,14 ve %98,57 olarak tespit edilmiştir.

## 1. INTRODUCTION

Breast cancer is a severe health problem, especially common in women, and its treatability is directly linked to early diagnosis. Early diagnosis can prevent disease progression and increase the chances of successful treatment [1–3].

According to a report published by the World Health Organization (WHO), 20 million new cancer cases occurred worldwide in 2022, resulting in 9.7 million deaths. Breast, colorectal, and lung cancers are among the most common types of cancer globally. It has been reported that 2.3 million breast cancer cases were diagnosed and 685,000 deaths occurred in 2020 [4]. Therefore, it is believed that research and development of early detection methods for breast cancer will play an important role in reducing mortality rates. The rapid development of artificial intelligence (AI) in the last decade shows that significant progress can be made in almost all areas in the future. These developments are in a position to radically change various aspects of human life and our interactions with society.

AI is used for many purposes in almost every field and is divided into different categories. In this context, in the field of medicine especially. AI systems are used effectively and successfully in disease detection and cancer classification. Studies show that ML techniques are essential, especially in medical applications [5,6].

The primary purpose of developing ML and other AI algorithms, as well as other biomedical technologies is to assist doctors in their evaluation processes in healthcare services. All these technologies are used to support doctors' decision-making processes and assist them in issues such as data analysis and image interpretation. The effectiveness and success of ML techniques are significant especially in disease diagnosis and cancer classification. In this context, using AI technologies in medicine provides substantial advantages, such as faster diagnosis of patients and the determination of appropriate treatment methods. In addition, developing and improving these technologies help improve the quality of service in the medical field and the quality of life of patients. Therefore, AI technologies in the medical field are constantly being developed and improved [7,8].

The application of ML techniques to classify of breast cancer has gained increasing attention in various studies. There are different studies on breast cancer diagnosis. A literature review of selected studies is presented for performance comparison and will be discussed here. The WBCD dataset has also been subjected to performance analysis using ML solutions by various researchers. For instance, Hasan et al. [9] used the WBCD and SEER 2017 Breast Cancer Dataset. The model achieved an accuracy rate of 99.1% on the reduced WBCD dataset and 89.3% on the SEER 2017 dataset. In another study, Mushtaq et al. [10] showed the highest accuracy of 99.20% for the Sigmoid-based Naive Bayes method. They also presented that the k Nearest Neighbour (k-NN) method performed

the best with PCA-based techniques. The accuracy rate was between 96.4% and 97.8%.

Kong [11] used five different ML models including LR, RF, SVM, k-NN and NB using WBCD. Performance evaluation was performed based on accuracy, precision and recall. The study uses initial tumour data to diagnose breast cancer using ML models. The study presents that the RF model achieved 98.25% prediction accuracy, and the SVM model achieved 100% prediction accuracy. Laghmati et al. [12] discusses the use of PCA and ML algorithms. Particularly the k-NN algorithm, for breast cancer classification and prediction. Sindhuja et al. [13] employed a deep neural network (DNN) incorporating PCA for feature selection to predict breast cancer types and recurrences. So, PCA is used to reduce the size and improve the performance of various ML algorithms. A study showed that integrating PCA with SVM increased the prediction accuracy from 94% to 96% while achieving high precision and recall scores [14]. Another study highlighted the effectiveness of PCA-based Deep Neural Network (PCA-DNN), which achieved an impressive accuracy of 98.83% on the WBCD [15]. Additionally, combining PCA with ensemble methods such as Gradient Boosting further enhances the prediction capabilities, allowing for robust classification of benign and malignant cases [16,17]. However, the need for larger datasets to improve model performance remains a common limitation across studies [16]. A hybrid approach of Convolutional Neural Networks (CNN) and PCA is proposed for early breast cancer diagnosis. This research uses unsupervised PCA for data understanding and supervises CNN for benign/malignant tumour classification from mammography images [18]. PCA is an important tool in optimizing ML models for breast cancer diagnosis [19].

The main objective of this research is to analyse the effects of different missing data imputation methods and PCA data reduction techniques used to improve the performance of ML models for early breast cancer diagnosis. PCA is mainly used as a dimensionality reduction technique that condenses many variables into a more manageable subset while preserving the most relevant information [20]. First, missing data imputation methods are used to appropriately fill in missing or empty values in cases where they exist in the dataset. These methods are essential for maintaining data integrity and ensuring that ML models produce more reliable results. Different missing data imputation methods may employ various strategies, considering the distribution of missing data and the dataset's characteristics. PCA identifies the principal components that emphasize the relationships between variables in the dataset and reduces the dimensionality of the dataset by selecting these components accurately. These results give a more readily understandable dataset. Also, it can improve the performance of ML models. The research detail will directly compare the effects of different missing data imputation methods and PCA-based data reduction techniques on the performance of ML models. This research was conducted on the WBCD [21]. The study's results were analysed using different metrics and



performance criteria to determine which method performed better.

The motivation of this study is to present a different approach to increase the accuracy and reliability of ML models in the diagnosis of breast cancer, which is a major health problem. Despite the advances in diagnostic technologies, the handling of missing data and the high dimensionality of medical datasets may pose varying degrees of challenges. This study emphasizes the importance of appropriate data completion techniques and the PCA method on model performance. It also demonstrates that model performance may be affected if these choices are not considered.

Our main contributions to this study are as follows.

- An analysis of different missing data imputation methods is presented in breast cancer diagnosis
- The effect of PCA on model accuracy was investigated on the new dataset, which was obtained by imputation missing data in the dataset.
- The performance analysis of PCA and missing data completion techniques on the same dataset was evaluated using ML methods.

This paper is organized as follows. Section 2 presents the materials and methods, providing information about the dataset and ML models used in the study. Section 3 presents the experimental results. This section shows the effects of missing data imputation techniques and PCA-based data reduction methods on the model performance. The performance of ML algorithms is compared. The evaluation of experimental results and findings related to other studies are discussed in Section 4. Finally, Section 5 summarizes the study's general conclusions and provides suggestions for future studies.

## 2. MATERIAL AND METHOD

Machine learning has shown significant advancements in the field of medicine in recent years. These algorithms have developed successful analyses and outcomes for various applications. Early diagnosis, particularly, holds critical importance in the treatment of breast cancer. ML algorithms contribute significantly to health professionals in areas such as early detection of breast cancer, risk analysis, managing treatment processes and decision support.

The analysis of classifiers used in the study was tested with the WBCD dataset. The WBCD dataset consists of 699 samples with 9 features. In the study, out of 9 features, the classification information was used for disease diagnosis, categorized as 4-malignant and 2-benign. Figure 1 shows the distribution of classification information.

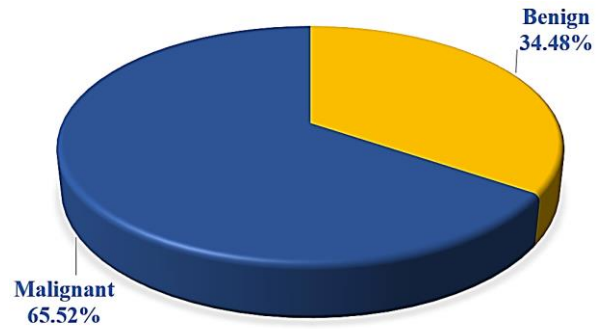


Figure 1. Classification of breast cancer diagnoses

The features used in the classification of tumours are crucial for obtaining the conclusion of whether a tumour is benign or malignant. These features represent various characteristics of the tumour and help determine the characteristics of tumour cells. These features are used to better understand the morphology and behaviour of tumours. ML algorithms can be used to predict whether a tumour is benign or malignant by analysing these features [22]. The dataset is structured as a table containing nine medical parameters and one output class. These parameters encompass various measurements and evaluations obtained during the examination, as illustrated in Table 1.

Table 1. Medical parameters

Specification	Average	Standard Deviation	Minimum Value	Maximum Value
Clump Thickness	4.42	2.82	1.00	10.00
Uniformity of Cell Size	3.13	3.05	1.00	10.00
Uniformity of Cell Shape	3.21	2.97	1.00	10.00
Marginal Adhesion	2.81	2.86	1.00	10.00
Single Epithelial Cell Size	3.22	2.21	1.00	10.00
Bare Nuclei	3.46	3.64	0.00	10.00
Bland Chromatin	3.44	2.44	1.00	10.00
Normal Nucleoli	2.87	3.05	1.00	10.00
Mitoses	1.59	1.72	1.00	10.00
Class	2.69	0.95	2.00	4.00

After the data content was received, an examination was first made to determine whether the data contained discrete and missing values. The analysis revealed that the data did not contain discrete values, but 16 missing data points were observed. Various approaches were explored concerning our studies identified 16 missing data points. The main reason for this decision is that although replacing missing data with a value of 0 has been preferred in previous studies on a similar dataset, the classification of the WBCD dataset has been performed between 1 and 10.

The correlation matrix is a statistical tool that measures the relationship between each pair of variables in a dataset. This relationship indicates how variables change together and how dependent they are on each other. The correlation matrix is presented in matrix form, where each cell contains the correlation coefficient between the corresponding two variables. These coefficients typically range from -1 to 1. As a coefficient approaches 1, the

relationship between variables is stronger and positively oriented; that is, as one variable increases, the other also increases. As it approaches -1, the relationship is negatively oriented; as one variable increases, the other decreases. Coefficients close to 0 indicate little to no relationship between variables, or a very weak relationship. When examining the correlation matrix, attention is paid to high correlation coefficients. High correlation indicates a strong relationship between variables and in such cases, these variables may need to be considered together or one may be preferred over the other in the modelling process. On the other hand, low or near-zero correlation coefficients indicate no or very weak relationship between variables, which helps in identifying unnecessary variables in the modelling process. The correlation matrix for the WBCD dataset is provided in Figure 2.

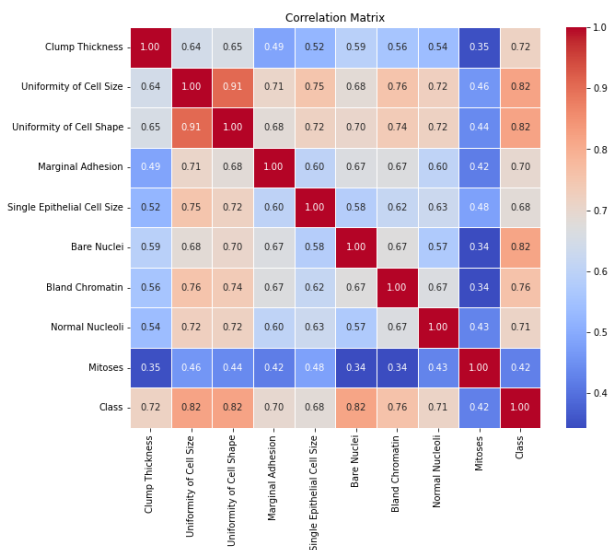


Figure 2. Correlation matrix

Four different methods were used to remove missing data. PCA was used as the dimensionality reduction technique. The obtained results enabled us to compare the effects of different imputation methods and PCA on the model performance. Data processed with PCA after replacing missing values with zero, mean, median values or by deleting missing data were evaluated for model performance. These analyses helped determine which imputation method and PCA component count provided the best performance for the model. In this way, effective handling of missing data and optimization of the model were achieved.

In the study, model performances were measured both across the entire dataset and with lower-dimensional data obtained using the PCA method for feature extraction. During feature extraction, features were transformed into linear combinations of features orthogonal to each other to reduce the dimensionality of the data and improve the accuracy and efficiency of the model. PCA takes the feature set as input and outputs a set of linear combinations of the elements of a subset of the feature set. This two-step approach was implemented as follows: In the first step, the data dimensionality was reduced using a fast and effective unsupervised feature extraction

technique like PCA. Subsequently, the obtained lower-dimensional data were used to train the models. Figure 3 depicts the process flow of the proposed method.

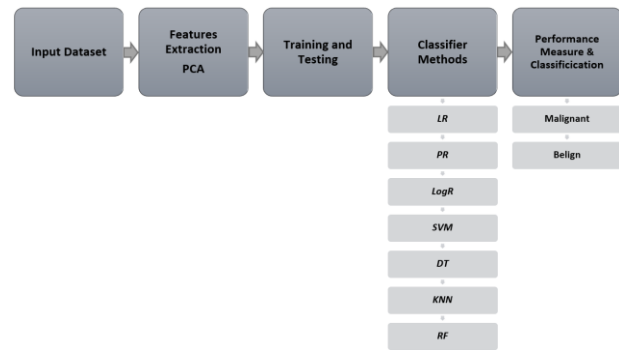


Figure 3. Flowchart of proposed system

ML algorithms exhibit different performances depending on the dataset, the type of problem and the metrics measured. Therefore, it is not always accurate to claim that one algorithm is superior to another. For instance, while one classifier may outperform others in a specific task, a different classifier may yield better results in another task.

In addition, different parameters such as label balance, size, and noise level of the dataset may affect the performance of the algorithms. This study used the Python programming language, Scikit-learn, and TensorFlow libraries within the Anaconda platform using the Spyder environment. The performances of the 16-missing data in the WBCD dataset and the methods of deleting, writing zero, and filling with mean and median values were evaluated. PCA is one of the dimensionality reduction techniques, and the number of components was assessed using LR, PR, LogR, SVM, DT, k-NN and RF algorithms. The obtained results were subjected to a detailed analysis to determine which algorithm performed better and provided the most accurate results for breast cancer diagnosis. It was determined which algorithm provided the best results and most accurate predictions for breast cancer diagnosis with the use of how many components.

### 3. EXPERIMENTAL RESULTS

In this study, there are a total of 699 data points in the WBCD dataset, with 16 of them containing missing values. Twenty percent of the dataset was set aside to evaluate the model's performance, while the remaining data was used for training the model. Various methods were applied to handle missing data such as zero imputation, mean, median and deletion of missing values. The results of these approaches are presented in Tables 2, 3, 4 and 5 respectively. When considered overall, applying the median imputation method for handling missing data resulted the highest performance among all ML algorithms, as demonstrated in Table 5.

**Table 2.** Assigning a zero value to replace missing data

Number of Components	LR	PR	LogR	SVM	DT	k-NN	RF
All Components	0.8500	0.8714	0.9643	0.9714	0.9429	0.9786	0.9643
PCA (n=8)	0.8571	0.8857	0.9643	0.9714	0.9357	0.9714	0.9714
PCA (n=7)	0.8500	0.9071	0.9643	0.9714	0.9357	0.9714	0.9714
PCA (n=6)	0.8500	0.9071	0.9571	0.9714	0.9357	0.9643	0.9786
PCA (n=5)	0.8500	0.9000	0.9571	0.9714	0.9429	0.9714	0.9643
PCA (n=4)	0.8571	0.8786	0.9643	0.9714	0.9429	0.9643	0.9714
PCA (n=3)	0.8571	0.8929	0.9714	0.9714	0.9214	0.9714	0.9643
PCA (n=2)	0.8643	0.9143	0.9571	0.9643	0.9429	0.9714	0.9500

**Table 3.** Assigning mean values instead of missing data

Number of Components	LR	PR	LogR	SVM	DT	k-NN	RF
All Components	0.8500	0.8786	0.9571	0.9643	0.9571	0.9857	0.9643
PCA (n=8)	0.8571	0.8929	0.9643	0.9643	0.9429	0.9714	0.9714
PCA (n=7)	0.8571	0.9000	0.9643	0.9714	0.9214	0.9714	0.9714
PCA (n=6)	0.8500	0.8929	0.9571	0.9714	0.9286	0.9643	0.9786
PCA (n=5)	0.8500	0.9000	0.9571	0.9714	0.9071	0.9714	0.9643
PCA (n=4)	0.8571	0.8786	0.9571	0.9714	0.9286	0.9643	0.9643
PCA (n=3)	0.8571	0.8929	0.9643	0.9714	0.9214	0.9714	0.9714
PCA (n=2)	0.8714	0.9143	0.9643	0.9643	0.9286	0.9714	0.9429

**Table 4.** Extraction of missing data

Number of Components	LR	PR	LogR	SVM	DT	k-NN	RF
All Components	0.7883	0.8613	0.9562	0.9489	0.9416	0.9489	0.9416
PCA (n=8)	0.7883	0.8613	0.9635	0.9489	0.9781	0.9562	0.9635
PCA (n=7)	0.7883	0.8832	0.9708	0.9562	0.9562	0.9562	0.9854
PCA (n=6)	0.7883	0.8832	0.9489	0.9562	0.9489	0.9562	0.9781
PCA (n=5)	0.7883	0.8686	0.9489	0.9562	0.9343	0.9635	0.9781
PCA (n=4)	0.7883	0.8759	0.9562	0.9562	0.9343	0.9635	0.9708
PCA (n=3)	0.7810	0.8759	0.9562	0.9708	0.9416	0.9781	0.9708
PCA (n=2)	0.7810	0.8978	0.9489	0.9635	0.9489	0.9854	0.9635

**Table 5.** Filling in missing data with median value

Number of Components	LR	PR	LogR	SVM	DT	k-NN	RF
All Components	0.8571	0.8857	0.9571	0.9714	0.9357	0.9857	0.9643
PCA (n=8)	0.8571	0.8929	0.9643	0.9714	0.9429	0.9714	0.9714
PCA (n=7)	0.8571	0.9071	0.9643	0.9714	0.9429	0.9714	0.9714
PCA (n=6)	0.8500	0.9071	0.9571	0.9714	0.9429	0.9643	0.9643
PCA (n=5)	0.8500	0.9000	0.9571	0.9714	0.9286	0.9714	0.9786
PCA (n=4)	0.8571	0.8786	0.9571	0.9714	0.9429	0.9643	0.9714
PCA (n=3)	0.8571	0.8929	0.9714	0.9714	0.9357	0.9786	0.9714
PCA (n=2)	0.8643	0.9143	0.9571	0.9643	0.9429	0.9714	0.9500

Figure 6 evaluates four methods for handling missing data and seven different ML algorithms. Among these methods, k-NN showed the best performance of 98.57% for mean imputation. In the case of deletion methods, the success rates of the algorithms are generally lower than other methods. The best performance was observed at the median imputation. ML methods using median

imputation are 98.57% for k-NN, 97.14% for SVM, and 96.43% for RF. Overall, it was found that deletion or imputation with zeros, with accurate data and PCA applications, led to lower success rates for all ML algorithms. In contrast, imputing missing data with mean or median values improved the overall performance of the algorithms.

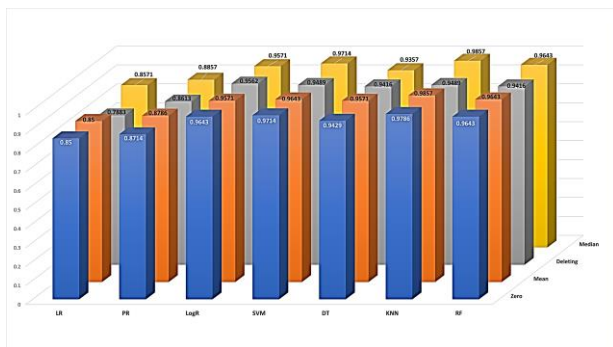


Figure 6. Missing data results for all data sets

#### 4. DISCUSSION

The findings of this study show that missing data management and PCA-based data reduction techniques significantly affect the performance of ML models in breast cancer diagnosis. Our analysis revealed that filling missing data with a median is more effective than other methods in improving model performance. The fact that the median filling method represents the data in a way that is suitable for the distribution in the dataset can be considered one of the main reasons for this effect.

In other studies, the MLTPBC system proposed by Narasimhaiah and Nagaraju [23] uses automatic systems for breast cancer identification using existing methods without PCA. Kong [11] emphasize that PCA achieves 100% in-sample prediction accuracy, especially with the PCA-RF combination, and demonstrates the effectiveness of PCA in classification tasks. Banerjee et al. [24] performed on the same dataset and 16 missing data were deleted. One was trained using Ensemble Learning, and the other without Ensemble Learning. The success rates were given as 95.6% and 82.59%, respectively. While their study was limited to a single method for removing missing data, it was also limited to only two different algorithms in the training part. In their research, Kadhim and Kamil [25] performed it on the same dataset, and 16 missing data were deleted. Eleven different classification models were analysed. The Extreme Random Trees (ERT) model was the most successful, with a success rate of 97.36%. In this study, only one method was used for missing data.

In our study, integrating ML algorithms with PCA with missing data management strategies provided significant improvements in model performance. It has been observed that reducing the data size using PCA leads to significant performance increases, especially in SVM and k-NN algorithms. These results are consistent with the findings obtained in other studies in the literature. It is seen that the combination of median filling and PCA further improves the performance of ML models.

In addition, only ML algorithms were used in [26,27] studies, and breast cancer diagnosis was predicted without using PCA. Unlike these studies, the contribution of the combined use of missing data management and PCA-based data reduction techniques to model performance is seen more clearly in our research. This study emphasizes the importance of using missing data management and

PCA-based data reduction techniques to increase the success of ML models in breast cancer diagnosis.

#### 5. CONCLUSION

This study evaluates PCA and ML algorithms with methods for eliminating missing data are used. In the study, the performances of the methods of deleting, writing zero, and filling with mean and median values among the missing data removal methods were evaluated for 16 missing data on the WBDC data set. For each method, the evaluation with different component numbers in the data reduction technique with PCA was tried in 7 different ML algorithms. When the results were analysed, it was observed that the method of deleting missing data generally performed lower. This finding causes low performance in the models because deleting missing data causes data loss. On the other hand, it was observed that the mean imputation method obtained results that were close to those of the median imputation method. Median imputation was effective, especially when the data distribution had a significant asymmetry. However, in some cases, the performance obtained with mean imputation is lower than zero imputation. This variation suggests that the selection of the imputation method may depend on the characteristics of the model and the data distribution. As a result, when the most successful two algorithms among seven were evaluated, the highest performance of the models was observed in filling with median with 97.14% success rates for SVM and 98.57% for k-NN. After filling the missing data with the median filling method, the number of components was evaluated in dimensionality reduction with PCA. The results showed that some models could slightly increase their accuracy rates or maintain their current performance. It was observed that LogR and PR models achieved the highest accuracy rate, especially when the number of components was reduced. However, in SVM and k-NN algorithms, there was no significant change in their success rates even when the number of components was reduced. When working on large data sets, it is thought that reducing the data size will speed up the analysis processes of the data set, which will provide time and cost savings. In future studies, examining the effects of missing data removal methods on large data sets with more missing data will be helpful. In addition to PCA, the effects of dimensionality reduction techniques such as T-distributed Stochastic Neighbor Embedding (t-SNE) and Uniform Manifold Approximation and Projection (UMAP) on model performance can be examined. Evaluating the performance of these methods by applying them to more ML methods and DNN will contribute to obtaining more detailed results.

#### REFERENCES

- [1] Sun YS, Zhao Z, Yang ZN, Xu F, Lu HJ, Zhu ZY, et al. Risk factors and preventions of breast cancer. *Int J Biol Sci* 2017;13:1387–97. <https://doi.org/10.7150/ijbs.21635>.
- [2] Cardoso F, Kyriakides S, Ohno S, Penault-Llorca F, Poortmans P, Rubio IT, et al. Early breast cancer: ESMO Clinical Practice Guidelines for diagnosis,

- treatment and follow-up. *Annals of Oncology* 2019;30:1194–220.  
<https://doi.org/10.1093/annonc/mdz173>.
- [3] Ginsburg O, Yip CH, Brooks A, Cabanes A, Caleffi M, Yataco JAD, et al. Breast Cancer Early Detection: A Phased Approach to Implementation. *Cancer* 2020;126:2379–93.  
<https://doi.org/10.1002/cncr.32887>.
- [4] Global Breast Cancer Initiative Implementation Framework Assessing, strengthening and scaling up services for the early detection and management of breast cancer. Geneva: 2023.
- [5] Ting Sim JZ, Fong QW, Huang W, Tan CH. Machine learning in medicine: what clinicians should know. *Singapore Med J* 2023;64:91–7.  
<https://doi.org/10.11622/smedj.2021054>.
- [6] Saturi S. Review on Machine Learning Techniques for Medical Data Classification and Disease Diagnosis. *Regen Eng Transl Med* 2023;9:141–64.  
<https://doi.org/10.1007/s40883-022-00273-y>.
- [7] Zhang B, Shi H, Wang H. Machine Learning and AI in Cancer Prognosis, Prediction, and Treatment Selection: A Critical Approach. *J Multidiscip Healthc* 2023;16:1779–91.  
<https://doi.org/10.2147/JMDH.S410301>.
- [8] Savić M, Kurbalija V, Ilić M, Ivanović M, Jakovetić D, Valachis A, et al. The Application of Machine Learning Techniques in Prediction of Quality of Life Features for Cancer Patients. *Computer Science and Information Systems* 2023;29:381–404.  
<https://doi.org/10.2298/CSIS220227061S>.
- [9] Hasan MM, Haque MR, Kabir MMJ. Breast Cancer Diagnosis Models Using PCA and Different Neural Network Architectures. 2019 International Conference on Computer, Communication, Chemical, Materials and Electronic Engineering (IC4ME2), 2019, p. 1–4.  
<https://doi.org/10.1109/IC4ME247184.2019.9036627>.
- [10] Mushtaq Z, Yaqub A, Hassan A, Su SF. Performance Analysis of Supervised Classifiers Using PCA Based Techniques on Breast Cancer. 2019 International Conference on Engineering and Emerging Technologies (ICEET), 2019, p. 1–6.  
<https://doi.org/10.1109/CEET1.2019.8711868>.
- [11] Kong D. Research on Prediction of Breast Cancer Type using Machine Learning. vol. 2023. 2023.
- [12] Laghmati S, Cherradi B, Tmiri A, Daanouni O, Hamida S. Classification of Patients with Breast Cancer using Neighbourhood Component Analysis and Supervised Machine Learning Techniques. 2020 3rd International Conference on Advanced Communication Technologies and Networking (CommNet), 2020, p. 1–6.  
<https://doi.org/10.1109/CommNet49926.2020.9199633>.
- [13] Sindhuja M, Poonkuzhali S, Vigneshwaran P. Breast Cancer Classification Model Using Principal Component Analysis and Deep Neural Network. *Smart Innovation, Systems and Technologies*, vol. 324, Springer Science and Business Media Deutschland GmbH; 2023, p. 137–49.  
[https://doi.org/10.1007/978-981-19-7447-2\\_13](https://doi.org/10.1007/978-981-19-7447-2_13).
- [14] Parman NH, Hassan R, Zakaria NH. Breast Cancer Prediction Using Support Vector Machine Ensemble with PCA Feature Selection Method. *International Journal of Innovative Computing* 2024;14:15–9.  
<https://doi.org/10.11113/ijic.v14n1.461>.
- [15] Rani P, Kumar R, Jain A, Lamba R, Sachdeva RK, Choudhury T. PCA-DNN: A Novel Deep Neural Network Oriented System for Breast Cancer Classification. *EAI Endorsed Trans Pervasive Health Technol* 2023;9.  
<https://doi.org/10.4108/eetpht.9.3533>.
- [16] Lou J. Prediction of breast cancer based on RF, SVM and PCA. *J Phys Conf Ser*, vol. 2646, Institute of Physics; 2023. <https://doi.org/10.1088/1742-6596/2646/1/012036>.
- [17] Bista C, M A, Slimanzay S, Sheikh MS, Srinivasa Rao P. Breast Cancer Prediction System Utilizing Machine Learning Algorithms, *Institute of Electrical and Electronics Engineers (IEEE)*; 2024, p. 80–4.  
<https://doi.org/10.1109/ieecon61558.2024.10585589>.
- [18] Eladallaoui HE, Elfazziki A, Sadgal M. A CNN and PCA Approach for Earlier Breast Cancer Diagnosis. *Proceedings - 17th International Conference on Signal-Image Technology and Internet-Based Systems, SITIS 2023, Institute of Electrical and Electronics Engineers Inc.*; 2023, p. 247–52.  
<https://doi.org/10.1109/SITIS61268.2023.00045>.
- [19] Yadav RK, Singh P, Kashtriya P. Diagnosis of Breast Cancer using Machine Learning Techniques -A Survey. *Procedia Comput Sci* 2023;218:1434–43.  
<https://doi.org/10.1016/j.procs.2023.01.122>.
- [20] Bharadiya JP. A Tutorial on Principal Component Analysis for Dimensionality Reduction in Machine Learning. *Int J Innov Res Sci Eng Technol* 2023;8.  
<https://doi.org/10.5281/zenodo.8002436>.
- [21] Wolberg Wi. Breast Cancer Wisconsin (Original) 1992.
- [22] Kaya S, Yağanoğlu M. An Example of Performance Comparison of Supervised Machine Learning Algorithms Before and After PCA and LDA Application: Breast Cancer Detection. 2020 Innovations in Intelligent Systems and Applications Conference (ASYU), 2020, p. 1–6.  
<https://doi.org/10.1109/ASYU50717.2020.9259883>.
- [23] Narasimhaiah P, Nagaraju C. Machine Learning Technique for Prediction of Breast Cancer. *International Journal on Recent and Innovation Trends in Computing and Communication* 2023;11:368–80.  
<https://doi.org/10.17762/ijritcc.v11i7s.7012>.
- [24] Baneriee C, Paul S, Ghoshal M. A Comparative Study of Different Ensemble Learning Techniques Using Wisconsin Breast Cancer Dataset. 2017 International Conference on Computer, Electrical & Communication Engineering (ICCECE), 2017, p. 1–6.  
<https://doi.org/10.1109/ICCECE.2017.8526215>.
- [25] Kadhim RR, Kamil MY. Comparison of breast cancer classification models on Wisconsin dataset. *International Journal of Reconfigurable and Embedded Systems* 2022;11:166–74.  
<https://doi.org/10.11591/ijres.v11.i2.pp166-174>.

- [26] Asharma S, Shinde S, Choudhary A, Raj U, Srivastava P. Machine Learning-Based Breast Cancer Detection. 2024 11th International Conference on Reliability, Infocom Technologies and Optimization (Trends and Future Directions), ICRITO 2024, Institute of Electrical and Electronics Engineers Inc.; 2024. <https://doi.org/10.1109/ICRITO61523.2024.10522209>.
- [27] Ahmed SS, Srivastava Y, Khan MohdG. Prediction and Diagnosis of Breast Cancer Using Machine Learning Algorithms. Asian Journal of Research in Medical and Pharmaceutical Sciences 2024;13:54–60. <https://doi.org/10.9734/ajrimps/2024/v13i3261>.

## Classification of Skin Diseases with Different Deep Learning Models and Comparison of the Performances of the Models

Ferdi DOĞAN<sup>1\*</sup>, Mikat AKTAŞ<sup>2</sup>, Mehmet İsmail GÜRSOY<sup>3</sup>

<sup>1</sup> Adıyaman University, Faculty of Engineering, Computer Engineering, Adıyaman, Türkiye

<sup>2</sup> Fırat University, Faculty of Technology, Software Engineering, Elazığ, Türkiye

<sup>3</sup> Adıyaman University, Technical Sciences Vocational School, Electrical Department, Adıyaman, Türkiye

Ferdi DOĞAN ORCID No: 0000-0002-9203-697X

Mikat AKTAŞ ORCID No: 0000-0002-0731-5668

Mehmet İsmail GÜRSOY SOYAD ORCID No: 0000-0002-2285-5160

\*Corresponding author: fdogan@adiyaman.edu.tr

(Received: 18.06.2024, Accepted: 25.08.2024, Online Publication: 26.09.2024)

### Keywords

Deep learning,  
Skin diseases  
classification,  
Disease detection,  
Dermatology,  
Quality of life

**Abstract:** Classification of skin diseases is a important issuse for early diagnosis and treatment. The process of determining the disease by the specialist physician also delays the treatment process to be applied to the patient. Computer-aided diagnosis systems play an important role in early diagnosis and initiation of treatment by minimizing such processes. In this study, high-performance classification of skin lesions was performed by using Deep Learning models. Dataset was ISIC data set, dataset were expanded by using data augmentation techniques. In the images in this dataset, there are images of Actinic Keratosis, Dermatofibroma, Pigmented Benign Keratosis, Seborrheic Keratosis, Vascular Lesion skin diseases. The data set was classified by Deep Learning models by using the supervised learning method.. SequeezeNet, AlexNet, GoogleNet, Vgg-19, ResNet101, DenseNet201, ResNet-50, ResNet-18, Vgg-16 DL models were used for classification. To evaluate of classification success of Deep Learning models, confusion matrix and F1-score, precision, sensitivity and accuracy metrics obtained from the matrix were used. According to the F1-score, the most successful model is Vgg16 with 97.41%, while the highest accuracy rate obtained by ResNet18 with 98.06%. High success rate shows that such systems can be used for diagnosis and treatment processes.

## Farklı Derin Öğrenme Modelleri ile Cilt Hastalıklarının Sınıflandırılması ve Modellerin Performanslarının Karşılaştırılması

### Anahtar Kelimeler

Derin öğrenme,  
Cilt hastalıkları  
sınıflandırması,  
Hastalık tespiti,  
Dermatoloji,  
Yaşam kalitesi

**Öz:** Deri hastalıklarının sınıflandırılması erken tanı ve tedavi açısından önemli bir konudur. Hastalığın uzman hekim tarafından tespit edilmesi süreci aynı zamanda hastaya uygulanacak tedavi sürecini de geciktirmektedir. Bilgisayar destekli teşhis sistemleri bu süreçleri en aza indirerek erken teşhis ve tedaviye başlanmasında önemli rol oynamaktadır. Bu çalışmada Derin Öğrenme modelleri kullanılarak cilt lezyonlarının yüksek performanslı sınıflandırması yapılmıştır. Veri seti ISIC veri seti olup, veri artırma teknikleri kullanılarak veri seti genişletilmiştir. Bu veri setindeki görsellerde Aktinik Keratoz, Dermatofibroma, Pigmentli Benign Keratoz, Seboreik Keratoz, Vasküler Lezyon cilt hastalıklarına ait görseller bulunmaktadır. Veri seti denetimli öğrenme yöntemi kullanılarak Derin Öğrenme modelleri ile sınıflandırılmıştır. Sınıflandırma için SequeezeNet, AlexNet, GoogleNet, Vgg-19, ResNet101, DenseNet201, ResNet-50, ResNet-18, Vgg-16 DL modelleri kullanılmıştır. Derin Öğrenme modellerinin sınıflandırma başarısını değerlendirmek için karışıklık matrisi ve matrizen elde edilen F1 skoru, kesinlik, duyarlılık ve doğruluk metrikleri kullanılmıştır. F1 skoruna göre en başarılı model %97,41 ile Vgg16 olurken, en yüksek doğruluk oranı %98,06 ile ResNet18 tarafından elde edildi. Başarı oranının yüksek olması bu tür sistemlerin teşhis ve tedavi süreçlerinde kullanılabileceğini göstermektedir.

## 1. INTRODUCTION

Skin diseases are one of the most common diseases in the world[1]. Diagnosis and treatment of skin diseases are quite difficult due to their complexity. In order to diagnose these diseases, comprehensive tests should be performed and examined[2]. The experience of the doctor and obtaining pathological results delay the diagnosis process of the patient considerably. Diagnosing and diagnosing the patient's condition is vital in some cases. Accelerating such processes is very important for medical processes [3]. Many known skin diseases are visually similar to each other. While some skin diseases are benign, some skin diseases can be malignant. In both cases, early diagnosis and treatment are valuable to improve the patient's quality of life. Skin lesions appearing in different parts of the body can have different meanings. The treatment processes of these skin lesions, which are very similar to each other, can be different from each other. When the specialist suspects the lesion, he performs a visual inspection. However, it is not possible

to perform visual inspection for all lesions [4-7]. There is no accepted definitive diagnostic method for visual inspection.

Image processing and its applications have become increasingly common with the increase in the high computational capacity of computer technologies,. It is used in many fields such as production, industry, defense and medicine[8, 9]. In recent years, computer-aided diagnosis systems related to medical diagnosis and treatment have become quite widespread. The systems with the highest rate in the performance of computer vision systems are artificial intelligence supported systems. Especially DL-based systems are used very popularly nowadays [10]. Deep Learning (DL) can be defined as a deep artificial intelligence system used especially on images. Thanks to its high depth artificial neural network layer structure, it gives quite successful results in image classification and detection processes [11]. The layers and classification process used in a DL architecture are shown in Figure 1.

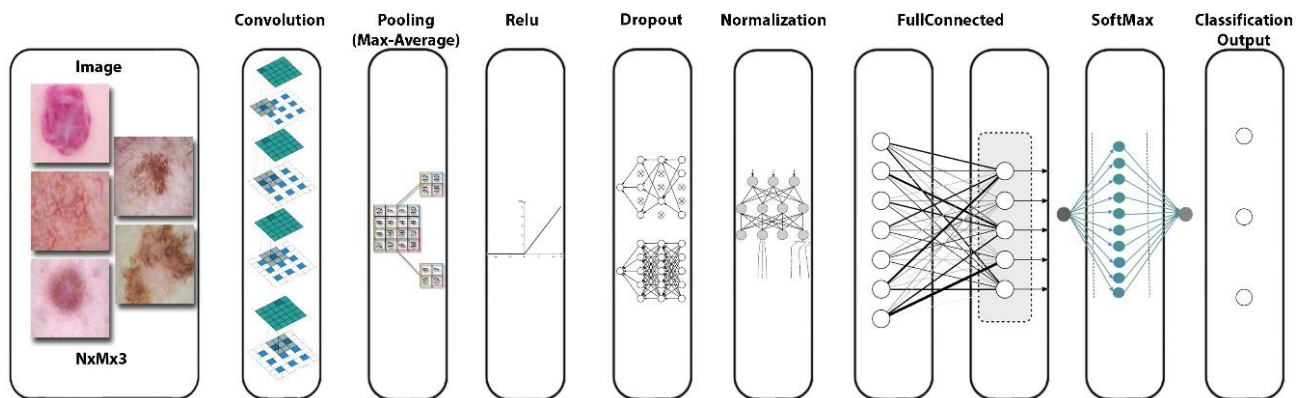


Figure 1. An example DL model and layers used in the model[12].

A dataset consisting of images of skin diseases, which is the input image in Figure 1, is put as input data to a sample DL model. Then, feature extraction is performed via convolutional layer. In the next layers, the image size used as input for the network is reduced by the polling process. Relu is used for activation function [13-15]. Probability of memorization of the network is reduced and some of the random weights in the network are discarded in the dropout layer,. The image data is standardized via normalization layer. Neurons in a fully connected layer are connected to neurons in the previous layer. This layer combines all the features (attributes) learned by previous layers in the image to identify larger patterns. The Softmax layer is the entropy layer and it makes probabilistic estimation and it is estimated which class the input image belongs to via the Classification layer [16,17].

9 DL models used for the classification of skin diseases. These models are SqueezeNet, AlexNet, GoogleNet, Vgg-19, ResNet101, DenseNet201, ResNet-50, ResNet-18, Vgg-16 [18-23]. These were used in the study because they were the most commonly encountered deep learning models in the literature reviews .

## 2. RELATED WORK

Classification of skin diseases is important for early diagnosis and early intervention of the disease [24]. Studies on this subject will make the doctor's work easier. It will provide early diagnosis and early intervention. On the other hand, it will lead the patients to start the treatment due to early diagnosis. When the studies are examined, the classification process was carried out using different datasets. Images obtained from different datasets were tried to be classified with different algorithms. Classification studies of skin diseases basically consist of two main parts. The first is classification using traditional methods. The second is classification using DL architectures. In traditional methods, features of the disease are determined and feature extraction is performed. These features are searched on the image and results are produced accordingly. In DL models, the processes are carried out by the layers in the model and the results are produced [25-27].

In a study, the images of 8 classes in the ISIC 2019 dataset were classified using a DL model with transfer learning. In the study, results were obtained by using a model whose weights were determined with GoogleNet. The skin diseases included in the study were classified as



melanoma, melanocytic nevus, basal cell carcinoma, benign keratosis, actinic keratosis, dermatofibroma, vascular lesion, and squamous cell carcinoma. The percentages of accuracy, sensitivity, specificity and precision respectively were 94.92%, 79.8%, 97% and 80.36% [28]. Another study sought to classify skin lesions as cancerous or non-cancerous images. In the study, the skin lesion was tried to be classified via AlexNet DL model. In a study using a two-stage method, an accuracy rate of 78% was achieved in cancerous and non-cancerous skin images [29]. In another study, skin diseases in the HAM10000 dataset were classified by using the DenseNet DL model [30]. AlexNet DL model was used in the study for the classification of skin diseases in the ISIC 2018 dataset, which consists of seven classes. The dataset of melanoma, melanocytic nevus, basal cell carcinoma,

actinic keratosis, benign keratosis, dermatofibroma, and vascular lesion images yielded 98.70% accuracy, 95.60% sensitivity, 99.27% specificity, and 95.06% accuracy [31].

### 3. MATERIAL AND METHOD

In this study, images belonging to 5 classes in the ISIC dataset containing skin diseases were classified. These classes were determined as dermatofibroma, pigmented benign keratosis, actinic keratosis, vascular lesion, seborrheic keratosis. DL from multilayer neural networks, one of the artificial intelligence methods, was used for the classification of skin diseases. 9 different DL models were used for classification.

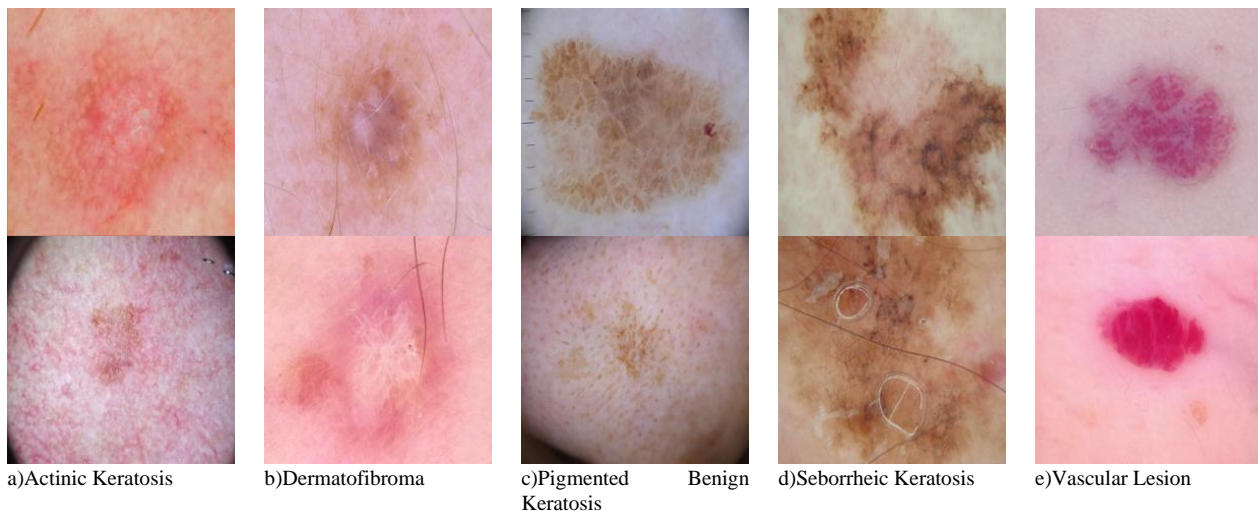


**Figure 2.** Example images used for classification

As seen in Figure 2, the sample images in the dataset are difficult to distinguish, so the diagnosis must be made by a specialist physician and evaluated in the light of pathological findings. The images in each class were

augmented by quadrupling with image reproduction techniques. The number of images in each class is given in

**Table 1.** Number of Image in the dataset used for classification

	Actinic Keratosis	Dermatofibroma	Pigmented Benign Keratosis	Seborrheic Keratosis	Vascular Lesion
Number Of Original Images	114	95	462	77	139
Number Of Augmented Images	456	380	1848	308	556
Total number of Images for Training				3548	

Used DL models and the detailed data of these models are given in Table 2. Table 1. It is known that training is better as the number of images increases in deep learning models. For this reason, the number of samples in the

dataset was increased by 4 times. As data augmentation methods, images were applied as reflection, inversion, 90-degree rotation, and 180-degree rotation.

**Table 2.** Features of used DL models[12]

Model	Number of Layers	Number of Connections	Depth	Number Of Parameter	Top-1 Error rate	Top-5 Error rate
AlexNet	25	-	8	61m	36.7	15.4
VGG16	41	-	16	138m	25.6	8.1
VGG19	47	-	19	144m	25.5	8
GoogleNet	144	170	22	7m	-	6.67
ResNet18	72	79	18	11.7m	30.43	10.76
ResNet50	177	192	50	25.6m	22.8	6.71
ResNet101	347	379	101	44.6m	21.75	6.05
SqueezeNet	68	75	18	1.2m	41.90	19.58
DenseNet201	708	805	201	20m	21.46	5.54

The DL models in Table 2 are frequently encountered in the literature. Each model is at different depths and has different number of layers. The error rates of the models and the number of parameters are important. As the number of parameters increases, the area occupied by the memory increases. Although the structure of each model is different, they can have their own special layer blocks. The dataset used for the classification of skin lesions was carried out using supervised learning. The weights of the models were determined by training the images in each class in the network. Weights were optimized by using transfer learning and classification performances were revealed.

The same hyperparameters were used for each of the deep learning models in Table 2. These hyperparameters are detailed in Table 3.

**Table 3.** Hyperparameters used for training

Hyperparameters	Value
MaxEpoch	50
MiniBatchSize	32
Solver	SGDM
InitialLearnRate	0.01
ValidationFrequency	50
Momentum	0.9
LearnRateDropFactor	0.1
LearnRateDropPeriod	10
L2Regularization	0.0001

**Table 4.** Classification evaluation result table of DL models

Model	Image Size	Number of Classes	Accuracy	Sensitivity	Precision	F1 Score
1 SqueezeNet	227*227	5	95.48	95.19	95.17	95.16
2 AlexNet	227*227	5	94.84	95.48	95.8	95.5
3 GoogleNet	224*224	5	95.00	95.8	95.97	95.74
4 Vgg-19	224*224	5	97.1	96.77	96.82	96.69
5 ResNet101	224*224	5	97.41	97.09	97.08	97.08
6 DenseNet201	224*224	5	96.61	97.09	97.13	97.1
7 ResNet-50	224*224	5	97.74	97.42	97.52	97.36
8 ResNet-18	224*224	5	98.06	97.42	97.58	97.37
9 Vgg-16	224*224	5	97.50	97.42	97.48	97.41

SqueezeNet, AlexNet, GoogleNet, Vgg-19, ResNet101, DenseNet20, , ResNet-50, ResNet-18, Vgg-16 were trained with images of different input sizes. Detailed information in the training is given in Table 4. Accuracy, sensitivity, precision and f1 evaluation metrics were used for the obtained results. The results were presented according to these evaluation metrics. It is seen that the results obtained from deep learning models have 94.84% and 98.5% accuracy and f1 score between 95.16 and 97.41. When the results are examined, the model with the highest F1 score among the given models is Vgg-16. It is seen that ResNet-18 has the highest result in the results

80% of the image in each class is reserved for the training of the network, and 20% for the test. All images were randomly selected during the training. Each model was trained three times and tested after each training. Average of three training and testing results were used for calculating final results. Accuracy, Sensitivity, Precision and F1-score metrics were used for evaluation result criteria. The equations for these metrics are Equation 1, Equation 2, Equation 3, Equation 4 below.

$$Accuracy = \frac{(TP+TN)}{(TP+FN+FP+TN)} \quad (1)$$

$$Sensitivity(Recall) = \frac{TP}{(TP+FN)} \quad (2)$$

$$Precision = \frac{TP}{(TP+FP)} \quad (3)$$

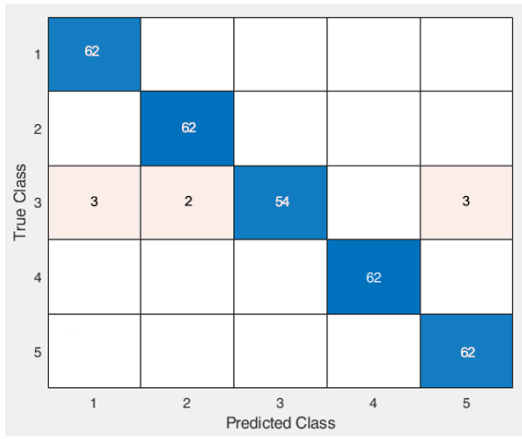
$$F - Score = 2 * \frac{(Precision*Recall)}{(Precision+Recall)} \quad (4)$$

### 3. RESULTS

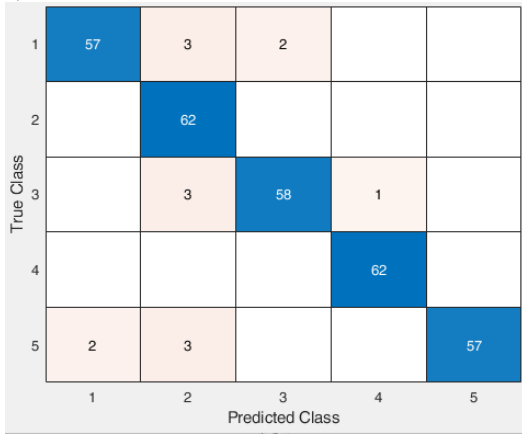
The detailed results obtained in the application for the classification of skin diseases are given in Table 4. In the table, the results of the DL models used for classification these 5 different type of skin diseases are compared in terms of accuracy, sensitivity, precision and F1-scores metrics. The metrics results show that the performance of DL models is quite high. 2810 images were used for training and 710 images were used for testing.

obtained according to the accuracy rate. It was found that the results obtained from these two models are quite close to each other.

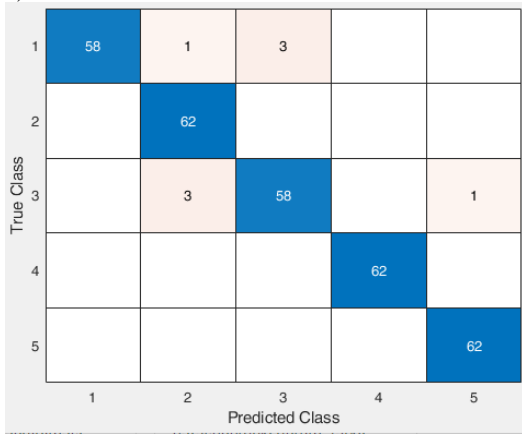
Even though there are small performance differences between the models, it has been observed in the literature studies that the performances of different deep learning models vary depending on the dataset and the study area. It is known in the literature that the Resnet architecture is used more for the dataset and medical images used in the study.



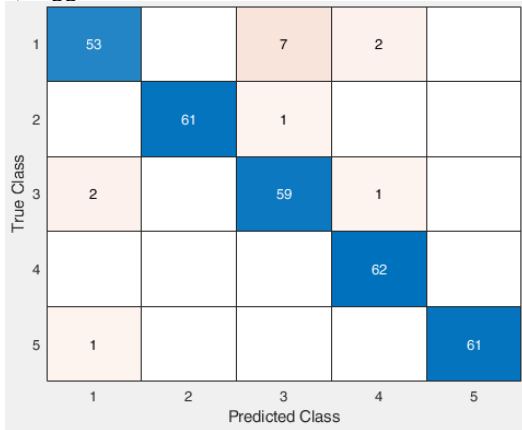
a) ResNet50



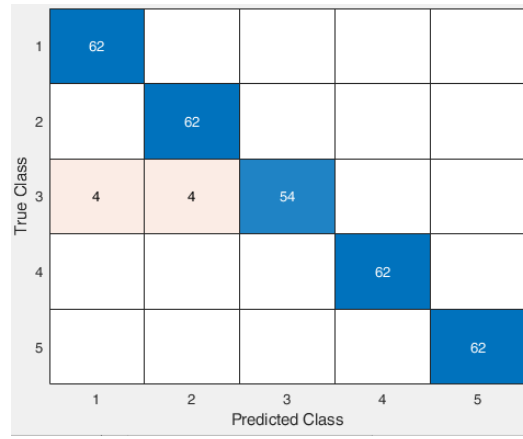
c) AlexNet



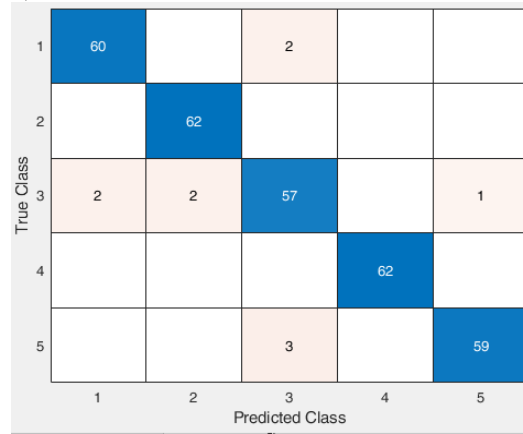
e) Vgg16



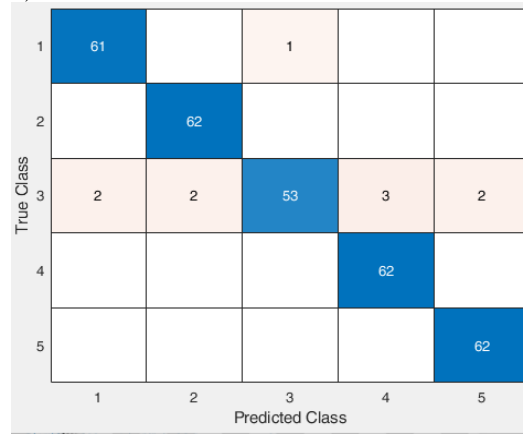
g) SequeezeNet



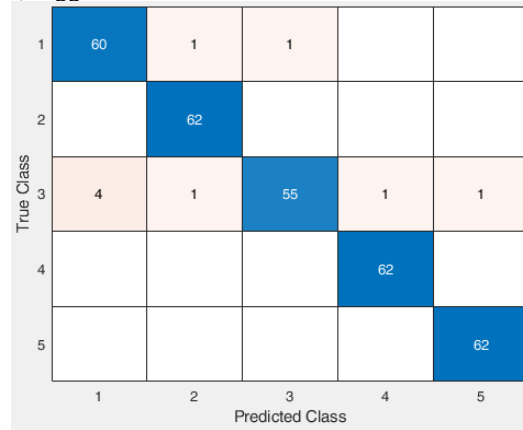
b) ResNet18



d) ResNet101



f) Vgg19



h) DenseNet201

1	62				
2		62			
3	7	1	53		1
4				62	
5		1			61
	1	2	3	4	5

i) GoogleNet

**Figure 3.** Confusion Matrix from DL models

In the figures shown in Figure 3, there are Confusion Matrices for each model. These matrices show the number of true and false classified images obtained in each model. According to the confusion matrix results, the highest results are obtained by Vgg-16 and ResNet18.

## REFERENCES

- [1] Hameed, N., A.M. Shabut, and M.A. Hossain. Multi-class skin diseases classification using deep convolutional neural network and support vector machine. in 2018 12th International Conference on Software, Knowledge, Information Management & Applications (SKIMA). 2018. IEEE.
- [2] Manoorkar, P., D. Kamat, and P. Patil. Analysis and classification of human skin diseases. in 2016 International Conference on Automatic Control and Dynamic Optimization Techniques (ICACDOT). 2016. IEEE.
- [3] Hu, Y., et al., Metabolic syndrome and skin diseases. *Frontiers in endocrinology*, 2019. 10: p. 788.
- [4] Flohr, C., & Hay, R. (2021). Putting the burden of skin diseases on the global map. *British Journal of Dermatology*, 184(2), 189-190.
- [5] Anand, V., Gupta, S., & Koundal, D. (2022). Skin disease diagnosis: challenges and opportunities. In *Proceedings of Second Doctoral Symposium on Computational Intelligence: DoSCI 2021* (pp. 449-459). Springer Singapore.
- [6] Saunte, D. M., Gaitanis, G., & Hay, R. J. (2020). Malassezia-associated skin diseases, the use of diagnostics and treatment. *Frontiers in cellular and infection microbiology*, 10, 112.
- [7] Outerbridge, C. A., & Owens, T. J. (2023). Nutritional management of skin diseases. *Applied Veterinary Clinical Nutrition*, 345-383.
- [8] Ari, A., O.F. Alcin, and D. Hanbay, Brain MR image classification based on deep features by using extreme learning machines. *Biomedical Journal of Scientific and Technical Research*, 2020. 25(3).
- [9] Toraman, S., T.B. Alakus, and I. Turkoglu, Convolutional capsnet: A novel artificial neural network approach to detect COVID-19 disease from X-ray images using capsule networks. *Chaos, Solitons & Fractals*, 2020. 140: p. 110122.
- [10] Alakus, T.B. and I. Turkoglu, Comparison of DL approaches to predict COVID-19 infection. *Chaos, Solitons & Fractals*, 2020. 140: p. 110120.
- [11] Aktaş, M., F. Doğan, and İ. Türkoğlu. Analysis Of Cracks In Photovoltaic Module Cells From Electroluminescence Images By DL. in 1st International Conference on Computing and Machine Intelligence. 2021.
- [12] Dogan, F. and I. Turkoglu, Comparison of DL models in terms of multiple object detection on satellite images. *Journal of Engineering Research*, 2021.
- [13] Das, B., & Toraman, S. (2022). Deep transfer learning for automated liver cancer gene recognition using spectrogram images of digitized DNA sequences. *Biomedical Signal Processing and Control*, 72, 103317
- [14] Demir, F., Sengur, A., Ari, A., Siddique, K., & Alswaitti, M. (2021). Feature mapping and deep long short term memory network-based efficient approach for Parkinson's disease diagnosis. *IEEE Access*, 9, 149456-149464.
- [15] Çalışan, M., Gündüzalp, V., & Olgun, N. Evaluation of U-Net and Resnet Architectures for Biomedical Image Segmentation. *International Journal of 3D Printing Technologies and Digital Industry*, 7(3), 561-570.
- [16] Sunnetci, K. M., Kaba, E., Beyazal Çeliker, F., & Alkan, A. (2023). Comparative parotid gland segmentation by using ResNet-18 and MobileNetV2 based DeepLab v3+ architectures from magnetic resonance images. *Concurrency and Computation: Practice and Experience*, 35(1), e7405.
- [17] Doğan, F. and İ. Türkoğlu. Derin öğrenme modelleri ve uygulama alanlarına ilişkin bir derleme. *Dicle Üniversitesi Mühendislik Fakültesi Mühendislik Dergisi*, 2019. 10(2): p. 409-445.
- [18] Szegedy, C., Ioffe, S., Vanhoucke, V., & Alemi, A. (2016). Inception-v4, inception-resnet and the impact of residual connections on learning. *arXiv preprint arXiv:1602.07261*.
- [19] Huang, G., Liu, Z., Van Der Maaten, L., & Weinberger, K. Q. (2017). Densely connected convolutional networks. In *Proceedings of the IEEE conference on computer vision and pattern recognition* (pp. 4700-4708).
- [20] He, K., Zhang, X., Ren, S., & Sun, J. (2016). Deep residual learning for image recognition. In *Proceedings of the IEEE conference on computer vision and pattern recognition* (pp. 770-778).
- [21] Krizhevsky, A., Sutskever, I., & Hinton, G. E. (2012). Imagenet classification with deep convolutional neural networks. In *Advances in neural information processing systems* (pp. 1097-1105).
- [22] Iandola, F. N., Han, S., Moskewicz, M. W., Ashraf, K., Dally, W. J., & Keutzer, K. (2016). SqueezeNet: AlexNet-level accuracy with 50x fewer parameters and < 0.5 MB model size. *arXiv preprint arXiv:1602.07360*
- [23] Simonyan, K., & Zisserman, A. (2014). Very deep convolutional networks for large-scale image recognition. *arXiv preprint arXiv:1409.1556*.

- [24] Selçuk, T., Beyoğlu, A., & Alkan, A. (2022). Automatic detection of exudates and hemorrhages in low-contrast color fundus images using multi semantic convolutional neural network. *Concurrency and Computation: Practice and Experience*, 34(6), e6768.
- [25] Zhou, H., et al., Mean shift based gradient vector flow for image segmentation. *Computer Vision and Image Understanding*, 2013. 117(9): p. 1004-1016.
- [26] Sadri, A.R., et al., Segmentation of dermoscopy images using wavelet networks. *IEEE Transactions on Biomedical Engineering*, 2012. 60(4): p. 1134-1141.
- [27] Xie, F. and A.C. Bovik, Automatic segmentation of dermoscopy images using self-generating neural networks seeded by genetic algorithm. *Pattern Recognition*, 2013. 46(3): p. 1012-1019.
- [28] Kassem, M.A., K.M. Hosny, and M.M. Fouad, Skin lesions classification into eight classes for ISIC 2019 using deep convolutional neural network and transfer learning. *IEEE Access*, 2020. 8: p. 114822-114832.
- [29] Kaymak, S., P. Esmaili, and A. Serener. DL for two-step classification of malignant pigmented skin lesions. in *2018 14th Symposium on Neural Networks and Applications (NEUREL)*. 2018. IEEE.
- [30] Carcagni, P., et al. Classification of skin lesions by combining multilevel learnings in a DenseNet architecture. in *International conference on image analysis and processing*. 2019. Springer.
- [31] Hosny, K.M., M.A. Kassem, and M.M. Fouad, Classification of skin lesions into seven classes using transfer learning with AlexNet. *Journal of digital imaging*, 2020. 33(5): p. 1325-1334.



## Some Identities Concerning Generalized Fibonacci and Lucas Numbers by Matrix Methods

Gülsüm LİMAN<sup>1\*</sup> , Refik KESKİN<sup>2</sup>

<sup>1</sup> Kağıthane Profilo Vocational and Technical Anatolian High School, İstanbul, Türkiye

<sup>2</sup> Department of Mathematics, Sakarya University, Sakarya, Türkiye

Gülsüm LİMAN ORCID No: 0000-0003-0214-6102

Refik KESKİN ORCID No: 0000-0003-2547-2082

\*Corresponding author: [rkeskin@sakarya.edu.tr](mailto:rkeskin@sakarya.edu.tr)

(Received: 15.12.2023, Accepted: 26.08.2024, Online Publication: 26.09.2024)

### Keywords

Generalized Fibonacci sequence, Generalized Lucas sequence

**Abstract:** In this study, we give some matrices whose powers consist of the terms of generalized Fibonacci and Lucas sequences. Then we give some identities concerning the terms of those sequences.

## Matris Yöntemleriyle Genelleştirilmiş Fibonacci ve Lucas Sayıları ile İlgili Bazı Özellikler

### Anahtar Kelimeler

Genelleştirilmiş Fibonacci dizisi, Genelleştirilmiş Lucas dizisi

**Öz:** Bu çalışmada kuvvetleri genelleştirilmiş Fibonacci ve Lucas dizilerinin terimlerinden oluşan bazı matrisler verilecektir. Daha sonra bu dizilerin terimlerine ilişkin bazı özdeşlikler elde edilecektir.

### 1. INTRODUCTION

Let  $k, t$  be nonzero integers with  $k^2 + 4t > 0$  and  $k > 0$ . Generalized Fibonacci and Lucas sequences  $(U_n(k, t))$  and  $(V_n(k, t))$  are defined by  $U_0(k, t) = 0, U_1(k, t) = 1, V_0(k, t) = 2, V_1(k, t) = k$  and  $U_{n+1}(k, t) = kU_n(k, t) + tU_{n-1}(k, t), V_{n+1}(k, t) = kV_n(k, t) + tV_{n-1}(k, t)$  for  $n \geq 0$ . These sequences are defined firstly by Lucas in [1].

For  $n < 0$ , we define

$$U_n(k, t) = -(-t)^n U_{-n}$$

and

$$V_n(k, t) = (-t)^n V_{-n}.$$

Then it is well known that

$$U_n(k, t) = \frac{\alpha^n - \beta^n}{\alpha - \beta}, V_n(k, t) = \alpha^n + \beta^n$$

for every integer  $n$ , where

$$\alpha = \frac{k + \sqrt{k^2 + 4t}}{2}, \beta = \frac{k - \sqrt{k^2 + 4t}}{2}$$

are the roots of the characteristic equation

$$x^2 - kx - t = 0.$$

The above formulas are known as Binet's formulas. If  $k = t = 1$ , we get Fibonacci sequence  $(F_n)$  and Lucas sequence  $(L_n)$  respectively. For  $k = 2, t = 1$ , we get Pell and Pell-Lucas sequences  $(P_n)$  and  $(Q_n)$ , respectively.

For briefly, we will write  $U_n$  and  $V_n$  instead of  $U_n(k, t)$  and  $V_n(k, t)$ . For more information and applications these sequences one can consult [2] and [5], respectively.

Many identities concerning the terms of these sequence can be proved by using Binet's formulas. Also, matrices can be used to obtain these identities. The most known matrix is  $\begin{pmatrix} k & t \\ 1 & 0 \end{pmatrix}$  and it is well known that

$$\begin{pmatrix} k & t \\ 1 & 0 \end{pmatrix}^n = \begin{pmatrix} U_{n+1} & tU_n \\ U_n & tU_{n-1} \end{pmatrix}$$

for every integer  $n$  (see [3,4]).

The most known identities are given below as (see [2] or [4])

$$\begin{aligned} V_n &= U_{n+1} + tU_{n-1}, \\ (k^2 + 4t)U_n &= V_{n+1} + tV_{n-1}, \\ U_n^2 - (k^2 + 4t)V_n^2 &= 4(-t)^n. \end{aligned}$$

In this study, we give some matrices whose powers consist of the terms of the above sequences. Then we will give some identities concerning the terms of these sequences. As we did not run into these identities in the literature, we think that these identities are new.

**2. MAIN THEOREMS**

**Theorem 1.** Let  $A = \begin{pmatrix} k & -\alpha \\ \beta & 0 \end{pmatrix}$  and  $B = \begin{pmatrix} 0 & \alpha \\ -\beta & k \end{pmatrix}$ . Then

$$A^n = \begin{pmatrix} U_{n+1} & -\alpha U_n \\ \beta U_n & tU_{n-1} \end{pmatrix} \text{ and } B^n = \begin{pmatrix} tU_{n-1} & \alpha U_n \\ -\beta U_n & U_{n+1} \end{pmatrix}$$

for every integer  $n$ .

**Proof:** It can be seen easily that eigenvalues of the matrix  $A$  are  $\alpha$  and  $\beta$ . Eigenvectors related to  $\alpha$  are of the form  $\begin{pmatrix} \alpha t \\ \beta t \end{pmatrix}$  for  $t \neq 0$ . And eigenvectors related to  $\beta$  are of the form  $\begin{pmatrix} t \\ t \end{pmatrix}$  for  $t \neq 0$ . Let  $P = \begin{pmatrix} \alpha & 1 \\ \beta & 1 \end{pmatrix}$ . As  $\det P \neq 0$ , we can write

$$A = PDP^{-1}, \text{ where } D = \begin{pmatrix} \alpha & 0 \\ 0 & \beta \end{pmatrix}.$$

Thus, it is easily seen that  $A^n = PD^nP^{-1}$  and therefore

$$\begin{aligned} A^n &= \frac{1}{\alpha - \beta} \begin{pmatrix} \alpha & 1 \\ \beta & 1 \end{pmatrix} \begin{pmatrix} \alpha^n & 0 \\ 0 & \beta^n \end{pmatrix} \begin{pmatrix} 1 & -1 \\ -\beta & \alpha \end{pmatrix} \\ &= \begin{pmatrix} \frac{\alpha^{n+1} - \beta^{n+1}}{\alpha - \beta} & \frac{-\alpha(\alpha^n - \beta^n)}{\alpha - \beta} \\ \frac{\beta(\alpha^n - \beta^n)}{\alpha - \beta} & \frac{-\alpha\beta(\alpha^{n-1} - \beta^{n-1})}{\alpha - \beta} \end{pmatrix} \\ &= \begin{pmatrix} U_{n+1} & -\alpha U_n \\ \beta U_n & tU_{n-1} \end{pmatrix}. \end{aligned}$$

The proof for the matrix  $B$  is similar with the matrix  $A$ . Therefore we omit the details.

Now we can give our main theorems.

**Theorem 2.** Let  $n$  be a natural number. Then

- a)  $U_{n+1} = t \sum_{j=0}^n \binom{n}{j} (-1)^{n-j} k^j U_{n-1-j},$
- b)  $U_n = - \sum_{j=0}^n \binom{n}{j} (-1)^{n-j} k^j U_{n-j},$
- c)  $tU_{n-1} = \sum_{j=0}^n \binom{n}{j} (-1)^{n-j} k^j U_{n+1-j},$
- d)  $V_n = \sum_{j=0}^n \binom{n}{j} (-1)^{n-j} k^j V_{n-j}$

**Proof.** Let the matrices  $A$  and  $B$  as in Theorem 1. Then, since  $A + B = \begin{pmatrix} k & -\alpha \\ \beta & 0 \end{pmatrix} + \begin{pmatrix} 0 & \alpha \\ -\beta & k \end{pmatrix} = kI$ , we get  $A = -B + kI$  and therefore

$$\begin{aligned} A^n &= (-B + kI)^n = \sum_{j=0}^n \binom{n}{j} (-B)^{n-j} k^j = \\ &= \sum_{j=0}^n \binom{n}{j} (-1)^{n-j} k^j B^{n-j}. \end{aligned}$$

Thus, it is seen that

$$\begin{pmatrix} U_{n+1} & -\alpha U_n \\ \beta U_n & tU_{n-1} \end{pmatrix} = \begin{pmatrix} \sum_{j=0}^n \binom{n}{j} (-1)^{n-j} k^j U_{n+1-j} & \alpha \sum_{j=0}^n \binom{n}{j} (-1)^{n-j} k^j U_{n-j} \\ -\beta \sum_{j=0}^n \binom{n}{j} (-1)^{n-j} k^j U_{n-j} & \sum_{j=0}^n \binom{n}{j} (-1)^{n-j} k^j U_{n+1-j} \end{pmatrix}$$

Then we get

$$U_{n+1} = t \sum_{j=0}^n \binom{n}{j} (-1)^{n-j} k^j U_{n-j-1}, \tag{1}$$

$$U_n = - \sum_{j=0}^n \binom{n}{j} (-1)^{n-j} k^j U_{n-j},$$

$$tU_{n-1} = \sum_{j=0}^n \binom{n}{j} (-1)^{n-j} k^j U_{n-j+1}. \tag{2}$$

If we add (1) to (2) and use  $V_r = U_{r+1} + tU_{r-1}$ , then we get

$$V_n = \sum_{j=0}^n \binom{n}{j} (-1)^{n-j} k^j V_{n-j}.$$

**Theorem 3.** Let  $n$  be a natural number. Then

- a)  $k^n = \sum_{j=0}^n \binom{n}{j} (-t)^j U_{n-2j+1},$
- b)  $k^n = t \sum_{j=0}^n \binom{n}{j} (-t)^j U_{n-2j-1},$
- c)  $0 = \sum_{j=0}^n \binom{n}{j} (-t)^j U_{n-2j},$
- d)  $2k^n = \sum_{j=0}^n \binom{n}{j} (-t)^j V_{n-2j}$

**Proof.** Let the matrices  $A$  and  $B$  as in Theorem 1. As  $A + B = kI$  and  $AB = BA = -tI$ , we get

$$\begin{aligned} k^n I &= (A + B)^n = \sum_{j=0}^n \binom{n}{j} A^{n-j} B^j \\ &= \sum_{j=0}^n \binom{n}{j} A^{n-2j} A^j B^j \\ &= \sum_{j=0}^n \binom{n}{j} A^{n-2j} (-tI)^j = \sum_{j=0}^n \binom{n}{j} (-t)^j A^{n-2j}. \end{aligned}$$

Therefore

$$\begin{pmatrix} k^n & 0 \\ 0 & k^n \end{pmatrix} = \begin{pmatrix} \sum_{j=0}^n \binom{n}{j} (-t)^j U_{n+1-2j} & -\alpha \sum_{j=0}^n \binom{n}{j} (-t)^j U_{n-2j} \\ \beta \sum_{j=0}^n \binom{n}{j} (-t)^j U_{n-2j} & t \sum_{j=0}^n \binom{n}{j} (-t)^j U_{n-1-2j} \end{pmatrix}.$$

Then the proof follows.

## REFERENCES

- [1] Lucas E. Théories des fonctions numériques simplement périodiques. *Amer. J. Math.* 1878;1:184-240.
- [2] Ribenboim P. *My numbers, my friends: Popular lectures on number theory.* Springer Verlag: Berlin-Heidelberg; 2000.
- [3] Kalman D, Mena R. The Fibonacci numbers-exposed. *Math. Mag.* 2003;76:167-181.
- [4] Şiar Z, Keskin R. Some new identities concerning generalized Fibonacci and Lucas numbers. *Hacet. J. Math. Stat.* 2013;42:211-222.
- [5] Ballot CJ.-C, Williams HC. *The Lucas sequences: Theory and applications.* Springer; 2023.



## Evaluation of the Efficacy of Propolis Extracts Based on Different Solvents Against Some Plant Pathogenic Fungi

Abdullah GÜLLER<sup>1\*</sup>, Işıl SARAÇ SİVRİKAYA<sup>2</sup>, Ersin KARAKAYA<sup>3</sup>, Gözdenur ÇAKAR KILIÇ<sup>4</sup>

<sup>1,2</sup> Bingöl University, Agriculture Faculty, Plant Protection Department, Bingöl, Türkiye

<sup>3</sup> Bingöl University, Agriculture Faculty, Biosystems Engineering Department, Bingöl, Türkiye

<sup>4</sup> Ankara University, Agriculture Faculty, Plant Protection Department, Ankara, Türkiye

Abdullah GÜLLER ORCID No: 0000-0003-3887-4208

Işıl SARAÇ SİVRİKAYA ORCID No: 0000-0002-5991-2173

Ersin KARAKAYA ORCID No: 0000-0002-6734-4962

Gözdenur ÇAKAR KILIÇ ORCID No: 0000-0002-2359-1312

\*Corresponding author: [aguller@bingol.edu.tr](mailto:aguller@bingol.edu.tr)

(Received: 31.05.2024, Accepted: 27.08.2024, Online Publication: 26.09.2024)

### Keywords

Propolis,  
Antifungal  
effect,  
*Fusarium  
oxysporum*,  
*Alternaria  
alternata*,  
*Verticillium  
dahliae*

**Abstract:** Propolis is a bee product produced as a natural defense mechanism by bees to protect their hives. It consists of plant resins, secretions from bees, and other substances collected from plants that, contain biologically active compounds with antimicrobial, antioxidant, and anti-inflammatory properties. Because of these characteristics, propolis has applications in various fields. In this study, pure propolis extracts obtained by Dimethyl Sulfoxide (DMSO), ethanol, methanol, glycerol, acetone and supercritical CO<sub>2</sub> extraction of propolis were tested for their antifungal activity against three phytopathogenic fungi, *Fusarium oxysporum*, *Alternaria alternata* and *Verticillium* spp. Antifungal activity tests were conducted in vitro using zone inhibition measurements on a PDA medium. Our findings revealed that the antifungal efficacy of propolis and its effect on mycelial growth parameters varied depending on the type of propolis extract used, demonstrating a dose-dependent relationship. In the present study, the ethanol + propolis preparation was found to be more successful in inhibiting the growth of fungal hyphae at a dose of 200 µL for all fungi than other solvents. The other solvents showed different levels of inhibition depending on the fungal species. In general, acetone, DMSO, and glycerol preparations of propolis were less effective in inhibiting fungal growth. The results obtained indicate that ethanol-based propolis extracts have the potential for control agriculturally important phytopathogenic fungi.

## Farklı Çözücülere Dayalı Propolis Ekstraktlarının Bazı Bitki Patojenik Funguslara Karşı Etkinliğinin Değerlendirilmesi

### Anahtar Kelimeler

Propolis,  
Antifungal etki,  
*Fusarium  
oxysporum*,  
*Alternaria  
alternata*,  
*Verticillium  
dahliae*

**Öz:** Propolis, arıların doğal savunma mekanizması olarak kovanlarını korumak için ürettikleri bir arı ürünüdür. Bitki reçinelerinden, arıların kendi salgılarından ve diğer bitkilerden topladıkları maddelerden oluşan propolis, antimikrobiyal, antioksidan ve anti-enflamatuar özelliklere sahip biyolojik olarak aktif bileşikler içerir. Bu özellikler nedeniyle, propolis çeşitli alanlarda kullanılmaktadır. Çalışmada, propolisin Dimetil Sülfoksit (DMSO), etanol, metanol, gliserol, aseton ve süperkritik CO<sub>2</sub> ekstraksiyon yöntemiyle elde edilen saf propolis ekstraktları üç fitopatojenik fungus türü olan *Fusarium oxysporum*, *Alternaria alternata* ve *Verticillium dahliae*'a karşı antifungal aktiviteleri test edilmiştir. Antifungal aktivite testleri, PDA ortamında yapılan zona inhibisyonu ölçümleri kullanılarak in vitro olarak gerçekleştirilmiştir. Bulgularımız, propolisin antifungal etkinliğinin ve miselyal büyüme parametrelerinin, kullanılan propolis ekstrakt türüne bağlı olarak değiştiğini ve doza bağlı bir ilişki gösterdiğini ortaya koymuştur. Çalışmada, Etanol+Propolis çözücüsünün, diğer çözücülere kıyasla tüm funguslar için 200 µl'lik dozunun fungal hif gelişimini inhibe etmede daha başarılı olduğu tespit edilmiştir. Diğer çözümler fungus türüne bağlı olarak farklı inhibisyon sergilemiştir. Genel olarak, fungal inhibisyon için, propolisin aseton, DMSO ve gliserol preparasyonları daha etkisiz olmuştur. Sonuç olarak, etanol bazlı propolis ekstraktlarının tarımsal açıdan önemli fitopatojenik fungusları kontrol etme potansiyeline sahip olduğunu göstermektedir.

## 1. INTRODUCTION

Propolis is a resinous substance with strong adhesive properties that bees produce from different plant secretions and use to close holes in the hive and protect the hive entrance from invaders. Propolis, a product with a long history of traditional use dating back to 300 BC, is well-known for its various biological and pharmacological properties. These properties include antibacterial, antifungal, antiviral, antiprotozoal, local anesthetic, anti-inflammatory, and immunostimulant effects [1, 2, 3]. It has a color ranging from yellow-green to dark brown and an aromatic odor, depending on the source and age of collection [4]. Propolis contains approximately 300 bioactive compounds, the contents of which varies according to the source of collection and season. To date, more than 180 compounds, mainly polyphenols, have been identified as the components of propolis. Propolis also contains other compounds such as essential oils, aromatic acids, waxes, pollen, vitamins, resins, balsams and various trace elements [5, 6]. Under *in vitro* conditions, propolis has demonstrated effectively inhibit both gram-positive and gram-negative bacterial strains [7, 8]. This antibacterial activity is attributed to the presence of flavonoids (such as galangin, pinocembrin, and pinostrobin), aromatic acids, and esters in propolis solutions [9]. Propolis has also shown inhibitory activity against a broad spectrum of viruses and fungal agents. Studies have indicated its effectiveness against various viruses of human and animal origin, including adonovirus, coronavirus, and rotavirus [10]. Additionally, propolis has been found to have antifungal effects against microfungi such as different *Candida* spp., *Trichosporon* spp., and *Pichia ohmeri* [11, 12, 13].

In recent years, propolis extracts have gained attention for their potential antiphytopathogenic effects against agricultural pathogens. Several *in vivo* and *in vitro* studies have investigated the antifungal activity of propolis against phytopathogenic fungi [14, 15]. Various propolis supernatants, including those extracted using ethanol, methanol, olive oil, and water, have been found to exhibit fungicidal activity against numerous plant-pathogenic fungi [16, 17, 18, 19]. In conclusion, propolis demonstrated remarkable antimicrobial properties, making it a promising candidate for further research and potential therapeutic applications.

Phytopathological fungi such as *Fusarium*, *Alternaria*, and *Verticillium* are common plant pathogens that can cause serious damage to agricultural crops, leading to yield and economic losses [20]. The long-term use of conventional chemical fungicides can cause environmental pollution, resistance development and risks to human health [21]. Therefore, the search for natural and environmentally friendly antifungal agents is of great importance. The mycelial growth activity of propolis extracts is commonly evaluated using dilution and diffusion methods [22, 23]. Mycelial growth inhibition is typically determined by comparing the radial growth diameter of the mycelium in the negative control (without propolis) with that in the tested solution

[24]. In line with this approach, our study aimed to investigate the mycelial inhibitory effects of different propolis extracts on *F. oxysporum*, *A. alternata*, and *Verticillium* spp. Specifically, we evaluated the dose-dependent antifungal activities of propolis extracts prepared using various solvents (ethanol, methanol, acetone, pure, glycerol) using agar diffusion methods under laboratory conditions. The results obtained from our study will not only help to determine the most effective solvent and dose of propolis but also contribute to demonstrating the usefulness of propolis as a natural protective agent against agricultural pathogens.

## 2. MATERIAL AND METHOD

### 2.1. Propolis Collection

Propolis was collected from plastic traps placed in beehives in Solhan district of Bingöl province (Turkey) and used in further studies.

### 2.2. Biological Material and PDA Medium

The test microorganisms, *V. dahliae*, *A. solani*, and *F. oxysporum*, were used from the available collection characterized in the Mycology Laboratory of Bingöl University, Faculty of Agriculture, Turkey. For inoculum preparation, all fungal species were grown for 7 days at 25 °C on Potato Dextrose Agar (PDA) (Merck, Darmstadt, Germany) prepared according to the company's instructions.

### 2.3. Preparing of Propolis Supernatants

In this study, six types of propolis supernatants were used: crude propolis purified by supercritical fluid extraction, acetone (ASP), ethanol (ESP), methanol (MSP), glycerol (GSP) and DMSO. The solvent concentration was 70% and the propolis/solvent ratio was used as 1/4 in the inhibition tests. For all supernatants, raw frozen propolis was pulverized using a grinder. The mixture of solvent and propolis in these proportions was incubated at 36 °C for 10 days on a magnetic stirrer, centrifuged at 1000 g for 5 minutes and then filtered. For the supercritical fluid extraction, 150 g of crude propolis was used, resulting in approximately 5 g of pure propolis supernatant. As in the previous method, it was homogenized with sterile distilled water. All the propolis supernatants were stored at +4 °C in the dark.

### 2.4. Antifungal Efficacy Assays

Antifungal assays were evaluated considering the inhibition of radial mycelium growth in the PDA culture medium [25]. Antifungal activity against phytopathogenic agents was tested in increasing doses (50, 100, and 200 µL) of each propolis supernatants added to the PDA medium. The negative control group consisted of PDA medium without supernatant and PDA medium with solvent added only at the concentrations indicated. All treatment and control groups were incubated at room temperature for one week. All tests

were performed in triplicate using a randomized design and radial fungal diameter was measured using a ruler and recorded. The percentage of inhibition was determined by assessing fungal growth in the control groups, following the equation provided by Deans and Sobada [26].

$$\text{Inhibition (\%)} = (gc - gt) / gc \times 100$$

Where gc refers to the mycelial growth diameter in the control plates; and gt is the mycelial growth diameter in the propolis suspension.

## 2.5. Statistical Analysis

Data were collected in triplicate using a factorial experimental design with randomized complete blocks. The statistical package program "JUMP 5.0" was used for the analysis. The data were analyzed using analysis of variance, and the treatment means were compared using Tukey's multiple comparison test.

## 3. RESULTS

Propolis possesses broad-spectrum anti-pathogenic properties against both plant and animal-derived agents. However, the direct use of propolis is not feasible. Therefore, the scientific community has been working to identify the most effective solvents for propolis extraction. Numerous studies have reported that ethanol is the most effective solvent for this purpose. Other commonly used solvents for propolis extraction include

water, oil, propylene glycol, and glycerol [27]. Although propolis solutions have been tested worldwide against various fungal pathogens, the antifungal activity of this natural product varies across different studies [19]. However, there is a lack of research on the efficacy of different solvent extracts of propolis, particularly against plant pathogenic fungi. Literature screening reveals that most studies on the antiphytopathogenic effects of propolis have focused on ethanol preparations in relation to plant pathogens. Ethanol extracts from propolis of different origins have been shown to negatively affect mycelial growth in several plant pathogens [16, 17, 15, 28, 29, 30].

In this study, six propolis preparations at three different doses were tested against three phytopathogenic fungi (*F. oxysporum*, *A. alternata*, and *V. dahliae*). The results of this study showed that propolis, especially its ethanol solutions, exhibited fungicidal activity. Different rates of inhibition of fungal mycelial growth were obtained depending on the microorganism tested, dose and solvent.

### 3.1. Inhibition in Mycelial Growth Based on Fungus Species

In all tests, the smallest mean fungal diameter was observed in *V. dahliae* (19.60 mm), followed by *A. solani* (32.87 mm) and *F. oxysporum* (48.20 mm) (Fig. 1). The differences between mean fungal diameters were statistically significant (Table 1).

**Table 1.** Descriptive values indicating the fungus species-specific inhibition zone

Fungal pathogens	Mean	Std. Deviation	Std. Error of Mean
<i>A. solani</i>	32,8 <sup>b</sup>	9,1	0,9
<i>V. dahliae</i>	19,6 <sup>c</sup>	5,7	0,5
<i>F. oxysporum</i>	48,2 <sup>a</sup>	13,0	1,3
<b>Average</b>	33,5	15,2	0,8

a,b,c: the difference between different letters in the same column is statistically significant ( $p \leq 0.01$ )

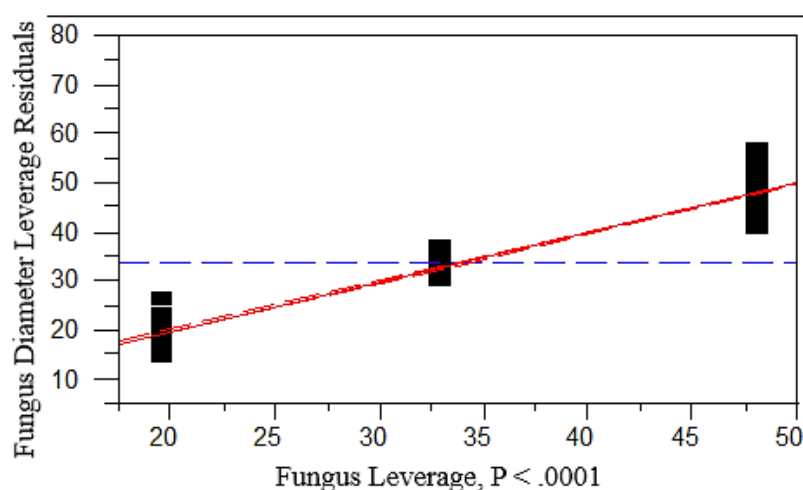


**Figure 1.** Diameter variation according to fungus species

### 3.2. Effect of Solvent and Propolis Extract Dose on Fungus Diameter

In this study, different solvents caused different rates of response inhibition in fungal species. The changes in

fungal diameter caused by propolis solvents are summarized in Table 2. Statistically significant differences were found between the mean diameters. The lowest fungal diameter values were obtained in the ethanol+propolis (22.0), pure propolis (25.1) and

methanol+propolis (25.7) preparations, respectively (Fig. 2). This indicated that ethanol was the best solvent in all treatments. The highest fungal diameter value was observed in the solvents without propolis,

indicating that solvent treatment alone has no activity in fungal inhibition. In addition, the mycelial growth diameter of the fungus decreased in all treated groups as the dose increased (data not shown).

**Table 2.** Fungal diameter values of solvent based propolis extracts

Solvent	Mean	Std. Deviation	Std. Error of Mean
Glycerol	43,7 <sup>b</sup>	18,1	3,5
Glycerol+propolis	35,7 <sup>d</sup>	16,2	3,1
Ethanol	46,6 <sup>a</sup>	18,6	3,5
Ethanol+propolis	22,0 <sup>h</sup>	11,4	2,2
DMSO	41,0 <sup>c</sup>	11,7	2,2
DMSO+propolis	29,6 <sup>f</sup>	9,5	1,8
Acetone	32,4 <sup>e</sup>	12,2	2,3
Acetone +propolis	30,3 <sup>f</sup>	12,9	2,4
Methanol	36,6 <sup>d</sup>	13,8	2,6
Methanol+propolis	25,7 <sup>g</sup>	10,2	1,9
Pure propolis	25,1 <sup>g</sup>	7,9	1,5
<b>Total</b>	<b>33,5</b>	<b>15,2</b>	<b>0,8</b>

a,b,c,d,e,f,g,h: the difference between different letters in the same column is statistically significant ( $p \leq 0.01$ )

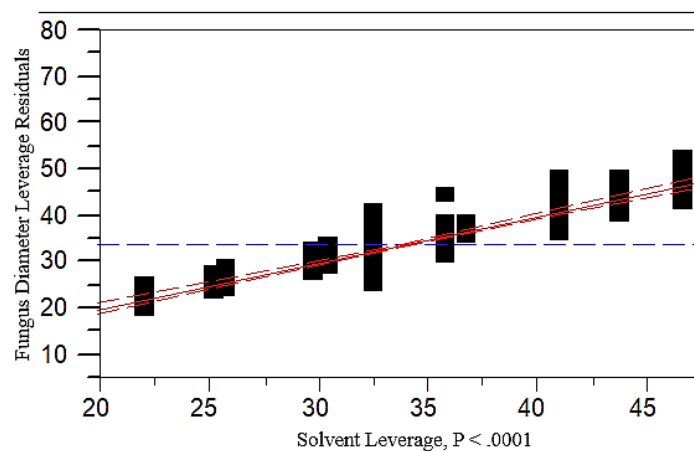


**Figure 2.** Change in fungus diameter with solvent treatment

### 3.3. Mean Values of Fungus-Solvent-Dose Interactions

The results showed that the effects of different solvent extracts of propolis varied according to the target fungal species. According to the analysis of variance, the model and effect tests were statistically significant

(Table 3, Table 4), and  $r^2$  and adjusted  $r^2$  values were calculated as 0.98 and 0.97, respectively. The model indicated that approximately 97% of the variation in the diameter of the fungal hyphae was due to differences in the fungal species, dose and solvent used (Table 5).

**Table 3.** Analysis of Variance

Source	DF	Sum of Squares	Mean Square	F Ratio
Model	98	67807,333	691,912	147,9465
Error	198	926,000	4,677	Prob > F
C. Total	296	68733,333		<.0001

**Table 4.** Effect Tests

Source	Nparm	DF	Sum of Squares	F Ratio	Prob > F
Fungus	2	2	40576,242	4338,065	<.0001
Solvent	10	10	17249,037	368,8239	<.0001
Dose	2	2	2475,717	264,6825	<.0001
Fungus *Solvent	20	20	5240,276	56,0246	<.0001
Fungus *Dose	4	4	196,525	10,5054	<.0001
Solvent*Dose	20	20	1287,246	13,7621	<.0001
Fungus *Solvent*Dose	40	40	782,290	4,1818	<.0001

**Table 5.** Summary of Model

RSquare	0,986528
RSquare Adj	0,97986
Root Mean Square Error	2,162584
Mean of Response	33,55556
Observations (or Sum Wgts)	297

In this study, the mean mycelial diameter varied depending on three variable factors. Depending on the solvent and dose, the mean mycelial diameter of *A. solani*, *V. dahliae*, and *F. oxysporum* was 32.8, 19.6 and 48.2, respectively. For all treatment groups, the highest dose (200 µL) of ethanol solution of propolis

had the best inhibitory activity, according to the statistical analysis of the three-way interaction (Table 3). This is probably because ethanol allows efficient dissolution of biologically active components in propolis [31].

**Table 3.** Distribution of Means for Fungus-Solvent-Dose Interactions

Treatment	<i>A. solani</i>				<i>V. dahliae</i>				<i>F. oxysporum</i>			
	50µl	100µl	200µl	Average	50µl	100µl	200µl	Average	50µl	100µl	200µl	Average
Glycerol	44,3±1,1	45,0±0,0	46,0±3,6	45,1±2,0	24,3±1,1	20,3±0,5	19,6±0,5	21,4±2,2	66,0±3,6	62,0±2,0	66,0±4,0	64,6±3,5
Glycerol + propolis	42,0±1,0	40,6±1,1	36,3±2,0	39,6±2,8	18,6±1,1	16,6±0,5	10,3±0,5	15,2±3,8	55,0±7,0	55,6±2,0	46,3±1,1	52,3±5,8
Ethanol	49,3±1,1	48,3±1,5	48,3±1,5	48,6±1,3	26,0±1,7	24,3±0,5	20,6±1,1	23,6±2,5	72,6±4,6	66,3±4,1	64,0±3,6	67,6±5,2
Ethanol + propolis	33,6±1,1	24,0±2,0	20,6±2,0	26,1±6,0	10,6±0,5	9,6±0,5	8,0±0,0	9,4±1,2	42,6±2,5	30,3±2,5	18,3±0,5	30,4±10,6
DMSO	43,0±2,6	39,3±0,5	35,6±1,1	39,3±3,5	31,3±6,1	25,3±0,5	28,6±1,1	28,4±4,0	56,0±1,7	53,6±1,1	56,3±3,2	55,3±2,2
DMSO + propolis	30,6±1,1	26,3±0,5	25,0±1,0	27,3±2,6	24,6±0,5	20,3±0,5	17,3±2,3	20,7±3,4	46,3±1,1	43,3±1,5	32,6±2,5	40,7±6,4
Acetone	31,6±1,5	26,3±1,1	26,6±1,5	28,2±2,8	24,0±1,0	20,0±3,0	19,0±1,7	21,0±2,9	51,6±2,0	44,6±7,2	47,6±6,8	48,0±5,9
Acetone + propolis	34,0±1,0	30,3±0,5	21,0±1,0	28,4±5,8	23,0±1,0	21,6±1,5	11,6±2,0	18,7±5,5	52,0±2,6	50,0±2,0	29,6±1,5	43,8±10,8
Methanol	33,6±0,5	31,6±1,1	31,3±1,1	32,2±1,3	23,3±0,5	22,6±0,5	22,3±0,5	22,7±0,6	55,6±1,5	56,0±1,0	53,3±1,5	55,0±1,7
Methanol + propolis	23,3±1,5	22,3±2,5	21,6±1,5	22,4±1,8	21,6±0,5	17,3±0,5	10,6±1,1	16,5±4,8	45,3±0,5	36,3±0,5	33,0±1,7	38,2±5,6
Pure propolis	27,3±0,5	24,0±1,0	20,6±1,1	24,0±3,0	20,3±0,5	17,6±1,1	14,3±0,5	17,4±2,6	41,0±1,7	32,0±1,7	28,6±1,1	33,8±5,6
Average	35,7±7,7	32,5±8,9	30,3±9,9	<b>32,8±9,1<sup>B</sup></b>	22,5±5,2	19,6±4,2	16,6±6,1	<b>19,6±5,7<sup>C</sup></b>	53,1±9,7	48,2±11,8	43,2±15,4	<b>48,2±13,0<sup>A</sup></b>

±: Standard deviation; ABC: The difference between the means shown with different letters in the same row is statistically significant ( $P \leq 0.01$ ).

However, other best solvents of propolis showed different inhibition effects depending on the fungus species. For *A. solani*, the second best inhibitor of mycelial growth was pure propolis obtained by the CO<sub>2</sub> extraction method, followed by methanol extract. DMSO and glycerol extracts were the least effective solvents. Compared to *A. solani*, glycerol and methanol were the second and third most inhibitory solvents of propolis extracts for *V. dahliae*. DMSO was the least

effective solvent. For *F. oxysporum*, the second and third highest inhibition values were measured in pure propolis and acetone extracts. However, the most ineffective solvents for the growth of this fungal pathogen were acetone and glycerol. In parallel with the statistical analyses, the percentage inhibition values of different extracts of propolis on fungal pathogens were also calculated (Table 4).

**Table 4.** Fungus and dose-based percentage inhibition rates of propolis extracts

Solvent/Fungus/Dose	<i>A. solani</i> (%)			<i>V. dahliae</i> (%)			<i>F. oxysporum</i> (%)		
	50µl	100µl	200µl	50µl	100µl	200µl	50µl	100µl	200µl
Glycerol	47,88	50	48,88	73	77,44	78,22	26,66	31,11	26,66
Glycerol +propolis	53,33	54,88	59,66	79,33	81,55	88,55	38,88	38,22	48,55
Ethanol	45,22	46,33	46,33	71,11	73	77,11	19,33	26,33	28,88
Ethanol+Propolis	62,66	73,33	77,11	88,22	89,33	91,11	52,66	66,33	79,66
DMSO	52,22	56,33	60,44	65,22	71,88	68,22	37,77	40,44	37,44
DMSO+Propolis	66	70,77	72,22	72,66	77,44	80,77	48,55	51,88	63,77
Acetone	64,88	70,77	70,44	73,33	77,77	78,88	42,66	50,44	47,11
Acetone+Propolis	62,22	66,33	76,66	74,44	76	87,11	42,22	44,44	67,11
Methanol	62,66	64,88	65,22	74,11	74,88	75,22	38,22	37,77	40,77
Methanol+Propolis	74,11	75,22	76	76	80,77	88,22	49,66	59,66	63,33
Pure Propolis	69,66	73,33	77,11	77,44	80,44	84,11	54,44	64,44	68,22

Apart from the antifungal activity of ethanol extracts of propolis against plant pathogens, some studies have focused on other solvents. Özcan et al. [32] tested methanol extracts of propolis from five different regions of Turkey against *Alternaria alternata* and *Fusarium oxysporum* f. sp. *melonis*. All the propolis extracts showed complete inhibition at a concentration of 5 %. Yang et al. [14] compared the inhibitory effects of different solvent solutions of Chinese propolis (ethanol, water, petroleum ether, n-butanol, ethyl acetate) on *Penicillium italicum* mycelial growth. The

results showed that ethyl acetate, ethanol, petroleum ether, n-butanol and water fractions were, in order, the most inhibitory at the same concentration (200 mg mL<sup>-1</sup>). Meneses et al. [16] tested different fractions of Colombian propolis (n-hexane/methanol fraction (EPEM), dichloromethane, ethyl acetate and methanol) against *Colletotrichum gloeosporioides* and *Botryodiplodia theobromae*. The results showed that two strains of *C. gloeosporioides* and *B. theobromae* were better inhibited by the dichloromethane and EPEM fractions, respectively. On the other hand, there

are very few studies on the DMSO extracts of propolis. Ertürk et al. [33] compared different solvents of propolis, including acetone, ethyl acetate, chloroform, ethanol, methanol, DMSO, and water, of animal-derived yeast *C. albicans* and other microorganisms. The DMSO solution of propolis showed weak inhibition against all tested microorganisms. Similarly, Ghasemi et al. [34] noted that PEE (propolis ethanol extract) exhibited broad-spectrum antibacterial activity against Gram-positive and Gram-negative bacteria compared to DMSO solutions. Solvent-based solutions showed different effects in a dose-dependent manner when comparing the antibacterial and antifungal activities of acetone and DMSO-based extracts against animal-derived pathogens. Overall, DMSO-based solutions have been reported to be more active than acetone-based solutions [35].

In this study, we found that ethanol was the most effective solvent for the extraction of propolis compared to other solvents. Our results indicate that ethanol extracts of propolis have the highest antiphytopathogenic activity. The superior performance of ethanol-propolis solutions in inhibiting fungal growth underscores the potential of this combination as a potent antifungal agent. Therefore, ethanol should be considered as the solvent of choice to maximise the bioactive properties of propolis in the control of plant pathogens. These results highlight the importance of the choice of the appropriate solvent in order to increase the efficacy of propolis in agricultural applications.

#### 4. CONCLUSION

The study carried out shows that the effect values of the application models and variables were statistically significant. Considering the solvent and dose applications of propolis, the soil-borne pathogen *V. dahliae* showed a greater inhibition of hyphal colony diameter compared to the others, indicating that this pathogen is more sensitive to propolis preparations. In addition, it was found that the ethanol+propolis solvent was more effective in inhibiting fungal diameter growth at the high dose of 200 µL for all fungi compared to other solvents.

These findings suggest that propolis, particularly in combination with ethanol, has significant potential as a natural antifungal agent. Its effectiveness in inhibiting the growth of soil-borne pathogens like *V. dahliae* highlights the possibility of developing propolis-based treatments for managing plant diseases. This study contributes to the growing body of research exploring natural alternatives for disease control, and it paves the way for further investigations into the commercialization and practical application of propolis in sustainable agriculture.

#### Conflicts of Interest

The article authors declare that there is no conflict of interest between them.

#### Author's Contributions

The authors declare that they have made equal contributions to this article.

#### REFERENCES

- [1] Banskota AH, Nagaoka T, Sumioka LY, Tezuka Y, Awale S, Midorikawa K, et al. Antiproliferative activity of the Netherlands propolis and its active principles in cancer cell lines. In *Journal of Ethnopharmacology*. 2002;80(1):67–73.
- [2] Abd-El-Rhman AM. Antagonism of *Aeromonas hydrophila* by propolis and its effect on the performance of Nile tilapia, *Oreochromis niloticus*. In *Fish & Shellfish Immunology*. 2009;27(3):454–459.
- [3] Bankova V, Galabov AS, Antonova D, Vilhelmova N, Di Perri B. Chemical composition of Propolis Extract ACF® and activity against herpes simplex virus. *Phytomedicine*. 2014; 21(11):1432-1438.
- [4] Ghisalberti EL. Propolis: a review. *Bee World*. 1979;60:59-84.
- [5] Castaldo S, Capasso F. Propolis, an old remedy used in modern medicine. *Fitoterapia*. 2002;73(1):1-6.
- [6] Toreti VC, Sato HH, Pastore GM, Park YK. Recent progress of propolis for its biological and chemical compositions and its botanical origin. *Evidence Based Complementary Alternative Medicine*. 2013;697390. DOI: 10.1155/2013/697390.
- [7] Hegazi AG. Propolis an overview. *Congreso Internacional de Propóleos*, Buenos Aires 1-2nd, September 2000.
- [8] Basim E, Basim H, Özcan M. Antibacterial activities of Turkish pollen and propolis extracts against plant bacterial pathogens. *Journal of Food Engineering*. 2006;77(4):992-996. DOI: 10.1016/j.jfoodeng.2005.08.027
- [9] Marcucci MC. Propolis: Chemical Composition, Biological Properties And Therapeutic Activity. In *Apidologie*. 1995;26:83-99.
- [10] Güneş F, Yılmaz M. Propolis'in kimyasal içeriği ile antibakteriyel, antiviral, antitümör, antifungal ve antioksidan aktivitesi. *Arcılık Araştırma Dergisi*. 2013;10: 25-28.
- [11] Lisa M, Leifertova I, Baloun J. Fungistatic effect of propolis. *Folia Pharm Univ Carol*. 1989;13:29-44.
- [12] Matsuno T, Chen C, Basnet P. A tumoricidal and antioxidant compound isolated from an aqueous extract of propolis. *Medical Science Research*. 1997;25:583–584.

- [13] Bogdanov S. Propolis: Composition, Health, Medicine: A Review. Bee Product Science, 2012. [www.bee-hexagon.net](http://www.bee-hexagon.net)
- [14] Yang SZ, Peng LT, Su XJ, Chen F, Cheng YJ, Fan G, et al. Bioassay-guided isolation and identification of antifungal components from propolis against *Penicillium italicum*. Food Chemistry. 2011;127(1):210-215. <http://dx.doi.org/10.1016/j.foodchem.2010.12.011>
- [15] Mattiuz BH, Ducamp-Collin MN, Mattiuz CFM, Vigneault C, Marques KM, Sagoua W, et al. Effect of propolis on postharvest control of anthracnose and quality parameters of 'Kent' mango. Scientia Horticulturae. 2015;184:60-168. DOI: 10.1016/j.scienta.2014.12.035
- [16] Meneses EA, Durango DL, García CM. Antifungal activity against postharvest fungi by extracts from Colombian propolis. Química nova. 2009;32:2011-2017.
- [17] Curifuta M, Vidal J, Salazar LA, Sánchez-Venegas J, Alvear M, Contreras A. The in vitro antifungal evaluation of a commercial extract of Chilean propolis against six fungi of agricultural importance. Ciencia e Investigación Agraria. 2012;39(2):347-359.
- [18] Ali A, Wei YZ, Mustafa MA. Exploiting Propolis as an Antimicrobial Edible Coating to Control Post-harvest Anthracnose of Bell Pepper. Packaging Technology and Science. 2014. DOI: 10.1002/pts.2088
- [19] Dudoit A, Mertz C, Chillet M, Cardinault N, Brat P. Antifungal activity of Brazilian red propolis extract and isolation of bioactive fractions by thin-layer chromatography-bioautography. Food Chemistry. 2020;327:1-8. DOI: 10.1016/j.foodchem.2020.127060
- [20] Agrios GN. Plant pathology. 5th Edition, Elsevier Academic Press, Amsterdam, 2005;26-27:398-401.
- [21] Lucas JA, Hawkins NJ, Fraaije BA. The evolution of fungicide resistance. Advances in applied microbiology. 2015;90:29-92.
- [22] Quiroga EN, Sampietro DA, Soberon JR, Sgariglia MA, Vattuone MA. Propolis from the northwest of Argentina as a source of antifungal principles. Journal of Applied Microbiology. 2006;101(1):103-110. DOI: 10.1111/j.1365-2672.2006.02904.x
- [23] Agüero MB, Svetaz L, Baroni V, Lima B, Luna L, Zacchino S, Tapia A. Urban propolis from San Juan province (Argentina): Ethnopharmacological uses and antifungal activity against *Candida* and dermatophytes. Industrial Crops and Products. 2014;57:166-173. DOI: 10.1016/j.indcrop.2014.03.009
- [24] Bosio K, Avanzini C, D'Avolio A, Ozino O, Savoia D. In vitro activity of propolis against *Streptococcus pyogenes*. Letters on Applied Microbiology. 2000;31:174-177. DOI: 10.1046/j.1365-2672.2000.00785.x
- [25] Ronald MA. Microbiologia, Compania Editorial Continental S. A. de C. V., Mexico, 1 D. 1990. F. pp. 505.
- [26] Deans SG, Sobada KP. Antimicrobial Properties of Marjoram (*Origanum marjorana* L.) Volatile Oil. Flavour Fragr. J. 1990;5:187-190.
- [27] Arslan S, Perçin D, Silici S. The in vitro effects of propolis extracts prepared with different solvents on mutans streptococci. J Health Sci. 2010;19:68-73.
- [28] Davari M, Ezazi R. Mycelial inhibitory effects of antagonistic fungi, plant essential oils and propolis against five phytopathogenic *Fusarium* species. Archives of Microbiology. 2022; 204:480.
- [29] Er Y. In vitro and in vivo antimicrobial activity of propolis extracts against various plant pathogens. Journal of Plant Diseases and Protection. 2021;128(3):693-701.
- [30] Costantin CR, de Oliveira HG, Roese LSM, Pancera MR, Silvestre WP, Siqueira GR, et al. Evaluation of the antifungal activity of propolis extracts from stingless bees on phytopathogenic fungi. Research, Society and Development. 2022;11(16):e445111638445-e445111638445.
- [31] Moura SALD, Negri G, Salatino A, Lima LDDC, Dourado LPA, Mendes JB, et al. Aqueous extract of Brazilian green propolis: primary components, evaluation of inflammation and wound healing by using subcutaneous implanted sponges. Evidence-Based Complementary and Alternative Medicine. 2011.
- [32] Özcan M, Ünver A, Ceylan DA, Yetisir R. Inhibitory effect of pollen and propolis extracts. Food/Nahrung. 2004;48(3):188-194.
- [33] Ertürk Ö, Yavuz C, Sıralı C. The Antimicrobial Activity of Propolis from Ordu Province of Turkey. HARUM. 2011;28:11-16.
- [34] Ghasemi FS, Eshraghi SS, Andalibi F, Hooshyar H, Kalantar-Neyestanaki D, Samadi A, et al. Anti-Bacterial Effect of Propolis Extract in Oil Against Different Bacteria. Zahedan J. Res. Med. Sci. 2017;19(3):7225.
- [35] Ugur A, Arslan T. An in vitro study on antimicrobial activity of propolis from Mugla province of Turkey. Journal of Medicinal Food. 2004;7(1):90-94.

## Investigation of Effects of Apilarnil and Imatinib Use on Liver and Kidney Tissues in Rats via PI3K/AKT/mTOR and JAK2/STAT3 Signaling Pathways

Cüneyt ÇAĞLAYAN<sup>1\*</sup>, Aydın GENÇ<sup>2</sup>, Sefa KÜÇÜKLER<sup>3</sup>, Hakan İNCİ<sup>4</sup>

<sup>1</sup> Bilecik Şeyh Edebali University, Medicine Faculty, Medical Biochemistry Department, Bilecik, Türkiye

<sup>2</sup> Bingöl University, Veterinary Faculty, Biochemistry Department, Bingöl, Türkiye

<sup>3</sup> Atatürk University, Veterinary Faculty, Biochemistry Department, Erzurum, Türkiye

<sup>4</sup> Bingöl University, Agriculture Faculty, Animal Science Department, Bingöl, Türkiye

Cüneyt ÇAĞLAYAN ORCID No: 0000-0001-5608-554X

Aydın GENÇ ORCID No: 0000-0001-5367-0743

Sefa KÜÇÜKLER ORCID No: 0000-0002-8222-5515

Hakan İNCİ ORCID No: 0000-0002-9791-0435

\*Corresponding author: [cuneyt.caglayan@bilecik.edu.tr](mailto:cuneyt.caglayan@bilecik.edu.tr)

(Received: 02.08.2024, Accepted: 06.09.2024, Online Publication: 26.09.2024)

### Keywords

Apilarnil,  
Imatinib,  
Liver,  
Kidney,  
Rat

**Abstract:** Imatinib, used in the field of molecular targeted therapy, has been reported to cause serious side effects, including liver and kidney failure. However, the mechanism of imatinib-induced liver and kidney toxicity remains unclear due to limited number of studies in this field. Apilarnil is a natural bee product produced from 3-7 day old drone larvae. The present study aimed to investigate the effects of apilarnil in rats with imatinib-induced liver and kidney toxicity using biochemical parameters. In the experiment, 35 wistar albino rats were divided into five groups (n=7): i) Control, ii) Apilarnil, iii) Imatinib, iv) Imatinib+Apilarnil-200, and v) Imatinib+Apilarnil-400. Rats were treated orally with imatinib (100 mg/kg) and apilarnil (200 and 400 mg/kg) for 14 days. Imatinib reduced PI3K, AKT and mTOR levels, while increasing JAK2 and STAT3 levels in liver and kidney tissues. Apilarnil given for treatment modulated these values and provided partial protection in liver and kidney tissue. In conclusion, it was determined that apilarnil has ameliorative effects against imatinib-induced liver and kidney damage.

134

## Sıçanlarda Apilarnil ve İmatinib Kullanımının Karaciğer ve Böbrek Dokuları Üzerine Etkilerinin PI3K/AKT/mTOR ve JAK2/STAT3 Sinyal Yolakları Aracılığı ile Araştırılması

### Anahtar

Kelimeler  
Apilarnil,  
İmatinib,  
Karaciğer,  
Böbrek,  
Rat

**Öz:** Moleküler hedefli tedavi alanında kullanılan imatinib'in karaciğer ve böbrek yetmezliği de dahil olmak üzere ciddi yan etkilere neden olduğu bildirilmiştir. Bununla birlikte, bu alanda sınırlı sayıda çalışma olduğu için imatinib kaynaklı karaciğer ve böbrek toksisite mekanizması belirsizliğini koruyor. Apilarnil, 3-7 günlük drone larvalarından üretilen doğal bir arı ürünüdür. Bu çalışmada, imatinib kaynaklı karaciğer ve böbrek toksisitesi olan sıçanlarda apilarnilin etkilerinin biyokimyasal parametreler kullanılarak araştırılması amaçlanmıştır. Deneyde, 35 wistar albino sıçan beş gruba ayrıldı (n=7): i) Kontrol, ii) Apilarnil, iii) İmatinib, iv) İmatinib+Apilarnil-200 ve v) İmatinib+Apilarnil-400. Sıçanlara 14 gün boyunca oral yoldan imatinib (100 mg/kg) ve apilarnil (200 ve 400 mg/kg) ile tedavi uygulandı. İmatinib, karaciğer ve böbrek dokularında PI3K, AKT ve mTOR düzeylerini düşürürken JAK2 ve STAT3 düzeylerini artırdı. Bununla birlikte, tedavi amacıyla verilen apilarnil ise bu değerleri modüle ederek karaciğer ve böbrek dokusunda kısmi koruma sağlamıştır. Sonuç olarak, imatinib kaynaklı karaciğer ve böbrek hasarına karşı apilarnilin iyileştirici etkilerinin olduğu tespit edilmiştir.

### 1. INTRODUCTION

Imatinib is one of the current anticancer drugs that is considered as a smart drug with antineoplastic effect used

in the treatment of many types of cancer [1]. Imatinib is a selective inhibitor of BCR-ABL tyrosine kinase, mainly used in chronic myeloid leukemia, acute lymphoblastic leukemia, metastatic or unresectable gastrointestinal



stromal tumors [2]. Today, imatinib, which is called a smart drug and is frequently used in addition to existing chemotherapeutics is considered a crucial example in terms of reflecting the importance of molecular targeted therapy and perhaps the future of cancer treatment, considering its significantly positive side effect profile and reliability compared to conventional cytotoxic treatments. Although it is frequently preferred due to its beneficial effects in the fight against cancer, it can commonly cause unwanted side effects such as vomiting, diarrhea, muscle pain, headache and rash even in overdose or normal dose intake. Severe side effects include fluid retention, gastrointestinal bleeding, bone marrow suppression, liver problems and heart failure. It has been reported that it can cause damage to tissues and organs such as testicles, heart, liver and spinal cord, which can be considered serious health problems as a result of its use in cancer treatments [3-6].

Apilarnil (bee drone larvae) is a bee product obtained by lyophilizing 3-7-day-old male bee larvae and has strong antioxidant properties. Apilarnil, which is homogeneous, milky, has the consistency of boza, is yellowish gray in color and has a bitter taste, is easily adulterated, and is a bee product that must be stored in a cold chain in raw form or lyophilized [7,8]. It gets its antioxidant properties from the vitamins (A, D, C, E, B1, B6, choline etc.), minerals (Ca, P, Na, Zn, Mn, Fe, Cu and K) and polyphenols it contains. In addition to its rich vitamin and mineral content, it contains 66% water, 14.5% carbohydrates, 4.5% lipids, 13% amino acids and some biologically active substances [9].

In the present study, the effects of apilarnil and imatinib use in rats on some biochemical parameters in liver and kidney tissues were investigated.

## 2. MATERIAL AND METHOD

### 2.1. Drug and Chemicals

Imatinib (Glivec®, 400 mg/tablet) was obtained from Novartis Pharmaceuticals (İstanbul, Turkey). Apilarnil samples were taken from the honeycomb into falcon tubes and immediately stored at -20 °C. Then, for the lyophilization process, they were taken to a freezer between -20 °C and -80 °C and lyophilization was performed by taking them into lyophilized flasks. The lyophilized apilarnil was dissolved in water according to the experimental protocol and given orally to the rats. ELISA kits for mammalian target of rapamycin (mTOR), phosphoinositide 3-kinase (PI3K), protein kinase B (AKT), janus kinase-2 (JAK2) and signal transducer and activator of transcription-3 (STAT3) were obtained from Sunred Biological Technology Company (Shanghai, China).

### 2.2. Animals

Thirty-five male Wistar albino rats, weighing 250-300 g and aged 12-13 weeks, was used in the experiment. The rats were obtained from Experimental Research Center, Bingol University (Bingol, Turkey). Animals were kept in

cages in a controlled room, providing a constant temperature of 24-25 °C and a twelve (12 h) hour light-dark cycle (07:00-19:00 light; 19:00-07:00 dark). They were provided with access to unlimited amounts of water and standard feed. The animal use protocol had been approved by the Animal Experimentation Ethics Committee of the Bingol University (Protocol No. 2022-02/01).

### 2.3. Experimental Procedure

Wistar albino male rats were randomly divided into 5 groups, with 7 rats in each group. Group I (Control): Physiological saline solution was given orally for 14 days. Group II (Apilarnil): Apilarnil at a dose of 400 mg/kg body weight was dissolved in physiological saline and given orally for 14 days [10]. Group III (Imatinib): Imatinib was dissolved in physiological saline and given orally at a dose of 100 mg/kg for 14 days [11]. Group IV (Imatinib + Apilarnil 200 mg/kg): Imatinib was dissolved in physiological saline and given orally at a dose of 100 mg/kg for 14 days. 30 minutes after imatinib application, apilarnil was given orally at a dose of 200 mg/kg. Group V (Imatinib + Apilarnil 400 mg/kg): Imatinib was dissolved in physiological saline and given orally at a dose of 100 mg/kg for 14 days. 30 minutes after imatinib application, apilarnil was given orally at a dose of 400 mg/kg. At the end of study period (15th day), the animals were sacrificed under mild sevoflurane anesthesia. The liver and kidney tissues from rats were evaluated for biochemical, analysis.

### 2.4. Determination of Liver and Kidney Tissues PI3K, mTOR, AKT, JAK2 and STAT3 by ELISA Method

Frozen liver and kidney tissues were ground with a tissue homogenizer machine (Tissue Lyser II, Qiagen, Netherlands) using liquid nitrogen. Then, 100 mg of ground liver and kidney tissues for each tissue were diluted 1:20 with phosphate buffer (0.1 M, pH 7.4) and homogenized with the homogenizer machine. Supernatants were prepared by centrifugation at 3500 rpm for 15 min. Measurements were performed using ELISA kits such as PI3K, mTOR, AKT, JAK2 and STAT3 in supernatants obtained from liver and kidney tissues according to the manufacturer's instructions and expressed as ng/g tissue.

### 2.5. Statistical Analysis

Biochemical data were analysed with ANOVA using SPSS (version 20.0; Chicago, IL). Results were expressed as mean  $\pm$  standard deviation (SD). One-way analysis of variance (ANOVA) and Tukey test were used to determine the difference and significance levels between the groups.  $p < 0.05$  were considered as statistically significant.

### 3. RESULTS

#### 3.1. Liver and Kidney PI3K levels

When liver and kidney PI3K levels were analyzed (Figure 1A and B), it was found that PI3K levels decreased in the imatinib group compared to the control group ( $p < 0.05$ ), and apilarnil 200 and 400 mg/kg doses administered together with imatinib were effective in increasing PI3K levels ( $p < 0.05$ ).

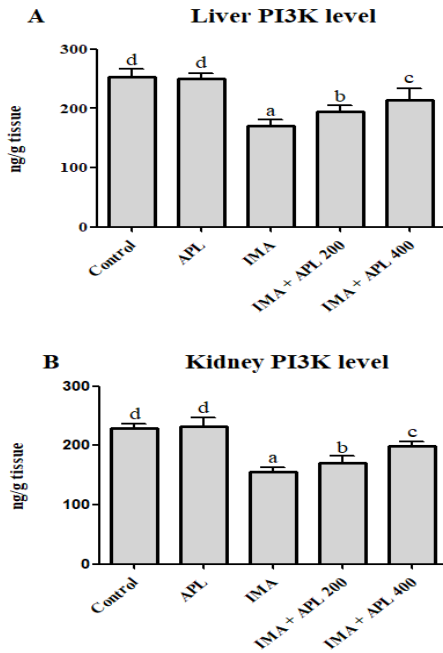


**Figure 1.** (A) Effect of oral administration of apilarnil (APL) on liver PI3K level in imatinib (IMA) treated rats. (B) Effect of oral administration of apilarnil (APL) on kidney PI3K level in imatinib (IMA) treated rats. Different letters (a–d) on the columns show a statistical difference ( $p < 0.05$ ).

#### 3.2. Liver and Kidney mTOR levels

When liver and kidney mTOR levels were examined (Figure 2A and B), it was found that there was no difference between the control and apilarnil groups ( $p > 0.05$ ), mTOR levels in the imatinib group decreased compared to the control group ( $p < 0.05$ ), apilarnil 200 and 400 mg/kg doses increased mTOR levels ( $p < 0.05$ ).

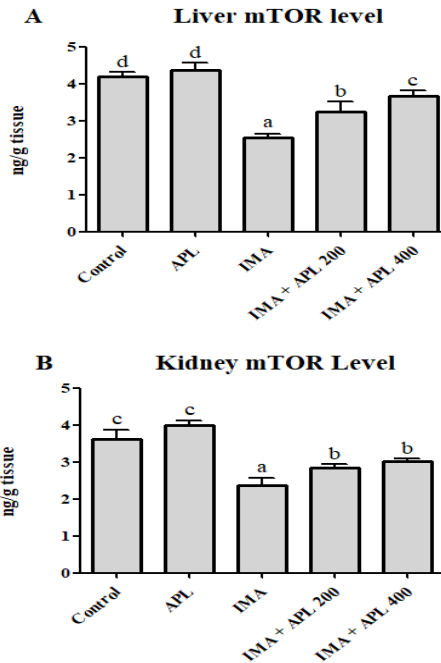


**Figure 2.** (A) Effect of oral administration of apilarnil (APL) on liver mTOR level in imatinib (IMA) treated rats. (B) Effect of oral administration of apilarnil (APL) on kidney mTOR level in imatinib (IMA) treated rats. Different letters (a–d) on the columns show a statistical difference ( $p < 0.05$ ).

#### 3.3. Liver and Kidney AKT levels

It was found that AKT levels in the imatinib group decreased compared to the control group ( $p < 0.05$ ), there was no difference between the control and apilarnil groups ( $p > 0.05$ ), and both doses of apilarnil given together with imatinib were effective in increasing AKT levels ( $p < 0.05$ ) (Figure 3).

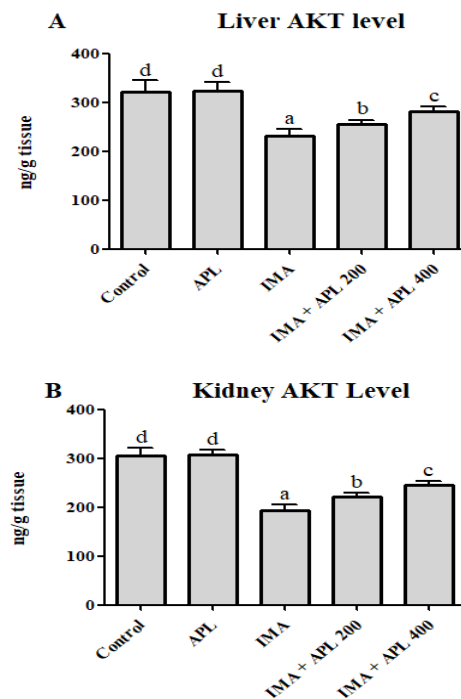


**Figure 3.** (A) Effect of oral administration of apilarnil (APL) on liver AKT level in imatinib (IMA) treated rats. (B) Effect of oral administration of apilarnil (APL) on kidney AKT level in imatinib (IMA) treated rats. Different letters (a–d) on the columns show a statistical difference ( $p < 0.05$ ).

### 3.4. Liver and Kidney JAK2 levels

While there was no difference between control and apilarnil group JAK2 levels ( $p > 0.05$ ), JAK2 levels in imatinib group increased compared to control and apilarnil groups ( $p < 0.05$ ), JAK2 levels in IMA + APL 200 and IMA + APL 400 groups decreased compared to imatinib group ( $p < 0.04$ ) (Figure 3). There was no statistical difference between the two groups (IMA + APL 200 and IMA + APL 400).

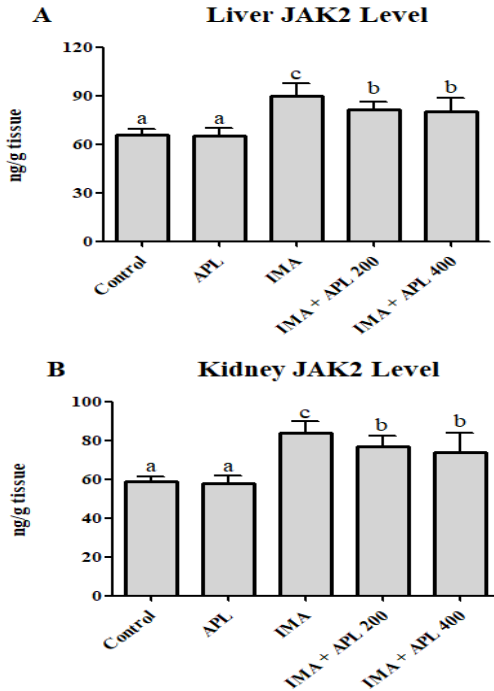


**Figure 4.** (A) Effect of oral administration of apilarnil (APL) on liver JAK2 level in imatinib (IMA) treated rats. (B) Effect of oral administration of apilarnil (APL) on kidney JAK2 level in imatinib (IMA) treated rats. Different letters (a-d) on the columns show a statistical difference ( $p < 0.05$ ).

### 3.5. Liver and Kidney STAT3 levels

When liver and kidney tissue STAT3 levels were examined, no difference was found between the control and apilarnil groups ( $p > 0.05$ ), STAT3 levels increased in the imatinib group compared to the control group ( $p < 0.05$ ), and 200 and 400 mg/kg doses of apilarnil given together with imatinib were found to be effective in reducing STAT3 levels ( $p < 0.05$ ).

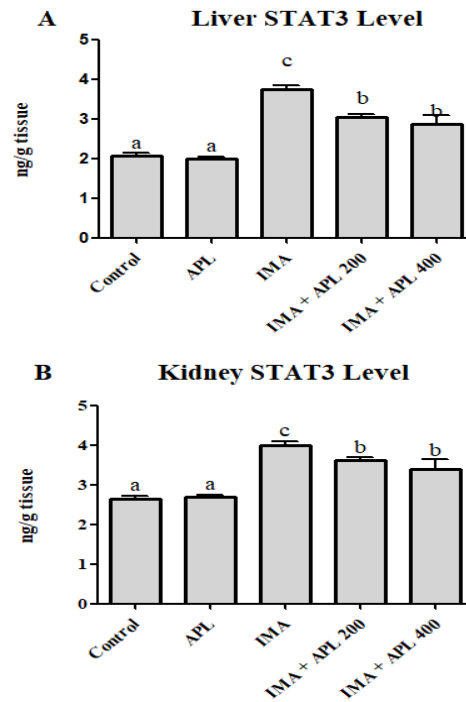


**Figure 5.** (A) Effect of oral administration of apilarnil (APL) on liver STAT3 level in imatinib (IMA) treated rats. (B) Effect of oral administration of apilarnil (APL) on kidney STAT3 level in imatinib (IMA) treated rats. Different letters (a-d) on the columns show a statistical difference ( $p < 0.05$ ).

## 4. DISCUSSION AND CONCLUSION

Imatinib is a drug used clinically against chronic myeloid leukemia and metastatic gastrointestinal stromal tumors. On the other hand, liver and kidney damage are associated with imatinib treatment [12, 13]. The current study investigated the possible effects of apilarnil against imatinib-induced liver and kidney toxicity in male rats from a biochemical perspective.

The PI3K/Akt/mTOR pathway is an important intracellular signal transduction pathway involved in regulating apoptosis, autophagy, cell proliferation, cell cycle, metabolism, and angiogenesis through communicating with its related downstream and upstream molecules [14]. PI3K is classified as type I, type II and type III. Among them, type I PI3K is a negative regulator of autophagy and its phosphorylation level plays an important role in regulating cell proliferation and death. AKT plays a role in regulating various signaling pathways including cell growth, proliferation, survival, chemoresistance and angiogenesis. It is a downstream effector of PI3K and an upstream regulatory molecule of mTORC1 [15]. The mTOR is a primary regulator with significant functions in autophagy and provides negative regulation of autophagy. mTOR is a serine/threonine kinase that is one of the major regulators of cellular functions such as growth, proliferation, and survival. While regulating cellular functions, mTOR; regulates cellular activities such as protein synthesis, energy metabolism, and stress response by bringing together different signaling pathways [16]. mTOR is considered an important downstream target of the PI3K/Akt pathway [15]. Many toxicants induce autophagy and apoptosis by downregulating the PI3K/AKT/mTOR pathway or

inhibiting mTOR [17]. Additionally, there is evidence from previous studies that imatinib inhibits the PI3K/AKT/mTOR pathway in various types of cancer [18,19]. However, there is no literature information on the PI3K/AKT/mTOR pathway regarding the effects of imatinib on liver and kidney damage. In this study, PI3K, AKT and mTOR levels in liver and kidney tissues were decreased by imatinib, while apilarnil given for treatment increased these parameters. In various toxicity studies conducted with experimental animals, it was reported that apilarnil protects liver and kidney tissues due to its antioxidant properties [10, 20].

The JAK2/STAT3 signaling pathway plays a role in regulating many important biological processes in the body, especially inflammation and oxidative stress. JAK2 can be activated by phosphorylation and then cause downstream STAT3 phosphorylation, which can be imported into the nucleus to initiate the expression of oxidative stress and inflammation-related genes and accentuate the oxidative stress and inflammation reaction in the tissue [21]. Activated STAT3 also stabilizes the mitochondrial membrane. Moreover, STAT3 is also recognized as an anti-apoptotic factor as it regulates several apoptosis-related genes such as Bcl-2 and Bcl-xL [22]. Previous studies have shown that the JAK2/STAT3 pathway plays a vital role in both liver and kidney injury [21, 23]. In another study, it was reported that low-dose imatinib (10 and 20 mg/kg) provided protection by reducing JAK2 and STAT3 protein levels in a model of ulcerative colitis experimentally induced with acetic acid in rats [24]. In this study, it was determined that imatinib increased JAK2 and STAT3 levels in liver and kidney tissues, while apilarnil given for treatment decreased JAK2 and STAT3 levels. There is no information in the literature about the relationship between apilarnil and the JAK2/STAT3 signaling pathway. However, it is thought that apilarnil has a therapeutic effect due to its rich content (vitamins, minerals and phenolic compounds).

As a result, it was determined that imatinib decreased PI3K, AKT and mTOR levels, increased JAK2 and STAT3 levels and triggered apoptosis and autophagy, while apilarnil application showed the opposite effect and tried to protect the tissues. In the light of the findings obtained, it is thought that more comprehensive studies are needed to clearly understand whether the use of apilarnil in imatinib-induced liver and kidney damage will be beneficial.

## REFERENCES

- [1] Droogendijk HJ, Kluin Nelemans HJ, van Doormaal JJ, Oranje AP, Loosdrecht AA, van Daele PL. Imatinib mesylate in the treatment of systemic mastocytosis. *Cancer*. 2006;107:345-351.
- [2] Banka N, Aljurf M, Hamadah I. Imatinib (STI-571)-induced exfoliative dermatitis in a Saudi patient with deck chair sign. *Dermatology*. 2003;207:329-330.
- [3] Al-Allaf LI, Al-Ashoo HA. Analysis of the Oxidative Stress Parameters in Testicular, Hepatic and Renal Tissues Homogenates of Albino Rats after Administration of Imatinib at Peripuberty. *Zoology*. 2018;27(5):26-33.
- [4] Herman EH, Knapton A, Rosen E, Thompson K, Rosenzweig B, Estis J, et al. A Multifaceted Evaluation of Imatinib-induced Cardiotoxicity in the Rat. *Toxicol Pathol*. 2011;39:1091-1106.
- [5] Al-Rasheed NM, El-Masry TA, Tousson E, Hassan HM, Al-Ghadeer A. Protective Potential of Grape Seed Proanthocyanidins Extract against Glivec (Imatinib Mesylate) Induced Liver Toxicity and Oxidative Stress in Male Rats. *Annu Res Rev Biol*. 2017;20(6):1-9.
- [6] Liu L, Zhou J, Wang Y, Qi T, Wang Z, Chen L, et al. Imatinib inhibits oxidative stress response in spinal cord injury rats by activating Nrf2/HO-1 signaling pathway. *Exp Ther Med*. 2020;(1):597-692.
- [7] Inci H., Izol E, Yilmaz MA, Ilkaya M, Bingöl Z, Gülçin I. Comprehensive phytochemical content by LC/MS/MS and anticholinergic, antiglaucoma, antiepilepsy, and antioxidant activity of apilarnil (drone larvae). *Chem Biodiversity*. 2023;20(10):e202300654.
- [8] Bărnuțiu LI, Mărghitaș LA, Dezmirean D, Bobiș O, Mihai C, Pavel C. Physico-chemical composition of apilarnil (bee drone larvae). *Lucrari Stiintifice, Seria Zootehnie*. 2013;59:199-202.
- [9] Sawczuk R, Karpinska J, Milyk W. What do we need to know about drone brood homogenate and what is known. *J Ethnopharmacol*. 2019;245:111581.
- [10] Inandiklioğlu N, Doganyigit Z, Okan A, Kayman E, Silici S. Nephroprotective effect of apilarnil in lipopolysaccharide-induced sepsis through TLR4/NF-κB signaling pathway. *Life Sci*. 2021;284:119875.
- [11] Emadi E, Abdoli N, Ghanbarinejad V, Mohammadi HR, Mobarakeh KM, Azarpira N, et al. The potential role of mitochondrial impairment in the pathogenesis of imatinib-induced renal injury. *Heliyon*. 2019;5(6):e01996.
- [12] Huang FR, Fang WT, Cheng ZP, Shen Y, Wang DJ, Wang YQ, et al. Imatinib-induced hepatotoxicity via oxidative stress and activation of NLRP3 inflammasome: an in vitro and in vivo study. *Arch Toxicol*. 2022;96(4):1075-1087.
- [13] Emadi E, Abdoli N, Ghanbarinejad V, Mohammadi HR, Mobarakeh KM, Azarpira N, et al. The potential role of mitochondrial impairment in the pathogenesis of imatinib-induced renal injury. *Heliyon*. 2019;5(6).
- [14] Sun EJ, Wankell M, Palamuthusingam P, McFarlane C, Hebbard L. Targeting the PI3K/Akt/mTOR pathway in hepatocellular carcinoma. *Biomedicine*. 2021;9(11):1639.
- [15] Yang H, Wang H, Liu Y, Yang L, Sun L, Tian Y, et al. The PI3K/Akt/mTOR signaling pathway plays a role in regulating aconitine-induced autophagy in mouse liver. *Res J Vet Sci*. 2019;24:317-320.
- [16] Wang Y, Liu Z, Shu S, Cai J, Tang C, Dong Z. AMPK/mTOR Signaling in Autophagy Regulation During Cisplatin-Induced Acute Kidney Injury. *Front Physiol*. 2020;11:619730.

- [17] Heras-Sandoval D, Pérez-Rojas JM, Hernández-Damián J, Pedraza-Chaverri J. The role of PI3K/AKT/mTOR pathway in the modulation of autophagy and the clearance of protein aggregates in neurodegeneration. *Cell signal*. 2014;26(12):2694-2701.
- [18] Fattahi S, Amjadi-Moheb F, Tabaripour R, Ashrafi GH, Akhavan-Niaki H. PI3K/AKT/mTOR signaling in gastric cancer: Epigenetics and beyond. *Life Sci*. 2020;262:118513.
- [19] Ma L, Huang K, Zhang H, Kim E, Kim H, Liu Z, et al. Imatinib inhibits oral squamous cell carcinoma by suppressing the PI3K/AKT/mTOR signaling pathway. *J Cancer* 2024;15(3):659.
- [20] Doğanyigit Z, Okan A, Kaymak E, Pandır D, Silici S. Investigation of protective effects of apilarnil against lipopolysaccharide induced liver injury in rats via TLR 4/HMGB-1/NF-κB pathway. *Biomed Pharmacother*. 2020;125:109967.
- [21] Zhang H, Liu Y, Wang LK, Wei N. Pyrrolidine dithiocarbamate alleviates the anti-tuberculosis drug-induced liver injury through JAK2/STAT3 signaling pathway: An experimental study. *Asian Pac J Trop Med*. 2017;10(5):520-523.
- [22] Zai W, Chen W, Luan J, Fan J, Zhang X, Wu Z, et al. Dihydroquercetin ameliorated acetaminophen-induced hepatic cytotoxicity via activating JAK2/STAT3 pathway and autophagy. *Appl Microbiol Biotechnol*. 2018;102:1443-1453.
- [23] Wang M, Zhou Y, Hao G, Wu YE, Yin R, Zheng Y, et al. Recombinant Klotho alleviates vancomycin-induced acute kidney injury by upregulating anti-oxidative capacity via JAK2/STAT3/GPx3 axis. *Toxicology*. 2023;499:153657.
- [24] Shalaby M, Abdelaziz RR, Ghoneim HA, Suddek GM. Imatinib mitigates experimentally-induced ulcerative colitis: Possible contribution of NF-κB/JAK2/STAT3/COX2 signaling pathway. *Life Sci*. 2023;321:121596.

## Investigation of the Effects of Rutin in Sprague Dawley Rats with Biochemical Parameters in Colistin-Induced Lung Injury

Özge KANDEMİR<sup>1\*</sup>, Sefa KÜÇÜKLER<sup>2</sup>

<sup>1</sup> Aksaray University, Aksaray Vocational School of Technical Sciences, Food processing Department, Aksaray, Türkiye

<sup>2</sup> Atatürk University, Veterinary Faculty, Veterinary Biochemistry Department, Erzurum, Türkiye

Özge KANDEMİR ORCID No: 0000-0001-8884-4168

Sefa KÜÇÜKLER ORCID No: 0000-0002-8222-5515

\*Corresponding author: [ozgekandemir@aksaray.edu.tr](mailto:ozgekandemir@aksaray.edu.tr)

(Received: 07.07.2024, Accepted: 06.09.2024, Online Publication: 26.09.2024)

### Keywords

Lung injury,  
Colistin,  
Oxidative stress,  
Rutin

**Abstract:** Colistin (COL), frequently used for Gram-negative bacteria, may cause pulmonary toxicity in a dose-dependent manner. Flavanoid-type antioxidants have started to be used frequently against toxicity caused by different chemical agents. Rutin (RUT) is one of the flavanoid-type antioxidants. The present study aimed to investigate the effects of RUT in rats with COL-induced lung injury using biochemical parameters. In the experiment, 35 Sprague Dawley rats were divided into five groups (n=7): Control, RUT, COL, COL+RUT50, and COL+RUT100. It was determined that COL increased lung tissue MDA values, decreased SOD, CAT, GPx activities, and GSH values, and triggered oxidative stress. COL administration increased NF- $\kappa$ B, TNF- $\alpha$ , IL-1 $\beta$ , MPO, and COX-2 levels, decreased mTOR levels, increased Beclin-1 levels and accelerated autophagy, increased Caspase-3 activity, and induced apoptosis. It was determined that RUT administration suppressed oxidative stress, inflammation, autophagy, and apoptosis by reversely regulating all these markers and reducing cell damage. The findings showed that the RUT application would be useful in COL-induced lung injury.

## Kolistin ile Akciğer Hasarı Oluşturulan Sprague Dawley Ratlarda Rutin'in Etkilerinin Biyokimyasal Parametreler ile Araştırılması

### Anahtar Kelimeler

Akciğer hasarı,  
Kolistin,  
Oksidatif stres,  
Rutin

**Öz:** Gram negatif bakteriler için sıklıkla kullanılan kolistin (COL) doza bağımlı olarak akciğer toksisitesinde neden olabilmektedir. Flavanoid türü antioksidanlar farklı kimyasal ajanların neden olduğu toksikasyonlara karşı günümüzde oldukça sık kullanılmaya başlamıştır. Rutin (RUT) flavanoid türü antioksidanlardan biridir. Sunulan çalışmada COL ile akciğer hasarı geliştirilen ratlarda RUT'in etkilerinin biyokimyasal parametreler ile araştırılması amaçlanmıştır. Deneyde 35 adet Sprague Dawley rat kontrol, RUT, COL, COL+RUT 50 ve COL+RUT100 olmak üzere 5 gruba (n=7) ayrıldı. COL' in akciğer dokusu MDA değerlerini artırıp, SOD, CAT, GPx aktiviteleri ile GSH değerlerini azalttığı ve oksidatif stresi tetiklediği tespit edildi. COL uygulamasının, inflamasyon belirteçlerinden NF- $\kappa$ B, TNF- $\alpha$ , IL-1 $\beta$ , MPO ve COX-2 seviyelerini artırdığı, mTOR düzeylerinin azalması ve Beclin-1 seviyelerini yükseltmekle otofajiyi hızlandırdığı, Kaspaz-3 aktivitesini artırarak apoptozisi indüklediği saptandı. RUT uygulamasının tüm bu belirteçleri tersine regüle ederek oksidatif stres, inflamasyon, otofaji ve apoptozisi baskıladığı ve hücredeki hasarı azalttığı belirlendi. Elde edilen bulgular COL kaynaklı akciğer hasarında RUT uygulamasının yararlı olacağını gösterdi.

## 1. INTRODUCTION

Antimicrobial resistance (AMR) has become an increasingly enormous worldwide health burden [1]. One of the most important reasons for this increase is inappropriately prescribed antibiotics, which are

especially prevalent in children. In some developed countries, 65-67% of antibiotics used to treat pediatric patients are reported to be ineffective and not the right choice. In 2017, the World Health Organization (WHO) published a list of drug-resistant bacteria (Pseudomonas aeruginosa, Acinetobacter baumannii, Escherichia coli,

etc.). The aforementioned report suggested exploring new treatment options to reduce the number of deaths from drug-resistant bacteria [2]. Polymyxin B and E (or colistin) is a last-line drug effective in the treatment of infections caused by drug-resistant gram-negative bacteria (*Pseudomonas aeruginosa*, *Acinetobacter baumannii*, *Klebsiella pneumoniae*, etc.). [1].

Colistin (COL) interacts with anionic lipopolysaccharides, displacing and neutralizing divalent cations (Ca and Mg) in the membrane of gram-negative bacteria (GNB). COL has an enormous molecular weight cannot easily pass through cell membranes, and is primarily distributed in the extracellular space. The pharmacokinetics of COL are very variable and have a narrow therapeutic window. In the 1980s, the clinical use of COL was abandoned due to its heavy side effects, but since the drug was effective in AMR, dose adjustment was prioritized to reduce side effects instead of banning it [3]. High doses cause undesirable clinical side effects, including pulmonary, neuro, and nephrotoxicity [1]. COL activates caspases 3, 8, and 9. Activation of caspases can potentially be triggered by two interacting pathways, the mitochondrial pathway (intrinsic) and the cell death receptor pathway (extrinsic). Concentration and time-dependent activation of all three caspases by COL in lung cells suggests that both the death receptor and mitochondrial pathways play a role in COL-induced apoptosis. [4]. Since 1960, there have been numerous reports of COL-induced acute respiratory failure and respiratory paralysis [5]. Direct delivery of COL to the lung is a promising strategy for pulmonary infection treatment, but high localized levels can cause pulmonary toxicity [6]. Ahmed et al. [4] reported that the drug accumulated at high levels in A549 human lung epithelial cells and caused apoptosis.

Flavonoids are natural compounds with many biological and pharmacological activities such as anti-inflammatory, anti-tumor, and anti-apoptotic, especially antioxidant properties. Research on the therapeutic effects of flavonoids against toxic damaging agents has been intensified [7, 8]. Flavonoids show antioxidant properties significantly by eliminating reactive oxygen species (ROS) and reactive nitrogen species and also by increasing antioxidant enzyme capacity [9]. Rutin (RUT) is a flavone derivative composed of the flavonol quercetin and the disaccharide rutinose and has the basic activities of flavonoids [10].

RUT is a significant flavonoid with four hydroxyl groups and the rutinose molecule in its structure, and these play a significant role in its biological activity. RUT is found in citrus fruits such as grapefruit, orange, lemon, and fruits and vegetables such as spinach, onion, and apple. In particular, the presence of rutinose increases the number of active sites of RUT, making it a more effective molecule [9,10].

In the presented study, the potential effects of RUT on Sprague Dawley rats with lung injury induced by COL were examined in terms of oxidative stress, inflammation, apoptosis and autophagic pathway

markers and possible damage mechanisms were tried to be revealed.

## 2. MATERIAL AND METHODS

### 2.1. Drug and Chemicals

COL (Colimycin® 150 mg/vial, Koçak Pharma, Istanbul, Turkey) was obtained from a local pharmacy. RUT ( $\geq 94\%$ ) and other chemicals were of analytical purity and purchased from Sigma Chemical Co. (St. Louis, MO, USA). ELISA kits for Nuclear factor kappa B (NF- $\kappa$ B) and Tumor necrosis factor alpha (TNF- $\alpha$ ) were obtained from YL Biont (Shanghai, China); Interleukin 1 beta (IL-1 $\beta$ ), Myeloperoxidase (MPO), Cyclooxygenase-2 (COX-2), Mammalian target of rapamycin (mTOR), Cysteine aspartate specific protease-3 (caspase-3) and Beclin-1 were obtained from Sunred Biological Technology Company (Shanghai, China).

### 2.2. Experimental Animals and Ethics Committee Approval

Thirty-five male Sprague Dawley rats from Atatürk University Animal Experimentation Center were used. Animals were kept in clean cages in a controlled room with a constant temperature of 24-25 °C and a 12-hour dark-light cycle. They were provided with unlimited access to water and standard chow. After the rats were allowed to rest in their cages for one week and adapted to the environment, the experiment was started. The ethics committee approval of the study was obtained from the Atatürk University Animal Experiments Local Ethics Committee with meeting number 2024/02 and decision number 34 dated 26.02.2024.

### 2.3. Experimental Design

In the dose selection of COL and RUT used in the study, Çelik et al. [11] were taken as a reference.

The rats were divided into five groups with seven rats in each group.

1. Control: 7 days oral and intraperitoneal (i.p.) saline was given.
2. RUT: 100 mg/kg RUT was given orally for seven days.
3. COL: 15 mg/kg COL was given i.p. for seven days.
4. COL+RUT50: 15 mg/kg COL was given i.p. for seven days. 50 mg/kg RUT was given orally for seven days 30 minutes after COL administration.
5. COL+RUT100: 15 mg/kg COL was given i.p. for seven days. 100 mg/kg RUT was given orally for seven days 30 minutes after COL administration.

Twenty-four hours after the last administration (day 8), the rats were decapitated under mild sevoflurane anesthesia, and lung tissue was removed and stored at -20°C until biochemical analyses were performed.

## 2.4. Evaluation of Oxidative Stress

Lung tissue was ground using liquid nitrogen (Tissue Lyser II, Qiagen). The lung tissues were homogenized in a 1:10 (weight/volume) ratio of tissue and 1.15% potassium chloride buffer. A portion of the homogenate was centrifuged at 10,000 rpm for 20 minutes at 4°C and the supernatant was used to measure glutathione peroxidase (GPx) activity and glutathione (GSH) level. The remaining homogenate was centrifuged at 3500 rpm for 15 minutes, and the supernatants were used for catalase (CAT), superoxide dismutase (SOD), and malondialdehyde (MDA) analysis. Measurements were performed as follows; CAT activity was determined by Aebi [12], GPx activity by Matkovic [13], SOD activity by Sun et al [14], MDA level by Placer et al [15], and GSH level by Sedlak and Lindsay [16]. The total protein in the homogenate was determined according to the Lowry et al. [17] method.

## 2.5. Determination of Lung Tissue NF- $\kappa$ B, TNF- $\alpha$ , IL-1 $\beta$ , MPO, COX-2, mTOR, Beclin-1 and Caspase-3 Levels by ELISA Method

The supernatants were prepared by centrifugation at 3500 rpm for 15 minutes and analyzed using the ELISA kit according to the manufacturer's protocol. 100 mg of ground lung tissue was diluted 1:20 with phosphate buffer (0.1 M, pH 7.4). The results were calculated using the standard graphs of the kits from the absorbance values obtained by reading the ELISA plates in a microplate reader (Bio-Tek, Winooski, VT, USA).

## 2.6. Statistical Analysis

One-way analysis of variance (ANOVA) and Tukey post hoc test (version 20.0; SPSS, Chicago, IL) was used to determine the difference between the groups and the significance levels.  $p < 0.05$  was considered a significant difference. All values were expressed as the mean  $\pm$  standard error of the mean (SEM).

## 3. RESULTS

### 3.1. MDA Levels

When lung tissue MDA levels were examined (Figure 1A), no difference was found between the control and RUT groups ( $p > 0.05$ ), MDA values increased in the COL group compared to the control group ( $p < 0.0001$ ), and 50 and 100 doses of RUT given together with COL were found to be effective in reducing MDA values ( $p < 0.0001$ ).

### 3.2. GSH Levels

It was found that GSH levels in the COL group decreased compared to the control group ( $p < 0.0001$ ), there was no difference between the control and RUT groups ( $p > 0.05$ ), and both doses of RUT given together with COL were effective in increasing GSH levels ( $p < 0.0001$ ) (Figure 1B).

### 3.3. GPx Activities

While there was no difference between control and RUT group GPx activities ( $p > 0.05$ ), GPx activities in COL group decreased compared to control and RUT groups ( $p < 0.0001$ ), GPx activities in COL+RUT50 and COL+RUT100 groups increased compared to COL group ( $p < 0.0001$ ) (Figure 1C).

### 3.4. SOD Activities

SOD activities in the COL group decreased compared to the control and RUT groups ( $p < 0.0001$ ), while both doses of RUT treatment increased these activities compared to the COL group ( $p < 0.0001$ ) (Figure 1D).

### 3.5. CAT Activities

When lung tissue CAT activities were examined (Figure 1E), it was found that there was no difference between the control and RUT groups ( $p > 0.05$ ), CAT activities in the COL group decreased compared to the control group ( $p < 0.0001$ ), RUT 50 doses administered together with COL was not effective in increasing the activity ( $p > 0.05$ ), and RUT 100 doses increased CAT activity ( $p < 0.01$ ).

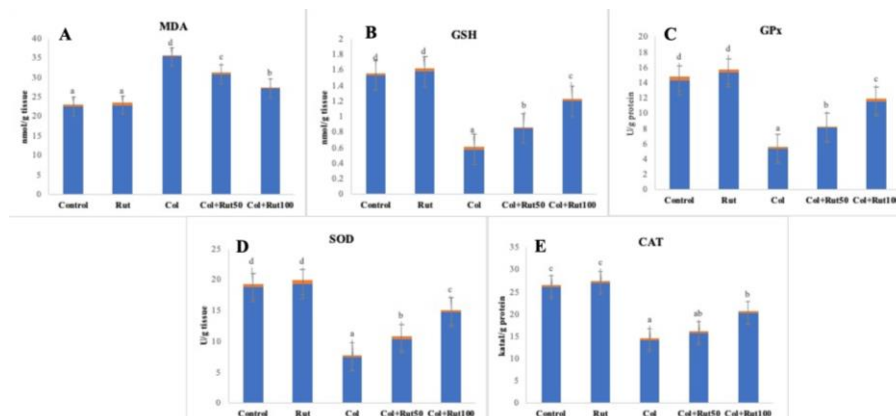


**Figure 1.** MDA (A), GSH (B) levels and GPx (C), SOD (D), CAT (E) activities in lung tissue after COL and RUT treatments. Different letters (a, b, c, d, e) indicate differences between groups ( $p < 0.05$ ).



### 3.6. NF- $\kappa$ B Levels

COL group NF- $\kappa$ B levels increased ( $p < 0.001$ ) when compared with control and RUT groups, and RUT 50 and 100 doses were effective in decreasing NF- $\kappa$ B levels ( $p < 0.0001$ ) (Figure 2A).

### 3.7. TNF- $\alpha$ Levels

While there was no difference between the control and RUT groups ( $p > 0.05$ ), TNF- $\alpha$  levels increased in the COL group compared to the control group ( $p < 0.0001$ ), and 50 and 100 doses of RUT given together with COL were effective in reducing TNF- $\alpha$  levels ( $p < 0.0001$ ) (Figure 2B).

### 3.8. IL-1 $\beta$ Levels

When lung tissue IL-1 $\beta$  levels were examined (Figure 2C), it was determined that there was no difference between the control group and the RUT group ( $p > 0.05$ ),

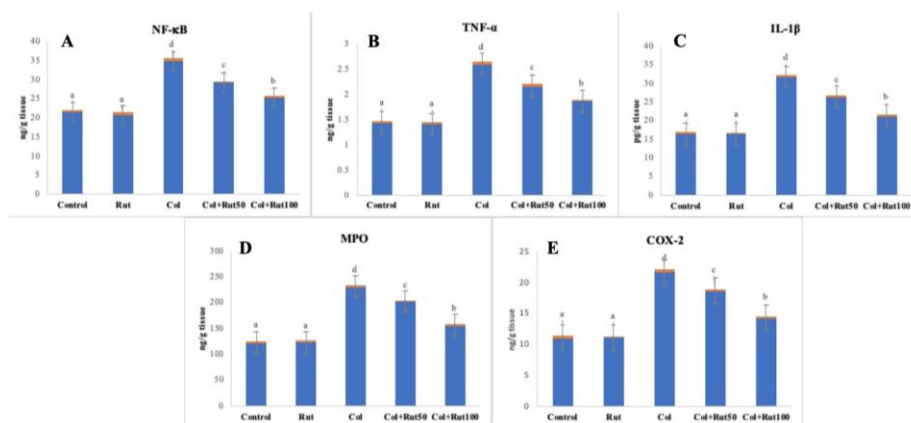


**Figure 2.** NF- $\kappa$ B (A), TNF- $\alpha$  (B), IL-1 $\beta$  (C) levels and MPO (D), COX-2 (E) activities in lung tissue after COL and RUT treatments. Different letters (a, b, c, d, e) indicate differences between groups ( $p < 0.05$ ).

### 3.11. mTOR Levels

When lung tissue mTOR levels were examined (Figure 3A), it was found that mTOR level decreased in COL-treated rats compared to the control and RUT groups ( $p < 0.0001$ ), and RUT 50 and 100 doses were effective in increasing mTOR levels ( $p < 0.0001$ ).

### 3.13. Beclin-1 Levels

When Beclin-1 levels were analyzed (Figure 3B), it was found that Beclin-1 level increased in the COL group compared to the control group ( $p < 0.0001$ ), and RUT 50

### 3.14. Caspase-3 activities

When Caspase-3 activity was examined (Figure 4), it was determined that there was no difference between the control group and the RUT group ( $p > 0.05$ ), the Caspase-3 activity in the COL group increased compared to the control and RUT groups ( $p < 0.0001$ ), both doses of RUT were effective in reducing Caspase-3 activity ( $p < 0.0001$ ), and there was no difference between RUT 50 and 100 doses in terms of effect ( $p > 0.05$ ).

and IL-1 $\beta$  levels in the COL group increased compared to the control and RUT groups ( $p < 0.0001$ ), both doses of RUT were effective and decreased IL-1 $\beta$  levels ( $p < 0.0001$ ).

### 3.9. MPO Activities

MPO activity in the COL group increased compared to the control and RUT group ( $p < 0.0001$ ), there was no difference between the control and RUT group ( $p > 0.05$ ), and RUT 50 and 100 doses were effective in decreasing the activity ( $p < 0.0001$ ) (Figure 2D).

### 3.10. COX-2 Activities

While there was no difference between the COX-2 activities of the control and RUT groups ( $p > 0.05$ ), it was determined that COX-2 activity increased in the COL group compared to the control group ( $p < 0.0001$ ), while COX-2 activity decreased with RUT 50 and 100 applications ( $p < 0.0001$ ) (Figure 2E).

and 100 doses administered together with COL were effective in reducing Beclin-1 levels ( $p < 0.0001$ ).

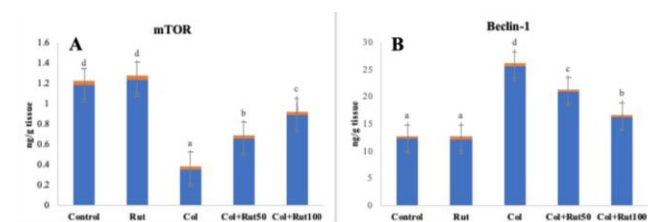


**Figure 3.** mTOR (A) and Beclin-1 (B) levels in lung tissue after COL and RUT treatments. Different letters (a, b, c, d, e) indicate differences between groups ( $p < 0.05$ ).

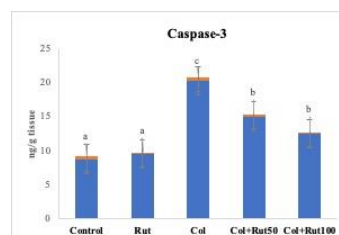


**Figure 4.** Caspase-3 activity in lung tissue after COL and RUT treatments. Different letters (a, b, c, d, e) indicate differences between groups ( $p < 0.05$ ).

#### 4. DISCUSSION AND CONCLUSION

COL (polymyxin E) is a glycopeptide antibiotic approved for medical use and used as a last resort in patients. It is commercially available in the form of COL sulfate for topical and oral use and colistimethate sodium for parenteral and inhalation use [18]. COL, a cationic polypeptide, has a bactericidal effect on multidrug-resistant GNB and is still one of the few options for the treatment of infections caused by GNB. COL is often used to treat GNB infections by intramuscular injection. In-vivo and in-vitro studies have demonstrated that COL use causes pulmonary toxicity, but the molecular mechanism underlying this toxicity has not been fully elucidated [1]. Therefore, in this study, the effects of RUT were investigated by oxidative stress, inflammation, apoptotic, and autophagic markers in rats with COL-induced lung injury.

Oxidative stress is recognized as one of the most important causes of tissue damage. Excessive production of ROS due to different reasons causes a decrease in antioxidant capacity, and this situation manifests itself as oxidative stress [19-21]. ROS produced in excessive amounts shape cell damage by affecting many macromolecules, especially proteins and lipids, one of the most significant components of the cell membrane [22, 23]. MDA, the end product of lipid peroxidation, is the most important marker of oxidative stress, and oxidative stress activates various defense systems in cells [24-26].

Antioxidants interact with unstable molecules such as ROS to stabilize them and prevent cell damage [27-29]. SOD, CAT, and GPx are at the base of the cellular antioxidant defense line. SOD is responsible for the scavenging of superoxide radicals, while CAT and GPx are responsible for the decomposition of H<sub>2</sub>O<sub>2</sub> into water and molecular oxygen. GSH, apart from being the substrate of GPx, also helps to maintain the redox state in cells [30, 31]. Studies have shown that COL increases MDA levels and causes cell damage by decreasing SOD, CAT, GPx activities, and GSH levels [1, 11, 32]. In the present study, it was determined that MDA levels increased, SOD, CAT, GPx activities and GSH levels decreased and oxidative stress developed in the cell of rats administered COL. It was determined that 50 and 100 doses of RUT administered together with COL protected the cell membrane and integrity by decreasing MDA levels, increased SOD, CAT, GPx activities, and GSH levels, and protected the cell from damage caused by oxidative stress by strengthening the antioxidant defense system. Aktaş et al. [33] reported that RUT decreased MDA levels by increasing antioxidant enzyme activities in lung damage and protected the cell from the effects of oxidative stress.

Inflammation, another damage pathway triggered by oxidative stress, is an important mechanism that causes an increase in lung damage. Increased oxidative stress in lung cells also increases the release of inflammatory cytokines and chemokines from the lung cells [34]. NF- $\kappa$ B is one of the transcription factors effective in

inflammatory damage and regulates the release of pro-inflammatory cytokines (such as TNF- $\alpha$ , IL-1 $\beta$ , and COX-2) [35-37]. ROS have been shown to play a role in the activation of pro-inflammatory mediators NF- $\kappa$ B and TNF- $\alpha$ , which promote tissue inflammation, and it has been reported that suppression of NF- $\kappa$ B will decrease TNF- $\alpha$  and suppress inflammation [37]. In a study conducted with different toxic agents, it was reported that inflammatory cytokines in lung tissue increased via ROS [38].

MPO, one of the enzymes that is effective in inflammation and oxidative stress damage at the cellular level, is a heme protein released by leukocytes. Its level is considered a reliable biomarker and indicates neutrophil infiltration when it increases [39]. In the present study, COL administration increased inflammation in lung tissue by causing an increase in NF- $\kappa$ B, TNF- $\alpha$ , IL-1 $\beta$ , COX-2, and MPO levels, while both doses of RUT administered together with COL suppressed TNF- $\alpha$ , IL-1 $\beta$ , COX-2 and MPO production and decreased inflammation by suppressing NF- $\kappa$ B release. In a study on rats, it was revealed that COL caused inflammation by increasing the levels of NF- $\kappa$ B, TNF- $\alpha$ , and IL-1 $\beta$  [40]. It has been reported that RUT has anti-inflammatory properties and reduces inflammation increased by chemical agents by suppressing cytokine production [7, 9, 41].

mTOR is a primary regulator with significant functions in autophagy and provides negative regulation of autophagy. mTOR is a serine/threonine kinase that is one of the major regulators of cellular functions such as growth, proliferation, and survival. While regulating cellular functions, mTOR; regulates cellular activities such as protein synthesis, energy metabolism, and stress response by bringing together different signaling pathways. [42]. Studies have shown that COL suppresses mTOR activity and accelerates autophagy [1]. In the present study, it was determined that mTOR activity decreased in COL-treated rats, while COL and RUT administration caused an increase in activity. It has been reported in different studies that RUT regulates mTOR activity and seriously increases dose-dependent mTOR levels [43, 44].

Autophagy is a program that manifests itself in situations such as nutrient, growth factor deficiency, and stress and is effective in cellular homeostasis, metabolism, and transport of material from the cytoplasm to lysosomes. Autophagy also allows cells to recycle nutrients, maintain cell energy balance, and break down toxic cytoplasmic components [45]. Beclin-1 is one of the most significant indicators interested in the autophagic process and determines the extent of autophagic damage [9]. A study revealed that COL accelerates autophagy by increasing Beclin-1 levels in lung tissue [1]. COL was also found to increase Beclin-1 levels in different studies on rats [2, 45]. In the present study, it was determined that COL administration accelerated autophagy by increasing Beclin-1 levels in rat lung tissue, while RUT administration suppressed autophagy by decreasing Beclin-1 levels. Studies have shown that rutin exhibits

anti-autophagic properties in organ toxicity models developed with different chemicals, suppresses the expression of Beclin-1, the most important marker of the autophagic pathway, and is effective in protecting the cell from autophagy [7, 9, 10].

Apoptosis, also known as programmed cell death, is a normal process for the elimination of unwanted cells and maintenance of tissue homeostasis [46, 47]. Caspase-3, one of the most significant markers of apoptosis, is a death protease that is often induced because it increases the specific cleavage of many cellular proteins and leads to DNA fragmentation, one of the characteristic cellular changes of apoptosis [48-50]. Cytokines such as TNF- $\alpha$  have also been reported to play a role in triggering apoptosis [51]. It has been reported in different studies that COL accelerates caspase-3 activity by increasing it [52, 53]. In the present study, it was found that caspase-3 activity increased and apoptosis accelerated in the lung tissue of COL-treated rats, and both doses of RUT suppressed apoptosis by decreasing this activity. It was reported by Gür and Kandemir [54] that RUT suppressed apoptosis by decreasing caspase-3 activity in lung tissue. In toxicity models developed with different chemicals in different organs, it has been reported that rutin exhibits antiapoptotic properties, suppresses the apoptotic pathway, especially Caspase-3, and protects the cell from apoptosis [55- 58].

As a conclusion, it was determined that COL triggered oxidative stress by increasing MDA level and causing a decrease in antioxidant enzyme activities and the increase in oxidative stress increased apoptosis and autophagy, especially inflammation, while RUT application showed the opposite effect, and tried to protect the cell. In light of the findings obtained, it is thought that the use of RUT in COL-induced lung damage will be beneficial.

## REFERENCES

- [1] Dai C, Li M, Sun T, Zhang Y, Wang Y, Shen Z, et al. Colistin-induced pulmonary toxicity involves the activation of NOX4/TGF- $\beta$ /mtROS pathway and the inhibition of Akt/mTOR pathway. *Food Chem Toxicol.* 2022;163:112966.
- [2] Kankılıç NA, Şimşek H, Akaras N, Gür C, İleritürk M, Küçükler S, et al. Protective effects of naringin on colistin-induced damage in rat testicular tissue: Modulating the levels of Nrf-2/HO-1, AKT-2/FOXO1A, Bax/Bcl2/Caspase-3, and Beclin-1/LC3A/LC3B signaling pathways. *J Biochem Mol Toxicol.* 2024;38(2):e23643.
- [3] Aksu EH, Kandemir FM, Küçükler S. The effects of hesperidin on colistin-induced reproductive damage, autophagy, and apoptosis by reducing oxidative stress. *Andrologia.* 2021;53(2):e13900.
- [4] Ahmed MU, Velkov T, Lin YW, Yun B, Nowell CJ, Zhou F, Zhou QT, Chan K, Azad MAK, Li J. Potential Toxicity of Polymyxins in Human Lung Epithelial Cells. *Antimicrob Agents Chemother.* 2017;61(6):e02690-16.
- [5] Shrestha A, Soriano SM, Song M, Chihara S. Intravenous colistin-induced acute respiratory failure: A case report and a review of literature. *Int J Crit Illn Inj Sci.* 2014;4(3):266-70.
- [6] Velkov T, Abdul Rahim N, Zhou QT, Chan HK, Li J. Inhaled anti-infective chemotherapy for respiratory tract infections: successes, challenges and the road ahead. *Adv Drug Deliv Rev.* 2015;85:65-82.
- [7] Gur C, Kandemir FM. Molecular and biochemical investigation of the protective effects of rutin against liver and kidney toxicity caused by malathion administration in a rat model. *Environ Toxicol.* 2023;38(3):555-565.
- [8] Simsek H, Akaras N. Acacetin ameliorates acetylsalicylic acid-induced gastric ulcer in rats by interfering with oxidative stress, inflammation, and apoptosis. *Int J Med Biochem* 2023;6(2):96-103.
- [9] Kandemir FM, İleritürk M, Gur C. Rutin protects rat liver and kidney from sodium valproate-induced damage by attenuating oxidative stress, ER stress, inflammation, apoptosis and autophagy. *Mol Biol Rep.* 2022;49(7):6063-6074.
- [10] Küçükler S, Kandemir FM, Özdemir S, Çomaklı S, Çağlayan C. Protective effects of rutin against deltamethrin-induced hepatotoxicity and nephrotoxicity in rats via regulation of oxidative stress, inflammation, and apoptosis. *Environ Sci Pollut Res Int.* 2021;28(44):62975-62990.
- [11] Çelik H, Kandemir FM, Çağlayan C, Özdemir S, Çomaklı S, Kucukler S, Yardım A. Neuroprotective effect of rutin against colistin-induced oxidative stress, inflammation and apoptosis in rat brain associated with the CREB/BDNF expressions. *Mol Biol Rep.* 2020;47(3):2023-2034.
- [12] Aebi H. Catalase in vitro. *Methods Enzymol.* 1984;105:121-6.
- [13] Matkovic B. Determination of enzyme activity in lipid peroxidation and glutathione pathways. *Laboratoriumi Diagnostika.* 1988;15:248-250.
- [14] Sun YI, Oberley LW, Li Y. A simple method for clinical assay of superoxide dismutase. *Clinical chemistry,* 1988;34(3):497-500.
- [15] Placer ZA, Cushman LL, Johnson BC. Estimation of product of lipid peroxidation (malonyl dialdehyde) in biochemical systems. *Analytical biochemistry.* 1966;16(2):359-64.
- [16] Sedlak J, Lindsay RH. Estimation of total, protein-bound, and nonprotein sulfhydryl groups in tissue with Ellman's reagent. *Analytical biochemistry,* 1968;25:192-205.
- [17] Lowry OH, Rosebrough NJ, Farr AL, Randall RJ. Protein measurement with the Folin phenol reagent. *Journal of Biological Chemistry.* 1951;193:265-75.
- [18] Nasrullah MZ, Eljaaly K, Neamatallah T, et al. Omeprazole Prevents Colistin-Induced Nephrotoxicity in Rats: Emphasis on Oxidative Stress, Inflammation, Apoptosis and Colistin Accumulation in Kidneys [published correction appears in *Pharmaceuticals* (Basel). 2024;17(4):540.
- [19] Kandemir FM, Ozkaraca M, Küçükler S, Çağlayan C, Hanedan B. Preventive effects of hesperidin on

- diabetic nephropathy induced by streptozotocin via modulating TGF- $\beta$ 1 and oxidative DNA damage. *Toxin reviews*. 2018;37(4):287-93.
- [20] Ekinçi Akdemir FN, Yıldırım S, Kandemir FM, Aksu EH, Guler MC, Kiziltunc Ozmen H, et al. The antiapoptotic and antioxidant effects of eugenol against cisplatin-induced testicular damage in the experimental model. *Andrologia*. 2019;51(9):e13353.
- [21] Zeren S, Bayhan Z, Kocak FE, Kocak C, Akcılar R, Bayat Z, et al. Gastroprotective effects of sulforaphane and thymoquinone against acetylsalicylic acid-induced gastric ulcer in rats. *J Surg Res*. 2016;203(2):348-59.
- [22] Kocak C, Kocak FE, Akcılar R, Isıklar OO, Kocak H, Bayat Z, et al. Molecular and biochemical evidence on the protective effects of embelin and carnosic acid in isoproterenol-induced acute myocardial injury in rats. *Life Sci*. 2016;147:15-23.
- [23] Kankılıç NA, Şimşek H, Akaras N, Gür C, Küçükler S, İleritürk M, et al. The ameliorative effects of chrysin on bortezomib-induced nephrotoxicity in rats: Reduces oxidative stress, endoplasmic reticulum stress, inflammation damage, apoptotic and autophagic death. *Food Chem Toxicol*. 2024;190:114791.
- [24] Şimşek H, Akaras N, Gür C, Küçükler S, Kandemir FM. Beneficial effects of Chrysin on Cadmium-induced nephrotoxicity in rats: Modulating the levels of Nrf2/HO-1, RAGE/NLRP3, and Caspase-3/Bax/Bcl-2 signaling pathways. *Gene*. 2023;875:147502.
- [25] Akaras N, İleritürk M, Gur C, Kucukler S, Oz M, Kandemir FM. The protective effects of chrysin on cadmium-induced pulmonary toxicity; a multi-biomarker approach. *Environ Sci Pollut Res Int*. 2023;30(38):89479-89494.
- [26] Keleş O, Can S, Cıgır G, Colak S, Erol H, Akaras N, et al. Hepatoprotective effects of B-1, 3-(D)-glucan on bortezomib-induced liver damage in rats. *Kafkas Üniversitesi Veteriner Fakültesi Dergisi*, 2014;20(6):929-38.
- [27] İleritürk M, İleritürk D, Kandemir O, Akaras N, Simsek H, Erdogan E, et al. Naringin attenuates oxaliplatin-induced nephrotoxicity and hepatotoxicity: A molecular, biochemical, and histopathological approach in a rat model. *J Biochem Mol Toxicol*. 2024;38(1):e23604.
- [28] Şimşek H, Gür C, Küçükler S, İleritürk M, Akaras N, Öz M, et al. Carvacrol Reduces Mercuric Chloride-Induced Testicular Toxicity by Regulating Oxidative Stress, Inflammation, Apoptosis, Autophagy, and Histopathological Changes. *Biol Trace Elem Res*. 2023 Dec 22.
- [29] Ozyigit F, Deger AN, Kocak FE, Ekici MF, Simsek H, Arık O. Protective effects of hesperidin in gastric damage caused by experimental ischemia-reperfusion injury model in rats. *Acta Cir Bras*. 2024;39:e391124.
- [30] Gur C, Akarsu SA, Akaras N, Tuncer SC, Kandemir FM. Carvacrol reduces abnormal and dead sperm counts by attenuating sodium arsenite-induced oxidative stress, inflammation, apoptosis, and autophagy in the testicular tissues of rats. *Environ Toxicol*. 2023;38(6):1265-1276.
- [31] Aydin M, Cevik A, Kandemir FM, Yuksel M, Apaydin AM. Evaluation of hormonal change, biochemical parameters, and histopathological status of uterus in rats exposed to 50-Hz electromagnetic field. *Toxicol Ind Health*. 2009;25(3):153-8.
- [32] Hanedan B, Ozkaraca M, Kirbas A, Kandemir FM, Aktas MS, Kilic K, et al. Investigation of the effects of hesperidin and chrysin on renal injury induced by colistin in rats. *Biomed Pharmacother*. 2018;108:1607-1616.
- [33] Aktas M, Kandemir F, Özkaraca M, Hanedan B, Kirbas A. Protective Effects of Rutin on Acute Lung Injury Induced by Oleic Acid in Rats. *Kafkas Üniversitesi Veteriner Fakültesi Dergisi*. 2017;23(3):445-51.
- [34] Yesildag K, Gur C, İleritürk M, Kandemir FM. Evaluation of oxidative stress, inflammation, apoptosis, oxidative DNA damage and metalloproteinases in the lungs of rats treated with cadmium and carvacrol. *Mol Biol Rep*. 2022;49(2):1201-1211.
- [35] Semis HS, Gur C, İleritürk M, Kandemir FM, Kaynar O. Evaluation of Therapeutic Effects of Quercetin Against Achilles Tendinopathy in Rats via Oxidative Stress, Inflammation, Apoptosis, Autophagy, and Metalloproteinases. *Am J Sports Med*. 2022;50(2):486-498.
- [36] Şimşek H, Küçükler S, Gür C, Akaras N, Kandemir FM. Protective effects of sinapic acid against lead acetate-induced nephrotoxicity: a multi-biomarker approach. *Environ Sci Pollut Res Int*. 2023;30(45):101208-22.
- [37] İleritürk M, Kandemir O, Akaras N, Simsek H, Genc A, Kandemir FM. Hesperidin has a protective effect on paclitaxel-induced testicular toxicity through regulating oxidative stress, apoptosis, inflammation and endoplasmic reticulum stress. *Reprod Toxicol*. 2023;118:108369.
- [38] Şimşek H, Küçükler S, Gür C, İleritürk M, Aygörmez S, Kandemir FM. Protective effects of zingerone against sodium arsenite-induced lung toxicity: A multi-biomarker approach. *Iran J Basic Med Sci*. 2023;26(9):1098-1106.
- [39] Çağlayan C, Kandemir FM, Yıldırım S, Kucukler S, Eser G. Rutin protects mercuric chloride-induced nephrotoxicity via targeting of aquaporin 1 level, oxidative stress, apoptosis and inflammation in rats. *J Trace Elem Med Biol*. 2019;54:69-78.
- [40] Yılmaz S, Küçükler S, Şimşek H, Aygörmez S, Kandemir FM. Naringin protects against colistin-induced sciatic nerve damage by reducing oxidative stress, apoptosis and inflammation damage. *J. Exp. Clin. Med*. 2024;41(1):53-9.
- [41] He Q, Hao H, Zhao K. (2024). Investigating the anti-inflammatory effects of rutin in carbon tetrachloride-induced hepatotoxicity: role of TLR4/MyD88/NF $\kappa$ B signaling pathway modulation. *Pharmacognosy Magazine*. 2024;20(1):107-15.

- [42] Wang Y, Liu Z, Shu S, Cai J, Tang C, Dong Z. AMPK/mTOR Signaling in Autophagy Regulation During Cisplatin-Induced Acute Kidney Injury. *Front Physiol.* 2020;11:619730.
- [43] Fei J, Sun Y, Duan Y, Xia J, Yu S, Ouyang P, et al. Low concentration of rutin treatment might alleviate the cardiotoxicity effect of pirarubicin on cardiomyocytes via activation of PI3K/AKT/mTOR signaling pathway. *Biosci Rep.* 2019;39(6):BSR20190546.
- [44] Wu X, Wang J, Li B, Gong M, Cao C, Song L, et al. Chlorogenic acid, rutin, and quercetin from *Lysimachia christinae* alleviate triptolide-induced multi-organ injury in vivo by modulating immunity and AKT/mTOR signal pathway to inhibit ferroptosis and apoptosis. *Toxicol Appl Pharmacol.* 2023;467:116479.
- [45] Lu Z, Miao Y, Muhammad I, Tian E, Hu W, Wang J, et al. Colistin-induced autophagy and apoptosis involves the JNK-Bcl2-Bax signaling pathway and JNK-p53-ROS positive feedback loop in PC-12 cells. *Chem Biol Interact.* 2017;277:62-73.
- [46] Akarsu SA, Gür C, İleritürk M, Akaras N, Küçükler S, Kandemir FM. Effect of syringic acid on oxidative stress, autophagy, apoptosis, inflammation pathways against testicular damage induced by lead acetate. *J Trace Elem Med Biol.* 2023;80:127315.
- [47] Akcılar R, Akcılar A, Koçak C, Koçak FE, Bayat Z, Şimşek H, et al. Effects of Ukrain on intestinal apoptosis caused by ischemia-reperfusion injury in rats. *Int J Clin Exp Med.* 2015;8(12):22158-66.
- [48] Şimşek H, Demiryürek Ş, Demir T, Atabay HD, Çeribası AO, Bayraktar R, et al. Assessment of expressions of Bcl-XL, b-FGF, Bmp-2, Caspase-3, PDGFR- $\alpha$ , Smad1 and TGF- $\beta$ 1 genes in a rat model of lung ischemia/reperfusion. *Iran J Basic Med Sci.* 2016;19(2):209-14.
- [49] Semis HS, Kandemir FM, Kaynar O, Dogan T, Arikian SM. The protective effects of hesperidin against paclitaxel-induced peripheral neuropathy in rats. *Life Sci.* 2021;287:120104.
- [50] Gur C, Kandemir FM, Caglayan C, Satici E. Chemopreventive effects of hesperidin against paclitaxel-induced hepatotoxicity and nephrotoxicity via amendment of Nrf2/HO-1 and caspase-3/Bax/Bcl-2 signaling pathways. *Chem Biol Interact.* 2022;365:110073.
- [51] Güçlü A, Erken HA, Erken G, Dodurga Y, Yay A, Özçoban Ö, et al. The effects of ozone therapy on caspase pathways, TNF- $\alpha$ , and HIF-1 $\alpha$  in diabetic nephropathy. *Int Urol Nephrol.* 2016;48(3):441-50.
- [52] Worakajit N, Thipboonchoo N, Chaturongakul S, Jutabha P, Soontornniyomkij V, Tuchinda P, et al. Nephroprotective potential of Panduratin A against colistin-induced renal injury via attenuating mitochondrial dysfunction and cell apoptosis. *Biomed Pharmacother.* 2022;148:112732.
- [53] Aksu EH, Kandemir FM, Küçükler S, Mahamadu A. Improvement in colistin-induced reproductive damage, apoptosis, and autophagy in testes via reducing oxidative stress by chrysin. *J Biochem Mol Toxicol.* 2018;32(11):e22201.
- [54] Gür C, Kandemir FM. Evaluation of the levels of metalloproteinases as well as markers of oxidative stress and apoptosis in lung tissues after malathion and rutin administrations to rats. *TJNS.* 2022;11(3):51-7.
- [55] Rafiee S, Nouri A, Heidarian E. Role of NF- $\kappa$ B/IL-1 $\beta$  Pathway and Caspase 3 in mediating the hepatoprotective effect of rutin against paraquat-induced liver toxicity in male rats. *Chem Biodivers.* 2023;20(4):e202200248.
- [56] Rahmani S, Naraki K, Roohbakhsh A, Hayes AW, Karimi G. The protective effects of rutin on the liver, kidneys, and heart by counteracting organ toxicity caused by synthetic and natural compounds. *Food Sci Nutr.* 2022;11(1):39-56.
- [57] Akaras N, Kandemir FM, Şimşek H, Gür C, Aygörmez S. Antioxidant, Antiinflammatory, and Antiapoptotic Effects of Rutin in Spleen Toxicity Induced by Sodium Valproate in Rats. *TJNS.* 2023;12(2), 138-144.
- [58] Caglayan C, Kandemir FM, Darendelioglu E, Yıldırım S, Kucukler S, Dortbudak MB. Rutin ameliorates mercuric chloride-induced hepatotoxicity in rats via interfering with oxidative stress, inflammation and apoptosis. *J Trace Elem Med Biol.* 2019; 56, 60-68.

## Investigation of the Effects of Maleic Acid and Vanillic Acid on Copper Toxicity in the *Drosophila melanogaster* Model

Emine TORAMAN<sup>1\*</sup> , Melike KARAMAN<sup>1</sup> 

<sup>1</sup> Atatürk University, Science Faculty, Molecular Biology and Genetics Department, Erzurum, Türkiye  
Emine TORAMAN ORCID No: 0000-0001-7732-6189  
Melike KARAMAN ORCID No: 0000-0002-0973-2561

\*Corresponding author: emine.toraman@atauni.edu.tr

(Received: 16.03.2024, Accepted: 06.09.2024, Online Publication: 26.09.2024)

**Keywords**  
Antioxidant,  
*Drosophila*,  
Maleic acid,  
Vanillic acid

**Abstract:** Copper is a metal that is necessary for the maintenance of biological functions in the all living organisms. Although copper is essential for the maintenance of cellular metabolism at low concentrations, at high concentrations it can cause toxic effects as it causes (Reactive Oxygen Species) ROS formation. In this study, toxicity was induced by CuSO<sub>4</sub> (1 mM) in larval and adult *Drosophila melanogaster*. The flies were then treated with maleic acid (MA) (2 mg) and vanillic acid (VA) (2 mg). The results showed that Cu toxicity caused a decrease in (Superoxide dismutase) SOD, Catalase (CAT), (Glutathione peroxidase) GPx, (Acetylcholinesterase) AChE and (Glutathione) GSH levels. There was a significant increase in (Malondialdehyde) MDA levels. However, it was found that treatment with MA and VA increased the amounts of SOD, CAT, GPx, AChE and GSH and decreased the amount of MDA. These results showed that MA and VA had ameliorative effects on ROS and oxidative stress caused by CuSO<sub>4</sub>. In conclusion, the effects of natural compounds on different biological parameters against metal-induced toxicity should be evaluated in future studies.

## *Drosophila melanogaster* Modelinde Maleik Asit ve Vanilik Asitin Bakır Toksikitesi Üzerine Etkilerinin Araştırılması

**Anahtar Kelimeler**  
Antioksidan,  
*Drosophila*,  
Maleik asit,  
Vanilik asit

**Öz:** Bakır, tüm canlı organizmaların biyolojik fonksiyonlarının sürdürülmesi için gerekli olan bir metaldir. Bakır, düşük konsantrasyonlarda hücrel metabolizmanın sürdürülmesi için gerekli olmasına rağmen, yüksek konsantrasyonlarda (Reaktif Oksijen Türleri) ROS oluşumuna neden olduğundan toksik etkilere neden olabilir. Bu çalışmada larva ve yetişkin *Drosophila melanogaster*'de CuSO<sub>4</sub> (1 mM) ile toksisite oluşturuldu. Sinekler daha sonra maleik asit (MA) (2 mg) ve vanilik asit (VA) (2 mg) ile işlendi. Sonuçlar Cu toksisitesinin (Süperoksitdismutaz) SOD, (Katalaz) CAT, (Glutasyon peroksidaz) GPx, (Asetilkolinesteraz) AChE ve (Glutasyon) GSH düzeylerinde azalmaya neden olduğunu gösterdi. (Malondialdehit) MDA düzeylerinde önemli bir artış oldu. Ancak MA ve VA tedavisinin SOD, CAT, GPx, AChE ve GSH miktarlarını artırdığı, MDA miktarını ise azalttığı belirlendi. Bu sonuçlar MA ve VA'nın CuSO<sub>4</sub>'ün neden olduğu ROS ve oksidatif stres üzerinde iyileştirici etkilere sahip olduğunu gösterdi. Sonuç olarak, gelecekteki çalışmalarda metal kaynaklı toksisiteye karşı doğal bileşiklerin farklı biyolojik parametreler üzerindeki etkileri değerlendirilmelidir.

### 1. INTRODUCTION

Heavy metals are elements that are frequently used in agriculture and industrial areas. Heavy metal pollution has reached dangerous levels in more than 5 million sites worldwide. Improper management of industrial wastes and widespread use of pesticides in agriculture are among the most important causes of heavy metal

pollution [1]. Copper is a metal that is necessary for the maintenance of biological functions of all living organisms [2]. Although Cu, which is used in many areas from construction to transportation, from health to cosmetics, is not harmful at low concentrations, exposure to high concentrations of Cu can cause toxic effects on the living body [3]. Studies have indicated that copper concentrations in water and soil are

approximately 7 and 50 ppm, and Cu in the atmosphere is between 5 and 200 ng/m<sup>3</sup>. The maximum concentration of copper that can be ingested by humans has also been determined to be 1.5 mg/L serum [4]. Copper metal is essential for the continuity of biological reactions of organisms, but more than the permissible amount of free copper ions can damage cellular structures [5]. Exposure to high levels of copper causes oxidative stress, DNA damage and reduced cell proliferation [6]. Oxidative stress resulting from Cu exposure has also been associated with dysregulation of Cu metabolism and neurodegenerative disorders [7]. Cu toxicity can affect many other organs, especially the liver, as high amounts of Cu in the body accumulate in the liver after entering the bloodstream [8,9]. Phytochemicals may be effective compounds in improving oxidative stress [10]. Maleic acid (MA) is an organic compound and a dicarboxylic acid. It is found as a metabolite in plants [11]. Vanillic acid (VA) is a common monohydroxybenzoic acid found in many plants and presents antioxidant, anti-inflammatory, anti-allergy, and anti-diabetes activities [10]. *Drosophila melanogaster*, a fruit fly, is an important model organism that can be used to study the molecular mechanisms of metal toxicity. In this study, the ameliorative effects of maleic and vanillic acids, both phytochemicals, against copper toxicity in *D. melanogaster* were investigated.

## 2. MATERIAL AND METHOD

### 2.1. Chemicals

CuSO<sub>4</sub> was used as the copper source in this study. All chemicals, including maleic acid (MA) and vanillic acid (VA), were purchased from Sigma.

### 2.2. Animals and Experimental Design

The wild-type Oregon R strain *Drosophila* culture used in the study was purchased from Carolina (172100). Under laboratory conditions, flies were fed with standard *Drosophila* medium (SDB) consisting of corn flour, agar, sucrose, dry yeast and propionic acid. Flies were reared in rooms with a temperature of 25 ± 1 °C and 40-60% humidity and kept on a 12 h light/12 h dark cycle. Third instar larvae obtained from these flies were used in all treatments. The larvae were divided into six groups.

**Group 1 (Control group):** Larvae in this group were treated with distilled water.

**Group 2 (Copper group):** Larvae in this group were treated with 1 mM Cu<sup>+2</sup> solution.

**Group 3 (MA group):** Larvae in this group were treated with 2 mg/mL MA solution.

**Group 4 (VA group):** Larvae in this group were treated with 2 mg/mL VA solution.

**Group 5 (MA+ copper group):** Larvae in this group were treated with 1 mM Cu<sup>+2</sup> solution and 2 mg/mL MA solution.

**Group 6 (VA+ copper group):** Larvae in this group were treated with 1 mM Cu<sup>+2</sup> solution and 2 mg/mL VA solution.

For each treatment, 1.5 g of Formula 4-24® Instant *Drosophila* Medium (Carolina) was wetted with 5 mL of test solution. Larvae were collected for analysis 24 hours after treatment. In addition, the heads of adult flies developed from larvae treated with the test solutions were dissected and used to analyze. The experimental design is schematized in Figure 1.

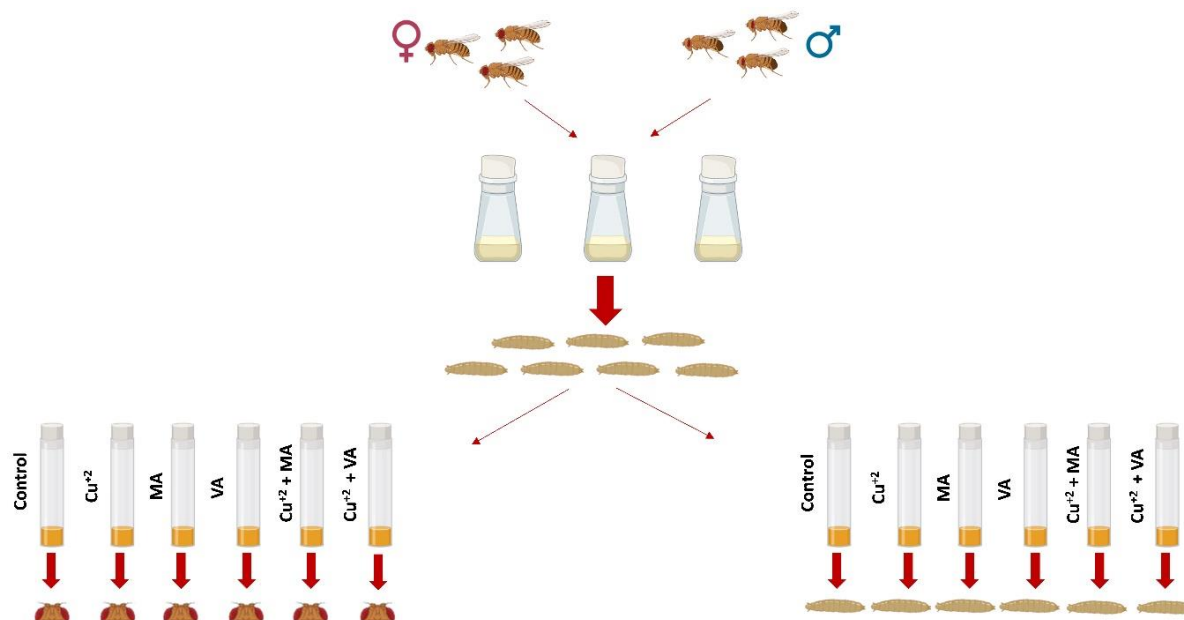


Figure 1. Schematization of the experimental design in adult flies and larvae

### 2.3. Determination of Total Glutathione (GSH)

The total GSH level was determined following the protocol suggested by Sedlak and Lindsay [12]. GSH

(mM) level at 412 nm was measured spectrophotometrically using the supernatant of homogenized fly head and larval samples.

## 2.4. Malondialdehyde (MDA) Formation Determination

Lipid peroxidation (LPO) levels in fly head and larval homogenates were determined by measuring MDA by thiobarbituric acid (TBA) assay [13]. The amount of MDA was determined by measuring the absorbance at 532 nm of a pink colored product formed by reaction with TBA [13].

## 2.5. Enzyme Activity Assays

Protein content in fly head tissue and larval homogenate was measured according to the Bradford method [14]. The activities of SOD (EC 1.15.1.1), CAT (EC 1.11.1.6), GPx (EC 1.11.1.9) and AChE (EC 3.1.1.7) enzymes were determined following the protocol suggested by Sun et al., 1988, Aebi et al., 1984, Beutler et al., 1975, and Ellman et al., 1961 respectively [15-18].

## 2.6. Statistical Analysis

Statistical analysis of the experimental results was performed using GraphPad Prism Software version 8.0 (GraphPad Software, San Diego, CA). Statistical comparisons were made by one-way ANOVA and Tukey's post-hoc tests. Symbol expressions are presented below: \*  $P < 0.05$  (significant); \*\*  $P < 0.01$  (highly significant); \*\*\*  $P < 0.001$  and \*\*\*\*  $P < 0.0001$  (highly significant).

## 3. RESULTS AND DISCUSSION

Copper (Cu) is an essential metal required for the maintenance of physiological functions of living organisms. Cu is essential for the maintenance of metabolic processes and biological functions in living organisms, and high levels of Cu in the body can cause many adverse effects. Studies have shown that prolonged exposure to toxic levels of Cu can cause organ dysfunction in humans and animals [19,20]. The formation and accumulation of reactive oxygen species (ROS) is one of the most important consequences of heavy metal exposure [21]. ROS interact with biological molecules and alter their structure or metabolic activity, leading to oxidation of proteins and nucleic acids and lipid peroxidation [22]. Antioxidant enzymes and compounds are agents that form the first line of cellular defense against oxidative damage [23]. Superoxide dismutases (SOD), which are antioxidant enzymes, provide the conversion of superoxide anions to dioxygen and hydrogen peroxide, while catalase (CAT) catalyzes the conversion of hydrogen peroxide to water. [24,7]. In a study, *Drosophila melanogaster* was exposed to 0.09

and 1.2 mg/mL dissolved copper for 7 days. The data obtained showed that  $\text{Cu}^{+2}$  increased mortality and decreased egg production and body size [25]. In a similar study, CAT and glutathione activity decreased while lipid peroxidation levels increased in flies treated with copper sulfate. After treatment with resveratrol (30 or 60 mg/kg), the antioxidant and anti-inflammatory capacities of the flies increased [26]. Copper toxicity can also cause locomotor dysfunction in living organisms. One study showed that exposure to 1 and 3 mM  $\text{CuSO}_4$  inhibited total AChE activity in *D. melanogaster* and caused impaired climbing ability (negative geotaxis) in adult flies [4]. Our study investigated the ameliorating effect of maleic acid (MA) and vanillic acid (VA) on  $\text{CuSO}_4$ -induced copper toxicity in flies.

Maleic acid is a dicarboxylic acid that acts as a fragrance agent and pH adjuster in cosmetics; it is used in low concentrations in several cosmetic product formulations [27]. In a study, the effect of MA on the toxicity caused by Cr stress in plants was investigated. The results showed that MA reduced oxidative stress by increasing the activities of antioxidant defense system enzymes inhibited by Cr stress [11]. In a similar study, MA was found to affect oxidative stress, lipid peroxidation and inflammatory response at the cellular level [28]. When the results obtained from our study were examined, it was observed that SOD, CAT and GPx activities increased significantly in the Cu-treated group, while the enzyme activities in the MA-treated group reached a level similar to the control. When compared with the Cu group, it was determined that the enzyme activities in the MA group were close to normal, but the enzyme activities in the  $\text{Cu}^{+2}$  + MA group were closer to the  $\text{Cu}^{+2}$  group (Figure 2a, 2b, 2c). When the enzyme activity changes in adults were examined, it was observed that there was a significant increase especially in SOD activity in the  $\text{Cu}^{+2}$  treated group. In the MA group, SOD, CAT and GPx activities approached the control (Figure 2e, 2f, 2g). These results showed that MA reduced  $\text{Cu}^{+2}$ -induced radical formation in *D. melanogaster* and improved the antioxidant buffering capacity of flies. Acetylcholinesterase enzyme activity is an effective and widely used mechanism to assess toxicological effects involving the nervous system. In a study, it was found that 1mM  $\text{CuSO}_4$  treatment caused a significant inhibition of total AChE activity in flies and an impairment in the climbing ability (negative geotaxis) of adult flies [4]. In our study, it was observed that AChE enzyme activity decreased significantly in the Cu-treated group in both larval and adult flies, but the activity increased with MA treatment and approached the control (Figure 2d and 2h).



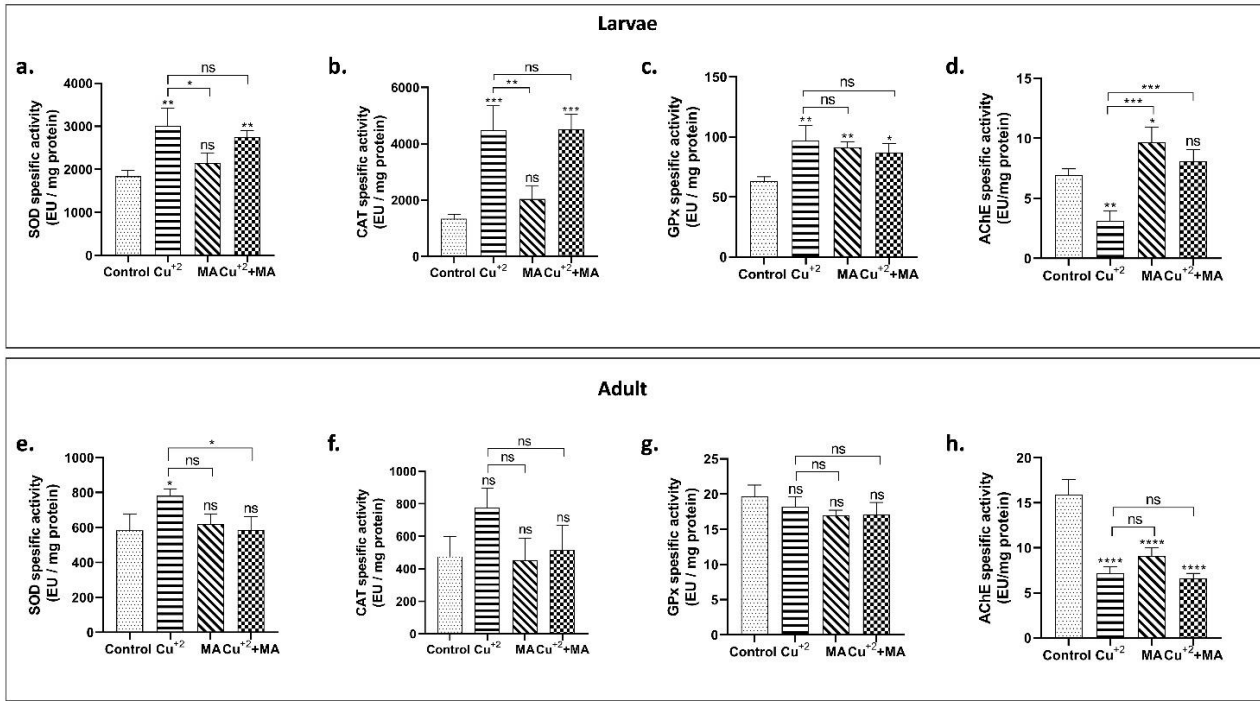


**Figure 2.** Changes in SOD, CAT, GPx and AChE enzyme activities in larval and adult *D. melanogaster* treated with maleic acid

Vanillic acid (VA, 4-hydroxy-3-methoxybenzoic acid) is an intermediate used in the production of vanillin from ferulic acid and is a phenolic derivative of edible plants. VA has antimicrobial activity and is an effective component in clearing free radicals [23]. When we examined the effect of vanillic acid against copper toxicity, it was found that SOD, CAT and GPx activities increased significantly in the Cu-treated group in larvae. In the VA-treated group, these enzyme activities were found to be similar to the control. In the Cu<sup>+2</sup> and VA groups, enzyme activities approached the control (Figure 3a, 3b and 3c). When the results in adult flies were

examined, it was found that SOD activity increased significantly in the Cu-treated group. It was observed that all enzyme activities in VA and Cu<sup>+2</sup> + VA group reached similar levels with the control. When all the results were evaluated together, it was determined that VA showed ameliorative effect against Cu toxicity by reducing oxidative stress (Figure 3e, 3f, 3g). When the change in AChE enzyme activity was examined, it was found that AChE activity decreased significantly in both larvae and adults in the Cu-treated group and increased as a result of VA treatment (Figure 3d and 3h).

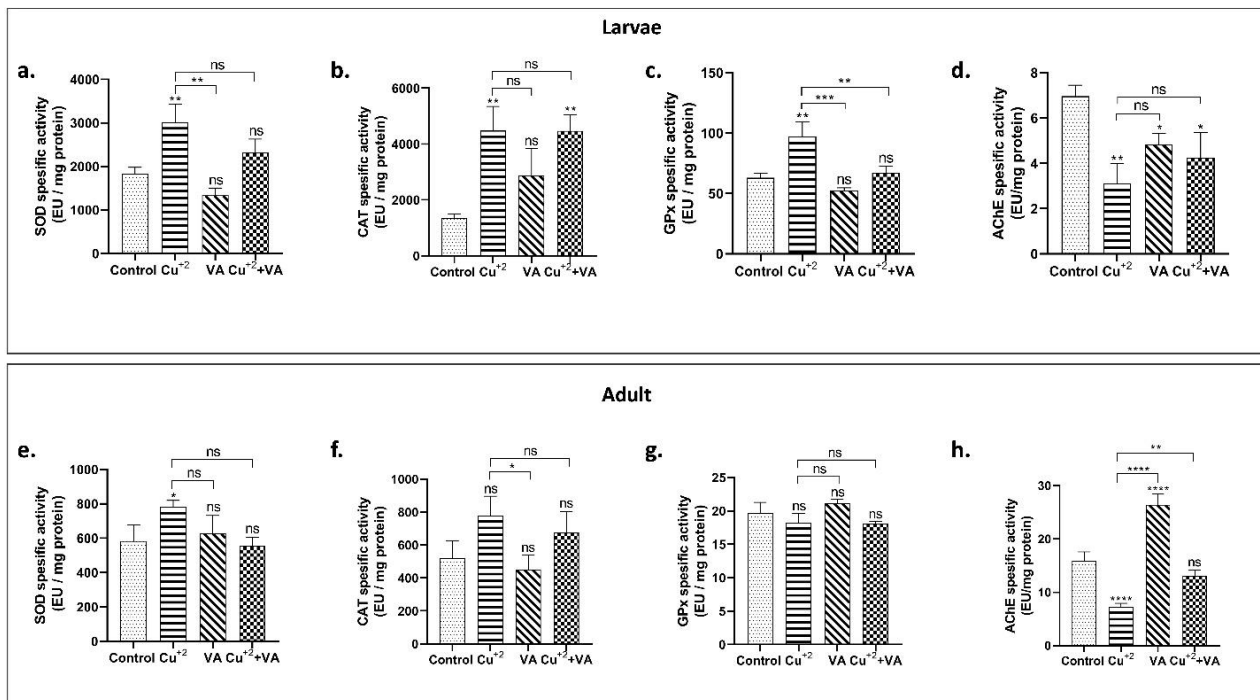


**Figure 3.** Changes in SOD, CAT, GPx and AChE enzyme activities in larval and adult *D. melanogaster* treated with vanillic acid

Exposure to toxic levels of Cu also causes peroxidation of lipids in membranes, which can damage cellular components [3]. In a study, it was found that GSH level decreased and MDA level increased in serum and liver in rats overloaded with Cu [29]. Reduced glutathione (GSH) is a non-enzymatic antioxidant. Decreased GSH levels in cells are an indicator of ROS accumulation and therefore oxidative stress [30]. In rats exposed to  $\text{Cu}^{+2}$  and  $\text{CuSO}_4$  for 21 and 42 days, GSH levels decreased significantly and triggered oxidative stress [9]. In our study, Cu toxicity significantly decreased GSH levels and increased MDA levels in both larval and adult flies.

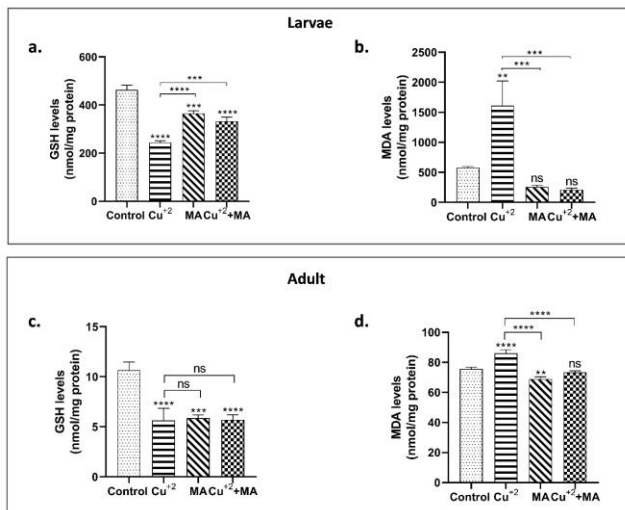


**Figure 4.** Changes in GSH and MDA enzyme activities in larval and adult *D. melanogaster* treated with maleic acid

#### 4. CONCLUSION

Although Cu metal is essential for the maintenance of many biological functions, exposure to high levels of Cu can damage cellular components and cause oxidative stress. This study showed that MA and VA reduced  $\text{Cu}^{+2}$ -induced radical formation in *D. melanogaster* and improved the antioxidant buffering capacity of flies. MA and VA can therefore be used to treat disorders involving oxidative stress. However, the concentrations of natural compounds, their interactions and their effects on different biological parameters against toxicity should be evaluated in future studies.

#### Acknowledgement

The authors acknowledge with thanks Ataturk University technical support.

#### REFERENCES

- [1] Everman ER, Macdonald SJ, Kelly JK. The genetic basis of adaptation to copper pollution in *Drosophila melanogaster*. *Frontiers in Genetics*. 2023;14.
- [2] Schlichting D, Sommerfeld C, Müller-Graf C, Selhorst T, Greiner M, Gerofke A, et al. Copper and zinc content in wild game shot with lead or non-lead ammunition – implications for consumer health protection. *Plos One*. 2017;12(9):e0184946.

When the post-treatment results were analyzed, it was observed that MA treatment increased GSH levels and decreased MDA levels in both larval and adult flies (Figure 4).

When we examined the effect of VA on Cu toxicity, it was observed that VA treatment increased GSH levels and decreased MDA levels in both larval and adult flies (Figure 5). The increase in GSH level and decrease in MDA level after VA treatment showed that VA may reduce the oxidative stress caused by Cu.

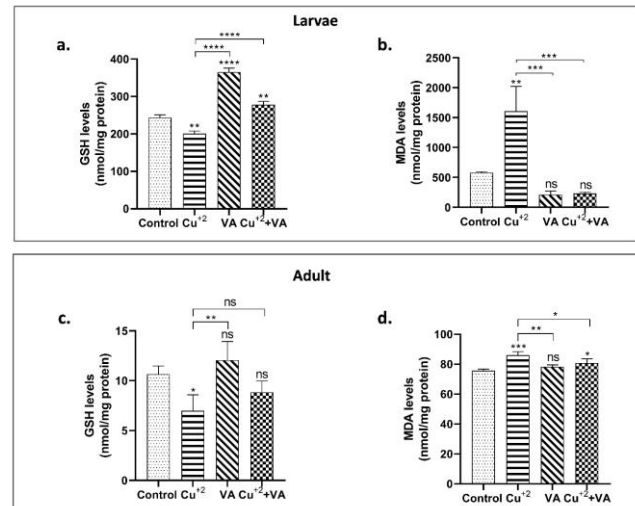


**Figure 5.** Changes in GSH and MDA enzyme activities in larval and adult *D. melanogaster* treated with vanillic acid

- [3] Gaetke L. Copper toxicity, oxidative stress, and antioxidant nutrients. *Toxicology*. 2003;189(1–2):147–163.
- [4] Halmenschelager PT, da Rocha JBT. Biochemical  $\text{CuSO}_4$  Toxicity in *Drosophila melanogaster* Depends on Sex and Developmental Stage of Exposure. *Biological Trace Element Research*. 2019;189(2):574–585.
- [5] Tapiero H, Townsend DM, Tew KD. Trace elements in human physiology and pathology. Copper. *Biomedicine & Pharmacotherapy*. 2003;57(9):386–398.
- [6] Oe S, Miyagawa K, Honma Y, Harada M. Copper induces hepatocyte injury due to the endoplasmic reticulum stress in cultured cells and patients with Wilson disease. *Experimental Cell Research*. 2016;347(1):192–200.
- [7] Uriu-Adams JY, Keen CL. Copper, oxidative stress, and human health. *Molecular Aspects of Medicine*. 2005;26(4–5):268–298.
- [8] Barber RG, Grenier ZA, Burkhead JL. Copper Toxicity Is Not Just Oxidative Damage: Zinc Systems and Insight from Wilson Disease. *Biomedicines*. 2021;9(3):316.
- [9] Liu H, Guo H, Jian Z, Cui H, Fang J, Zuo Z, et al. Copper Induces Oxidative Stress and Apoptosis in the Mouse Liver. *Oxidative Medicine and Cellular Longevity*. 2020;2020:1–20.
- [10] Jasemi SV, Khazaei H, Morovati MR, Joshi T, Aneva IY, Farzaei MH, et al. Phytochemicals as

- treatment for allergic asthma: Therapeutic effects and mechanisms of action. *Phytomedicine*. 2024;122:155149.
- [11] Mahmud J Al, Hasanuzzaman M, Nahar K, Rahman A, Hossain MdS, Fujita M. Maleic acid assisted improvement of metal chelation and antioxidant metabolism confers chromium tolerance in *Brassica juncea* L. *Ecotoxicology and Environmental Safety*. 2017;144:216–226.
- [12] Sedlak J, Lindsay RH. Estimation of total, protein-bound, and nonprotein sulfhydryl groups in tissue with Ellman's reagent. *Analytical Biochemistry*. 1968;25:192–205.
- [13] Ohkawa H, Ohishi N, Yagi K. Assay for lipid peroxides in animal tissues by thiobarbituric acid reaction. *Analytical Biochemistry*. 1979;95(2):351–358.
- [14] Bradford MM. A rapid and sensitive method for the quantitation of microgram quantities of protein utilizing the principle of protein-dye binding. *Anal Biochem*. 1976;72(1–2):248–254.
- [15] Sun Y, Oberley LW, Li Y. A simple method for clinical assay of superoxide dismutase. *Clin Chem*. 1988;34(3):497–500.
- [16] Aebi H. [13] Catalase in vitro. In: *Methods in enzymology*. 1984: 121–126.
- [17] Beutler E. *Red Cell Metabolism Manual of Biochemical Methods*. 1971. London, UK: Academic Press.
- [18] Ellman GL, Courtney KD, Andres V, Featherstone RM. A new and rapid colorimetric determination of acetylcholinesterase activity. *Biochem Pharmacol*. 1961;7(2):88–95.
- [19] Pujol J, Fenoll R, Macià D, Martínez-Vilavella G, Alvarez-Pedrerol M, Rivas I, et al. Airborne copper exposure in school environments associated with poorer motor performance and altered basal ganglia. *Brain and behavior*. 2016;6(6):e00467.
- [20] Mitra S, Keswani T, Dey M, Bhattacharya S, Sarkar S, Goswami S, et al. Copper-induced immunotoxicity involves cell cycle arrest and cell death in the spleen and thymus. *Toxicology*. 2012;293(1–3):78–88.
- [21] Bellion M, Courbot M, Jacob C, Blaudez D, Chalot M. Extracellular and cellular mechanisms sustaining metal tolerance in ectomycorrhizal fungi. *FEMS Microbiology Letters*. 2006;254(2):173–181.
- [22] Cavalcanti Luna MA, Vieira ER, Okada K, Campos-Takaki GM, Nascimento AE do. Copper-induced adaptation, oxidative stress and its tolerance in *Aspergillus niger* UCP1261. *Electronic Journal of Biotechnology*. 2015;18(6):418–427.
- [23] Kumar S, Prahalathan P, Raja B. Antihypertensive and antioxidant potential of vanillic acid, a phenolic compound in L-NAME-induced hypertensive rats: a dose-dependence study. *Redox Report*. 2011;16(5):208–215.
- [24] Okado-Matsumoto A, Fridovich I. Subcellular Distribution of Superoxide Dismutases (SOD) in Rat Liver. *Journal of Biological Chemistry*. 2001;276(42):38388–38393.
- [25] Budiyanti DS, Moeller ME, Thit A. Influence of copper treatment on bioaccumulation, survival, behavior, and fecundity in the fruit fly *Drosophila melanogaster*: Toxicity of copper oxide nanoparticles differ from dissolved copper. *Environmental Toxicology and Pharmacology*. 2022;92:103852.
- [26] Igharo OG, Ebaluegberifoh LO, Aikpitan-Idutua GA, Oshilonyah HU, Momodu IB. Resveratrol protects against copper and iron toxicity in *Drosophila melanogaster*. *Universa Medicina*. 2023;42(1):29–40.
- [27] Yeon J, Park AR, Nguyen HTT, Gwak H, Kim J, Sang MK, et al. Inhibition of Oomycetes by the Mixture of Maleic Acid and Copper Sulfate. *Plant Disease*. 2022;106(3):960–965.
- [28] Wu C, Chen H-C, Chen S-T, Chiang S-Y, Wu K-Y. Elevation in and persistence of multiple urinary biomarkers indicative of oxidative DNA stress and inflammation: Toxicological implications of maleic acid consumption using a rat model. *PLOS ONE*. 2017;12(10):e0183675.
- [29] Zhang SS, Noordin MM, Rahman SO, Haron J. Effects of copper overload on hepatic lipid peroxidation and antioxidant defense in rats. *Veterinary and human toxicology*. 2000;42(5):261–4.
- [30] Toraman E, Budak B, Bayram C, Sezen S, Mokhtare B, Hacımuftuoğlu A. Role of parthenolide in paclitaxel-induced oxidative stress injury and impaired reproductive function in rat testicular tissue. *Chemico-Biological Interactions*. 2024;387:110793.

## Investigation Of Friction Welding Dissimilar AISI 304 And AISI 1040 Steels

Zülküf BALALAN<sup>1\*</sup>, Mehmet YAZ<sup>2</sup>, Sedat BULDAĞ<sup>3</sup>

<sup>1</sup> Bingöl University, Faculty of Engineering and Architecture, Mechanical Engineering, Bingöl, Türkiye

<sup>2</sup> Firat University, Vocational School Of Technical Sciences/Department Of Machinery And Metal Technologies/Machinery, Elazığ, Türkiye

<sup>3</sup> Bingöl University, Faculty of Engineering and Architecture, Mechanical Engineering, Bingöl, Türkiye

Zülküf BALALAN ORCID No: 0000-0001-5808-6263

Mehmet YAZ ORCID No: 0000-0002-5422-7433

Sedat BULDAĞ ORCID No: 0009-0000-3877-6320

\*Corresponding author: zbalalan@bingol.edu.tr

(Received: 28.05.2024, Accepted: 09.09.2024, Online Publication: 26.09.2024)

### Keywords

Joining,  
Dissimilar steels,  
Microstructure,  
Tensile strength,  
Microhardness

**Abstract:** Friction time is one of the important parameters in friction welding. The effect of friction time on the mechanical and microstructural properties of the weld was investigated in the friction welding of AISI 304 and AISI 1040 steels. With the enhancement of friction time, the temperature at the welding region naturally increased. Increasing the friction time resulted in the formation of a stronger weld. The highest tensile strength of 755 MPa was found in the S3 weld sample made at the highest friction time of 9 seconds. An increase in the friction time also provided a significant increase in the weld tensile elongation. S2 and S3 weld samples were broken as ductile during the tensile test, while S1 weld sample was broken as a mixture of brittle and ductile. The highest microhardness value of approximately 310 HV was determined at the joint area of the S1 weld produced with the lowest friction time. Hardness at the weld interface slightly decreased with an increase in the friction time. The weld interface shape changed depending on the friction time.

## Farklı AISI 304 Ve AISI 1040 Çeliklerinin Sürtünme Kaynağının Araştırılması

### Anahtar Kelimeler

Birleştirme,  
Farklı çelikler,  
Mikroyapı,  
Çekme mukavemet  
Mikrosertlik

**Öz:** Sürtünme süresi sürtünme kaynağında önemli parametrelerden biridir. AISI 304 ve AISI 1040 çeliklerinin sürtünme kaynağında sürtünme süresinin kaynağın mekanik ve mikroyapısal özelliklerine etkisi araştırıldı. Sürtünme süresinin artmasıyla birlikte kaynak bölgesindeki sıcaklık da doğal olarak artmıştır. Sürtünme süresinin artırılması daha sağlam bir kaynak oluşumuyla sonuçlandı. En yüksek çekme gerilmesi 9 saniyelik en yüksek sürtünme süresinde yapılan S3 kaynak numunesinde 755 MPa olarak bulunmuştur. Sürtünme süresindeki artış, kaynağın çekme uzamasında da önemli bir artış sağladı. Çekme testi sırasında S2 ve S3 kaynak numuneleri sünek olarak kırılırken, S1 kaynak numunesi gevrek ve sünek karışımı olarak kırılmıştır. En düşük sürtünme süresiyle üretilen S1 kaynağının birleşim bölgesinde yaklaşık 310 HV ile en yüksek mikrosertlik değeri belirlendi. Kaynak arayüzündeki sertlik, sürtünme süresinin artmasıyla birlikte hafifçe azalmıştır. Kaynak ara yüzeyinin şekli sürtünme süresine bağlı olarak değişmiştir.

### 1. INTRODUCTION

Friction welding, a solid-state joining technique, generates heat through mechanical friction between the surfaces of workpieces without the use of external heat. When an external force is applied, the workpieces deform plastically, allowing materials that are similar or dissimilar to be joined without melting. Friction welding is a solid-state method as opposed to fusion welding,

which is a melting process [1]. Since friction welding influences a small surface area, less stress, flaws, and material loss result, lowering the chance of welding problems and material effects [2]. Combining dissimilar materials would enable more efficient and economical constructions in many applications [3]. Many defects such as pores and intermetallic phases that seriously affect the weld quality seen in fusion welding techniques do not occur in solid-state welding techniques because

the materials are welded without melting [4]. Joining dissimilar materials via conventional fusion welding techniques is not practical because of the production of brittle and low melting intermetallics due to metallurgical incompatibility, broad melting point differences, thermal mismatch, etc. In these kinds of circumstances, friction welding is commonly used [5, 6]. Friction welding offers significant advantages including notable material savings, short manufacturing times, and the ability to join different metals or alloys [7]. For instance, even completely different AZ31B magnesium alloy and AISI 304 stainless steel were reported to be successfully welded by the solid-state technique [8, 9]. Friction welding parameters (friction time, rotation speed, friction pressure, etc.) have a significant effect on heat generation, material flow, microstructure, residual stress, and weld quality. The impact of each parameter is greatly affected by the materials that are joined [1]. Balalan and Ekinici [10] investigated the effect of rotation speed on the mechanical characteristics of the welds of the AISI 1040 parts via the friction welding method. They obtained the strongest weld with 400 MPa at 1500 rpm. Celik et al. [11] studied the joining of AISI 304 and AISI 1040 steels by friction welding and reported that joint strength is proportional to friction pressure and these steels can be reliably joined for

industrial applications. Paventhan et al. [12] studied friction welding of AISI 1040 and AISI 304 steel and reported that friction time significantly affects the weld strength. Various material combinations such as aluminum alloy and magnesium alloy [13], aluminum and copper [14], magnesium alloy and stainless steel [15], and stainless steel and zinc [16] have been successfully joined using the friction welding process.

The impact of friction time, which is an important friction welding parameter in joining AISI 304 and AISI 1040 steels by friction welding, on the weld's mechanical and microstructural properties has not been much researched. Therefore, in this study, AISI 304 and AISI 1040 steels which are widely used in many applications were combined through the friction welding technique. The influence of friction time on macro and microstructure, tensile strength, and microhardness were investigated.

## 2. MATERIAL AND METHOD

The chemical composition of the materials produced by the cold drawing method used in the experiments is given in Table 1, and their mechanical properties are presented in Table 2.

**Table 1.** Chemical compositions of materials (wt.%)

Materials	C	Mn	Cr	S	Ni	P	Mo
AISI 1040	% 0,37-0,44	0.60-0.90	-	0.050	-	0.040	-
AISI 304	0,042	1.47	18.25	0.032	8.09	0.032	0.30

**Table 2.** Mechanical properties of materials

Materials	Yield Strength (MPa)	Tensile Strength (MPa)	Elongation (%)	Microhardness (HV <sub>0.3</sub> )		
AISI 304	310	616	35	205	203	207
AISI 1040	361	600	25	149	152	156

The materials were lathe machined to 100x12mm and prepared for friction welding. The friction welding parameters used are given in Table 3. Friction welding

processes were done on the continuously driven friction welding machine shown in Figure 1. Macro photography of welded joints is given in Figure 2.

**Table 3.** Friction welding variables

Experiment Samples	Number of Revolutions (rpm)	Friction Pressure (da. N/cm <sup>2</sup> )	Friction Time (s)	Upset Pressure (da. N/cm <sup>2</sup> )	Upset Time (s)
S1	2200	30	5	60	6
S2	2200	30	7	60	6
S3	2200	30	9	60	6

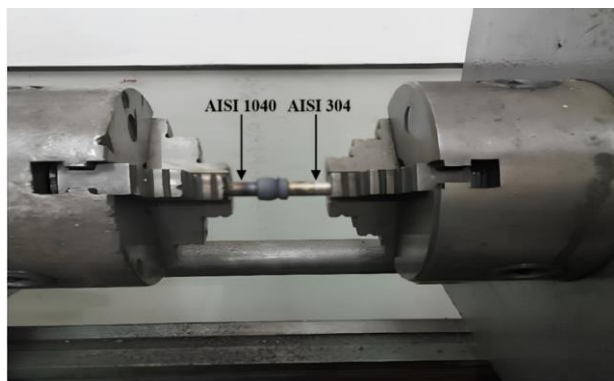


**Figure 1.** Friction welding process



**Figure 2.** Macro-photograph of the friction welds

After the friction welding process, the tensile strength test samples were produced from the welded joints according to TS 138 EN 895 the tensile strength test standard in Figure 3. Tensile strength tests were carried out on INSTRON brand tensile device. Three of each sample were subjected to tensile tests.

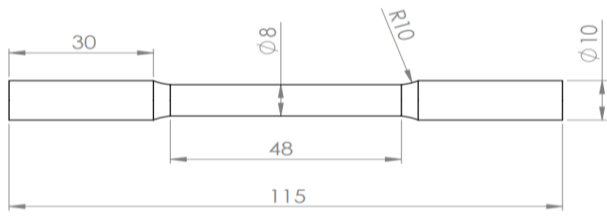


Figure 3. Dimension of the tensile strength test sample



Figure 4. Raynger 3i plus infrared temperature measurement device

To detect the microstructures of the welded samples, cross-section areas of the welds were sanded with sandpapers and then polished. After that, electrolytically etched using 47.6% HCl + 47.6% pure water + 4.8% NHO<sub>3</sub> nitric acid solution. Then optical photographs were taken. In the microstructure analysis studies of the samples, the chemical content of the phase occurring in the weld area was determined by EDS. JEOL JSM6510 brand scanning electron microscope test device was used. To detect the intermetallic compounds formed, X-ray diffraction patterns (XRD) analysis from the etched cross-sectional area was performed using a Rigaku Ultima IV brand device. Microhardness measurement was carried out to detect the hardness in heat-affected zone (HAZ) and weld areas. Microhardness measurement was measured on the Vickers microhardness device, model THV-1D, by applying a load of 300 g and a waiting time of 10 seconds, with 0.5 mm intervals, as shown in Figure 5.

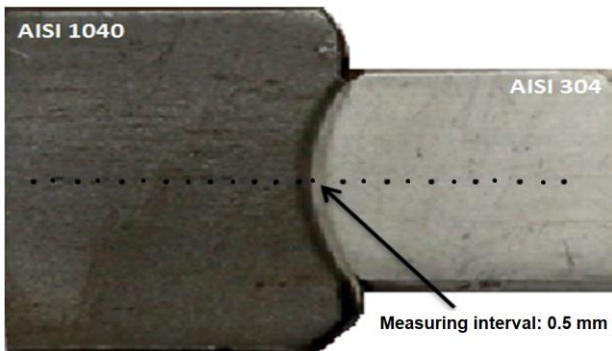


Figure 5. Microhardness measurement taken on the weld cross-section

### 3. RESULTS AND DISCUSSION

#### 3.1. Measuring the Temperature of The Weld Region and Welded Sample Dimensions

Maximum temperatures measured from the welding areas are given in Table 4. As the friction time increased, the temperature increased slightly. Therefore, the flash material (the amount of material protruding from the interface) increased. The demonstration of measuring flash dimensions is shown in Figure 6. Flash widths and lengths, and length shortenings of the welded

samples are given in Tables 5 and 6. The temperature at the weld region rose with a rise in the friction time, resulting in larger flash formation and sample length reduction.

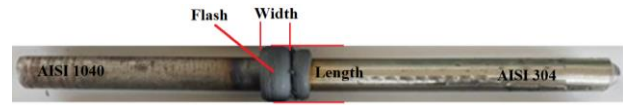


Figure 6. Flash dimensions

Table 4. Weld area maximum temperature

Samples	Maximum Temperatures (°C)
S1	980
S2	1000
S3	1100

Table 5. Weld samples flash dimensions

Length	Material	S1	S2	S3
Flash Width (mm)	AISI 1040	5.01	6.55	7.24
	AISI 304	2.98	3.45	3.90
Flash Length (mm)	AISI 1040	18.87	20.06	20.50
	AISI 304	16.36	17.30	18.27

Table 6. Length reduction amounts of the weld samples

Samples	Shortening in length (mm)
S1	13.11
S2	16.15
S3	17.10

#### 3.2. Metallographic Examination

Figure 7 shows the schematic demonstration of the weld cross-section. Four different zones were identified. The base material zone, heat-affected zone, deformed zone, and extremely deformed zone, which is within the deformation zone but shows structural differences. The heat-affected, deformed, and extremely deformed areas were determined to be larger on the AISI 1040 side. It is consistent with the literature that the size of these four defined regions varies depending on the process parameter [17].

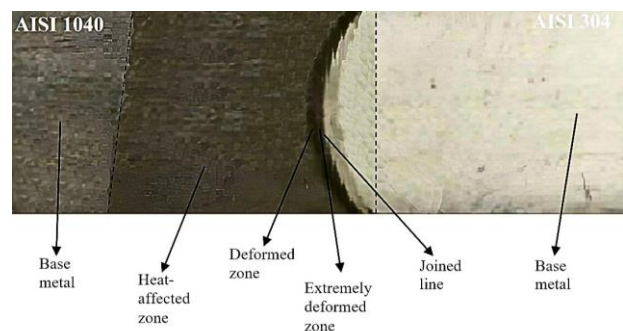


Figure 7. Schematic picture of the joint cross-section in friction welded samples

The SEM photograph of AISI 304 austenitic stainless steel and the AISI 1040 steel is given in Figure 8. As a source of austenitic stainless steel, chromium carbide precipitation occurs in some stainless steels such as 18/8 steel at a temperature in the temperature range of 450-850 °C. Since 90% of the chromium carbide formed consists of Cr by weight, even a very small amount of carbon at the grain boundary reduces the chromium level around the austenite grain excessively. When the

material remains in a corrosive area, corrosion occurs in the chromium-weakened grain [12].

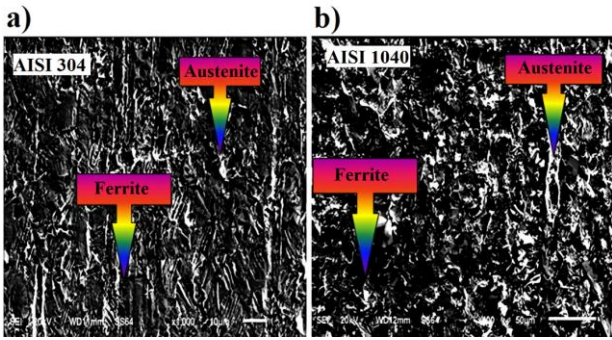


Figure 8. Microstructure SEM photographs of AISI 304 and AISI 1040 steel

SEM photographs of samples S1-S3, expressing the structural change, are shown in Figure 9. Structural changes in the weld area in the joints with different friction times and the effect of friction time on the structural change are seen. It has been observed that the width of the extremely deformed region at the weld interface in S1 and S2, due to the effect of temperature and pressure changes depending on the friction process. Microstructure grain quality is enhanced by friction welding. But, because of the combined influence of mechanical and thermal stresses, grains become thinner in the weld zone. It has been determined that the plastic deformation of austenitic-stainless steel AISI 304 has no effect on the friction welding variables or weld strength [18]. Increasing friction time can lead to the expansion of the high plastic deformation zone thus resulting in a hard zone at the joint interface [19]. Similar weld interfaces in Figure 9 were observed in the study of joining AISI 304 and AISI 1040 steels via friction welding conducted by [11].

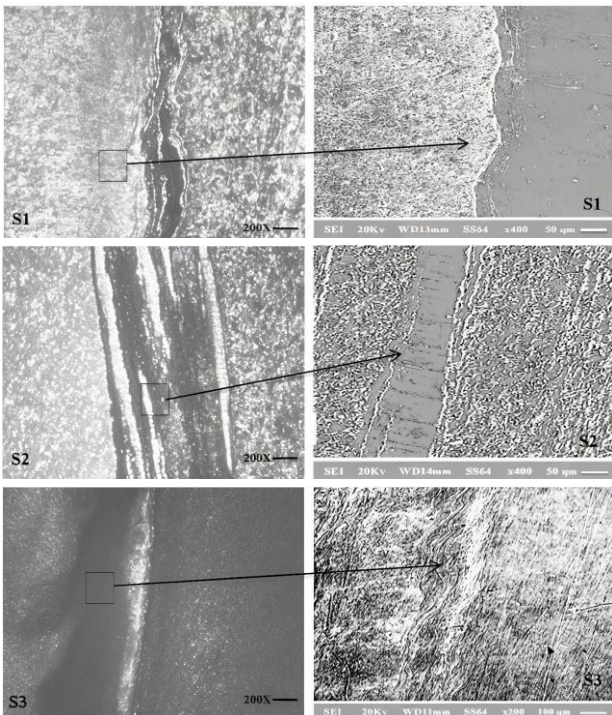


Figure 9. Optical and SEM images of samples S1, S2 and S3

Point EDS elemental analysis image on the weld cross-section of sample S3 is shown in Figure 10. The obtained results are given in Table 7. As can be seen from Table 1, the main steel material AISI 1040 contains almost no Cr, but AISI 304 contains 18.25 percent by weight. As can be seen from Table 7, in region 4, which is the weld region close to AISI 1040, there is an increase in the Cr rate, and in weld region 5 close to AISI 304, there is a decrease in the Cr rate. This is an indication of the mixing and diffusing of 304 and 1040 steels.

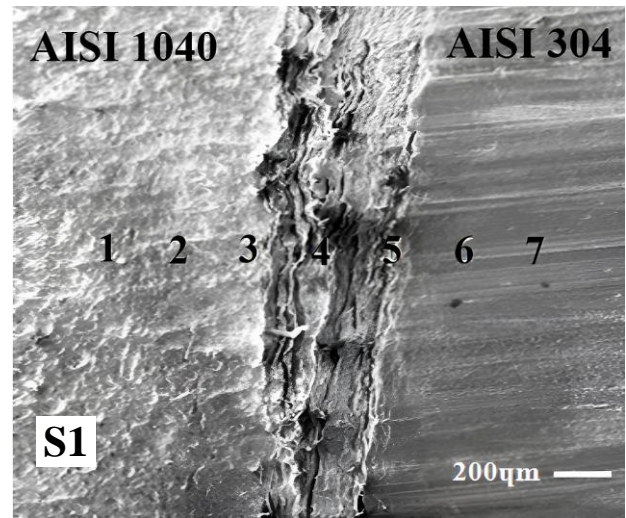


Figure 10. Point EDS analysis image of Sample S3

Figure 11 shows the XRD results of the S3 weld sample. Cr<sub>1.35</sub>Fe<sub>0.52</sub>, Cr<sub>23</sub>C<sub>6</sub>, Fe<sub>3</sub>C, and austenite phases were detected. In similar studies [20-23], ferrite, retained austenite and chromium (Cr) phases were formed in the weld. It is considered that the austenite phase occurs at ferrite grain boundaries and within the grain. The absence of XRD patterns of other phases such as carbides in the weld region means the welding process did not provide sufficient time for carbide formation [23].

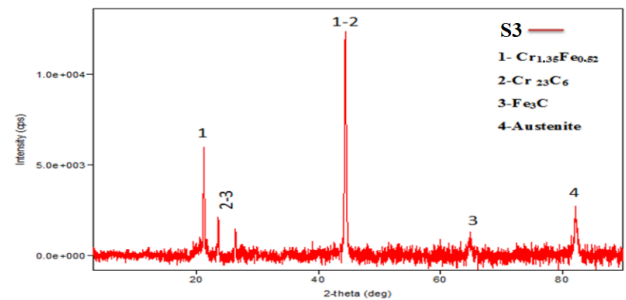


Figure 11. XRD graph of sample S3

**Table 7.** EDS values taken from 7 regions of the S3 sample

Elt.	Line	Units	1. AISI 1040 Main Material	2. HAZ Area	3. Deformed Area	4. Weld Area	5. Deformed Area	6. HAZ Area	7. AISI 304 Main Material
C	Ka	wt. %	0.000	0.000	0.000	0.000	0.000	0.000	0.000
Si	Ka	wt. %	0.449	1.285	0.503	0.237	0.129	0.594	0.473
Cr	Ka	wt. %	0.073	0.097	4.101	10.923	11.165	18.600	18.722
Mn	Ka	wt. %	0.675	0.709	1.570	2.432	2.249	1.405	1.461
Fe	Ka	wt. %	98.703	97.855	93.483	73.420	85.659	71.428	71.464
Ni	Ka	wt. %	0.099	0.054	0.342	2.988	0.798	7.974	7.880
		wt. %	100.000	100.000	100.000	100.000	100.000	100.000	100.000

**3.3. Tensile Strength Test Results**

The tensile strength diagram drawn according to the results obtained is shown in Figure 12. Sample S3 had the highest tensile strength and elongation while S1 had the lowest tensile strength and elongation. It has been observed that tensile strength and elongation increase with the increase in the friction time. The error bars for the tensile strength of the welded samples are provided in Figure 13. Three tensile tests were performed for each sample. Average tensile strengths of 661, 696 and 755 MPa for S1, S2 and S3, respectively. Celik et al. [11] joined AISI 304 and AISI 1040 different steels using friction welding and produced the weld with the highest tensile strength of an average of 792.4 MPa. Paventhan et al. [12] also investigated friction welding AISI 1040 and AISI 304 steels by optimizing welding parameters of friction time, friction pressure, forging pressure, and forging time. According to the results obtained, the strongest weld with a tensile strength of 543 MPa in which 6 s friction time was used. It was also concluded that friction time has the most effect on weld strength than other welding parameters.

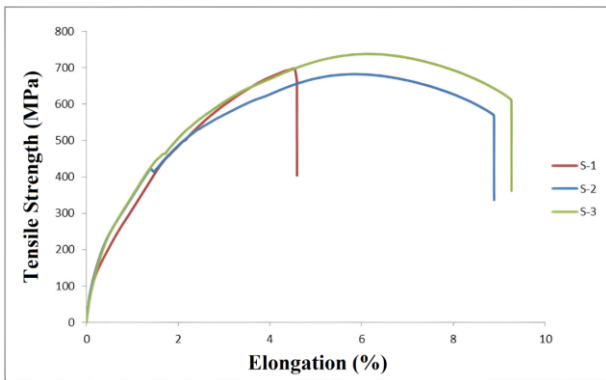


**Figure 12.** Stress-strain curves of S1, S2, S3 welded samples

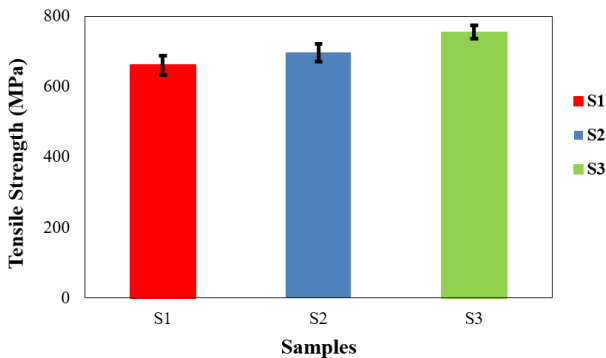


**Figure 13.** Tensile strength of the welded samples



**Figure 14.** Tensile test broken pictures of samples S1, S2, and S3

When the broken surface photographs sample S1 are examined in Figure 15, some dimples and cleavages can be seen, meaning a mix of ductile and brittle fracture occurred. Tensile strength test broken pictures of samples S1, S2, and S3 are shown in Figure 14, it can be seen that there is necking in S2 and S3, but almost straight fracture perpendicular to the load direction for S1. It is evident from Figure 12 and the necking fracture in Figure 14 that S2 and S3 fracture ductile. All the samples failed from the welded areas. Celik et al. [11] examined the friction weld tensile fracture surface of the 1040 and 304 steels and determined the signs indicating brittle and ductile fractures.

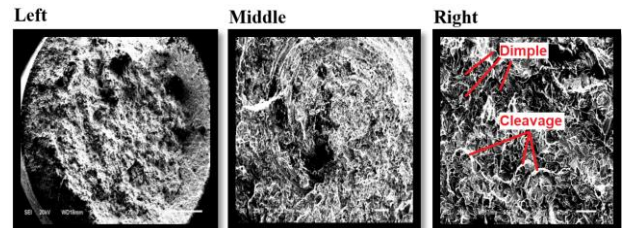


**Figure 14.** SEM photos taken from the left, middle, and right sides of the tensile fractured surface of sample S1

**3.4. Microhardness Test Results**

The results of the microhardness tests are given graphically in Figure 15. It was observed that the hardness value in the AISI 304 heat-affected region (HAZ) region decreased. The highest hardness values were in the weld areas due to deformation hardening with martensite formation upon sudden cooling. The hardness in the weld area decreased slightly with increasing of friction time. The hardness values at the weld zone of welds S1, S2 and S3 were found to be approximately 310, 270 and 240 HV, respectively. So, the lowest hardness value was obtained in the weld sample S3. This is probably due to the S3 having the highest friction time and thus heat input resulting in softening. Similar results were reported by [24, 25]. Higher friction time caused higher heat input. According to Ekinici and Balalan [26], higher heat input caused



larger grains in the microstructure, leading to softening. Celik et al. [11] found that the microhardness of HAZ regions was lower compared to the weld zones having microhardness values ranging between 210 and 260 HV for friction welding of dissimilar AISI 304 and AISI 1040 steels. The increase in the hardness of the weld zone was attributed to the Cr transformation from AISI 304 to AISI 1040 side, resulting in the formation of chromium-carbide by heat. In this study, Cr transformation was also seen in Table 7.

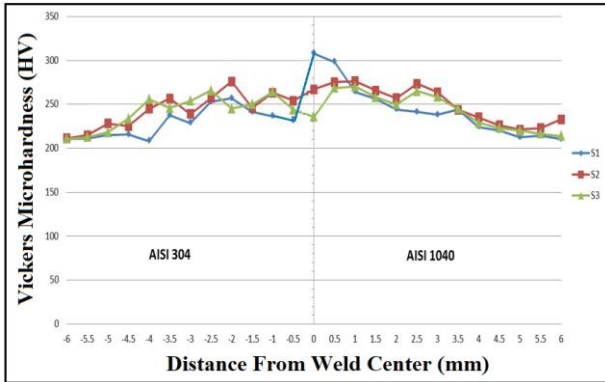


Figure 15. Microhardness distribution of the samples (S1, S2 and S3) on the horizontal axis

#### 4. CONCLUSIONS

In the joining of dissimilar AISI 304 and AISI 1040 steels by friction welding, 3 different friction times (5, 7 and 9 seconds) were used and the influence of friction time on the mechanical and microstructural properties of the weld was determined. Accordingly,

1. It has been found that the surface temperature taken from the surface of welded joints increases in parallel with the increase of friction time.
2. The highest tensile stress of 755 MPa was seen in the S3 sample having the highest friction time while the lowest tensile stress of 661 MPa was determined in the S1 sample with the lowest friction time. The tensile strength and also elongation of the weld increased by increasing friction time.
3. Microhardness values around 310, 270 and 240 HV were reached at the joint areas of S1, S2 and S3 welds, respectively.
4. A decrease in the hardness value at the weld interface was observed when the friction time was increased.
5. It has been observed that the width and shape of the excessively deformed region on both sides of the joint interface changed due to the effect of temperature and pressure depending on the friction time.
6. S2 and S3 weld samples exhibited a ductile fracture during the tensile strength test. However, S1 weld sample was broken as a mixture of brittle and ductile.

#### REFERENCES

- [1] Dahlan H, Nasution AK, Rusli M. Preliminary study on effect of inertia and continuous friction welding on mechanical properties of SS 316-Zn alloys friction welded joint. *Journal of Advanced Joining Processes*. 2024;9:100187.
- [2] Kumar Rajak D, Pagar DD, Menezes PL, Eyvazian A. Friction-based welding processes: friction welding and friction stir welding. *J. Adhes Sci. Technol*. 2020;34(24):2613-2637.
- [3] Mortezaie A, Shamanian M. An assessment of microstructure, mechanical properties and corrosion resistance of dissimilar welds between Inconel 718 and 310S austenitic stainless steel. *International Journal of Pressure Vessels and Piping*. 2014;116:37-46.
- [4] Dinc D. Investigation of weldability of AISI 1020 and AISI 304 steels by friction welding. M.Sc. Thesis. Balikesir University, Institute of Science, Balikesir; 2006.
- [5] Meshram SD, Mohandas T, Madhusudhan Reddy G. Friction welding of dissimilar pure metals. *J Mater Process Technol* 2008;184:330-337.
- [6] Sathiyha P, Aravindan S, Noorul Haq A. Some experimental investigations on friction welded stainless steel joints. *Mater Des*. 2007;29:1099-1109.
- [7] Sahin M. Simulation of friction welding using a developed computer program. *J Mater Process Technol*. 2004;153(4):1011-8.
- [8] Ekinci O. Effect of tool rotational speed on friction stir spot welds of AZ31B Mg alloy to AISI 304 stainless steel. *Materials Testing*. 2024;66(4):534-43.
- [9] Ekinci O. Friction stir lap welding of AZ31B magnesium alloy to AISI 304 stainless steel. *Materials Testing*. 2024;66(9):1367-78.
- [10] Balalan Z, Ekinci O. Effect of Rotation Speed Parameter on Mechanical Properties of Similar AISI 1040 Parts Joined by Friction Welding. *Metallofiz. Noveishie Tekhnol*. 2018;40(12):1699-707.
- [11] Celik S, Dinc D, Yaman R, and Ay I. An Investigation on Weldability of AISI 304 and AISI 1040 Steels on Friction Welding. *Practical Metallography*. 2010;47(4):188-205.
- [12] Paventhan R, Lakshminarayanan PR, Balasubramanian V. Optimization of Friction Welding Process Parameters for Joining Carbon Steel and Stainless Steel. *Journal of Iron and Steel Research, International*. 2012;19(1):66-71.
- [13] Guo W, You G, Yuan G, Zhang X. Microstructure and mechanical properties of dissimilar inertia friction welding of 7A04 aluminum alloy to AZ31 magnesium alloy. *J. Alloys Compd*. 2017;695:3267-77.
- [14] Pratyusha M, Ramana PV, Prasanthi G. Evaluation of tensile strength of dissimilar metal pure aluminium and pure copper friction welds. *Mater. Today Proc*. 2021;38:2271-74.
- [15] Nasution AK, Nawangsari P, Junaidi A, Hermawan H. Friction welding of AZ31-SS316L for partially-

- degradable orthopaedic pins. IOP Conf. Ser. Mater. Sci. Eng. 2019;532:012014.
- [16] Dahlan H, Nasution AK, Zuhdi SA, Rusli M. Study of the effect of friction time and preheating on the joint mechanical properties of friction welded SS 316- Pure Zn. Appl. Sci. 2023;13(2):988.
- [17] Adin MS, Okumuş M. Investigation of Microstructural and Mechanical Properties of Dissimilar Metal Weld Between AISI 420 and AISI 1018 Steels, Arabian Journal for Science and Engineering. 2022;47:8341-50.
- [18] Sahin M. Characterization of properties in plastically deformed austenitic-stainless steels joined by friction welding. Materials & Design. 2009;30(1):135-44.
- [19] Shi Y, Li W, Tian L, Sun Y, Zhang J, Zhao HJL, Xu L, Han Y. Effect of ferrite and grain boundary characteristics on corrosion properties of thermal simulated 316 L heat affected zone. Corrosion Science. 2023;222:111384.
- [20] Kumar NN, Ram GJ, Bhattacharya S, Dey H, Albert S. Spark plasma welding of austenitic stainless steel AISI 304L to commercially pure titanium. Trans. Indian Inst. Met. 2015;68:289-97.
- [21] Mohammed M, Omar M, Sajuri Z, Al-Zubaidi S. Characterization of metallurgical and mechanical properties of thixowelded AISI D2 and AISI 304 steels. J. Mater. Eng. Perform. 2020;29:739-49.
- [22] Kumar AS, Khadeer SA, Rajinikanth V, Pahari S, Kumar BR. Evaluation of bond interface characteristics of rotary friction welded carbon steel to low alloy steel pipe joints. Materials Science and Engineering: A. 2021;824:141844.
- [23] Saeidi K, Zapata DL, Lofaj F, Kvetkova L, Olsen J, Shen Z, et al. Ultra-high strength martensitic 420 stainless steel with high ductility. Addit. Manuf. 2019;29:100803.
- [24] Fu L, Duan L. The coupled deformation and heat flow analysis by finite element method during friction welding. Welding journal. 1998;77(5):202-7.
- [25] Sluzalec A. Thermal effects in friction welding. Int. J. Mech. Sci. 1990;32(6):467-78.
- [26] Ekinçi O, Balalan Z. Influence of tool pin shape and rotation speed for friction stir spot welding of AZ91 magnesium alloy sheets. Materials Testing. 2023;65(8):1281-91.

## Anticholinergic Evaluation, Antioxidant Effects, and DNA Protection Potential of *Chenopodium spp* Depending on Its Phenolic Content

Enver Fehim KOÇPINAR<sup>1\*</sup> 

<sup>1</sup> Muş Alparslan University, Vocational School of Health Services, Department of Medical Laboratory Techniques, Mus, Türkiye

Enver Fehim KOÇPINAR ORCID No: 0000-0002-6031-4664

\*Corresponding author: [ef.kocpinar@alparslan.edu.tr](mailto:ef.kocpinar@alparslan.edu.tr)

(Received: 07.05.2024, Accepted: 10.09.2024, Online Publication: 26.09.2024)

### Keywords

Antioxidant,  
DNA protection,  
Inhibition,  
Phenolics,  
LC-MS/MS

**Abstract:** Plants are important food sources and natural therapeutics, and they are preferred as an alternative instead of synthetic medicines with harmful side effects in the treatment of routine diseases. Their unique effects are mostly attributed to specific herbal metabolites based on soil, climatic, and biogeography. *Chenopodium* species growing on barren and alkaline soils with nitrogen content are important candidates for unique biological effects. Due to their acceptance as food and wild, searching the biological activities and knowing the metabolite content are important. A series of *in vitro* biological activity tests were performed to determine the effects of *Chenopodium spp* (*Cspp*). First, leaf and flower samples were prepared using a Soxhlet device. Antioxidant tests including radical scavenging and heavy metal reduction were performed. Their phenolic contents were determined by LC-MS/MS to better interpreting the antioxidant results. Their inhibitory effects on AChE and BChE were tested and were shown to have quite significant total inhibition effect compared to Galantamine used as standard. Finally, their DNA protective effects were evaluated. In conclusion, it has been understood that phenolic content and the other biological effects are mostly parallel, and the samples have antioxidant effects at acceptable levels depending on dose.

161

## Fenolik İçeriğine Bağlı Olarak *Chenopodium spp*'nin DNA Koruma Potansiyeli, Antioksidan Etkileri ve Antikolinergik Değerlendirilmesi

### Anahtar Kelimeler

Antioksidan,  
DNA koruma,  
İnhibisyon,  
Fenolikler,  
LC-MS/MS

**Öz:** Bitkiler önemli besin kaynakları ve doğal terapötiklerdir. Bu nedenle onlar özellikle rutin hastalıkların tedavisinde yan etkilere sahip olan sentetik ilaçların yerine alternatif olarak tercih edilirler. Bitkilerin özgün etkileri çoğunlukla büyüdükleri biyocoğrafya, toprak türü ve iklim şartlarına bağlı olarak değişebilen bitkisel metabolitlerine atfedilir. Kurak ve nitrojen içeriği bol olan topraklarda büyüyen *Chenopodium* türleri özgün etkiler için önemli adaylardır. Yiyecek veya vahşi bitki olarak kabul edilmelerinden dolayı kullanmadan önce onların biyolojik yönden araştırılması ve bu etkilerin arkasındaki moleküllerin bilinmesi önem arz eder. Bu çalışmada bu türün kendine has biyolojik bazı etkilerini belirlemek amacıyla bir dizi *in vitro* biyolojik aktivite testi gerçekleştirilmiştir. İlk olarak Soxhlet ekstraksiyon aparatı kullanılarak bitkiden yaprak ve çiçek örnekleri hazırlanmıştır. Radikal süpürme ve ağır metal indirgeme testlerini içeren antioksidan testler gerçekleştirilmiş, ardından elde edilen verileri daha anlamlı hale getirmek amacıyla LC-MS/MS ile bitkinin fenolik içeriği belirlenmiştir. Daha sonra örneklerin AChE ve BChE enzimleri üzerindeki inhibitör etkileri test edilmiş ve numunelerin standart olarak kullanılan galantamine kıyasla önemli inhibisyon etkisi göstermiş olduğu anlaşılmıştır. Son olarak DNA koruyucu özellikleri test edilmiştir. Sonuçta, fenolik içerik ile diğer biyolojik etkilerin çoğunlukla paralel olduğu ve örneklerin doza bağlı olarak kabul edilebilir düzeyde antioksidan etkilere sahiptir

### 1. INTRODUCTION

The plants grown in wild nature have been our primary food for thousands of years and have been used as

medicine because of pharmaceutical benefits [1, 2]. Although access to synthetic medicines with specific effects has become easier in today's pharmacology, public awareness about the adverse effects of modern

medicines supports the tendency on herbal products in the treatment of diseases. Due to their low cost, low adverse effects, and known benefits, plants are used by approximately 80% of the world's population in the treatment of diseases and as the primary nutrition source [1, 3, 4]. In parallel with this trend, it is stated that the global herbal products market size will gradually increase in recent years [5]. Most studies state that the beneficial benefits of plants depend on their secondary metabolites with low molecular weight [5]. Alkaloids, glycosides, amines, steroids, flavonoids, carotenoids, xanthophylls, vitamins, tocopherols, phenolic acids, flavonoids, and lignans are known as secondary metabolites protecting the plants against microbes, herbivores, bacteria, insects, and various adverse environmental conditions [4, 6-9]. Also, herbal molecules, including alkaloids, polyphenols, and phytoestrogens, are promising actors for natural nutrition and alternative therapy based on biological effects [10]. Depending on the pharmaceutical effects of these biomolecules, they are essential for investigations that focus on the treatment of many diseases such as cancer and Alzheimer's diseases [11, 12]. For this reason, it is stated that herbal and natural products should be added to the diet regularly, based on the positive relationship between diet and health [13].

The strong relationship between cognitive impairment depending on Alzheimer's and neurotransmitters is well known [10] and Alzheimer's disease (AD) is a cholinergic dysfunction due to impaired neuronal activity and neurotoxicity with amyloid/tau proteinopathy [14]. The cognition and recollection processes are known to greatly improve by stabilizing acetylcholine concentration via AChE enzyme inhibition [14]. Hence, the discovery of acetylcholine regulatory agents is great and promising to hold the progression of AD. Regarding this, there are some inhibitors used pharmaceutically such as tacrine, donepezil, and galantamine that are known to cause some undesirable side effects [15] and plants can be considered as anticholinergic agents. Carcinogenic molecules such as H<sub>2</sub>O<sub>2</sub> can cause DNA damage. The damage in DNA has been associated with cardiovascular, many neurodegenerative diseases, and cancer [16, 17]. Plants can influence the fate of DNA through dose-dependent beneficial and lethal effects [18, 19].

The Amaranthaceae family includes 104 genera and more than 1400 species [6]. *Chenopodium* is a member of this family and is also known as white crow's feet. *Chenopodium* encompasses numerous species of perennial or annual herbaceous flowering plants that can be seen in continental climates in many parts of the world [12, 20]. *Chenopodium spp* has a widespread growth network and adaptation all over the world [12]. They are consumed as food in Northern India, Nepal, and Pakistan, as opposed to being considered wild plants in North America and Europe.

The limited data on *Chenopodium spp* (*Cspp*), its ability to survive even under stressful conditions, and the possibility of specific secondary metabolite potential

raises the curiosity to investigate their biological activities and unique contents. For this purpose, *Chenopodium spp* (*Cspp*) was collected from Muş-Varto region (latitude and longitude information; 39.1929920 and 41.4457306) in Turkey, *in vitro* antioxidant activity, some herbal antioxidant contents, anticholinergic effects, and DNA protective activity were evaluated in *Chenopodium spp*. extracts.

## 2. MATERIAL AND METHOD

### 2.1. Plant Acquisition and Sample Preparation

*Chenopodium spp* (*Cspp*) samples were collected during the vegetation period and stored as herbarium material in Muş Alparslan University, Research Laboratory of Technology Research Project Coordination Unit. The flower and leaf tissues of the herbarium material were separated from each other. Leaf (*CsppL*) and Flower (*CsppF*) samples were prepared by extraction of tissues in ethanol (EtOH) using a Soxhlet apparatus. The solvents of stock samples were completely evaporated and stored at +4 °C until the experimental phase. The test samples with different concentrations were prepared by diluting in the same solvent.

### 2.2. *In Vitro* Antioxidant Studies

#### 2.2.1. DPPH radical scavenging assay

1,1-Diphenyl 2-picrylhydrazyl (DPPH) radical scavenging assay was performed the method of Blois [21]. This method is a measurement based on the relative scavenging of DPPH radicals in alcohol by hydrogen donor molecules such as antioxidants. The absorbance values of samples were measured spectrophotometrically at 517 nm and different concentrations (15, 30, and 45mg/mL). Butylated hydroxyanisole (BHA) and ascorbic acid (ACS) were used as standard antioxidants. DPPH radical scavenging activity (DPPH<sub>RSA</sub>) was calculated using the following equation (Equation 1) and Trolox standard curve.

$$\text{DPPH}_{\text{RSA}} = \frac{(\text{ABS}_{\text{Control}} - \text{ABS}_{\text{Sample}})}{(\text{ABS}_{\text{Control}})} \quad (1)$$

#### 2.2.2. ABTS radical scavenging assay

ABTS radical scavenging activities were determined following the method of Wu [22]. According to this, the ABTS radical scavenging of a molecule is determined by measuring the colorless ABTS solution after the addition of the antioxidant molecule to the dark blue ABTS radical solution. The samples were prepared at 15, 30, and 45mg/mL concentrations and were incubated for 2 hours. Butylated hydroxyanisole (BHA) and ascorbic acid (ACS) were used as standard antioxidants. The absorbance values were recorded at 734nm. ABTS radical scavenging activity (ABTS<sub>RSA</sub>) was calculated using the following Equation 2 (Equation 2) and the Trolox standard curve.

$$ABTS_{RSA} = \frac{(ABS_{Control} - ABS_{Sample})}{(ABS_{Control})} \quad (2)$$

### 2.2.3. CUPRAC assay

Cupric ion reducing power (CUPRAC) assay was applied by following the teachings of the method proposed by [23]. This test is based on the spectrophotometric measurement of cuprous ion ( $Cu^{1+}$ ) with blue color formed by the reduction of cupric ion ( $Cu^{2+}$ ) after the treatment with reductive molecules such as antioxidants. The absorbance values of different concentrations of the samples were recorded at 450 nm. Butylated hydroxyanisole (BHA) and ascorbic acid (ACS) were used as standard antioxidants. The  $Cu^{2+}$  reducing activity was calculated using the following Equation 3 (Equation 3) and the curve of Trolox as a reference. The elements in the equation are as follows;  $ABS_{sample}$ ; The absorbance value of sample,  $\epsilon$ ; Molar absorption coefficient of Trolox molecule ( $16700 \text{ L mol}^{-1} \cdot \text{cm}^{-1}$ ),  $V_T$ ; Total volume,  $V_S$ ; Sample volume, DF; dilution factor,  $V_{MS}$ ; main sample volume, and  $m$ ; The amount of dry material in the main sample.

$$CUPRAC = \frac{ABS_{Sample}}{\epsilon} \times \frac{V_T}{V_S} \times DF \times \frac{V_{MS}}{m} \quad (3)$$

### 2.2.4. FRAP assay

The ferric ion ( $Fe^{3+}$ ) reducing antioxidant power assay (FRAP) was performed using the method of Oyaizu [24]. FRAP assay is based on reducing capacity of an antioxidant to reduce a ferric salt ( $Fe^{3+}$ ) to ferrous salt ( $Fe^{2+}$ ) with blue color by electron transfer reaction. The absorbance values of the samples at 15, 30, and 45mg/mL concentrations were recorded at 700 nm. Butylated hydroxyanisole (BHA) and ascorbic acid (ACS) were used as standard antioxidants. FRAP was calculated by accepting the Trolox as a reference and using following Equation 4 (Equation 4). The elements in the equation are as follows;  $c$ ; sample concentration obtained from Trolox standard curve equation,  $V$ ;

Sample volume, DF; dilution factor, and  $m$ ; Dry material weight [25].

$$FRAP = c \times V \times \frac{t}{m} \quad (4)$$

### 2.2.5. Iron chelating assay

The iron chelating activity was performed according to the basic teachings of the method proposed by Decker, Welch [26]. The essence of this method is a measure of the binding affinity between a metal ion such as  $Fe^{2+}$  and a reagent. Butylated hydroxyanisole (BHA) and ascorbic acid (ACS) were used as standard antioxidants. The absorbances of the samples at 15, 30, and 45mg/mL concentrations were recorded at 562nm and converted to concentrations with the help of trolox standard curve, and  $Fe^{2+}$  chelating activity was calculated by following Equation 5 (Equation 5).

$$Fe^{2+} \text{ chelating activity} = \frac{(ABS_{Control} - ABS_{Sample})}{(ABS_{Control})} \quad (5)$$

## 2.3. Chromatographic Assay

Quantitative phenolic compounds were determined chromatographically in LC-MS/MS device (Agilent 6460 Triple Quadrupole LC-MS/MS (Liquid Chromatography-Tandem Mass/Mass Spectrometer, Agilent Technologies) equipped with a Zorbax SB-C18 (4.6x100mm; 3.5 Micron) column). The analyzes were performed in Atatürk University, Eastern Anatolia Advanced Technologies Research and Application Center (DAYTAM) laboratories. The analysis mode is a multiple reaction monitoring mode (MRM). The mobile phase was filtered with a 0.45  $\mu\text{m}$  Millipore membrane filter before loading to LC-MS/MS. Samples were then maintained at a concentration level of 5 mg/mL. The identification of the samples was done by comparison with the standard samples. Injection volume was studied as 5  $\mu\text{l}$  and working time was determined as 20 min. Solvent A contains 0.1% (v/v) formic acid in water and solvent B contains 0.1% (v/v) formic acid in acetonitrile.

**Table 1.** Order of samples loaded into electrophoresis wells and the component amounts of the samples.

Well No	DNA( $\mu\text{L}$ )	$H_2O_2$ ( $\mu\text{L}$ )	DMSO( $\mu\text{L}$ )	<i>Cspp</i> extract (10 $\mu\text{L}$ )	Water ( $\mu\text{L}$ )
1	10	-	-	-	15
2	10	5	-	-	10
3	10	5	10	-	-
4	10	-	10	-	5
5	10	-	-	<i>Cspp</i> L (0.25 mg/ml)	5
6	10	5	-	<i>Cspp</i> L (0.25 mg/ml)	-
7	10	-	-	<i>Cspp</i> L (0.5 mg/ml)	5
8	10	5	-	<i>Cspp</i> L (0.5 mg/ml)	-
9	10	-	-	<i>Cspp</i> L (1 mg/ml)	5
10	10	5	-	<i>Cspp</i> L (1 mg/ml)	-
11	10	-	-	<i>Cspp</i> F (0.25 mg/ml)	5
12	10	5	-	<i>Cspp</i> F (0.25 mg/ml)	-
13	10	-	-	<i>Cspp</i> F (0.5 mg/ml)	5
14	10	5	-	<i>Cspp</i> F (0.5 mg/ml)	-
15	10	-	-	<i>Cspp</i> F (1 mg/ml)	5
16	10	5	-	<i>Cspp</i> F (1 mg/ml)	-

## 2.4. DNA Protection Assay

DNA protection assay was performed according to the method proposed by Siddall [27]. pUC18 plasmid DNA was used as model DNA in the DNA protection assay and the protective effects of the samples were tested on. In this scope, stock samples were prepared as 200mg/ml by dissolving the dry extraction products in ethanol, and by diluting the stock samples, fresh samples were prepared at 0.25mg/mL, 0.5mg/mL, and 1mg/mL concentrations. Electrophoresis samples were incubated at 37 °C and dark for 24 hours before loading. 15 µl from each sample were loaded into agarose gel electrophoresis and run at 40 Volts for 2 hours. The electrophoresis product was visualized using the BIORAD ChemiDoc XRS imaging system. The component amounts of the electrophoresis samples are shown in Table 1.

## 2.5. Cholinesterase Inhibition Assay

Acetylcholinesterase (AChE) isolated from *Electrophorus electricus* (Electric eel) and butyrylcholinesterase (BChE) isolated from equine serum were purchased from Sigma- Aldrich (St. Louis, MO). Acetylthiocholine iodide (AChI) and butyrylcholine iodide (BChI) were used as a substrate, and 5'-dithiobis - 2 - nitrobenzoic acid (DTNB) were used as Ellman's reagent in the measurement of inhibition. The inhibitory effects of the samples on AChE and BChE were evaluated by following the teachings of the spectrophotometric method proposed by [28]. Absorbance values showing the inhibition effects were recorded at 412 nm at 1 min intervals for 5 min. Inhibition effect of each sample were recorded in 3 replications and calculations were made using the averages of these results. %Activity graphs were plotted to determine the inhibitory effects of samples and IC<sub>50</sub> values showing inhibition effects of the samples were calculated.

## 2.6. Statistical Analyses

The tests for each study were performed in at least 3 replicates. All statistical data were represented as Mean ± Standard Deviation (SD), and  $p < 0.05$  was considered significant. In the antioxidant studies, sample results were compared statistically with standard results using One-way ANOVA followed by Dunnett's Multiple Comparisons Test, and the statistical significance levels were represented as follows;  $P > 0.05$  (not significant, ns);  $*P < 0.05$  (significant);  $**P < 0.01$  (very significant);  $***P < 0.001$  and  $****P < 0.0001$  (extremely significant). Inhibition values according to the increase in concentration were normalized in the range of 0-100, and LogIC<sub>50</sub>, IC<sub>50</sub>, and R<sup>2</sup> values were calculated. In

addition to this, the band intensities in the results of the electrophoresis study were analyzed using the ImageJ 2x software for windows. The band density values of the samples were statistically compared with the control values of the same study, and the stabilization effects of the samples on DNA were calculated as a percentage. Finally, compatibility between quantitative phenolic results and biological activity results was analyzed using Spearman's correlation test. The p values and r values showing the direction of the correlation were calculated.

## 3. RESULTS

### 3.1. In vitro antioxidant results

#### 3.1.1. Radical scavenging activities

The scavenging effect of *Cspp* samples removing the half effects of DPPH and ABTS radicals were calculated as IC<sub>50</sub> values, and the results were evaluated statistically (Figure 1 A and D). Trolox Equivalent Antioxidant Capacity (TEAC) values of DPPH and ABTS were calculated (Figure 1 B and E). In addition, heavy metal reduction and radical scavenging capacities were expressed as µM TE/g (Figure 1 C and F). IC<sub>50</sub> values of *Cspp* samples were detected to be higher than standards and TEAC results were determined as lower than standards.

#### 3.1.2. Heavy metal reduction activities

Reduction activities of Fe<sup>3+</sup> and Cu<sup>2+</sup> ions were determined using FRAP and CUPRAC methods, respectively. The results were shown as IC<sub>50</sub>, TEAC, and µM TE/g (Figure 2). In the FRAP results, the similarity of *CsppF* IC<sub>50</sub> values to BHA results was noteworthy. However, the IC<sub>50</sub> value of *CsppL* was found to be quite high compared to the standards (Figure 2A). Similarly, unlike *CsppL*, it was observed that *CsppF* TEAC result was close to the BHA result (Figure 2B). The CUPRAC results clearly show that the samples have a higher IC<sub>50</sub> and lower TEAC results compared to the standards (Figure 2D and 2E). Better heavy metal reduction activities depend on sample concentrations were observed however, the results at the same concentrations were weaker than standards (Figure 2C and 2F). The iron-chelating activities of *Cspp* samples were also determined. When compared with the results of standards, the IC<sub>50</sub> values of iron chelation as lower and the TEAC values as higher were calculated (Figure 2G and 2H). However, interestingly, the iron chelating capacities of the samples were detected to be quite close to the standards (Figure 2I).

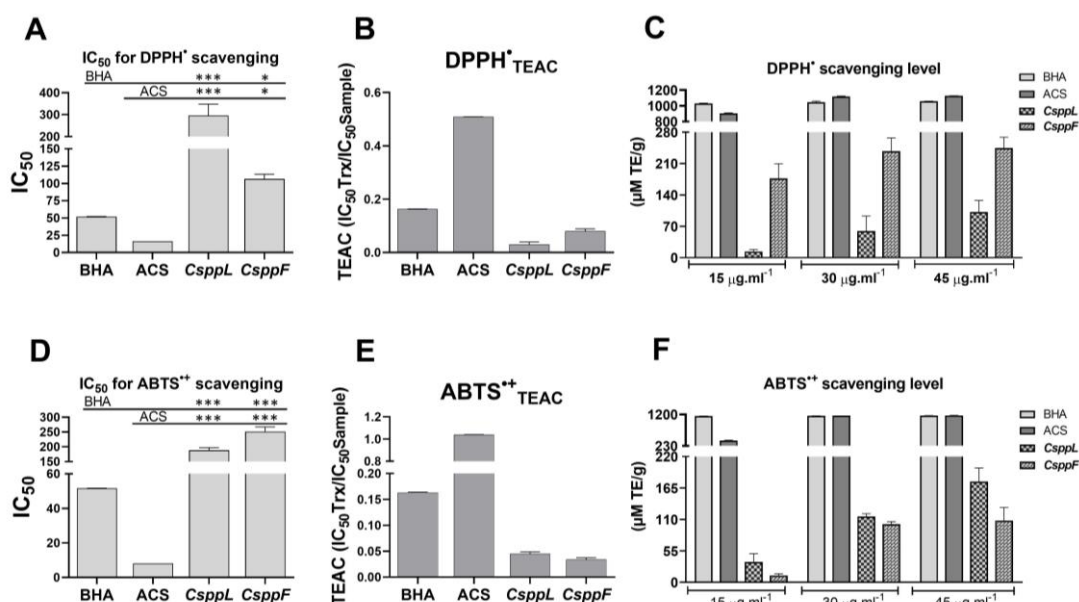


**Figure 1.** Radical scavenging results of the samples **A)** The IC<sub>50</sub> values based on DPPH radical scavenging, **B)** The TEAC results of DPPH radical scavenging using Trolox reference (DPPH<sub>TEAC</sub>), **C)** DPPH radical scavenging levels based on sample concentration, **D)** The IC<sub>50</sub> values based on ABTS radical scavenging, **E)** The TEAC results of ABTS radical scavenging using Trolox reference (ABTS<sub>TEAC</sub>), **F)** ABTS radical scavenging levels based on sample concentration.

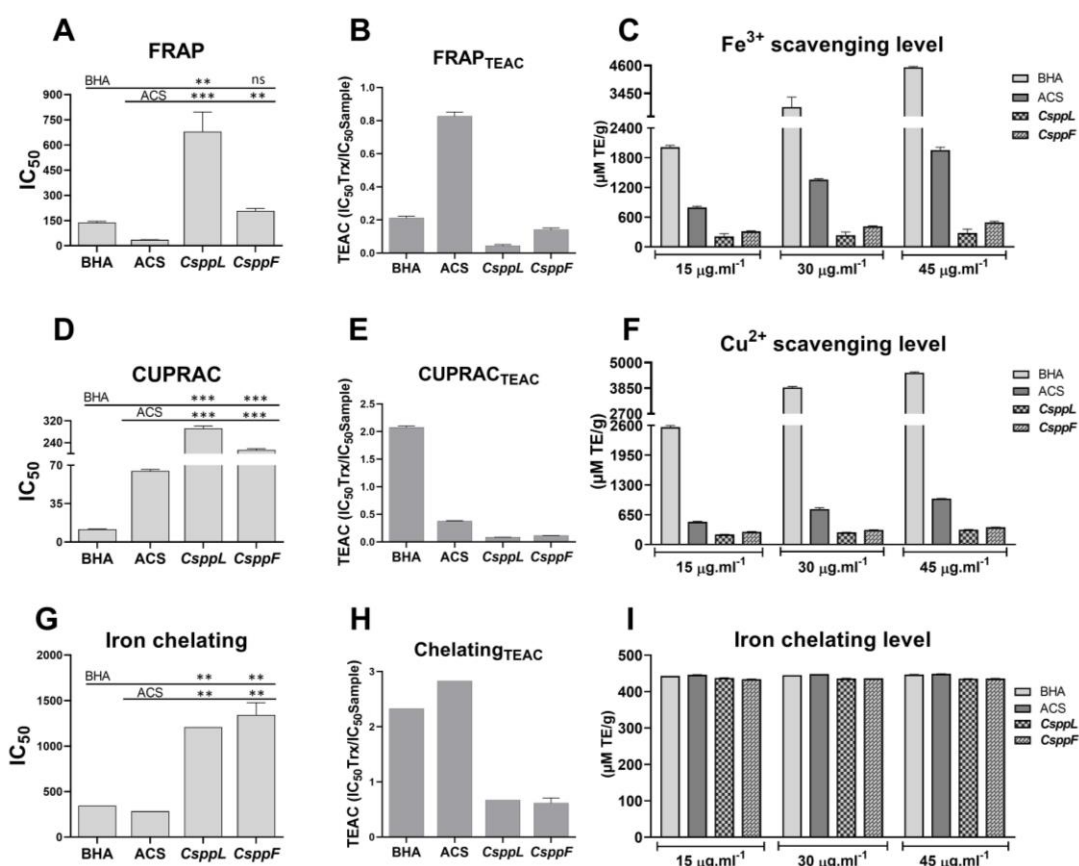


**Figure 2.** The evaluation of heavy metal eliminations in the samples. **A)** IC<sub>50</sub> values based on Fe<sup>3+</sup> reduction, **B)** TEAC based on FRAP results using Trolox reference (FRAP<sub>TEAC</sub> results), **C)** Fe<sup>3+</sup> reduction levels based on sample concentration, **D)** IC<sub>50</sub> values based Cu<sup>2+</sup> reduction, **E)** TEAC based on CUPRAC results using Trolox reference (CUPRAC<sub>TEAC</sub> results), **F)** Cu<sup>2+</sup> reduction levels based on sample concentrations, **G)** IC<sub>50</sub> values based on Fe<sup>2+</sup> chelating capacity, **H)** TEAC based on Fe<sup>2+</sup> chelating capacity using Trolox reference (Chelating<sub>TEAC</sub> results), and **I)** Fe<sup>2+</sup> chelating levels based on sample concentration.

### 3.2. Chromatographic Analysis by LC-MS/MS

To interpret the antioxidant activities more accurately, the phenolic contents of the samples were determined by LC-MS/MS. The phenolic content of *CsppF* sample was found to be higher than *CsppL* sample (11.7199 μg/mL and 21.3057 μg/mL, respectively). Resveratrol as the

lowest level (0.0004 μg/mL and 0.0002 μg/mL, respectively) and Rosmarinic acid as the highest level (7.2489 μg/mL and 11.6250 μg/mL, respectively) were detected in both samples and the concentration of some phenolics could not be determined (Table 2).

**Table 2.** LC-MS/MS results showing the phenolic concentrations of *CsppL* and *CsppF* as  $\mu\text{g/mL}$ 

Phenolics	<i>CsppL</i>	<i>CsppF</i>	Phenolics	<i>CsppL</i>	<i>CsppF</i>
4-OH-Benzoic Acid	0.1714	0.3793	Keracyanin Chloride	0.0015	0.0029
Apigenin	0.0000	0.0000	Luteolin	0.0000	0.0000
Caffeic Acid	0.0600	0.1801	Myricetin	0.0000	0.0000
Catechin	0.0000	0.0000	Naringenin	0.0000	0.0000
Chlorogenic Acid	0.0000	0.0460	Naringin	0.0000	0.3507
Chrysin	0.0000	0.0000	p-Coumaric Acid	0.0872	0.1813
Curcumin	0.0000	0.0000	Peonidin-3-o-glucoside	0.0048	0.0036
Cyanidin-3-o-glucoside	0.0352	0.0357	Pyrogallol	0.0000	0.0000
Ellagic Acid	0.0000	0.0340	Quercetin	0.1075	0.3373
Epicatechin	0.2366	0.5592	Quinic Acid	0.0906	0.4604
Epigallocatechin Gallate	0.0000	0.0000	Resveratrol	<b>0.0004</b>	<b>0.0002</b>
Ferulic Acid	0.8641	1.8680	Rosmarinic Acid	<b>7.2489</b>	<b>11.625</b>
Fumaric Acid	1.2148	2.4987	Sinapic Acid	0.0000	0.0000
Galangin	0.0000	0.0000	Syringic Acid	0.0000	0.0071
Gallic Acid	0.0000	0.0000	Taxifolin	0.0000	0.0000
Hesperidin	1.5940	2.7309	Vanillic Acid	0.0015	0.0000
Isohamnetin	0.0000	0.0000	Vanillin	0.0014	0.0056
<b>Total Content in <i>CsppL</i></b>	<b>11.7199</b>		<b>Total Content in <i>CsppF</i></b>	<b>21.3057</b>	

### 3.3. Anticholinergic Activity

The inhibition effects of the samples were tested on AChE and BChE enzymes and galantamine, known as the commercial inhibitor, was used as the standard. It was understood from the results that *CsppF* was detected

to have more effective inhibition compared to *CsppL* (Figure 3). The samples showed a significantly higher inhibitory effect on AChE compared to galantamine (Figure 3 A, A<sub>1</sub>, and A<sub>2</sub>). However, its inhibitory effect on BChE was found to be quite close to galantamine (Figure 3 B, B<sub>1</sub>, and B<sub>2</sub>).

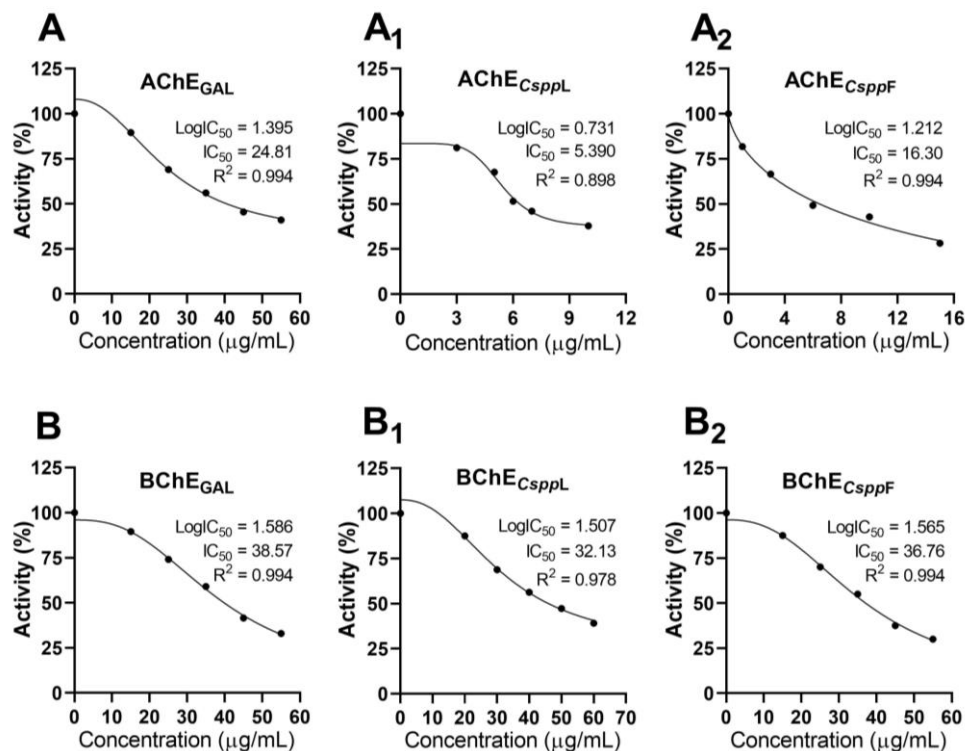


**Figure 3.** Inhibition effects of standard and samples on AChE and BChE enzymes. **A)** The inhibition effect of Galantamine on AChE, **A<sub>1</sub>)** The inhibition effects of *CsppL* on AChE, **A<sub>2</sub>)** The inhibition effects of *CsppF* on AChE, **B)** The inhibition effect of Galantamine on BChE, **B<sub>1</sub>)** The inhibition effects of *CsppL* on BChE, **B<sub>2</sub>)** The inhibition effects of *CsppF* on BChE. Galantamine (GAL) is a well-known inhibitor of AChE and BChE enzymes and was used as a standard inhibitor.

### 3.4. DNA Protection Activity

The nucleic acid protective effects of *Cspp* samples were tested on pUC18 plasmid DNA. Following the treatments given in Table 1, the samples were incubated at 36 °C for 24 hours. The samples were then loaded into gel electrophoresis and the fate of plasmid DNA was visualized (Figure 4). Following 24 hours of incubation, the DNA forms disappeared in wells treated with H<sub>2</sub>O<sub>2</sub> alone and H<sub>2</sub>O<sub>2</sub>+DMSO (Figure 4 well 2 and well 3,

respectively), and plasmid DNA was not affected by DMSO alone (Figure 4, well 4). Accordingly, plasmid DNA forms were not affected by the different concentrations of *Cspp* samples. Interestingly, form II was preserved by the 0.25mg/mL *CsppL* (Figure 4, well 6). However, this effect could not be displayed in other wells. In conclusion, *Cspp* could not protect the plasmid DNA against the scavenging effect of H<sub>2</sub>O<sub>2</sub>, and no significant effect on the stabilization of form I and form II was also observed when applied alone (Figure 4).



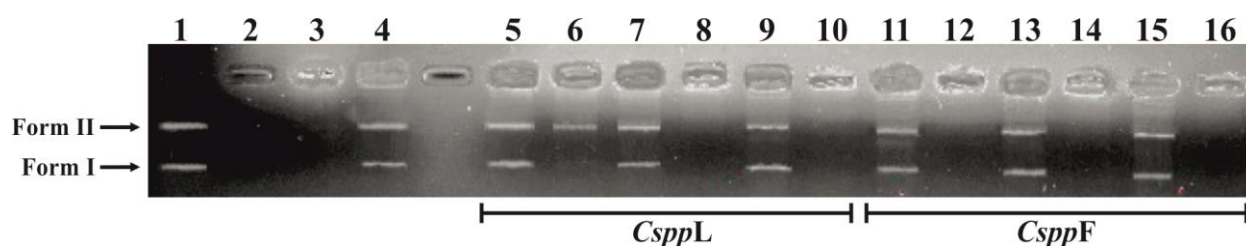


**Figure 4.** Electrophoresis image showing the effect of samples on pUC18 DNA in the environment with H<sub>2</sub>O<sub>2</sub> and H<sub>2</sub>O<sub>2</sub> free. The effect of *CspplL* was visualized in wells 5-10 and the effect of *CspplF* was visualized in well 11-16. H<sub>2</sub>O<sub>2</sub> free samples were loaded into wells 5, 7, 9, 11, 13 and 15 and the samples with H<sub>2</sub>O<sub>2</sub> were loaded into wells 6, 8, 10, 12, 14, and 16.

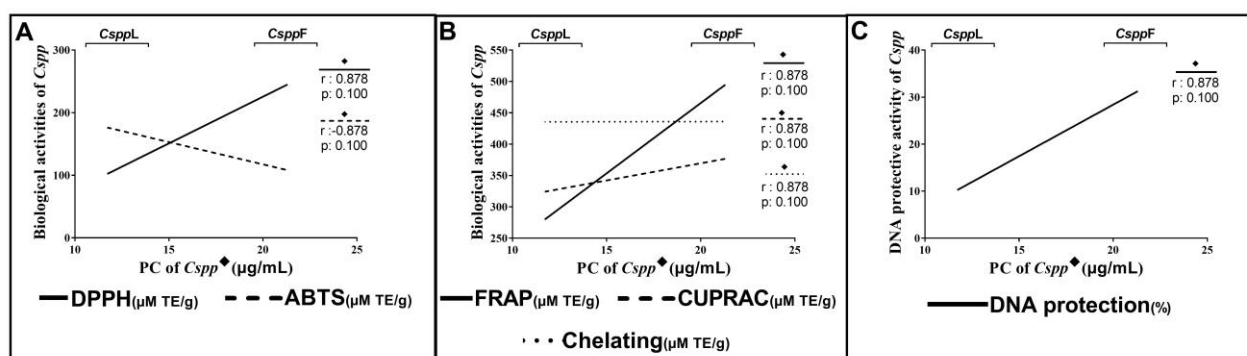


**Figure 5.** Correlation of biological activities depending on phenolic content in leaf (*CspplL*) and Flower (*CspplF*) samples. **A)** Correlation between phenolic content and radical scavenging activities in *Csppl* samples, **B)** Radical scavenging activities depending on the phenolic content of the samples, **C)** Heavy metal reduction activities depending on the phenolic content of the samples. (♦); was used as the symbol for phenolic content (PC). The x-axis represents the change in phenolic content, and the y-axis represents the change in biological activities. *r* and *p* values were shown on correlation graphs. The biological changes in each of the 3 graphs was shown with different line graphs. The closeness of *r* to 1 indicates the same directional correlation and the closeness of *r* to -1 indicates the opposite directional correlation.

### 3.5. Correlation of Phenolics and Biological Activities

The comparative interpretation of phenolic content and biological activities is essential to better understand the heavy metal and radical elimination based on phenolics. The results of phenolics and biological activities were compared by nonparametric Spearman's correlation test. The *p* and *r* values were calculated and displayed by a line graph (Figure 5). Accordingly, it was generally observed that the biological activities of flower samples were higher than leaf samples. These results are consistent with phenolic contents. However, the opposite situation was detected in ABTS radical scavenging activity. The band intensities were evaluated using the ImageJ 2.0 software program for Windows and these values were expressed as % protective activity.

## 4. DISCUSSION AND CONCLUSION

ROS can be produced by heavy metal accumulation such as iron and copper. The high oxidation power of ROS affects cell physiology negatively [14, 29, 30]. It is well known that excessive ROS has a lethal potential for cancerization and some neurodegenerative disease formation [14, 17, 31]. Plants are known as good regulators to balance the ROS and the heavy metal, and the biogeography of the plants is the architect of their unique biological character. Feeble antioxidant activities were demonstrated compared to the standards (Figure 1 and Figure 2), and the phenolic results from LC-MS/MS supported the antioxidant activity results. Previous studies document that herbal samples show lower antioxidant activity than commercial antioxidants [32,

33]. A lower effect is a situation expected compared to the commercial pure antioxidants because of the other molecules in plants limiting the expected effects. Even if their low effects, plants are highly preferred due to the lack of side effects and holistic beneficial effects across a wide range. A study emphasized that plants have low radical scavenging activities but are still considered good radical scavengers [34]. In this case, radical scavenging and heavy metal reduction activities are at acceptable levels. The higher IC<sub>50</sub> values and the lower TEAC values were calculated in the iron chelating activity results. Accordingly, it is possible that the samples may be able to chelate Fe<sup>2+</sup> effectively depending on the incubation time (Figure 2I). Zulfqar [35] stated that some *Chenopodium* species accumulate heavy metals in their leaves by absorbing them from the soil and they reduce some antioxidant molecules such as carotenoids. The results of iron chelation tests support this situation. That is, the *Chenopodium* species may have absorbed the iron from the soil, and this may be the reason for the low activities observed in antioxidant studies. Low heavy metal reduction was observed in FRAP and CUPRAC assays. This may be a result of possible chelation in plant metabolism using its own secondary metabolites. Furthermore, chromatographic results support this data. Phenolics known as secondary metabolites have a significant role in herbal antioxidant capacity [36] and they offer many beneficial effects such as strengthening the cellular defense against cancer and Alzheimer's [4, 10, 14]. Plant biogeography has an impact on their unique biological characteristics [37]. Therefore, the determination of herbal biological activities is important for the development process of alternative therapy.

It is known that some *Chenopodium* species can absorb nickel, chromium, and cadmium from soil and accumulate in their leaves. Heavy metal accumulation may be a reason for the low phenolic amount in plant content. The chelation results are consistent with this idea. Previous studies emphasizing the high and protein in *Chenopodium* content suggests their nutritional value. However, nutrition and biological effects are different properties.

Plants may be natural candidates for preventing AD formation by neurotransmitter regulation and the inhibition of AChE and BChE enzymes. Based on this, the inhibition potential of the samples on AChE and BChE was tested to reveal their importance in Alzheimer's treatment, and the samples were shown to have a higher total inhibition effect on AChE and BChE compared to galantamine. Accordingly, the samples may be natural and strong inhibitor candidates, however, the background of the inhibition may be based on possible heavy metal accumulation in the plant body.

Antioxidant activity and chromatography results revealed the necessity of investigating the DNA protective effects of the samples. DNA protective results largely supported the antioxidant activity and phenolic contents. Interestingly, form II was preserved by *CsppL* at 0.25mg concentration (Figure 4 well 6). Except for this, DNA forms were degraded by H<sub>2</sub>O<sub>2</sub> in all wells. Comparative interpretation of biological activity results obtained from the different tissues is essential to better understand the relationship between phenolic content and biological activities. Apart from the chelating activity, a general compatibility was observed between the phenolic results and the biological activities. The chelation effect of the samples is highly similar to the standards (Figure 2). This strengthens the possibility of using phenolics for chelating purposes. The inverse relationship between chelation activity and phenolic content could be evidence of this.

In summary, when thinking about the purity of the standards, it is clear that the samples showed quite sufficient heavy metal reduction and radical scavenging activity. Iron chelation results support the possibility of heavy metal accumulation in the leaves. That is, rather than radical scavenging and heavy metal reduction, this result may be assumed as evidence indicating the possibility of effective chelation in leaves. That is, the low phenolic content may be associated with the use of some metabolites such as carotenoids in the heavy metal chelation and the high iron chelation results may also be proof of this. Based on the study results, the samples can be assumed as natural AChE and BChE inhibitors. The study data contains valuable data supporting the improvements in the treatment of AD with the regulation of neurotransmitters. Plants can influence the fate of DNA against carcinogenic molecules. low antioxidant activity and quantitative phenolic content greatly support the DNA protective activity results. Despite the increase in sample concentration, decreases in DNA protection activity were noticed. This reverse effect in DNA protective activity may be related to the predominance of

toxicity based on metal accumulation and thus the masking of antioxidant effects.

### Acknowledgement

I would like to express my gratitude to Prof. Dr. Murat KURŞAT from Bitlis Eren University for supporting me in the identification of plant used in the study.

### REFERENCES

- [1] Singh R, Upadhyay SK, Tuli HS, Singh M, Kumar V, Yadav M, et al. Ethnobotany and herbal medicine: Some local plants with anticancer activity. *Bulletin of Pure & Applied Sciences-Botany*, 2020; 1: p. 57-40
- [2] Shori AB, Kee LA, Baba AS. Total phenols, antioxidant activity and sensory evaluation of bread fortified with spearmint. *Arabian Journal for Science and Engineering*, 2021; 46: p. 5257-5264
- [3] El Omari N, Sayah K, Fettach S, El Blidi O, Bouyahya A, Faouzi MEA, et al. Evaluation of in vitro antioxidant and antidiabetic activities of *Aristolochia longa* extracts. *Evidence-Based Complementary and Alternative Medicine*, 2019; 2019
- [4] Jain C, Khatana S, Vijayvergia R. Bioactivity of secondary metabolites of various plants: a review. *Int. J. Pharm. Sci. Res*, 2019; 10(2): p. 494-504
- [5] Reddy PRK, Elghandour M, Salem A, Yayaswini D, Reddy PPR, Reddy AN, et al. Plant secondary metabolites as feed additives in calves for antimicrobial stewardship. *Animal Feed Science and Technology*, 2020; 264: p. 114469
- [6] Khomarlou N, Aberoomand-Azar P, Lashgari AP, Hakakian A, Ranjbar R, Ayatollahi S. Evaluation of antibacterial activity against multidrug-resistance (mdr) bacteria and antioxidant effects of the ethanolic extract and fractions of *Chenopodium album* (sub sp striatum). *International Journal of Pharmaceutical Sciences and Research*, 2017; 8(9): p. 3696-3708
- [7] Akyüz M, İnci Ş, Kırbağ S. Evaluation of Antimicrobial, Antioxidant, Cytotoxic and DNA Protective Effects of Oyster Mushroom: *Pleurotus pulmonarius* (Fr.) Quel. *Arabian Journal for Science and Engineering*, 2022: p. 1-11
- [8] Wei S, Wang Y, Tang Z, Xu H, Wang Z, Yang T, et al. A novel green synthesis of silver nanoparticles by the residues of Chinese herbal medicine and their biological activities. *RSC advances*, 2021; 11(3): p. 1411-1419
- [9] Hemeg HA, Moussa IM, Ibrahim S, Dawoud TM, Alhaji JH, Mubarak AS, et al. Antimicrobial effect of different herbal plant extracts against different microbial population. *Saudi Journal of Biological Sciences*, 2020; 27(12): p. 3221-3227
- [10] Bose B, Tripathy D, Chatterjee A, Tandon P, Kumaria S. Secondary metabolite profiling, cytotoxicity, anti-inflammatory potential and in vitro inhibitory activities of *Nardostachys jatamansi* on key enzymes linked to hyperglycemia,

- hypertension and cognitive disorders. *Phytomedicine*, 2019; 55: p. 58-69
- [11] Vujanović M, Zengin G, Đurović S, Mašković P, Cvetanović A, Radojković M. Biological activity of extracts of traditional wild medicinal plants from the Balkan Peninsula. *South African Journal of Botany*, 2019; 120: p. 213-218
- [12] Yang L, Li Q, Zhao G. Characterization of the complete chloroplast genome of *Chenopodium* sp.(Caryophyllales: Chenopodiaceae). *Mitochondrial DNA Part B*, 2019; 4(2): p. 2574-2575
- [13] Umar MF, Ahmad F, Saeed H, Usmani SA, Owais M, Rafatullah M. Bio-mediated synthesis of reduced graphene oxide nanoparticles from *Chenopodium album*: their antimicrobial and anticancer activities. *Nanomaterials*, 2020; 10(6): p. 1096
- [14] Mollica A, Stefanucci A, Macedonio G, Locatelli M, Luisi G, Novellino E, et al. Chemical composition and biological activity of *Capparis spinosa* L. from Lipari Island. *South African Journal of Botany*, 2019; 120: p. 135-140
- [15] Kaya AÇ, Özbek H, Yuca H, Yılmaz G, Bingöl Z, Kazaz C, et al. Phytochemical Analysis and Screening of Acetylcholinesterase and Carbonic Anhydrase I and II Isoenzymes Inhibitory Effect of *Heptaptera triquetra* (Vent.) Tutin Root. *FABAD Journal of Pharmaceutical Sciences*, 2022; 47(3): p. 381-392
- [16] Sicari V, Pellicano T, Giuffrè A, Zappia C, Capocasale M, Poiana M. Physical chemical properties and antioxidant capacities of grapefruit juice (*Citrus paradisi*) extracted from two different varieties. *International Food Research Journal*, 2018; 25(5)
- [17] Jaradat N, Qneibi M, Hawash M, Sawalha A, Qtaishat S, Hussein F, et al. Chemical composition, antioxidant, antiobesity, and antidiabetic effects of *Helichrysum sanguineum* (L.) Kostel. from Palestine. *Arabian Journal for Science and Engineering*, 2021; 46: p. 41-51
- [18] Papanastasiou SA, Bali E-MD, Ioannou CS, Papachristos DP, Zarpas KD, Papadopoulos NT. Toxic and hormetic-like effects of three components of citrus essential oils on adult Mediterranean fruit flies (*Ceratitis capitata*). *PloS one*, 2017; 12(5): p. e0177837
- [19] Ismael MA, Elyamine AM, Moussa MG, Cai M, Zhao X, Hu C. Cadmium in plants: uptake, toxicity, and its interactions with selenium fertilizers. *Metallomics*, 2019; 11(2): p. 255-277
- [20] Zhu G, Mosyakin SL, Clemants SE. *Chenopodium Linnaeus*. *Flora of China*, 2004; 5: p. 352-378
- [21] Blois MS. Antioxidant determinations by the use of a stable free radical. *Nature*, 1958; 181(4617): p. 1199-1200
- [22] Wu L-c, Chang L-H, Chen S-H, Fan N-c, Ho J-aA. Antioxidant activity and melanogenesis inhibitory effect of the acetonic extract of *Osmanthus fragrans*: A potential natural and functional food flavor additive. *LWT-Food Science and Technology*, 2009; 42(9): p. 1513-1519
- [23] Apak R, Guclu K, Ozyurek M, Karademir SE, Ercag E. The cupric ion reducing antioxidant capacity and polyphenolic content of some herbal teas. *International Journal of Food Sciences and Nutrition*, 2006; 57(5-6): p. 292-304
- [24] Oyaizu M. Studies on products of browning reaction antioxidative activities of products of browning reaction prepared from glucosamine. *The Japanese journal of nutrition and dietetics*, 1986; 44(6): p. 307-315
- [25] Xiao F, Xu T, Lu B, Liu R. Guidelines for antioxidant assays for food components. *Food Frontiers*, 2020; 1(1): p. 60-69
- [26] Decker EA, Welch B. Role of ferritin as a lipid oxidation catalyst in muscle food. *Journal of Agricultural and Food Chemistry*, 1990; 38(3): p. 674-677
- [27] Siddall TL, Ouse DG, Benko ZL, Garvin GM, Jackson JL, McQuiston JM, et al. Synthesis and herbicidal activity of phenyl-substituted benzoylpyrazoles. *Pest Management Science: formerly Pesticide Science*, 2002; 58(12): p. 1175-1186
- [28] Ellman GL, Courtney KD, Andres Jr V, Featherstone RM. A new and rapid colorimetric determination of acetylcholinesterase activity. *Biochemical pharmacology*, 1961; 7(2): p. 88-95
- [29] Kocpinar EF, Gonul Baltaci N, Ceylan H, Kalin SN, Erdogan O, Budak H. Effect of a Prolonged Dietary Iron Intake on the Gene Expression and Activity of the Testicular Antioxidant Defense System in Rats. *Biol Trace Elem Res*, 2020; 195(1): p. 135-141
- [30] Salahshour B, Sadeghi S, Nazari H, Soltaninejad K. Determining undeclared synthetic pharmaceuticals as adulterants in weight loss herbal medicines. *International Journal of Medical Toxicology and Forensic Medicine*, 2020; 10(1): p. 26253
- [31] Skanda S, Vijayakumar B. Antioxidant and antibacterial potential of crude extract of soil fungus *Periconia* sp.(SSS-8). *Arabian Journal for Science and Engineering*, 2022; 47(6): p. 6707-6714
- [32] Campestrini LH, Melo PS, Peres LE, Calhelha RC, Ferreira IC, Alencar SM. A new variety of purple tomato as a rich source of bioactive carotenoids and its potential health benefits. *Heliyon*, 2019; 5(11): p. e02831
- [33] Wangsawat N, Nahar L, Sarker SD, Phosri C, Evans AR, Whalley AJ, et al. Antioxidant activity and cytotoxicity against cancer cell lines of the extracts from novel *Xylaria* species associated with termite nests and LC-MS analysis. *Antioxidants*, 2021; 10(10): p. 1557
- [34] Kucukoglu K, Nadaroglu H. Assessment of the antioxidant and antiradical capacities in vitro of different phenolic derivatives. *Free Radicals and Antioxidants*, 2014; 4(1): p. 24-31
- [35] Zulfqar S, Wahid A, Farooq M, Maqbool N, Arfan M. Phytoremediation of soil cadmium using *Chenopodium* species. *Pak. J. Agri. Sci*, 2012; 49(4): p. 435-445

- [36] Mwamatope B, Tembo D, Chikowe I, Kampira E, Nyirenda C. Total phenolic contents and antioxidant activity of *Senna singueana*, *Melia azedarach*, *Moringa oleifera* and *Lannea discolor* herbal plants. *Scientific African*, 2020; 9: p. e00481
- [37] Gajanayake A, Abeywickrama P, Jayawardena R, Camporesi E, Bundhun D. Pathogenic *Diaporthe* from Italy and the first report of *D. foeniculina* associated with *Chenopodium* sp. *Plant Pathology & Quarantine*, 2020; 10(1): p. 172-197

## SAR Ship Detection Using Image Histograms and Machine Learning Approach

Kazım HANBAY<sup>1\*</sup>, Mücahit ÇALIŞAN<sup>2</sup>, Taha Burak ÖZDEMİR<sup>3</sup>

<sup>1</sup> İnönü University, Engineering Faculty, Software Engineering Department, Malatya, Türkiye

<sup>2</sup> Bingöl University, Engineering-Architecture Faculty, Computer Engineering Department, Bingöl, Türkiye

<sup>3</sup> İnönü University, Engineering Faculty, Computer Engineering Department, Malatya, Türkiye

Kazım HANBAY ORCID No: 0000-0003-1374-1417

Mücahit ÇALIŞAN ORCID No: 0000-0003-2651-5937

Taha Burak ÖZDEMİR ORCID No: 0000-0002-8546-9662

\*Corresponding author: [kazimhanbay@gmail.com](mailto:kazimhanbay@gmail.com)

(Received: 05.08.2024, Accepted: 12.09.2024, Online Publication: 26.09.2024)

### Keywords

Remote sensing,  
Synthetic  
aperture radar,  
Machine learning,  
Eigenvalues

**Abstract:** Ship detection and classification in SAR images is an important and active research area. It provides effective surveillance by facilitating applications such as surveillance and tracking of commercial and military ships. In this study, SAR images were classified using Hessian matrix and HOG algorithm. Using the eigenvalues of the Hessian matrix, the angle and orientation information of the HOG method was calculated. Thus, distinctive pixel characteristics were coded. Our method has obtained desired results in terms of classification accuracy. The proposed method achieved 94.50% classification success.

## Görüntü Histogramları ve Makine Öğrenmesi Yaklaşımı Kullanarak SAR Gemi Tespiti

171

### Anahtar

### Kelimeler

Uzaktan algılama,  
Sentetik  
açıklıklı radar,  
Makine öğrenmesi,  
Özdeşler

**Öz:** SAR görüntülerinde gemi tespiti ve sınıflandırması önemli ve aktif bir araştırma alanıdır. Ticari ve askeri gemilerin gözetimi ve takibi gibi uygulamalarda kolaylık sağlayarak etkin gözetim imkânı sunar. Bu çalışmada SAR görüntüleri Hessian matrisi ve HOG algoritması kullanılarak sınıflandırılmıştır. Hessian matrisinin özdeşleri kullanılarak HOG yönteminin açı ve yönelim bilgisi hesaplanmıştır. Böylece ayırt edici piksel özellikleri kodlanmıştır. Yöntemimiz, sınıflandırma doğruluğu açısından istenilen sonuçlar elde etmiştir. Önerilen metot %94.50 sınıflandırma başarısı elde etmiştir.

## 1. INTRODUCTION

Ship detection and classification in remote sensing images is an important element in maritime surveillance, military missions and commercial operations. The main purpose of ship detection is to detect the type and location of ships in the images. Synthetic aperture radar images provide effective images in all weather conditions. For this reason, images taken from these radars are used extensively in ship detection. Important Synthetic Aperture Radar (SAR) satellites such as Sentinel-1 and TerraSAR-X provide a wide range of SAR data.

Image processing and artificial intelligence methods are used effectively in studies detecting ships in SAR images. The most basic approach is the Constant False Alarm Rate (CFAR) method [1]. The CFAR method detects ships with the generated polarization features and appropriate statistical models. However, achieving the fabrication of handcrafted features that require extensive

prior knowledge is a key shortcoming of CFAR-based methods. Huo et al. [2] use maximally-stable extremal region method to detect proper image regions, and calculate threshold for detecting ships. The attention-guided balanced pyramid and the refined detection head are combined by Fu et al. [3] to identify ships using an anchor-free approach that aims to strike a fair balance between speed and accuracy. In order to enhance detection performance, Pan et al. [4] look into the ship's scattering mechanisms and suggest a unique ship detection technique based on the main contribution of scattering mechanisms. Liu et al. [5] proposed an optimization filter set to detect ships. They combining a polarimetric whitening filter and a polarimetric matched filter. Thus the probability of false alarm was reduced.

Successful results have been achieved with the traditional feature extraction methods mentioned above. In addition, deep learning-based ship detection methods have also been developed. The main motivation for turning to these methods is the desire to develop

methods that do not require hand-crafted feature extraction. Gao et al. [6] proposed a dualistic cascade convolution neural network to PolSAR image ship detection. They used a backbone feature calculation architecture by means of parallel cascade architecture. Thus robust geometric features and polarization features were fused to improve the network performance. Zhu et al. [7] developed a hybrid deep neural network architecture. Their model consists of a detection Network, a duplicate bilateral feature pyramid network, and a feature extraction network. Thus they reduced redundant model parameters and, they detected the small-scale ships. Currently, one difficulty is to maintain acceptable generalization performance while using a deep CNN model with limited training sets for PolSAR target identification and classification. A CenterNet++ deep neural network architecture was developed for small ship detection [8]. A feature refinement module was designed to detecting small ship detection. Complex backgrounds were eliminated using feature pyramids and discriminative feature of foreground. Efficient results have been obtained on AIR-SARShip, SSDD, and SAR-Ship datasets. To estimate ship velocity, a multitask deep learning model has been developed [9]. This study does not require prior wake detection to estimate ship speed. A dataset including 30000 ship images from Sentinel-1 SAR scenes has been constructed. Multi-scale features need to be extracted to detect ships of different scales. This prevents ships of different sizes from being overlooked. In a current study, an appropriate solution to this problem was developed by designing a Swin transformer [10]. In order to address the multi-scale ship problem, they offer a cross-level modulated deformable convolution (CLMD-Conv) for multi-scale feature fusion.

Studies in the literature show that very powerful methods have been developed for ship detection. Methods have been developed using both deep learning and traditional hand-crafted features. It is an easy method to distinguish ship areas in SAR images with the help of pixel brightness information. However, this simple approach does not give good results in the presence of noise and in detecting ships of different sizes. In this study, a ship detection method has been developed by using both the derivative approach and the Histogram Oriented Gradient (HOG) approach, which is a hand-crafted feature extraction method. The proposed method is an expanded and updated version of the study presented as an abstract conference paper [11]. By calculating the Hessian matrix of SAR images, simple pixel brightness changes were encoded. HOG features were calculated using the Hessian matrix, allowing ship regions to be identified and classified.

This paper is designed as follows: In Section 2, the proposed method is presented. The results obtained are presented in Section 3. Some conclusions are presented in Section 4.

## 2. THE PROPOSED METHODOLOGY

### 2.1 Database Construction

There are different SAR ship databases in the literature. Developed ship detection and classification methods are tested using these databases. In this study, a database of 10000 images was created using the Copernicus OpenAccess Hub [12] database, where SAR images are available for sharing free of charge. It is aimed to shed light on future studies for the development of new solutions by using Earth Observation Satellite Data and geospatial Information, which can be obtained free of charge from different sources. Images in this database are labeled as those with or without ships. In creating the database, SAR images were taken from different sea and port areas. The following basic steps were followed to create a database of images taken from the Sentinel-1 SAR satellite:

- 1) The raw SAR images to be obtained have a TIFF format. SAR images with TIFF format were converted to .jpg file format so that image processing and machine learning algorithms can work more accurately and interpretably. Thus, images can be stored with PASCAL VOC format. Geospatial Data Abstraction Library (GDAL) library was used to convert images into jpg extension files.
- 2) After the raw SAR images taken from the Copernicus OpenAccess Hub database were converted to jpg format, the jpeg images, each with an average size of 24000x16000, were divided into sub-images. Literature research shows that the size of subimages can be between 600x600 and 900x900 pixels. In this study, it is aimed to create sub-images of 800x800 size. It has been observed that many ship types of different sizes can be expressed with sufficient resolution in images of this size. It also makes a positive contribution to the computational cost. Each sub-image is divided into subparts so that there is no overlap.

With the studies carried out, a SAR ship database containing 10000 images was created. Sample images in the database are given in Figure 1. The images are divided into 2 folders: with ships and without ships. Thus, the machine learning method will be used for two-class data. Studies on different database construction models are ongoing to label images in the database for use in future deep learning-based studies.

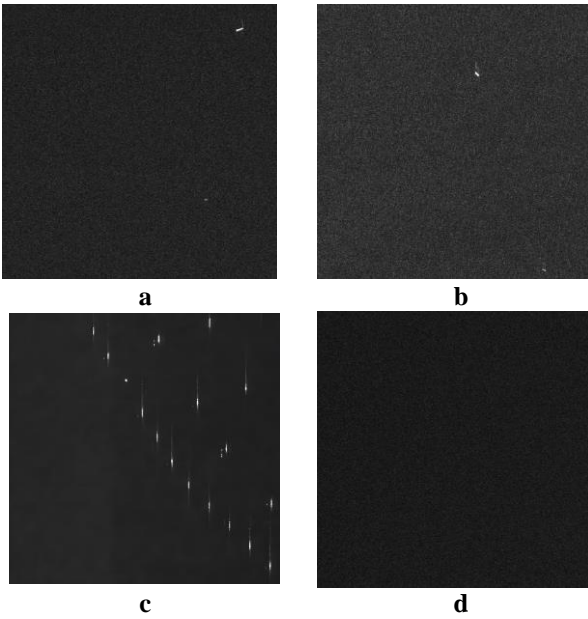


Figure 1. SAR ship and sea images, (a-b-c:ship, d:sea)

## 2.2 The Proposed Model

In this study, a hybrid approach was used to detect ships in SAR images. The main purpose of the hybrid approach is to extract the distinctive features of pixel shadows with different characteristics in images. Figure 1 shows SAR images containing ships. There is a difference in pixel brightness between shadows with and without ships. However, small ships can be found in some SAR images. In addition, under some imaging conditions, the brightness of ships cannot be detected sufficiently. In this case, some light reflections in the ship area and the background are mixed together. Derivative-based approaches give good results in distinguishing between light reflections on the sea surface and ship brightness. Starting from this point, the Hessian matrices of SAR images were calculated and the pixel change information was encoded. Based on this information, feature vectors of ship objects were calculated using the current HOG approach [13].

The Hessian matrix at the scale of any  $(x,y)$  pixel in a gray level image  $I$  is calculated as follows [14]:

$$H_{\sigma}(x, y) = \begin{bmatrix} D_{xx} & D_{xy} \\ D_{yx} & D_{yy} \end{bmatrix} = \begin{bmatrix} I * G_{xx} & I * G_{xy} \\ I * G_{xy} & I * G_{yy} \end{bmatrix} \quad (1)$$

where  $*$  shows the convolution operation,  $D_{xx}$ ,  $D_{yy}$ ,  $D_{xy}$  show the second-order derivations of image for the horizontal, vertical and diagonal directions, respectively.  $G_{xx}$ ,  $G_{yy}$ ,  $G_{xy}$  shows the Gaussian horizontal, vertical and diagonal derivative filters, respectively.

The basic idea in calculating the eigenvalues and eigenvectors of the Hessian matrix is to mathematically reveal the basic directions and basic curvatures on the image surface. Therefore, the local second order differential structure of the image should be examined. By calculating the eigenvalues of the Hessian matrix, the behavior of the pixels in the image and the differential relationship of neighboring pixels with each other can be

analyzed. Because eigenvalues contain the magnitude information of the basic change directions in an image. The eigenvalues of the Hessian matrix are called principal curvatures and are not affected by rotation. The eigenvalues of the Hessian matrix are calculated as follows:

$$\lambda = \pm \sqrt{\frac{(I * G_{xx} - I * G_{yy})^2}{4} + (I * G_{xy})^2} + \frac{I * G_{xx} - I * G_{yy}}{2} \quad (2)$$

where  $\lambda$  shows the eigenvalues of Hessian matrix.

In this paper, eigenvalue information was used instead of traditional gradient calculation in the HOG method. Gradient orientations and gradient magnitudes of the HOG method can be calculated using the  $\lambda_1$  and  $\lambda_2$  eigenvalues matrices.

In the HOG method, the gradient magnitude is calculated as follows [14]:

$$I_{\theta gradient} = \sqrt{(\lambda_1)^2 + (\lambda_2)^2} \quad (3)$$

The gradient orientation of the HOG algorithm is calculated using the eigenvalue information as follows:

$$\theta = \tan^{-1} \left( \frac{\lambda_2}{\lambda_1} \right) \quad (4)$$

The HOG method is used extensively in object recognition problems such as pedestrian detection [13]. It was also used in the ship detection problem discussed, thus enabling the method to be used in a different field. The calculated eigenvalue information was used to calculate the gradient orientation bins in the HOG method. Histogram labeling was done with 9 different angle values. In the next step of the HOG method, histogram divisions are defined with the help of eigenvalue information. Thus, feature vectors of  $1 \times 128$  size of SAR images were calculated. This feature vector contributes to the discrimination capacity of the classifier.

The artificial neural network was used to classify the resulting feature vectors. 80% of the images were used as the training set and 20% as the test set. The artificial neural network was run 10 times to obtain robust results. All experimental studies were carried out in the Matlab environment.

## 3. EXPERIMENTAL RESULTS

In this section, the results of ship classification studies obtained using the SAR database created are mentioned. Since the developed method was tested on a new database, the number of methods used in the comparison was limited. The proposed method is compared with the original LBP method [15]. The LBP method is used

extensively in texture classification. Distinguishing ship regions from the background is also a type of texture classification problem. At this point, the LBP method was used with its original parameters.

Four different performance metrics are used to compare the methods. These metrics have been explained as follows;

- Accuracy: It is used to express the accuracy percentage of the prediction made. It is the ratio of correctly predicted values to the sum of all predicted values.
- Precision: It helps to express how much of the positive predictions made are actually positive. Precision is the ratio of true positive predictions to all positive predictions.
- Recall: It provides information about how many true positive values of the prediction operations resulted correctly.
- F1 Score: It is the harmonic average of precision and recall values.

The classification results of the methods are given in Table 1. As seen from the results, the proposed hybrid approach achieved higher classification results. The main reason for this is the use of a hybrid feature extraction scheme. In many SAR images, ship regions appear as small collections of bright pixels. While methods such as LBP interpret these bright regions, they fail due to the effects of noise. Because pixel behavior should be analyzed in more detail by calculating precise statistical properties from images. At this point, a more precise feature calculation should be made. In the proposed method, these drawbacks are prevented with a hybrid approach. By calculating the eigenvalue/eigenvector of the image, changes in the background were distinguished from the sea surface and noise. Even small pixel intensity changes have been detected with precise derivative calculations.

**Table 1.** Classification results (%)

Method	Accuracy	Precision	Recall	F1-score
LBP method	89.00	88.82	89.05	88.73
Our proposed method	94.50	94.23	94.98	95.09

These differential calculations were effective in improving the object detection success of the HOG method. Eigenvalues were used in the gradient and orientation calculations of the HOG method. Thus, more precise derivative information was used to label the histogram regions. The 94.50% classification success achieved is satisfactory. However, it is predicted that the success of the method will increase, especially by eliminating noise components.

#### 4. CONCLUSION

In this study, a new method for ship classification was developed using the newly created SAR ship database. The developed method used a hybrid approach. An effective feature extraction process was performed using the second order derivatives of the images. In the feature calculation of the HOG method, eigenvalue information

was used instead of the traditional gradient. Gradient magnitudes and orientations calculated with eigenvalues increased the success of the HOG method. Thus the current HOG method can be used to detect ships in SAR images.

It is planned to improve the database with future studies. It is also considered to develop more powerful feature extraction and classification methods such as deep learning.

#### Acknowledgement

This work has been supported by the Scientific and Technological Research Council of Turkey under the project number TÜBİTAK 123E344.

#### REFERENCES

- [1] Huang S qi, Liu D zhi, Gao G qing, Guo X jian. A novel method for speckle noise reduction and ship target detection in SAR images. *Pattern Recognit* 2009;42:1533–42. <https://doi.org/10.1016/J.PATCOG.2009.01.013>.
- [2] Huo W, Huang Y, Pei J, Zhang Q, Gu Q, Yang J. Ship Detection from Ocean SAR Image Based on Local Contrast Variance Weighted Information Entropy. *Sensors* 2018, Vol 18, Page 1196 2018;18:1196. <https://doi.org/10.3390/S18041196>.
- [3] Fu J, Sun X, Wang Z, Fu K. An Anchor-Free Method Based on Feature Balancing and Refinement Network for Multiscale Ship Detection in SAR Images. *IEEE Trans Geosci Remote Sens* 2021;59:1331–44. <https://doi.org/10.1109/TGRS.2020.3005151>.
- [4] Pan X, Wu Z, Yang L, Huang Z. Ship Detection Method Based on Scattering Contribution for PolSAR Image. *IEEE Geosci Remote Sens Lett* 2022;19. <https://doi.org/10.1109/LGRS.2021.3138796>.
- [5] Liu T, Jiang Y, Marino A, Gao G, Yang J. The Polarimetric Detection Optimization Filter and its Statistical Test for Ship Detection. *IEEE Trans Geosci Remote Sens* 2022;60. <https://doi.org/10.1109/TGRS.2021.3055801>.
- [6] Gao G, Bai Q, Zhang C, Zhang L, Yao L. Dualistic cascade convolutional neural network dedicated to fully PolSAR image ship detection. *ISPRS J Photogramm Remote Sens* 2023;202:663–81. <https://doi.org/10.1016/J.ISPRSJPRS.2023.07.006>.
- [7] Zhu H, Xie Y, Huang H, Jing C, Rong Y, Wang C. DB-YOLO: A Duplicate Bilateral YOLO Network for Multi-Scale Ship Detection in SAR Images. *Sensors* 2021, Vol 21, Page 8146 2021;21:8146. <https://doi.org/10.3390/S21238146>.
- [8] Guo H, Yang X, Wang N, Gao X. A CenterNet++ model for ship detection in SAR images. *Pattern Recognit* 2021;112:107787.
- [9] Heiselberg P, Sørensen K, Heiselberg H. Ship velocity estimation in SAR images using multitask deep learning. *Remote Sens Environ* 2023;288:113492. <https://doi.org/10.1016/J.RSE.2023.113492>.



- [10] Liu L, Fu L, Zhang Y, Ni W, Wu B, Li Y, et al. CLFR-Det: Cross-level feature refinement detector for tiny-ship detection in SAR images. *Knowledge-Based Syst* 2024;284:111284. <https://doi.org/10.1016/J.KNOSYS.2023.111284>.
- [11] Hanbay K, Özdemir TB. SAR Ship Detection Based on Differential Image Analysis and Machine Learning Approach. *Int. Conf. Eng. Soc. Sci. Humanit., Mecca*: 2024, p. 46.
- [12] Copernicus Data Space Ecosystem | Europe's eyes on Earth 2024. <https://dataspace.copernicus.eu/>.
- [13] Dalal N, Triggs B. Histograms of oriented gradients for human detection. *Proc - 2005 IEEE Comput Soc Conf Comput Vis Pattern Recognition, CVPR 2005* 2005;I:886–93. <https://doi.org/10.1109/CVPR.2005.177>.
- [14] Hanbay K, Alpaslan N, Talu MF, Hanbay D, Karci A, Kocamaz AF. Continuous rotation invariant features for gradient-based texture classification. *Comput Vis Image Underst* 2015;132:87–101. <https://doi.org/10.1016/J.CVIU.2014.10.004>.
- [15] Ojala T, Pietikäinen M, Mäenpää T. Multiresolution gray-scale and rotation invariant texture classification with local binary patterns. *IEEE Trans Pattern Anal Mach Intell* 2002;24:971–87. <https://doi.org/10.1109/TPAMI.2002.1017623>.

## Classification of Temporary and Real E-mail Addresses with Machine Learning Techniques

Caner BALIM<sup>1\*</sup>, Nevzat OLGUN<sup>2</sup>

<sup>1</sup> Afyon Kocatepe University, Engineering Faculty, Software Engineering Department, Afyonkarahisar, Türkiye

<sup>2</sup> Afyon Kocatepe University, Engineering Faculty, Software Engineering Department, Afyonkarahisar, Türkiye

Caner BALIM ORCID No: 0000-0002-1010-129X

Nevzat OLGUN ORCID No: 0000-0003-2461-4923

\*Corresponding author: cbalim@aku.edu.tr

(Received: 20.07.2024, Accepted: 12.09.2024, Online Publication: 26.09.2024)

### Keywords

E-mail  
classification,  
Natural  
language  
processing,  
Artificial neural  
network,  
Machine  
learning

**Abstract:** Temporary e-mail addresses are e-mail addresses that users can quickly create without signing up. These e-mail addresses are useful for privacy and to avoid spam. However, they also pose several serious cyber threats, including fraud, spam campaigns, and fake account creation. In this study, a method utilizing natural language processing and machine learning techniques is proposed to classify real and temporary e-mail addresses. First, temporary and real e-mail addresses are analyzed, and features are developed to identify the differences between them. These features include lexical structures, broad contexts, and structural features of e-mail addresses. Various machine learning algorithms were then applied on the resulting feature set to differentiate e-mail addresses. The results were evaluated with K-fold cross-validation method and an accuracy rate of 96% was obtained. This success rate shows that the developed method can successfully distinguish between real and temporary e-mail addresses.

## Geçici ve Gerçek E-posta Adreslerinin Makine Öğrenme Teknikleriyle Sınıflandırılması

### Anahtar Kelimeler

E-mail  
sınıflandırma,  
Doğal dil  
işleme,  
Yapay sinir  
ağı,  
Makine  
öğrenmesi

**Öz:** Geçici e-posta adresleri, kullanıcıların üye olmadan hızlı bir şekilde oluşturabildikleri e-posta adresleridir. Bu e-posta adresleri gizlilik ve istenmeyen e-postalardan kaçınmak için yararlıdır. Fakat bu e-postalar adreslerinin dolandırıcılığa, spam kampanyalarında kullanılma ve sahte hesap oluşturmaya kadar bir dizi ciddi siber tehdidi de bulunmaktadır. Bu çalışmada, gerçek ve geçici e-posta adreslerini sınıflandırmak için doğal dil işleme ve makine öğrenme tekniklerinden yararlanan bir yöntem önerilmiştir. Öncelikle, geçici ve gerçek e-posta adresleri analiz edilmiş ve arasındaki farkları belirlemeye yönelik öznitelikler geliştirilmiştir. Bu öznitelikler, e-posta adreslerinin leksik yapılarını, geniş bağlamlarını ve yapısal özelliklerini içermektedir. Sonrasında elde edilen öznitelik seti üzerinde, çeşitli makine öğrenme algoritmaları uygulanmış ve e-posta adresleri ayırt edilmeye çalışılmıştır. Elde edilen sonuçlar, K-katlı çapraz doğrulama yöntemiyle değerlendirilmiş ve %96 doğruluk oranı elde edilmiştir. Bu başarı oranı, geliştirilen yöntemin gerçek ve geçici e-posta adreslerini başarılı bir şekilde ayırt edebileceğini göstermektedir.

## 1. INTRODUCTION

Temporary e-mail addresses are mainly used for short-term, anonymous e-mail communication. Such addresses are usually valid for periods ranging from a few minutes to a few days, after which they automatically disappear. Temporary e-mail services allow users to create e-mail addresses quickly and without registration. These services are often used during online registrations, forums, or various downloads over the Internet. In this way, users do not risk their personal or business e-mail addresses for

such temporary activities. They are also widely used to avoid spam e-mails and to protect online privacy.

While temporary e-mails are helpful, they also have the potential for misuse. For example, some users may use such addresses to create multiple accounts, violate terms of service, or engage in illegal activities. This can lead to security and management challenges for online platforms and services. Therefore, detecting and managing temporary e-mail addresses has become an important issue, especially for businesses and service providers.

There are not many arguments that can be used to identify temporary e-mail addresses other than their addresses. Classification based solely on e-mail addresses seems to be a technically simpler process when performed on the basis of certain criteria, but it has its own difficulties. Although the structure of the addresses is generally standardized, it is very difficult to make inferences based on features such as the information contained in the address and the domain name used. In order to develop a good classification algorithm, it is very important to know the structure of e-mail addresses. E-mail addresses can be structurally divided into two main parts:

1. Local part: The part of the e-mail address that comes before the "@" sign. It may contain the user's name, alias, or other identifying information. The local part may be case-sensitive.
2. Domain part: The part of the e-mail address that comes after the "@" sign. This part is usually associated with the name of a website (example.com, etc.) and is not case-sensitive. The domain part includes the Top-Level domain (TLD). TLDs located within the domain are used to provide more specific addressing. Different sub-domains such as ".com", ".edu", and ".gov" can be defined.

The at ("@") and dot (".") Symbols are very important in e-mail addresses. The at sign is used to distinguish between the local part and the domain part. The dot can be used both in the local and domain parts. The dot sign is used in the local part to separate different words or sections, while in the domain it is used to separate TLDs. In addition to the period, signs such as underscore (\_) and plus (+) can be used in the local part of e-mail addresses. However, the use of special characters in the domain part is very limited.

There are various studies on e-mail address classification in the literature [1], [2], [3], [4]. It was observed that Enron and Spam Assassin data sets are used in the majority of the studies [5], [6]. Since there is limited information about e-mail addresses, it has been observed that most of the classification studies have been used with the content of the e-mail address. Also, it has been observed that in most studies, researchers focus on ham-spam classification and security analysis (ham-phishing, etc.).

Ham-spam e-mail classification is one of the issues that has attracted the attention of researchers since long ago. The term "ham" means "clean" or "correct" in the context of e-mail classification. Many important works have been proposed in this area. Nowadays, many models show excellent performance with over 90% accuracy. Most of the current work is carried out using deep learning-based approaches. In particular, Long Short-Term Memory (LSTM), which is a type of Recurrent Neural Network (RNN), and Transformer-based BERT (Bidirectional Encoder Representations from Transformers) approaches are widely used [7]. Debnath and Kar obtained 99.14% accuracy by using BERT, LSTM, and natural language processing (NLP) techniques on the Enron e-mail dataset

[8]. In their study on the Enron dataset, Krishnamoorthy et al. used an LSTM-based hybrid deep learning approach and obtained an accuracy rate of approximately 98% [9]. AbdulNabi and Yaseen used BERT to demonstrate the effectiveness of word embedding in spam e-mail classification [10]. In addition to the successful results obtained with deep learning techniques, some traditional algorithms also give very successful results [2], [11], [12]. Dedeturk and Akay proposed a method combining logistic regression with artificial bee colony algorithm for spam detection [11]. Saidani et al. proposed a two-step semantic analysis for e-mail spam analysis [2]. In the first step, the categorization of the e-mail is performed; in the second step, domain-specific semantic features are extracted.

Another important issue on e-mail classification that attracts the attention of researchers is the detection of phishing attacks. Phishing attacks are a type of cyber-attack in which hackers aim to mislead users into accessing sensitive information. Attackers mostly aim to steal important information such as usernames, passwords, credit cards. Such attacks are often conducted through e-mails that appear legitimate but are malicious. Rastenis et al. created a taxonomy of e-mail-based phishing attacks [13]. For more detailed information, this study can be reviewed.

An analysis of the studies in the literature shows that NLP and Machine Learning (ML) techniques have been applied to the task of ham-phishing email classification, as well as ham-spam classification [3]. Gholampour and Verma developed an enriched ham-phishing e-mail dataset on different phishing attacks using GPT-2 [14]. Kumar et al. developed a hybrid phishing detection system combining SVM classification and feature extraction [15]. Fang et al. first analyzed the e-mail structure and then used a special recurrent convolutional neural network model to model e-mails according to their features, such as header, body, and character level [16]. More details on phishing mail detection using natural language processing techniques can be found in the review by Salloum et al [17].

In this study, a model that performs the classification of temporary e-mail addresses and real e-mail addresses is proposed. Temporary e-mail addresses are services that have good features, such as providing anonymity to users, but also have the possibility of abuse (violating the terms of service or engaging in illegal activities, etc.). Within the scope of research, no previous study on this subject and no data set has been found in the literature. In the study, NLP and ML techniques, which are frequently studied by researchers, are utilized. The study's main contributions can be summarized as follows:

- A model is proposed to detect temporary e-mail addresses using NLP and ML techniques. A hybrid approach is followed, and different type of feature categories are combined.
- The impact of different feature types (lexical structures, broad contexts and structural features) on e-mail address classification is shown. In addition,

the effect of different feature pairs on classification is also shown.

- A new dataset that can be used in e-mail classification tasks has been produced. When building the dataset, care was taken to ensure that the e-mail addresses collected were from different domains and TLDs. The dataset contains a close ratio of temporary and real e-mail addresses.

The article is structured as follows: Section 2 describes the material and method used for problem solving. Section 3 presents experimental results and comments. Finally, Section 4 concludes and makes suggestions for future research.

## 2. MATERIAL AND METHODOLOGY

In this section, firstly, the material on which the presented methods are applied is explained, and then the general steps of the method are explained in detail.

### 2.1. Material

There are over 100 different temporary email providers on the Internet. These providers usually provide valid email addresses for 10 minutes with different domain addresses. As a result of the research carried out, a new data set was created since there was no publicly available data set on this subject before. For this purpose, e-mail addresses were collected from different temporary e-mail address providers. Then, verified publicly available email addresses were collected. While collecting real email addresses, sample addresses were also taken from different institutions and organizations, such as universities, governments, and e-commerce sites, for a fair approach. In order to create a balanced data set while collecting email addresses, care was taken to have a close number of samples in each class. As a result, statistics about the email addresses collected are shown in Table 1.

Table 1. Dataset Statistic

Real	Temporary	Total
719	765	1484

### 2.2. Methodology

The methodology aims to predict whether the e-mail is temporary or real based on combining different features extracted from e-mail addresses. The proposed approach consists of two main parts: Feature extraction and classification.

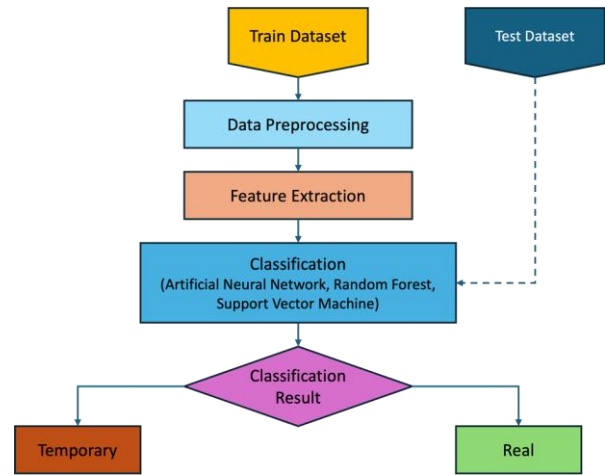


Figure 1. Schematic of the proposed system

#### 2.2.1. Feature extraction

In the process of classifying e-mail addresses, the strategic use of NLP techniques for feature extraction is critical. While deep learning methodologies have delivered impressive results in various text analysis and processing areas, direct deep learning-based feature extraction on specialized and structured data types such as e-mail addresses presents significant challenges due to the data's limited context and its specific structural properties. Therefore, to extract features in the proposed model, weighting methods such as Term Frequency-Inverse Document Frequency (TF-IDF), which have proven successful in text classification and analysis, and spelling control techniques such as the Levenshtein distance are used to extract meaningful and actionable features from e-mail addresses.

In this study, traditional NLP techniques have been utilized to classify between temporary and real e-mail addresses. A hybrid approach that combines different types of features has been employed for better classification performance.

##### 2.2.1.1. Term frequency-inverse document frequency (TF-IDF)

TF-IDF is a statistical method used in text mining and information retrieval. It is used to determine the importance of a term in a document relative to a corpus. TF-IDF is frequently used for NLP tasks such as e-mail classification [4], [18], [19]. It comprises two components: Term Frequency (TF) and Inverse Document Frequency (IDF).

Term Frequency (TF) quantifies the frequency of a term in a document relative to the total number of terms in that document. It is calculated using the formula:

$$TF(t, d) = \frac{\text{Number of occurrences of term } t \text{ in the document}}{\text{Total number of terms in the document}} \quad (1)$$

Inverse Document Frequency (IDF) measures the significance of a term across the corpus. It is calculated as:

$$IDF(t,D) = \log\left(\frac{\text{Total number of documents in the corpus}}{\text{Number of documents containing term}}\right) \quad (2)$$

The TF-IDF score is obtained by multiplying the TF and IDF scores for each term:

$$TF-IDF(t,d,D) = TF(t,d) \times IDF(t,D) \quad (3)$$

In this study, TF-IDF is used to extract features from e-mail addresses. Before applying TF-IDF, e-mail addresses are preprocessed by removing punctuation marks (@, +, etc.) to standardize the representation and remove non-informative characters. In the next step, a character-level approach is adopted using 1-2 n-grams. This involves breaking the e-mail addresses into substrings of 1 to 2 characters and computing TF-IDF scores for these character n-grams. In this way, it is aimed to capture patterns and features in the structure of e-mail addresses that may not be noticeable at the word level.

### 2.2.1.2. Top-level domain features

In an e-mail address, the term "Top-Level Domain" (TLD) refers to the last part of the domain name, typically following the final dot ("."). This part of the domain name provides information about the type or purpose of the domain. Common examples of TLDs include ".com", ".org", ".net", ".gov", and ".edu". For example, ".gov" indicates a government organization, ".edu" represents an educational institution, and ".org" often denotes a non-profit organization.

In this study, the most common TLDs in the dataset were compiled and the 15 most used TLDs are added to the model as attributes. This process aimed to capture the potential influence of TLDs on the classification task. The inclusion of TLD-related features enhances the model's ability to distinguish between different types of e-mail addresses based on their domain structure, thereby improving the overall performance of the classification system. Table 2 shows the most common TLDs in the e-mail addresses in the data set.

**Table 2.** The 15 most mentioned TLDs in the data set.

No	TLDs
1	.com
2	.edu
3	.org
4	.gov
5	.bel
6	.net
7	.kep
8	.co
9	.app
10	.email
11	.digital
12	.info
13	.site
14	.xyz
15	.store

### 2.2.1.3. Spelling features

Detecting spelling errors in the local and domain parts of e-mail addresses can play an important role in determining temporary e-mail addresses. Systems that provide temporary e-mail addresses often consist of domains with irregular structures or generate usernames that do not follow spelling rules. Spell checking evaluates the meaning and integrity of local or domain domains, and the domain names of real and reliable e-mail addresses usually have a meaningful and consistent structure.

In this study, the English and Turkish dictionaries of Open Office, an open-source application, were used for spell checking [20]. The words in the dictionaries were compared with the local and domain parts of the e-mail addresses and labelled according to their presence in the dictionary. Non-matching parts are evaluated with Levenshtein distance.

The Levenshtein distance, used to measure the difference between two sequences, is a metric announced by V. I. Levenshtein in 1965 [21]. It has a wide range of applications, including plagiarism detection, spell checking, and bioinformatics [22]. The Levenshtein distance algorithm attempts to find the minimum number of edits required to compare two sequences character by character and convert one sequence into the other. It uses a dynamic programming technique to calculate the distance between sequences of different lengths.

If there are two sequences  $x$  and  $y$  and the lengths of these sequences are  $m$  and  $n$  respectively, the Levenshtein distance ( $L(x,y)$ ) between the two sequences is calculated as follows:

- If both  $m$  and  $n$  are 0, then  $L(x,y) = 0$ .
- If  $m$  is 0 and  $n$  is not,  $L(x,y)$  is equal to  $n$ .
- Similarly, if  $n$  is 0 and  $m$  is not,  $L(x,y)$  is equal to  $m$ .
- If both  $m$  and  $n$  are not 0. Their last characters  $x_{(m-1)}$  and  $y_{(n-1)}$ . The Levenshtein distance can be calculated by considering the following scenarios:

1. If  $x_{m-1} = y_{n-1}$ , no operation is needed. In this case,  $L(x,y) = L(x_{m-2}, y_{n-2})$ .
2. If  $x_{m-1} \neq y_{n-1}$ , calculate the minimum cost among three operations (insertion, deletion, substitution):

- a. Insertion:

$$L(x, y_{n-1}) = L(x, y_{n-2}) + 1 \quad (4)$$

- b. Deletion:

$$L(x_{m-1}, y) = L(x_{m-2}, y) + 1 \quad (5)$$

- c. Substitution:

$$L(x_{m-1}, y_{n-1}) = L(x_{m-2}, y_{n-2}) + 1 \quad (6)$$

This operation is performed as the product of the dimensions of the two sequences (mxn).

In this study, for each e-mail address in the dataset, both the local and domain parts of the e-mail address are checked for spelling separately and the Levenshtein score is calculated according to the close values found in the dictionaries and a feature vector is created.

#### 2.2.1.4. Handcrafted features

In the context of machine learning and data analytics, the term "handcrafted features" refers specifically to features designed and selected by human experts from the raw data in the dataset. In this study, five handcrafted features are used that are considered to be discriminative in classifying temporary and real e-mail addresses:

- **Check for punctuation in the local part:** This feature checks whether the local part of the e-mail address contains punctuation (".", "-", "\_", etc.). When the local parts of both types are compared, it is seen that very few punctuation marks are used in the local fields of temporary e-mail addresses.
- **Number of letters in the local part:** This feature counts the number of alphabetic characters in the local part of the e-mail address. An examination of the local parts of temporary and real e-mail addresses shows that the number of letters in the local parts of temporary e-mail addresses is in most cases less than the number of letters in the local parts of real e-mail addresses.
- **Number of digits in the local part:** This feature counts the number of digits in the local part of the e-mail address. Analyses of the local parts of temporary and real e-mail addresses show that the number of digits in the local parts of temporary e-mail addresses is in most cases higher than the number of digits in the local parts of real e-mail addresses.
- **Number of punctuation marks in the local and domain parts:** This feature counts the number of punctuation marks in the local and domain parts of the email address. Analysis has shown that the number of punctuation marks used in temporary e-mail addresses is lower than the number of punctuation marks found in real e-mail addresses.
- **Country-code Top Level Domain(ccTLD) existence check:** ccTLDs are two-letter TLDs that represent a specific country or region. This feature examines whether the domain part of the e-mail address has a country or region representation. In the scans, it has been observed that the use of ccTLD in temporary e-mail addresses is quite low.

In this study, values are generated for each e-mail address in the training and test sets using the five discriminative features mentioned above and feature vectors are created with the generated values.

### 2.2.2. Classifiers

The classifier uses extracted features to classify e-mails as transient or real. Depending on the selected feature pairs, the classifiers detect temporary e-mails from the input data after the training phase.

#### 2.2.2.1. Artificial neural networks (ANNs)

Artificial Neural Networks (ANNs) are an advanced machine learning method that excels in processing nonlinear data inspired by the human nervous system. ANNs operate through two main phases: Forward propagation and backward propagation. Forward propagation refers to the process by which data moves from input to output layers through transformations. The process by which the weights and biases of the network are adjusted through gradient descent to minimize errors between predicted and actual outputs is called backward propagation. This cycle repeats until the network's performance meets the desired criteria. ANNs' ability to learn from data iteratively and model complex relationships makes them highly versatile and effective for various applications, from pattern recognition to predictive modeling.

In the proposed method, a multilayer perceptron (MLP) based classifier model is used as the ANN classifier [23]. Three hidden layers are identified in the MLP model; There are 500 neurons in the first hidden layer, 100 neurons in the second hidden layer and 50 neurons in the third hidden layer. Rectified Linear Unit (ReLU) is used as the activation function. Adaptive Moment estimation (Adam) is chosen as the optimization algorithm.

#### 2.2.2.2. Support vector machines (SVMs)

Support Vector Machines (SVM) is an ML method for classification and regression tasks [24]. SVMs are designed to classify data into distinct categories by constructing a hyperplane in a high-dimensional space. This method hinges on maximizing the margin between the hyperplane and the nearest data points from each category, known as support vectors. SVM aims to find the optimal hyperplane that separates the classes with the greatest possible margin. The effectiveness of SVM lies in its ability to transform the original feature space into a higher dimensional space where a linear separation is feasible, thanks to the kernel trick, thereby accommodating complex and nonlinear relationships between data points.

#### 2.2.2.3. Random forest (RF)

Random Forest (RF) is a powerful ensemble learning technique for both classification and regression tasks where many decision trees are trained together [25]. Based on the concept of bootstrap aggregation (bagging), RF improves the decision tree algorithm by creating a 'forest' of trees where each tree is trained on a random subset of data and features, thus reducing variance and preventing overfitting. By combining predictions from multiple trees, RF can achieve higher accuracy and

stability than a single decision tree. RF is frequently used in classification problems such as spam detection.

**2.2.3. Evaluation metrics**

The evaluation metrics such as accuracy, precision, and recall values were measured by the proposed method. The formula for accuracy, precision and recall were shown in equations (7) – (9).

In Equation 7 and the following, TP defines the number of instances of correctly classified temporary e-mails, while FP defines the number of e-mails that may be incorrectly classified as temporary when an e-mail is real. TN defines the number of instances of e-mails correctly classified as real e-mails. FN refers to the case where an e-mail that is actually temporary is mistakenly classified as real.

$$Accuracy = \frac{TP + TN}{TP + TN + FP + FN} \tag{7}$$

Precision refers to the ratio of temporary e-mail addresses predicted by the model to actual temporary e-mail addresses. The precision formula is given in Equation 8. A high precision value indicates that the model keeps the number of false positives to a minimum and produces mostly correct results.

$$Precision = \frac{TP}{TP + FP} \tag{8}$$

Recall refers to the rate at which actual temporary e-mail addresses are correctly predicted. The Recall formula is shown in Equation 9. A high recall value means that the model does not miss actual temporary e-mail addresses and classifies most of them correctly.

$$Recall = \frac{TP}{TP + FN} \tag{9}$$

**3. EXPERIMENT RESULT**

This section presents the experimental studies and discussion. The e-mail addresses in the dataset were first pre-processed with the techniques described in the previous section, and then the features were extracted and combined. The performance measurements of the proposed model are obtained by using the relations between Equations 7-9. The training and test rates were set as 70% and 30%, respectively. The training and test data of the temporary and real e-mail addresses in the dataset were separated according to the K-Fold technique. The results are shown in Table 3.

**Table 3.** Accuracy values of the proposed model according to K Fold options.

Classifier	1	2	3	4	5	Average
ANN	<b>0.9663</b>	0.9494	<b>0.9730</b>	0.9494	<b>0.9662</b>	<b>0.9609</b>
SVM	0.9360	0.9495	0.9428	<b>0.9529</b>	0.9392	0.9441
RF	0.9495	<b>0.9596</b>	0.9394	<b>0.9529</b>	0.9493	0.9501

As shown in Table 3, five different results were obtained with the KFold-5 technique and these results were averaged. When examined according to average values, it is seen that a test accuracy rate of 0.9609 was achieved with the ANN technique. It is observed that the most successful technique after the ANN technique is the RF technique with an accuracy value of 0.9501.

A comparison of the performance of the ANN model using various feature sets on the task of ephemeral e-mail detection is shown as a heat map in Figure 2.

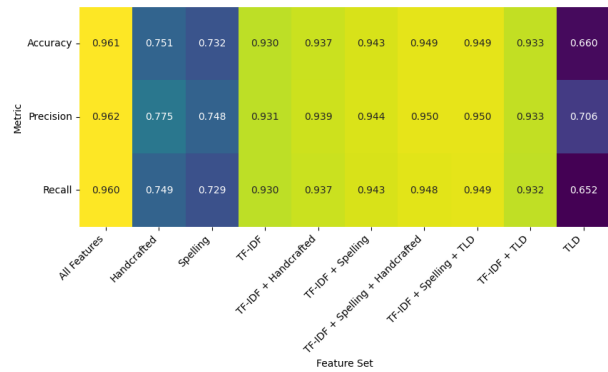


**Figure 2.** Performance comparison of ANN classification based on various feature sets.

When Figure 2 is examined, it shows that the feature sets used are effective in distinguishing between temporary and real e-mail addresses. When the features are evaluated individually, it is observed that the TF-IDF feature achieves more successful results compared to others. In individual evaluation, the handcrafted features are seen to be the most successful single feature after TF-IDF. When the features are evaluated in pairs with TF-IDF, it is seen that TF-IDF and spelling features (TF-IDF + Spelling) complement each other and produce more successful results than the others. However, in the three-group valuation, the results are not observed to be much different from those obtained with TF-IDF and Spelling features (TF-IDF + Spelling).

It is seen that the TLDs produces the lowest results in the experiments. The reason for this may be the presence of TLDs such as ".com" in almost all e-mail addresses. In addition, it was observed that the TLD ".edu", which was thought to be distinctive in the analyses, is also found in some temporary e-mail addresses. This explains the reason for the lower success of TLD features.

According to Figure 2, the "All Features" set shows the highest performance because it contains the most comprehensive information. However, the use of specific feature sets, such as TF-IDF and Spelling, may be sufficient to achieve nearly similar or better results in certain cases. This shows that the success of the classification model depends on the quality and relevance of the features used.

The accuracy of the proposed method with various feature sets and classifiers is shown in Figure 3. While the TF-IDF feature set has the highest accuracy value when used with the ANN model, the RF model shows higher

accuracy values in models where TF-IDF is not included. It was observed that the TLD feature was the most ineffective feature when considered alone, but when combined with other features, it improved the results. Although the Handcrafted feature set has low accuracy values when used with ANN, it is observed that its performance improves when used with SVM and RF models.

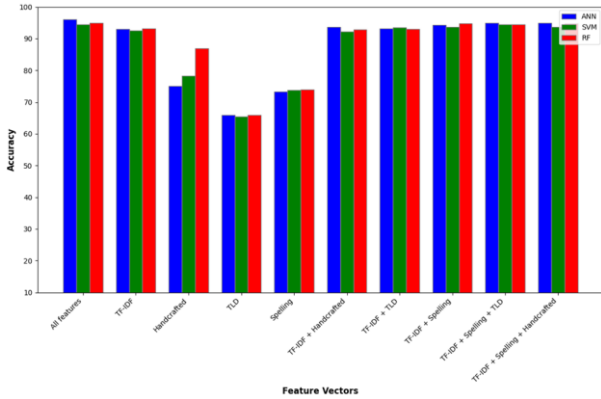


**Figure 3.** Accuracy of temporary e-mail detection with various feature vectors and classifiers.

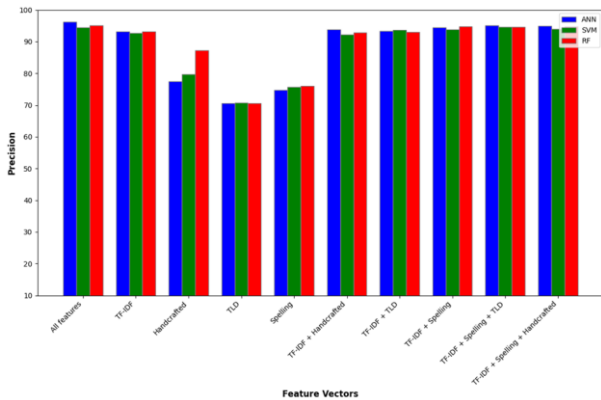


**Figure 4.** Precision of temporary e-mail detection with various feature vectors and classifiers

In Figure 4 and Figure 5, the precision and recall values of the proposed method are compared for various classifiers and feature sets, respectively. When the TF-IDF feature set is used, the ANN model achieved the highest precision and recall values. However, when TF-IDF and other feature sets (spelling, handcrafted, TLD) are used, different machine learning models also gave good results. In particular, the “All features” set provided the highest precision and recall values for the ANN model. When all features set is used, the precision value of the ANN model is approximately 0.962, while the precision value of the SVM model is approximately 0.945 and the precision value of the RF model is approximately 0.951. Similarly, when the all-feature set is used, the recall value of the ANN model is approximately 0.960, while the recall value of the SVM model is approximately 0.944 and the recall value of the RF model is approximately 0.950.

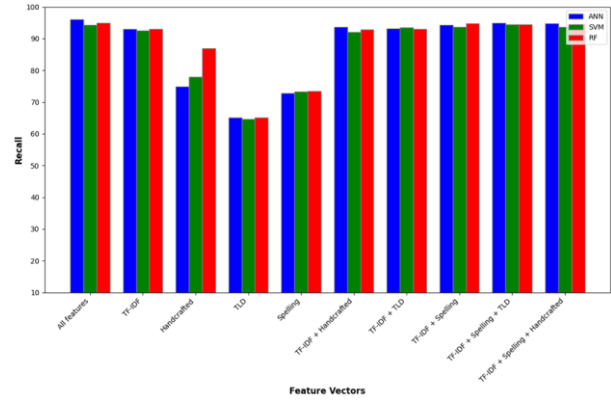


**Figure 5.** Recall of temporary e-mail detection with various feature vectors and classifiers

#### 4. CONCLUSION

Temporary e-mail addresses allow users to protect their privacy and avoid potentially harmful situations such as receiving spam e-mail. However, when misused, they bring a number of serious cyber threats ranging from cyber security breaches to fraud, spam e-mails, and fake account creation. In this study, a method using various feature sets and machine learning techniques is proposed to classify temporary and real e-mail addresses. As a result of the experiments, an accuracy value of 0.9606 was obtained for the classification of temporary and real e-mail addresses, and the performance of different feature sets and machine learning models were compared in detail.

As a result of the experiments, it is observed that especially the TF-IDF feature set and its combinations with various feature sets achieve high accuracy rates. In particular, the combination of TF-IDF and spelling features is found to produce quite adequate results for this task.

When a comparison is made on a model basis, it is observed that the ANN method mostly performs the best. The ability of the ANN model to effectively handle the complexities in the dataset and the interactions between the features is considered to be an important factor in the classification success. The other methods used in the experiments, RF and SVM, also obtained competitive results, but they were not as successful as ANN. The robust structure and high generalization capacity of ANN is thought to make it prominent for this type of classification problems.

The results obtained from the experiments show that the selection of the right feature sets and learning models can significantly affect the classification performance. It is thought that the findings obtained will contribute to research in areas such as the development of e-mail classification systems and the improvement of spam filtering techniques. Future studies are planned to investigate the effectiveness of different feature selection techniques and machine learning models in this task.



## REFERENCES

- [1] Diale, M., Celik, T., & Van Der Walt, C. (2019). Unsupervised feature learning for spam email filtering. *Computers & Electrical Engineering*, 74, 89–104. <https://doi.org/10.1016/j.compeleceng.2019.01.004>
- [2] Saidani, N., Adi, K., & Allili, M. S. (2020). A semantic-based classification approach for an enhanced spam detection. *Computers & Security*, 94, 101716. <https://doi.org/10.1016/j.cose.2020.101716>
- [3] Salloum, S., Gaber, T., Vadera, S., & Shaalan, K. (2021). Phishing email detection using natural language processing techniques: A literature survey. *Procedia Computer Science*, 189, 19–28. <https://doi.org/10.1016/j.procs.2021.05.077>
- [4] Sanghani, G., & Kotecha, K. (2019). Incremental personalized e-mail spam filter using novel TFDCR feature selection with dynamic feature update. *Expert Systems with Applications*, 115, 287–299. <https://doi.org/10.1016/j.eswa.2018.07.049>
- [5] Kaggle. (2024). The Enron email dataset. Kaggle. <https://www.kaggle.com/datasets/wcukierSKI/enron-email-dataset>
- [6] Kaggle. (2024). The Spam Assassin email dataset. Kaggle. <https://www.kaggle.com/datasets/ganiyuolalekan/spam-assassin-email-classification-dataset>
- [7] Vaswani, A., Shazeer, N., Parmar, N., Uszkoreit, J., Jones, L., Gomez, A. N., Kaiser, Ł., & Polosukhin, I. (2017). Attention is all you need. In *Advances in Neural Information Processing Systems* (pp. 5999–6009). <https://arxiv.org/abs/1706.03762v5>
- [8] Debnath, K., & Kar, N. (2022). Email spam detection using deep learning approach. In *2022 International Conference on Machine Learning, Big Data, Cloud and Parallel Computing (COM-IT-CON)* (pp. 37–41). <https://doi.org/10.1109/COM-IT-CON54601.2022.9850588>
- [9] Krishnamoorthy, P., Sathiyarayanan, M., & Proença, H. P. (2024). A novel and secured email classification and emotion detection using hybrid deep neural network. *International Journal of Cognitive Computing in Engineering*, 5, 44–57. <https://doi.org/10.1016/j.ijce.2024.01.002>
- [10] AbdulNabi, I., & Yaseen, Q. (2021). Spam email detection using deep learning techniques. *Procedia Computer Science*, 184, 853–858. <https://doi.org/10.1016/j.procs.2021.03.107>
- [11] Dedeturk, B. K., & Akay, B. (2020). Spam filtering using a logistic regression model trained by an artificial bee colony algorithm. *Applied Soft Computing*, 91, 106229. <https://doi.org/10.1016/j.asoc.2020.106229>
- [12] Gibson, S., Issac, B., Zhang, L., & Jacob, S. M. (2020). Detecting spam email with machine learning optimized with bio-inspired metaheuristic algorithms. *IEEE Access*, 8, 187914–187932. <https://doi.org/10.1109/ACCESS.2020.3030751>
- [13] Rastenis, J., Ramanauskaitė, S., Janulevičius, J., Čenys, A., Slotkienė, A., & Pakrijauskas, K. (2020). E-mail-based phishing attack taxonomy. *Applied Sciences*, 10(7), 72363. <https://doi.org/10.3390/app10072363>
- [14] Mehdi Gholampour, P., & Verma, R. M. (2023). Adversarial robustness of phishing email detection models. In *Proceedings of the 9th ACM International Workshop on Security and Privacy Analytics (IWSPA '23)* (pp. 67–76). <https://doi.org/10.1145/3579987.3586567>
- [15] Kumar, A., Chatterjee, J. M., & Díaz, V. G. (2020). A novel hybrid approach of SVM combined with NLP and probabilistic neural network for email phishing. *International Journal of Electrical and Computer Engineering (IJECE)*, 10(1), 486–493. <https://doi.org/10.11591/ijece.v10i1.pp486-493>
- [16] Fang, Y., Zhang, C., Huang, C., Liu, L., & Yang, Y. (2019). Phishing email detection using improved RCNN model with multilevel vectors and attention mechanism. *IEEE Access*, 7, 56329–56340. <https://doi.org/10.1109/ACCESS.2019.2913705>
- [17] Salloum, S., Gaber, T., Vadera, S., & Shaalan, K. (2022). A systematic literature review on phishing email detection using natural language processing techniques. *IEEE Access*, 10, 65703–65727. <https://doi.org/10.1109/ACCESS.2022.3183083>
- [18] Barushka, A., & Hajek, P. (2018). Spam filtering using integrated distribution-based balancing approach and regularized deep neural networks. *Applied Intelligence*, 48(10), 3538–3556. <https://doi.org/10.1007/s10489-018-1161-y>
- [19] Srinivasarao, U., & Sharaff, A. (2023). Spam email classification and sentiment analysis based on semantic similarity methods. *International Journal of Computer Science and Engineering*, 26(1), 65–77. <https://doi.org/10.1504/ijcse.2023.129147>
- [20] Apache OpenOffice. (2024). Apache OpenOffice extensions. OpenOffice. <https://extensions.openoffice.org/>
- [21] Levenshtein, V. (1965). Binary codes capable of correcting deletions, insertions, and reversals. *Soviet Physics Doklady*.
- [22] Berger, B., Waterman, M. S., & Yu, Y. W. (2021). Levenshtein distance, sequence comparison and biological database search. *IEEE Transactions on Information Theory*, 67(6), 3287–3294. <https://doi.org/10.1109/TIT.2020.2996543>
- [23] Russell, S. J., & Norvig, P. (2010). *Artificial intelligence: A modern approach* (3rd ed.). Prentice Hall.
- [24] Cortes, C., & Vapnik, V. (1995). Support-vector networks. *Machine Learning*, 20(3), 273–297. <https://doi.org/10.1007/BF00994018>
- [25] Liaw, A., Wiener, M., & others. (2002). Classification and regression by randomForest. *R News*, 2(3), 18–22.

## Microbial Quality of Drinking and Utility Water in Tourism Facilities in Antalya

Rişan Elif NURAL<sup>1</sup> , Nadide SEYHUN<sup>1\*</sup> 

<sup>1</sup> Bursa Technical University, Faculty of Engineering and Natural Sciences, Department of Food Engineering, Bursa, Türkiye

Rişan Elif NURAL ORCID No: 0000-0002-6073-890X

Nadide SEYHUN ORCID No: 0000-0002-0086-8374

\*Corresponding author: nadide.seyhun@btu.edu.tr

(Received: 26.08.2024, Accepted: 12.09.2024, Online Publication: 26.09.2024)

### Keywords

*E. coli*,  
Total coliform,  
Microbiological  
water quality,  
Tourism  
facilities,  
Water hygiene

**Abstract:** The microbial quality of drinking and utility water is important for public health, environmental safety, and overall well-being. Contaminated water can harbor harmful microorganisms that can cause a wide range of diseases. Governments set standards for the microbiological quality of drinking water, and it is required to regularly test and monitor the microbial content of water to meet these standards. This study investigated the microbial quality of drinking and utility water in different hotels in Antalya during high season (June – July – August – September) in 2022 and 2023. 270 water samples for each year – 540 samples in total were collected from 12 different hotels. Total coliform and *E. coli* analyses were performed via membrane filtration analysis, and the results were verified by using oxidase test and indole test. The results showed that only 1 hotel out of 12 have met the safety criteria required in the legislation. All the other 11 hotels had overall microbial counts over the legal limits. In 2022, total coliforms were detected in 8 hotels at 29 different sample spots, and *E. coli* growth was found in the water used for washing vegetables only in 1 establishment. In 2023, total coliforms were found in 11 hotels at 53 different spots, and *E. coli* was detected in the samples taken from the ice machines at 3 facilities. The results concluded that microbiological contamination occurs in drinking and utility water, especially originated from ice machines, in tourism facilities if the required hygiene and sanitation criteria are not provided.

## Antalya’da Bulunan Bazı Otellerdeki İçme ve Kullanma Sularının Mikrobiyal Kalitesi

### Anahtar

### Kelimeler

*E. coli*,  
Toplam koliform,  
Mikrobiyolojik  
su kalitesi,  
Turizm  
işletmeleri,  
Su hijyeni

**Öz:** İçme ve kullanma suyunun mikrobiyal kalitesi halk sağlığı, çevre güvenliği ve genel refah açısından önemlidir. Kirlenmiş su, çok çeşitli hastalıklara neden olabilecek zararlı mikroorganizmaları barındırabilir. Hükümetler içme suyunun mikrobiyolojik kalitesine ilişkin standartlar belirlemiştir ve bu standartları karşılamak için suyun mikrobiyal içeriğinin düzenli olarak test edilmesi ve izlenmesi gerekmektedir. Bu çalışmada, 2022 ve 2023 yıllarında Antalya’daki farklı otellerde yoğun sezonda (Haziran – Temmuz – Ağustos – Eylül) içme ve kullanma suyunun mikrobiyal kalitesi araştırılmıştır. Her yıl için 270 su örneği – 12 farklı otelden toplam 540 örnek toplanmış, membran filtrasyon analizi ile toplam koliform ve *E. coli* analizleri yapıldıktan sonra sonuçlar oksidaz testi ve indol testi kullanılarak doğrulanmıştır. Sonuçlar, 12 otelden yalnızca 1’inin mevzuatın gerektirdiği güvenlik kriterlerini karşıladığını göstermiştir. Diğer 11 otelin tamamında genel mikrobiyal sayımlar yasal limitlerin üzerinde çıkmıştır. 2022 yılında 8 otelde 29 farklı numune noktasında toplam koliform tespit edilirken, sadece 1 işletmede sebze yıkamada kullanılan suda *E. coli* üremesine rastlanmıştır. 2023 yılında 11 otelde 53 farklı noktada toplam koliformlara rastlanırken, 3 tesisdeki buz makinelerinden alınan numunelerde *E. coli* tespit edilmiştir. Sonuç olarak, turizm tesislerinde gerekli hijyen ve sanitasyon kriterlerinin sağlanmaması durumunda, içme ve kullanma sularında özellikle buz makinelerinden kaynaklanan mikrobiyolojik kirlenmelerin meydana geldiği sonucuna varılmıştır.

## 1. INTRODUCTION

Water is a vital resource for humans, but its quality is often compromised by microbial contamination. The microbiological quality of drinking and utility water is a significant public health concern globally, as contaminated water can lead to various waterborne diseases and associated mortality [1, 2]. Vulnerable populations, including the elderly, immunocompromised individuals, and infants, are at higher risk of severe outcomes from waterborne infections.

According to Turkish regulations, drinking and utility water is defined as “water that is generally used for drinking, cooking, cleaning and other domestic purposes; and for the preparation, processing, storage and marketing of foodstuffs and other products intended for human consumption; regardless of its origin, whether in its original or treated form, whether supplied from the spring or from the distribution network; and is not offered for sale for commercial purposes” [3].

Coliforms and fecal coliforms are key indicators used in the monitoring of water quality. Their presence signals potential contamination and the risk of waterborne disease, prompting necessary actions to protect public health. By serving as early warning indicators, these bacteria help ensure that water supplies remain safe for consumption and recreational use. Total coliforms are used as an initial screening tool in water quality testing because they can be easily detected [2, 4]. If total coliforms are detected, further testing is usually conducted to determine the presence of fecal coliforms or other specific pathogens. Fecal coliforms are a subset of the total coliform group, specifically originating from the intestines of warm-blooded animals, including humans [4]. They are more specific indicators of fecal contamination than total coliforms. The most well-known fecal coliform is *Escherichia coli* (*E. coli*), which is used as a primary indicator of fecal pollution. The presence of coliforms, and especially fecal coliforms, in water is a significant public health concern. It indicates the potential for waterborne diseases, such as diarrhea, cholera, typhoid fever, and hepatitis, which are caused by pathogens that may be present in fecal matter [1, 2, 4]. The multiple-tube fermentation (MTF), a.k.a. most probable number (MPN), and membrane filtration (MF) methods are the popular reference methods used for monitoring the quality of drinking water. MTF requires 3 to 4 days while MF provides results just after 24 hours [2, 5].

Membrane filtration analysis is a widely used method for detecting and quantifying microorganisms, particularly bacteria, in drinking and utility water samples. It is commonly used in routine water quality monitoring, particularly for detecting indicator bacteria such as total coliforms and *E. coli*. These bacteria are indicators of fecal contamination and are used to assess the safety of drinking water. This method is based on membrane filtration followed by culture on a chromogenic coliform agar (CCA) medium and counting the number of the colonies of target organisms in the sample [2, 5].

Antalya is one of the biggest and busiest cities in Türkiye, which maintains its vitality in all four seasons and has many tourism facilities. Antalya is the 5th most visited city in the world according to the statistics and has long been a popular beach travel destination [6]. So the city welcomes domestic and international visitors more than ten times its own population throughout summer season, resulting in overcrowded tourism facilities. The objective of this study was to investigate the microbial quality of drinking and utility water in different hotels in Antalya during high season.

## 2. MATERIAL AND METHOD

For this study, drinking and utility water samples were collected from 12 different hotels which were selected from different districts of Antalya. One of the hotels was in Manavgat, 2 were in Side, 3 were in Türkler, 1 was in Avsallar, 3 were in Konaklı, and the remaining 3 hotels were in Alanya. The capacity of the hotels varied between 60 – 490 rooms. The water samples were collected aseptically with the necessary precautions during high season summer months (June – July – August – September), both for 2022 and 2023. Same hotels were included for both years of the study.

### 2.1. Sample Collection

Sterile glass sample containers of 500 ml capacity were used for sampling, and the containers were filled with no air pockets. All water samples were taken and transported carefully, protected from sunlight and avoided any contact to prevent contamination. Each year 270 different samples were collected for the study, and the number of samples to be analyzed from the hotels were determined according to the capacity of the hotels. Samples were delivered to the laboratory within 1 hour after collection and stored at  $4\pm 2^{\circ}\text{C}$ .

### 2.2. Membrane Filtration Analysis

In order to determine the quality of drinking and utility water, all analyses were done according to the current Turkish regulations. TS EN ISO 9308-1:2004 standard method [7] was conducted by using a membrane filtration system (Sartorius T500, Germany). The samples were passed through a membrane filter with a pore size of  $0.45\ \mu\text{m}$  (Membrane Solutions, USA). The membrane filter was then placed on Chromogenic Coliform Agar (CCA) (Biolife, Italy). The filter, along with the medium, is incubated at  $37^{\circ}\text{C}$  for 24 hours. After the incubation period, colonies with a color change (pink to red is marked as coliform, and blue to dark purple is marked as *E. coli*) were counted as positive.

### 2.3. Verification

The colonies marked as coliform were verified by using oxidase test. The oxidase test helps to differentiate between oxidase-negative coliforms and other non-coliform bacteria that might also be present. The colonies were picked from the membrane filter, and transferred on oxidase test strips. A positive result was indicated by a

color change (typically to dark purple or blue) within 20-60 seconds, which were not taken into consideration. Colonies with negative oxidase test results were verified as coliforms.

The colonies marked as *E. coli* were verified by using indole test. The indole test is particularly useful in distinguishing between indole-positive bacteria like *E. coli* and indole-negative bacteria. The colonies were picked and inoculated into a broth containing tryptophan (Biolife, Italy). The inoculated broth was incubated at 37°C for 2 to 7 days, to allow bacteria to produce indole. After incubation, 0.5 ml Kovac's reagent was added to the broth. If indole is present, the reagent reacts with it to produce a red or pink color which floats on top of the broth. A positive indole test was indicated by this red or pink color change, i.e. verifying *E. coli*. A negative indole test resulted in no color change or a yellowish color, indicating that the bacterium did not produce indole.

#### 2.4. Calculation

The number of confirmed colonies counted on the membrane filter was calculated based on the number of *E. coli* and coliform bacteria present in the water samples. Total coliform count was calculated as the sum of all oxidase-negative colonies plus all indole-positive colonies. The number of indole positive colonies was taken into account for the *E. coli* count. These counts were used to estimate the concentration of bacteria in the original water samples, expressed as colony-forming units per 100 milliliters (CFU/100 ml).

### 3. RESULTS AND DISCUSSION

This study was performed to explore the microbiological quality of drinking and utility water in the tourism facilities in Antalya during June – July – August – September of 2022 and 2023. Twelve hotels were inspected, and 270 water samples for each year – 540 water samples in total were collected for microbiological analysis, and total coliform and *E. coli* analyses were performed via membrane filtration method. The results obtained from membrane filtration analysis were verified by using oxidase test for total coliforms and indole test for *E. coli*. The results are summarized in Table 1.

The first two columns in Table 1 show the hotels and the number of samples taken from each hotel. The samples were taken from different spots at each hotel, depending on the size and the capacity of the hotels. Samples were taken from preparation areas in the kitchen, snack bars, pool bars, and ice machines located in different spots. The total coliform and *E. coli* counts given in the other columns are the sum of the results of the water samples per each month obtained from all different spots.

The microbiological quality of drinking and utility water is a critical component of public health. In Türkiye, the legal limits of total coliform count and *E. coli* count for drinking and utility water are 0/100 ml [3]. In other words, no coliforms or *E. coli* are allowed in drinking and utility water.

**Table 1.** *E. coli* and total coliform counts for drinking and utility water samples taken from 12 different hotels

Hotel	Number of samples	Months	2022		2023	
			<i>E. coli</i> (CFU/100 ml)	Total coliform (CFU/100 ml)	<i>E. coli</i> (CFU/100 ml)	Total coliform (CFU/100 ml)
A	18	June	0	60	0	0
		July	0	0	0	60
		August	0	290	0	580
		September	0	280	0	840
B	24	June	0	0	0	280
		July	0	160	0	60
		August	0	0	0	2060
		September	0	0	0	0
C	24	June	0	750	0	0
		July	0	0	0	4300
		August	800	4500	0	1940
		September	0	220	0	0
D	24	June	0	200	0	0
		July	0	0	0	30
		August	0	0	0	390
		September	0	0	0	240
E	24	June	0	0	0	450
		July	0	0	0	1900
		August	0	1100	0	0
		September	0	0	0	1800
F	15	June	0	0	0	0
		July	0	0	0	0
		August	0	0	0	0
		September	0	0	0	0
G	24	June	0	0	0	1890
		July	0	0	0	0
		August	0	0	0	0
		September	0	0	0	40
H	15	June	0	0	0	0
		July	0	0	0	80
		August	0	0	0	0
		September	0	0	0	60
I	24	June	0	140	0	230
		July	0	0	0	900
		August	0	0	0	850
		September	0	610	0	60
K	24	June	0	800	0	0
		July	0	400	10	4070
		August	0	0	0	60
		September	0	0	0	290
L	24	June	0	0	20	150
		July	0	0	0	1400
		August	0	0	0	500
		September	0	0	0	300
M	24	June	0	0	0	350
		July	0	0	0	700
		August	0	280	0	0
		September	0	0	0	450

Table 1 states that only 1 hotel (Hotel F) out of 12 have met the safety criteria required in the legislation. That hotel was a relatively small and new boutique hotel compared to the other facilities. The results for all the other 11 hotels indicated that overall microbial counts for those hotels were over the limits throughout summer season.

In Hotel A, total coliform growth was observed at 6 different spots in June – July – August and September in 2022, while total coliform growth was observed at 10 different spots in 2023. These spots were mainly kitchen (water used for washing vegetables) and several ice

machines at the restaurant, pool, lobby and snack bars. There was no *E. coli* growth observed for both years.

The results for Hotel B showed that there was almost no microbial growth for June and September for both 2022 and 2023. But all the positive counts for the other months came from ice machines located in lobby and beach bars. A total coliform count of 2000 CFU/100 ml of the total count (2060 CFU/100 ml) for August 2023 was from only one ice machine at the beach bar.

Hotel C had the highest total coliform counts among all the hotels. Total coliform growth was detected at 9 different spots for 2022, and at 6 different spots for 2023. These spots were ice machines at the snack bar and lobby bar, and the water used for washing vegetables and preparing breakfast. In August 2022, a total coliform count of 2600 CFU/100 ml and an *E. coli* count of 800 CFU/100 ml was found in the water sample used for washing vegetables, while the rest of total coliform count comes from other sample points such as ice boxes and water sample used in snack bars. All water samples were positive for total coliforms in August 2022, indicating a possible problem with the water system.

The microbial counts for Hotel D were relatively low, and the positive results were mainly from the water samples taken from ice machines and kitchen. There was no *E. coli* growth for both years.

In Hotel E, total coliform growth was observed at 2 different spots in 2022, while total coliform growth was observed at 3 different spots in 2023, but the total coliform counts were really high for each sample spot.

Hotel F was the only hotel that has clean and safe water. No microbial growth was observed for both 2022 and 2023.

Hotel G also had mostly clean water, except June 2023. In June 2023, water samples from kitchen and ice machines at the pool and lobby bars were tested positive for total coliforms.

Hotel H was a relatively small facility compared to others, and there were only 2 spots in 2023 where total coliform counts were above the legal limits. Both of these spots were water dispensers in the lobby and the restaurant.

In Hotel I, total coliform growth was observed at 5 different spots in June – July – August and September in 2022 and in 2023. There was no *E. coli* growth observed for both years. These spots were mainly kitchen and several ice machines at the restaurant, pool, lobby and snack bars.

Hotel K water samples were tested positive for total coliforms at 3 different spots in 2022, and 5 different spots in 2023. There was also *E. coli* growth at one spot in July 2023. The water sample taken from the ice machine at the pool had 10 CFU/100 ml *E. coli* and 4000 CFU/100 ml total coliforms in July 2023.

There was no microbial growth observed for Hotel L in 2022, but in 2023 *E. coli* was found in one sample spot and total coliforms in 4 different spots. 20 CFU/100 ml *E. coli* and 150 CFU/100 ml total coliforms were found in the water used at the pool bar in June 2023. Other sample spots tested positive were the ice machines at the restaurant and the pool bar.

The water samples taken from Hotel M were almost clean in 2022, there was only one sample from the kitchen tested positive for total coliforms. In 2023, total coliform growth was observed at 4 different spots, all spots being ice machines at the pool bars.

The present study investigated the microbiological quality of drinking and utility water in selected tourism facilities in Antalya, and the results showed that the water used in 11 out of 12 hotels was contaminated throughout the high season summer months. The studies in literature investigating the microbial water quality also stated similar results [8 - 10]. A study was conducted to evaluate water quality of several hotels in Brazil. They investigated 15 hotels and 31 water samples, and they concluded that approximately 50% of the water samples were contaminated with total coliforms. The authors suggested that there is a need for stricter control of the quality of the water used, through monitoring the internal water distribution system, adapting and complying with the requirements of the legislation [8]. Çetin et al. [9] studied the microbiological quality of the water used by food production enterprises in Kırklareli, Türkiye. The results showed that 84.3% of 83 samples exceeded the legal limit for total coliform bacteria, 37.3% for total aerobic mesophilic bacteria, 27.7% for psychrophilic bacteria, and 10.8% for *E. coli*. Kireççi et al. [10] conducted a study to determine the microbiological quality of drinking and utility water used in Kars and Sarıkamış military units. As a result, they detected *E. coli* in 30% of 1469 drinking and utility water samples. These findings state the importance of regular monitoring of microbiological water quality.

In 10 of the 12 different hotels, microbial growth was observed at the ice samples taken from different areas of the hotels. World Health Organization (WHO) stated that the water used in the production of ice that will come into contact with food must have the same chemical and microbiological quality as drinking water [11]. Microbial growth observed in ice machines and ice boxes used in hotel bars is mainly caused by inadequate hygiene and sanitation, placing ice shovels outside the shovel container in places that may cause pollution and as a result not ensuring hygiene and sanitation of the shovel container, the staff using ice shovels with dirty hands, and possible cross contamination during the transfer of ice cubes from the machine to the ice boxes. The findings observed in the present study regarding the microbiological risk of ice were in accordance with similar studies conducted in literature [12 - 14]. Gaglio et al. [12] analyzed ice cubes collected from houses, bars and pubs prepared with ice machines and produced in industrial plants, and found that almost all samples had members of the *Enterobacteriaceae* family. Hampikyan et al. [13] collected water and ice samples from 75

restaurants, 20 bars and 10 fish markets located in different regions of Istanbul. They showed that 13 water and 54 ice samples were tested positive for total coliforms, and 7 ice samples exceeded the limits for *E. coli*. Another study performed to determine the microbiological and chemical quality of ice in Georgia, USA, and they found that none of the manufactured ice had unacceptable microbial levels and 37% of the samples contained a high level of coliforms and 1% contained *E. coli* [14].

#### 4. CONCLUSION

In this study, 270 samples were taken in 2022 and total coliform and *E. coli* analyzes were performed. In 2022, total coliform growth was observed in 8 of the hotels in different months and at 29 different spots (10.7%), and *E. coli* growth was observed in the water used for washing vegetables in only 1 hotel (0.3%). In 2023, 270 samples were taken from the same sample spots of the hotels and total coliform and *E. coli* analyzes were performed. In 2023, total coliform growth was detected in 11 of the hotels in different months and at 53 different points (19.6%), and *E. coli* was detected in the ice machines from 2 hotels and in the pool bar drinking water in one other hotel (1.1%). It was revealed that the microbial counts obtained at these samples exceeded the legal limit of 0 CFU/100 ml for total coliform bacteria and *E. coli*. The results concluded that microbiological contamination occurs in drinking and utility water in tourism facilities if the required hygiene and sanitation is not provided. The old plumbing instalments, well water usage, the increase in the high season and the staff not paying enough attention to the hygiene rules were the main reasons for the failure to provide hygiene and sanitation. Another important result of this study is the most contaminated areas in these hotels were ice machines and ice boxes. Ice quality is an often overlooked but crucial aspect of food safety. Ensuring the microbiological safety of ice requires attention to the quality of the water used, the cleanliness of ice machines, proper storage, and handling practices. Regular monitoring and adherence to regulatory standards are essential to prevent the transmission of waterborne diseases and to protect public health.

#### Acknowledgement

The authors would like to thank Alanya Çevre Laboratuvarı for their support.

#### REFERENCES

- [1] Liguori G, Cavallott, I, Arnese A, Amiranda C, Anastasi D, Angelillo IF. Microbiological quality of drinking water from dispensers in Italy. BMC Microbiology 2010; 10: 1-5.
- [2] Tambi A, Brighu U, Gupta AB. Methods for detection and enumeration of coliforms in drinking water: a review. Water Supply 2023; 23(10): 4047-4058.
- [3] İnsani Tüketim Amaçlı Sular Hakkında Yönetmelik, 2005.

- <https://www.mevzuat.gov.tr/mevzuat?MevzuatNo=7510&MevzuatTur=7&MevzuatTertip=5>
- [4] Eden R. Enterobacteriaceae, Coliforms and *E. coli* | Classical and modern methods for detection and enumeration. In: Encyclopedia of Food Microbiology. 2nd ed. Editors: Batt CA, Tortorello ML. London: Academic Press, 2014. pp 667-673.
  - [5] Hannan A, Shan S, Arshad MU. Bacteriological analysis of drinking water from 100 families of Lahore by membrane filtration technique and chromagar. Biomedica 2010; 26: 152-156.
  - [6] Euromonitor International Statistics; 2024 [cited 2024 Jun 28]. Available from: <https://wptravel.io/most-visited-cities-in-the-world/>
  - [7] Türk Standartları Enstitüsü, 2014. Su kalitesi - *Escherichia coli* ve koliform bakterilerin tespiti ve sayımı - Bölüm 1: Düşük bakterili zemin floralı sular için membranla süzme yöntemi (ISO 9308-1:2014).
  - [8] Souza M, Aparecida MN, Mendes ES, Alves L. *Escherichia coli* producer of virulence factors in water used in hotel food service. COINTER PDVAgro 2020 – 5th International Congress of Agricultural Sciences; Brazil 2020.
  - [9] Çetin B, Aloğlu HŞ, Harun U, Karabulut ŞY. Gıda işletmelerinde kullanılan suların gıda güvenliği yönünden incelenmesi. Akademik Gıda 2016; 14(4): 375-381.
  - [10] Kireççi E, Savaşçı M, Uslu H. Kars ve Sarıkamış çevresindeki içme suyu kaynaklarından membran filtrasyon yöntemi ile *Escherichia coli* izolasyonu. Atatürk Üniversitesi Veteriner Bilimleri Dergisi 2006; 1(2): 29-32.
  - [11] World Health Organization, 2018. Developing drinking-water quality regulations and standards: general guidance with a special focus on countries with limited resources. ISBN: 978-92-4-151394-4.
  - [12] Gaglio R, Francesca N, Di Gerlando R, Mahony J, De Martino S, Stucchi C, et al. Enteric bacteria of food ice and their survival in alcoholic beverages and soft drinks. Food Microbiology 2017; 67: 17-22.
  - [13] Hampikyan H, Bingol EB, Cetin O, Colak, H. Microbiological quality of ice and ice machines used in food establishments. Journal of Water and Health 2017; 15(3): 410-417.
  - [14] Mako SL, Harrison MA, Sharma V, Kong F. Microbiological quality of packaged ice from various sources in Georgia. Journal of Food Protection 2014; 77(9), 1546-1553.